RUSSIAN ACADEMY OF SCIENCES
INSTITUTE FOR PROBLEMS IN MECHANICAL ENGINEERING
PETER THE GREAT ST. PETERSBURG POLYTECHNIC UNIVERSITY

Proceedings of the XLVI Summer School – Conference

ADVANCED PROBLEMS IN MECHANICS

A P M 2 0 1 8

St. Petersburg

http://apm-conf.spb.ru

St. Petersburg, 2018

Scientific Committee and Editorial Board

Preface

Dear Reader,

in this book you will find the Proceedings of the Summer School – Conference "Advanced Problems in Mechanics (APM) 2018". The conference had been started in 1971. The first Summer School was organized by Prof. Ya.G. Panovko and his colleagues. In the early years the main focus of the School was on nonlinear oscillations of mechanical systems with a finite number of degrees of freedom. Since 1994 the Institute for Problems in Mechanical Engineering of the Russian Academy of Sciences organizes the Summer School. The traditional name of "Summer School" has been kept, but the topics covered by the School have been much widened, and the School has been transformed into an international conference. Now it is held under the patronage of the Russian Academy of Sciences. The topics of the conference cover now almost all fields of mechanics, being concentrated around the following main scientific directions:

— aerospace mechanics;
— computational mechanics;
— dynamics of rigid bodies and multibody dynamics;
— fluid and gas;
— mechanical and civil engineering applications;
— mechanics of media with microstructure;
— mechanics of granular media;
— nanomechanics;
— nonlinear dynamics, chaos and vibration;
— molecular and particle dynamics;
— phase transitions;
— solids and structures;
— wave motion.

The Summer School – Conference has two main purposes: to gather specialists from different branches of mechanics to provide a platform for cross-fertilization of ideas, and to give the young scientists a possibility to learn from their colleagues and to present their work. Thus the Scientific Committee encouraged the participation of young researchers, and did its best to gather at the conference leading scientists belonging to various scientific schools of the world.

We believe that the significance of Mechanics as of fundamental and applied science should much increase in the eyes of the world scientific community, and we hope that APM conference makes its contribution into this process.

The Conference is organized by Institute for Problems in Mechanical Engineering of Russian Academy of Sciences (IPME RAS) and Peter the Great St.Petersburg Polytechnic University (SPbPU) under the patronage of Russian Academy of Sciences (RAS), St.Petersburg Scientific Center, Ministry of Education and Science of Russian Federation (project indentificator RFMEFI 60715X0120) and the University of Seville (Universidad de Sevilla). APM 2018 is partially supported by Russian Foundation for Basic Research. Minisymposium in memoriam of Antonio Castellanos Mata is partially sponsored by the Vicerrectorado de Investigacion de la Universidad de Sevilla (Vice-Rectorate for Research, University of Seville, Spain).

We hope that you will find the materials of the conference interesting, and we cordially invite you to participate in the coming APM conferences. You may find the information on the future "Advanced Problems in Mechanics" Schools – Conferences at our website:

`http://apm-conf.spb.ru`

With kind regards,

Co-Chairmen of APM 2018

Dmitri A. Indeitsev, Anton M. Krivtsov

Contents

On axial movement and transverse vibrations of layered thin-walled membrane-plate structures and the problems of stability

Nikolay V. Banichuk, Svetlana Yu. Ivanova, Evgeniy V. Makeev
banichuk@gmail.com

Abstract

This study concentrated on stability analysis and optimization of thermoelastic web travelling between two rollers. It is presented a model for a layered travelling web (continuous layered panel composed from isotropic materials) restricting the consideration on one open draw. The web is mechanically simply supported at the inflow and outflow ends of the span with the rest boundaries of the span unsupported. The considered part of the layered web is effectively isotropic, homogeneous and occupies the domain having a rectangular shape in plan. The web is symmetrically composed with respect to a middle plane and it is consisted of thermoelastic layers characterized by some important parameters (mass per unit area, Young modulus, Poisson ratio and distances from the middle plane). The movement of layered membrane-plate structure with constant axial velocity is considered [1]. Various mechanical and temperature actions and characteristic properties of the moving media are taken into account [2], [8]. Transverse vibrations arising in the process of axial movement are supposed to be small. The loss of stability of thin-walled thermoelastic plate-like moving structures is studied in the static form (divergence) and the stability domain is determined in the space of basic considered parameters.

1 Introduction

In this paper we present mechanical models for a homogeneous (continuous, isotropic) and for a layered (effectively isotropic and homogeneous) travelling webs, restricting the consideration to one open draw. The webs are mechanically simply. supported at the inflow ($x = 0$) and outflow ($x = l$) ends of the span. The webs are travelling at a constant velocity V_0 in the x-direction of the rectangular global coordinate system xz and are loaded by axial tension T_0 and thermal loads. The length l and the total thickness H are supposed to be given, while $0 < x < l$ and $-H/2 < z < H/2$. For given problem parameters we study stability problems and derive the expressions for critical temperature and critical web velocity. As a result we find safety domain of stability.

2 Homogeneous thermoelastic web

Free transverse vibrations of homogeneous web axially moving with constant velocity and loaded by axial tension and heated by some temperature are described by the following equation for transverse displacement w and simply supported boundary conditions

$$m\left(\frac{\partial^2 w}{\partial t^2}+2V_0\frac{\partial^2 w}{\partial x\partial t}+V_0^2\frac{\partial^2 w}{\partial x^2}\right)=\left(T-\frac{EH}{1-\nu}\varepsilon_\theta\right)\frac{\partial^2 w}{\partial x^2}-D\frac{\partial^4 w}{\partial x^4}, \tag{1}$$

$$(w)_{x=0}=0,\quad \left(\frac{\partial^2 w}{\partial x^2}\right)_{x=0}=0,\quad (w)_{x=l}=0,\quad \left(\frac{\partial^2 w}{\partial x^2}\right)_{x=l}=0, \tag{2}$$

where m, E, ν, D are, respectively, the mass per unit area, Young's modular, Poisson ratio, bending rigidity ($D=EH^3/12(1-\nu^2)$) and the deformation ε_θ is defined as

$$\varepsilon_\theta=\alpha_\theta\theta,\quad \theta=\theta_a-\theta_0. \tag{3}$$

Here α_θ is the linear expansion coefficient, θ is the temperature discrepancy, θ_0 is the temperature of zero deformation, θ_a is the actual temperature.
In the stationary case, when

$$\frac{\partial w}{\partial t}=\frac{\partial^2 w}{\partial t^2}=0, \tag{4}$$

the transverse displacement $w=w(x)$ satisfies the equation

$$\frac{d^4 w}{dx^4}+\lambda\frac{d^2 w}{dx^2}=0, \tag{5}$$

where parameter λ (eigenvalue) is given by the expression

$$\lambda=\frac{1}{D}\left(mV_0^2+\frac{EH}{1-\nu}\alpha_\theta\theta-T_0\right)\equiv f\left(V_0^2,\theta\right). \tag{6}$$

If we introduce new unknown variable $\psi(x)$ as

$$\psi(x)=\frac{d^2 w}{dx^2},\quad 0\le x\le l, \tag{7}$$

we obtain the following spectral problem

$$\frac{d^2\psi}{dx^2}+\lambda\psi=0, \tag{8}$$

$$\psi(0)=0,\quad \psi(l)=0. \tag{9}$$

Here the value λ plays the role of an eigenvalue. Nontrivial solution of the formulated eigenvalue problem can be represented as

$$\psi(x)=C_1\sin\left(\sqrt{\lambda}x\right)+C_2\cos\left(\sqrt{\lambda}x\right) \tag{10}$$

with two arbitrary coefficients C_1, C_2 and unknown value λ. Taking into account (9), (10) we will have $C_2 = 0$ and

$$\lambda = \left(\frac{j\pi}{l}\right)^2, \quad j = 1, 2, ..., \tag{11}$$

$$\psi(x) = C_1 sin\left(\frac{j\pi x}{l}\right) \tag{12}$$

with arbitrary constant C_1.
Thus, for given problem parameters D, E, ν, H, l, T_0, m, V_0, α_θ we obtain the critical temperature θ^{div} of instability (divergence or buckling)

$$\theta^{div} = \frac{1-\nu}{EH\alpha_\theta}\left[D\left(\frac{\pi}{l}\right)^2 + T_0 - mV_0^2\right] \tag{13}$$

and

$$\lambda_{min} = \left(\frac{\pi}{l}\right)^2 \tag{14}$$

corresponding the minimal $j = 1$ in (11). Analogously we find the critical instability velocity (squared) $(V_0^2)^{div}$ as

$$\left(V_0^2\right)^{div} = \frac{1}{m}\left[D\left(\frac{\pi}{l}\right)^2 + T_0 - mV_0^2\right], \tag{15}$$

where D, E, ν, H, l, T_0, m, θ, α_θ are considered as a given positive parameters.
Safety domain for stability in the values (θ, V_0^2) is defined by the inequality

$$f\left(V_0^2, \theta\right) < \lambda_{min} = \left(\frac{\pi}{l}\right)^2 \tag{16}$$

that is reduced to the condition

$$F\left(V_0^2, \theta\right) \equiv \frac{1}{D}\left(\frac{l}{\pi}\right)^2 f\left(V_0^2, \theta\right) = C_V V_0^2 + C_\theta \theta - C_0 < 0, \tag{17}$$

where

$$C_V = \frac{m}{D}\left(\frac{l}{\pi}\right)^2, \quad C_\theta = \frac{EH\alpha_\theta}{D(1-\nu)}\left(\frac{l}{\pi}\right)^2, \quad C_0 = \frac{T_0}{D}\left(\frac{l}{\pi}\right)^2 + 1.$$

Safety domain of the values V_0^2, θ has a triangular shape OAB shown in Fig. 1

3 Layered thermoelastic web

Consider the layered web that is symmetrically composed with respect to a middle plane (Fig. 2) and consisted of $2n+1$ (odd number) thermoelastic layers characterized by mass per unit area m_i, Young's modulus E_i, Poisson's ratio ν_i, coefficient

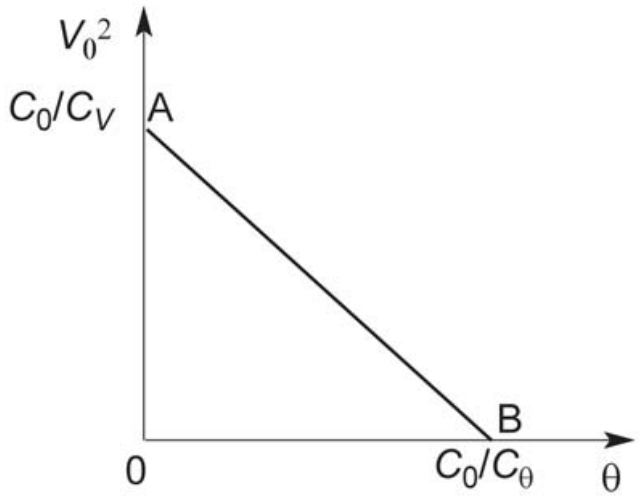

Figure 1: Safety domain OAB

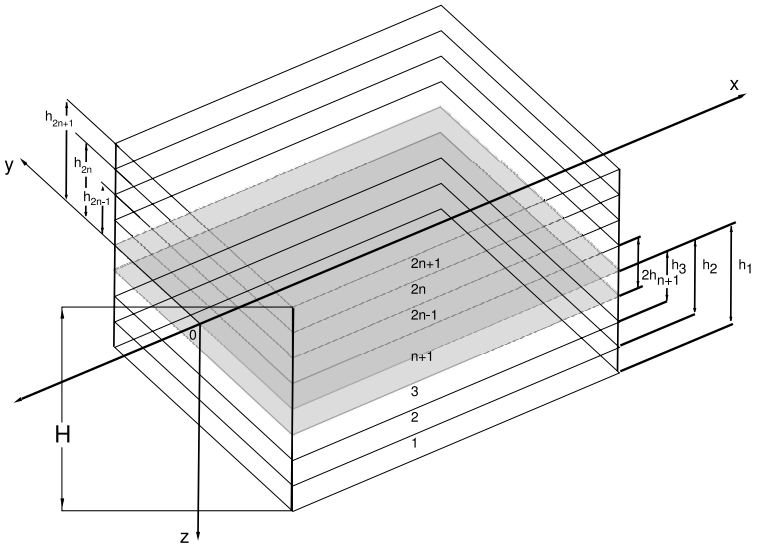

Figure 2: Layered web

$(\alpha_\theta)_i$, and distances h_i from the middle plane. We will take into account the symmetry of internal web structure, i.e.

$$E(z) = E(-z), \quad \nu(z) = \nu(-z), \quad \alpha_\theta(z) = \alpha_\theta(-z) \tag{18}$$

and derive the expressions for effective moduli D^{ef}, ν^{ef}, ε_θ^{ef} and m^{ef}. To this end we apply the formulas for stresses and strains and the expression for bending moment

$$\int_{-H/2}^{H/2} \sigma_x z dz = \left[2 \int_0^{H/2} \frac{z^2 E(z) dz}{1 - (\nu(z))^2} \right] \frac{d^2 w}{dx^2} = D^{ef} \frac{d^2 w}{dx^2}. \tag{19}$$

Thus we find the expression for effective bending rigidity in the form

$$D^{ef} = 2\int_0^{H/2} \frac{z^2 E(z)dz}{1-(\nu(z))^2}. \tag{20}$$

Using mechanical and geometric characteristics of the web layers E_i, ν_i, h_i we evaluate the integral in (20). We will have the following formula

$$D^{ef} = \frac{2}{3}\frac{E_{n+1}}{1-\nu_{n=1}^2}h_{n+1}^3 + \frac{2}{3}\sum_{i=1}^{n}\frac{E_i}{1-\nu_i^2}\left(h_i^3 - h_{i+1}^3\right). \tag{21}$$

In analogous manner we derive the formulas for effective Poisson's ratio ν^{ef} and for effective thermal deformation ε_θ^{ef} of nonhomogeneous isotropic layered web. We have

$$\nu^{ef} = \frac{2}{D^{ef}}\int_0^{H/2}\frac{z^2\nu(z)E(z)}{1-(\nu(z))^2}dz = \frac{2}{3D^{ef}}\left[\frac{\nu_{n+1}E_{n+1}h_{n+1}^3}{1-\nu_{n+1}^2} + \sum_{i=1}^{n}\frac{E_i\nu_i}{1-\nu_i^2}\left(h_i^3 - h_{i+1}^3\right)\right], \tag{22}$$

$$\varepsilon_\theta^{ef} = \frac{2}{H}\int_0^{H/2}\alpha_\theta(z)\theta dz = \frac{2}{H}\left[(\alpha_\theta)_{n+1}\theta_{n+1}h_{n+1} + \sum_{i=1}^{n}(\alpha_\theta)_i\theta_i(h_i - h_{i+1})\right], \tag{23}$$

if $\theta_1 = \theta_2 = ... = \theta_{n+1} = \theta$ then

$$\varepsilon_\theta^{ef} = \frac{2\theta}{H}\left[(\alpha_\theta)_{n+1}h_{n+1} + \sum_{i=1}^{n}(\alpha_\theta)_i(h_i - h_{i+1})\right], \tag{24}$$

$$m^{ef} = m_{n+1} + 2\sum_{i=1}^{n} m_i. \tag{25}$$

If we define

$$a = \frac{EH}{1-\nu}\varepsilon_\theta, \quad a = a(z) = \frac{E(z)H}{1-\nu(z)}\varepsilon_\theta(z) = \frac{HE(z)}{1-\nu(z)}\alpha_\theta(z)\theta(z),$$

then

$$a^{ef} = 2\int_0^{H/2}\frac{E(z)\alpha_\theta(z)\theta(z)}{1-\nu(z)}dz = 2\left[\frac{(\alpha_\theta)_{n+1}E_{n+1}\theta_{n+1}}{1-\nu_{n+1}}h_{n+1} + \sum_{i=1}^{n}\frac{(\alpha_\theta)_iE_i\theta_i}{1-\nu_i}(h_i - h_{i+1})\right]. \tag{26}$$

If the temperature of each layer are the same, then

$$a^{ef} = 2\theta\left[\frac{(\alpha_\theta)_{n+1}E_{n+1}h_{n+1}}{1-\nu_{n+1}} + \sum_{i=1}^{n}\frac{(\alpha_\theta)_iE_i(h_i - h_{i+1})}{1-\nu_i}\right]. \tag{27}$$

In this case the domain for stability in the values (θ, V_0^2) is defined analogy (17)

$$F\left(V_0^2,\theta\right) \equiv \frac{1}{D^{ef}}\left(\frac{l}{\pi}\right)^2 f\left(V_0^2,\theta\right) = C_V^{ef}V_0^2 + C_\theta^{ef}\theta - C_0^{ef} < 0,$$

where

$$C_V^{ef} = \frac{m^{ef}}{D}\left(\frac{l}{\pi}\right)^2, \quad C_0^{ef} = \frac{T_0}{D^{ef}}\left(\frac{l}{\pi}\right)^2 + 1.$$

$$C_\theta^{ef} = \frac{2}{D^{ef}}\left(\frac{l}{\pi}\right)^2 \left[\frac{(\alpha_\theta)_{n+1}E_{n+1}h_{n+1}}{1-\nu_{n+1}} + \sum_{i=1}^{n}\frac{(\alpha_\theta)_i E_i(h_i - h_{i+1})}{1-\nu_i}\right].$$

Acknowledgements

The study was performed in Ishlinsky Institute for Problems in Mechanics RAS and supported by the Russian Science Foundation (project 17-19-01247).

References

[1] Nikolay Banichuk, Juha Jeronen, Pekka Neittaanmaki, Tytti Saksa, Tero Tuovinen. Mechanics of Moving Materials. 2014. Springer International Publishing Switzerland.

[2] Kovalenko, A.D. Thermoelasticity. 1975. Kiev: Vishcha Shkola. 216p. (in Russian).

[3] Timoshenko, S.P., Woinowsky-Kriger, S. Theory of plates and shells, 2nd edn. 1959. New York: Tokyo: McGraw-Hill.

Nikolay V. Banichuk, 119526, Ishlinsky Institute for Problems in Mechanics RAS, Prospekt Vernadskogo, 101, bld.1, Moscow, Russia
Svetlana Yu. Ivanova, 119528, Ishlinsky Institute for Problems in Mechanics RAS, Prospekt Vernadskogo, 101, bld.1, Moscow, Russia
Evgeniy V. Makeev, Ishlinsky Institute for Problems in Mechanics RAS, Prospekt Vernadskogo, 101, bld.1, Moscow, Russia
[1] Nikolay Banichuk, Juha Jeronen, Pekka Neittaanmaki, Tytti Saksa, Tero Tuovinen. Mechanics of Moving Materials. Springer International Publishing Switzerland. 2014. 253p. [2] Timoshenko, S.P., Woinowsky-Kriger, S. Theory of plates and shells, 2nd edn. New York: Tokyo: McGraw-Hill. 1959. 595p. [3] Kovalenko, A.D. Thermoelasticity. Kiev: Vishcha Shkola.1975. 216p. (in Russian).

Mechanical characterization of polymer-based composite materials at micro- and nanoscale using AFM

Eduard S. Batyrshin, Yuriy S. Zamula, Svyatoslav S. Chugunov, Ivan V. Sergeichev, Iskander S. Akhatov
batyrshine@mail.ru

Abstract

The mechanical characterization of fiber-reinforced polymer composites at micro- and nanoscale is an essential experimental approach for the development of multi-scale mechanical representation of macroscopic composite parts. The study of elastic moduli variation within fiber and matrix phases, as well as properties of the fiber-matrix interface, is of particular importance. In this paper, we present the results of studying of the mechanical properties of fiber-reinforced polymer composite materials, using atomic force microscopy (AFM) based force modulation technique. The force modulation AFM operates in a contact mode with the tested material surface. It uses low frequency excitation of the probe, exploiting the fact that the amplitude of excited probe oscillation is sensitive to the elasticity of the sample surface. As the result of composite material characterization with AFM technique, the surface elastic moduli was quantitatively mapped. We additionally studied the effect of AFM operating parameters and probe characteristics on the resulting maps.

1 Introduction

Fiber reinforced polymer composite materials are the key components in modern technological applications. Due to their low specific gravity, high mechanical strength and resistance to external impacts, they are being applied in aeronautics, automotive industry, energy applicaitons, and other industrial fields. Predicting behaviour of a part, made of composite material, under the action of a complex mechanical load is an important task. Despite the considerable progress achieved to the date in general understanding of deformation processes in composite materials, exact mechanisms affecting composite behavior at microscale have not been thoroughly studied yet. Destruction of the composite material, under the action of mechanical loads, is a complex multi-stage process [1] that involves destruction of the polymer matrix, fibers and matrix-fiber interface. Such multiphase nature of composite failure, indicates the importance of studying the mechanical properties of

composites at micro- and nanoscale, which corresponds to the typical spatial scale of fibers and the interface between the fibers and the matrix.
AFM based techniques provide solid advantage in studying mechanical properties of polymer composites at micro- and nanoscale. In particular, AFM implements a few variants of nanoindentation technique, which is direct and easy to interpret method for determining local elastic properties of the studied material. The well developed models of AFM tip contact mechanics help in estimation of effective Young modulus of the sample in the contact region of AFM tip and sample surface. For instance, sequential nanoindentation with AFM allows construction of 2D maps of elastic moduli over a selected region of interest. Despite the relative simplicity of the method, the construction of a two-dimensional map of the mechanical properties of the surface takes considerable time when traditional nanoindentation technique is utilized. AFM based force modulation methods of material characterization are more efficient than the traditional technique; additionally, they provide better spatial resolution [2, 3]. During the use of AFM force modulation mode, the scanning probe remains in permanent contact with the surface of the sample. The force that presses the tip of AFM probe to sample's surface has two components: the first component is represented with a small constant loading force which presses probe's tip into sample's surface for only a few nanometers, so that interaction between the probe and the material remains elastic; the second component is represented with harmonic osciallations (tens to hundreds of kHz) imposed on the constant loading force. As a result of the scaning procedure, the surface topography, the amplitude and the phase of the probe oscillations are recorded. These properties are correlated to mechanical properties of the studied material at the next steps of the analysis.

2 Experimental details

The samples of a glass fiber/epoxy unidirectional composite material were used in this work. The fiber glass roving contained approximately 800 elementary filaments with an average diameter of $10\mu m$ each. A bundle of roving threads was tightly packed into a polyurethane tube and impregnated with a compound, consisting of epoxy resin ED-20 and TETA hardener, taken at 10:1 mass ratio. The sample was polymerized at room temperature for 24 hours and heated in an oven for 4 hours at 60°C. The cured sample was fragmented by circular diamond saw in a direction perpendicular to the fibers. The obtained cylindrical samples, 3 mm high and 4 mm in diameter, were glued onto a 1.5cm$\times$1.5cm glass substrate with a hot melt adhesive. The samples were polished with sandpaper with a gradual decrease of grit size from 500 to 7000 grit. The grinding direction was altered by 90° after every change of grit. After the grinding, the sample surface was additionally polished with a suspension containing colloidal nano-silica particles, approximately 30 nm in size. Surface quality was controlled with an optical microscope. After polishing, the samples were cleaned in an ultrasonic bath for 5 minutes, washed with deionized water and dried at 60°C for 1 hour. Scanning of the samples was carried out on an atomic force microscope Agilent 5500AFM (Agilent, USA) using the force modulation mode (FMM). Three cantilevers with different force constants were used. The characteristics of the cantilevers are provided in Table 1. All tested AFM probe cantilevers

had diamond coated tips with radius R=100nm (according to manufacturers).

Table 1: Characteristics of AFM probes

#No.	Probe	Manufacturer	Force constant, N/m
1	HA_HR_DCP-B	NT-MDT, Russia	17
2	HA_HR_DCP-A	NT-MDT, Russia	34
3	HA_HR_DCP-A	TipsNano, Estonia	85

3 Results and discussions

The modulation of the force on AFM probe is performed with a piezo element (Fig.1a). The oscillations are transmitted to AFM probe through the probe holder, probe substrate, cantilever beam, and other components of AFM system. A signal proportional to the deflection of the cantilever $D(t)$ is recorded (Fig.1b) during AFM scanning. The tip deforms the surface of the sample and partially penetrates into it, to a depth of $\delta(t)$. If the tip deformation is neglected, the probe position, the cantilever deflection, and the indentation depth are interrelated $z(t) = D(t) + \delta(t)$. The AFM keeps constant drive of the piezo element during the scan, so that the alternating amplitude of the $z(t)$ is also constant. As a result, for stiffer sample areas, where the deformation of the material is relatively low, the FM amplitude $D(t)$ increases, and for softer areas of the surface the FM amplitude decreases. A 2D map of the oscillation amplitude of the cantilever implicitly characterizes the stiffness of the material over the entire scaned area.

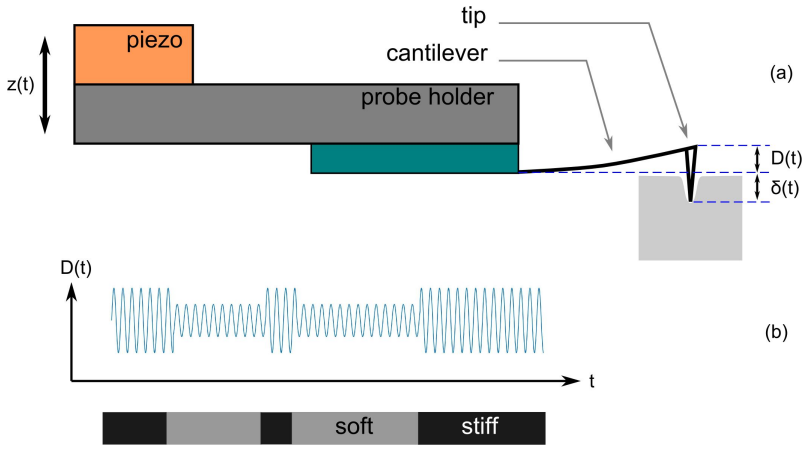

Figure 1: Schematics of force modulation mode (FMM) of AFM (a) and a typical profile of the signal obtained during FMM scanning (b)

It should be noted that, in addition to the contact of AFM probe and sample surface, AFM system contains a number of other mechanical contacts (AFM probe to probe holder, etc.) that affect the response of the system. To minimize this effect, the scanning frequency is selected far from the resonant peaks of the system; in this study, it was set at 60kHz, 85kHz and 20kHz for cantilevers #1, #2 and #3,

respectively. The amplitude of the piezo element oscillation is determined by the amplitude of the voltage U_{piezo}., applied to the piezo element. With each cantilever, the sample surface was scanned at $U_{piezo} = 1$, 2 and 4 V_{pp}.
Typical results of material characterization with AFM are shown in Fig.2. On the image of topography (Fig.2a) there can be clearly seen some scratches, which result from mechanical polishing of sample surface, and defects of epoxy matrix (dark areas), which, apparently, are the voids formed during fabrication of the sample. The fiber surface, although not everywhere, is located somewhat higher than the surface of the polymer matrix - by tens of nanometers (Fig.2b) - which is also a result of mechanical polishing of sample surface. During polishing operations, softer materials, such as epoxy, are removed in excess to harder materials, such as glass fibers. The height difference between the highest and the lowest point at the studied sample surface, not accounting for voids, is less than 100 nm.

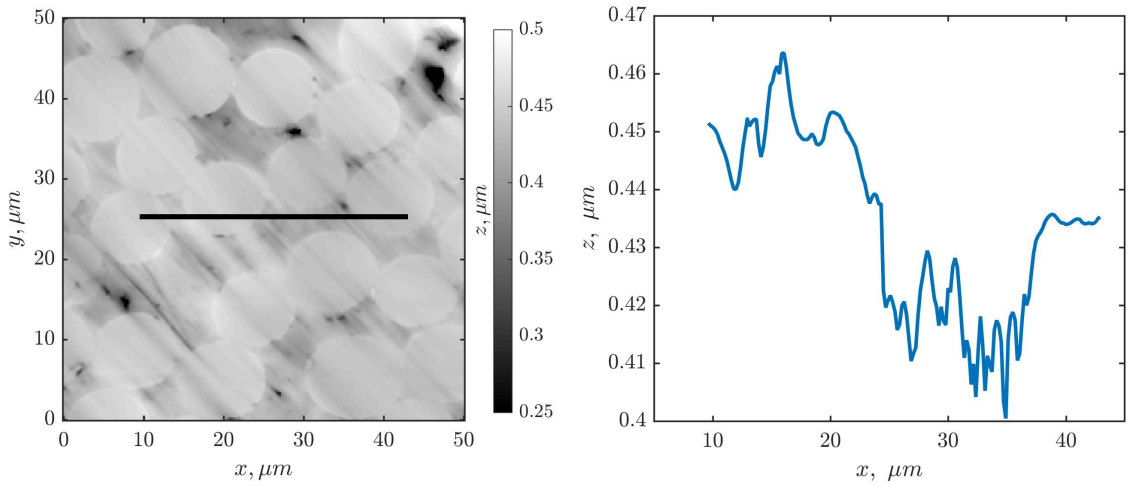

(a) (b)

Figure 2: AFM image of the surface topography (a) and a surface profile along a dark line (b) (probe #2, $U_{piezo} = 2$ V_{pp})

The two-dimensional map of the amplitude of the cantilever oscillations (Fig.3a) shows correlation between stiffness of the surface and FM amplitude level - on glass fibers, that are stiffer than the epoxy matrix, FM amplitude increases. The histogram of the FM amplitude values (Fig.3b), collected over the scanned area, clearly demonstrates two narrow peaks corresponding to the fibers and the matrix. The analysis of FM amplitude and FM phase maps results in quantitative estimates of viscoelastic parameters of the sample [4, 5].
The elasticity map is constructed from FM amplitude values, using a technique based on results of [6, 7]. The main assumption is based on the fact that the typical values of YoungвЂ™s modulus for epoxy resins (several GPa) are significantly smaller than those for glass fibers (70 GPa). Hence, the deformation of the glass fibers during contact with the AFM tip can be neglected. In this case, an analytical expression that relates the stiffness of the tip-matrix contact to the values of FM amplitude of glass fibers and epoxy matrix can be obtained:

$$k_m = \frac{k_c}{< A_f > /A_m - 1}, \tag{1}$$

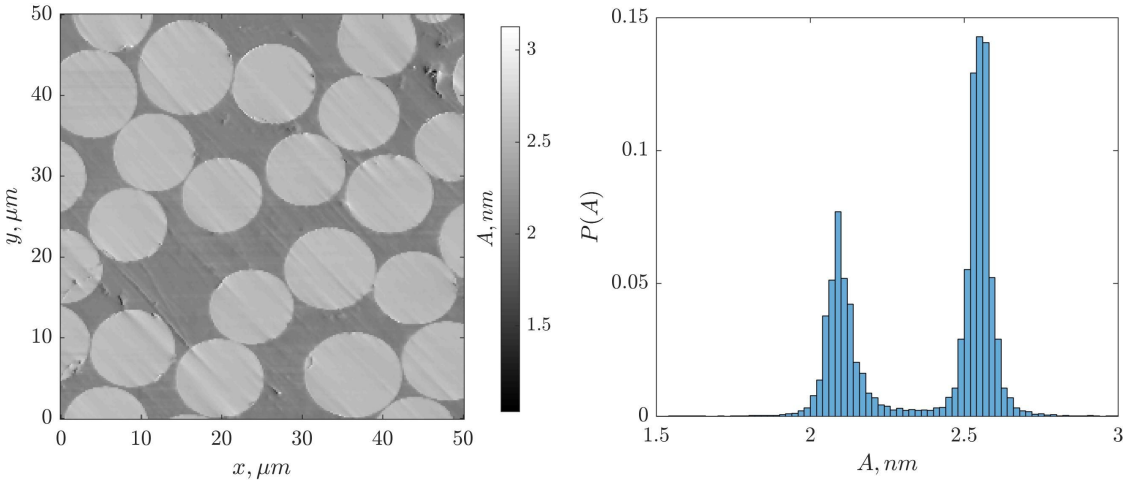

(a) (b)

Figure 3: A 2D map of the FM Amplitude (a) and a histogram of FM Amplitude values collected from map (b) (probe #2, $U_{piezo} = 2\ V_{pp}$)

here $< A_f >$ is the average FM amplitude over the fibers surface, A_m is the FM amplitude over the polymer matrix. Alternatively, the contact stiffness can be calculated in the framework of the Hertz contact mechanics [6, 8], with the correction for adhesion force, that provides the following relation:

$$k_m = 6^{1/3} E^{*2/3} R^{1/3} (F_0 + F_{ad})^{1/3}, \tag{2}$$

where R is the tip radius, F_0 is the constant component of the indentation force (set point), F_ad is the adhesion force, E^* is the reduced Young's modulus of the epoxy matrix, which can be expressed as $E^* = E_m/(1-\nu_m^2)$ if the tip deformation is negligible. E_m and ν_m are the Young's modulus and the Poisson's ratio of the matrix. The constant force F_0 is a predefined scanning parameter, and F_{ad} was determined from the standard AFM force-distance curves. The values of the tip radius used for calculations is R=100nm. The relations (1) and (2) are employed to calculate the elasticity modulus of the epoxy matrix of the samples.
Elasticity map is obtained using AFM probes characterized with different force constants; there are three different driving voltages used for piezo element $U_{piezo} = 1V_{pp}$, $2V_{pp}$ and $4V_{pp}$. Figure 4a shows the map of the effective modulus of elasticity of the epoxy matrix. Due to the assumption of abscence of fiber deformation, the fiber part remain uncomputed in the map. The histogram of the modulus of elasticity (Fig.4b) shows the average value of $E^* \approx 5$GPa which is typical for epoxy resins [9]. Considering influence of piezo element driving voltage and cantilever stiffness on the estimation of elastic modulus (Fig.5), the estimates obtained for probes #1 and #2 provide quite high values. There may be several reasons for this, including variations of the true radius of AFM tip, degradation of the tip during the scan, irregularity of amplitude-frequency response of the measuring mechanical system (Fig.1), which contains a lot of peaks of resonant frequencies. Under such circumstances, selecting a scanning frequency far from the resonant peaks of the system does not guarantee a constant amplitude of the probe during the scan. Thus, quantitative estimates of the elastic moduli should be done with care. The estimates of elastic moduli,

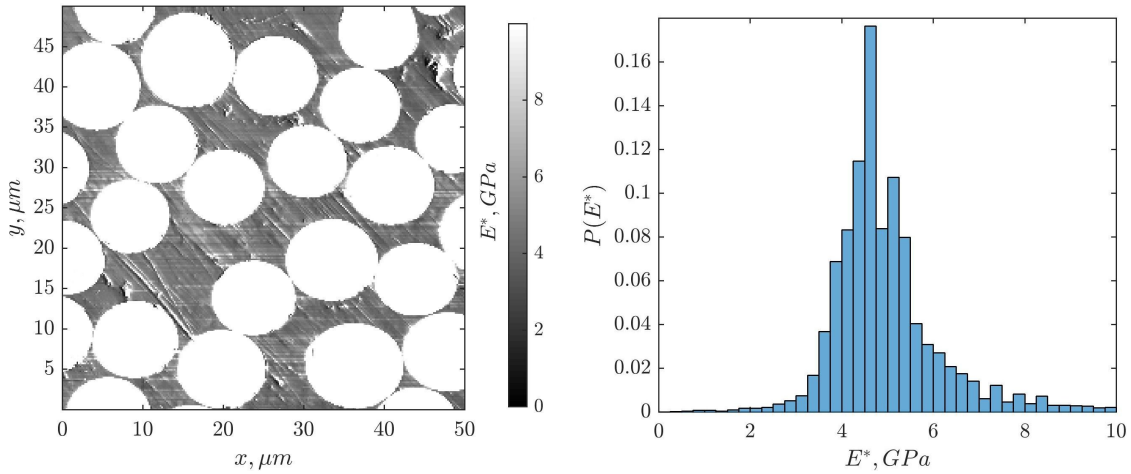

Figure 4: Map of the effective modulus of elasticity of the epoxy matrix (a) and the histogram of these data(b) (probe #2, $U_{piezo} = 2\ V_{pp}$)

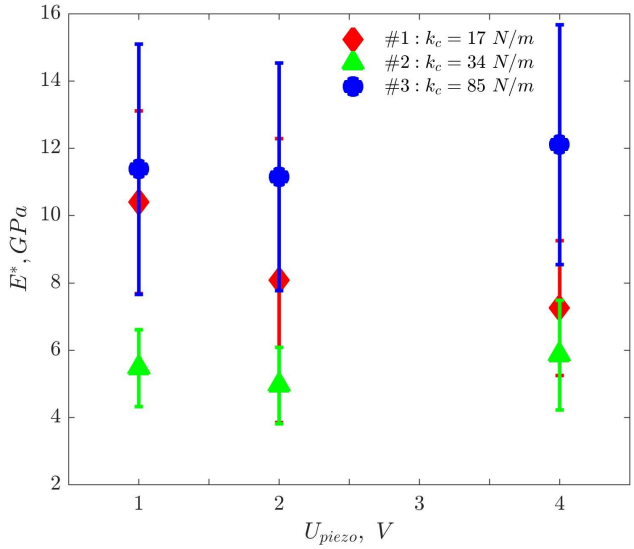

Figure 5: Effective Young's modulus of the epoxy matrix estimations obtained using various AFM probes and piezo driving voltage

obtained with stiffer probes #2 and #3, remain unchanged when the driving voltage of piezo element, U_{piezo}, changes. In the case of softer probe #1, the estimation of E^* decreases with increase of modulation amplitude. The use of stiffer cantilevers increases stability of the obtained results.

Despite the described difficulties, the AFM force modulation technique can be very efficient in the study of relative changes in surface elasticity, in characterizing the degree of polymer matrix spatial homogeneity, in detecting the change of elasticity under the action of external forces, and in studies of the properties of the fiber-matrix interface.

4 Conclusions

The application of AFM in the force modulation mode for characterizing mechanical properties of materials at micro and nano scales is demonstrated. The AFM offers several scanning modes for evaluating elastic moduli of a material. The force modulation approach seems to be better suitable for studying elastic moduli of the material, than traditional nanoindentation approaches. The use of AFM probes with a stiffer cantilever beam increases stability of the obtained signal and eads to overally better results. The applied method of AFM-based nanoindentation allows 2D mapping of surface elasticity, even in the case of multicomponent materials, where mechanical properties of components differ by orders of magnitude. This method, owing to the high accuracy (up to nanometers) of AFM probe positioning and to the high contrast of the resulting image, is an excellent tool for investigating mechanical characteristics of thin elements of the material, including sample matrix and reinforcing fibers.

Acknowledgements

This work was supported by Skoltech Partnership Program

References

[1] Talreja R., Assessment of the fundamentals of failure theories for composite materials // Compos. Sci. Technol. Elsevier Ltd, 2014. Vol. 105. P. 190вЃ“201.

[2] Kulik A.J. et al. Nanoscale Mechanical Properties вЃ“ Measuring Techniques and Applications // Nanotribology and Nanomechanics / ed. Bharat Bhushan. Springer-Verlag Berlin Heidelberg, 2005.

[3] Klapetek P. Force and Mechanical Properties // Quantitative Data Processing in Scanning Probe Microscopy. Elsevier, 2013. P. 127вЃ“172.

[4] Yang N. et al. Frequency-dependent viscoelasticity measurement by atomic force microscopy // Measurement Science and Technology. 2009. Vol. 20, No. 2.

[5] Zlotnikov I. et al. Nano-scale modulus mapping of biological composite materials: theory and practice // Progress in Materials Science. 2017. Vol. 87. P. 292вЃ“320

[6] Maivald P. et al. Using force modulation to image surface elasticities with the atomic force microscope // Nanotechnology. 1991. Vol. 2, No. 2. P. 103вЃ“106.

[7] Xu X. et al. Dynamics of surface-coupled microcantilevers in force modulation atomic force microscopy - magnetic vs. dither piezo excitation // Journal of Applied Physics. 2012. Vol. 111, No. 5.

[8] Bhushan B. Nanotribology and nanomechanics. Berlin/Heidelberg : Springer-Verlag, 2005. ISBN 3-540-24267-8.

[9] Lapitskiy V.A., Kritsuk A.A. Fiziko-mekhanicheskie svoystva epoksidnyh polimerov i stekloplastikov, Kiev/Naukova dumka, 1986

Eduard S. Batyrshin, Bashkir State University, Zaki Validi Street 32, 450076 Ufa, Russia
Yuriy S. Zamula, Bashkir State University, Zaki Validi Street 32, 450076 Ufa, Russia
Svyatoslav S. Chugunov, Skolkovo Institute of Science and Technology, Nobel Street 3, 143026 Moscow, Russia
Ivan V. Sergeichev, Skolkovo Institute of Science and Technology, Nobel Street 3, 143026 Moscow, Russia
Iskander S. Akhatov, Skolkovo Institute of Science and Technology, Nobel Street 3, 143026 Moscow, Russia

Modern advances in mechanics of materials with hydrogen

Alexander K. Belyaev, Ksenia P. Frolova, Anatoliy M. Polyanskiy, Vladimir A. Polyanskiy, Yuriy A. Yakovlev
vapol@mail.ru

Abstract

Accumulation of hydrogen inside metals leads to hydrogen embrittlement. Examination of the hydrogen influence on the mechanical properties of materials, as well as explanation of the mechanisms of its transport, especially diffusion, is one of the most actual problems in mechanics of materials. Within the framework of this paper we review existing models of hydrogen diffusion and describe the phenomenon of localization of plastic deformations. According to the retrospective of the models development, the most well-known and universally recognized mathematical description of hydrogen transport is based on the elementary diffusion equation and a number of equations for the chemical reactions of hydrogen trap filling. Moreover, the main experimental method for studying the hydrogen motion in a solid generally does not take into account diffusion. Another important fact is that most of the existing results have been obtained by studying specimens charged with hydrogen. According to our analysis this approach can not be used for investigation of the hydrogen influence on the mechanical properties of materials. In this regard we developed the model of multichannel diffusion of hydrogen. On the basis of this model, we also developed an experimental-calculation method for measuring the binding energies of hydrogen. In this study we also observe modern approaches for modeling of localization of plastic deformation, considering it as a process of loss of stability of motion. We underline that all problems of localization of plastic deformation intersect with the problems of formation of local areas of hydrogen embrittlement. The dynamic instability caused by hydrogen is associated with its diffusion. One can conclude that it is necessary to consider dynamic unstable processes when solving problems of mechanics of materials. Finally, it is necessary to take into account the spatial inhomogeneity of both plastic deformations and the distribution of hydrogen when calculating the strength.

1 Introduction

Modern problems in mechanics are closely related to the special properties of materials due to technology development. Exploitation of most of the metal structural

components is realized with minimal stock factor and under stress levels equal or even exceeding the yield stress. The mass fraction of special high-strength steels in the modern car body is 70 %. Highly alloyed high-strength steels are the only ones that are used in construction of pipelines. Forged titanium is widely used in aviation. Details of modern building constructions are connected by high-strength hardware instead of rivets. Nowadays superhigh-strength steels and nanostructured materials with tensile strength three to four times higher than that of common ones are developed and used.
Elastic modules are fundamental values underlines the binding energy in a metal matrix. Metals with extreme properties are generally obtained by changing the internal structure. It means that the yield line of the original matrix is used to increase strength. In this case, the maximum plastic deformations substantially decrease down to zero in some nanocrystalline metals.
Under these conditions, the influence of relatively small imperfections and local defects becomes determinative. One of these factors is dissolved hydrogen. Unlike other components of alloys, it has a large diffuse mobility and can enter the metal from the external medium, both directly in the gaseous state, and due to various corrosive processes. Therefore, one can say that in nature there are no metals completely hydrogen free.

2 Mechanics of materials containing hydrogen

The significant effect of dissolved hydrogen on the metal properties was first discovered by M.Fremy in 1861 in his investigation of the effect of gases on the steels properties. He studied the meteorite iron specimens and found that steel can be obtained from these specimens only if hydrogen is removed. Since then, any new technology for the metals production and production of many other materials is faced with the problem of the destructive effect of hydrogen at an increasingly low level of its concentrations in the solid material.
At the beginning of the 20th century, one had to contend with the Kruppovaya disease, or in other words, discontinuities of rolled metal due to the mass production of rolled steel. The relative mass concentrations of hydrogen that cause these deviations are of the order of $4 \cdot 10^{-6}$ in steels. Later, the problem of the brittleness of aluminum alloys wasappeared. The corresponding level of hydrogen concentrations was of the order of $4 \cdot 10^{-7}$. "Hydrogen problems" appeared in the production of titanium, zirconium, heat-resistant nickel alloys.
There is a vast amount of reference devoted to the examination and investigation of “hydrogen problems”. The number of scientific publications related to the investigation of hydrogen influence on the materials structure and properties represents between 20 and 30 thousand over the last 150 years.
Nowadays elimination of the negative effect of hydrogen on strength, plasticity, cold-brittle strength, fatigue strength, impact strength and other physical and mechanical properties of materials can be considered as one of the main research direction for mechanics.
The accumulation of hydrogen inside metals always leads to hydrogen embrittlement. Hydrogen transport occurs mainly due to its diffusion in a solid. Therefore, both

explanation of the hydrogen influence on the mechanical properties of materials, and explanation of the mechanisms of its transport are important in terms of mechanics.

Initially, the process of hydrogen transport in a solid was considered as a diffusion process described by the Fick equation with a diffusion coefficient depending on temperature according to the Arrhenius law. The parameter of this law is the diffusion activation energy. Moreover, in 1930s Gorsky established that the deformation of the material matrix changes its concentration gradient and thus can lead to diffusion induced by mechanical stresses.

Experimental studies have shown that the application of the Fick equation for the data approximation leads to a huge scatter in the values of the diffusion coefficients and the activation energy for the same materials. Danken and Smith [7] explained this variation by the fact that there is a threshold value of the concentration depending on the method and temperature regime of the sample treatment when hydrogen saturation of metals. Therefore, they introduced the concept of bound hydrogen and distributed in the material hydrogen traps in the explanation of hydrogen transport in a solid. Traps were understood as boundaries of multicrystalline grains, foreign inclusions, internal defects (dislocations, microcrack vacancies, etc.) [22, 36, 37]. As the "traps theory" for description of the hydrogen transport developed, more and more complex mathematical models were used, from McNabb and Foster [28] to the Oriani model [30]. At hte same time, the equation of the hydrogen diffusion did not change, only additional equations for filling and emptying the distributed hydrogen traps were introduced. In case of presence of a large number of parameters, such as concentration, diffusion activation energy, the capacity of traps, different activation energies for the collection and desorption of hydrogen from traps, they can be selected to approximate almost any experimental result. Generalization of all models and a comparison of the experimental results with the results of mathematical modeling are carried out in [16, 19]. In [19], in addition to the values вГЌвГЌof activation energies and diffusion constants, different activation energies of hydrogen capture and release fro, traps were introduced.

The Oriani model is supported by an experimental technique for measuring the binding energies of hydrogen, which is called the "thermal desorption spectra (TDS) method". The justification of this method was given 60 years ago by Kissinger [20]. According to this paper, the energy state changing and the hydrogen diffusion process in a solid are described as first-order chemical reactions. Therefore, diffusion is considered as a fast process in relation to the process of hydrogen releasing from the traps. In this regard, the experimental procedure for interpreting the obtained experimental data neglects the diffusion equations in the transport model. Hydrogen diffusion was taken into account in one paper [32], but in the framework of the Oriani model [30].

Thus, the most well-known and universally recognized mathematical description of hydrogen transport is based on the most elementary diffusion equation and the set of equations of chemical reactions of trap filling. The main experimental method for examination the hydrogen movement in a solid generally does not take into account diffusion. It leads to the fact that in the fundamental physical handbook [14] it is written that the values of the hydrogen diffusion coefficient and its activation energy, which are given in the tables of the handbook, are the result of averaging of

numerous experimental data and are fair "at best, only for magnitude order".

This situation can be explained by the great importance of the hydrogen problem. According to the long history of the technology development, all scientific research in this area has been repeatedly checked up experimentally. Therefore, despite the great importance of specific data, significant technological failures has been avoided due to large-scale tests.

Several basic approaches for the modeling of the influence of hydrogen on the strength of materials can be identified, such as taking into account the influence of hydrogen on the nucleation and motion of dislocations, taking into account the influence of hydrogen on the development of cracks, taking into account the internal pressure of hydrogen in the metal and, finally, "physical approaches", based on taking into account the potential energy of hydrogen-material matrix interaction.

The motion and formation of dislocations and their effect on local plasticity near the peaks of cracks lead to local plasticity because of the very high concentration of dislocations. The mechanism of hydrogenenhanced local plasticity (HELP) was first described by Birnbaum H.K., Sofronis P. [6]. The constitutive equations for the material taking into account local changes in material properties at the mouth of the microcrack were proposed later in [40] and [9, 10]. These equations were obtained on the basis of physical considerations on the interaction potentials between hydrogen and dislocations.

At the same time, according to calculations performed by the authors of the model presented in [40], significant changes in mechanical properties in HELP occur at local relative mass concentrations of hydrogen of the order of 10^{-2}. For most metals it is an unattainable high concentration. Steels, as well as more aluminum alloys, crack themselves up to complete destruction without any external load even at much lower concentrations.

Calculation of local plasticity in the framework of the theoretical examination of a crack with a spherical tip shows that the local hydrogen concentrations at the tip of the crack are only 100 times higher than the average ones [42]. Given that the average values are usually about 10^{-6}, the local concentrations do not exceed 10^{-4}. Thus, the verification calculation does not confirm that local accumulation of hydrogen necessary for triggering physical mechanisms of local plasticity is possible under the influence of external mechanical loads.

There are still many uncertainties surrounding the model noticed by the authors. In particular, there is a nonlinear dependence of the internal potential on the stresses magnitude and hydrogen concentration. Since huge local concentrations many times greater than observed in practice are considered, all nonlinearities are of significant importance.

It was noted in [17] that the HELP model requires enormous computational resources in solving any applied problem, therefore, the only way out is to use the continuum model of dislocation development, however, this replacement is often inadequate and the authors propose to use the growth criterion for submicrocrack, ie, reduce all hydrogen problems to Modeling the development of a crack with a manually adjustable reduction in fracture toughness.

In [17] it was noted that the HELP model requires enormous computational resources in solving any applied problem. Therefore, the only way out is to use the continuum

model of dislocation development. However, this replacement is often inadequate and as a result authors propose to use the growth criterion for submicrocrack, i.e., to reduce all hydrogen problems to modeling the development of a crack with a manually adjustable crack resistance reduction.
The hydrogenenhanced decohesion model (HEDE) is similar to HELP [43]. The difference is that HEDE takes into account the decrease in the formation energies of free fracture surfaces with increasing local hydrogen concentration.
It should be noted that the HELP and HEDE models have become generally recognized in state-of-art science. Explicit discrepancies, including mentioned above discrepancies with experimental data, are ignored. The latest scientific discussions are reduced to using these models simultaneously to describe the same material [11, 12]. This is very difficult to realize because of the computational complexity. Therefore, only quasistatic problems considering uniaxial stretching of cylindrical samples are solved.
Standard modeling of the hydrogen-induced cracks development, taking into account the reduction in crack resistance, is also a common approach. At the same time, the model does not relate to real physical mechanisms of hydrogen influence. In addition, it turns out that the consideration of the same model within the framework of problems with different scales yields significantly different results [1, 2].
The stress tensor changing based on the internal pressure created by hydrogen penetrating into the crystal structure of metal also does not allow to examine the effect of low hydrogen concentrations. Within the framework of this approach, the visible effect of hydrogen is detected only at average concentrations above 10^{-5} [15], which are about ten times greater than the real threshold for steels.
Molecular dynamics is also used to model hydrogen embrittlement [41, 44]. Nevertheless, it allows to describe only micromechanisms at the apex of a microcrack or dislocation because of the smallness of the modeled ensembles. The same disadvantage is possessed by the quantum mechanical approach [8, 39]. It can be used only to describe the behavior of cracks in ideal crystals or to model the behavior of individual microcracks and dislocations because of the large heterogeneity of real metals.

3 New approaches to description of hydrogen destruction

It is necessary to underline one more discrepancy of modern approaches to hydrogen research. Almost all results and models were obtained by investigation of specimens charged with hydrogen. Initially, the saturation was carried out in gaseous hydrogen under pressure. Nowadays, 99% of the results are obtained by hydrogen saturation in salts solutions or in an electrolyte under the action of an electrical potential.
We detected experimentally the skin effect when saturating the metal samples with hydrogen in a solution of salts according to the NACE Standard TM0284-2003. After saturation of the samples, hydrogen is concentrated in a thin surface layer less than 50 μm thick. Our results in combination with the latest data from other studies devoted to the uneven distribution of hydrogen concentrations during cathodic

hydrogenation [26, 45] actually put an end to the technology of charging samples with hydrogen to study the effect of hydrogen on the properties of metals.
Developed by us model of multichannel diffusion of hydrogen has been verified by using various materials. It is also confirmed by the experiments of other scientists. We suppose this model to be promising for describing the transport of small concentrations of hydrogen in a solid. On the basis of this model, we constructed an experimental-calculation method for measuring the binding energies of hydrogen.
We have established that the limitations of the quasistatic approaches, as well as the methods of separation of motions, do not allow us to obtain certain predictive results in the case of complex systems involving several contacting details, which is important for practical applications [5]. Also, it is not possible to describe the process of loss of stability of deformation, which is characteristic for hydrogen embrittlement of steels, when zones of local hydrogen saturation and associated zones of local plastic deformations are formed.
This problem is especially important in terms of the fact that zones of plastic deformations localization are sources for the microcracks initiation, their formation triggers the destruction process.

4 Localization of plastic deformations

The inhomogeneity of the plastic deformation of metals and the "stress dropping" accompanying its formation in case of uniform deformation are the main manifestations of the Portevin-Le Chatelier effect [35]. Later detailed studies of plastic deformation fields made it possible to establish that during plastic deformation, plastic deformation bands are formed. The characteristic distance between these bands depends, in particular, on the grain size [46].
A lot of references are devoted to the explanation and modeling of the Portevin-Le Chatelier effect, see the review [38]. The main mechanism is the motion or even “jumping” of dislocations inside the metal during plastic deformation and their interaction with vacancies, foreign inclusions and other structural imperfections that contribute to the unstable motion of dislocations and the formation of plastic deformation bands. Moreover, the effect itself is often used for testing various models of displacement of dislocations and their interaction with the metal structure [46].
This dislocation approach has a significant drawback. The mechanical characteristics calculated on the base of this approach highly depend on the dislocation density on the grain surface (for example, see [31]). This value can not be directly measured. Simulation of the behavior of a large number of dislocations requires the specification of the generalized energy characteristics of this ensemble, which requires the building of additional physical microparameters. The presence of a large number of parameters in the material characteristics makes it possible to approximate any experimental dependences and ensure fully correspondence between results of the dislocation modeling and the experimental data [46]. It is difficult and sometimes impossible to measure these parameters even in case of complete destruction of the test specimen (for example, in case of beam irradiation in an electron microscope). In other words, the dislocation model does not allow us to obtaine a quantitative prediction without preliminary adjusting of the parameters based on the the results

of testing the material with the same initial dislocation density.
These problems led to the emergence of generalized models of the localization of plastic deformation, considering it as a process of loss of stability of motion. In this regard, deformation with a small constant velocity is considered. Elements cause instability of solutions are introduced into the equations of a continuum.
There are three main approaches:

1. Determination of the dependence of the speed of change of stresses on the speed of change of deformations, which has a site with a negative slope, see for example [21, 34].

2. Introduction of non-linear dependencies based on simulation of the diffusion of vacancies and associated dislocations and non-linear constitutive equations of the material in the equations of continuum, for example [18, 27].

3. Description of the dislocations formation as a random process developing in time, transition to stochastic dynamic equations of continuum[23]. In this case, the nonuniformity of the deformation process is described as stochastic instability.

Thus, the loss of stability of a uniform uniaxial deformation of material is modeled either by direct violation of the energy conservation law (by specifying an unstable part of its characteristic or by instability in a stochastic system describing the behavior of dislocations) or by complicating the continuum model by introducing moment stresses, grains rotations and plastic shears, or by means of a bifurcation point arising from the introduction of additional nonlinear relations in the constitutive equations [24]. These nonlinear relationships are often obtained from consideration of the processes of nucleation and migration of dislocations. The process of localization of plastic deformations is considered as dynamic and wave process.
These assumptions contradict some experimental data and the initial statement of the problem, as underlined by the authors of the models described above. For example, in [3], the interaction of dislocations with structural inhomogeneities is considered as the main physical mechanism for localization of plastic deformation. In [46] an experimental dependence of the geometric characteristics of local bands on grain sizes was obtained.
One way or another, the authors of all the above-mentioned articles agree that the original natural heterogeneity of the material can play an essential role in the occurrence of localization of plastic deformation.
At the same time, except for [4], in all the papers known to us such an inhomogeneity is taken into account binary. For example, in [13] it is given as a soft metal model containing more rigid grains of another metal. In [25], the inhomogeneity is given as a separate deformation model for grain boundaries.
An important manifestation of the effect of localization of plastic deformation is the formation of a system of intersecting bands on the surface of a material such as a “chessboard”. For the first time this term was proposed by V.E. Panin in [33]. According to his research, the effect of the “chess” distribution of normal and tangential stresses on interfaces was experimentally discovered and theoretically

confirmed. Also conclusion about the important role of the observed effect in various phenomena of nature was made.
An alternative explanation for the formation of the "chess" surface character is given in Morozov [29]. The authors considered the compression of different elastic bodies. Within the framework of a geometrically linear formulation, both isotropic elastic bodies in a two-dimensional formulation (plates, plates on an elastic base) and transversely isotropic elastic half-spaces and layers were investigated. It was shown that exceeding of the critical value of the compressive load lead to yield of material from the loading plane. In this case, wave formation occurs in the material, which leads to the appearance of a regular structure on the surface, which also resembles the "chessboard".

5 Localization of plastic deformations and hydrogen embrittlement as a single problem of modern mechanics of solids

All problems of localization of plastic deformation intersect with the problems of formation of local zones of hydrogen embrittlement. They are a manifestation of the dynamic instability of the material. The only difference is that the dynamic instability caused by hydrogen is associated with its diffusion, whereas in the case of plastic flow it is associated with the migration of dislocations. That is, additional degrees of freedom, which can give energy for the development of instability, appear. It is difficult to model an unstable process related to localization, since all approximate approaches have an approximation error that increases in time and can not be estimated from above.
Many continuum material makes it possible to describe the emerging instability as a structural transition. Nevertheless, recent data indicate failure of a homogeneous material model, since localization of plastic deformations leads to volumetric heterogeneity of mechanical properties. The surface effect, both in redistribution of hydrogen concentrations and in plasticity, leads to talk about new approaches to modeling the behavior of materials outside the elastic region.
These new approaches shall take into account the redistribution of diffusely mobile components and the special role of the solid surface during plastic deformation and material destruction.

6 Conclusion

Accounting of dynamic unstable processes in the framework of solution of mechanics problems is necessary due to the logic of research development and the problems of state-of-art technology. The main problem is that the accuracy of any approximations falls with time, since the error is also an unstable process.
When calculating the strength, it is necessary to take into account the spatial inhomogeneity of both plastic deformations and the distribution of hydrogen, since they directly affect the mechanical properties of materials.

Plastic waves are accompanied by the transfer of diffusely mobile hydrogen. The presence of a boundary surface layer makes the influence of the boundary conditions on these processes not essential.
Under these circumstances, it is natural to use the wave approximation when studying the processes of redistribution of natural small hydrogen concentrations in structural materials under the influence of external loads, taking into account the mutual influence of hydrogen diffusion, hydrogen accumulation in critical areas, heterogeneity of plastic deformations and changes in the mechanical properties of the material associated with the accumulation of hydrogen.

Acknowledgements

This work was supported by the Russian Foundation for Basic Research (projects Nos. 18-08-00201, 17-08-00783 and 18-31-00329 mol-a).

References

[1] Alvaro A., Olden V., Akselsen O.M. 3D cohesive modelling of hydrogen embrittlement in the heat affected zone of an X70 pipeline steel // International Journal of Hydrogen Energy, 38(18), 2013, pp. 7539–7549

[2] Alvaro A., Olden V., Akselsen O.M. 3D cohesive modelling of hydrogen embrittlement in the heat affected zone of an X70 pipeline steel // Part II. Int. J. of Hydrogen Energy, 39(7), 2014, pp. 3528–3541

[3] Ananthakrishna G. Current theoretical approaches to collective behavior of dislocations // Physics Reports, 2007, 440(4), pp 113–259

[4] Balokhonov R.R., Stefanov Yu.P., P.V. Makarov P.V., Smolin I.Yu. Deformation and fracture of surface-hardened materials at meso- and macroscale levels // Theoretical and Applied Fracture Mechanics, 33, 2000, pp. 9–15

[5] Belyaev A.K., Polyanskiy V.A., Yakovlev Y.A. Hydrogen as an indicator of high-cycle fatigue // Procedia IUTAM, 13, 2015, pp. 138–143

[6] Birnbaum H.K., Sofronis P. Hydrogen-enhanced localized plasticity – a mechanism for hydrogen-related fracture // Mat. Sci. and Eng.: A. 176(1-2) 1994, pp. 191–202

[7] Darken L.S., Smith R.P. Behavior of Hydrogen in Steel During and After Immersion in Acid // Corrosion, 5(1), 1949, pp. 1–16

[8] Daw M.S., Baskes M.I. Semiempirical quantum mechanical calculation of hydrogen embrittlement in metals // Phys. Rev. Lett. 50(17), 1983, pp. 1285–1288

[9] Delafosse D., Magnin T. Hydrogen induced plasticity in stress corrosion cracking of engineering systems // Eng. Fract. Mech., 68(6), 2001, pp. 693–729

[10] Delafosse D., Magnin T. Interfaces in stress corrosion cracking: a case study in duplex stainless steels // Solid State Phenomena, 59-60, 1998, pp. 221–250

[11] Djukic M.B., Bakic G.M., Zeravcic V.S., Sedmak A., Rajicic B. Hydrogen Embrittlement of Industrial Components: Prediction, Prevention, and Models // Corrosion, 72(7), 2016, pp. 943–961

[12] Djukic M.B., Zeravcic V.S., Bakic G.M., Sedmak A., Rajicic B. Hydrogen damage of steels: A case study and hydrogen embrittlement model, Engineering Failure Analysis, 58, 2015, pp. 485–498

[13] Gaskell J., Dunne F., Farrugia D., Lin J. A multiscale crystal plasticity analysis of deformation in a two-phase steel // Journal of Multiscale Modelling, 1(1), 2009, pp. 1–19

[14] Grigorev I.S. Physical quantities (in Russian). Handbook, M.: Energoatomizdat, 1991, p. 1232

[15] Hu Z., Fukuyama S., Yokogawa K., Okamoto S. Hydrogen embrittlement of a single crystal of iron on a nanometer scale at a crack tip by molecular dynamics // Modelling and Simulation in Materials Science and Engineering, 7(4), 1999, pp. 541–551

[16] Hurley C., Martin F., Marchetti L., Chene J., Blanc C., Andrieu E. Numerical modeling of thermal desorption mass spectroscopy (TDS) for the study of hydrogen diffusion and trapping interactions in metals // International Journal of Hydrogen Energy, 40(8), 2015, pp. 3402–3414

[17] Ignatenko A.V., Pokhodnya I.K., Paltsevich A.P., Sinyuk V.S. Dislocation model of hydrogen-enhanced localizing of plasticity in metals with BCC lattice // The Paton Weld J., 3, 2012, pp. 15–19

[18] Kalk A., Nortmann A., Schwink C. Dynamic strain ageing and the boundaries of stable plastic deformation in Cu-Mn single crystals // Philosophical Magazine A., 72(5), 1995, pp. 1239–1259

[19] Kirchheim R. Hydrogen solubility and diffusivity in defective and amorphous metals // Progress in Materials Science, 32(4), 1988, pp. 261–325

[20] Kissinger H.E. Reaction Kinetics in Differential Thermal Analysis // Analytical Chemistry, 29(11), 1957, pp. 1702–1706

[21] Lebyodkin M. et al. Statistical behaviour and strain localization patterns in the Portevin-Le Chatelier effect // Acta materialia, 1996, 44(11), pp. 4531–4541)

[22] Lecoester F., Chene J., Noel D. Hydrogen embrittlement of the Ni-base Alloy 600 correlated with hydrogen transport by dislocations // Materials Science and Engineering: A, 262(1–2), 1999, pp. 173–183

[23] Leoni F., Zapperi S. Dislocation mutual interactions mediated by mobile impurities and the conditions for plastic instabilities // Physical Review E, 2014, 89(2), p. 022403

[24] Madej L., Hodgson P.D., Pietrzyk M. Development of the Multi-scale Analysis Model to Simulate Strain Localization Occurring During Material Processing // Arch. Comput. Methods Eng., 2009, 16, pp. 287–318

[25] Makarov P.V., Romanova V.A., Balokhonov R.R. Numerical modeling of heterogeneous plastic deformation with consideration for generation of localized plastic shears at interfaces and free surfaces // Physical Mesomechanics, 4(5), 2001, pp. 29–38

[26] Martinsson Å, Sandström R. Hydrogen depth profile in phosphorus-doped, oxygen-free copper after cathodic charging // Journal of Materials Science, 47(19), 2012, pp. 6768–6776

[27] McCormigk P.G. A model for the Portevin-Le Chatelier effect in substitutional alloys // Acta Metallurgica, 1972, 20(3), pp. 351–354

[28] McNabb A., Foster, P.K. A new analysis of the diffusion of hydrogen in iron and ferritic steels // Trans. Aime, 227, 1963, pp. 618–627

[29] Morozov N.F., Tovstik P.E. On Chessboard of buckling modes in compressed materials // Acta Mechanica, 223(8), 2012, pp. 1769–1776

[30] Oriani R.A. The diffusion and trapping of hydrogen in steel // Acta Metallurgica, 18(1), 1970, pp. 147–157

[31] Ovid'ko I.A., Skiba N.V. Enhanced dislocation emission from grain boundaries in nanocrystalline materials // Scripta Mater., 2012, 67(1), pp. 13–16

[32] Padhy G.K., Ramasubbu V., Murugesan N., et all. Determination of apparent diffusivity of hydrogen in 9Cr-1MoVNbN steel using hot extraction-PEMHS technique // International Journal of Hydrogen Energy, 38(25), 2013, pp. 10683–10693

[33] Panin V.E., Panin A.V., Moiseenko D.D. "Chess" meso-effect of the interface in heterogeneous media in fields of external influences (in Russian) // Fiz. mezomeh., 2006, 9(6), pp. 5–15

[34] Penning P. Mathematics of the Portevin-Le Chatelier effect // Acta Metallurgica, 1972, 20(10), pp. 1169–1175

[35] Portevin A., Le Chatelier F. Sur un phinomune observi lors de l'essai de traction d'alliages en cours de transformation // Comptes Rendus de l'Acadimie des Sciences Paris., 1923, 176, pp.507–510

[36] Pressouyre, G.M. A classification of hydrogen traps in steel // Metallurgical Transactions A, 10(10), 1979, pp. 1571–1573

[37] Pressouyre, G.M. Hydrogen traps, repellers, and obstacles in steel; Consequences on hydrogen diffusion, solubility, and embrittlement // Metallurgical Transactions A, 14(10), 1983, pp. 2189–2193

[38] Rizzi E., Hähner P. On the Portevin–Le Chatelier effect: theoretical modeling and numerical results // International Journal of Plasticity, 2004, 20(1), pp. 121–165

[39] Serebrinsky S., Carter E.A., Ortiz M. A quantum-mechanically informed continuum model of hydrogen embrittlement // Journal of the Mechanics and Physics of Solids., 52(10), 2004, pp. 2403 –2430

[40] Sofronis P., Liang Y., Aravas N. Hydrogen induced shear localization of the plastic flow in metals and alloys // European J. of Mech. A. Solids, 20(6), 2001, pp. 857–872

[41] Song J., Curtin W.A. A nanoscale mechanism of hydrogen embrittlement in metals // Acta Materialia, 59(4), 2011, pp. 1557–1569

[42] Taha A., Sofronis P. A micromechanics approach to the study of hydrogen transport and embrittlement // Eng. Fract. Mech, 68(6), 2001, pp. 803–837

[43] Varias A.G., Massih A.R. Simulation of hydrogen embrittlement in zirconium alloys under stress and temperature gradients // J. of Nuclear Mat., 279(2-3), 2000, pp. 273–285

[44] Wen M., Xu X.-J., Omura Y., et al. Modeling of hydrogen embrittlement in single crystal Ni // Computational Materials Science, 30(3-4), 2004, pp. 202–211

[45] Wu R. , Ahlström J., Magnusson H., Frisk K., Martinsson A. Charging, degassing and distribution of hydrogen in cast iron // Swerea KIMAB, Swedish Nuclear Fuel and Waste Management Co., 2015, pp. 1–41

[46] Zuev L.B., Semuhin B.S., Zarikovskaya N.V. Dependence of the wavelength of localized deformation on the grain size when tensile aluminum samples (in Russian) // Prikladnaya mehanika i tehnicheskaya fizika, 43(2), 2002, pp. 166–169

Alexander K. Belyaev, Institute of Problems of Mechanical Engineering RAS, V.O., Bolshoj pr., 61 St. Petersburg, Russia
Ksenia P. Frolova, Institute of Problems of Mechanical Engineering RAS, V.O., Bolshoj pr., 61 St. Petersburg, Russia
Anatoliy M. Polyanskiy, RDC Electron & Beam Technology Ltd., Bronevaya, 6, St. Petersburg, Russia
Vladimir A. Polyanskiy, Institute of Problems of Mechanical Engineering RAS, V.O., Bolshoj pr., 61 St. Petersburg, Russia
Yuriy A. Yakovlev, Institute of Problems of Mechanical Engineering RAS, V.O., Bolshoj pr., 61 St. Petersburg, Russia

Solution of nonlinear non-autonomous Klein-Fock-Gordon equation

A.N. Bulygin, Yu.V. Pavlov
bulygin_an@mail.ru

Abstract

This paper presents methods of obtaining of functionally-invariant solutions $U(x, y, z, t)$ of nonautonomous nonlinear Klein-Fock-Gordon equation. Solutions $U(x, y, z, t)$ are obtained in the form of an arbitrary function which depends on one $\tau(x, y, z, t)$ or two $\alpha(x, y, z, t)$, $\beta(x, y, z, t)$ specially constructed functions. These functions are called ansatzes. Ansatzes (τ, α, β) are defined as solutions of separate equations (algebraic or mixed forms — algebraic and partial differential equations). Equations defining ansatzes contain arbitrary functions depending on (τ, α, β). Proposed methods allow to find $U(x, y, z, t)$ for the special class of nonautonomous nonlinear Klein-Fock-Gordon equations. General methods of solution are illustrated by examples of finding particular exact analytical solutions of nonautonomous Liouville equation.

1 Introduction

Nonlinear Klein-Fock-Gordon equation (NKFG)

$$U_{xx} + U_{yy} + U_{zz} - \frac{U_{tt}}{v^2} = F(U), \tag{1}$$

where $F(U)$ is an arbitrary nonlinear function U and lower symbolic index denotes partial derivative by the corresponding variable, plays a fundamental role in the modern natural sciences.
Equations (1) for particular forms of function $F(U)$ are well known in the mathematical physics. Eq. (1) with $F(U) = \exp U$ first came in the theory of surfaces with constant negative curvature. It was solved by Liouville [1]. Eq. (1) with $F(U)$ which equals to the sum of exponents describes oscillations of chain of nonlinear pendulums [2], and with $F(U)$ in the form of truncated series by functions $\sinh nU$, $\cosh nU$ $(n = 1, 2, \ldots)$ modells orientational structure of ferromagnetic media in the magnec field [3]. Many papers in mathematics, applied and theoretical physics are devoted to the analysis of nonlinear equations [4] including the equation (1) with $F(U)$ in the form of truncated Fourier series (sine-Gordon, double sine-Gordon etc.) and truncated Taylor series (Ginzburg-Landau equation). Outlined equations describe various physical phenomena and model numerous technological procecces [5].

Though it is necessary to idealize both physical phenomena and technological procecces making assumptions about uniformity of media and fields of external actions. Various physical phenomena and technological procecces are described by nonautonomous nonlinear Klein-Fock-Gordon equation

$$U_{xx} + U_{yy} + U_{zz} - \frac{U_{tt}}{v^2} = p(x, y, z, t)\, F(U). \tag{2}$$

Here $p(x, y, z, t)$ is some function.
Analytical methods of solving equation (2) are practically absent in the literature. This paper presents an approach to finding of exact analytical solutions of nonautonomous NKFG equation based on the methods of building of functionally-invariant solutions of partial differential equations.

2 Methods of obtaining of analytical solutions of nonautonomous Klein-Fock-Gordon equation

Solution of the differential equation is called functionally-invariant if it is in the form of an arbitrary function $U = f(W)$ depending on another definite function W called ansatz. The ansatz is a solution of one or several equations. Equations can be algebraic or differential or a mixed type. There are functionally invariant solutions depending on two or more ansatzes.
The idea of the existence of functionally invariant solutions was suggested by C.Jacobi [6]. A.Forsyth [7] found functionally invariant solutions of the Laplace equation, wave equation, and of the Helmholtz equation. In studying electromagnetic waves, Bateman [8] fundamentally and consistently developed the Jacobi idea as applied to the wave equation. S.L.Sobolev and V.I.Smirnov [9]–[12] successfully used the method to construct functionally invariant solutions to solve problems of diffraction and sound wave propagation in uniform and layered solid media. N.P.Erugin [13] made a large contribution to developing the theory of this method. Functionally-invariant solutions of both autonomous and nonautonomous NKFG equation in particular sine-Gordon equation were obtained by authors of [14]–[18].
We will find solutions of nonautonomous NKFG equation (2) in the form of composite function $U = f(W)$. Then Eq. (2) is as follows

$$f''\left[W_x^2 + W_y^2 + W_z^2 - \frac{W_t^2}{v^2}\right] + f'\left[W_{xx} + W_{yy} + W_{zz} - \frac{W_{tt}}{v^2}\right] = p\, F[f(W)]. \tag{3}$$

Here and elsewhere prime denotes ordinary derivative with respect to the argument. Two obvious propositions could be made on the basis of (3).
Proposition 1. If function W satisfies to equations

$$W_x^2 + W_y^2 + W_z^2 - \frac{W_t^2}{v^2} = 0, \qquad W_{xx} + W_{yy} + W_{zz} - \frac{W_{tt}}{v^2} = p(x, y, z, t), \tag{4}$$

then solution of equation (2) is given by inversion of the integral

$$\int \frac{df}{F(f)} = W(x, y, z, t). \tag{5}$$

Proposition 2. If function W satisfies to equations

$$W_x^2 + W_y^2 + W_z^2 - \frac{W_t^2}{v^2} = p(x,y,z,t), \qquad W_{xx} + W_{yy} + W_{zz} - \frac{W_{tt}}{v^2} = 0, \tag{6}$$

then solution of equation (2) is given by inversion of the integral

$$\int \frac{df}{\sqrt{E+V}} = \pm\sqrt{2}W(x,y,z,t). \tag{7}$$

Here $F(U) = V'(U)$ and E is constant of integration.
For analytical expressions $F(U)$ listed in the Introduction integral (5) by corresponding substitution of variable reduces to the integration of rational fraction. Function f defined by (7) is obtained by inversion of elliptical or hyperelliptical integral with genre defined by number of summands in the function $F(U)$. Because problem of finding function f from equations (5) and (7) is solved in literature the key problem of solving nonautonomous NKFG equation reduces to finding ansatz W satisfying to equations (4) and (6). This problem could be solved by application of methods of building functinally-invariant solutions of partial differential equations.
First method. We will seek the soutions of equations (4) in the form

$$W = \varphi(\tau). \tag{8}$$

Here $\varphi(\tau)$ is arbitrary function τ and $\tau(x,y,z,t)$ is root of algebraic equation

$$x\,\xi(\tau) + y\,\eta(\tau) + z\,\zeta(\tau) - v^2 t\tau = \frac{s^2+q^2}{2}, \tag{9}$$
$$s^2 = x^2 + y^2 + z^2 - v^2t^2, \qquad q^2 = \xi^2(\tau) + \eta^2(\tau) + \zeta^2(\tau) - v^2\tau^2,$$

and $\xi(\tau), \eta(\tau), \zeta(\tau)$ are arbitrary functions τ.
Equation (9) implicitly defines dependence τ from time and space coordinates. Therefrom using rules of implicit functions differentiation we obtain partial derivatives τ of first and second order and make sure that τ satisfies to equations

$$\tau_x^2 + \tau_y^2 + \tau_z^2 - \frac{\tau_t^2}{v^2} = 0, \qquad \tau_{xx} + \tau_{yy} + \tau_{zz} - \frac{\tau_{tt}}{v^2} = \frac{2}{\nu}, \tag{10}$$

$$\nu = \xi_\tau(x-\xi) + \eta_\tau(y-\eta) + \zeta_\tau(z-\zeta) - v^2(t-\tau). \tag{11}$$

In deriving equations (10) the following relations were taken into account

$$\xi_\tau\tau_x + \eta_\tau\tau_y + \zeta_\tau\tau_z + \tau_t = 1, \tag{12}$$

$$\nu_x\tau_x + \nu_y\tau_y + \nu_z\tau_z - \frac{\nu_t\tau_t}{v^2} = 1. \tag{13}$$

On the basis of the Proposition **1** and equations (10) we obtain that (8) is the solution of equation (2) if function $f(W)$ is obtained from equation (5) and

$$p(x,y,z,t) = \frac{2}{\nu}\varphi_\tau. \tag{14}$$

We note that in spite of the simplicity of the analytic dependence (14) computed solution of nonautunomous NKFG equation is sufficiently general. Note first that $\varphi(\tau)$ is arbitrary function τ and as well we seek anzats τ from the equation (9) which contains three arbitrary functions $\xi(\tau)$, $\eta(\tau)$, $\zeta(\tau)$.
We seek function W in the form

$$W = \Psi(\nu, \tau). \tag{15}$$

For this anzats equations (4), (6) takes the form

$$W_x^2 + W_y^2 + W_z^2 - \frac{W_t^2}{v^2} = \Psi_\nu^2(2\sigma - q^2) + 2\Psi_\nu\Psi_\tau + \Psi_\tau\frac{2}{\nu}, \tag{16}$$

$$W_{xx} + W_{yy} + W_{zz} - \frac{W_{tt}}{v^2} = \frac{1}{\nu}(2\sigma - q_1^2)(\nu\Psi_\nu + \Psi)_\nu + \frac{2}{\nu}\Psi_\nu(\nu\Psi_\nu + \Psi). \tag{17}$$

Here

$$\sigma = \xi_{\tau\tau}(x - \xi) + \eta_{\tau\tau}(y - \eta) + \zeta_{\tau\tau}(z - \zeta), \tag{18}$$

$$q_1^2 = \xi_\tau^2 + \eta_\tau^2 + \zeta_\tau^2 - v^2. \tag{19}$$

In deriving equations (16), (17) account must be taken of (13) and equations which are satisfied by function $\nu(x, y, z, t)$

$$\nu_x^2 + \nu_y^2 + \nu_z^2 - \frac{\nu_t^2}{v^2} = 2\sigma - q_1^2, \tag{20}$$

$$\nu_{xx} + \nu_{yy} + \nu_{zz} - \frac{\nu_{tt}}{v^2} = \frac{2}{\nu}(2\sigma - q_1^2). \tag{21}$$

From (17) it is seen that $\Psi(\nu, \tau)$ is the solution of the second equation (6) i.e. wave function if

$$\nu\Psi_\nu + \Psi = 0, \quad \Psi(\nu, \tau) = \frac{\varphi(\tau)}{\nu}. \tag{22}$$

For this solution

$$W_x^2 + W_y^2 + W_z^2 - \frac{W_t^2}{v^2} = \frac{\varphi^2}{\nu^4}\left[2\sigma - q_1^2 - 2\nu\frac{\varphi_\tau}{\varphi}\right]. \tag{23}$$

On the basis of Proposition **2** we arrive at conclusion that (22) is solution of the equation (2) if

$$p(x, y, z, t) = \frac{\varphi^2}{\nu^4}\left[2\sigma - q_1^2 - 2\nu\frac{\varphi_\tau}{\varphi}\right]. \tag{24}$$

More general solution of nonautonomous NKFG equation could be obtained assuming that

$$W = \Psi(\tau, \lambda, \nu), \tag{25}$$

where

$$\lambda = l(\tau)(x-\xi) + m(\tau)(y-\eta) + n(\tau)(z-\zeta) - v^2 w(\tau)(t-\tau). \tag{26}$$

Here $l(\tau)$, $m(\tau)$, $n(\tau)$, $w(\tau)$ are arbitrary functions. We impose on them the following relationships

$$l\xi_\tau + m\eta_\tau + n\zeta_\tau - v^2 w = 0, \tag{27}$$

$$l^2 + m^2 + n^2 = v^2 w^2. \tag{28}$$

For anzats W defined by (25), equations (4), (6) are reduced to the form

$$W_x^2 + W_y^2 + W_z^2 - \frac{W_t^2}{v^2} = \frac{2}{\nu}\left(\Psi_\tau + \omega\Psi_\lambda + \sigma\Psi_\nu\right)\left(\lambda\Psi_\lambda + \nu\Psi_\nu\right) - \frac{q_1^2}{\nu}\Psi_\nu(2\lambda^2\Psi_\lambda + \nu\Psi_\nu), \tag{29}$$

$$W_{xx} + W_{yy} + W_{zz} - \frac{W_{tt}}{v^2} =$$

$$= \frac{2}{\nu}\left(\frac{\partial}{\partial\tau} + \omega\frac{\partial}{\partial\lambda} + \sigma\frac{\partial}{\partial\nu}\right)\left(\lambda\Psi_\lambda + \nu\Psi_\nu + \Psi\right) - \frac{q_1^2}{\nu}\left(4\lambda\Psi_{\lambda\nu} + \nu\Psi_{\nu\nu}\right). \tag{30}$$

From (29) it is seen that $\Psi(\tau, \lambda, \nu)$ will be a solution of equations (4) if

$$q_1^2 = \xi_\tau^2 + \eta_\tau^2 + \zeta_\tau^2 - v^2 = 0, \tag{31}$$

$$\lambda\Psi_\lambda + \nu\Psi_\nu = 0. \tag{32}$$

General solution of the equation (32) has the form

$$\Psi(\tau, \lambda, \nu) = g\left(\frac{\lambda}{\nu}\right)\varphi(\tau). \tag{33}$$

Here $g(\lambda/\nu)$ is arbitrary homogenous function of zero order. For the solution (33)

$$p(x, y, z, t) = -\frac{2}{\nu^2} g^2 \varphi^2 \left[\frac{\varphi_\tau}{\varphi} - \frac{\sigma}{\nu} + \frac{g'}{\nu g}(\omega + \sigma\lambda)\right]. \tag{34}$$

Hence (25), (33) will be solutions of the equation (2) if $f(W)$ is the inversion of integral (5) and function p is given by (34).
It follows from (30) that $W = \Psi(\tau, \lambda, \nu)$ will be a wave function if condition (31) is satisfied and function $\Psi(\tau, \lambda, \nu)$ satisfies the equation

$$\lambda\Psi_\lambda + \nu\Psi_\nu + \Psi = 0. \tag{35}$$

Solution of equation (35) will be arbitrary homogeneous function of negative first order

$$\Psi(\tau, \lambda, \nu) = \frac{1}{\nu}\, g\left(\frac{\lambda}{\nu}\right)\varphi(\tau). \tag{36}$$

According to the Proposition **2** anzats $W = \Psi(\tau, \lambda, \nu)$ given by (36) will be a solution of nonautonomous NKFG equation (2) if

$$p(x, y, z, t) = -\frac{2}{\nu}\Psi(\Psi_\tau + \omega\Psi_\lambda + \sigma\Psi_\nu). \tag{37}$$

3 Examples of construction of analytic solutions of nonautonomous Liouville equation

Proposed method of solutions of NKFG equation is applicable for obtaining of exact analytic solutions of nonautonomous Liouville wave equation

$$U_{xx} + U_{yy} + U_{zz} - \frac{U_{tt}}{v^2} = p(x, y, z, t)\, e^U. \tag{38}$$

However we will not attempt to find general solutions. Contrary having the aim to illustrate general methods we will represent simple particular solutions.
According to (5) solution of thq equation (38) is given by

$$U = \ln \frac{1}{C - W}, \tag{39}$$

if function $W(x, y, z, t)$ satisfies to equations (4). In the case then $W(x, y, z, t)$ satisfies equations (6) solution of (38) according to (7) will be

$$U = -2 \ln \sinh \frac{W + C}{\sqrt{2}}. \tag{40}$$

In solutions (39), (40) C is contant of integration. Function $W(x, y, z, t)$ as is explained above could be constructed in a variety of ways. If to find the solution of equation (38) according to the first method then $W(x, y, z, t)$ it is an arbitrary function of anzats $\tau(x, y, z, t)$ and anzats is a root of an algebraic equation (9). In order to find particular solutions it is necessary to define arbitrary functions $\xi(\tau)$, $\eta(\tau)$, $\zeta(\tau)$. Assume that

$$\xi = 0, \quad \eta = 0, \quad \zeta = 0. \tag{41}$$

Then

$$\tau = t \pm \frac{R}{v}, \quad R = \sqrt{x^2 + y^2 + z^2}, \tag{42}$$

$$p(x, y, z, t) = \frac{2}{\nu} W_\tau, \quad \nu = \pm v R. \tag{43}$$

Therefore for the case (41) solution of the Liouville equation (38) is given by formula (39) in which W is an arbitrary function τ and $\tau(x, y, z, t)$ and $p(x, y, z, t)$ are given by (42), (43).
Let

$$\xi = a_1 v\tau, \quad \eta = a_2 v\tau, \quad \zeta = a_3 v\tau, \quad a_1^2 + a_2^2 + a_3^2 = 1. \tag{44}$$

For this selection of functions ξ, η, ζ solution of (38) is (39) if

$$\tau = \frac{s^2}{2\nu}, \quad s^2 = x^2 + y^2 + z^2 - v^2 t^2, \tag{45}$$

$$p(x, y, z, t) = \frac{2}{\nu} W_\tau, \quad \nu = v(a_1 x + a_2 y + a_3 z - vt), \tag{46}$$

and W as in the case (41) is an arbitrary function τ.
New solutions of the equation (38) could be constructed if to introduce a function λ. According to the definition (26) it depends on functions $\xi(\tau)$, $\eta(\tau)$, $\zeta(\tau)$ which determine an anzats $\tau(x,y,z,t)$ and other arbitrary functions $l(\tau)$, $m(\tau)$, $n(\tau)$, and $w(\tau)$. Last functions are related to the first equations (27), (28). We find from them

$$\begin{aligned} l &= \frac{v\,w(\tau)}{\sqrt{q_1^2+v^2}}\left\{v\cos A+\sqrt{q_1^2}\left[\cos\delta\cos f(\tau)-\sin\delta\cos B\sin f(\tau)\right]\right\},\\ m &= \frac{v\,w(\tau)}{\sqrt{q_1^2+v^2}}\left\{v\cos B+\sqrt{q_1^2}\sin C\sin f(\tau)\right\}, \qquad (47)\\ n &= \frac{v\,w(\tau)}{\sqrt{q_1^2+v^2}}\left\{v\cos C-\sqrt{q_1^2}\left[\sin\delta\cos f(\tau)+\cos\delta\cos B\sin f(\tau)\right]\right\}. \end{aligned}$$

Here

$$\cos A=\frac{\xi_\tau}{\sqrt{q_1^2+v^2}},\ \cos B=\frac{\eta_\tau}{\sqrt{q_1^2+v^2}},\ \cos C=\frac{\zeta_\tau}{\sqrt{q_1^2+v^2}},\ \sin\delta=\frac{\xi_\tau}{\sqrt{\xi_\tau^2+\zeta_\tau^2}}, \quad (48)$$

and $f(\tau)$ is an arbitrary function τ.
If to define functions $\xi(\tau)$, $\eta(\tau)$, $\zeta(\tau)$ then from the equation (9) anzats could be find $\tau(x,y,z,t)$ and formula (26) helps with (47) compute the function λ.
Let

$$\xi=av\tau,\quad \eta=0,\quad \zeta=0. \qquad (49)$$

Then

$$l=\frac{v}{a}w(\tau),\quad m=\frac{\sqrt{a^2-1}}{a}v\,w(\tau)\sin f(\tau),\quad n=-\frac{\sqrt{a^2-1}}{a}v\,w(\tau)\cos f(\tau). \quad (50)$$

On the basis of (49) and (50) we obtain

$$\begin{aligned} \tau &= \frac{1}{v(a^2-1)}\left[ax-vt\pm\sqrt{(x-avt)^2-(a^2-1)(y^2+z^2)}\right],\\ \nu &= \mp v\sqrt{(x-avt)^2-(a^2-1)(y^2+z^2)}, \qquad (51)\\ \lambda &= \frac{v\,w(\tau)}{a}\left[x-avt+\sqrt{a^2-1}(y\sin f-z\cos f\right]. \end{aligned}$$

Determinig functions τ,ν,λ by formulas (15), (22) we obtain an anzats W and by formula (40) obtain the solution of nonautonomous Liouviville equation (38). We note that for the case (49) formulas (33) and (36) will not give the solution of the equation (38) because condition (31) is not satisfied for it. It will be satisfied if $a=1$. In this case

$$\tau=\frac{s^2}{2\nu},\quad \nu=v(x-vt),\quad \lambda=\nu w(\tau). \qquad (52)$$

Function $\varphi(\tau)$ satisfies the system of equations (4) and $\varphi(\tau)/\nu$ – system of equations (6). Threfore using functions (τ,ν,λ) (52) solution of nonautonomous Liouville

equation (38) could be constructed using formulas obtained above. Therefore solution of (38) will be (40) if

$$W = \frac{1}{x^2+y^2+z^2-v^2t^2}, \quad p(x,y,z,t) = \frac{4}{(x^2+y^2+z^2-v^2t^2)^3}. \tag{53}$$

This Lorentz invariant solution is obtained if τ and ν defined by (52) and

$$W = \frac{\varphi(\tau)}{\nu}, \quad \varphi(\tau) = \frac{1}{2\tau}.$$

Examples of particular solutions of the equation (38) are given below. They are defined by the formula (39) in which W is an arbitrary function of an anzats τ and τ and function $p(x,y,z,t)$ are defined by a particular form of functions (ξ,η,ζ,θ).

1. $\xi = v\tau\cos\alpha\cos\beta, \quad \eta = v\tau\cos\alpha\sin\beta, \quad \zeta = v\tau\sin\alpha, \quad \theta = \tau,$

$$\tau = t \pm \frac{R}{v}, \quad p(x,y,z,t) = \pm\frac{2}{vR}W_\tau,$$

2. $\xi = v\tau\cos\alpha, \quad \eta = v\tau\sin\alpha, \quad \zeta = 0, \quad \theta = \tau,$

$$\tau = \frac{s^2}{\sqrt{x^2+y^2}-vt}, \quad p(x,y,z,t) = \frac{1}{\sqrt{x^2+y^2}-vt}\left[4 - \frac{\tau}{\sqrt{x^2+y^2}}\right]W_\tau,$$

3. $\xi = \tau\cos\alpha, \quad \eta = \tau\sin\alpha, \quad \zeta = \tau\sinh\beta, \quad \theta = \frac{\tau}{v}\cosh\beta,$

$$\tau = \sqrt{x^2+y^2} - \sqrt{v^2t^2-z^2}, \quad p(x,y,z,t) = \left[\frac{1}{\sqrt{x^2+y^2}} + \frac{1}{\sqrt{v^2t^2-z^2}}\right]W_\tau,$$

4. $\xi = \tau\cos\alpha\sinh\beta, \quad \eta = \tau\sin\alpha\sinh\beta, \quad \zeta = \tau, \quad \theta = \frac{\tau}{v}\cosh\beta,$

$$\tau = z + \sqrt{v^2t^2-x^2-y^2}, \quad p(x,y,z,t) = -\frac{2}{\sqrt{v^2t^2-x^2-y^2}}W_\tau.$$

In Fig. 1. spatial image of the solution **3** is given for the case $W(\tau) = \sin\tau$.
Solutions of two-dimensional nonautonomous Liouville equations for some particular cases of function $p(x,y,t)$ have been obtained in papers [19, 20].

4 Conclusion

Methods of obtaining exact analytic solutions of nonautonomous NKFG equation are divised. They are based on the ideas and methods of construction of functionally-invariant solutions of partial differential equations. Proposed methods allow to construct solutions of NKFG equation in the form of an arbitrary function depending on one or several anzatses. Equations for determining of anzatses are given and methods of their solution are discussed. Developped methods allow to find analytic solutions of the equation (2) for functions $p(x,y,z,t)$ of the special form. Distinctive feature consists in simultaneous obtaining of solutions and analytic form of the function $p(x,y,z,t)$. Solutions are particular but the have sufficiently general form

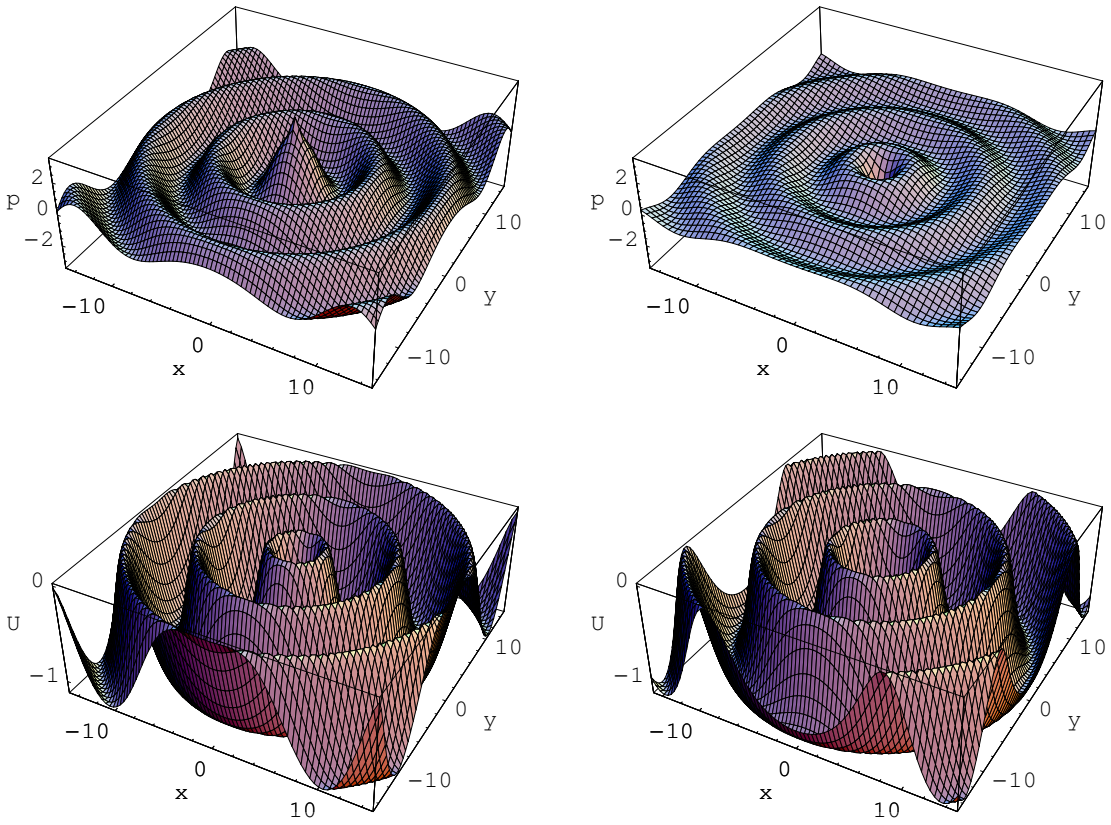

Figure 1: Function p and solution **3** for $z = 0$, $t = 1$ (left) and $t = 3$ (right).

because the include arbitrary functions. Untill now the problem of their selection in order to get given beforehand function $p(x, y, z, t)$ is not solved. This task needs further studies.

General methods of construction of functionally-invariant solutions of NKFG equation are illustrated by examples of finding particular exact analytical solutions of nonautonomous Liuoville equation.

Methods of solution of nonautonomous NKFG equation are described for the three-dimesional space. However they could be easily extended for the space of any dimension. We expect that proposed methods could be useful for the realization of nonlinear models which describe real physical phenomena and technological processes more adequately.

Acknowledgements

This work was supported by the Russian Foundation for Basic Researches, Grant Nos. 16-01-00068-a, 17-01-00230-a and 17-02-00365-a.

References

[1] J. Liouville. Sur lвЃ Ґéquation aux différences partielles $\frac{d^2 \log \lambda}{du\, dv} \pm \frac{\lambda}{2a^2} = 0$. Journal de mathématiques pures et appliquées **18** (1853) 71–72.

[2] M. Toda. Vibration of a chain with nonlinear interaction. J. Phys. Soc. Jpn. **22** (1967) 431–436.

[3] R. M. Vakhitov, O. G. Ryakhova. Nonlinear dynamics of cubic ferromagnets in the range of magnetoelastic resonance. Technical Physics **50** (2005) 1021–1025.

[4] N. A. Kudryashov. Methods of Nonlinear Mathematical Physics [In Russian]. Intellekt Publ., Moscow, Dolgoprudnyi, 2010.

[5] A. V. Porubov, E. L. Aero, G. A. Maugin. Two approaches to study essentially nonlinear and dispersive properties of the internal structure of materials. Phys. Rev. E **79** (2009) 046608.

[6] C. G. J. Jacobi. Über eine particuläre Lösung der partiellen Differentialgleichung $\frac{\partial^2 V}{\partial x^2} + \frac{\partial^2 V}{\partial y^2} + \frac{\partial^2 V}{\partial z^2} = 0$. Crelle Journal für die reine und angewandte Mathematik **36** (1848) 113–134. (*Reprinted in* C. G. J. Jacobi's Gesammelte Werke. Zweiter Band. Herausgegeben von Weierstrass K. Verlag von G.Reimer, Berlin, 1882, s. 191–216).

[7] A. R. Forsyth. New solutions of some of the partial differential equations of mathematical physics. Messenger of Mathematics **27** (1898) 99–118.

[8] H. Bateman. The Mathematical Analysis of Electrical and Optical Wave–Motion on the Basis of MaxwellвЃ Ґs Equations. Cambridge University Press, Cambridge, 1915.

[9] V. Smirnov, S. Sobolev. Sur une méthode nouvelle dans le problème plan des vibrations élastiques. Tr. Seism. Inst. **20** (1932) 1–37 [English transl.: On a new method in the plane problem on elastic vibrations. *In* Selected Works of S.L. Sobolev, vol. I, Springer, New York, 2006, p. 45–80].

[10] V. Smirnoff, S. Soboleff. Sur le problème plan des vibrations élastiques. C. R. Acad. Sci. Paris **194** (1932) 1437–1439.

[11] S. L. Sobolev. Functionally invariant solutions of the wave equation. Tr. Fiz.-Mat. Inst. Steklova **5** (1934) 259–264 [English transl. in: Selected Works of S. L. Sobolev, vol. I, Springer, New York, 2006, p. 195–199].

[12] Selected Works of S. L. Sobolev. Eds. G. V. Demidenko, V. L. Vaskevich. Springer, New York, 2006.

[13] N. P. Erugin. On functionally invariant solutions [In Russian]. Uchenye Zapiski Leningrad University, Vyp. **15**, N 96 (1948) 101–134.

[14] E. L. Aero, A. N. Bulygin, Yu. V. Pavlov. Solutions of the three-dimensional sine-Gordon equation. Theor. Math. Phys. **158** (2009) 313–319.

[15] E. L. Aero, A. N. Bulygin, Yu. V. Pavlov. Solutions of (3+1)-dimensional generalized sine-Gordon equation [In Russian]. Nelineinyi Mir **7** (2009) 513–517.

[16] E. L. Aero, A. N. Bulygin, Yu. V. Pavlov. New approach to the solution of the classical sineвГYGordon equation and its generalizations. Differential Equations **47** (2011) 1442–1452.

[17] E. L. Aero, A. N. Bulygin, Yu. V. Pavlov. Functionally invariant solutions of nonlinear Klein-Fock-Gordon equation. Appl. Math. Comput. **223** (2013) 160–166.

[18] E. L. Aero, A. N. Bulygin, Yu. V. Pavlov. Solutions of the sine-Gordon equation with a variable amplitude. Theor. Math. Phys. **184** (2015) 961–972].

[19] I. Kh. Sabitov. Solutions of the equation $\Delta u = f(x, y)e^{cu}$ in some special cases. Sbornik: Mathematics **192** (2001) 879–894.

[20] É. I. Semenov. New exact solutions to the nonautonomous Liouville equation. Siberian Mathematical Journal **49** (2008) 166–174.

A. N. Bulygin, Yu. V. Pavlov,
Institute for Problems in Mechanical Engineering of Russian Academy of Sciences,
61 Bol'shoy, V.O., Saint Petersburg, 199178, Russia

The algorithm of numerical solution for thermo-viscoelastic model composite material synthesis based on Ni-Al

Yu.A. Chumakov, T.A. Krylova
chya@ispms.ru

Abstract

The model of the synthesis of a composite based on a Ni-Al system with refractory carbide (TiC) particles is suggested. The various multiscale processes are considered in the model. The model takes into account an interaction of mechanical and thermal processes. The change in the structure of the composite is considered in the two-level approach: an evaluation of the stress-strain state of the system, calculation of thermal and concentration fields during the synthesis are conducted at the macrolevel; the effective properties of the composite are determined at the microlevel. The heat release from chemical reactions is determined by solving the problem of the reaction cell. The algorithm for the numerical solution of the problem is proposed.

1 Introduction

Synthesis of composites in the combustion regime [1-3] or in the thermal explosion mode [4-6] has attracted the attention of researchers [7-9]. The external electric and magnetic fields, as well as various types of mechanical loading are usually used to control the synthesis process. However, the exothermic synthesis process is poorly controlled. Therefore, the predictions of the composition and properties of composites, depending on the conditions of synthesis, use mathematical modeling.
The present work represents the evolution of previous investigations [10-13]. In this paper, we propose a model of the synthesis of a multiphase composite from a mixture of metal powders (Ni and Al), including those with additives of refractory inclusions such as titanium carbide TiC under heating conditions combined with loading. Since a change in the structure of the reaction system is possible during the synthesis process, and the macroscopic model is unable to describe the local structural inhomogeneities of the reaction medium, in this work, in order to take into account the influence of the particle size of the reagents, their distribution, formation of the reaction product layer at the particle level and their correlation with the characteristics of the synthesis process is used the two-level approach. The microstructural model of the reaction cell is considered at the microlevel (the level of individual powder particles) to determine the effective properties of the composite

and the heat release from chemical reactions. The methods of continuous medium mechanics, the dynamics of multiphase media, the theory of structural macrokinetics and thermodynamics are used at the macro level to determine the characteristics of the solid-phase synthesis process (the field of temperature, component concentration, stress and deformation).

2 PROBLEM FORMULATION

A flat layer of reagent that can be subjected to external thermal heating and mechanical loading is considered to describe the process of synthesis of composite material. In the model we use the following assumptions:
- in the investigated sample a flat layer of the regent of length L_x, width L_y, thickness L_z is considered. The conditions $L_z << L_y$, $L_z << L_x$ are satisfied, which allows us to use the hypothesis of the plane-stressed state of the plate to estimate the mechanical stresses arising in the system; i.e. $\sigma_{zz} = 0$ (rotations are also not taken into account);
- in the energy equation we take into account the work of dissipative forces and interaction of thermal and mechanical processes
- the properties of the composite are effective ones and the properties are calculated based on the sintering theory and dynamics of multiphase media
-the heat release from chemical reactions is determined from the solution of the problem of chemical reaction in the reaction cell.
- To take into account the melting of the components of the system, we use an abrupt specific heat changing in the vicinity of the melting point

$$c_\varepsilon \rho = \begin{cases} (c_\varepsilon \rho)_S + L_m \delta (T - T_m), & T <= T_m \\ (c_\varepsilon \rho)_L + L_m \delta (T - T_m), & T > T_m \end{cases},$$

where subscripts "s" and "L" refer to the properties of the solid and liquid (molten) material, respectively; T_m is the melting point, L_m is the heat of the phase transition, and δ is the Dirac delta function.
The mathematical formulation of the problem includes the heat conduction equation associated with deformations and containing two types of heat sources - due to a chemical reaction and due to viscous dissipation.

$$\sigma_{ij} \frac{d\varepsilon_{ij}}{dt} + c_\varepsilon \rho \frac{dT}{dt} = \nabla \cdot \lambda_T \nabla T + \sum_{i=1}^{n} Q_i \phi_i (\eta, T) - 3K\, T \alpha_T \frac{d\varepsilon_{kk}}{dt} \quad (1)$$

where c_ε, ρ and λ_T are the effective heat capacity, density and thermal conductivity coefficient, respectively; T is the temperature, x and y are spatial coordinates, $\varepsilon_{kk} = \varepsilon_{xx} + \varepsilon_{yy} + \varepsilon_{zz}$ is the first invariant of strain tensor, α_T is the thermal expansion coefficient, K is the isothermal bulk modulus, σ_{ij} , ε_{ij} are the components of stress and strains tensors, η is the conversion level or the fraction of the reaction product, Q is the heat of the total reaction, $\phi_i(\eta,T)$ is the chemical reaction rate,

$$\frac{\partial ...}{\partial t} + V \cdot \nabla ... \quad (2)$$

To determine the stressed-strain state of plane layer, we consider the problem of the mechanical equilibrium of the plate in the approximation of generalized plane stress state. Therefore, the problem involves the equilibrium equations, rheological relations and boundary conditions corresponding [14].

$$\frac{\partial \sigma_{xx}}{\partial x} + \frac{\partial \sigma_{xy}}{\partial y} = 0; \quad \frac{\partial \sigma_{yx}}{\partial x} + \frac{\partial \sigma_{yy}}{\partial y} = 0 \tag{3}$$

We use the Cauchy equations [14]

$$\varepsilon_{xx} = \frac{\partial u_x}{\partial x}; \quad \varepsilon_{yy} = \frac{\partial u_y}{\partial y}; \varepsilon_{xy} = \frac{1}{2}\left(\frac{\partial u_y}{\partial x} + \frac{\partial u_x}{\partial y}\right) \tag{4}$$

We assume that the stress tensor is the sum of the elastic and viscous components:

$$\sigma_{ij} = \sigma_{ij}^e + \sigma_{ij}^V.$$

We use the Duhamel-Neumann relations for "elastic" stresses

$$\sigma_{ij}^e = 2\mu \cdot \varepsilon_{ij} + \delta_{ij}\left[\lambda \varepsilon_{kk} - K\omega\right],$$

where

$$\omega = 3\left[\alpha_T(T - T_0) + \sum_{k=1}^{n} \alpha_k \eta_k\right],$$

n is the number of components involved in the reactions; α_k are the coefficients of concentration expansion.
Elastic stress increments are linearly related to the increments of any deformations. Viscous - linearly related to the rates of deformation. By analogy with the previous one, for viscous stresses we have

$$\sigma_{ij}^V = 2\mu_V \cdot \dot{\varepsilon}_{ij} + \delta_{ij}\left[\lambda \dot{\varepsilon}_{kk} - 3K\left(\alpha_T \dot{T} + \sum_{k=1}^{n} \alpha_k \dot{\eta}_k\right)\right],$$

where μ_V is the coefficient of viscosity; δ_{ij} is Kronecker symbol.
For the total reaction, we obtain the expression

$$\sigma_{ij} = 2\mu\varepsilon_{ij} + 2\mu_v\dot{\varepsilon}_{ij} + \delta_{ij}\left[\lambda\varepsilon_{kk} + \lambda\dot{\varepsilon}_{kk} - 3K\left\{(\alpha_p - \alpha_r)\eta + (\alpha_p - \alpha_r)\dot{\eta}\right\}\right] \tag{5}$$

The boundary conditions correspond to the character layer loading (tension, compression, shear) and to the conditions of external heating.

$$\begin{gathered} t = 0 : T = T_0, \quad \sigma_{ij} = 0; \ \varepsilon_{ij} = 0 \\ x = 0 : \ -\lambda \frac{\partial T}{\partial x} = \begin{cases} q_0, t \le t_i \\ \alpha\left(T - T_0\right), t > t_i \end{cases}, x = L_x : \ \frac{\partial T}{\partial x} = 0; \\ y = 0 : \ \frac{\partial T}{\partial y} = 0, y = L_y : \ \frac{\partial T}{\partial y} = 0, \end{gathered} \tag{6}$$

where t_i is the heat flux time; q_0 is the heat flow power; and α is the external heat exchange coefficient.
For the case of uniaxial extension, the boundary conditions have the form

$$\begin{aligned} &x = 0,\ x = L_x: \ \ \sigma_{xx} = P,\ \ \sigma_{yy} = 0,\ \ \sigma_{xy} = 0; \\ &y = 0,\ \ y = L_y: \ \ \sigma_{xx} = 0,\ \ \sigma_{yy} = 0,\ \ \sigma_{xy} = 0.x \end{aligned} \tag{7}$$

For the case of uniaxial compression, the load was taken with a negative sign. For the pure shear condition we have

$$\begin{aligned} &x = 0,\ x = L_x: \ \ \sigma_{xx} = P_1,\ \ \sigma_{yy} = 0,\ \ \sigma_{xy} = 0 \\ &y = 0,\ \ y = L_y: \ \ \sigma_{xx} = 0,\ \ \sigma_{yy} = P_2,\ \ \sigma_{xy} = 0 \end{aligned} \tag{8}$$

where $P_1 = P{\cdot}\cos(\alpha)$, $P_2 = P{\cdot}\sin(\alpha)$, $\mathrm{tg}(\alpha) = L_x/L_y$.

Algorithm of numerical solution

The algorithm for the numerical solution of the problem under investigation was as follows. For the numerical solution of the heat equation (1) finite-difference approximation using the four-point pattern and the splitting scheme by coordinates were used. The finite-difference scheme for (1) has the form

$$\begin{aligned} c_{ij}\rho_{ij}\frac{\tilde{T}_{ij} - \overset{\vee}{T}_{ij}}{dt} &= \frac{1}{dx}\left[\frac{\lambda_{i+1j} + \lambda_{ij}}{2}\frac{\tilde{T}_{i+1j} - \tilde{T}_{ij}}{dx} - \frac{\lambda_{ij} + +\lambda_{i-1j}}{2}\frac{\tilde{T}_{ij} - \tilde{T}_{i-1j}}{dx}\right] \\ c_{ij}\rho_{ij}\frac{T_{ij} - \tilde{T}_{ij}}{dt} &= \frac{1}{dy}\left[\frac{\lambda_{ij+1} + \lambda_{ij}}{2}\frac{T_{ij+1} - T_{ij}}{dy} - \frac{\lambda_{ij} + \lambda_{ij-1}}{2}\frac{T_{ij} - T_{ij-1}}{dy}\right] + \\ &+ \overset{\vee}{W}_{ij} - \overset{\vee}{U}_{ij} + \sum_{i=1}^{n} Q_i\phi\left(\overset{\vee}{\eta}_{ij}, \overset{\vee}{T}_{ij}\right) \end{aligned} \tag{9}$$

where

$$W = \sigma_{ij}\frac{\partial\varepsilon_{ij}}{\partial t}, U = 3K\,T\alpha_T\frac{\partial\varepsilon_{kk}}{\partial t}.$$

The parameters denoted by the symbol "$\vee$" are the values on the previous time layer. Further, the resulting system of linear algebraic equations was solved by a sweep method with initial and boundary conditions (6). The temperature value for each k time layer ($T_{ij}^k(x,y)$) was used in kinetic equations and rheological relations. To determine the kinetic function of $\phi(\eta,T)$ and the total heat release from chemical reactions, a special problem of chemical reaction is solved at the level of the representative volume (reaction cell). The method used to solve the system of differential equations in the model of the reaction cell is analogous to the solution method for the energy equation presented above.
To find the components of the stress tensor σ_{ij} and deformation ε_{ij} we use the Cauchy equation and the deformation rate relations.

$$V_x = \frac{\partial u_x}{\partial t}; V_y = \frac{\partial u_y}{\partial t}; \quad \frac{\partial\varepsilon_{xx}}{\partial t} = \frac{\partial V_x}{\partial x}; \quad \frac{\partial\varepsilon_{yy}}{\partial t} = \frac{\partial V_y}{\partial y}; \frac{\partial\varepsilon_{xy}}{\partial t} = \frac{1}{2}\left(\frac{\partial V_y}{\partial x} + \frac{\partial V_x}{\partial y}\right) \tag{10}$$

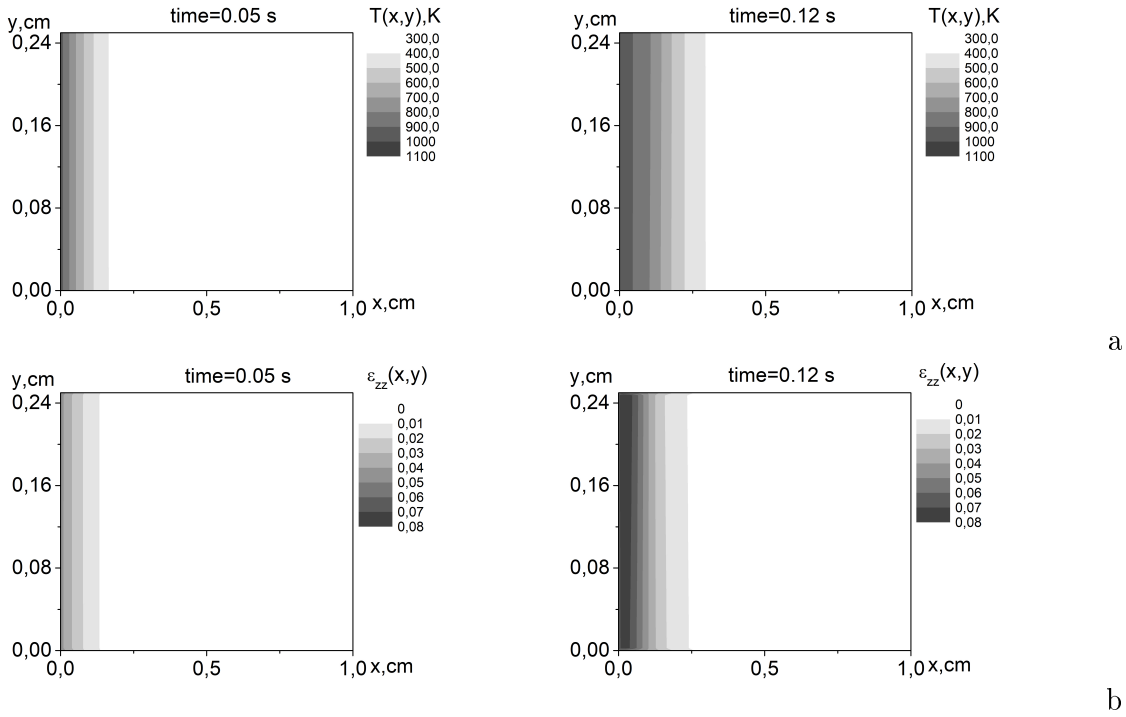

Fig.1. Spatial distributions of the plate temperature (a) and component of strain tensor (b) $q^0 = 10^7 W/m^2, P = 1GPa$

The relations (10) were substituted into the rheological relations (5) and the equilibrium equations (3).Then the differential equations were replaced by difference equations, and the resulting system was solved by the relaxation method. In view of the cumbersomeness, we not represent the founded expressions in the article. The results of calculations based on the proposed algorithm for the viscoelastic Maxwell's body and the case of pure shear are shown in Fig. 1.

Acknowledgements

The work was carried out in the framework of the Fundamental Research Program of the State Academies of Sciences for 2013-2020. Project 23.2.2.

References

[1] Widodo T., Riyadi B., Zhang T., Combustion Synthesis of Ti3Al Composite by Induction Heating,Proceedings of the 3rd Applied Science for Technology Innovation, 2014, 18-23.

[2] Kobashi M., Ichioka D., Kanetake N., Combustion Synthesis of Porous TiC/Ti Composite by a Self-Propagating Mode Materials 2010, 3,3939-3947.

[3] Feng G., Li Zh., Jacob R.J., Yang Y., Wang Y., Zhou Z., Sekuli D.P., Zachariah

M.P., Laser-induced exothermic bonding of carbon fiber/Al composites and TiAl alloys, Materials and Design, 126, 2017, 197-206.

[4] Liang Y., Zhao Q., Han Zh., Zhang Zh., Li X., Ren L., Reaction behavior of TiC/Cu composite via thermal explosion reaction (TE) under Ar and air atmosphere, Corrosion Science, Vol.93, 2015, 283-292.

[5] Shokati A.A., Parvin N., Shokati M., Combustion synthesis of NiAl matrix composite powder reinforced by TiB2 and TiN particulates from Ni-Al-Ti-BN reaction system, Journal of Alloys and Compounds, Vol. 585, 5 February 2014, 637-643.

[6] Liua Ya., Cai X., Sun Zh., Jiao X., Akhtar F., Wang J., Feng P., A novel fabrication strategy for highly porous FeAl/Al2O3 composite by thermal explosion in vacuum, Vacuum, Vol. 149,March 2018,225-230.

[7] Rogachev A.S., Mukasyan A.S. Combustion for Material Synthesis, Taylor Francis Group, 2015.

[8] Moore J.J.,Feng H.J. Combusion synthesis of advanced materials: part I. Reaction parameters,Progress in material science, 1995, Vol.39, 243-273.

[9] Moore J.J.,Feng H.J. Combusion synthesis of advanced materials: Part II: Classification, application and modeling, Progress in material science, 1995. Vol.39, 275-316.

[10] Chumakov Yu.A., Knyazeva A. G. The influence effect of coupling on solid-phase conversion in the plate from composition materials under condition of axial tension and shifting, AIP Conference Proceedings,1623, 2014, 95-98.

[11] Chumakov Yu.A., Knyazeva A.G. Influence of method used for calculating of effective properties on stressed-strain state of composite plate under nonstationary heating, Applied Mechanics and Materials, 756, 2015, 402-407.

[12] Chumakov Yu.A.,Knyazeva A.G. Model of behavior of the viscoelastic system with a melting component under external load, IOP Conf. Series: Materials Science and Engineering,124,012049, 2016.

[13] Chumakov Yu.A., Knyazeva A.G. Porosity evolution during composite synthesis under loading, AIP Conference Proceedings 1909,020028, 2017.

[14] Boley B., Weiner J. Theory of Thermal Stresses, New York, Wiley, 1960.

Yu.A. Chumakov, ISPMS SB RAS, pr. Akademicheskii, 2/4, Tomsk, Russia
T.A. Krylova, ISPMS SB RAS, pr. Akademicheskii, 2/4, Tomsk, Russia

Numerical simulation of non-Newtonian fluid flow in a T-shaped channel under the given pressure boundary conditions

Olga A. Dyakova, Evgeniy I. Borzenko
dyakova_o@ftf.tsu.ru

Abstract

The planar steady-state flow of non-Newtonian incompressible fluid in a T-shaped channel is considered. The motion of the fluid is caused by a given pressure difference between inlet/outlet boundaries. The flow is described by momentum and continuity equations written in dimensionless variables. On the solid walls, no slip boundary conditions are assigned. The viscosity of non-Newtonian fluid is determined by the Ostwald-de Waele power law. The problem is solved numerically using the finite difference method based on the SIMPLE procedure. The parametric studies of the flow kinematics depending on the pressure values given at the inlet/outlet boundaries have been performed. The typical flow regimes characterized by redistribution and reversal of the fluid flow have been found. The effect of main parameters on the kinematic and dynamic characteristics has been estimated.

1 Introduction

Pipelines networks using for transportation of fluids and gases consist of branched or connected elements. One such element is a T-shaped channel. The fluid flow in a T-channel is characterized by separation of the flow into two parts. In engineering practice, it is essential to understand the main characteristics of the flow in separating and reattaching flows [1, 2].

Nowadays, a large number of investigations of the flows of both Newtonian [3, 4, 5, 6, 7] and non-Newtonian [1, 2, 8, 9, 10] fluids with given flow rate at the boundaries of a T-shaped channel were carried out. There are a few works in which values of the pressure are given at the boundaries of a T-shaped channel. Among these results we find the works [11, 12] where numerical simulation of the flow of a Newtonian incompressible fluid in channels of complex geometry including fluid flow in a T-channel was performed.

The primary purpose of this work is to investigate characteristics of the flow of a power-law fluid in a T-shaped channel under the given pressure difference between boundary sections.

2 Problem Formulation

The planar steady-state flow of a non-Newtonian incompressible fluid in a T-channel is investigated. The flow region is limited by solid walls *MKF*, *EDC*, *AB* (Fig.1). The fluid flow is driven by pressure difference between boundary sections *AM*, *FE*, *BC* of the T-shaped channel. Mathematical problem statement includes momentum and continuity equations which in dimensionless vector form are written as follows:

$$(\mathbf{U}\cdot\nabla)\,\mathbf{U} = -\nabla p + \nabla\cdot(2\eta\mathbf{E})\,, \tag{1}$$

$$\nabla\cdot\mathbf{U} = 0. \tag{2}$$

Here, U is dimensionless velocity vector with components (u,v) in the Cartesian coordinate system (x, y), p is dimensionless pressure, E is the strain rate tensor.

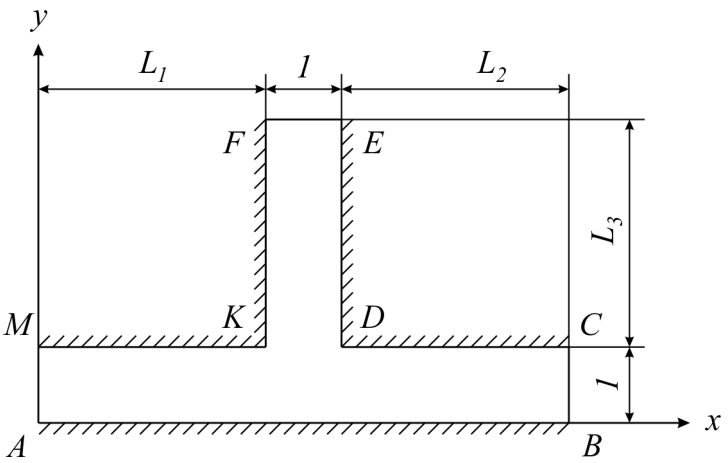

Figure 1: Flow region

The viscosity of non-Newtonian fluid is determined by the Ostwald-de Waele power law [13]:

$$\eta = (A)^{n-1}, \tag{3}$$

where $A = \sqrt{2\left(\frac{\partial u}{\partial x}\right)^2 + \left(\frac{\partial u}{\partial y} + \frac{\partial v}{\partial x}\right)^2 + 2\left(\frac{\partial v}{\partial y}\right)^2}$ is dimensionless intensity of the strain rate tensor, n is the power-law index. Needless to say that the model describes the rheology of Newtonian fluids at *n=1*.
To scale the length and the velocity, L (the width of the boundary section *AM*) and $U_0 = \left(\frac{k}{\rho L^n}\right)^{\frac{1}{2-n}}$ are used, respectively. Dimensionless pressure is prescribed by following expression:

$$p = (P - P_{FE}) \,/ \left(\frac{k^2}{\rho^n L^{2n}}\right)^{\frac{1}{2-n}},$$

where k is the power-law consistency index, ρ is the fluid density, P is dimension pressure, P_{FE} is dimension pressure in the cross-section *FE*.

In the through-flow sections AM, FE, and BC, zero tangential components of the velocity vector and values of the pressure are specified

$$\begin{aligned} &v = 0,\ p_{AM} = p_1,\ x = 0,\ 0 \le y \le 1 \\ &u = 0,\ p_{FE} = 0,\ L_1 \le x \le L_1 + 1,\ y = L_3 + 1 \\ &v = 0,\ p_{BC} = p_3,\ x = L_1 + L_2 + 1,\ 0 \le y \le 1 \end{aligned} \tag{4}$$

On the solid walls, the no slip boundary conditions hold

$$\mathbf{U} = 0. \tag{5}$$

The problem solution is reduced to finding both the velocity and pressure fields which satisfy Eqs. (1)-(3) with given boundary conditions (4)-(5).

3 Numerical Method and Validation

The problem is solved numerically. An asymptotic time solution of the unsteady flow equation is used to obtain steady-state velocity and pressure fields [20]. Such method of solution assumes the addition of time derivative of the function U in Eq.(1). The obtained system is discretized by the finite difference method based on the SIMPLE procedure [15]; rectangular staggered grid is used.
The rheological model for shear-thinning fluid ($n < 1$) has peculiarity of "infinite" viscosity, as $A \to 0$. To ensure the stability and accuracy of calculations in the regions of small values of A, the modified model of the rheological equation is used [16-17]. According to this model, the viscosity is determined by expression

$$\eta = (A + \varepsilon)^{n-1},$$

where ε is the regularization parameter. The approximate convergence of the method of calculating with using regularized rheological model is presented in [16, 5].

4 Results and Discussion

The flow characteristics of the problem are depending on geometric sizes of the channel and three parameters: the power-law index (n) and values of the pressure given at boundaries AM and BC, respectively, (p_1 and p_3). In present work, all calculations have been performed in the T-shaped channel with branches of the same width equal to one dimensionless unit and the same length L_1=L_2=L_3=3 (Fig. 1). Investigation of the flow characteristics depending on the parameters p_1 and p_3 at n=0.8 has been carried out.
In Fig. 2, distribution of the flow characteristics at p_1=-300 and p_3=-400 are presented. The fluid flow enters through the boundary section FE. The inlet flow divides into two parts in the vicinity of the junction of the branches and leaves the channel through the boundary sections AM and BC. The planar-parallel flow of the non-Newtonian fluid with the fully developed velocity profile occurs near the

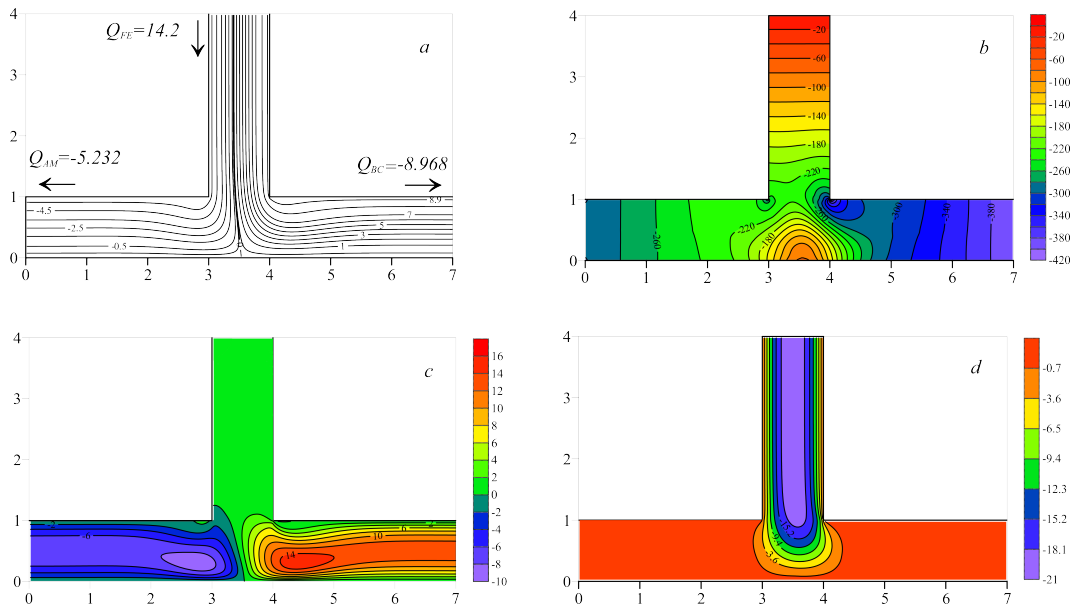

Figure 2: Distribution of the flow characteristics at n=0.8, p_1=-300 and p_3=-400 (a — the stream function contours, b — the pressure field, c — the field of velocity u, d — the field of velocity v)

through-flow sections AM, FE, and BC. Transient regions of the flow appear in the vicinity of the sections with corner points K and D.

The Reynolds Number is imposed to analyse the results and use the similarity theory as follows:

$$\mathrm{Re} = \frac{\rho {U_{avg}}^{2-n} L^n}{k}.$$

Here, U_{avg} is the average velocity in the cross section of the channel which is characterized by maximum flow rate. For case plotted in Fig. 2, $\mathrm{Re} = |Q_{FE}|^{2-n} = 24.1$.

The research has been carried out over the range of values of the pressure -2000$\leq p_1, p_3 \leq$2000. Four characteristic flow regimes have been determined for this range of main parameters. Regime I (Fig. 3a) corresponds to the case describing above. The fluid flow enters through the boundary section FE and leaves the channel through the boundary sections AM and BC. This regime is observed when values of the pressure given in the boundary sections AM and BC are less than the value of the pressure in the section FE. The increase of the pressure in the through-flow section AM, ($p_1 >$0), leads to reversal of the flow in the branch containing the through-flow section AM if all other parameters remaining equal (Regime II). The fluid flow enters through two boundary sections AM and FE. After confluence of entering flows, the fluid leaves the channel through the boundary section BC (Fig. 3b). As the parameter p_1 is further increased, the fluid flow changes the direction in the branch containing the through-flow section FE (Regime III). The fluid flow entering through the boundary section AM divides into two parts in the vicinity of the junction of the branches and leaves the channel through the boundary sections FE and BC (Fig. 3c). Regime IV (Fig. 3d) corresponds to the case when two fluid flows entering through the

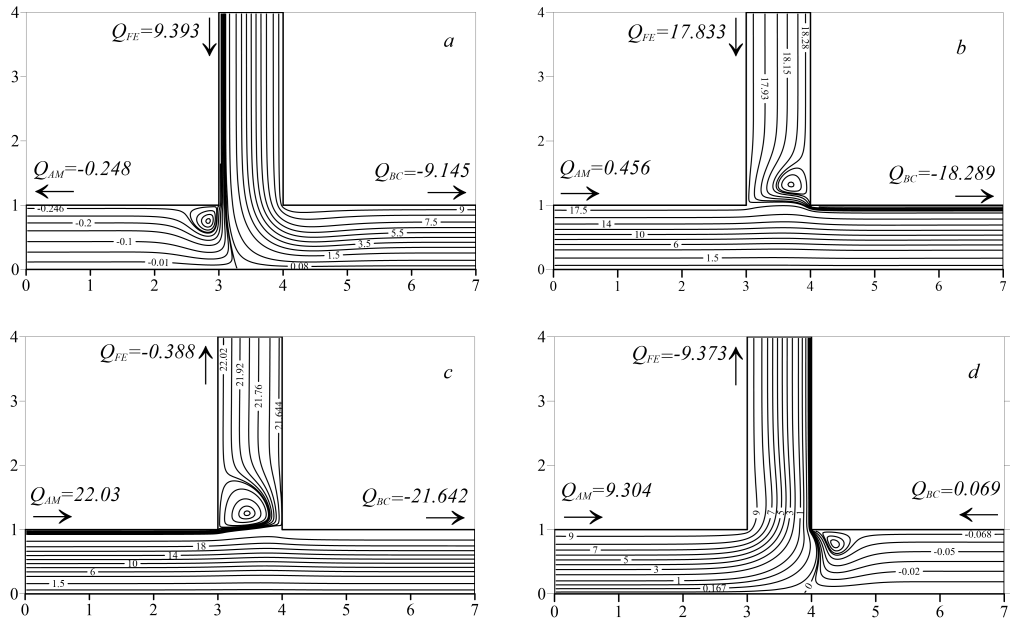

Figure 3: Flow regimes at n=0.8 (a — p_1=-160 and p_3=-400, b — p_1=250 and p_3=-400, c — p_1=320 and p_3=-400, c — p_1=400 and p_3=280)

boundary sections AM and BC merge into one in the vicinity of the the junction of the branches and run out through the boundary sections FE. This regime is observed for positive values of p_1 and p_3.

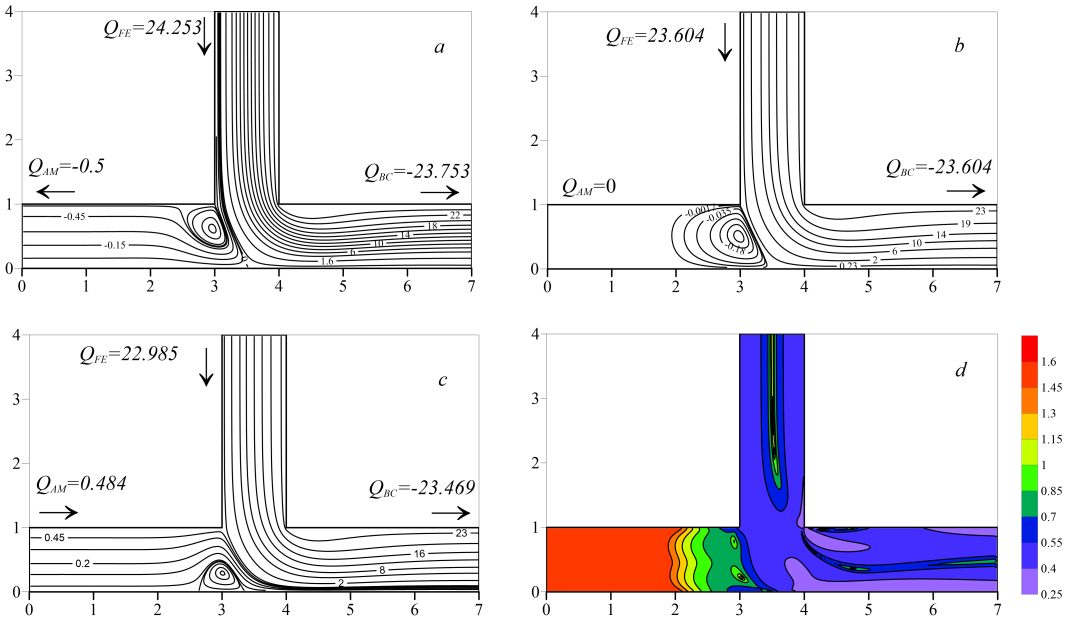

Figure 4: Distribution of the streamlines (a,b,c) and the viscosity (d) at different values of p_1 (n=0.8, p_3=-1000, a — p_1=-230, b,d — p_1=-214.95, c — p_1=-200)

Fig. 4 demonstrates change of the flow kinematics during transition from regime I to regime II at critical pressure $p_1 = p_{crit}$ and fixed value p_3 =-1000. Regime I without recirculation zone in the flow of the fluid is observed at $p_1 \ll p_{crit}$. The recirculation

zone in the vicinity of the corner point K appears with increasing parameter p_1 (Fig. 4a). As the pressure p_1 is further enhanced, sizes of formed recirculation zone become larger and, subsequently, reach its maximum at $p_1 = p_{crit}$ =-214.95 (Fig. 4b). Thus, the recirculation zone closes the cross-section, and the flow rate through the boundary section AM attains zero. The viscosity field for this case is plotted in Fig. 4d. It can be seen that the apparent viscosity of the fluid is maximum in the branch containing the cross section AM. Regime II is observed at $p_1 > p_{crit}$ (Fig. 4c). The recirculation zone turns around, decreases and shifts to the solid wall AB with further increase of the parameter p_1. Similarly, the change of other regimes occurs; and the recirculation zone appears in the branch of the T-shaped channel in which the reorientation of the flow happens.

5 Conclusions

The planar flow of the power-law incompressible fluid in the T-channel has been studied. The fluid flow is driven by pressure difference between boundary sections AM, FE, and BC of the T-shaped channel. On the solid walls, the no slip boundary conditions have been used.
Investigation of the flow characteristics depending on values of the pressure given in the through-flow sections AM and BC (-2000$\leq p_1, p_3 \leq$2000) has been carried out. The range of change of these parameters has been chosen so that the planar-parallel flow of the non-Newtonian fluid with the fully developed velocity profile has been realized in the vicinity of the through-flow sections AM, FE, and BC.
As a result of the parametric studies, four regimes of the flow have been determined for this range of parameters p_1 and p_3. Estimation of the influence of main parameters on the flow pattern has been performed. Characteristics of the flow for these regimes have been presented. The results describing transition from one regime to another have been demonstrated.

Acknowledgements

This research was supported by the Grant of the President of the Russian Federation for the Young Russian Scientists (MK-3085.2018.1) and the Grant of the Russian Foundation for Basic Research (Project No.18-38-00259).

References

[1] Khandelwal V., Dhiman A., Baranyi L. Laminar flow of non-Newtonian shear-thinning fluids in a T-channel. Computers and Fluids, V.108, pp.79-91, 2015.

[2] Matos H.M., Oliveira P.J. Steady and unsteady non-Newtonian inelastic flows in a planar T-junction. Int.J.Heat and Fluid Flow, V.39, pp.102-126, 2013.

[3] Liepsch D., Moravec S., Rastogi A.K., Vlachos N.S. Measurements and calculation of laminar flow in a ninety degree bifurcation. J.Biomech., V.15-7. pp.473-485, 1982.

[4] Khodadadi J.M., Nguyen T.M., Vlachos N.S. Laminar forced convective heat transfer in a two-dimensional 90-degree bifurcation. Numer.Heat Transfer, V9-6, pp.677-695, 1986.

[5] Grace J.L., Priest M.S. Division of flow in open channel junctions. Auburn, Ala.: Engineering Experiment Station, Alabama Polytechnic Institute, 1958.

[6] Shamloo H., Pirzadeh B. Investigation of characteristics of separation zones in T-Junctions. WSEAS Transactions on Mathematics, V.7-5, pp.303-312, 2008

[7] Benes L., Louda P., Kozel K., Keslerova R., Stigler J. Numerical simulations of flow through channels with T-junction. Applied Mathematics and Computation, V.219, pp.7225-7235, 2013.

[8] Miranda A.I.P., Oliveira P.J., Pinho F.T. Steady and unsteady laminar flows of Newtonian and generalized Newtonian fluids in a planar T-junction. Int.J.Numerical Methods in Fluids, V.57-3, pp.295-328, 2008.

[9] Khodadadi J.M., Vlachos N.S., Liepsch D., Moravec S. LDA measurements and numerical prediction of pulsatile laminar flow in a plane 90-degree bifurcation. J.Biomech.Eng., V110-2, pp.129-136, 1988.

[10] Khodadadi J.M. Wall pressure and shear stress variations in a 90-deg bifurcation during pulsatile laminar flow. J.Fluids Eng., V.113-1, pp.111-115, 1991.

[11] Moshkin N., Yambangwi D. Steady viscous incompressible flow driven by a pressure difference in a planar T-junction channel. Int.J.Comput.Fluid Dyn., V.23-3, pp.259-270, 2009.

[12] Kuznetsov B.G., Moshkin N.P., Smagulov S.H. Numerical investigation of the viscous incompressible fluid flow in channels of the complex geometry with given pressure [in Russian]. Proceedings of the Institute of the Theoretical and Applied Mechanics of the Siberian Branch of the Academy of Sciences of the USSR, V.14, 1983.

[13] Shulman Z.P. Convective Heat and Mass Transfer of Rheologically Complex Liquids [in Russian]. Moscow: Energiya, 1975.

[14] Godunov S.K., Ryabenkii V.S. Difference Schemes. North-Holland, Elsevier Science Ltd, 1987.

[15] Patankar S. Numerical Heat Transfer and Fluid Flow. New York: Taylor and Francis, 1980.

[16] Dyakova O.A., Frolov O.Yu. Pressure driven laminar flow of a power-law fluid in a T-channel. IOP Conf. Series: Journal of Physics, V.894, pp.1-7, 2017.

[17] Borzenko E.I., Dyakova O.A. Flow a power-law fluid in a T-channel under the given pressure difference. Journal of Engineering Physics and Thermophysics, V.92-3, 2018. (in print)

Evgeniy I. Borzenko, Tomsk State University, Lenina pr. 36, Tomsk, Russia, 634050
Olga A. Dyakova, Tomsk State University, Lenina pr. 36, Tomsk, Russia, 634050

Coherent structures and localized modes in collective models of accelerator physics

Antonina N. Fedorova, Michael G. Zeitlin
zeitlin@math.ipme.ru, anton@math.ipme.ru

Abstract

We present applications of our multiresolution approach to various popular models of accelerated physics. Mostly we are interested in the description of complex beam motions with the internal collective behaviour generated by background electromagnetic fields: Vlasov-Maxwell-Poisson systems, envelope/momentum RMS approximation, a beam-beam interaction model. We obtain the representation for all dynamical variables as multiresolution expansion via high-localized nonlinear eigenmodes in the base of various compactly supported wavelet-like functions. Numerical modelling demonstrates the creation of coherent structures, generated by internal hidden symmetry on the level of the underlying functional spaces and appearance of (meta)stable patterns.

1 Introduction

In this paper we consider the applications of a new numerical-analytical technique which is based on the methods of local nonlinear harmonic analysis (LNHA) a.k.a. wavelet analysis in the case of affine group as a group of internal symmetries, to three (nonlinear) beam/accelerator physics problems which can be characterized by the collective type behaviour: some forms of Vlasov-Maxwell-Poisson equations[1], RMS envelope dynamics[2], the model of beam-beam interactions [3]. Such an approach may be useful in all models in which it is possible and reasonable to reduce all complicated problems related with statistical distributions to the problems described by systems of nonlinear ordinary/partial differential equations with or without some (functional)constraints. LHNA is a relatively novel set of mathematical methods, which gives us the possibility to work with well-localized bases in functional spaces and gives the maximum sparse forms for the general type of operators (differential, integral, pseudodifferential) in such bases. Our approach is based on the variational-multiscale approach developed by us [4]-[15] and allows to consider the polynomial and rational type of nonlinearities. Multiscale representation for the solutions has

the following multiresolution decomposition via nonlinear high-localized eigenmodes

$$u(t,x) = \sum_{(i,j)\in Z^2} a_{ij} U^i(x) V^j(t), \quad (1)$$

$$V^k(t) = V_N^{k,slow}(t) + \sum_{i\geq N} V_i^k(\omega_i^1 t), \quad \omega_i^1 \sim 2^i \quad (2)$$

$$U^k(x) = U_M^{k,slow}(x) + \sum_{j\geq M} U_j^k(\omega_j^2 x), \quad \omega_j^2 \sim 2^j, \quad (3)$$

which corresponds to the full multiresolution expansion in all underlying time/space scales (x are the generalized space coordinates or phase space coordinates, t is time coordinate). The representation (1) provides the expansion into the slow part $u_{N,M}^{slow}$ and fast oscillating parts for arbitrary N, M. So, we may move from coarse scales of resolution to the finest one for obtaining more detailed information about our dynamical process. The first terms in the RHS of formulas (1)-(3) correspond, on the global level of function space decomposition, to the resolution space and the second ones to detail space. In this way we give contribution to our full solution from each scale of resolution or each time/space scale or from each high-localized nonlinear eigenmode (Fig.1). The same is correct for the contribution to power spectral density (energy spectrum): we can take into account contributions from each level/scale of resolution. In all these models, numerical modelling demonstrates the appearance of coherent high-localized structures and (meta)stable patterns formation. In part 2 we start from the description of Vlasov-Maxwell-Poisson equations, root-mean-square (RMS) envelope dynamics and beam-beam interaction model, after that in part 3 we consider our generic approach based on variational-multiresolution formulation. We give explicit representation for all dynamical variables in the base of compactly supported wavelets or nonlinear eigenmodes. Our solutions are parametrized by solutions of a number of reduced algebraical problems, one from which is nonlinear with the same degree of nonlinearity and the rest are the linear problems which correspond to a particular method of calculation of scalar products of functions from wavelet bases and their derivatives. In part 4, we consider numerical modelling based on our analytical approach.

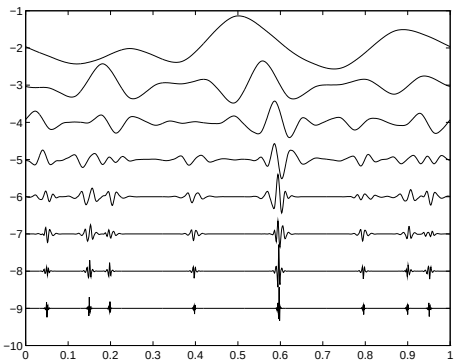

Figure 1: Multiscale/high-localized eigenmodes decomposition.

2 Collective models

2.1 Vlasov-Maxwell-Poisson equations

Analysis based on the full form of nonlinear Vlasov-Maxwell-Poisson equations leads to more clear understanding of the collective effects and nonlinear beam dynamics of high intensity beam propagation in the periodic-focusing and uniform-focusing transport systems. We consider the following form of equations ([1],[2] for setup and designation):

$$\Big\{\frac{\partial}{\partial s}+p_x\frac{\partial}{\partial x}+p_y\frac{\partial}{\partial y}-\Big[k_x(s)x+\frac{\partial\psi}{\partial x}\Big]\frac{\partial}{\partial p_x}-$$
$$\Big[k_y(s)y+\frac{\partial\psi}{\partial y}\Big]\frac{\partial}{\partial p_y}\Big\}f_b(x,y,p_x,p_y,s)=0, \tag{4}$$
$$\Big(\frac{\partial^2}{\partial x^2}+\frac{\partial^2}{\partial y^2}\Big)\psi=-\frac{2\pi K_b}{N_b}\int \mathrm{d}p_x\mathrm{d}p_y f_b, \tag{5}$$
$$\int \mathrm{d}x\mathrm{d}y\mathrm{d}p_x\mathrm{d}p_y f_b=N_b \tag{6}$$

The corresponding Hamiltonian for transverse single-particle motion is given by

$$H(x,y,p_x,p_y,s)=\frac{1}{2}(p_x^2+p_y^2)+\frac{1}{2}[k_x(s)x^2 \tag{7}$$
$$+k_y(s)y^2]+H_1(x,y,p_x,p_y,s)+\psi(x,y,s),$$

where H_1 is nonlinear (polynomial/rational) part of the full Hamiltonian. In case of Vlasov-Maxwell-Poisson system we may transform (4) into invariant form

$$\frac{\partial f_b}{\partial s}+[f,H]=0. \tag{8}$$

2.2 RMS equations

We consider an approach based on the second moments of distribution functions for calculation of the evolution of RMS envelope of a beam. The RMS envelope equations are the most useful for analysis of the beam self–forces (space–charge) effects and also allow to consider both transverse and longitudinal dynamics of space-charge-dominated relativistic high–brightness axisymmetric/asymmetric beams, which under short laser pulse–driven radio-frequency photoinjectors have fast transition from nonrelativistic to relativistic regime [2]. Analysis of halo growth in beams, appeared as result of bunch oscillations in the particle-core model, is also based on three-dimensional envelope equations [2]. We can consider the different forms of RMS envelope equations, which are not more than nonlinear differential equations with rational nonlinearities and variable coefficients from the formal point of view. Let $f(x_1,x_2)$ be the distribution function which gives full information about noninteracting ensemble of beam particles regarding to trace space or transverse phase coordinates (x_1,x_2). Then we may extract the first nontrivial effects of collective dynamics from the second moments

$$\sigma^2_{x_ix_j} \;=\; <x_ix_j>=\int\int x_ix_jf(x_i,x_j)\mathrm{d}x_i\mathrm{d}x_j. \tag{9}$$

RMS emittance ellipse is given by $\varepsilon^2_{x,rms} =< x_i^2 >< x_j^2 > - < x_i x_j >^2$ $(i \neq j)$. Expressions for twiss parameters are also based on the second moments. We will consider the following particular cases of RMS envelope equations, which describe the evolution of moments (9) ([2] for full designation): for asymmetric beams we have the system of two envelope equations of the second order for σ_{x_1} and σ_{x_2}:

$$\sigma^{''}_{x_1} + \sigma^{'}_{x_1}\frac{\gamma'}{\gamma} + \Omega^2_{x_1}\left(\frac{\gamma'}{\gamma}\right)^2 \sigma_{x_1} = I/(I_0(\sigma_{x_1}+\sigma_{x_2})\gamma^3) + \varepsilon^2_{nx_1}/\sigma^3_{x_1}\gamma^2, \qquad (10)$$
$$\sigma^{''}_{x_2} + \sigma^{'}_{x_2}\frac{\gamma'}{\gamma} + \Omega^2_{x_2}\left(\frac{\gamma'}{\gamma}\right)^2 \sigma_{x_2} = I/(I_0(\sigma_{x_1}+\sigma_{x_2})\gamma^3) + \varepsilon^2_{nx_2}/\sigma^3_{x_2}\gamma^2.$$

The envelope equation for an axisymmetric beam is a particular case of preceding equations. Also we have the related Lawson equation for evolution of RMS envelope in the paraxial limit, which governs evolution of cylindrical symmetric envelope under external linear focusing channel of strenght K_r:

$$\sigma^{''} + \sigma^{'}\left(\frac{\gamma'}{\beta^2\gamma}\right) + K_r\sigma = \frac{k_s}{\sigma\beta^3\gamma^3} + \frac{\varepsilon_n^2}{\sigma^3\beta^2\gamma^2}, \qquad (11)$$

where $K_r \equiv -F_r/r\beta^2\gamma mc^2$, $\quad \beta \equiv \nu_b/c = \sqrt{1-\gamma^{-2}}$. According to [2] we have the following form for envelope equations in the model of halo formation by bunch oscillations:

$$\begin{aligned} \ddot{X} + k_x^2(s)X - \frac{3K}{8}\frac{\xi_x}{YZ} - \frac{\varepsilon_x^2}{X^3} &= 0, \\ \ddot{Y} + k_y^2(s)Y - \frac{3K}{8}\frac{\xi_y}{XZ} - \frac{\varepsilon_y^2}{Y^3} &= 0, \\ \ddot{Z} + k_z^2(s)Z - \gamma^2\frac{3K}{8}\frac{\xi_z}{XY} - \frac{\varepsilon_z^2}{Z^3} &= 0, \end{aligned} \qquad (12)$$

where X(s), Y(s), Z(s) are bunch envelopes, ξ_x, ξ_y, $\xi_z = F(X,Y,Z)$.
After transformations to the Cauchy form we can see that all these equations from the formal point of view are not more than ordinary differential equations with rational nonlinearities and variable coefficients Also, we may consider regimes in which γ, γ' are not fixed functions/constants but satisfy some additional differential constraints/equations, but this case does not change our general approach of the next part.

2.3 Beam-beam modelling

In A. Chao e.a. model [3] for simulation of beam-beam interaction, the initial collective description for distribution function $f(s,x,p)$

$$\frac{\partial f}{\partial s} + p\frac{\partial f}{\partial x} - (k(s)x - F(x,s))\frac{\partial f}{\partial p} = 0 \qquad (13)$$

is reduced to Fockker-Planck (FP) equations on the first stage and after that to a very nontrivial dynamical system with complex behaviour:

$$\begin{aligned} &\frac{\mathrm{d}^2\sigma_k}{\mathrm{d}s^2} + \Gamma_k\frac{\mathrm{d}\sigma_k}{\mathrm{d}s} + F_k\sigma_k = \frac{1}{\beta_k^2 a_k^2\sigma_k^3}, \\ &\frac{\mathrm{d}a_n}{\mathrm{d}s} = \Gamma_k a_k(1 - a_k^2\sigma_k^2). \end{aligned} \qquad (14)$$

The solutions of dynamical system (14) provides the parameters of enveloping gaussian anzatz for solution of initial FP equations on the second stage of this global reduction which encodes stochastic collective motion into the data describing behaviour of nonlinear dynamic system.

3 Rational dynamics

After some anzatzes ([4]-[15]) all problems above may be reduced to the dynamical systems (cases 2.2 and 2.3 (system (14)) above):

$$Q_i(x)\frac{\mathrm{d}x_i}{\mathrm{d}t} = P_i(x,t), \quad x = (x_1, ..., x_n), \tag{15}$$
$$i = 1, ..., n, \quad \max_i deg\ P_i = p, \quad \max_i deg\ Q_i = q$$

or a set of such systems (cases 2.1, 2.3 (full equation (13)) above) corresponding to each independent coordinate in phase space. They have the fixed initial (or boundary) conditions $x_i(0)$, where P_i, Q_i are not more than polynomial functions of dynamical variables x_j and have arbitrary dependence of time. Because of time dilation we can consider only next time interval: $0 \leq t \leq 1$. Let us consider a set of functions

$$\Phi_i(t) = x_i\frac{\mathrm{d}}{\mathrm{d}t}(Q_i y_i) + P_i y_i \tag{16}$$

and a set of functionals

$$F_i(x) = \int_0^1 \Phi_i(t)dt - Q_i x_i y_i \mid_0^1, \tag{17}$$

where $y_i(t)$ $(y_i(0) = 0)$ are dual (variational) variables. It is obvious that the initial system and the system

$$F_i(x) = 0 \tag{18}$$

are equivalent. Of course, we consider regular $Q_i(x)$ at $t = 0$ or $t = 1$, i.e. $Q_i(x(0)), Q_i(x(1)) \neq \infty$. Now we consider formal expansions for x_i, y_i:

$$x_i(t) = x_i(0) + \sum_k \lambda_i^k \varphi_k(t) \quad y_j(t) = \sum_r \eta_j^r \varphi_r(t), \tag{19}$$

where $\varphi_k(t)$ are basis functions for proper functional space (L^2, L^p, Sobolev, etc.), which corresponds to concrete particular problem. It should be noted that initial conditions demand only $\varphi_k(0) = 0$ and for $r = 1, ..., N, \quad i = 1, ..., n$, we collect the "generalized Fourier coefficients" in the following data set:

$$\lambda = \{\lambda_i\} = \{\lambda_i^r\} = (\lambda_i^1, \lambda_i^2, ..., \lambda_i^N), \tag{20}$$

where the lower index i corresponds to expansion of dynamical variable with index i, i.e. x_i and the upper index r correspond to the numbers of terms in the expansion of dynamical variables in the formal series. Then we put (19) into the functional

equations (18) and as a result we have the following reduced algebraical system of equations on the set of unknown coefficients λ_i^k of expansions (19):

$$L(Q_{ij}, \lambda, \alpha_I) = M(P_{ij}, \lambda, \beta_J), \tag{21}$$

where operators L and M are algebraization of RHS and LHS of initial problem (15) and the data set λ (20) are unknowns of Reduced System of Algebraical Equations (RSAE)(21). Here Q_{ij} are the coefficients (with possible time dependence) of LHS of initial system of differential equations (15) and as a consequence the coefficients of RSAE, while P_{ij} are coefficients (with possible time dependence) of RHS of initial system of differential equations (15) and as a consequence the coefficients of reduced RSAE too. $I = (i_1, ..., i_{q+2})$, $J = (j_1, ..., j_{p+1})$ are multiindexes by which are labelled α_I and β_I, which are the other coefficients of RSAE (21). So, we have:

$$\beta_J = \{\beta_{j_1 ... j_{p+1}}\} = \int \prod_{1 \le j_k \le p+1} \varphi_{j_k}, \tag{22}$$

where p is the degree of polinomial operator P (15)

$$\alpha_I = \{\alpha_{i_1} ... \alpha_{i_{q+2}}\} = \sum_{i_1, ..., i_{q+2}} \int \varphi_{i_1} ... \dot{\varphi_{i_s}} ... \varphi_{i_{q+2}}, \tag{23}$$

where q is the degree of polynomial operator Q (15), $i_\ell = (1, ..., q+2)$, $\dot{\varphi_{i_s}} = \mathrm{d}\varphi_{i_s}/\mathrm{d}t$. Now we can solve RSAE (21) and determine unknown coefficients of the formal expansion (19), therefore we can obtain the solution for our initial problem (15). It should be noted that during modelling we consider only the truncated expansions (19) with N terms, so we have, from (21), the system of $N \times n$ algebraical equations with degree $\ell = max\{p, q\}$ and the degree of this algebraical system coincides with the degree of initial differential system. Finally, we have the solution of the initial nonlinear (rational) problem in the following form (it is a particular form of our general multiscale representation (1)-(3)):

$$x_i(t) = x_i(0) + \sum_{k=1}^{N} \lambda_i^k X_k(t), \tag{24}$$

where coefficients λ_i^k are roots of the corresponding reduced algebraical (polynomial) problem RSAE (21). Consequently, we have a parametrization of solution of initial problem by solution of reduced algebraical problem (21). The first main problem is a problem of computations of the coefficients α_I (23), β_J (22) of the reduced algebraical system. These problems may be explicitly solved inside multiresolution approach [4]-[15]. The obtained solutions are given in the form (24), where $X_k(t)$ are basis functions and λ_k^i are roots of reduced system of equations. In our case $X_k(t)$ are obtained via multiresolution expansions and represented by compactly supported wavelets and λ_k^i are roots of the corresponding general polynomial system (21). Because affine group of translation and dilations is inside the approach, this method resembles the action of a microscope. We have contribution to final result from each scale of resolution from the whole infinite scale of spaces. More exactly, the closed subspace $V_j (j \in \mathbf{Z})$ corresponds to level j of resolution, or to scale j.

We consider multiresolution analysis on $L^2(\mathbf{R}^n)$ [16] (of course, we may consider any different and proper functional space), which is a sequence of increasing closed subspaces V_j: $...V_{-2} \subset V_{-1} \subset V_0 \subset V_1 \subset V_2 \subset ...$ satisfying the following properties: let W_j be the orthonormal complement of V_j with respect to $V_{j+1} : V_{j+1} = V_j \bigoplus W_j$, then

$$L^2(\mathbf{R}) = \overline{V_0 \bigoplus_{j=0}^{\infty} W_j}. \tag{25}$$

Such a functional space decomposition corresponds to the exact nonlinear (maximally) localized eigenmode decomposition (1)-(3). It should be noted that such representations give the best possible localization properties in the corresponding (phase)space/time coordinates. In contrast with different approaches formulas (1)-(3), (24) or, in general, (25) do not use perturbation technique or linearization procedures and represent exact dynamical evolution via generalized nonlinear localized eigenmodes. Finally, by using multiresolution decomposition which provides best localization in the underlying functional space, we can construct high-localized coherent structures in spatially–extended stochastic systems with collective behaviour. Definitely, coherence is a consequence of action of internal hidden symmetry which is a generic property of mutiresolution decomposition.

4 Modelling

Resulting multiresolution/multiscale representations for solutions of equations from part 2 in the high-localized bases/eigenmodes are demonstrated on Fig. 2–Fig. 7. Multiscale modelling [17] demonstrates the appearance of (meta)stable patterns formation from high-localized coherent structures. Fig. 2, Fig. 3 present contribution to the full expansion (1)-(3) from level 1 and level 4 of decomposition (25). Figures 4, 5 show the representations for full solutions, constructed from the first 6 eigenmodes (6 levels in formula (25)). Figures 6, 7 show (meta)stable patterns formation based on high-localized coherent structures.

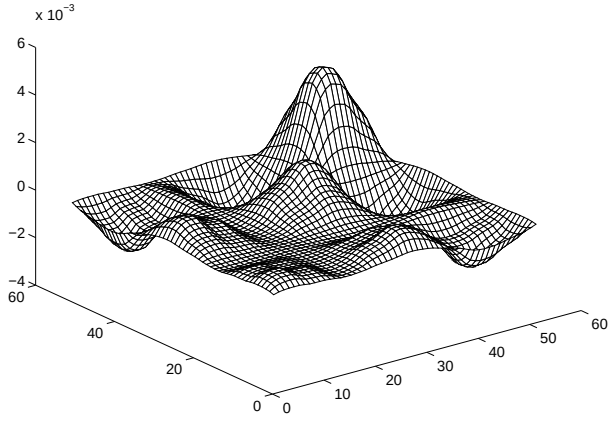

Figure 2: Base localized eigenmode

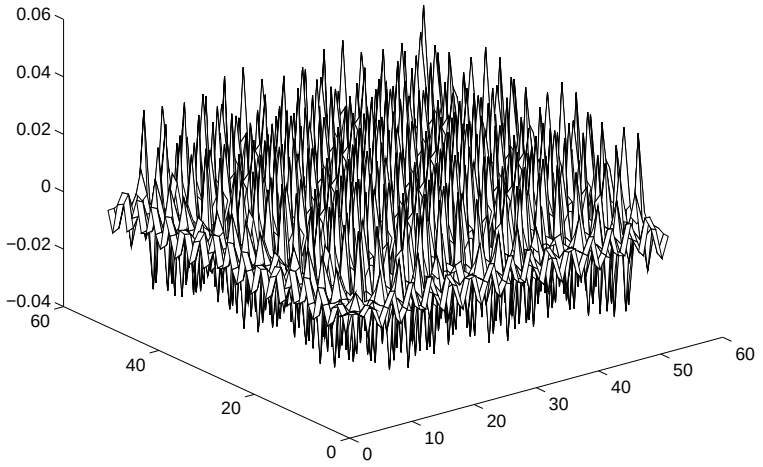

Figure 3: Four-eigenmodes decomposition

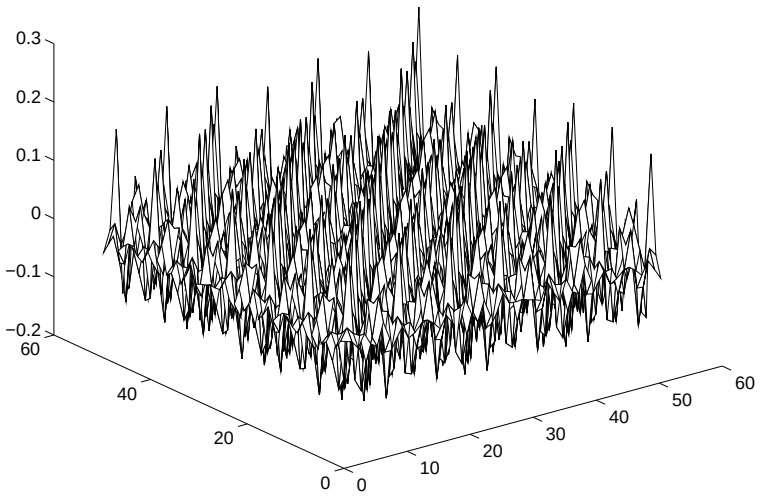

Figure 4: Appearence of coherent structure

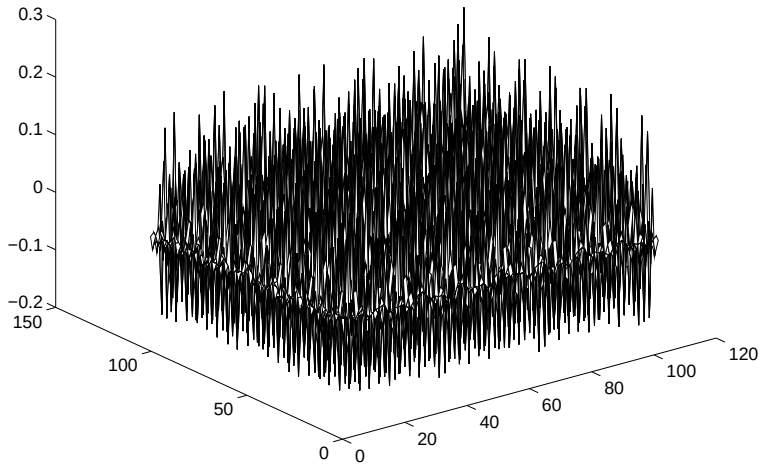

Figure 5: Six-eigenmodes decomposition

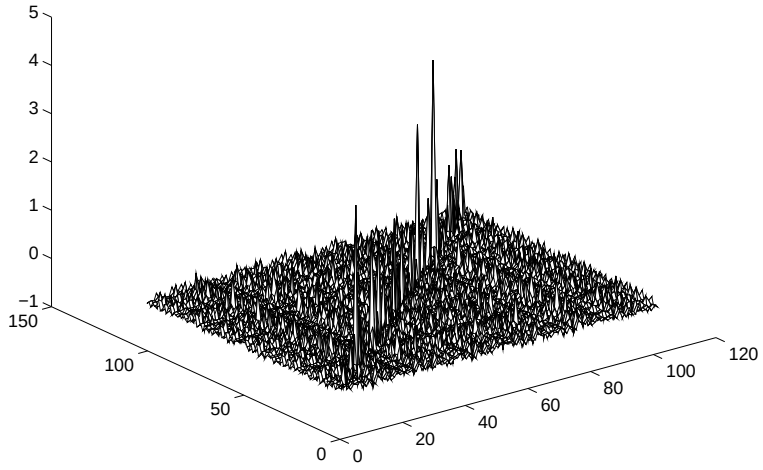

Figure 6: (Meta)Stable pattern 1

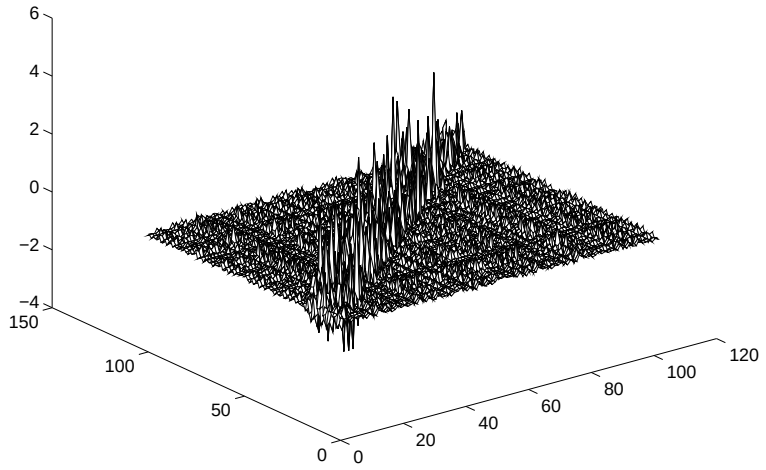

Figure 7: (Meta)Stable pattern 2

References

[1] R. Davidson, H. Qin, P. Channel, PRSTAB, 2, 074401, 1999.

[2] J.B. Rosenzweig, Fundamentals of Beam Physics, e-version: http://www.physics.ucla.edu/class/99F/250Rosenzweig/notes/ L. Serafini and J.B. Rosenzweig, *Phys. Rev. E* **55**, 7565, 1997; C. Allen, T. Wangler, papers in UCLA ICFA Proc., World Sci., 2000.

[3] A. Chao, e.a., Los Alamos preprint, physics/0010055.

[4] A.N. Fedorova and M.G. Zeitlin, Wavelets in Optimization and Approximations, *Math. and Comp. in Simulation*, **46**, p. 527, 1998.

[5] A.N. Fedorova and M.G. Zeitlin, Wavelet Approach to Mechanical Problems. Symplectic Group, Symplectic Topology and Symplectic Scales p.31; Wavelet Approach to Polynomial Mechanical Problems, p. 101, in *New Applications of Nonlinear and Chaotic Dynamics in Mechanics*, Ed. F. Moon, Kluwer, 1998.

[6] A.N. Fedorova and M.G. Zeitlin, Nonlinear Dynamics of Accelerator via Wavelet Approach, in **CP405**, p. 87, American Institute of Physics, 1997.
Los Alamos preprint, physics/9710035.

[7] A.N. Fedorova, M.G. Zeitlin and Z. Parsa, Wavelet Approach to Accelerator Problems, parts I, II, III, in Proc. PAC97 **2**, pp. 1502, 1505, 1508, American Physical Society/IEEE, 1998.

[8] A.N. Fedorova, M.G. Zeitlin and Z. Parsa, Nonlinear Effects in Accelerator Physics: from Scale to Scale via Wavelets, p. 930; Wavelet Approach to Hamiltonian, Chaotic and Quantum Calculations in Accelerator Physics, p. 933, in Proc. EPAC98, Institute of Physics, 1998.

[9] A.N. Fedorova, M.G. Zeitlin and Z. Parsa, Variational Approach in Wavelet Framework to Polynomial Approximations of Nonlinear Accelerator Problems, p. 48, in **CP468**, American Institute of Physics, 1999. Los Alamos preprint, physics/990262.

[10] A.N. Fedorova, M.G. Zeitlin and Z. Parsa, Symmetry, Hamiltonian Problems and Wavelets in Accelerator Physics, p. 69, in **CP468**, American Institute of Physics, 1999. Los Alamos preprint, physics/990263.

[11] A.N. Fedorova, M.G. Zeitlin, Nonlinear Accelerator Problems via Wavelets, Parts 1-8, in Proc. PAC99, pp. 1614, 1617, 1620, 2900, 2903, 2906, 2909, 2912, American Institute of Physics/IEEE, New York, 1999. Los Alamos preprints: physics/9904039,physics/9904040, physics/9904041, physics/9904042, physics/9904043, physics/9904045, physics/9904046, physics/9904047.

[12] A.N. Fedorova, M.G. Zeitlin, Variational-Wavelet Approach to RMS Envelope Equations, p. 235, in The Physics of High Brightness Beams, World Scientific, 2000. Los Alamos preprint: physics/0003095.

[13] A.N. Fedorova, M.G. Zeitlin, Spin-Orbital Motion: Symmetry and Dynamics, p. 415; Local Analysis of Nonlinear RMS Envelope Dynamics, p. 872; Multiresolution Representation for Orbital Dynamics in Multipolar Fields, p. 1101; Quasiclassical Calculations in Beam Dynamics, p. 1190; Multiscale Representations for Solutions of Vlasov-Maxwell Equations for Intense Beam Propagation, p. 1339; Nonlinear Beam Dynamics and Effects of Wigglers, p. 2325, in Proc. EPAC00, Austrian Acad. Sci., 2000. Los Alamos preprints: physics/0008045, physics/0008046, physics/0008047, physics/0008048, physics/0008049, physics/0008050.

[14] A.N. Fedorova, M.G. Zeitlin, Multiscale Analysis of RMS Envelope Dynamics, p. 300; Multiresolution Representations for Solutions of Vlasov - Maxwell - Poisson Equations,p. 303, in Proc. 20 International Linac Conf., SLAC, Stanford, 2000. Los Alamos preprints: physics/0008043, physics/0008200.

[15] A.N. Fedorova, M.G. Zeitlin, Localized Coherent Structures and Patterns Formation in Collective Models of Beam Motion, p. 527; Quasiclassical Calculations for Wigner Functions via Multiresolution, p. 539, in Quantum Aspects of Beam Physics, ed. P. Chen, World Scientific, 2002. Los Alamos preprints:physics/0101006, physics/0101007.

[16] Y. Meyer, Wavelets and Operators, CUP, 1990.

[17] D. Donoho, WaveLab, Stanford, 1998.

Antonina N. Fedorova, Michael G. Zeitlin
Mathematical Methods in Mechanics Group, IPME RAS, V.O. Bolshoj pr., 61, 199178, St. Petersburg, Russia
http://math.ipme.ru/zeitlin.html, http://mp.ipme.ru/zeitlin.html

Wigglers: nonlinearities in multiscales. From smart storage rings to synchrotron radiation in pulsar wind nebulae

Antonina N. Fedorova, Michael G. Zeitlin
zeitlin@math.ipme.ru, anton@math.ipme.ru

Abstract

We consider dynamics of high-energy beams in storage rings in the presence of external insertion devices like wigglers and undulator magnets which provide: (a) an additional damping of betatron and synchrotron oscillations to create a smart beam storage system, (b) the generation of high-power synchrotron radiation, very important as for a lot of applications as well for the understanding of a number of (astrophysical) phenomena, e.g. the evolution of pulsar wind nebulae. Our machinery is based on applications of our variational–multiscale approach for the analytical/numerical treatment of the effects of insertion devices on beam dynamics. We consider the dynamical models which have polynomial nonlinearities and variable coefficients. Our approach provides all dynamical variables by exact multiscale decomposition on the whole tower of the underlying scales starting with coarse one. The generalized dispersion relations provide, in principle, the possibility for the control of dynamics on the pure algebraical level. It is very important that the description of natural nonlinearities are considered on each scale of the whole multiscale decomposition separately in the framework of the general paraproducts technique.

1 Introduction

In this paper, we consider the applications of our numerical-analytical technique [1]-[12] which is based on the methods of Local Nonlinear Harmonic Analysis (LNHA) (or wavelet analysis in the simplest case), to the treatment of effects of insertion devices on beam dynamics. Our approach is based on a generalization of the variational-multiscale approach that allows to consider both the polynomial and rational type of nonlinearities. We present the solution via full multiresolution expansion in all time/space/phase space scales, which gives us the expansion into a slow (coarse) part and fast oscillating parts. So, we may decompose our dynamical process into coarse scales of resolution and the finest one for obtaining more detailed (full, in principle) information about our dynamical process. In this way we give contribution to our exact solution from each scale of resolution. The same

is correct for the contribution to power spectral density (energy spectrum): we can take into account contributions from all underlying high-localized modes. In Part 2 we consider initial set-up for generic dynamical problem: how we may take into the account the effects of insertion external devices, like bending magnets, wigglers, undulators, on complex beam dynamics. In Part 3 we consider general framework for construction of the explicit representation for all dynamical variables in the base of maximally high localized eigenmodes (compactly supported wavelets or wavelet packets). Then, in Part 4, we consider further extension of our previous results to the case of variable coefficients. Part 5 is devoted to very important facilities that allow to consider the natural nonlinearities on each scale of the whole multiscale decomposition separately in the framework of the general paraproducts technique. These last chapters are very important for the description of Free Electron Laser and general Synchrotron Radiation considered in details in separate publications. Finally, in Part 6 we consider some numerical experiments and perspectives based on our machinery here.

2 Effects of insertion devices on beam dynamics

Assuming a sinusoidal field variation, we may consider according to [13] the analytical treatment of the effects of insertion devices on beam dynamics. One of the major harmful aspects of the installation of insertion devices is the resulting reduction of dynamic aperture. The introduction of non-linearities leads to enhancement of the amplitude-dependent tune shifts and distortion of phase space. The nonlinear fields will produce significant effects at large betatron amplitudes such as excitation of n–order resonances. The components of the insertion device vector potential used for the derivation of equations of motion are as follows:

$$\begin{aligned} A_x &= \cosh(k_x x)\cosh(k_y y)\sin(ks)/(k\rho) \\ A_y &= k_x \sinh(k_x x)\sinh(k_y y)\sin(ks)/(k_y k\rho) \end{aligned} \tag{1}$$

with $k_x^2 + k_y^2 = k^2 = (2\pi/\lambda)^2$, where λ is the period length of the insertion device, ρ is the radius of the curvature in the field B_0. After a canonical transformation to betatron variables, the Hamiltonian is averaged over the period of the insertion device and hyperbolic functions are expanded to the fourth order in x and y (or arbitrary order). Then we have the following Hamiltonian:

$$\begin{aligned} H &= \frac{1}{2}[p_x^2 + p_y^2] + \frac{1}{4k^2\rho^2}[k_x^2 x^2 + k_y^2 y^2] \\ &+ \frac{1}{12k^2\rho^2}[k_x^4 x^4 + k_y^4 y^4 + 3k_x^2 k^2 x^2 y^2] \\ &- \frac{\sin(ks)}{2k\rho}[p_x(k_x^2 x^2 + k_y^2 y^2) - 2k_x^2 p_y xy] \end{aligned} \tag{2}$$

We have in this case also the nonlinear (polynomial with degree 3) dynamical system with variable (periodic) coefficients. After averaging motion over the magnetic

period we have the following generic dynamical system:

$$\begin{aligned} \ddot{x} &= -\frac{k_x^2}{2k^2\rho^2}\left[x+\frac{2}{3}k_x^2x^3\right]-\frac{k_x^2xy^2}{2\rho^2} \\ \ddot{y} &= -\frac{k_y^2}{2k^2\rho^2}\left[y+\frac{2}{3}k_y^2y^3\right]-\frac{k_x^2x^2y}{2\rho^2} \end{aligned} \tag{3}$$

3 Wavelet framework

The first main part of our consideration is some variational approach to this problem, which reduces the initial problem to the problem of solution of functional equations at the first stage and some algebraical problems at the second stage. Multiresolution expansion is the second main part of our construction. Because affine group of translation and dilations is inside the approach, this method resembles the action of a microscope. We have contribution to final result from each scale of resolution from the whole infinite scale of the increasing closed subspaces V_j: $...V_{-2} \subset V_{-1} \subset V_0 \subset V_1 \subset V_2 \subset ....$ The solution is parameterized by solutions of several reduced algebraical problems, one is nonlinear and the rest ones are some linear problems, which are obtained by the method of Connection Coefficients (CC) [14]. We use here the generic compactly supported wavelet basis. Let our multiscale wavelet expansion be:

$$f(x) = \sum_{\ell\in\mathbf{Z}} c_\ell\varphi_\ell(x) + \sum_{j=0}^{\infty}\sum_{k\in\mathbf{Z}} c_{jk}\psi_{jk}(x) \tag{4}$$

If $c_{jk} = 0$ for $j \geq J$, then $f(x)$ has an alternative expansion in terms of dilated scaling functions only: $f(x) = \sum\limits_{\ell\in\mathbf{Z}} c_{J\ell}\varphi_{J\ell}(x)$. This is a finite wavelet expansion, it can be written solely in terms of translated scaling functions. To solve our second associated linear problem we need to evaluate derivatives of $f(x)$ in terms of $\varphi(x)$. Let $\varphi_\ell^n = \mathrm{d}^n\varphi_\ell(x)/\mathrm{d}x^n$. We consider computation of the wavelet - Galerkin integrals. Let $f^d(x)$ be d-derivative of function $f(x)$, then we have $f^d(x) = \sum_\ell c_l\varphi_\ell^d(x)$, and values $\varphi_\ell^d(x)$ can be expanded in terms of $\varphi(x)$:

$$\begin{aligned} \varphi_\ell^d(x) &= \sum_m \lambda_m\varphi_m(x) \\ \lambda_m &= \int_{-\infty}^{\infty} \varphi_\ell^d(x)\varphi_m(x)\mathrm{d}x \end{aligned} \tag{5}$$

where λ_m are wavelet-Galerkin integrals. The coefficients λ_m are 2-term connection coefficients. In general we need to find $(d_i \geq 0)$:

$$\Lambda_{\ell_1\ell_2\ldots\ell_n}^{d_1d_2\ldots d_n} = \int_{-\infty}^{\infty}\prod\varphi_{\ell_i}^{d_i}(x)dx \tag{6}$$

For the case of degree three we need to evaluate two and three connection coefficients

$$\Lambda_\ell^{d_1 d_2} = \int_{-\infty}^{\infty} \varphi^{d_1}(x)\varphi_\ell^{d_2}(x)dx, \tag{7}$$
$$\Lambda^{d_1 d_2 d_3} = \int_{-\infty}^{\infty} \varphi^{d_1}(x)\varphi_\ell^{d_2}(x)\varphi_m^{d_3}(x)dx$$

According to CC method [14] we use the next construction. When N in scaling equation is a finite even positive integer, the function $\varphi(x)$ has compact support contained in $[0, N-1]$. For a fixed triple (d_1, d_2, d_3) only some $\Lambda_{\ell m}^{d_1 d_2 d_3}$ are nonzero: $2-N \le \ell \le N-2$, $2-N \le m \le N-2$, $|\ell - m| \le N-2$. There are $M = 3N^2 - 9N + 7$ such pairs (ℓ, m). Let $\Lambda^{d_1 d_2 d_3}$ be a M-vector, whose components are numbers $\Lambda_{\ell m}^{d_1 d_2 d_3}$. Then we have the first reduced algebraical system, where Λ satisfy the following system of equations ($d = d_1 + d_2 + d_3$):

$$A\Lambda^{d_1 d_2 d_3} = 2^{1-d}\Lambda^{d_1 d_2 d_3} \tag{8}$$
$$A_{\ell,m;q,r} = \sum_p a_p a_{q-2\ell+p} a_{r-2m+p}$$

By moment equations we have created a system of $M + d + 1$ equations in M unknowns. It has rank M and we can obtain unique solution by combination of LU decomposition and QR algorithm. The second reduced algebraical system gives us the 2-term connection coefficients ($d = d_1 + d_2$):

$$A\Lambda^{d_1 d_2} = 2^{1-d}\Lambda^{d_1 d_2}, \quad A_{\ell,q} = \sum_p a_p a_{q-2\ell+p} \tag{9}$$

For degree more than three we have analogous additional linear problems for generic objects (6). Solving these linear problems we obtain the coefficients of the reduced nonlinear algebraical system and after that we obtain the coefficients of wavelet expansion (4). As a result we obtain the explicit exact solution of our problem in the base of compactly supported wavelets. On Fig. 1 we present an example of the base wavelet function which satisfies some boundary conditions. In the following we consider extension of this approach to the case of arbitrary variable coefficients.

4 Variable coefficients

To cover the general treatment of possible insertion device, in addition to the model described by the nonlinear (rational) differential equations, we need to consider the extension of the previous approach to the case when we take into account any type of variable coefficients (periodic, regular or singular). We can do that rather simple: we add to our construction above an additional refinement equation, which encoded all information about variable coefficients [15]. According to our variational approach we need to compute only additional integrals of the form:

$$\int_D b_{ij}(t)(\varphi_1)^{d_1}(2^m t - k_1)(\varphi_2)^{d_2}(2^m t - k_2)\mathrm{d}x, \tag{10}$$

where $b_{ij}(t)$ are arbitrary functions of time and trial functions φ_1, φ_2 satisfy the refinement equations:

$$\varphi_i(t) = \sum_{k \in \mathbf{Z}} a_{ik} \varphi_i(2t - k) \tag{11}$$

If we consider all computations in the class of compactly supported wavelets, then only a finite number of coefficients do not vanish. To approximate the non-constant coefficients, we need to choose a different refinable function φ_3 along with some local approximation scheme:

$$(B_\ell f)(x) := \sum_{\alpha \in \mathbf{Z}} F_{\ell,k}(f) \varphi_3(2^\ell t - k), \tag{12}$$

where $F_{\ell,k}$ are suitable functionals supported in a small neighborhood of $2^{-\ell}k$ and then replace b_{ij} in (10) by $B_\ell b_{ij}(t)$. In the particular case one can take a characteristic function and thus approximate non-smooth coefficients locally. To guarantee the sufficient accuracy of the resulting approximation of (10) it is important to have the flexibility of choosing φ_3 different from φ_1, φ_2. In the case when D is some domain, we can write

$$b_{ij}(t) \mid_D = \sum_{0 \le k \le 2^\ell} b_{ij}(t) \chi_D(2^\ell t - k), \tag{13}$$

where χ_D is the characteristic function of D. So, if we take $\varphi_4 = \chi_D$, which is again a refinable function, then the problem of computation of (10) is reduced to the problem of calculation of the integrals:

$$H(k_1, k_2, k_3, k_4) = H(k) = \int_{\mathbf{R}^s} \varphi_4(2^j t - k_1) \cdot \varphi_3(2^\ell t - k_2) \varphi_1^{d_1}(2^r t - k_3) \varphi_2^{d_2}(2^s t - k_4) \mathrm{d}x \tag{14}$$

The key point is that these integrals also satisfy some sort of refinement equation [15]:

$$2^{-|\mu|} H(k) = \sum_{\ell \in \mathbf{Z}} b_{2k-\ell} H(\ell), \qquad \mu = d_1 + d_2 \tag{15}$$

This equation can be interpreted as the problem of computing an eigenvector. Thus, after all that, we reduced the problem of extension of our method to the case of variable coefficients to the same standard algebraical problem as in the preceding sections. So, the general scheme is the same one and we have only one more additional linear algebraic problem by which we can parameterize the solutions of the corresponding problem in the same way.

On Fig. 2 we present, as a sample, a toy model for insertion device and on Fig. 3 the corresponding multiscale representation via localized eigenmodes according to formula (4).

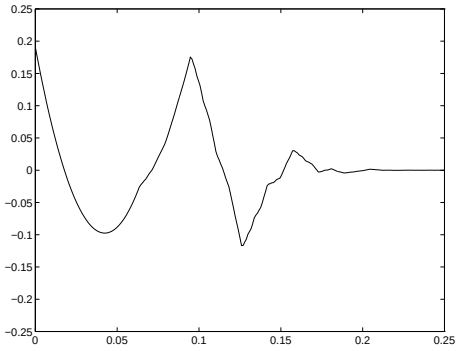

Figure 1: Base wavelet with fixed boundary conditions

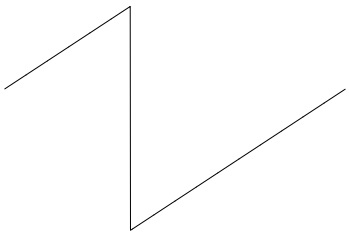

Figure 2: Sample insertion

5 Evaluation of Nonlinearities Scale by Scale

Here we present the modification of our variational–multiscale approach to the case that allows to consider separately different scales of general multiresolution. For this reason we need to compute the errors of approximations. The main problems come of course from nonlinear terms. We follow the approach from [15].
Let P_j be projection operators on the subspaces $V_j, j \in \mathbf{Z}$:

$$\begin{aligned} P_j &: L^2(\mathbf{R}) \to V_j \\ (P_j f)(x) &= \sum_k < f, \varphi_{j,k} > \varphi_{j,k}(x) \end{aligned} \tag{16}$$

and Q_j are projection operators on the subspaces W_j:

$$Q_j = P_{j-1} - P_j \tag{17}$$

So, for $u \in L^2(\mathbf{R})$ we have $u_j = P_j u$ and $u_j \in V_j$, where $\{V_j\}, j \in \mathbf{Z}$ is a multiresolution decomposition of $L^2(\mathbf{R})$. It is obviously that we can represent u_0^2 in the following form:

$$u_0^2 = 2\sum_{j=1}^{n}(P_j u)(Q_j u) + \sum_{j=1}^{n}(Q_j u)(Q_j u) + u_n^2 \tag{18}$$

In this formula there is no interaction between different scales. We may consider each term of (18) as the bilinear mappings:

$$M_{VW}^j : V_j \times W_j \to L^2(\mathbf{R}) = V_j \oplus_{j' \geq j} W_{j'} \tag{19}$$

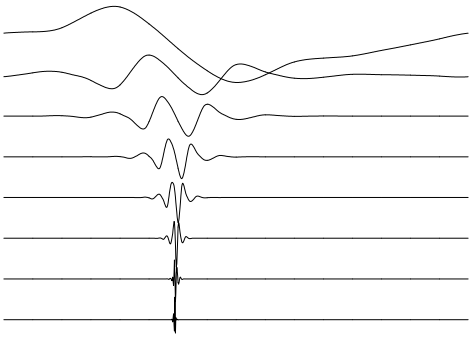

Figure 3: Multiscale representation via localized eigemodes

$$M^j_{WW} : W_j \times W_j \to L^2(\mathbf{R}) = V_j \oplus_{j' \geq j} W_{j'} \tag{20}$$

For numerical purposes we need decomposition like (18) with a finite number of scales, but when we consider limits $j \to \infty$ we will have:

$$u^2 = \sum_{j \in \mathbf{Z}} (2P_j u + Q_j u)(Q_j u), \tag{21}$$

which is para-product of Bony, Coifman and Meyer [15].
Now we need to expand (18) into the wavelet basis. To expand each term in (18) into such a wavelet basis, we need to consider the integrals of the products of the basis functions, e.g.:

$$M^{j,j'}_{WWW}(k,k',\ell) = \int_{-\infty}^{\infty} \psi^j_k(x)\psi^j_{k'}(x)\psi^{j'}_{\ell}(x)\mathrm{d}x, \tag{22}$$

where $j' > j$ and

$$\psi^j_k(x) = 2^{-j/2}\psi(2^{-j}x - k) \tag{23}$$

are the basis functions. If we consider compactly supported wavelets then

$$M^{j,j'}_{WWW}(k,k',\ell) \equiv 0 \quad \text{for} \quad |k - k'| > k_0, \tag{24}$$

where k_0 depends on the overlap of the supports of the basis functions and

$$|M^r_{WWW}(k - k', 2^r k - \ell)| \leq C \cdot 2^{-r\lambda M} \tag{25}$$

Let us define j_0 as the distance between scales such that for a given ε all the coefficients in (25) with labels $r = j - j'$, $r > j_0$ have absolute values less than ε. For the purposes of computing with accuracy ε we replace the mappings in (19), (20) by

$$M^j_{VW} : V_j \times W_j \to V_j \oplus_{j \leq j' \leq j_0} W_{j'} \tag{26}$$

$$M^j_{WW} : W_j \times W_j \to V_j \oplus_{J \leq j' \leq j_0} W_{j'} \tag{27}$$

Since

$$V_j \oplus_{j \le j' \le j_0} W_{j'} = V_{j_0 - 1} \tag{28}$$

and

$$V_j \subset V_{j_0-1}, \qquad W_j \subset V_{j_0-1} \tag{29}$$

we may consider bilinear mappings (26), (27) on $V_{j_0-1} \times V_{j_0-1}$. For the evaluation of (26), (27) as mappings $V_{j_0-1} \times V_{j_0-1} \to V_{j_0-1}$ we need significantly fewer coefficients than for mappings (26), (27). It is enough to consider only the coefficients

$$M(k, k', \ell) = 2^{-j/2} \int_{\infty}^{\infty} \varphi(x-k)\varphi(x-k')\varphi(x-\ell)\mathrm{d}x, \tag{30}$$

where $\varphi(x)$ is scale function. Also we have

$$M(k, k', \ell) = 2^{-j/2} M_0(k-\ell, k'-\ell), \tag{31}$$

where

$$M_0(p, q) = \int \varphi(x-p)\varphi(x-q)\varphi(x)\mathrm{d}x \tag{32}$$

Now, by the ideology of Part 3, we may derive and solve a system of linear equations to find $M_0(p, q)$ and as a result obtain the explicit representation for the solution at each scale separately.

6 Vista

We concentrated here on the general computation/analytical set-up and postponed applications to a separate paper but we need to mention that all applications, we are interested in, are covered by such a machinery. Our goals in this direction are two-fold. First of all we are interested in precise dynamics of high-energy beams in storage rings in the presence of external insertion devices like bending magnets, wigglers and undulators, which provide an additional damping of betatron and synchrotron oscillations and promise the smart beam storage systems in accelerator physics. Secondly, we hope to describe correctly the generation of high-power synchrotron radiation (including Free Electron Laser radiation), which is very important as for a lot of practical applications as well for the understanding of a number of (astrophysical) phenomena, e.g. the evolution of Crab Nebula (important experiment for understanding Lorentz violation and possible experimental signs of Quantum Gravity). In any case, the full zoo of possible patterns and coherent structures generated by hidden internal high localized modes via multiresolution representation was described by us in a companion paper in this Volume [16]. So, on the qualitative level, Figures 3 –7 [16] present all possible dynamical features, that we hope to characterize by our approach in present context: isolated high localized modes (Fig. 2 [16]), chaotic, coherent and (meta)stable localized patterns/waveletons (Figures 3–7 [16]).

References

[1] A.N. Fedorova and M.G. Zeitlin, Wavelets in Optimization and Approximations, *Math. and Comp. in Simulation*, **46**, p. 527, 1998.

[2] A.N. Fedorova and M.G. Zeitlin, Wavelet Approach to Mechanical Problems. Symplectic Group, Symplectic Topology and Symplectic Scales p.31; Wavele t Approach to Polynomial Mechanical Problems, p. 101, in *New Applications of Nonlinear and Chaotic Dynamics in Mechanics*, Ed. F. Moon, Kluwer, 1998.

[3] A.N. Fedorova and M.G. Zeitlin, Nonlinear Dynamics of Accelerator via Wavelet Approach, in **CP405**, p. 87, American Institute of Physics, 1997.
Los Alamos preprint, physics/9710035.

[4] A.N. Fedorova, M.G. Zeitlin and Z. Parsa, Wavelet Approach to Accelerator Problems, parts I, II, III, in Proc. PAC97 **2**, pp. 1502, 1505, 1508, American Physical Society/IEEE, 1998.

[5] A.N. Fedorova, M.G. Zeitlin and Z. Parsa, Nonlinear Effects in Accelerator Physics: from Scale to Scale via Wavelets, p. 930; Wavelet Approach to Hamiltonian, Chaotic and Quantum Calculations in Accelerator Physics, p. 933, in Proc. EPAC98, Institute of Physics, 1998.

[6] A.N. Fedorova, M.G. Zeitlin and Z. Parsa, Variational Approach in Wavelet Framework to Polynomial Approximations of Nonlinear Accelerator Problems, p. 48, in **CP468**, American Institute of Physics, 1999. Los Alamos preprint, physics/990262.

[7] A.N. Fedorova, M.G. Zeitlin and Z. Parsa, Symmetry, Hamiltonian Problems and Wavelets in Accelerator Physics, p. 69, in **CP468**, American Institute of Physics, 1999. Los Alamos preprint, physics/990263.

[8] A.N. Fedorova, M.G. Zeitlin, Nonlinear Accelerator Problems via Wavelets, Parts 1-8, in Proc. PAC99, pp. 1614, 1617, 1620, 2900, 2903, 2906, 2909, 2912, American Institute of Physics/IEEE, New York, 1999. Los Alamos preprints: physics/9904039,physics/9904040, physics/9904041, physics/9904042, physics/9904043, physics/9904045, physics/9904046, physics/9904047.

[9] A.N. Fedorova, M.G. Zeitlin, Variational-Wavelet Approach to RMS Envelope Equations, p. 235, in The Physics of High Brightness Beams, World Scientific, 2000. Los Alamos preprint: physics/0003095.

[10] A.N. Fedorova, M.G. Zeitlin, Spin-Orbital Motion: Symmetry and Dynamics, p. 415; Local Analysis of Nonlinear RMS Envelope Dynamics, p. 872; Multiresolution Representation for Orbital Dynamics in Multipolar Fields, p. 1101; Quasiclassical Calculations in Beam Dynamics, p. 1190; Multiscale Representations for Solutions of Vlasov-Maxwell Equations for Intense Beam Propagation, p. 1339; Nonlinear Beam Dynamics and Effects of Wigglers, p. 2325, in Proc. EPAC00, Austrian Acad. Sci., 2000.

Los Alamos preprints: physics/0008045, physics/0008046, physics/0008047, physics/0008048, physics/0008049, physics/0008050.

[11] A.N. Fedorova, M.G. Zeitlin, Multiscale Analysis of RMS Envelope Dynamics, p. 300; Multiresolution Representations for Solutions of Vlasov - Maxwell - Poisson Equations,p. 303, in Proc. 20 International Linac Conf., SLAC, Stanford, 2000. Los Alamos preprints: physics/0008043, physics/0008200.

[12] A.N. Fedorova, M.G. Zeitlin, Localized Coherent Structures and Patterns Formation in Collective Models of Beam Motion, p. 527; Quasiclassical Calculations for Wigner Functions via Multiresolution, p. 539, in Quantum Aspects of Beam Physics, ed. P. Chen, World Scientific, 2002. Los Alamos preprints:physics/0101006, physics/0101007.

[13] A. Chao, e.a., Handbook on Accelerator Physics, 1999; A. Ropert, CERN, 98-04.

[14] A. Latto, H.L. Resnikoff and E. Tenenbaum, Aware Technical Report AD910708, 1991.

[15] W. Dahmen, C. Micchelli, *SIAM J. Numer. Anal.*, **30**, 507 (1993), Y. Meyer, Wavelets and Operators, Volumes 1-3, CUP, 1990.

[16] A.N. Fedorova, M. G. Zeitlin, Coherent structures and localized modes in collective models of accelerator physics, companion paper, This Volume.

Antonina N. Fedorova, Michael G. Zeitlin
Mathematical Methods in Mechanics Group, IPME RAS, V.O. Bolshoj pr., 61, 199178, St. Petersburg, Russia
http://math.ipme.ru/zeitlin.html, http://mp.ipme.ru/zeitlin.html

Backwards waves in a cylindrical shell: comparison of 2D shell theories with 3D theory of elasticity

G.V. Filippenko, M.V. Wilde
g.filippenko@gmail.com, g.filippenko@spbu.ru, mv_wilde@mail.ru

Abstract

Dispersion of elastic waves in an infinite circular cylindrical shell is studied with special attention to backwards waves. Two types of boundary conditions on the surfaces of the shell are considered: free faces and the spring-type boundary condition on the outer surface, analogous to Winkler foundation for a plate. For each fixed wavenumber in the circumferential direction three lowest modes are investigated both on the basis of 3D theory of elasticity and on the basis of 2D approximate shell theories. For the shell with spring-type boundary condition the results of analytical and numerical investigations of backwards waves are presented. The limits of applicability of 2D theories are illustrated by comparison with the 3D solution. For the shell with free faces it is shown that there are no backwards waves in the range of applicability of long-wave asymptotic approximations.

1 Introduction

Dispersion of elastic waves in a cylindrical shell has been investigated in numerous publications. The three-dimensional theory of elasticity [1] and approximate shell theories [2] were used to govern the motion of the shell. A number of papers are concerned with analysis of the accuracy of the classical Kirchhoff–Love theory of shells and its refinements [3, 4]. But in such a rich system as a shell the peculiar phenomena may occur which require a special study. In this paper the accuracy of approximate shell theories in the case of an anomalous dispersion characterized by opposite signs of the phase and group velocities (backwards waves) is investigated. For a shell with free faces, it is shown that this phenomenon does not occur in the range of applicability of 2D theories. The existing of a backward wave in the framework of the classical Kirchhoff–Love theory is not confirmed by 3D theory of elasticity. But it suggest that this wave can exist in a shell with some other material properties or under other boundary conditions on the faces, if the changes lead to increasing of the flexural stiffness of the shell. As an example of such a situation we consider a shell with spring-type boundary condition on the outer surface.

2 Statement of the problem

Consider an infinite cylindrical shell occupying in cylindrical coordinate system (r, θ, z) the domain $\{R - h/2 < r < R + h/2, 0 \leqslant \theta < 2\pi, -\infty < z < \infty\}$, where R is the radius of the midsurface, h is the thickness of the shell. Let us assume that the action of environment can be modeled as a normal load proportional to the transverse displacement with the coefficient K_0 (this model can be considered as an analogue of a plate on the Winkler foundation [5]). The harmonic vibrations with the circular frequency ω_0 are considered, the factor $\exp(-\mathrm{i}\omega_0 t)$ is omitted everywhere. Let us introduce curvilinear coordinates (θ, z) on the midsurface $r = R$. The equations of motion according to the Kirchhoff–Love-type theory of shells [6] can be written in the form

$$\begin{gathered}\left[\alpha_1\left(\partial_\theta{}^2+\nu_-\widetilde{\partial}_z^2\right)+\omega^2\right]u_1+\nu_+\widetilde{\partial}_z\partial_\theta u_2+\partial_\theta\left(1+2\alpha^2[1-\partial_\theta^2-\widetilde{\partial}_z^2]\right)u_n=0,\\ \nu_+\widetilde{\partial}_z\partial_\theta u_1+\left(\nu_-\partial_\theta^2+\widetilde{\partial}_z^2+\omega^2\right)u_2+\nu\widetilde{\partial}_z u_n=0,\\ -\partial_\theta(1+2\alpha^2[1-\partial_\theta^2-\widetilde{\partial}_z^2])u_1-\nu\widetilde{\partial}_z u_2\\ +\left[\alpha^2(2\partial_\theta^2-1+2\nu\widetilde{\partial}_z^2-[\partial_\theta^2+\widetilde{\partial}_z^2]^2)-1+\omega^2-4\nu_+\nu_-h_*^{-1}K\right]u_n=0,\end{gathered}\tag{1}$$

where u_1, u_2, u_n are components of the midsurface displacement in the circumferential, longitudinal and radial directions, respectively, $\widetilde{\partial}_z = R\partial_z$, $\alpha^2 = \frac{1}{12}\left(\frac{h}{R}\right)^2$, $\alpha_1 = 1 + 4\alpha^2$, $\nu_\pm = (1 \pm \nu)/2$, $h_* = h/R$ is the relative thickness of the shell, $K = K_0R/E$, $\omega = \omega_0 R/c_s$ is the dimensionless frequency, $c_s = \sqrt{E/((1-\nu^2)\rho)}$, E, ν, ρ are Young's modulus, Poisson's ratio and the density of the material.

In paper [7] the classical theory with modified inertia is proposed, which is constructed as higher order long-wave asymptotic approximation of 3D equations of elasticity. Let us present the equations of this theory in the form

$$\begin{gathered}\left[\partial_\theta{}^2\left(1+\alpha^2\right)+\nu_-\widetilde{\partial}_z^2\left(1+4\alpha^2\right)\right]u_1+\nu_+\widetilde{\partial}_z\partial_\theta u_2\\ +\partial_\theta\left(1-\alpha^2[\partial_\theta^2+(2-\nu)\widetilde{\partial}_z^2]\right)u_n+\left(I_{tg}\mathrm{u}_{tg}\right)_1=0,\\ \nu_+\widetilde{\partial}_z\partial_\theta u_1+\left(\nu_-\partial_\theta^2+\widetilde{\partial}_z^2\right)u_2+\nu\widetilde{\partial}_z u_n+\left(I_{tg}\mathrm{u}_{tg}\right)_2=0,\\ -\partial_\theta(1-\alpha^2[\partial_\theta^2+(2-\nu)\widetilde{\partial}_z^2])u_1-\nu\widetilde{\partial}_z u_2\\ +\left[-\alpha^2[\partial_\theta^2+\widetilde{\partial}_z^2]^2-1+I_{tr}-4\nu_+\nu_-h_*^{-1}K\right]u_n=0\end{gathered}\tag{2}$$

with operators of modified inertia

$$I_{tg}\mathrm{u}_{tg}=\omega^2\left[\mathrm{u}_{tg}+\eta^2\omega^2\sum_{k=1}^{3}d_k\left(-\nu_-^{-1}\eta^2\omega^2\right)^{k-1}\mathrm{grad}_{tg}\left(\partial_\theta u_1+\widetilde{\partial}_z u_2\right)\right],$$

$$I_{tr}=\omega^2\sum_{k=0}^{1}\left(-\nu_-^{-1}\eta^2\omega^2\right)^k\left[a_k+\eta^2 b_k\left(\partial_\theta^2+\widetilde{\partial}_z^2\right)\right],$$

where $\mathrm{u}_{tg} = (u_1, u_2)^{\mathrm{T}}$, $\eta = h/(2R)$, $\mathrm{grad}_{tg} = (\partial_\theta, \widetilde{\partial}_z)^{\mathrm{T}}$, $a_0 = 1$, a_1, b_k, d_k are coefficients depending on ν, which can be found in [7]. The term $4\nu_+\nu_-h_*^{-1}K$ should also

be refined in order to retain the asymptotic error of equations (2), but it requires an additional asymptotic analysis of the corresponding 3D equations. In this paper we restrict ourselves with refinements in describing the motion of the shell, which are expressed through operators of modified inertia.
To analyze the accuracy of equations (1) and (2) we use three-dimensional theory of elasticity. Let us introduce dimensionless variables

$$\begin{gathered} r = R\tilde{r}, z = R\tilde{z}, \{ u_r, u_\theta, u_z\} = R\{ \tilde{u}_r, \tilde{u}_\theta, \tilde{u}_z\}, \tilde{\omega} = R\omega c_2^{-1} = \omega/\sqrt{\nu_-}, \\ \{ \sigma_{rr}, \sigma_{\theta\theta}, \sigma_{zz}, \sigma_{r\theta}, \sigma_{rz}, \sigma_{\theta z}\} = E\left[2(1+\nu)\right]^{-1} \{ \tilde{\sigma}_{rr}, \tilde{\sigma}_{\theta\theta}, \tilde{\sigma}_{zz}, \tilde{\sigma}_{r\theta}, \tilde{\sigma}_{rz}, \tilde{\sigma}_{\theta z}\}, \end{gathered} \tag{3}$$

where $\mathrm{u} = (u_r, u_\theta, u_z)^{\mathrm{T}}$ is the displacement vector, σ_{rr}, $\sigma_{\theta\theta}$, $\sigma_{zz}, \sigma_{r\theta}$, σ_{rz}, $\sigma_{\theta z}$ are components of the stress tensor, $c_2 = \sqrt{E/(2(1+\nu)\rho)}$ is transverse wave speed. The displacement vector can be presented in the terms of wave potentials φ, $\boldsymbol{\psi}$ as

$$\widetilde{\mathrm{u}} = \operatorname{grad}\varphi + \operatorname{rot}\boldsymbol{\psi} \tag{4}$$

with additional condition $\operatorname{div}\boldsymbol{\psi} = 0$. After introducing the dimensionless variables (3) the equations for the potentials take the form

$$\Delta\varphi + \kappa^2\tilde{\omega}^2\varphi = 0, \quad \Delta\boldsymbol{\psi} + \tilde{\omega}^2\boldsymbol{\psi} = 0 \tag{5}$$

with $\kappa = \sqrt{(1-2\nu)(2\,(1-\nu))^{-1}}$. The expressions of the stresses in terms of φ, $\boldsymbol{\psi}$ can be found in [8]. Boundary conditions on the faces of the shell $\tilde{r} = 1 \pm \eta$ are

$$\tilde{\sigma}_{rr}|_{\tilde{r}=1+\eta} = -K\,\tilde{u}_r|_{\tilde{r}=1+\eta}, \;\; \tilde{\sigma}_{rr}|_{\tilde{r}=1-\eta} = 0, \;\; \tilde{\sigma}_{r\theta}|_{\tilde{r}=1\pm\eta} = \tilde{\sigma}_{rz}|_{\tilde{r}=1\pm\eta} = 0. \tag{6}$$

Further we will investigate the normal modes that propagate along the z-axis. The dependence on z is assumed to be in the form $\exp(\mathrm{i}\lambda z/R)$, where λ is the dimensionless wavenumber. The dispersion equations corresponding to approximate theories (1) and (2) can be derived by the method described in [9]. In the case of 3D problem (4)–(6) we use approach proposed in [8]. The variable θ is separated by assuming the law $\sin(m\theta)$ for functions u_1, u_θ and $\cos(m\theta)$ for u_2, u_n, u_z, u_r $(m = 0, 1, 2, \ldots)$. In the case of 3D theory the infinite series of modes exists for each m, but only the lowest three of them can be described on the basis of equations (1) and (2). The real branches of dispersion curves $\omega(\lambda)$ start from cut-off frequencies ω_k $(k = 1, 2, \ldots)$. We are interested in the backwards waves arising in the vicinity of a cut-off frequency, when it coincides with some other one. For the sake of convenience we will refer this point as coincidence frequency.

3 Shell with free surfaces

In the case of free faces $(K = 0)$ the asymptotic behavior of cut-off frequencies in the framework of the Kirchhoff–Love theory can be presented as [10]

$$\omega_1 = \frac{\eta m(m^2-1)}{\sqrt{3(m^2+1)}}\left(1 + O\left(\eta^2\right)\right), \; \omega_2 = m\sqrt{\nu_-}, \; \omega_3 = \sqrt{m^2+1}\left(1 + O\left(\eta^2\right)\right). \tag{7}$$

It can be easily verified that the frequencies ω_2 and ω_3 cannot coincide. The coincidence of frequencies ω_1 and ω_2 requires $m \sim \eta^{-1}$ or $q = 1$, where q is the variability

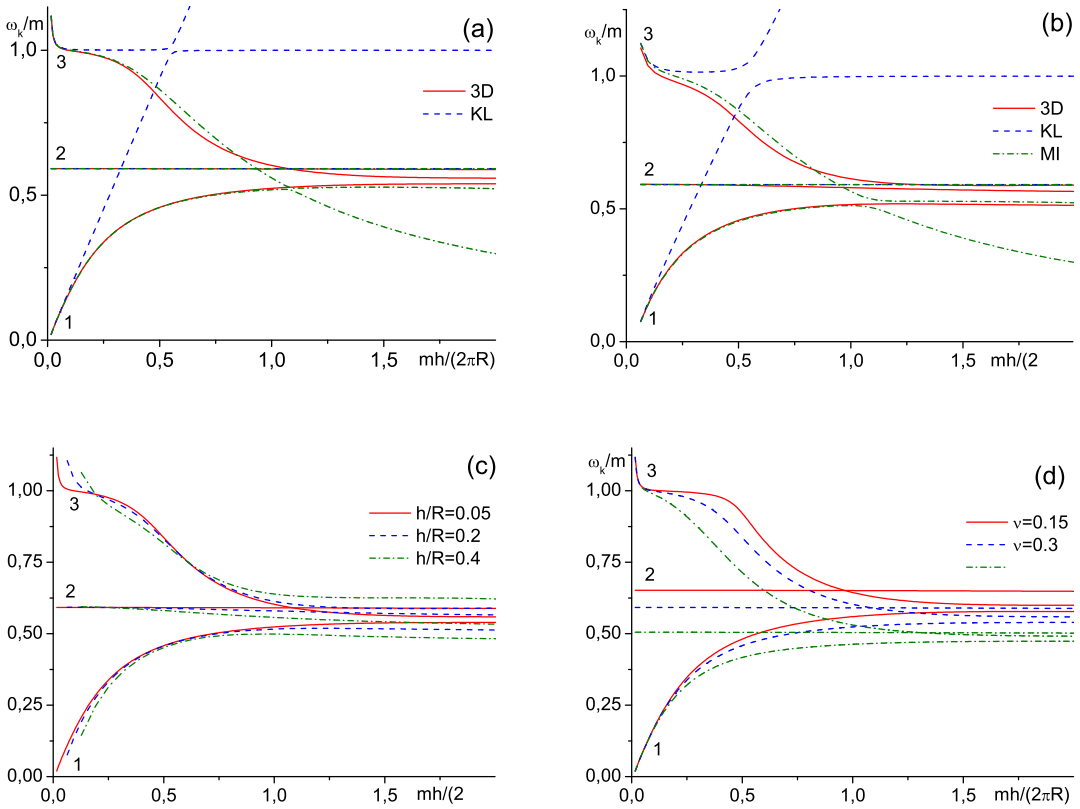

Figure 1: Numerical results for cut-off frequencies: $\nu = 0.3, h/R = 0.05$ (a), $\nu = 0.3, h/R = 0.2$ (b), $\nu = 0.3$ (c), $h/R = 0.05$ (d)

index in terms of [7]. The range of applicability of Kirchhoff–Love theory was defined in [7] as $q < 1$, thus the coincidence frequency does not belong to it. But this reason does not exclude the existence of the coincidence frequency and, consequently, the backwards waves by large values of m or in a thick shell. To investigate this matter a series of numerical experiments was performed, in which the cut-off frequency were calculated on the basis of each of the three theories formulated in Sec. 2. The most interesting results are shown in Fig. 1. As one can see, the coincidence of ω_1 and ω_2 predicted by Kirchhoff–Love theory is not confirmed by 3D theory of elasticity. The theory with modified inertia has much greater range of applicability and predicts the behavior of cut-off frequencies ω_1 and ω_2 with a good accuracy (see Fig. 1,a,b). The investigation on the basis of 3D theory for different values of h/R and ν has shown that apparently the coincidence of ω_1 and ω_2 is not possible (see Fig. 1,c,d). But for some not very great values of h/R there is a coincidence frequency $\omega_2 = \omega_3$. For example, in Fig. 1,c we can see it at $h/R = 0.05$ (red lines) but cannot see it at $h/R = 0.2, 0.4$ (blue and green lines). Since parameter m for this point corresponds to $q \geqslant 1$, it cannot be described by 2D theories of shells. Calculations show that the backward wave arises in the vicinity of ω_2, but the domain of its existence on the axis ω is very narrow ($\lesssim 10^{-5}$ for the dimensionless frequency introduced as in (1)). The investigation of that backward wave in more detail does not match the goal of this paper.

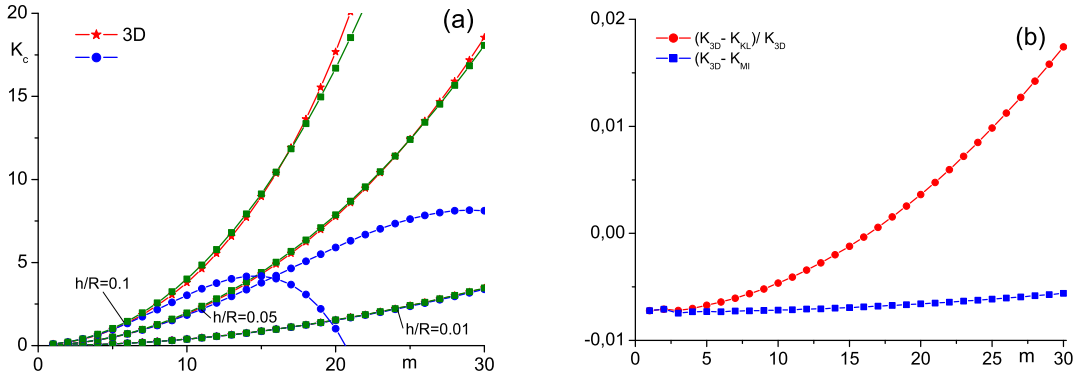

Figure 2: Comparison of three theories for coincidence parameter K_c (a); relative errors of 2D theories for $h/R = 0.01$ (b)

The numerical results presented in Fig. 1 show that the curves for ω_1 and ω_2 have a tendency of drawing closer to one another. In the next section we consider a shell model in which these curves intersect.

4 Shell with spring-type boundary conditions on the outer surface

In the case $K \neq 0$ there is one additional parameter of the problem. An analysis of the dispersion equations corresponding to the problems formulated in Sec. 2 shows that at $\lambda = 0$ all three of them are separated into two independent equations. One of the pair is an equation for the cut-off frequency ω_2, which is independent on K and is equal to that in the case of free surface. Substituting ω_2 in the second equation we obtain an explicit expression for the value of $K = K_c$, at which ω_1 coincides with ω_2. For the Kirchhoff–Love theory (1) the coincidence parameter $K_c = K_{KL}$ is

$$K_{KL} = \frac{4\nu_+\nu_-h_*}{2\nu_+ + 8\alpha^2}\left[2(\nu_- - \nu_+\alpha^2) + \left(2\nu_+\nu_- + 2\alpha^2(5-3\nu)\right)m^2 - 2\alpha^2\nu_+m^4\right],$$

for the other theories the expressions are too cumbersome to be presented here. Further we denote them as K_{MI} for the theory with modified inertia and K_{3D} for the 3D theory of elasticity. The asymptotic behavior of K_{KL} at $m \sim 1$

$$K_{KL} = 4\nu_+\nu_-h_*\left[\frac{1-\nu}{1+\nu} + \frac{1-\nu}{2}m^2 + O\left(\alpha^2\right)\right]$$

shows that at the small values of m the coincidence parameter nearly proportional to relative thickness.

In Fig. 2,a the dependence $K_c(m)$, calculated on the basis of each of the three theories, is shown for the different values of h/R. Here the Kirchhoff–Love-type theory can give qualitatively correct results, but only for small m. As in the case of free faces, the range of applicability of the theory with modified inertia is much greater (see also the relative errors on Fig. 2,b).

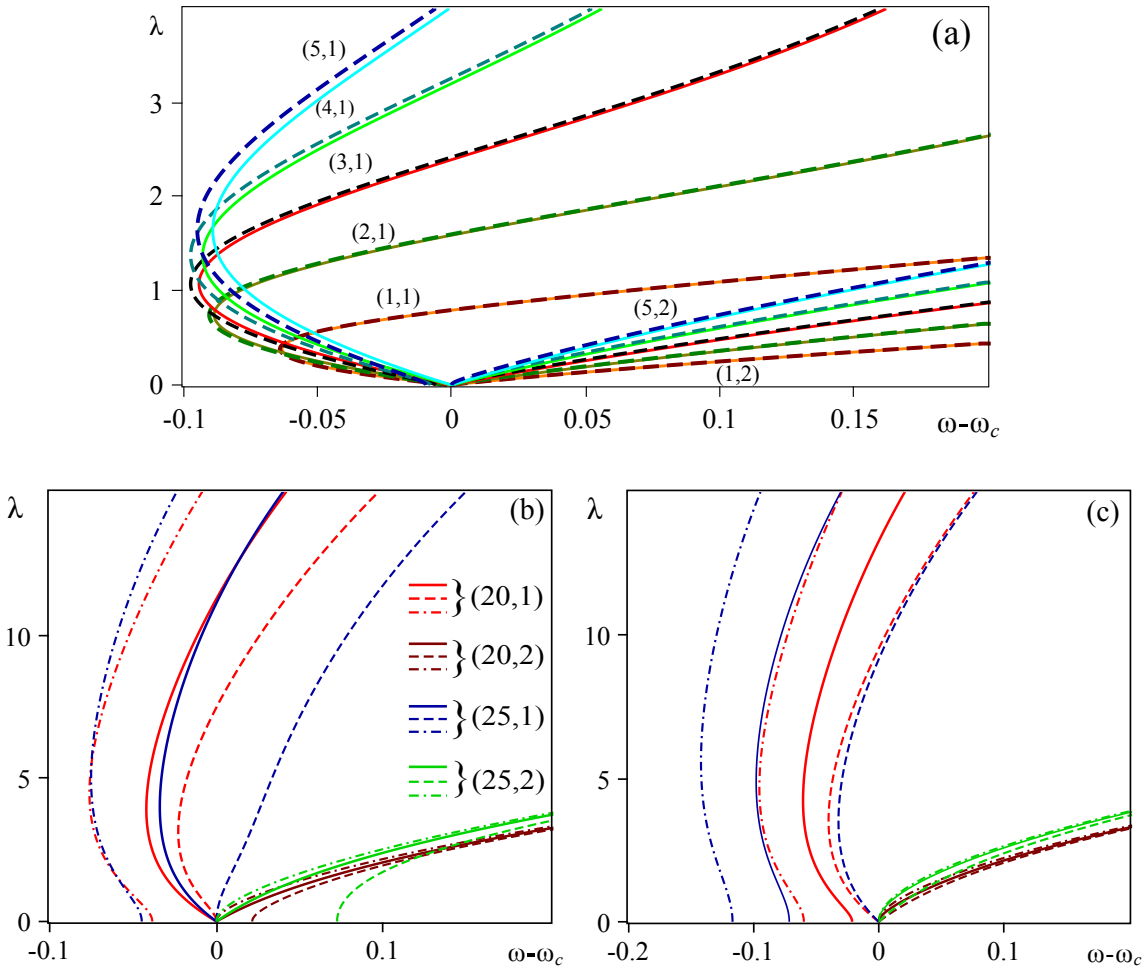

Figure 3: Dispersion curves for $\nu = 0.3$, $h/R = 0.01$, $K = K_{3D}$: $m = \overline{1,5}$ (a), $m = 20, 25$ (b), and the same as (b) for $K = K_{KL}$ (c). Solid lines: 3D theory, dashed lines: KL theory, dash-dotted lines: theory with MI

In Fig. 3 the comparison of dispersion curves in the vicinity of the coincidence frequency $\omega_c = \omega_1 = \omega_2$ is presented. Here the numbers of modes are indicated by pairs (m, k) with $k = 1, 2$. Because of the difference between parameters K_c calculated on the basis of 3D theory of elasticity and 2D shell theories there is no coincidence of cut-off frequencies for the latter. The error of Kirchhoff–Love theory at $m = 25$ leads to a qualitatively incorrect result: according to it, the backwards wave does not exist at $K = K_{3D}$, although the calculations on the basis of 3D theory of elasticity shows its existence (see Fig. 3,b, blue lines). On the other hand, at $K = K_{KL}$ there is the backwards wave according to Kirchhoff–Love theory (see Fig. 3,c). Notice, that at $n = 25$ the relative error of K_{KL} is less than 2% (see Fig. 2,b). But it reveals itself to be essential in the problem under consideration. The theory with modified inertia gives the qualitative correct results in both cases.

In Fig. 4 the behavior of eigenfunctions calculated on the basis of 3D and Kirchhoff–Love theories is investigated near the coincidence frequency ω_2 at $m = 5$, $h/R = 0.01$ and the values of K indicated on the graphs. Since the dependence of displacements along the thickness coordinate is very close to linear one at these values of parame-

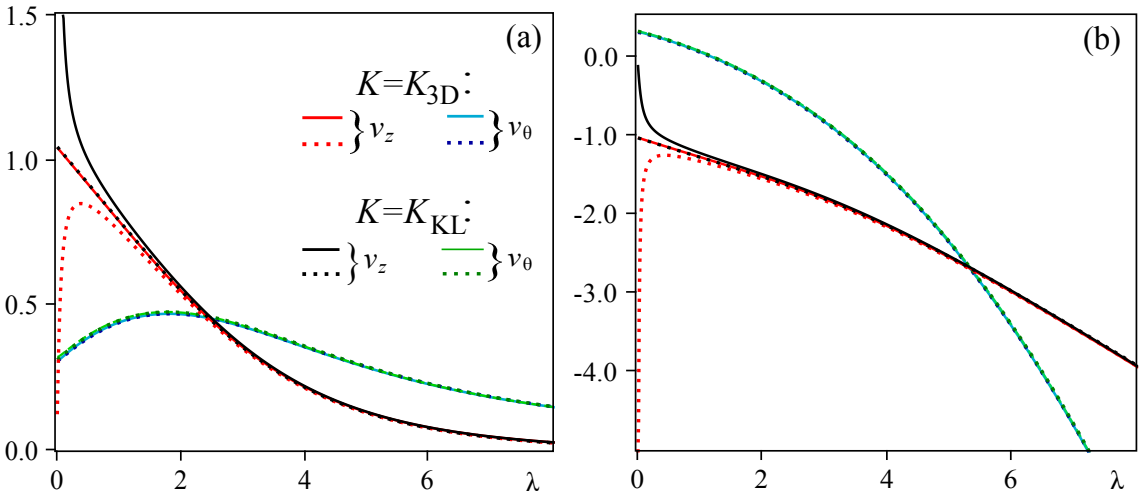

Figure 4: Evolution of normalized tangential displacements for modes $(5,1)$ (a) and (5.2) (b) for $\nu = 0.3$, $h/R = 0.01$ and indicated values of K. Solid lines: 3D theory, dotted lines: KL theory

ters, it can be characterized by quantities v_θ, v_z representing normalized amplitudes of displacements $\mathrm{Re}(u_\theta/\,u_r|_{r=R+h/2})$, $\mathrm{Im}(u_z/\,u_r|_{r=R+h/2})$ averaged in respect to the coordinate $r \in [R-h/2, R+h/2]$. When using the Kirchhoff–Love theory, we put $v_\theta = \mathrm{Re}(u_1/u_n)$, $v_z = \mathrm{Im}(u_2/u_n)$. In the case of 3D theory, for both modes $(5,1)$ and $(5,2)$ the displacement u_r is distributed nearly uniformly along the thickness coordinate in the whole domain shown in Fig. 4, so the normalized and averaged displacement u_r is nearly equal to unity for any λ. Taking this into account, we can see from Fig. 4 that mode $(5,1)$ becomes a flexural one ($|u_\theta|\,,\ |u_z| \ll |u_r|\,$) when the wavenumber grows, while mode $(5,2)$ tends to torsional one ($|u_z|\,,\ |u_r| \ll |u_\theta|\,$). In the domain of the backwards wave (cf. Fig. 3,a) both modes have mixed character. The Kirchhoff–Love theory describes the behavior of displacements with good accuracy except the displacement v_z in the vicinity of $\lambda = 0$. This effect is apparently caused by the coupling between the tangential and flexural motions of the shell, which is absent at $\lambda = 0$ if there is no coincidence of the cut-off frequencies. The accuracy of Kirchhoff–Love theory seems to be improved after setting $K = K_{KL}$, but is still has a great error comparing with the solution of 3D problem calculated at the same value of K.

5 Conclusion

The investigation presented above shows that the using of 2D shell theories requires a careful analysis of their range of applicability, when some special effects are studied. The classical theory with modified inertia proposed in [7] can be effectively used in such an analysis. It was also noticed that the errors of approximate shell theories increase in the domains characterized by presence of backwards waves. For an isotropic shell with free faces it was shown that there are no backwards waves which could be described by long-wave approximations of the 3D equations of elasticity. But such an effect is still possible in some anisotropic or laminated shell.

References

[1] Gazis D. C., 1959. Three-dimension investigation of the propagation of waves in hollow circular cylinders. I. Analytical foundation. II. Numerical results. *J. Acoust. Soc. Am.*, **31**, 568–578.

[2] Ainola L, Nigul U. K., 1965. Wave processes in deformation of elastic plates and shells. *Izvestiya Akademii Nauk Estonskoi SSR, Ser. Fiz.-Mat. Tekhn. Nauk*, **14**(1), 3–63.

[3] Greenspon J. E., 1960. Vibrations of a thick-walled cylindrical shell. Comparison of the exact theory with approximate theories. *J. Acoust. Soc. Am.*, **32**, 571–578.

[4] Berezin V. L. Kaplunov J. D., Kossovich L. Yu., 1995. Synthesis of the dispersion curves for a cylindrical shell on the basis of approximate theories. *J. of Sound and Vibration*, **186**, 37–53.

[5] Selvadurai A., 1979. Elastic analysis of soil-foundation interaction, Developments in Geotechnical Engineering 17. Amsterdam, The Netherlands: Elsevier.

[6] Yeliseev V.V., 2003, *Mechanics of elastic bodies*, SPb., SPbSPU, Russia, 336 p. (in Russian).

[7] Kaplunov J. D., Kossovich L. Yu., Nolde E. V., 1998. *Dynamics of thin walled elastic bodies*, Academic Press, San Diego, 226 p.

[8] Ardazishvili R. V., Wilde M. V., Kossovich L. Yu., 2015. Three-dimensional fundamental edge waves in a thin shell. *I. Yakovlev Chuvash State Pedagogical University Bulletin*, **4(26)**, 109–124. (In Russian)

[9] Filippenko G. V., 2017. Waves with the negative group velocity in cylindrical shell of Kirchhoff–Love type. *Proc. of the XLV Summer School–Conference "Advanced problems in mechanics (APM)"*, 161–167.

[10] Filippenko G. V., 2014. Energy aspects of wave propagation in an infinite cylindrical shell fully submerged in liquid. *Vycisl. meh. splos. sred – Computational Continuum Mechanics*, **7**(3), 295–305.

G. V. Filippenko, Institute of Mechanical Engineering of RAS, Vasilievsky Ostrov, Bolshoy Prospect 61, St.Petersburg, 199178, Russia, g.filippenko@gmail.com
Saint Petersburg State University, 7-9, Universitetskaya nab., St.Petersburg, 199034, Russia, g.filippenko@spbu.ru
M. V. Wilde, Saratov State University, Astrakhanskaya street, 83, Saratov, 410012, Russian Federation, mv_wilde@mail.ru

Microshungite – perspective fillers for rubber compounds used in the tire industry

Oleg K. Garishin, Vladimir V. Shadrin, Anton Yu. Belyaev, Yuri V. Kornev
gar@icmm.ru

Abstract

Strength and viscoelastic properties of nanocomposites based on butadiene-styrene rubber (SBR-1500) with dispersed mineral filler (micro-shungite) were studied experimentally. In its structure shungites represent natural composite with a uniform distribution of finely crystalline silicate particles in the carbon matrix. These minerals sufficiently disperse readily into particles globular (spherical) form, with appropriate processing. The mineral is characterized by high density, chemical resistance and electrical conductivity. Currently, shungite is being used in the tire industry to produce active and semi-active fillers of a new generation. The tests were carried out on samples with various volumetric concentrations. The average particle size of the micro-shungite filler was about 500 nm. Experiments on uniaxial tensile at break showed that micro-shungite input leads to a significant increase in the material strength. At the same time, its deformability grew, but not so much. Thus, it can be said that the good chemical affinity of the filler and matrix contributes to improving the material's ultimate characteristics. Studies of the thermo-visco-elastic properties of these materials on a dynamo-mechanical analyzer (DMA) were also carried out. As a result, the dynamic and viscous modulus dependences on the frequency (at 20 °C) and their temperature dependences (from −50 to +100 °C) were constructed.

1 Introduction

The use of various mineral fillers in the production of elastomeric composites with improved performance properties (in particular automobile tires) is a relatively new and very promising perspective direction of material science development. These materials are characterized by a combination of such important properties as increased thermal stability, resistance to burning, low diffusion permeability, ecological purity and relative cheapness of production [1, 2]. At its core, they represent a complex structural heterogeneous systems consisting of a low-modulus highly elastic matrix, which embedded by a much more rigid and durable particles of the particulate filler. Such materials are characterized by a complex mechanical behavior (finite deformations, nonlinear elasticity, viscoelasticity), which is caused by a different

nature reversible and irreversible structural changes occurring under deformation [3, 4, 5]. Currently, elastomer composites with various mineral fillers are the subject of intensive research, both experimental and theoretical [6, 7, 8, 9, 10, 11, 12].
One of the most promising areas of use of elastomers with mineral fillers are automobile tires. Rubbers with such filling are cheaper and have higher wear resistance [13, 14].

2 The object of study

The main object of research was elastomeric nanocomposites based on SBR-1500 synthetic butadiene rubber, filled with micro-shungite (granular particles with a typical average size of about 500 nm). This is a relatively new (for elastomers) type of filler. Shungite represent natural mineral composite with a uniform distribution of highly disperse silicate particles in the carbon matrix [15, 16, 17]. Depending on the deposit, the composition of shungite rocks can vary within fairly wide limits. On average, these materials contain about 60–70%-wt. of silicates and 30%-wt. of shungite carbon with an admixture of other inorganic substances (<4%-wt., $A_{l2}O_3$, FeO, MgO, CaO, etc.). Reliably established that the shungite carbon in the rock is lined up by globules connected together, that is, particles of approximately spherical shape. The diameter of the shungite globules is about 10 nm (which is unique for materials of natural origin). There is a strong bond between the carbon and silicate components. The rock is characterized by high density (1.9–2.4 g/cm^3), chemical resistance and electrical conductivity [18, 19]. Such a structure and composition give shungite materials several unusual physical-chemical and technological properties. The particles of shungite powder, even micron-sized, contain phases different in polarity. Due to bipolarity, powders of shungite rocks mix well with most known substances (aqueous suspensions and fluoroplastics, rubbers, resins and cements, etc.). Therefore, they are one of the promising modern fillers. Currently, shungite is being used in the tire industry to produce active and semi-active fillers of a new generation. In general, the experimental testing of shungite in rubber compounds revealed the following main effects [13, 14, 20]:
1) Improving the ability of rubber compounds to process (in comparison with carbon black and white soot).
2) Shungiton-filled rubber has improved dynamic properties: resistance to growth of cracks in bending with puncture, reduced heat generation under alternating bending, dynamic endurance under angular rotation.
3) Filling rubber with shungite significantly increases their thermal and fire resistance.

3 Experiment and results discussion

All experiments were performed on samples prepared in IAPM RAS. The volume micro-shungite concentration φ was 0% (pure rubber), 10%, 18%, and 27%. The studies consisted of two stages: 1) uniaxial stretching up to rupture rupture; 2) tests on a dynamo-mechanical analyzer (DMA). Experimental studies were carried out on the universal tensile testing machine Testometric FS100kN CT. Samples were manufactured in accordance with the standard ISO 527-25A with working part 2 on 2 by 10 mm. During the test, each sample was monotonically stretched to a break at a rate of 25 %/min. 9–12 samples were tested for each filling. The averaged results of the experiments are shown in Fig. 1.

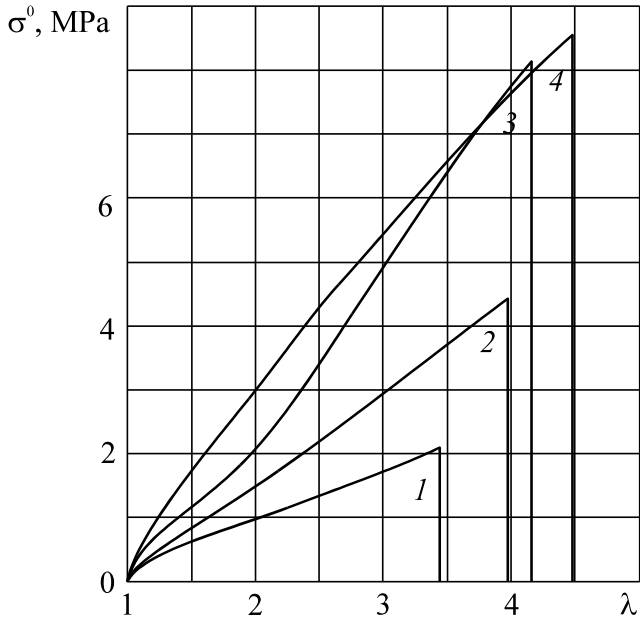

Figure 1: Nominal stresses σ^0 versus extension ratio λ at stretching of elastomers filled by micro-schungite particles; $\varphi = 0\%$ (*1*), 10% (*2*), 18% (*3*), 27% (*4*)

It was found that the addition of micro-shungite filler leads to a significant increase in the strength of the elastomer. For example: for $\varphi = 27\%$ it was more than 3 times. At the same time, its deformability grew, but not so much (from 10 to 30%). Thus, it can be said that the good chemical affinity of the filler and matrix contributes to improving the ultimate characteristics of the material. In the near future, it is planned to carry out the similar experiments with nano-shugite filler. There, we think, these effects should appear even stronger.

The thermo-visco-elastic properties of these composite materials were investigated in the second stage. The experiments were held on a dynamo-mechanical analyzer DMA/STDA861^e (METTLER TOLEDO STAR^e). This device allows to obtain information about the change in the viscoelastic characteristics of the material under the action of a dynamic cyclical load (linear viscoelasticity model) for given temperature values from -150 to $+500\,^\circ$C. Rectangular samples were used for the tests: base (working part) 10 mm, width 3 mm, thickness 2 mm. One-point loading scheme was applied: cyclic uniaxial stretching–compression of a pre-stretched sample with dynamic load applied according to a harmonic law.

The frequency range f varied from 1 to 20 Hz, which corresponds to the rolling speed of a standard automotive wheel (landing diameter 15 inches) in the range from 6 to 136 km/h, respectively. The amplitude of deformations ε_0 was set at 3% in all cases.

As a result, the dependences of the dynamic (E') and viscous (E'') modules on the loading frequency f were plotted. Their temperature dependences (-50 to $+100$°C) at a constant frequency of 13 Hz (which corresponds to approximately 90 km/h) were built too. The corresponding graphs are shown in Figures 2–4.

The analysis of results obtained by DMA showed the following.

Frequency tests:

The addition of micro-shungite filler to rubber promoted an increase in both E' and E'', and with concentration growth this effect intensified. It was also found that in this frequency range the dynamic and viscous modules retained almost constant values. Thus, we can assume that these composites have sufficiently stable viscoelastic characteristics in this frequency range of tire rotation.

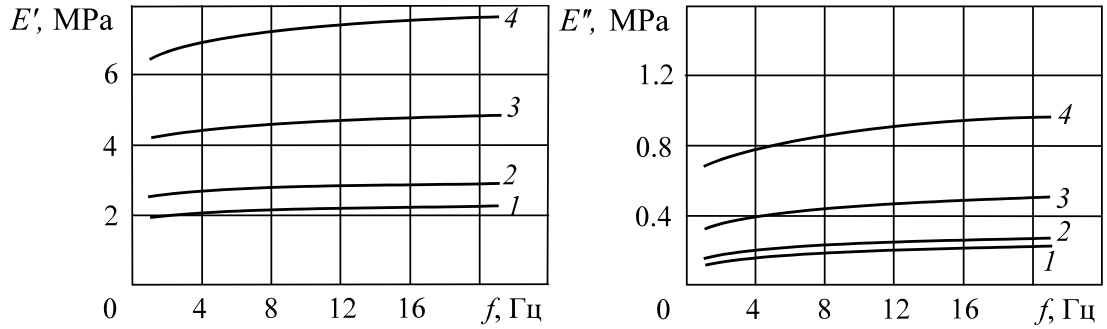

Figure 2: Frequency dependences of dynamic (E') and viscous (E'') modules for microchungite filler concentrations of $\varphi = 0\%$ (*1*), 10% (*2*), 18% (*3*), 27% (*4*)

Temperature tests:

At temperatures below -30 °C there was a sharp increase in E' and E'', while for shungite-filled rubbers the values increased by several orders of magnitude. The pure elastomer changed its properties considerably less. From the analysis of the temperature dependences of the loss tangent ($\tan\delta = E''/E'$), it is seen that when a micro-shungite is added, the characteristic peak corresponding to the glass transition temperature shifts from -45°C (pure elastomer) to -25°C (27%). Consequently, the use of tires with only such fillers in such low temperatures is quite problematic — some special additives are needed in the tire compound. At higher temperatures, all samples demonstrated the stability of their mechanical properties.

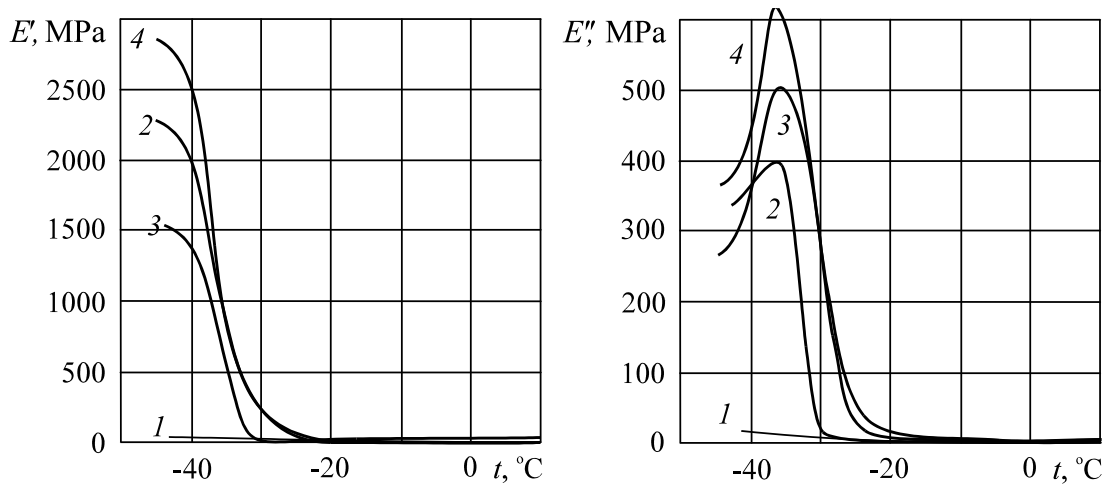

Figure 3: Temperature dependences of dynamic (E') and viscous (E'') modules for microchungite filler concentrations of $\varphi = 0\%$ (*1*), 10% (*2*), 18% (*3*), 27% (*4*)

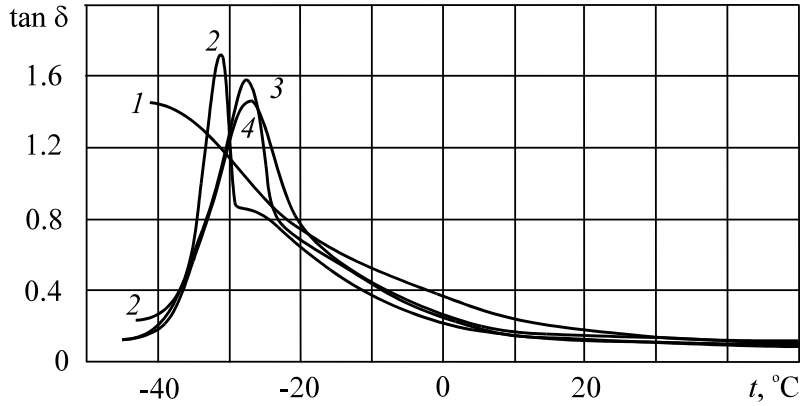

Figure 4: Temperature dependences of loss tangent ($\tan\delta = E''/E'$) for microchungite filler concentrations of $\varphi = 0\%$ (*1*), 10% (*2*), 18% (*3*), 27% (*4*)

Acknowledgements

This work is executed at a financial support of RFBR Grant 16-08-00756.

References

[1] Fengge G. Clay/polymer composites: the story // Materials Today, 2004, N 11, P. 50–55.

[2] Theng B.K.G. Some Practical Applications of the Clay-Polymer Interaction // Developments in Clay Science, 2012, V. 4, P. 153–199 and P. 201–241.

[3] Moshev V.V., Svistkov A.L., Garishin O.K., Evlampieva S.E., Rogovoy A.A., Kovrov V.N., Komar L.A., Golotina L.A., Kozhevnikova L.L. Structural mechanisms for the formation of mechanical properties and strength of granular polymer composites. UB RAS, Ekaterinburg, 1997, 508 p. (in Russian)

[4] Moshev V.V. Garishin O.K. Structural mechanics of dispersed filled elastomeric composites // Achievements in Mechanics, 2005, V. 4, N 2, P. 3–36. (in Russian)

[5] Garishin O.K. Mechanical properties and destruction of dispersely filled elastomers. Structural modeling. Germany, Saarbrucken: Palmarium Academic Publishing (LAP), 2012, 286 p. (in Russian)

[6] Rooj S., Das A., Stuckelhuber K.W., Reuter U., Heinrich G. Highly exfoliated natural rubber/clay composites by "propping-open procedure": the influence of fatty acid chain length on exfoliation // Macromol. Mater. Eng., 2012, V. 297, P. 369–383.

[7] Rooj S., Das A., Stuckelhuber K.W., Mukhopadhyay N., Bhattacharyya A.R., Jehnichen D. Pre-intercalation of long chain fatty acid in the interlayer space of layered silicates and preparation of montmorillonite/natural rubber nanocomposites // Appl. Clay. Sci., 2012, V. 67-68, P. 50–56.

[8] Rooj S., Das A., Morozov I.A., Stuckelhuber K.W., Stocek R., Heinrich G. Influence of "expanded clay" on the microstructure and fatigue crack growth behavior of carbon black filled NR composites // Composites Science and Technology, 2013, V. 76, P. 61–68.

[9] Lvov Y., Fakhrullin R., Wang W., Zhang L. Hallousite clay nanotubes for loading and sustained release of functional compounds // Advanced Materials, 2016, V 28, N 6, P. 1227-1250.

[10] Garishin O.K., Shadrin V.V., Svistkov A.L., Sokolov A.K., Stockelhuber W.K. Visco-elastic-plastic properties of natural rubber filled with carbon black and layered clay nano-particles. Experiment and simulation // Polymer Testing, 2017, V. 63, P. 133-140.

[11] Garishin O.K., Shadrin V.V., Svistkov A.L., Sokolov A.K. Experimental studies of rubbers filled by layered clay nanoparticles // XLV Summer School-Conference "Advanced problems in mechanics": Proceedings, St.-Petersburg, 2017, P. 168-174.

[12] Mokhireva K.A., Svistkov A.L., Solod'ko V.N., Komar L.A., Stockelhuber K.W. Experimental analysis of the effect of carbon nanoparticles with different geometry on the appearance of anisotropy of mechanical properties in elastomeric composites // Polymer Testing, 2017, V. 59, P. 46-54.

[13] Kornev Yu.V., Chirkunova C.V. Boiko O.V., Simonova M.A., Shugaeva V.O., Yanovsky Yu.G. Investigation of the effect of dispersion of mineral shungite on the complex properties of elastomeric compositions based on rubber SKTN-A // Caoutchouc and rubber, 2012, N 6. P. 10-14. (in Russian)

[14] Kornev Yu.V., Yanovskiy G., Boiko V., Semenov N.A., Chirkunova S. Investigating the influence of the degree of dispersion of mineral shungite on the properties of elastomeric materials based on butadiene-styrene rubber // International Polymer Science and Technology, 2013, V. 40, N 3,P. 17-22.

[15] Buseck P.R. Geological fullerenes: review and analysis // Earth and Planetary Science Letters, 2002, V. 203, P. 781-792.

[16] Ignatov I., Mosin O.V. Composition and structural properties of the natural fullerene-containing shungite mineral // Nanoengineering, 2012, N 6, P. 17-23.

[17] Yushkin N.P. Globular supramolecular structure of schungite: data from scanning tunneling microscopy // DAN, 1994, V. 337, N 6, P 800-803.

[18] Kovalevski V. V., Prikhodko A. V., Buseck P. R. Diamagnetism of natural fullerene-like carbon // Carbon, 2005, V. 43, N 2, P. 401-405.

[19] Kwiecinska B., Pusz S., Krzesinska M., Pilawa B. Physical properties of shungite // International J. of Coal Geology, 2007, V. 71, N 4, P. 455-461.

[20] Grishin B.S., Kalinin Yu.K. Fine disperse shungite powders — perspective filler of polyfunctional action for elastomer composites. ISP, Moscow, Petrozavodsk, 2005. 20p.

Oleg Konstantinovich Garishin, Institute of Continuous Media Mechanics UB RAS, Perm, Russia
Vladimir Vasilyevich Shadrin, Institute of Continuous Media Mechanics UB RAS, Perm, Russia, Perm State National Research University, Perm, Russia
Anton Yu. Belyaev, Institute of Continuous Media Mechanics UB RAS, Perm, Russia, Perm State National Research University, Russia
Yuri V. Kornev, Institute of Applied Mechanics RAS, Moscow, Russia

Biaxial tests of elastomeric nanocomposites with various types of dispersed fillers

Oleg K. Garishin, Vladimir V. Shadrin, Yury V. Kornev
shadrin@icmm.ru

Abstract

Mechanical tests under biaxial cyclic loading of elastomeric nanocomposites with various types of filler under biaxial cyclic loading were carried out. The object of research were elastomeric composites based on synthetic butadiene-styrene rubber SBR-1500 (matrix) and the following fillers: nanoshungite; silicic acid (fumed silica), carbon black, carbon nanofibers.

The biaxial tests were carried out on a four-vector test rig Zwick/Roell (the only one in Russia), which allows to define complex deformation trajectories in two mutually perpendicular directions. Original cross-shaped specimens were used. Their form and dimensions were established on the basis of special theoretical studies held in ICMM UB RAS (Perm).

The experiments carried out made it possible to study the effects of softening and the appearance of induced anisotropy in filled elastomers under the action of a biaxial load. It is established that the nature of their manifestation depends on the type of filler. It is also shown that in the case of pure rubber they are practically absent.

In samples filled with nanoshungite particles or carbon black, cyclic deformation along one axis causes a corresponding softening along the same axis, but does not affect the mechanical behavior of the material in the perpendicular direction.

When using the filler as a mixture of carbon black and carbon nanofibers cyclic deformation along one axis causes similar softening the other axis. In elastomers filled with silica particles (fumed silica), this effect is also present, but it is much weaker than in case of carbon nanofibers.

Thus, one can say, that it is possible to change the mechanical properties of the composite to the desired side, making the system more or less anisotropic, due to the variation in the filler composition.

1 Introduction

Disperse-filled elastomeric composites are systems consisting of a highly elastic low modulus rubber matrix (continuous phase) into which solid particulate filler particles (dispersed phase) are embedded. Their industrial analogs can be considered rubbers for various purposes (from automobile tires to current-conducting high-elastic

gaskets), solid rocket fuels, etc. At present they are the object of intensive research both theoretical and experimental [1, 2]. Such materials have complex mechanical behavior (finite deformations, nonlinear elasticity, viscoelasticity), which is due to various reversible and irreversible structural changes occurring during deformation [3 –11]. In particular, they are characterized by a phenomenon such as "softening" during repeated deformation (the Patrikeev-Mullins effect) [12, 13, 14, 15], which causes certain problems in their operation.

2 The object of study

The main object of research was the synthetic butadiene-styrene rubber SBR-1500, in which various fillers different in their mechanical and physicochemical properties were added: 1) nano-shugite; 2) technical carbon (carbon black); 3) carbon nanofibers with technical carbon; 4) silicic acid (white soot). In addition, similar tests were carried out for the pure elastomer without filler. Shungite is a clay mineral consisting mainly of fullerene-like carbon (30%) and silicon dioxide SiO_2 (60%) [16, 17, 18]. It is fairly widely distributed in nature, inexpensive and characterized by high ecological safety. Nanoparticles of the globular type are formed when shungite is dispersed. Rubbers filled with shungite nanoparticles are characterized by increased wear resistance. Currently, they are used in the tire industry [19, 20]. In our case, the composite samples contained 65 parts by weight (phr) of shungite nanoparticles with an average size of 60–80 nm. Carbon black grade N220 (ASTM standard) was taken: the average particle size was about 30 nm, the mass concentration was 60 phr. Carbon nanofibers VGCF [21, 22] were of length from 10 to 20 μm and a diameter of 150–200 nm. Their concentration was 5 phr. This concentration is rather significant for fibers, because, these particles (by their shape and size) "extend their influence" to much larger distances than granular inclusions. The filler of silicic acid BS-120 (white soot) was a particulate hydrated silicon dioxide with an average size of 20–30 nm [23]. Its concentration was also 65 phr.

3 Experiment and results discussion

The biaxial tests were carried out using the four-vector test rig Zwick/Roell (the only one in Russia), which allows to define complex deformation trajectories in two mutually perpendicular directions (Fig. 1). The original cross-shaped samples were used (Fig. 2). Their shape and dimensions were set on the basis of special theoretical studies carried out in ICMM UB RAS. These samples are optimal from the viewpoint of obtaining uniform stress fields at the working part of the specimen and minimizing the size of the non-working part [24].

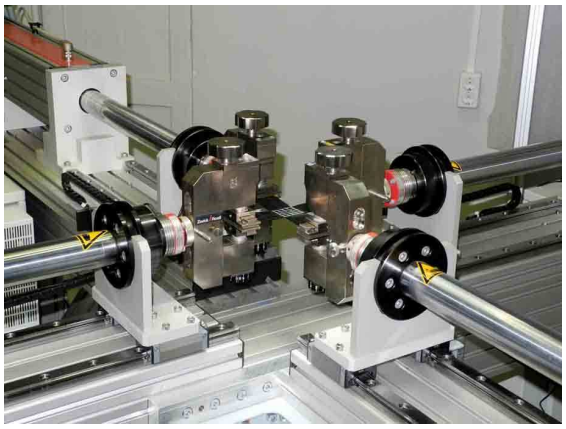

Figure 1: The four-vector test rig Zwick/Roell

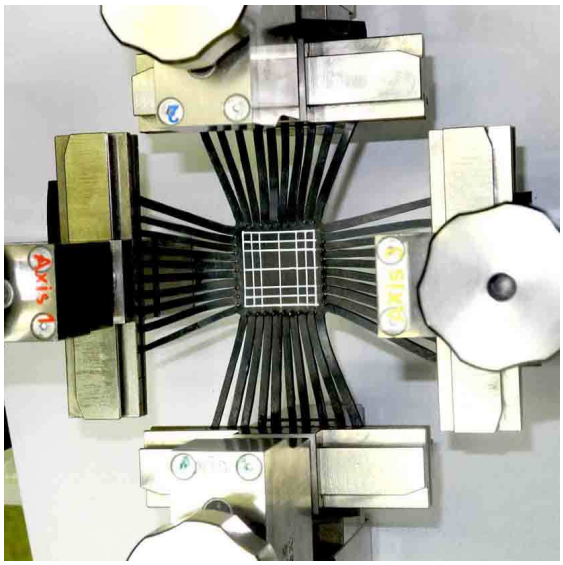

Figure 2: General view of cross-shaped specimens used in biaxial tests

Tests for pure elastomer and composites filled with nanoshungite and silicic acid were performed according to a program of 4 cycles (Program I). Each cycle consisted of the following steps: Stretching along one axis (direction X) to a given deformation, stopping for stress relaxation, compressing to the initial state and again stopping for relaxation. The rate of deformation was 25%/min, the stop for relaxation was 30 min. In the first and second cycles, the sample was stretched along the X axis to a deformation of 25% and 50%, respectively. In the third and fourth cycles, the same procedure was repeated along the Y axis.
For samples filled with carbon black, as well as carbon fibers with technical carbon, the Program II was applied (deformation rate 25%/min, stop time for relaxation 20 min.):
1) Stretching along the X axis to a deformation of 150% and stopping for relaxation.
2) Compression along the X axis to the initial state and stopping for relaxation.
Procedures 1) and 2) were repeated 3 times.
3) Stretching along the Y axis to a deformation of 150% and stopping for relaxation.
4) Compression along the Y axis to the initial state and stopping for relaxation.
Procedures 3) and 4) were also repeated 3 times.

Testing of pure rubber SBR-1500 according to Program I established (Fig. 3) that uniaxial cyclic deformation practically does not affect its properties in other directions. The hysteresis loops in the "load-unload" mode are also very weakly expressed. That is, such material can be considered as a high degree of reliability to be elastic and isotropic.

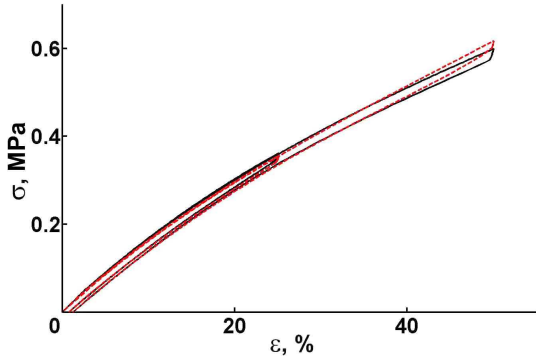

Figure 3: Biaxial tests of pure elastomer; solid lines — tensile curves along the X axis, dashed lines — along the Y axis (σ — nominal stress, ε – stretching deformation)

A different picture is observed for samples with nanoshungite (Fig. 4). The graphs show that the addition of this filler enhances the viscosity properties of the composite — hysteresis loops appear. At the same time softening of the material under repeated loading does not occur. Dependences of stresses on deformation, constructed under loading along the X and Y axes, practically coincide, i.e. the appearance of anisotropy induced by the deformation is not observed.

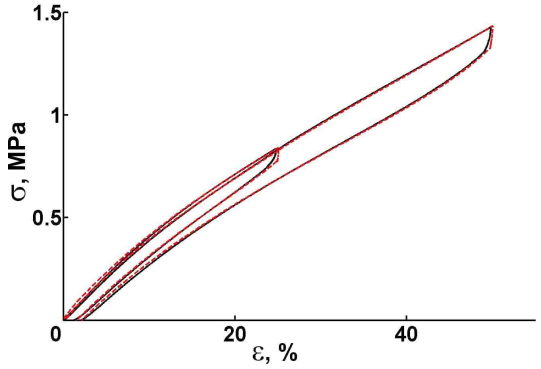

Figure 4: Biaxial testing of an elastomer filled by shungite nanoparticles; solid lines — tensile curves along the X axis, dashed lines — along the Y axis

Fig. 5 shows the results of tests of composites with white soot as a filler. In this case, the hysteresis curves turned out to be larger than in the previous experiment which indicates an increase in the viscosity properties of the composite. The stiffness decreases with repeated loading (the Patrikeev-Mullins effect) for curves corresponding to deformation along the same axis. Also, the appearance of an induced anisotropy of properties is observed for these samples. The curves $\sigma(\varepsilon)$ obtained under loading along the Y axis lie lower than those constructed for the X axis.

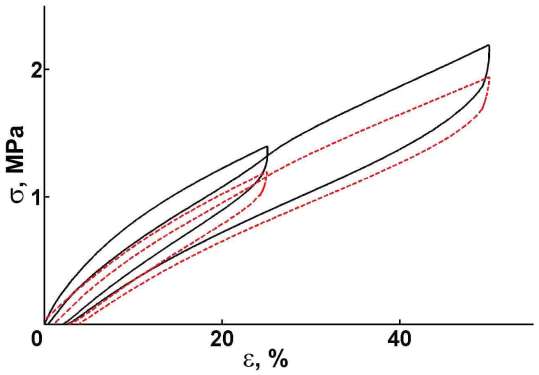

Figure 5: Biaxial testing of an elastomer filled by white soot nanoparticles; solid lines — tensile curves along the X axis, dashed lines — along the Y axis

Experiments for composites filled by carbon black and nanofibers with carbon black (program II) are represented in Fig. 6 and Fig. 7. Fig. 6 presents the dependences of σ on ε for the composite with the carbon black filler only. These plots show that the material as a result of cyclic loading along the first axis (X) undergoes considerable softening after the first cycle, in the second and third cycles the situation stabilizes. The hysteresis loop on the first cycle is also much larger than in the second and third ones. Most interestingly, almost exactly the same curves were obtained for subsequent loading in the perpendicular direction (Y-axis), that is, for a given composite, the load history for X has no effect on the Y loading history.

The addition of just 5 phr of carbon nanofibers to this composite significantly changes the behavior of the material. Fig. 7a shows the results of the first three cyclic loads along the X axis, and in Fig. 7b — the three subsequent cycles along the Y axis. When loaded along X, the plot is qualitatively the same as in the case of a only carbon black filler: the first cycle is characterized by the largest area of hysteresis and the greatest softening of the material. The curves corresponding to the second and third cycles lie nearby. In the subsequent deforming along Y, the material behaves quite differently. The previous deformation in the perpendicular direction led to the fact that all three cycles in Y coincide with the second and third cycles in X, that is, the uniaxial "training" of this composite causes its isotropic softening.

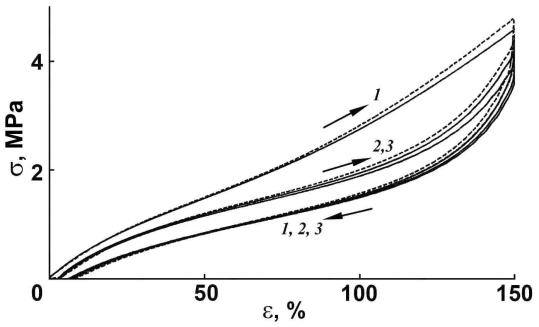

Figure 6: Biaxial testing of an elastomer filled by carbon black nanoparticles; solid lines — tensile curves along the X axis, dashed lines — along the Y axis

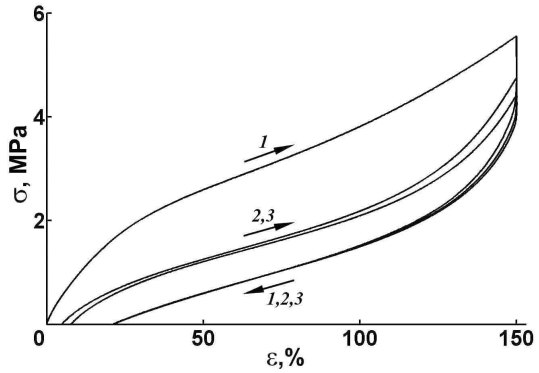

a

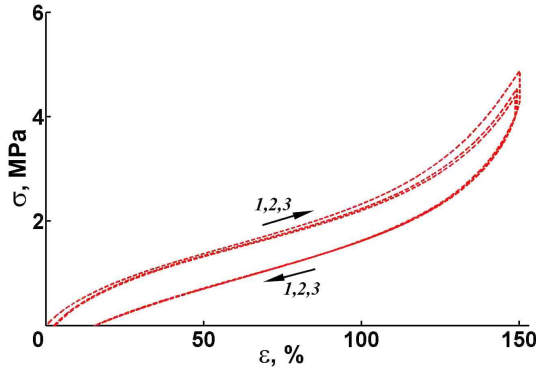

b

Figure 7: Biaxial testing of an elastomer filled by nanofibers and carbon black; (a) — deformation along the X axis, (b) — deformation along the Y axis. 1, 2 и 3 — cycle numbers

4 Summary

Experimental studies showed that the mechanical behavior of dispersed filled elastomers (induced anisotropy of the module and viscoelastic properties) at biaxial tests depends on what materials are used as filler. Pure rubber remains practically elastic and isotropic material, regardless of the type of applied load. For samples with shungite or technical carbon as filler, cyclic deformation along one axis causes a corresponding softening along the same axis, but does not affect the mechanical behavior of the material in the perpendicular direction. In the case of filler made of carbon black with nanofibers, cyclic deformation along one axis causes similar softening along another axis (isotropic softening). This effect can also be observed for the filler of silicic acid particles, but it is much weaker than for carbon nanofibers.

Acknowledgements

This work is executed at a financial support of RFBR Grant 17-08-01118.

References

[1] Moshev V.V. Garishin O.K. Structural mechanics of dispersed filled elastomeric composites // Achievements in Mechanics, 2005. V. 4, N 2. P. 3–36. (in Russian)

[2] Garishin O.K. Mechanical properties and destruction of dispersely filled elastomers. Structural modeling. Germany, Saarbrucken: Palmarium Academic Publishing (LAP), 2012. 286 p. (in Russian)

[3] Rooj S., Das A., St*ö*ckelhuber K.W., Reuter U., Heinrich G. Highly exfoliated natural rubber/clay composites by "propping-open procedure": the influence of fatty acid chain length on exfoliation // Macromol. Mater. Eng., 2012. V. 297. P. 369–383.

[4] Rooj S., Das A., St*ö*ckelhuber K.W., Mukhopadhyay N., Bhattacharyya A.R., Jehnichen D. Pre-intercalation of long chain fatty acid in the interlayer space of layered silicates and preparation of montmorillonite/natural rubber nanocomposites // Appl. Clay. Sci., 2012. V. 67–68, P. 50–56.

[5] Rooj S., Das A., Morozov I.A., St*ö*ckelhuber K.W., Stocek R., Heinrich G. Influence of "expanded clay" on the microstructure and fatigue crack growth behavior of carbon black filled NR composites // Composites Science and Technology, 2013. V. 76. P. 61–68.

[6] Lvov Y., Fakhrullin R., Wang W., Zhang L. Hallousite clay nanotubes for loading and sustained release of functional compounds // Advanced Materials, 2016. V 28, N 6. P. 1227–1250.

[7] Garishin O.K., Shadrin V.V., Svistkov A.L., Sokolov A.K., St*ö*ckelhuber K.W. Visco-elastic-plastic properties of natural rubber filled with carbon black and layered clay nano-particles. Experiment and simulation // Polymer Testing, 2017. V. 63. P. 133–140.

[8] Garishin O.K., Shadrin V.V., Svistkov A.L., Sokolov A.K. Experimental studies of rubbers filled by layered clay nanoparticles // XLV Summer School-Conference "Advanced problems in mechanics": Proceedings, St.-Petersburg, 2017. P. 168–174.

[9] Mokhireva K.A., Svistkov A.L., Solod'ko V.N., Komar L.A., St*ö*ckelhuber K.W. Experimental analysis of the effect of carbon nanoparticles with different geometry on the appearance of anisotropy of mechanical properties in elastomeric composites // Polymer Testing, 2017. V. 59. P. 46–54.

[10] Kornev Yu.V., Chirkunova C.V. Boiko O.V., Simonova M.A., Shugaeva V.O., Yanovsky Yu.G. Investigation of the effect of dispersion of mineral shungite on the complex properties of elastomeric compositions based on rubber SKTN-A // Caoutchouc and rubber, 2012. N 6. P. 10–14. (in Russian)

[11] Kornev Yu.V., Yanovskiy G., Boiko V., Semenov N.A., Chirkunova S. Investigating the influence of the degree of dispersion of mineral shungite on the

properties of elastomeric materials based on butadiene-styrene rubber // International Polymer Science and Technology, 2013. V. 40, N 3. P. 17–22.

[12] Mullins L. Effect of stretching in the properties of rubber// J. of Rubber Research, 1947. V. 16, N 12. P. 245–289.

[13] Shadrin V.V. Recovery of the mechanical properties of rubber under thermal treatment // Polymer Science, Ser. B, 2005. V. 47, N 7–8. P. 220–222.

[14] Diani J., Fayolle B, Gilormini P. A review on the Mullins effect // European Polymer Journal, 2009. V. 45. P. 601–612.

[15] Sokolov A.K., Svistkov A.L., Komar L.A., Shadrin V.V., Terpugov V.N. Stress softening effect on changes in the stress-strain state of a tire / Computational Continuum Mechanics, 2016. V. 9, N 3. P. 358–365. (in Russian)

[16] Buseck P.R. Geological fullerenes: review and analysis // Earth and Planetary Science Letters, 2002. V. 203. P. 781–792.

[17] Kwiecinska B., Pusz S., Krzesinska M., Pilawa B. Physical properties of shungite // International J. of Coal Geology, 2007. V. 71, N 4. P. 455–461.

[18] Ignatov I., Mosin O.V. Composition and structural properties of the natural fullerene-containing shungite mineral // Nanoengineering, 2012. N 6. P. 17–23.

[19] Kornev Yu.V., Yanovskiy Yu.G., Boiko O.V., Chirkunova S.V. Guseva M.A. The effect of carbon nanotubes on the properties of elastomeric materials filled with the mineral shungite // International Polymer Science and Technology, 2013. V. 40, N 2. P. 29–32.

[20] Kornev Yu.V., Yanovskiy Yu.G., Boiko O.V., Semenov N.A., Chirkunova S.V. Investigating the influence of the degree of dispersion of mineral shungite on the properties of elastomeric materials based on butadiene-styrene rubber // International Polymer Science and Technology, 2013. V. 40, N 3. P. 17–22.

[21] Koyama T, Endo M. Structure and Growth Processes of Vapor-Grown Carbon Fibers // O. Buturi, 1973. V. 42. P. 690–696. (in Japanese)

[22] Tibbetts. G. Lengths of carbon fibers grown from iron catalyst particles in natural gas // Journal of Crystal Growth, 1985. V. 73, N 3. P. 431–438.

[23] Chemical Encyclopedia / Knuniants I.L. and etc. — M.: Soviet encyclopedia, 1990 — 671 p. (in Russian)

[24] Mokhireva K.A., Svistkov A.L., Shadrin V.V. Determination of the optimal shape of the samples for experiments on biaxial stretching // Computational Continuum Mechanics. 2014. V. 7, N 4. P. 353–362. (in Russian)

Oleg K. Garishin, Institute of Continuous Media Mechanics, Perm, Russia

Vladimir V. Shadrin, Institute of Continuous Media Mechanics UB RAS, Perm, Perm State National Research University, Russia

Yuri V. Kornev, Institute of Applied Mechanics RAS, Moscow, Russia

Laser thermoelasticity of brittle and ductile materials in the initial and modified states

Alexei L. Glazov, Nikita F. Morozov, Kyrill L. Muratikov
glazov.holo@mail.ioffe.ru

Abstract

Non-destructive evaluation of samples made from brittle and ductile materials with various structures with residual stresses was performed by the laser thermoelastic method with piezoelectric signal registration. Main attention was paid to experimental investigations of thermoelastic effect near specially made defects like indentation or holes under external loading. The stress distribution was studied near crack tips, small shallow holes, Vickers indentations and 3D-printed steel samples. It is shown that the laser ultrasonic signal is very sensitive to residual stresses especially in metals. The possible reasons for this signal behavior are discussed and an effect of residual stress on the thermoelastic signal is estimated.

1 Introduction

Laser generation of sound is an important area of modern mechanics and physics of solids [1, 2]. Laser ultrasonic methods also play an increasingly important role in solving problems of non-destructive testing of solids and structures [3, 4, 3, 6]. The basic mechanisms of laser generation of sound in solids are based on thermoelasticity. Important details of laser thermoelasticity depend on the radiation power, the time range of the laser exposure, the type of material [7]. The characteristic times of modern laser sound generation methods ranges from femtoseconds to milliseconds. Materials of various types are being actively studied at present by means of laser thermoelastic methods. Both the time scale and the type of material can impose significant features on thermoelastic processes. Of particular interest are studies that establish specific features of the effects of laser thermoelasticity in materials with a complex rheological structure and containing defects of various types. Attention to these issues is strongly stimulated by the need to develop new methods of nondestructive testing [8, 9].

In this paper, thermoelasticity problems are considered in brittle and ductile materials. The specific feature of this article is that when considering thermoelasticity, pre-stressed state of the material and the presence of plastic deformations in it are taken into account [10]. The main results on laser thermoelasticity were obtained for ceramics as a brittle material [10, 11], and for metals as a plastic material [12, 13, 14]. Near-surface defects in samples is modeled by Vickers and Rockwell

indentations and hole drilling. The laser thermoelastic (TE) signal was measured by a piezoelectric detector. The behavior of laser thermoelastic signals under the action of external unidirectional compressive stress in these materials was studied in details. For ceramics such investigations were carried out for regions near the tips of vertical cracks.

2 Theoretical part

Classical thermoelastic theory is based on two coupled equations, namely, the heat conduction and motion equations. However, for many cases the coupling is small and may be omitted. Then the system of thermoelastic equations may be represented as [15].

$$\nabla^2 T - \frac{1}{\kappa}\dot{T} = -\frac{Q}{\lambda_T}, \tag{1}$$

$$\rho\ddot{\vec{u}} = \mu\nabla^2\vec{u} + (\lambda+\mu)\mathrm{graddiv}\vec{u} - K_\epsilon \mathrm{grad}T, \tag{2}$$

where T is the change of the temperature of the body comparing to the environmental temperature, $\vec{u}$ denotes deformations of the body, Q is the heat produced in the body by external sources, λ and μ are Lam*é* elastic constants, λ_T and κ are the thermal conductivity and diffusivity, K_ϵ is the thermoelastic parameter of the material.

The first equation may be solved independently and the solution is inserted in the equation of motion. The thermoelastic parameter takes place at the equation of motion as well as at the boundary conditions for stresses through the Duhamel-Neiman relation. Because the main aim of the paper is to reveal the relations between the TE signal and the residual stress, we studied a possible stress dependence of elastic parameters.

First of all we will be interested in the dependence of laser ultrasonic signals on mechanical stresses. For this purpose we compare the degree of influence of stresses on the coefficient of thermal expansion and on the mechanical parameters of the material. Let us first consider such dependence for the coefficient of thermoelastic coefficient.

It was shown by thermodynamic methods [16] that in adiabatic conditions and at the independence of PoissonIs ratio on the temperature the thermoelastic parameter is related to the first stress invariant as follows

$$K_\epsilon = K_\epsilon^{(0)} + K_\epsilon^{(1)} = 3K\left(\alpha_T - \frac{1}{E^2}\frac{\partial E}{\partial T}\sigma\right), \tag{3}$$

where α_T is the coefficient of linear thermal expansion, E is Young's modulus, $\sigma = \sigma_{ii}$ is the first stress invariant, K is the bulk modulus, $K_\epsilon^{(0)} = 3K\alpha_T$ is the thermoelastic parameter of a body in the unstressed state.

To get the stress dependence of other elastic parameters one needs to use non-linear elastic theory. Expression for the pressure dependence of the bulk modulus K and

shear modulus μ were obtained in [17]. Coefficients $\frac{dK}{d\sigma}$ and $\frac{d\mu}{d\sigma}$ were derived on the base of non-linear MurnaghanIs model:

$$K(\sigma) = \lambda + \frac{2}{3}\mu - \frac{18l + 2n}{9\lambda + 6\mu}\sigma, \tag{4}$$

$$\mu(\sigma) = \mu - \frac{6m - n + 6\lambda + 6\mu}{6\lambda + 4\mu}\sigma, \tag{5}$$

here λ and μ are Lam*é* constants for the unstressed state, l, m and n are Murnaghan constants. Experiments on the measurement of various sound velocities made it possible to determine the numerical values of $dK/d\sigma$ and $\frac{d\mu}{d\sigma}$ for some materials, and in particular for steel they amounted to $\frac{dK}{d\sigma} = 2.7\pm1.6$ and $\frac{d\mu}{d\sigma} = 6.3\pm1.0$. Note that for other materials these coefficients may be negative.
Scholz and Frankel [18] based on the above approach have estimated the dependence of the Young's modulus and the Poisson's ratio on the uniaxial pressure σ_{11} for steel grade 4340, and obtained the following expressions

$$E = 206.2 \times 10^{-9}(1 - 2.56 \times 10^{-11}\sigma_{11})(\text{Pa}),$$
$$\nu = 0.29(1 - 4.89 \times 10^{9}\sigma_{11}),$$

where σ_{11} is expressed in Pa. Numerical data are obtained on the basis of measurements of sound velocities and subsequent determination of elastic constants of the second and third order (λ=11.04, μ=7.99, l=-38.8±3.6, m=-62.4±2.4, n=-74.7±1.6). That is, these values vary by a few percent near the yield point.
To estimate the influence of the obtained dependences on the TE signal, we consider a simple model of signal generation, which assumes its proportionality to the displacement speed of the sample surface attached to the piezoelectric detector. Let the infinite sample of thickness L be uniformly illuminated by laser radiation, modulated in time according to the harmonic law $I(t) = I_0 \exp(i\omega t)$. Then the time dependent functions will have the form $T(t) = T\exp(i\omega t)$, $u_{xx}(t) = u_{xx}\exp(i\omega t)$, $Q(t) = Q\exp(i\omega t)$, where Q is the thermal flow on the sample surface $x = 0$.
Then, for surface absorption, the temperature is determined from the heat equation

$$\frac{\partial^2 T}{\partial x^2} = \frac{i\omega}{\kappa}T \tag{6}$$

with the boundary conditions

$$K_T \frac{\partial T}{\partial x}\Big|_{x=0} = -Q, T\Big|_{x=L} = 0. \tag{7}$$

The motion equation

$$-\rho\omega^2 u_{xx} = (\lambda + \mu)\frac{\partial^2 u_{xx}}{\partial x^2} - K_\epsilon \frac{\partial T}{\partial x} \tag{8}$$

with the boundary conditions, for instance, for the free surfaces

$$\sigma_{xx}(x = 0) = \sigma_{xx}(x = L) = 0 \tag{9}$$

allows us to calculate u_{xx}. For a thermally thick sample with $L\sqrt{\frac{\omega}{2\kappa}} >> 1$,

$$u_{xx}(L) = 2QK_\epsilon \left(c(\sigma)(K + 4\mu/3) \sin(c(\sigma)L) K_T \sqrt{i\omega/\kappa} \right)^{-1}, \quad (10)$$

where $c(\sigma) = \omega\sqrt{\rho/(K + 4\mu/3)}$. Substituting the above values we get the 4% increase of u_{xx} at σ=1 GPa.

3 Experimental part

3.1 Experimental set-up

All TE images were obtained by scanning laser TE microscope. Thermal and acoustic waves in samples were excited by a solid-state laser radiation at the wavelength 532 nm. The DC laser radiation intensity was periodically temporal modulated by an acousto-optic modulator and focused on the sample surface into a spot of 5 Bxm in diameter. Acoustic waves in a sample were excited at one of the resonant frequencies of a piezoelectric transducer attached to its rear unilluminated side. The PZT detector size was $32 \times 14 \times 7$ mm^3. The operating resonant frequency of the used piezoelectric transducer was near 140 kHz. The voltage from the detector was applied to an input of an amplifier for a piezoelectric signal and then to a lock-in amplifier. The block-schema of the experimental set-up is presented in Fig. 1. Laser TE images were obtained by scanning the sample surface by the laser beam over two coordinates with a 2.5 Bxm step. The known uni-axial compressive mechanical stress was applied during the measurements to the side surfaces of the samples parallel to the illuminated surface.

3.2 Thermoelastic study of cracks in brittle materials

Experimental and theoretical studies of laser TE signals in ceramics near the ends of radial cracks showed the presence of strong peculiarities in their behavior in these regions [10, 11]. Experiments with the external uni-axial stress have demonstrated a strong effect of these stresses on the behavior of laser TE signals near the tips of cracks. By laser photoacoustic microscopy methods the distribution of these features was investigated near the ends of cracks. The analysis of the results obtained in the frequency domain showed that signal formation is primarily due to laser excitation of thermal and thermoelastic waves, and not due to the subsequent generation of acoustic waves.

Experiments with a different orientation of the Vickers indentations in ceramics relative to the direction of the external stress action allowed us to estimate the degree of influence of normal and tangential components of stress on laser TE signals near the tips of radial cracks [19]. It was shown that their behavior corresponds well to the theoretical distribution of normal and tangential stresses near the ends of the surface cracks. Up to a certain magnitude of the indentation load, an increase in the amplitude of the laser signals was observed near the ends of the cracks, which, after reaching it, was saturated. Our experiments on ceramics of silicon nitride and ceramics based on aluminum oxides showed very similar results

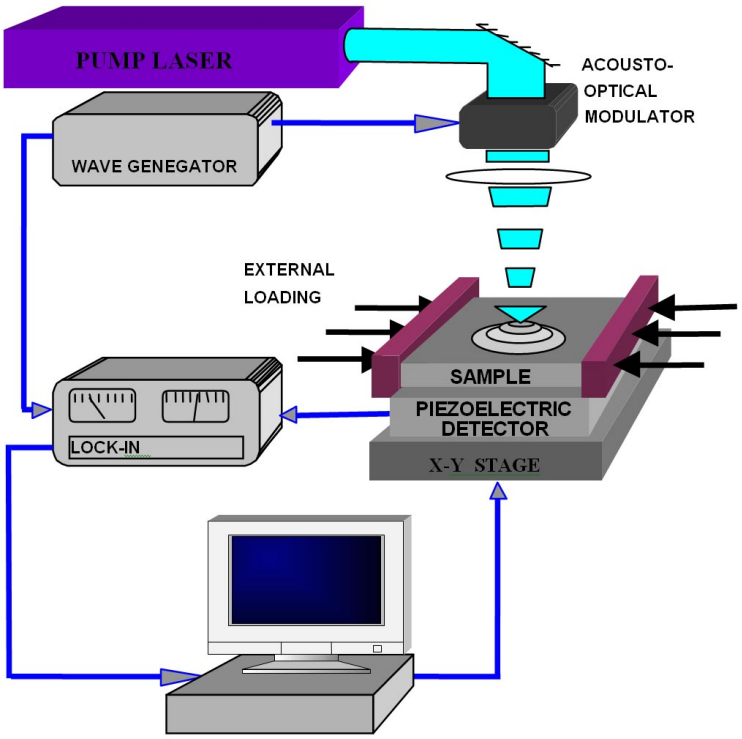

Figure 1: Experimental set-up.

Various ceramics were investigated as brittle materials. The system of cracks was created in the samples by the method of indentation by Vickers. This method allows the reproduction of cracks of a certain length, depending on the load on the indenter. Fig. 2 presents the TE images of the region around the print. On the TE image in the ends of the cracks, a significant increase in the signal is observed. The application of an external uniaxial load at different angles to the cracks made it possible to determine the intensity coefficients.
The stress intensity factors of the crack in general case are determined by the total action of residual stresses and stresses produced by external loading. In linear crack mechanics mechanics the normal and shear components of the total stress intensity factors of a crack can be represented in the form [20]

$$K_I = K_I^{(0)} + K_I^{(1)} \sin^2\phi,\ K_{II} = K_{II}^{(0)} + K_{II}^{(1)} \cos\phi \sin\phi, \tag{11}$$

where $K_I^{(0)}$ and $K_{II}^{(0)}$ are the stress intensity factors which are related to residual stresses, $K_I^{(1)}$ and $K_{II}^{(1)}$ are the stress intensity factors that characterize the crack behavior under external loading, ϕ is the angle between the crack and direction of the external loading.
For small strains near the surface, the change of the TE signal due to the stress may be estimated as

$$\Delta S = AS_0(\sigma_{xx} + \sigma_{yy}), \tag{12}$$

where S_0 is the TE signal from the unstrained sample, constant A depends on the thermoelastic parameters including third-order elastic constants.

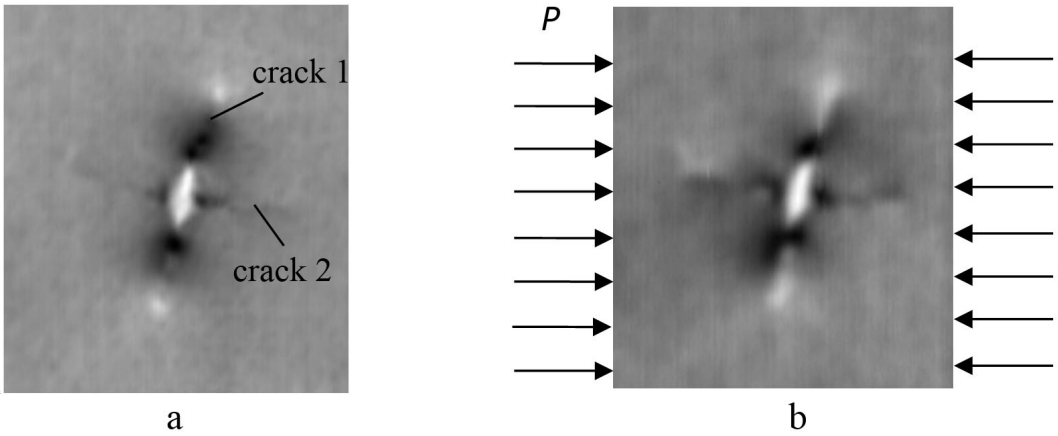

Figure 2: The TE image of Vickers indentation in Al_2O_3-SiC-TiC ceramic a - without external load, b - under the external load of 170 MPa. The indentation load is 98 N, the area is 480×500 μ m^2.

According to [Sedov], the stress tensor components near a crack tip accounting an external loading are

$$\sigma_{xx}+\sigma_{yy}=\sqrt{\frac{2}{\pi r}}\left(K_I\cos\frac{\theta}{2}-K_{II}\sin\frac{\theta}{2}\right), \tag{13}$$

where we used the polar coordinate system with the center at the crack tip.
For residual stress near the tips of radial cracks produced by Vickers indentation with a load P, the stress intensity factors are given by [21]

$$K_I^{(0)}=\chi P/L^{(3/2)},\ K_{II}^{(0)}=0, \tag{14}$$

where χ is a dimensionless factor depending on the crackIs shape and L is the length of the crack.
Then the TE signal near the radial crack tips can be expressed in the form [11]

$$\Delta S=AS_0\sqrt{\frac{2}{\pi r}}\left[\left(K_I^{(0)}+K_I^{(1)}\sin^2\phi\right)cos\frac{\theta}{2}-K_{II}^{(1)}\sin\phi\cos\phi sin\frac{\theta}{2}\right], \tag{15}$$

The detailed analysis of experimental data given in Fig. 2 allows us to estimate ratio $K_I^{(1)}/K_{II}^{(1)}$. For example, the ratio is about 1.4 for crack 1. This result correlates well with a theory of vertical cracks in thick plates [Sedov]. In this case, the theory predicts $K_I^{(1)}=K_{II}^{(1)}$.

3.3 Thermoelastic studies of plastic materials

As a rule, there are no cracks in plastic materials, but many different structures with complex rheology can be formed that contain stress concentrators of various shapes and intensities that can lead to a strong dependence of the TE signal on both internal and external stresses.

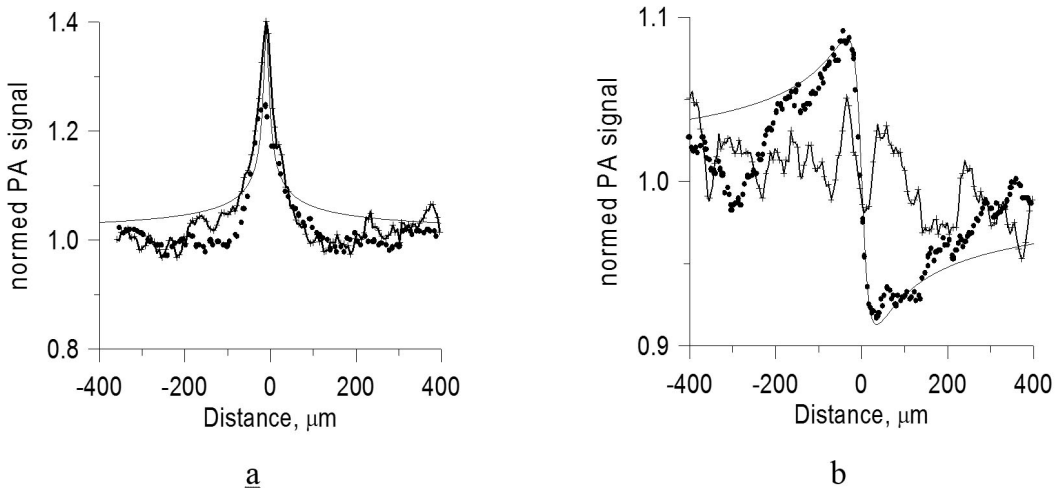

Figure 3: The behavior of the PA signal across the tips of radial cracks. a - for crack 1, b - for crack 2. + denotes the experimental data for the sample without external loading, • denotes the experimental data for the sample under the external loading of 170 MPa, solid line is a theoretical curve.

3.3.1 Method of drilling holes.

The method of drilling holes for the determination of internal stresses is well developed in combination with strain gauges or holographic interferometry [22, 23]. This is primarily determined by the fact that the problem of stress distribution around a small hole in a pre-stressed object was solved quite a long time [8].
The radial and tangential stresses are written as follows

$$\sigma_r = \frac{P}{2}\left(1 - \frac{a^2}{r^2}\right) + \frac{P}{2}\left(1 + \frac{3a^4}{r^4} - \frac{4a^2}{r^2}\right)\cos 2\vartheta, \tag{16}$$

$$\sigma_\vartheta = \frac{P}{2}\left(1 + \frac{a^2}{r^2}\right) - \frac{P}{2}\left(1 + \frac{3a^4}{r^4}\right)\cos \vartheta, \tag{17}$$

where P is the pressure along the axis from which the angle ϑ is measured, a is the radius of the hole, and r is the polar radius. In the case of the formation of the TE signal, we will be interested in the total stress, which in the plane of the surface is equal to

$$\sigma = \sigma_r + \sigma_\vartheta = P - P\frac{2a^2}{r^2}\cos 2\vartheta. \tag{18}$$

Fig.4 demonstrates the graph corresponding to this formula. In mechanics, tensile stresses are positive. However, in our thermoelastic experiments, the TE signal usually increases with compressive stresses, which correlates, for example, with the formula for the coefficient of thermal expansion. When using modulation frequencies in the region of hundreds of kilohertz, the thermal wave length in metallic alloys is of the order of a dozen microns, so even with relatively shallow holes this formula can be considered a good approximation.
A sample for such research was made of a duralumin alloy D16 measuring $6 \times 3 \times 3.6$ mm^3, in the center of which a drill hole of 0.2 mm diameter was drilled at a depth

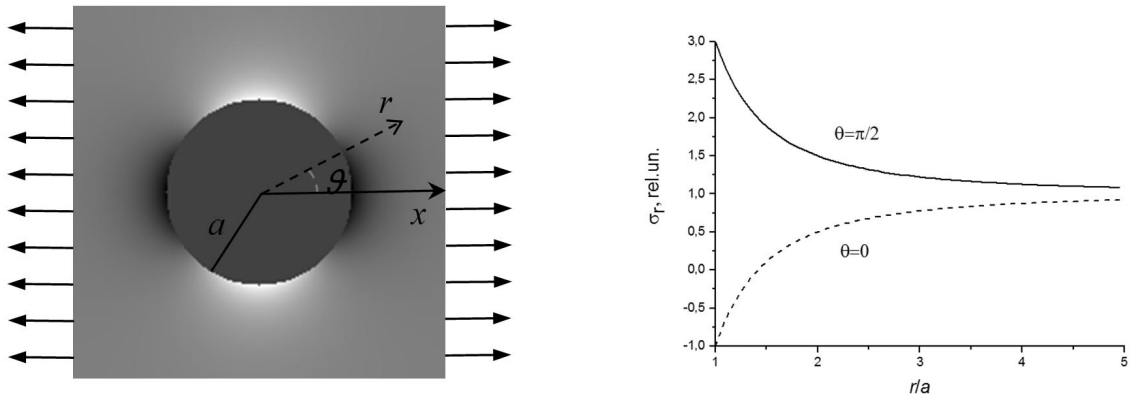

Figure 4: Distribution of stresses around the hole under uniaxial tension P=1.

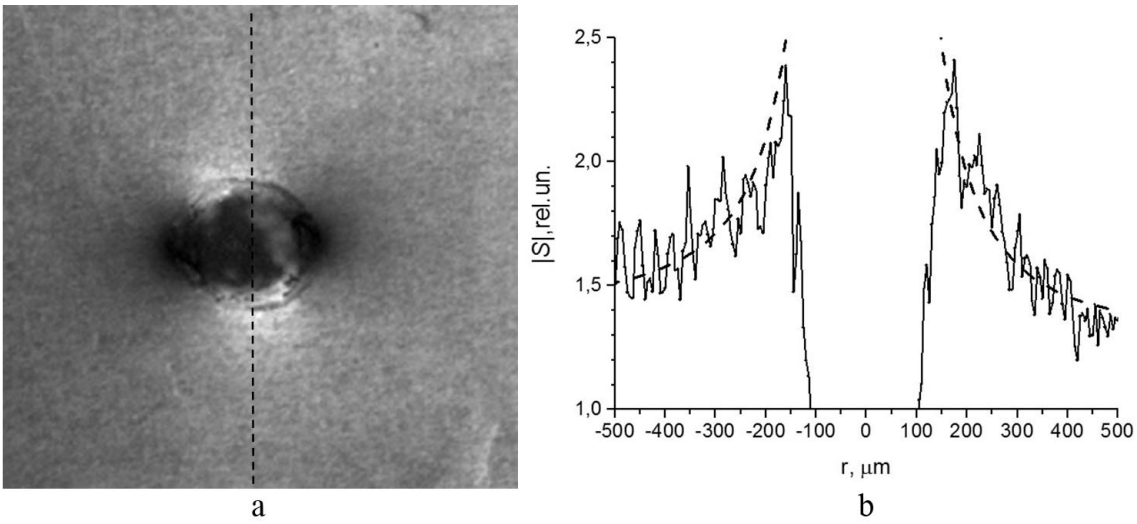

Figure 5: (A) The TE image of a sample from alloy D16 around a small hole. The image size is 1.1×1.1 mm^2. (B) is the cross-section of the TE of the image along the line of the hole through the center at an angle of 90° to the horizontal axis x. The dash curves are the theoretical fitting.

of 0.25 mm. The surface of the sample was previously polished. The TE image of a part of the surface around the hole is shown in Fig. 5. First of all, it should be noted that the length of the thermal wave in the alloy at the used modulation frequency was 15 μm, the effect of the hole on the temperature change did not extend beyond this distance from its edge.

To analyze the behavior of the signal, we have made cross-sections of this image in two perpendicular directions passing through the center of the hole and two circles with a radius of 195 and 225 μm passing in the region of homogeneous heating. A trajectory of the section is shown in Fig. 5 by the dashed line. Minor changes in the signal relative to the trend are reproducible and are determined by the granular structure of the alloy. In accordance with our experimental data, compressive stresses lead to an increase in the signal, and tensile stresses lead to a decrease. In Fig.6 theoretical dependences are also shown in accordance with the Eq.17 for P

= 0.7 and 0.647 for the left and right branches, respectively. It can be seen that although the experimental curves do not have strict symmetry, on the whole they correspond to the theoretical model of stress distribution and, apparently, the TE signal is determined by them entirely. Particular attention should be paid to the strong dependence of the TE signal on internal stresses.
Our further work suggests the study of samples with a calibrated external load.

3.4 Additive technologies

Non-destructive testing of the properties and quality of products obtained with the help of additive technologies becomes more and more relevant in connection with the avalanche expansion of the field of applications and materials. Extremely promising is the use of metal microgranules, which are layer-by-layer sintered. Currently, it is believed that laser ultrasound diagnostics is the most informative and convenient method for these purposes [25].
We used our approach to study samples obtained by 3D printing a steel profile on the surface of a steel plate. As a starting material for printing, a powder from stainless steel 316L was used. The diameter of the initial microgranules was 15/40 μm, and the total thickness of the layer was 3 mm. The general view of the sample is shown in Fig.6a: a homogeneous substrate layer is on the left, a layer obtained by 3D printing is on the right. The image size is 1.5×2 mm^2. The TE image (Fig.6b) demonstrates a strong difference between the signals from the two halves of the sample. In contrast to the substrate, where a sufficiently uniform signal is observed, the change in the normalized signal for the "printed" layer is from 0 to 17. A particularly strong signal increase is observed along the substrate-deposited material boundary. In addition, zones of increased signal around individual grains are observed. In Fig. 6 various images of the border region of the sample are given. Black spots on the optical image are visible open cavities in the material obtained by additive technology. In other places, the heterogeneous structure of the regions seeming to be uniform under the microscope is seen. These inhomogeneities of the TE signal can be caused both by inhomogeneous heating due to the presence of cavities and by the presence of stresses, similar to the distribution of internal stresses arising near the apertures, as was demonstrated in the previous section. When an external load is applied to the TE, the image changes. A characteristic feature of these changes is the decrease in the signal (black regions), mainly around the inhomogeneities elongated along the boundary. This indicates that the residual stresses in these regions were directed across the boundary and, when squeezed in this direction, the total stress decreased. This is consistent with the results of our studies of TE signals around cracks in brittle materials.
For clarity of signal distribution Fig.7 presents a cross section of the TE image along the lines shown in Fig. 6 by the dotted lines. The cross section demonstrates homogeneous behavior at $x < 0$ and very strong signal changes on the right side. Near the border, there are places where the TE signal in 17 times more than that for the homogeneous part. This signal may be reduced by applying pressure perpendicular to the border. Other places, e.g., at x=800 μm, demonstrate strong enhance of the signal, which corresponds to a defect concentrating stress.

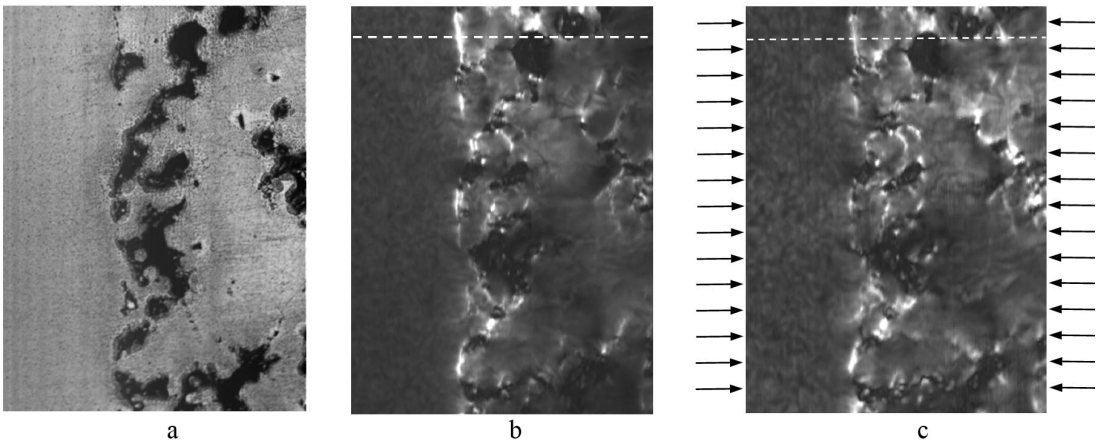

Figure 6: Images of the border region of the sample made of steel with a size of 1.5×2 mm^2. (A) is the optical image, (b) is the TE image, (c) is the TE image of the sample at the uniaxial compression 35 MPa.

Thus, laser thermoelastic diagnostics makes it possible to reveal not only the structure of materials obtained by additive technology, but also the distribution of internal stresses, and this can be done in the production process.

3.5 Indentations in metals

As in the case of ceramics, the indentation method is used in plastic materials for hardness testing. However, in this case, the indenter produces only plastic deformations without cracking. At the same time, however, a system of residual stresses is formed, which is stably reproduced. For the interpretation of the behavior of laser TE signals from indents by Vickers and Rockwell, theoretical models were proposed that take into account their complex rheological structure. Investigation of laser dynamic processes involving thermal, thermoelastic and mechanical processes in such structures are of great interest [26, 27]. Experimentally we found that laser signals have significantly more pronounced features for Vickers indents. We showed by the TE microscopy method that the stress distribution after removing the load on the indenter depends on the state of the sample before indenting [12, 13, 14]. Moreover, the external load can significantly change the stress distribution in the imprint area. Depending on the orientation of the print with respect to the direction of action of the external load, the change in the stress distribution can be reversible or irreversible with the same load. As an example, Fig.8 presents the TE images of Vickers prints in steel in the initial state and under the influence of an external load. The TE signal changes strongly under the load 24 MPa and returns mainly to the initial state after the load relief. This shows that the load has produced elastic effect on the sample and the signal changes were due to the stresses rather than plastic deformation. Again we see that the signal increase was more than 2 times.

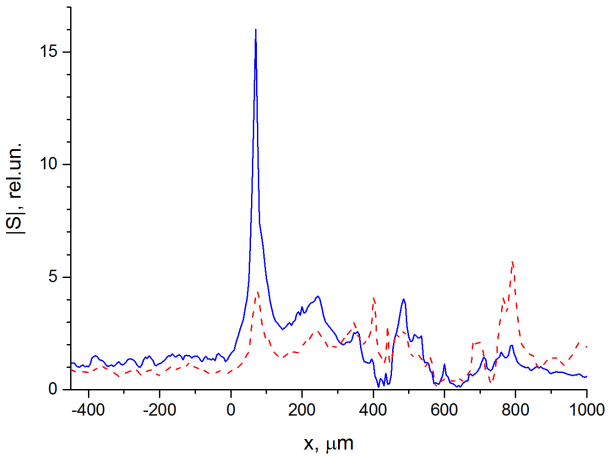

Figure 7: A cross-section of the TE image along the dash line shown in Fig. 7b. Solid blue line is the TE signal for the sample in the initial state, red dash line is the TE signal for the sample under the uniaxial external compressive pressure 35 MPa.

4 Discussion

The study of strained samples from various materials and various inhomogeneities showed a strong dependence on stresses, which is not explained completely by the known dependence of the elastic parameters. At the same time, in brittle materials, the effect of stress on the TE signal was less than in metals. For example, the maximum increase in the TE signal at compressive stresses was about 40% compared to the unstressed state. In metal samples, the excess of the signal from the stressed regions was hundreds of percent. The influence of tensile stresses could suppress the signal practically to zero. The behavior of the signal in cases with a known stress distribution confirms the proportionality of the signal to the first invariant of the stress tensor.

The reasons for an additional increase in the signal in metals can be several. The main reason may be that a two-component model should be used for metals. The main part of the laser radiation is absorbed by the electrons and then is given to the lattice as a result of the electron-phonon interaction. In the general case, to describe such a process, it is necessary to use a two-temperature model that takes into account the electron and lattice temperature difference [28]. Taking into account, however, that the electron-lattice relaxation processes are carried out over times of the order of a few tens of ps, when modulating laser radiation with frequencies in the megahertz range, this difference can be neglected. The classical equations of thermoelasticity take into account the effect of laser excitation of elastic waves only through thermal and thermoelastic phenomena in the crystal lattice. For metals, the contribution of the electronic system to mechanical processes should also be taken into account. As is known, the presence of an electron gas in metals leads to the appearance of a new thermoelastic constant, which takes into account the effect of electrons on lattice deformation. In addition to the dynamic processes in the lattice, conductors in

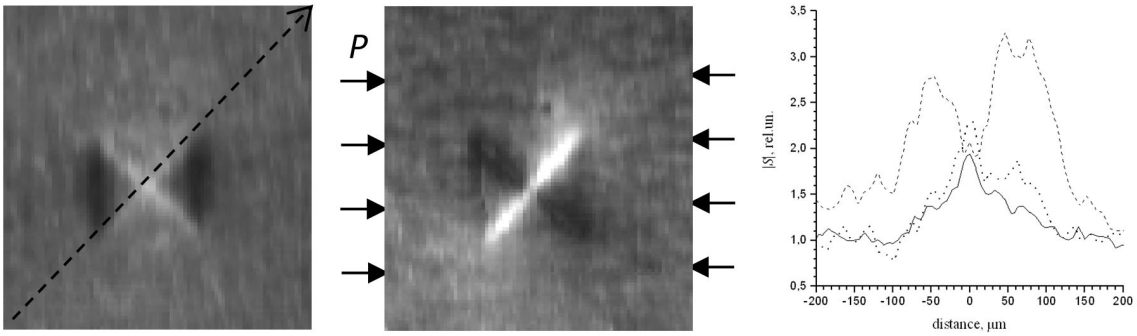

Figure 8: The TE images of Vickers prints in steel grade U8. The load on the indentor is 98N, the image size is 430×430 μm^2. (A) is the sample in the initial state, (b) is the sample under load of 24 MPa, (c) is the TE signal along an indentation diagonal shown as a dash line in (a). The solid, dashed, and dotted curves correspond to the initial sample state, the sample under load, and the sample after load relief, respectively.

parallel have kinematic processes in the electron gas [29, 30]. In the pico-femtosecond range, the interaction of electrons and lattices leads to the effect of an electron shock wave [31]. In the low-frequency range, the absorption of energy by electrons leads to an additional pressure on the lattice, which can lead to an increase in the TE signal.

In the study of imprints from different indenters, a strong change in the TE signal is observed at places of sharp changes in the surface geometry, namely, at the edges of prints and diagonals. These elements are stress concentrators and can lead to an increase in stresses [32] We estimated the stress increase at the diagonals of Vickers indentation up to two orders [13].

In addition, the entire region under the indenter is subject to strong plastic deformation, in which the thermoelastic effect can differ significantly from such an effect in an initial material. First, Young's modulus in the zone of plastic deformation decreases, which, according to Eq. 2, leads to an increase in the influence of stresses on the termoelastic parameter. Secondly, we can talk about nonlinear kinking elasticity observed in solids with plastic anisotropy. These include materials with a layered microstructure and regions with a large number of dislocations. The important mechanical feature of these materials consists in the formation of the stable closed hysteretic loops on their load-displacement curves under cycle loading and unloading. Such a stabilization of the hysteretic loops occurs after several cycles (usually less than 10). It is explained by the formation of reproducible and completely reversible dislocation motion appear in them after several cycles [33, 34, 35]. This circumstance can explain the formation of stable TE signals from the plastically deformed zones of materials during their cyclic laser illumination.

When a certain threshold load is exceeded, reproducible and completely reversible dislocation motion appear in them [33]. These hysteretic loadвГYdisplacement loops can additionally transmit thermal energy into acoustic vibrations.

5 Conclusion

The presented experimental and theoretical results exhibit a strong effect of mechanical stress on the laser TE signals near the tips of cracks in ceramics and from Vickers indented areas in metals. The registered characteristic features of the photoacoustic effect are common for various ceramics and metals subjected to external stress, which goes to show its general nature. The performed analysis has revealed the difficulties of internal and external stress registration by a conventional photoacoustic method that does not use the indentation. In this case, even significant internal or external stresses cause weak changes in the photoacoustic signals generated in metal samples. The presence of stress concentrators significantly enhances the stress influence on the laser TE ultrasonic signal.

Acknowledgments

This work was supported by Russian Science Foundation, project no. 15-19-001892.

References

[1] D. Cerniglia, A. Pantano, C. Mineo, Applied Physics: A, vol.105, pp.959-967, 2011.

[2] T.C. Truong, A.D. Abetew, J.-R. Lee, J.-B. Ihn, ASME J. Nondestructive Evaluation, vol.1, p.021001 (6 pages), 2017.

[3] D. Cerniglia, M. Scafidi, A. Pantano, J. Rudlin, Ultrasonics, vol.62, pp.292-298, 2015.

[4] D. Levesque, C. Bescond, M. Lord, X. Cao, P. Wanjara, J.-P. Monchalin, AIP Conf. Proc., vol.1706, p.130003, 2016.

[5] D. Cerniglia, N. Montinaro, Procedia Structural Integrity, pp.154-162, 2018.

[6] S. Everton, P. Dickens, C. Tdutton, The Journal of the Minerals, Metals (JOM), vol.70, pp.378-383, 2018.

[7] A. C. Tam, Rev. Mod. Phys., vol.58, pp.381-431, 1986.

[8] H. Huan, A. Mandelis, L. Liu, A. Melnikov, NDT&E International, vol.84, pp.47-53, 2016.

[9] H. Huan, A. Mandelis, L. Liu, Int. J. Thermophys., vol.39, pp.39-55, 2018.

[10] K.L.Muratikov, A.L.Glazov, D.N.Rose, and J.E.Dumar, J. Appl. Phys., vol.88, pp.2948-2955, 2000.

[11] K.L. Muratikov, A.L. Glazov, D.N. Rose and J.E. Dumar. Rev. Sci. Instrum., vol.74, pp.3531-3535, 2003.

[12] A.L. Glazov, N.F. Morozov, K.L. Muratikov, Tech. Phys. Lett., vol.42, pp.67-70, 2016.

[13] A.L. Glazov, N.F. Morozov, K.L. Muratikov, Phys. Solid State, vol.58, pp.1735-1743, 2016.

[14] A.L. Glazov, N.F. Morozov, K.L. Muratikov, Int. J. Thermophys, vol.38, p.113, (13 pages) 2017.

[15] L.D. Landau and E.M. Lifshitz. Theory of Elasticity, 187 p., Pergamon, New York (1986).

[16] A.K. Wong, R. Jones and J.G. Sparrow, J. Phys. Chem. Solids, vol.48, pp.749-753, 1987.

[17] D.S. Hughes and J. L. Kelly , Phys Rew., vol.92, pp.1145-1149, 1953.

[18] W. Scholz and J. Frankel, Technical report ARCCB-TR-86004, vol.46, 8 p., 1986.

[19] K. L. Muratikov, A. L. Glazov, D. N. Rose, J. E. Dumar, High Temperatures-High Pressures, vol.34, pp.585-590, 2002.

[20] L. M. Sedov, Mechanics of Continuous Medium, vol.1, 528 p., Nauka, Moscow (1994) (in Russian)

[21] S.M. Smith, and R.O. Scattergood, J. Am. Ceram. Soc., vol.75, pp.305-315, 1992.

[22] A.A. Antonov, Weld Prod., vol.30, pp.29-31, 1983.

[23] ASTM Standard E837-01 Standard Test Method for Determining Residual Stresses by the Hole-Drilling Strain-Gage Method, 2001.

[24] S.Timoshenko and J.N.Goodier, Theory of elasticity, 506p., McGrow-Hill book company, Inc. N.Y, (1951)

[25] Zhong Yang Chua1, Il Hyuk Ahn1, Seung Ki Moon, International journal of precision engineering and manufacturing-green technology, vol.4, pp.235-245, 2017.

[26] D. A. Indeitsev, Yu. I. Meshcheryakov, A. Yu. Kuchmin, D. S. Vavilov, Acta Mechanica, vol.226, pp.917-930, 2015.

[27] D. A. Indeitsev, D. Y. Skubov, D. S. Vavilov, Mechanics and Model-Based Control of Advanced Engineering Systems , Springer, Vienna, pp.181-188, 2014.

[28] L. Jiang, H.L. Tsai, J. of Heat Transfer, vol.127, pp.1167-1173, 2005.

[29] M. Cutler, N.F. Mott, Phys. Rev., vol.181, pp.1336-1340, 1969.

[30] A. Eisenbach, T. Havdala, J. Delahaye, T. Grenet, A. Amir, A. Frydman, Phys. Rev. Lett., vol.117, p.116601 (5 pages)., 2016.

[31] D.Y. Tzou, J.K. Chen, J.E. Beram, J. of Thermal Stresses, vol.28, pp.563-594, 2005.

[32] M.P. Savruk, A. Kazberuk, Int. Appl. Mech, vol.43, pp.182-197, 2007.

[33] P. Finkel, A.G. Zhou, S. Basu, O. Yeheskel, M.W. Barsoum, Appl. Phys. Lett., vol.94, p.241904 (3 pages), 2009.

[34] A. G. Zhou, S. Basu, G. Friedman, P. Finkel, O. Yeheskel, M. W. Barsoum, Phys. Rev. B, vol.82, p.094105 (10 pages), 2010.

[35] B. Anasory, M.W. Barsoum, MRS Communications , vol.3, pp.245вГY248, 2013.

Alexei L. Glazov, Ioffe Physical-Technical Institute, Polytekhnicheskaya 26, 124021 St.Peterburg, Russia
Nikita F. Morozov, Institute of Problems of Mechanical Engineering, Bolshoi pr.VO 61,199178 St.Petersburg, Russia
Kyrill L. Muratikov, Ioffe Physical-Technical Institute, Polytekhnicheskaya 26, 124021 St.Peterburg, Russia

An Analogy of the Equilibrium of a Two-legged Robot on a Cylinder for the Problem of Transfer by a Manipulator With a Two-finger Grasp of a Cylinder

Yury F. Golubev, Elena V. Melkumova
elena_v_m@mail.ru

Abstract

We consider a walking robot with m legs that ensure the desired motion of the robot body. Each of the robot legs contacts the surface in a single foothold. We describe the robot motion within the framework of general dynamics theory, with six differential equations for the robot motion derived from the momentum and angular momentum theorems. In the case of two-legged robot, $n = 2$, we reduce the problem of the existence of the solution to a system of algebraic inequalities. We present the classification of footholds positions for different values of the friction coefficient k.

We show an analogy of the problem of the equilibrium of a two-legged robot on an inclined rough cylinder for the problem of transfer by a manipulator with a two-finger grasp of a rough cylinder.

1 A cylinder grasping problem

In this paper, we discuss the problem of walking robot dynamics on one-side constraint. While the general walking robot motion on a plane was analyzed in detail in Ref. [1] the case of the dynamics on a curved surface is far more complicated. Model dynamics and control problems was considered in [2]. Equilibrium conditions for a solid on a rough plane was considered in [3]. Walking robot parameters optimization for the motion in tubes was considered in [4]. The special case of a robot with eight legs whose up porting points are restricted to the inner surface of a tube was considered in [5]. In the present work, we consider the more general case of a robot with two arbitrary supporting points on a rough cylinder and on a curved surface.

Then we consider the problem of curved object grasping by the fingers of the robot-manipulator. For example we discussed monkey-robot with 10 arms and 10 legs fingers or two legged human-robot with 10 arms fingers. The robot can hold the object by one and grasp by two-fingers. An object grasping problem is equivalent to the problem of the walking robot with n legs [6], [7]. Consider a grasp with m fingers. Each finger contacts an object in one foothold.

Let the point O is an origin fixed in absolute space. Suppose that robot arms fingers accomplish the desired motion with respect to the body of the robot. Using general dynamics theorems to describe the cylinder motion, we obtain six different equations for the cylinder dynamics from the momentum and angular momentum theorems. Among them there are three equations of the body translation with point A and another three describe body rotation about point A. For prescribed motion be realized then reaction in m footholds should satisfy following kinetostatic equations [8], [9]:

$$\sum_{i=1}^{m} \tilde{\mathbf{R}}_i = -\tilde{\mathbf{\Phi}}, \qquad \sum_{i=1}^{m} \tilde{\mathbf{r}}_i \times \tilde{\mathbf{R}}_i = -\tilde{\mathbf{M}}, \tag{1}$$

where $\tilde{\mathbf{R}}_i$ is reaction component, $\tilde{\mathbf{r}}_i$ corresponds to the i-th finger supporting point vector, $\tilde{\mathbf{\Phi}}$ is the sum of the external active forces plus time derivative of desired momentum, and $\tilde{\mathbf{M}}$ is the sum of external active forces momentum and time derivative of desired angular momentum with respect to the point O. In two vector equations in (1), the former corresponds to the momentum of the object (and is equivalent to three scalar equations when projected onto the basis vectors), while the latter defines the desired change of the angular momentum.
Assuming that $\tilde{\mathbf{\Phi}}$ is orthogonal to $\tilde{\mathbf{M}}$, we obtain [10] that the system $\{\tilde{\mathbf{\Phi}}, \tilde{\mathbf{M}}\}$ can be also used at the point C

$$\tilde{\mathbf{r}}_C \times \tilde{\mathbf{\Phi}} = \tilde{\mathbf{M}}, \qquad \tilde{\mathbf{r}}_C = -\frac{\tilde{\mathbf{M}} \times \tilde{\mathbf{\Phi}}}{\tilde{\Phi}^2}, \qquad \tilde{\Phi} = |\tilde{\mathbf{\Phi}}|,$$

where $\tilde{\mathbf{r}}_C$ is the vector $\mathbf{OC}$, and C corresponds to the point at which the resultant of the reactions is acting.
Further problem of reactions distribution $\tilde{\mathbf{R}}_i$ in some fixed point of time is investigated by the proposal that force $\tilde{\mathbf{\Phi}}$ is acting at the point $\tilde{\mathbf{r}}_C$ and force moment there is zero. Motion equations (1) for finding reactions of fingers prescribed motion can be transformed [11]:

$$\sum_{i=1}^{m} \tilde{\mathbf{R}}_i = \tilde{\mathbf{\Phi}}, \quad \sum_{i=1}^{m} \tilde{\mathbf{r}}_i \times \tilde{\mathbf{R}}_i = \tilde{\mathbf{r}}_C \times \tilde{\mathbf{\Phi}}. \tag{2}$$

For example point C can be the grasping object center of mass.
Assuming that the robot footholds are on the surface of a rough cylinder of radius ρ with a friction coefficient k, we introduce the coordinate system $Oxyz$ such that the axis Ox is directed along the cylinder axis (so that the projection of $\tilde{\mathbf{\Phi}}$ on the axis Ox is negative – see Fig. 1.), the axis Oz is parallel to the vector $\tilde{\mathbf{\Phi}}$, and the angle between the cylinder axis and the vector $\tilde{\mathbf{\Phi}}$ is α.
The problem of finding the reaction forces (2) is similar to the foothold reactions distribution problem for walking robot, when the footholds are on the external surface of a rough inclined cylinder where the axis has an angle α with respect to the vector $\tilde{\mathbf{\Phi}}$. It has been considered in Ref. [9] the problem of searching of the reactions components along the cylinder axis when $\alpha = 0$.
In the coordinates $Oxyz$ we define $\tilde{\mathbf{R}}_i = (\tilde{R}_i^x, \tilde{R}_i^y, \tilde{R}_i^z)$, $\tilde{\mathbf{r}}_C = (\tilde{x}_C, \tilde{y}_C, \tilde{z}_C)$, and $\tilde{\mathbf{\Phi}} = (-\tilde{\Phi}\sin\alpha, 0, -\tilde{\Phi}\cos\alpha)$, $i = 1, \cdots, m$. In case of a one-sided surface, and the grasp inside the cylinder, we have additional restrictions on normal reactions $\tilde{N}_i$ [13]:

$$\tilde{N}_i = \tilde{\mathbf{R}}_i \cdot \mathbf{e}_\nu^i \geq 0, \tag{3}$$

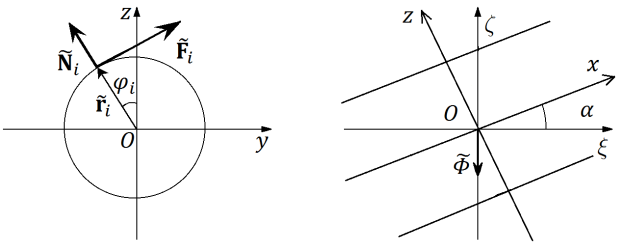

Figure 1: Cylinder.

where $\mathbf{e}^i_\nu$ is an external normal to i-th supporting point on the cylinder, while the tangential components are given by $\tilde{\mathbf{F}}_i = \tilde{\mathbf{R}}_i - \tilde{N}_i \mathbf{e}^i_\nu$.
For the reactions to be in the friction cones (2), we have following inequalities:

$$|\tilde{\mathbf{F}}_i| \leq k\tilde{N}_i, \tag{4}$$

i.e. the tangential reactions $\tilde{\mathbf{F}}_i$ are restricted by Coulomb limiting friction value. When $\tilde{\mathbf{F}}_i$ exceeds this limiting value, the robot legs and arms begin to slide along a surface.
The reaction distribution problem then reduces to the solution of equations (2), and inequalities (3), (4), for reactions limited to the friction cones. The restricted motion can only be realized if the solution of Eqns. (2)-(4) does exist.
The same inequalities are for walking robot on the cylinder [9]. If the grasp is out the cylinder this inequalities (3) have opposite sign.
For example if m is even. And one of each par of the supporting points is on and another is in the thin surface such that we consider them like one geometrical point. Then we need only inequalities (4).
For $\mathbf{r}_i = \tilde{\mathbf{r}}_i/\rho = (x_i, y_i, z_i)$, in the cylinder coordinate: $\mathbf{r}_i = (x_i, -\sin\varphi_i, \cos\varphi_i)$, $\mathbf{e}^\nu_i = (0, -\sin\varphi_i, \cos\varphi_i)$, $N_i = \tilde{\mathbf{N}}_i/\tilde{\Phi} = (0, -N_i \sin\varphi_i, N_i \cos\varphi_i)$, where φ_i is the angles between axis Oz and cylinder normal $\mathbf{e}^\nu_i$. We define $\mathbf{e}_x$ as the unitary vector in the Ox axis, while $\mathbf{e}^\tau_i = (0, \cos\varphi_i, \sin\varphi_i)$ as the tangential to the cylinder. Then the tangential reaction: $\mathbf{F}_i = (F^x_i, F^{yz}_i \cos\varphi_i, F^{yz}_i \sin\varphi_i)$, where $F^x_i = \mathbf{F}_i \cdot \mathbf{e}_x$, $F^{yz}_i = \mathbf{F}_i \cdot \mathbf{e}^\tau_i$, $\mathbf{R}_i = \tilde{\mathbf{R}}_i/\tilde{\Phi} = (R^x_i, R^y_i, R^z_i)$, $\mathbf{r}_C = \tilde{\mathbf{r}}_C/\rho = (x_C, y_C, z_C)$.
Let $p = R^x_1 - R^x_2$. We further define the coordinate differences, and the supporting points difference of angles of axis Oz are $\Delta x = x_2 - x_1$, $\Delta y = y_2 - y_1$, $\Delta z = z_2 - z_1$, $\Delta\varphi = \varphi_2 - \varphi_1$, and $s_{21} = \sin\varphi_2 - \sin\varphi_1$, $c_{21} = \cos\varphi_2 - \cos\varphi_1$. We then project system (2) onto the axes $Oxyz$. For arbitrary surface we find that the second equation of (2) (corresponding to the moment) has the skew-symmetric matrix with respect to the component R^x_i [9]. These are 2 independent equation, while the third equation corresponds to the restriction of the point C to the plane containing the two footholds. As a result, the system (2) yields 5 independent equation and a restriction.

2 A Two-finger Grasp

During the robot motion one-supporting and two-supporting points phases are changed. First, we consider the one-supporting phase of the grasp. Let $m = 1$,

then the motion existing condition is reaction is equal to force $\mathbf{\Phi}$ and supporting point and the point C are on the line along $\mathbf{\Phi}$, while the angle between $\mathbf{\Phi}$ and the normal do not exceed the friction angle.
If the grasp inside the surface then point C is under the surface. In opposite case the grasp is under the surface. Then point C is inside the surface.
If m is even. And one of each par of the supporting points is on and another is in the thin surface such that we consider them like one geometrical point. Then it does not matter where the point C is on the line.
Let $n = 2$, and $x_1 \neq x_2$. Then $p = F_2^x - F_1^x$, and from (2):

$$\begin{gathered} F_1^x = (\sin\alpha + p)/2, \qquad F_2^x = (\sin\alpha - p)/2, \\ N_1 = \frac{-p\sin^2\dfrac{\Delta\varphi}{2} + (x_2 - x_C)\cos\varphi_1\cos\alpha}{\Delta x} + N_1^\alpha, \\ N_2 = \frac{-p\sin^2\dfrac{\Delta\varphi}{2} + (x_C - x_1)\cos\varphi_2\cos\alpha}{\Delta x} + N_2^\alpha, \\ F_1^{yz} = \frac{-p\sin\Delta\varphi + 2(x_2 - x_C)\sin\varphi_1\cos\alpha}{2\Delta x} + F_1^{(yz)\alpha}, \\ F_2^{yz} = \frac{p\sin\Delta\varphi + 2(x_C - x_1)\sin\varphi_2\cos\alpha}{2\Delta x} + F_2^{(yz)\alpha}, \\ \tan\alpha = \frac{\Delta x(\sin\varphi_2 + y_c) + (x_C - x_2)s_{21}}{y_C c_{21} + z_C s_{21} - \sin\Delta\varphi}, \end{gathered} \tag{5}$$

where N_i^α and F_i^{yz} are the functions of x_i, φ_i, y_C and z_C.
From the conditions (3)

$$p \le \frac{(x_2 - x_C)\cos\varphi_1\cos\alpha + N_1^\alpha\Delta x}{\sin^2\Delta\varphi/2}, \qquad p \le \frac{(x_C - x_1)\cos\varphi_2\cos\alpha + N_2^\alpha\Delta x}{\sin^2\Delta\varphi/2}. \tag{6}$$

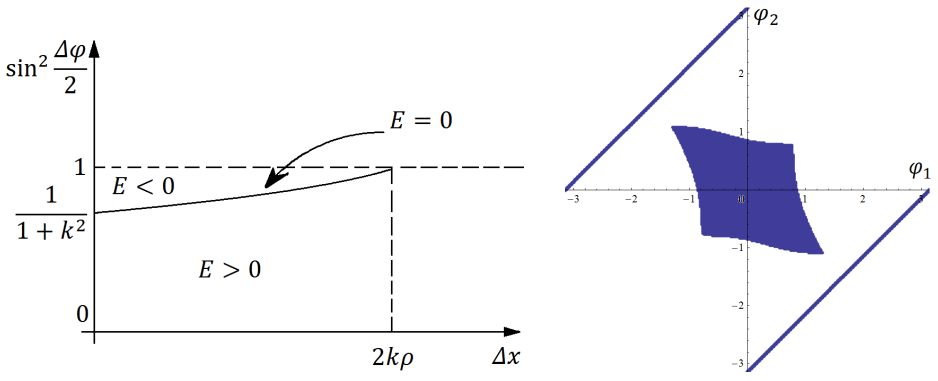

Figure 2: The analytical and the numerical parameter diagrams.

The conditions (4) can be displayed in the form

$$Ep^2 + B_1 p + C_1 \le 0, \qquad Ep^2 + B_2 p + C_2 \le 0, \tag{7}$$

where

$$E = (\Delta x)^2 + \sin^2 \Delta\varphi - 4k^2 \sin^4 \left(\frac{\Delta\varphi}{2}\right),$$

B_i, C_i are the functions of x_i, φ_i, x_C, y_C and z_C.

The boundaries between different regimes can be determined analytically. For example, in the case of $E < 0$, the solution exists, and can be obtained analytically [9], as shown in Fig. 2, on the left. Note that in this case it's limited to the range $\Delta x \leq 2k\rho$. In contract to this behavior, for $E \geq 0$ there is no such restriction and an additional step is required to address the question of the existence of the solution. At the point $(0, 0)$ we find $E = 0$, which means that two footholds are orthogonal to the cylinder axis. Here, two possible solution are either identical, or limited to a single diameter. In the latter case, point C and the reaction have to be in one plane, parallel to force Φ, and the problem has a solution.

For the desired legs or fingers configurations and given point C, the problem can be solved numerically. In Fig. 2, on the right, we present the numerical solution for the example when $x_2 = -x_1 = \rho = k = 1$. Note that in this case $E > 0$.

In the numerical simulations, we use a 300×300 array for the points (φ_1, φ_2), in the interval $[-\pi, \pi]$, and for each point verify the conditions (6), (7). Specifically, the condition (7) was analyzed in two cases, when $E = 0$ and $E > 0$, and when the solution of the problem does exist, the solutions were shown in the plot.

When $E = 0$, the reaction distribution problem reduces to the linear inequalities (6), (7) for the parameter p.

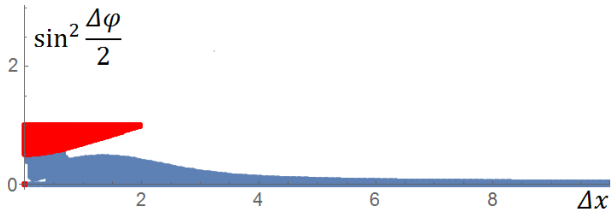

Figure 3: For $\alpha = \pi/4$; $x_2 = -x_1$, $\varphi_2 = -\varphi_1$.

For $E > 0$, we need to consider two conditions. First is the restriction on the determinants $D \geq 0$, while the second is the requirement of a non-empty intersection of the set of point of the intervals between the roots of quadratic equations. From this plot we see that, if two points are on one diameter, then the solution of the reaction distribution problem exists. The two lines in the plot, correspond to $\varphi_1 = \varphi_2 + \pi$ or $\varphi_1 = \varphi_2 - \pi$. The rhombus form represents the requirement on the determinants $D_i \geq 0$, while additional conditions further restrict the range [11].

In Fig. 3 we present the results for $E > 0$ and $E \leq 0$, when $x_2 = -x_1$, $\varphi_2 = -\varphi_1$ and shows the case of $\alpha = \pi/4$. The figures for $\alpha = 0$ and increased to $\pi/2$ are shown in [12]. Note that when $\alpha = \pi/2$, the solutions exists only for diametrical footholds.

For two-finger robot when E is negative, the solution exists, and obtained analytically [13]. Using numerical simulations we explain the reaction distribution problem existing and build this problem solution existing fields for given footholds and point C position. For example, for two-foothold phase, we consider symmetric, about

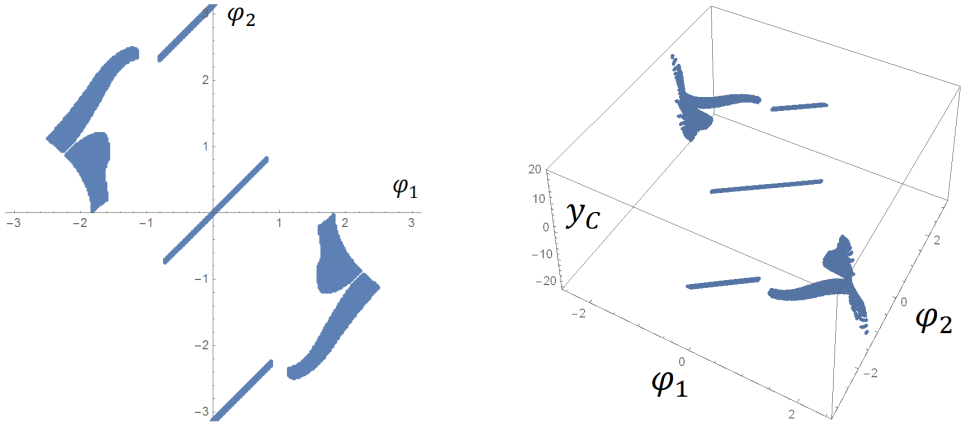

Figure 4: Admissible area for $\alpha = \pi/3$; $\Delta x = 1,1$.

point C, along and orthogonal cylinder axis, robot configurations. For first of these configurations examined three cases with nonnegative E coefficient, for distance x, between point C and footholds: $0,9$; 1 and $1,1$ at ρ and k equal 1, α from 0 to π (in all 13 different values cylinder inclination angles). Reactions distribution problem solution existing fields constructed on the two angles plane, correspond to footholds projections on the cylinder base and three dimensional fields which supplement this plane by point C z-coordinate altitude. When α equals to 0, x equals to 1, the field consist of three separate situated subregions. On the angle plane each of pair parallel lines corresponds to support on the cylinder diameter plane section contained point C [14]. There is connected field between these lines. It contains the line segment corresponding to the angles equality, robot supported above on the line which is parallel to cylinder axis and satisfy force direction deviation restriction. The indicated segment on the plot disappear when x equals to $0,9$ for α equals $\pi/4$, and at increasing x, later, for $4\pi/9$. It corresponds to the robot beginning sliding down the cylinder. When x equals to $1,1$ for α equals $\pi/3$ in three-dimensional fields observed bundles of separate points, Fig. 4. That means that the point C altitude position more harsh change while changing the angles [15].

3 Conclusion

During the robot motion, one-supporting point and two-supporting point phases are changed. The reaction distribution problem have a solution in following cases.
1. One-supporting point phase. So the motion existing condition is reaction is equal to force $\mathbf{\Phi}$ and supporting point and the point C are on the line along $\mathbf{\Phi}$. And the angle between $\mathbf{\Phi}$ and the normal not exceed friction angle.
1.1 If the grasp inside the surface then point C is under the surface. In opposite case the grasp is under the surface. Then point C is inside the surface.
1.2 If m is even. And one of each par of the supporting points is on and another is in the thin surface such that we consider them like one geometrical point. Then it does not matter where the point C is on the line.
2. Two-supporting point phases. In case when the grasp is inside the cylinder. The

point C and the reactions have to be in the plane parallel to force $\mathbf{\Phi}$.
2.1 If supporting points are on one diameter.
2.2 When coefficient $E < 0$. And in some fields with connected set of points, when $E \geq 0$.
So the robot can transfer the cylinder by one or two fingers.

Acknowledgements

This work was supported by the Russian Foundation for Basic Researches (grant no. $16-01-00131$ *A).*

References

[1] D. E. Okhotsimski and Yu. F. Golubev. Mechanics and Motion Control of Automatic Locomotion Apparatus. Moscow Nauka Publishers, 1984. (In Russian.)

[2] V. V. Beletski. Two-legged Locomotion. Model Dynamics and Control Problems. Moscow Nauka Publishers, 1984. (In Russian.)

[3] F. L. Chernousko. Equilibrium conditions for a solid on a rough plane. Izvestiya RAN, ser. Solid Mechanics, No. 6, pp. 6-17, 1988.

[4] F. L. Chernousko and N. Bolotnik. Walking robot parameters optimization for the motion in tubes. Izvestiya RAN, ser. Solid Mechanics, No. 6, pp. 27-41, 1995.

[5] F. Pfeiffer et al., Optimization of Structural Parameters and Gates of a Pipe Crawling Robot, IUTAM Symposium on Optimization of Mechanical Systems, D. Bestli; W. Schiehlen. IAF, Kluwer Academic Publisgers, 1996, pp. 231-238.

[6] Yu. F. Golubev. The Fundamentals of Theoretical Mechanics. Moscow State University, 2000. (In Russian.)

[7] Yu. F. Golubev and E. V. Melkumova. Static-Stability Conditions for a Walking Apparatus in Horizontal Cylinder and on Two Planes. Journal of Computer and Systems Sciences International. Robotics. Pleiades Publishing, Ltd., vol. 38, є 2, pp. 278-284, 1999. (Translated from Izvestiya Akademii Nauk. Teoriya i Sistemy Upravleniya, є 2, pp. 116-122, 1999.)

[8] Yu. F. Golubev and E. V. Melkumova. On Stability of Equilibrium Positions for Walking Robot in a Smooth Horizontal Tube. Proc. of the Third International Conference on Climbing and Walking Robots, Madrid, Spain, pp. 433-440, 2000.

[9] Yu. F. Golubev and E. V. Melkumova. Equilibrium Problem for a Two-Legged Robot on Rough Horizontal Cylinder Taking into Account the Reaction Components Along the Cylinder Axis, Moscow, Russia: MAKS Press, 2010. (In Russian.)

[10] Yu. F. Golubev and E. V. Melkumova. “Walking Robot Dynamics on a Rough Inclined Cylinder,” in 8-th European Solid Mechanics Conference, Book of Abstracts, edited by Gerhard A. Holzapfel and R. W. Ogden, (Technische Universitat Graz, Graz, 2012), pp. 1-2.

[11] Yu. F. Golubev and E. V. Melkumova. Prescribed Motion of a Two-legged Walking Robot on a Rough Cylinder. Proc. of the 2016 International Conference YStability and Oscillations of Nonlinear Control SystemsŸŸ (PyatnitskiyŸs Conference), ISBN 978-1-4673-9975 IEEE Catalog Number CFP16E79-ART RUSSIA, MOSCOW, V.A. TRAPEZNIKOV INSTITUTE OF CONTROL SCIENCES, pp. 1-4, DOI: 10.1109/STAB.2016.7541184

[12] Yu. F. Golubev and E. V. Melkumova, The existence of solution for robot motion on a cylinder pipe. All-Russian Meeting of University Lecturers and Department Heads on Theoretical Mechanics, Robotics and Mechatroinics. Conference Materials. Edited by V. A. Samsonov. Makhachkala.: Publishing center Master (Didkovskaya N.V.), 2016, pp. 30-33. (In Russian.)

[13] Yu. F. Golubev and E. V. Melkumova. Footholds Admissible Areas Structure Properties for a Two-legged Walking Robot on an Inclined Cylinder. in The Lomonosov Readings. Mechanics Section. (Lomonosov Moscow State University, Moscow, 2017), pp. 64-65. (In Russian.)

[14] Yu. F. Golubev and E. V. Melkumova. Footholds Admissible Areas Structure of a Two-legged Walking Robot on an Inclined Cylinder. Abstracts. International Scientific Conference. Fundamental and Applied Problems of Mechanics, Dedicated to the 170th Anniversary of a Distinguished Russian Scientist N. E. Zhukovsky. Bauman Moscow State Technical University, 2017, pp. 83–84. (In Russian.)

[15] Yu. F. Golubev and E. V. Melkumova. Two-legged Walking Robot Prescribed Motion on a Rough Cylinder. The Eighth PolyakhovŸs Reading. Book of Abstracts. January 30 - February 2, Saint Petersburg, Russia. 2018, p. 15.

Yury F. Golubev, Keldysh Institute of Applied Mathematics, RAS,
Moscow, Russia
Elena V. Melkumova, Lomonosov Moscow State University,
Moscow, Russia

Tube-deployable unmanned aerial vehicle multiphysical simulation

M. Gusev, S. Nikolaev, D. Padalitsa, E. Mozhenkov, I. Uzhinsky
m.gusev@skoltech.ru

Abstract

The flight dynamics mathematical model for a small tube-deployable unmanned aerial vehicle (UAV) and its flight trajectory optimization is presented in this paper. The optimal stiffness of torsion spring which mechanically deploys the wings of a UAV is found from the optimization. The flight of a UAV consists of several steps. At first step, the UAV is launched from the tube with folded wings. After launching, UAV is deploying the wings over the period of 0.5 – 1 sec, which depends on the torsion spring stiffness. Due to the wings mass-inertial characteristics, the speed of wings deployment and hence spring stiffness has to be constrained in order to minimize negative influence of the inertia forces on the UAV flight trajectory. This multiphysics problem includes ballistics, flight dynamics, aerodynamics, control system simulation, deployment mechanism stiffness identification and the optimal trajectory determination. This paper is devoted to the approach which allows solving such a complex task with different physical phenomena using the combination of software packages for numerical simulation (LMS Imagine.Lab Amesim, Matlab) and optimization tools (Optimus). The described approach could be extended to different applications in aerospace industry.

1 Introduction

A deployable wing UAVs are becoming more widespread due to their packing capabilities and they find their application in civil and military fields [1]. Despite the simplicity of the deployable wing concept, the developing and modelling of this concept is enough complicated task. At first, there are a lot of opportunities how to realize the deployable wings: with mechanical tools, such as rotational or linear spring, with stepper motor or with usual motor and reducer and others. Detailed review and classification of various deploying mechanism implementations is presented in paper [1]. But this ongoing research doesn't focus on the system modeling or selecting appropriate technology for implementation of the deploying mechanism, but focuses on multiphysical simulation modeling of the already selected concept of a small UAV and mechanism of deploying. A multiphysical simulation for a small UAV in the general includes flight dynamics equations of motion which are well

Figure 1: Concept of launch system and tube deployable small UAV

known for fixed-wing aircraft [2, 3, 4], aerodynamics [4], strength and vibration calculations [5]. This paper presents a solution of a rather non-trivial optimization task: at what time should the UAV open its wings after launch from the tube, since in the initial state of the UAV the wings are folded and the UAV is located inside the pneumatic tube. Together with that some constraints arise because of specific structure of a small UAV.
This article describes stages of solving of presented problem. These stages include modelling of flight dynamics, the approach to consider deployable wings instead of fixed wings, some results of aerodynamics calculations to understand lift and drop coefficients of a UAV in the flight.

2 The design of a tube-deployable UAV

This article considers tube-deployable small UAV which flies out of the pneumatic tube at first stage, then the wings open and finally the UAV flies with fixed wing. The concept of a pneumatic tube and some views of UAV is presented in Figure 1. The deployable mechanism is designed with the rotational pair and the rotational spring unfolds the wings. The cruising speed of a UAV is about 100 km/h. Altitude is up to 200 m. The critical speed of a UAV at which it capable to fly is 54 km/h. At a lower speed, the required lift force will not be achieved. During launch, this required speed is achieved by a pneumatic tube with high pressure inside. But it is not obvious without a preliminary calculation in what time it needs to start open the wings. Also, the spring stiffness directly influences on the wings deployment time, and specific spring and its stiffness must be correctly selected. All these challenges were solved by mathematical modeling and optimization performed in LMS Amesim and Noesis Optimus software.

3 Flight dynamics of a small UAV

It is proposed to consider two stages of a flight: the first stage is only flight out from a tube with subsequent opening of the wings and the second stage is the flight with unfolded wings. Also at the first stage, the problem of determining the wings opening time is solved, depending on the stiffness of the spring. The following assumption is introduced: the dynamics of a UAV flight for the intermediate state are not considered when the wings are opening. This is due to the changing mass-

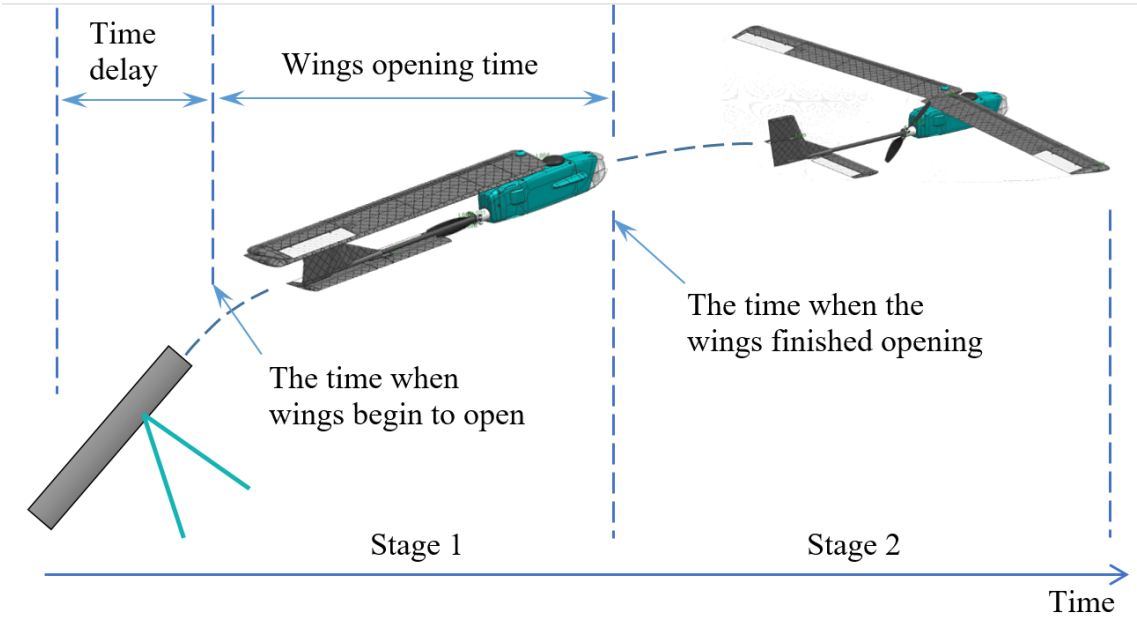

Figure 2: Stages of a flight for mathematical modelling

inertial characteristics in this state. At the second stage, the wings have already fully opened. The outline of a considered problem is presented in Figure 2.
As mentioned above, the mathematical model for flight dynamics of UAV with fixed unfolded wings is fairly well known. The body-axes equation of motion are as follows [2]:
Force equations:

$$\dot{U} = rV - qW - g\cos\theta + (X_A + X_T)/m$$

$$\dot{V} = -rU + pW + g\sin\psi\cos\theta + (Y_A + Y_T)/m$$

$$\dot{W} = qU + pV + g\cos\psi\sin\theta + (Z_A + Z_T)/m$$

Moment equations:

$$J_x\dot{p} - J_{xz}(\dot{r} + pq) + (J_z - J_y)qr = \vec{L}$$

$$J_y\dot{q} + (J_x - J_z)pr + J_{xy}(p^2 + r^2) = M$$

$$J_z\dot{r} + J_{yz}(\dot{p} - qr) + (J_y - J_x) = N$$

Moment equations:

$$\dot{\phi} = p + \tan\theta(q\sin\phi + r\cos\phi)$$

$$\dot{\theta} = p\cos\phi - r\sin\phi$$

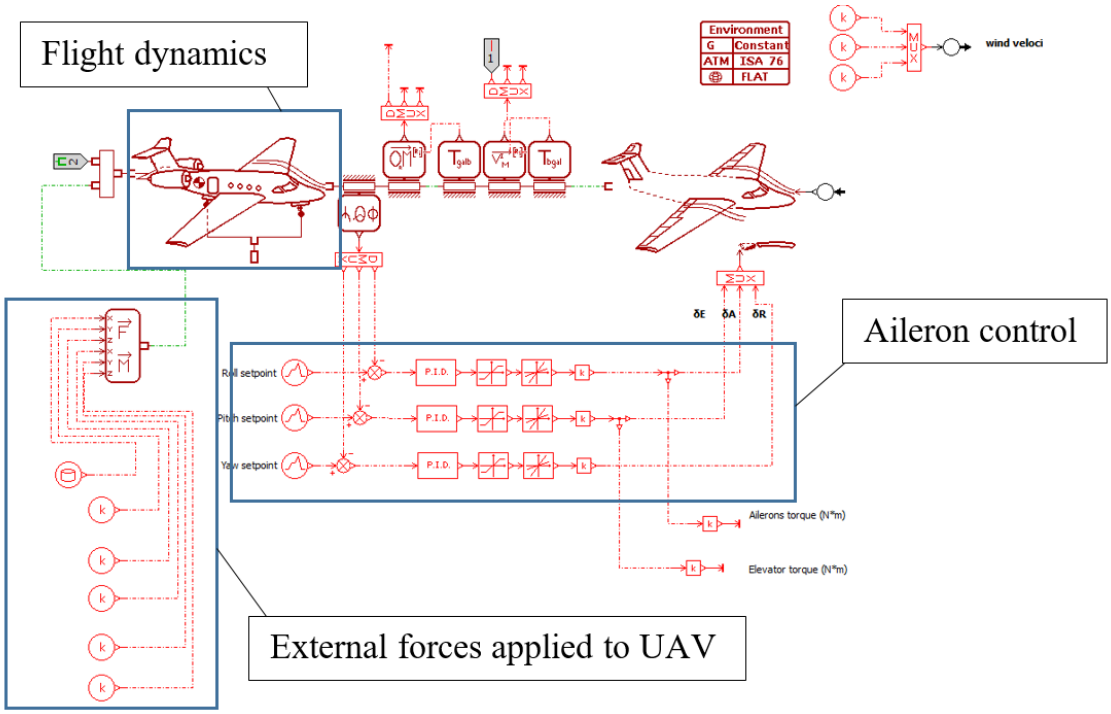

Figure 3: Mathematical model for UAV flight in LMS Amesim

$$\dot{\psi} = (q \sin\phi - r\cos\phi)/\cos\theta$$

Navigation equations:

$$\dot{p^N} = Uc\theta c\psi + V(-c\phi s\psi + s\phi s\theta c\psi) + W(c\phi s\psi + c\phi s\theta c\psi)$$

$$\dot{p^E} = Uc\theta s\psi + V(c\phi c\psi + s\phi s\theta s\psi) + W(-s\phi c\psi + c\phi s\theta s\psi)$$

$$\dot{p^D} = -Us\theta + Vs\phi c\theta + Wc\phi c\theta$$

The definition of each variable in equations is found in Ref. [2].
The equations for two stages was solved in LMS Amesim software [6]. This software includes validated library of components for many engineering applications including flight dynamics library. The circuit visualization of the mathematical model for considered UAV is presented in Figure 3.
The distinctive feature of creating models in LMS Amesim is that engineer do not need to create equations and next to translate them into hundreds of code lines. It decreases number of errors during modelling. There are some initial parameters in each element of a mathematical model. The flight dynamics element contains the most significant initial parameters, such as: mass, components of the inertia matrix, initial speed, altitude, pitch, roll and yaw angles, lift and drag coefficients, wing span, wing area. Since at the first step the wings are folded, the wing span of for analysis is taken about zero: 0.001 m. The wing span and wing area are taken as actual: 1.6 m and 0.24 m2 for the second stage.

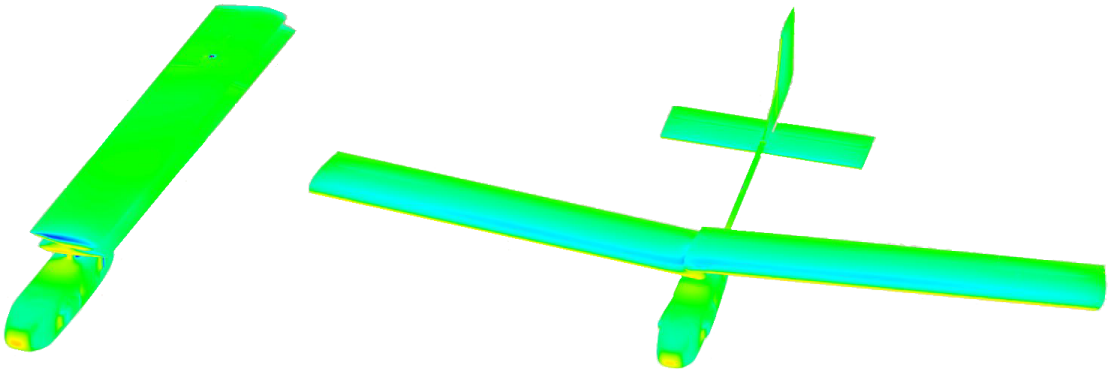

Figure 4: Results of CFD analysis for two stages of a flight. Pressure acting on the UAV

4 Determination of lift and drag coefficients

The lift and drag coefficients were obtained by CFD analysis by means of Ansys CFX. The results of calculations are presented in Figure 4.
Numerical results are summarized in the table 2.

Table 2: Lift and drug coefficients

	Deployed wing	**Folded wing**
C_{yo}	0.18	0
C_y^α	0.0677 1 deg	0.0117 $1/deg$
C_{xo}	0.0575	0.04
C_x^α	0.0031 1 deg	0.002 $1/deg$

Numerical results of CFD analysis were the initial data for flight dynamics calculations.

5 Mathematical model for the wings opening

Mathematical model for time determination of a wing deployment takes into consideration inertia of a wings, wind speed and the UAV speed. The equation of motion for this problem is as follows [7].

$$J\ddot{\varphi} + B\dot{\varphi} + K\varphi = M(t)$$

,
where J is moment of inertia, $П\Ъ$ is the rotational angle,B is damping coefficient,K is stiffness coefficient, $M(t)$ is applied external moment acting on the wings.
External forces, specifically the moments from wind speed and the UAV speed are taken from the flight dynamics calculation. The problem was solved in LMS Amesim software and some results of calculations are presented below. The dependency of

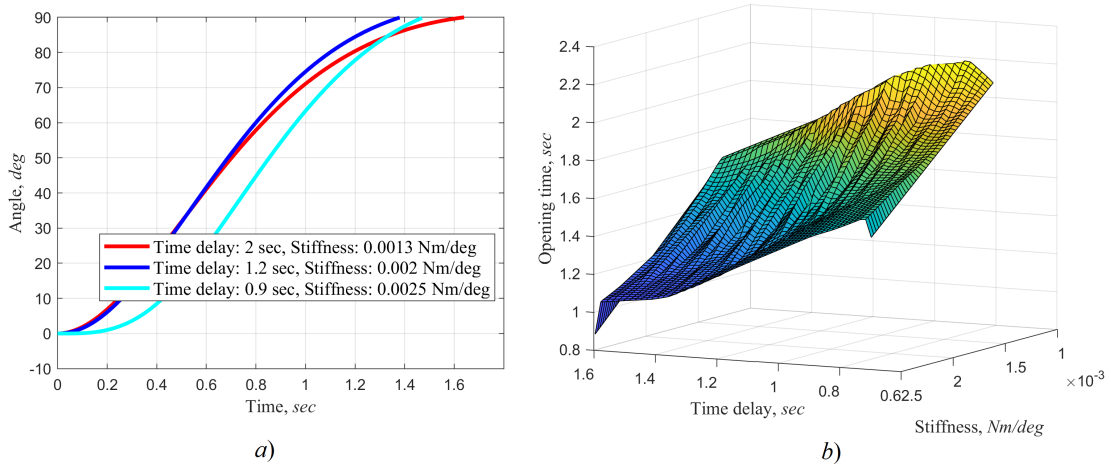

Figure 5: Results of calculations obtained from mathematical model of the wing opening: a) Angle over time; b) Opening time depending on the time delay and stiffness

angle over time is presented in Figure 5a and the opening time of a wing depending on time delay and stiffness is presented in Figure 5b. Time delay is the time when the wings begin to open (Figure 2).

The results of calculations shown in 5 pointed on the nonlinear dependency of opening time from time delay and stiffness. This is explained by the non-constant moment applied to wings. This moment strongly depends on the delay time.

6 Flight dynamic calculation results

In order to clarify the described problem, the flight trajectory of a UAV on the first and on the second stage are presented separately. The trajectories of a flight are presented below in Figure 6.

It is obvious that, the UAV should fall with folded wings at the first stage. But not clearly in what exactly time it should the wings should be deployed and what stiffness of a spring should be chosen to achieve maximum altitude at the second stage. It is proposed to solve these problems by means of optimization.

Important point is to understand limits for the initial parameters when optimization is applied. For the considered problem, there are two initial parameters: the stiffness of a spring and the time delay before starting to deploy the wings. Limits for the rotational spring stiffness are taken from the required dimensions and 3D calculations of a spring: 0.001–0.0025 Nm/deg. The low limit for the delay time is determined by physical restriction: the UAV cannot deploy the wing inside the tube, therefore the low limit is the time when UAV already has flown out from the tube (Figure 2). The value for that time was calculated for the tube length 2 m and is 0.1 s. The upper bound is determined by the time when the altitude of a UAV becomes less than zero (Figure 6) and this time is equal 5 s.

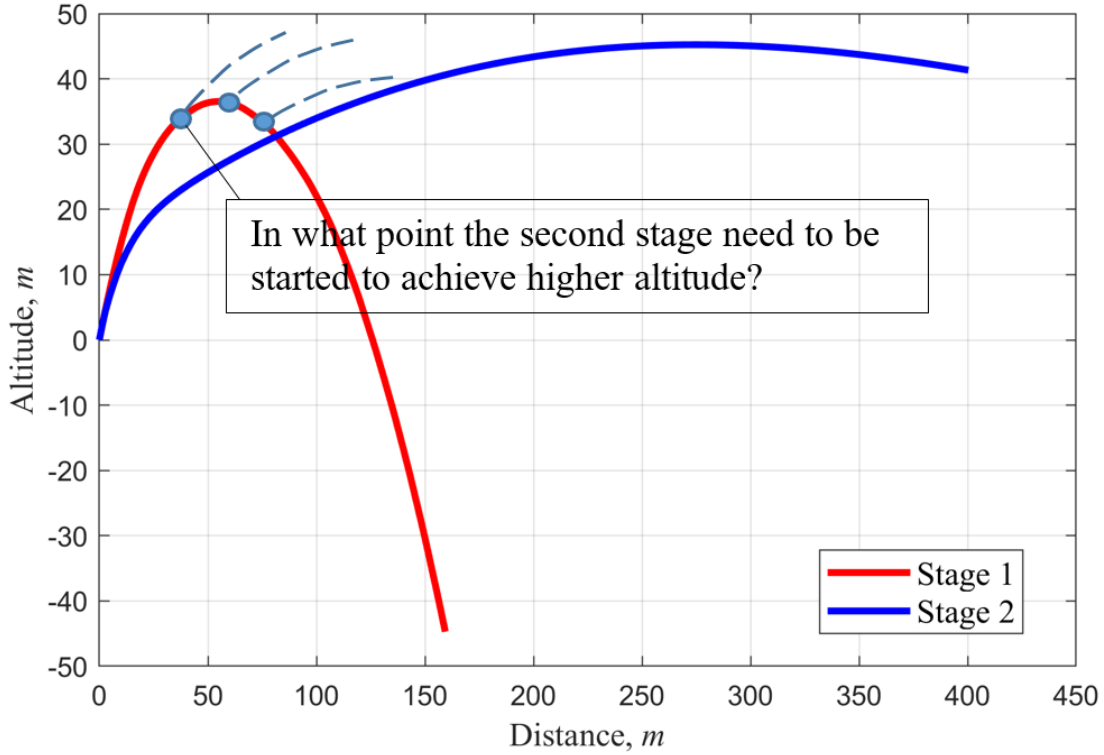

Figure 6: Trajectories of stage 1 and 2 separately

7 Statement of the optimization problem

Considering all the above, optimization problem is proposed as follows: to find the best combination of time delay and stiffness of a rotational spring which will lead to the maximum of altitude at the end of stage 2. To solve this problem, the calculation chain was created which involved three mathematical models: time opening and two stages of a flight dynamics. The calculation chain was created in Noesis Optimus Software and the outline of this chain is presented in Figure 7.

The results of the optimization problem are presented as a set of figures and also the specific recommendations on the choice for stiffness of a spring and the delay time. The goal altitude, which is at the end time of stage 2 depending on the stiffness at the specific time delay and depending on time delay at the specific stiffness are presented in Figure 8 a) and b).

The results presented in Figure 8 show dependencies which describe the optimal solution slices. The results summarize the multiphysics simulations and allow to obtain the best combination of initial parameters to achieve higher altitude. For example, one could choose time delay about 0.4 sec and achieve 70 m altitude with stiffness of a spring about 0.0015 Nm/deg.

The important result is nonlinear dependency between altitude and time delay (Figure 8b). From there it's shown that there is specific time delay from 0.8 up to 1.2 s which leads to low altitude almost with all values of stiffness. In this case, the optimization results did not lead to a specific optimal pair of the values but the range of poor initial points which leads to low altitude was calculated.

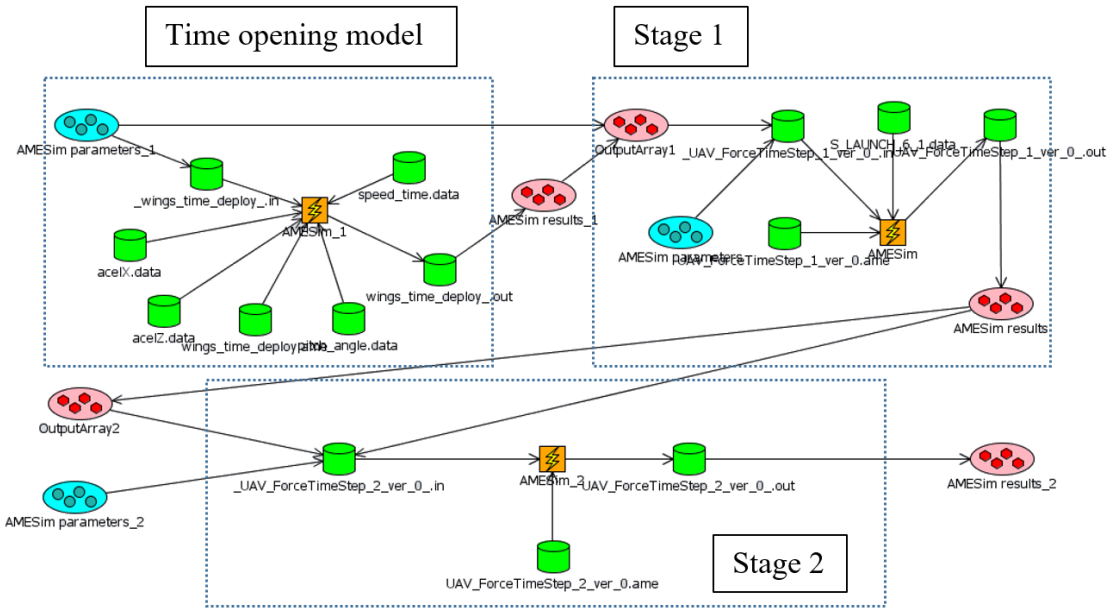

Figure 7: Outline of the calculation chain

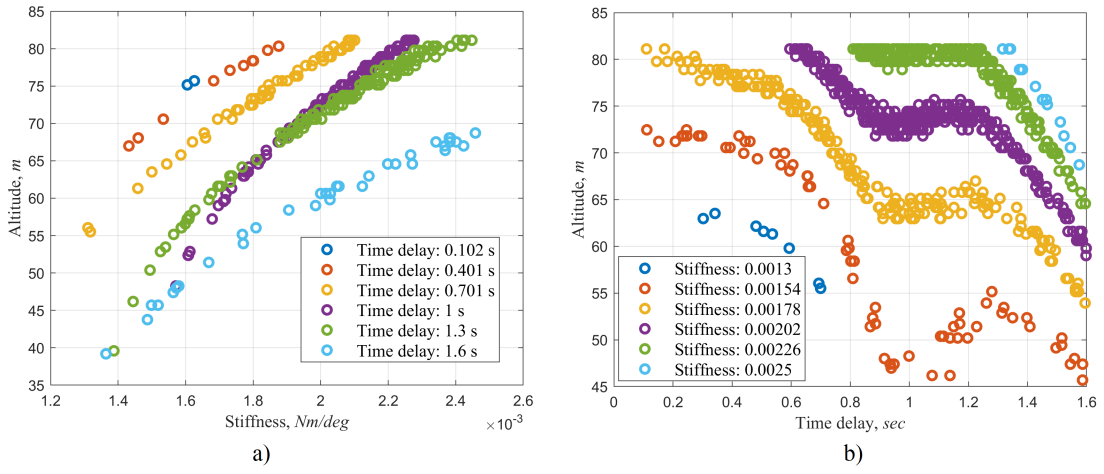

Figure 8: Results of optimization: a) Altitude depending on stiffness changing, b) Altitude depending on time delay changing

Although UAV considered in this paper is not the industrial case but this approach of multiphysics simulations and optimization can be extended to the real product development.

References

[1] Jacob, Jamey, and Suzanne Smith. "Design limitations of deployable wings for small low altitude UAVs." 47th AIAA Aerospace Sciences Meeting Including The New Horizons Forum and Aerospace Exposition. 2009.

[2] Stevens, Brian L., Frank L. Lewis, and Eric N. Johnson. Aircraft control and simulation: dynamics, controls design, and autonomous systems. John Wiley and Sons, 2015.

[3] Etkin, Bernard, and Lloyd Duff Reid. Dynamics of flight: stability and control. Vol. 3. New York: Wiley, 1996.

[4] Selig, Michael S. "Real-time flight simulation of highly maneuverable unmanned aerial vehicles." Journal of Aircraft 51.6 (2014): 1705-1725.

[5] Anderson, Kevin, et al. "Vibration Analysis of a Solar Powered UAV." World Academy of Science, Engineering and Technology, International Journal of Mechanical, Aerospace, Industrial, Mechatronic and Manufacturing Engineering 9.9 (2015): 1651-1656.

[6] Lemmens, Yves, et al. "Simulation and validation of energy and thermal management of an electrically-powered UAV." (2012).

[7] Corben, Herbert Charles, and Philip Stehle. Classical mechanics. Courier Corporation, 2013.

M. Gusev, Skolkovo Institute of Science and Technology, Nobelya Ulitsa 3, Moscow, Russia 121205

Numerical study of fracture mechanism in ceramic armor under impact load

M.K. Khan, M.A. Iqbal, V. Bratov, N.K. Gupta, N.F. Morozov
ashraf@rediffmail.com

Abstract

A numerical investigation has been carried out for studying the fracture mechanics and the ballistic response of ceramic target. The ceramic considered was Alumina 95, the backing plate was Aluminium alloy 2024-T3 and the projectile was made up of Steel 4340. The diameter to length ratio of conical and blunt nosed projectiles has been varied as 0.25, 0.5 and 1.1 keeping the mass constant in order to study the effect of diameter of projectile. The Johnson-Holmquist (JH2) constitutive model has been used for ceramic and the Johnson-Cook (JC) model has been used for the metallic backing material and the projectile. The thickness of target plate and backing plate was 6 mm both, and the size of the plates considered was 150 mm × 150 mm. A range of velocity has been considered to explore the effect on higher as well as lower velocities. The residual velocities being compared and presented here for different diameters. The ballistic limit velocity (BLV) was also found for different projectile diameter. The BLV was found to be higher with the increase in the projectile diameter. Three dimensional numerical simulation have been performed using ABAQUS/explicit finite element. The simulations were validated with the experimental data.

1 Introduction

Ceramic is used as an armor material due to its high compressive strength, hardness and low density. Ceramic possesses low fracture toughness and less tensile strength that cannot be overlooked as these properties are equally important for proper function of armor. Metallic plates or composite layers are used with the ceramic to impart ductility and tensile strength to the protective system. With ceramics as front layer, metals or composites are used as a backing material. Bi-layer armors are found to be efficient in protection as well as being lightweight in comparison to monolithic armors. If ceramic is used with no backing plate or cover, under high impact load it will break instantaneously due to very little toughness it possesses. The function of ceramic layer is to shatter and blunt the projectile, during this process, the ceramic is also fractured but the backing layer keeps the ceramic in its place and absorbs the energy of the projectile by deforming.
The use of bi-layer armor systems, comprising a hard ceramic front face and an

energy absorbing metal backing layer, results in a lighter design compared to monolithic metallic armor providing the same ballistic protection level, against armor-piercing (AP) projectiles. A negligible proportion of the projectile's kinetic energy (0.2 %) dissipates into fracture of the ceramic. The major energy dissipating mechanisms were identified as plastic deformation of both the backing plate (20-40 %) and the penetrator (10-15 %), and the kinetic energy picked up by the ceramic debris (45-70 %) [1990, Woodward].

During high velocity impact a compressive shock wave travels through the thickness of the target, which result in radial cracks in front of the projectile head. A tensile wave came back from the interface and it originates circumferential cracks in the rear face and ceramic conoid is formed. The projectile pushes the comminuted ceramic which is restrained by the backing plate, the backing plate is deformed and bent, it provides space for the comminuted ceramic to move. New fracture conoid with smaller diameter is formed and segregated from the adjoining material and the procedure kept on repeating up to when the diameter of the conoid is closer to the diameter of the deformed projectile. The backing plate reaches its strength and plugs are ejected from the plates having diameter same as the diameter of deformed projectile.

The high velocity impact is a complex process which is affected by many factors. Thickness of the plates, constrained conditions, angle of impact and properties of the materials are few of the factors that affects the fracture mechanics.

Many researchers studied various factors and conditions affecting the ballistic properties in case of bi-layer ceramic-metal armor. Woodward (1990) [1] develops a simple set of models for the perforation of ceramic composite armour, illustrating the relation and effects of various physical properties and impact parameters on the ballistic resistance of the armor. Various aspects like the inertial response of the system components, cone crack formation and projectile erosion and backing deformation were modelled realistically. Woodward (1994) [2] concluded that ballistic performance may be influenced by the nature and thickness of the ceramic, the confining and backing layers and the geometry of the impacting projectile. Zaera and Galvez (1998) [3] presented a new analytical model for simulation of impact problem in case of bi-layer ceramic-metal armor. The model was based on Tate and AlekseevskiiвЂ™s equation for projectile penetration and on the ideas of WoodwardвЂ™s and den ReijerвЂ™s models for metallic backing and was validated by comparing experimental and analytical results. Some of the experimental works involve Wang and Lu [4]. Based on an existing model, a design criterion has been developed by Wang and Lu (1994), which gives the optimum thickness ratio that gives the best ballistic limit performance of two-component ceramic armour under a given total thickness. The ceramic was used 94 % purity alumina and for backing plate aluminium 6061 T6 and the projectile was NATO 7.62 AP, 0.5 (12.7 mm) calibre. The model used was given by Florence (1969). The model assumes a short cylindrical rod striking normally into the ceramic, and forcing it to break progressively into a cone of fractured material, which distributes all the impact energy to the backing plate over a larger area than the projectile's diameter. The backing plate will deform as a uniform membrane under constant tension. As the energy dissipated in ceramic fracture and projectile erosion is ignored, the failure mechanisms of the backing plate

are simplified significantly. Based on the above assumption, Florence managed to obtain a fairly simple expression for the ballistic limit for two-component armour. To provide a specified level of protection at minimum weight Hetherington (1992) [5] developed an equation for obtaining the optimum thickness ratio. The model was developed under a given aerial density with the total thickness of the armour not being constant. Programme of trials with 7.62AP ammunition against alumina/aluminium combinations confirmed the usefulness of the model. Hetherington observed that for a given areal density, better performance can be obtained with ratios of ceramic to the backing plate as one, or more, and that ratios of less than one can lead to greatly reduced performance. For a normal impact on ceramic target with thin metallic backing plate a model was proposed by Cortes et al. [6] that was based on finite difference Lagrangian formulation. No front confinement was considered there and penetrator considered was made up of steel, and target was constituted of Alumina front plate and aluminium backing plate. The macroscopic material behaviour in the zone of пæЃnely pulverized ceramic ahead of the penetrator was modelled by means of a constitutive relation taking into account internal friction and volumetric expansion. When the ceramic is pulverized in front of projectile head, the projectile starts to push it rather than penetration. Lee and Yoo (2001) [7] done experimental and simulation work to find optimum ratio of thicknesses of ceramic and back plate in bi-layer armor as it can also affect the penetration process. Experimental works involve ballistic limit velocity determination of different thickness ratios and the results were used for verification of numerical approach. The armor was constituted of alumina ceramic (3380 kg/m^3) front plate and 5083 aluminium back plate and the projectile used was made up of steel (7850 kg/m^3). The MohrвЃ“YCoulomb (MC) strength model and linear equation of state (EOS) were used for simulation in AUTODYN hydrocode by using SPH (Smoothed particle hydrodynamics).
Using available experimental data Chi et al. (2013) [8] validated numerical simulation model and proposed a semi-analytic ballistic limit velocity model. Using numerical simulations they concluded that for a particular bi-layer armor under same geometric ratios the residual velocity remains same. Serjouei et al. (2015) [9] validated numerical simulation model by using the data of experiments they performed. The numerical simulations then used for validating the model proposed by chi et al. (2012). Numerical simulation was used for finding optimum thickness ratios of ceramic and metal plates. For lower velocities they suggested monolithic metallic armor and for higher velocities ratios of 0.5 and 0.6 was found to be optimum. Venkatesan et al. (2017) [10] studied the behaviour of different aluminum alloys backing plate against ogive nose projectile by using numerical simulation. Venkatesan et al. (2017)[11] compared the ballistic performance of Alumina and Silicon Carbide ceramic using numerical simulation and found Silicon Carbide performance better in a bi-layer armor.
In the present study, numerical simulation model was validated by using experimental data of serjouei et al. (2015). The effect of diameter on residual velocities was studied by comparing the residual velocities for different length to diameter ratios, with mass being constant. Blunt and ogival nose shape has been considered. The ballistic limit velocity was found to be higher in lower length to diameter ratios.

2 Numerical Simulation

The ballistic experiments are tedious and also too expensive to perform large number of experiments to gain a full insight of the complex phenomenon. Numerical simulation helps in by giving many detailed observations if proper model and parameters are used. There are many models available, among which Johnson-Holmquist models is widely used for ceramic under high velocity impact, high strain rate and large deformation. The Johnson and Holmquist вГУ 2 [12] model was used for ceramic and Johnson- Cook model was used for metallic projectile and backing plate. The parameters taken from Serjouei et al. (2015) are presented in table 1 and 2.

Johnson and Holmquist-2 Model

The normalized equivalent stress is

$$\sigma^* = \sigma_i^* D(\sigma_i^* - \sigma_f^*) \tag{1}$$

Where σ_i^* is the normalized intact equivalent stress, and σ_f^* the normalized fracture stress, and D is the damage ($0 \leq \mathrm{D} \leq 1.0$).

The normalized equivalent stresses $(\sigma^*, \sigma_i^*, \sigma_i^*)$ have the general form

$$\sigma^* = \frac{\sigma}{\sigma_{HEL}} \tag{2}$$

Where σ is the actual equivalent stress and σ_{HEL} is the equivalent stress at the HEL. The normalized intact strength is given by

$$\sigma_i^* = A(P^* + T^*)^N (1 + C \ln \dot{\epsilon}^*) \tag{3}$$

and the normalized fracture strength is given by

$$\sigma_f^* = B(P^*)^M (1 + C \ln \dot{\epsilon}^*) \tag{4}$$

The material constants are A, B, C, M, N, and SFMAX.

The normalized pressure is

$$P^* = \frac{P}{P_{HEL}} \tag{5}$$

Where, P is the actual pressure and PHEL is the pressure at the HEL. The normalized maximum tensile hydrostatic pressure is

$$T^* = \frac{T}{P_{HEL}} \tag{6}$$

Where, T is the maximum tensile hydrostatic pressure the material can withstand. The dimensionless strain rate is

$$\epsilon^* = \frac{\dot{\epsilon}}{\dot{\epsilon}_0} \tag{7}$$

where Ох МЉ is the actual strain rate and
$\dot{\epsilon} = 1.0\ s^I$ is the reference strain rate.

The damage for fracture is accumulated in a manner similar to that used in the JH-1 model and the Johnson-Cook fracture model. It is expressed as

$$D = \Sigma \frac{\Delta \epsilon^p}{\Delta \epsilon_f^p} \tag{8}$$

Where, $\Delta \epsilon^p$ is the plastic strain during a cycle of integration and $\epsilon_f^p = f(P)$ is the plastic strain to fracture under a constant pressure, P. The specific expression is

$$\epsilon_f^p = D_1 (P^* + T^*)^(D_2) \tag{9}$$

Where D_1 and D_2 are constants.
The hydrostatic pressure before fracture begins (D = 0) is simply

$$P = K_1 \mu + K_2 \mu^2 + K_3 \mu^3 \tag{10}$$

Where, K_1, K_2 and K_3 are constants (K_1 is the bulk modulus); and

$$\mu = \frac{\rho}{\rho_0} - 1 \tag{11}$$

For current density ρ and initial density ρ_0. After damage begins to accumulate (D > 0), bulking (pressure increase and/or volumetric strain increase) can occur. Now an additional incremental pressure, ΔP, is added, such that

$$P = K_1 \mu + K_2 \mu^2 + K_3 \mu^3 + \Delta P \tag{12}$$

Johnson-Cook Model
The Johnson-Cook (JC) constitutive model describes the strength of engineering alloys at large strains, high strain rates and high temperatures. The flow stress is expressed as an explicit function of strain, strain rate and temperature as follows [13]:
The equivalent stress of the model is defined as

$$\sigma_0 = [A + B(\bar{\epsilon}^{pl})^n][1 + C(\frac{\dot{\bar{\epsilon}}^{pl}}{\dot{\epsilon}_0})][1 - T^m] \tag{13}$$

Where, $\bar{\epsilon}^{pl}$ is equivalent plastic strain, A, B, n and m are material parameters measured at or below the transition temperature, T_0. The non-dimensional temperature $\hat{T}$ is defined as:

$$\hat{T} = \begin{cases} 0, & \text{for} T < T_0 \\ \frac{T - T_0}{T_{melt} - T_0}, & \text{for } T_0 \leq T \leq T_{melt} \\ 1, & \text{for} T > T_{melt} \end{cases}$$

Where, T is the current temperature, T_{melt} is the melting point temperature and T0 is the transition temperature defined as the one at or below which there is no temperature dependence on the expression of the yield stress.
When $T > T_{melt}$ the material melts down and behaves like fluid and hence does not

Table 3: Parameters for Alumina 95%

S.No.	Parameter	Values
1.	Density(Kg/m^3)	3741
2.	EOS	Polynomial
3.	Bulk Modulus K_1 (GPa)	184.56
4.	Pressure Constant, K_2 (GPa)	185.87
5.	Pressure Constant, K_3 (GPa)	157.54
6.	Strength Model	JH-2
7.	Shear Modulus G (GPa)	120.34
8.	Hugoniot,elastic limit (HEL) (GPa)	6
9.	Intact strength constant, A	0.889
10.	Intact strength exponent, N	0.764
11.	Strain rate constant, C	0.0045
12.	Fracture strength constant, B	0.29
13.	Fracture strength exponent, M	0.53
14.	Normalized maximum fractured strength	1
15.	Failure model	JH-2
16.	Normalized hydrostatic tensile limit, T^* (GPa)	-0.3
17.	Damage constant, d1	0.005
18.	Damage constant, d2	1
19.	Bulking factor, β	1

offer shear resistance.

The projectile of nominal diameter 7.56 mm and a nominal length of 30.54 mm was used. The target was a bi-layer with a front plate of size 100 mm $\times$ 100 mm and back layer size was 160 mm $\times$ 160 mm. The materials of projectile, front layer and back layer of target were hardened steel 4340, Alumina 95% and Aluminium alloy 2024-T3 respectively.

Three dimensional finite element model of the bi-layer armor and projectile was made in ABAQUS/CAE. The projectile and target plates both were modelled as deformable bodies with Lagrangian elements. The four peripheral boundaries of the target was restrained against all degree of freedom. The size of the mesh for target plates was kept constant in all cases i.e. 0.6 mm in the inner part of 60 mm and increasing gradually towards the peripheral boundaries. The mesh of size 0.65 mm was kept for projectile. Eight node brick element (C3D8R) were considered for plates. The numerical simulation was found to be in good agreement with the experiments and found to be suitable for predicting the failure behaviour of concerned bi-layer ceramic armor.

Table 4: Parameters for Aluminium and Steel.

S. No.	Parameters	Al-2024-T3	Steel 4340
1.	Density	2785	7770
2.	EOS	Shock	Linear
3.	Bulk Modulus, K_1 (GPa)		159
4.	Gruneisen constant	2	
5.	Parameter C1 (m/s)	5328	
6.	Parameter S1	1.338	
7.	Specific heat, Cr (J/kg.K)	874.9	477
8.	Strength Model	JC	JC
9.	Shear Modulus, G (GPa)	26.92	77
10.	Static yield strength, A (GPa)	0.167	0.950
11.	Strain hardening constant, B (GPa)	0.596	0.725
12.	Strain hardening exponent, n	0.551	0.375
13.	Strain rate constant	0.001	0.015
14.	Thermal softening exponent, m	0.859	0.625
15.	Melting temperature, (K)	893	1793
16.	Reference strain rate	1	1
17.	Failure model	JC	JC
18.	Damage constant, d1	0.112	-0.8
19.	Damage constant, d2	0.123	2.1
20.	Damage constant, d3	1.5	-0.5
21.	Damage constant, d4	0.007	0.002
22.	Damage constant, d5	0	0.61

3 Results and Discussion

3.1 Validation

The experimental data of Serjouei et al. (2015) was used. The size of the ceramic front layer and metallic backplate target plates was kept 150 mm × 150 mm. The thickness of the plates was considered to be 6 mm. During the experiments, an obliquity was experienced, the impact was not perfectly normal to the target surfaced. That inherited yaw angle was considered in the numerical simulation model also as shown in fig. 1.

A comparison was made in residual velocity and residual length of the projectile. After perforation of the target plates, the hole created in the plates was measured at the rear side of the backing plate in two mutually perpendicular directions namely a1 and a2. The errors in residual velocity, residual length, a1 and a2 was found to be very less, and reported in table 3. The numerical simulation was found to be in good agreement with the experiments and found to be suitable for predicting the failure behaviour of concerned bi-layer ceramic armor.

Table 5: My caption

Parameter	Experiment	Simulation	%Error
Residual Length	23.4 mm	25.2 mm	7.6
Residual Velocity	351 m/s	355 m/s	1.1
a1	14 mm	12.9	7.8
a2	16 mm	15.1	5.6

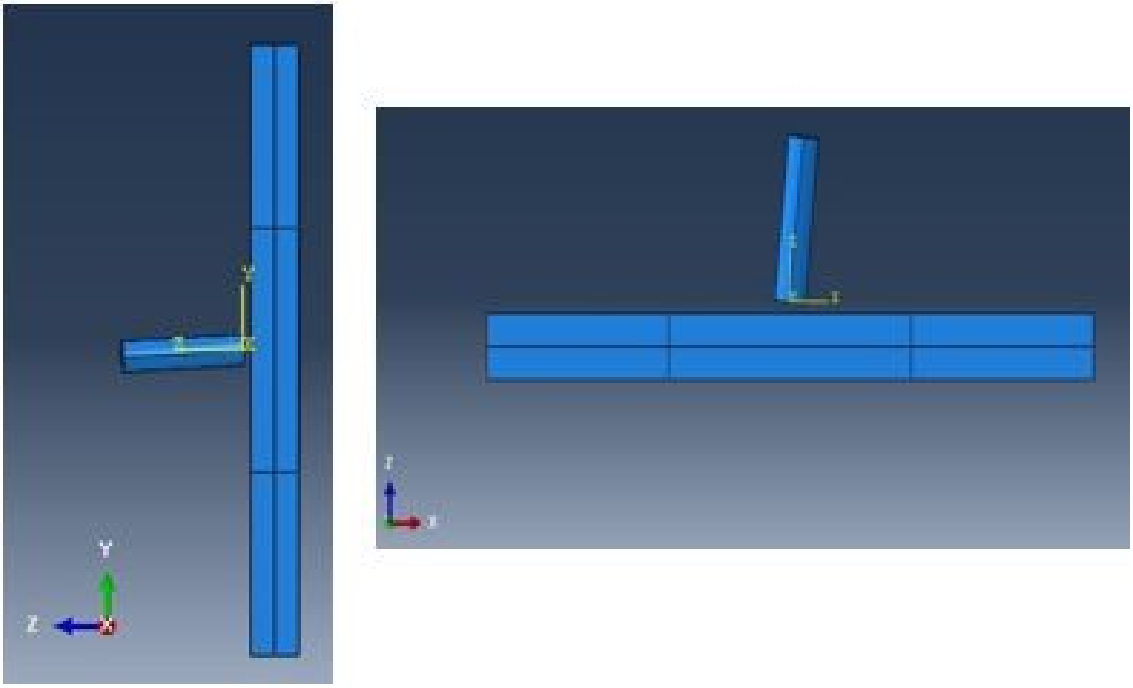

Figure 1: Angel of yaw.

3.2 Effect of diameter variation

The nominal diameter of the projectile in study of Serjouei et al. (2015) was 7.56 mm with a nominal length of 30.54 mm. The ballistic limit was worked out by using numerical simulation and was found to be 435 m/s. The diameter of the projectile here taken as 10 mm and 12.5 mm. The length of projectile was changed accordingly as 17.45 mm and 11.17 mm to maintain the mass of the projectile to be constant. In both the cases of blunt head and ogival nose head the residual velocity was found to be increasing with decreasing diameter to length ratios. The comparison for blunt nose head projectile have been shown in fig. 3.

Table 6: BLV for different D/L ratios.

S.No.	D/L Ratio	BLV (m/s)
1.	0.25	435
2.	0.5	565
3.	1.1	615

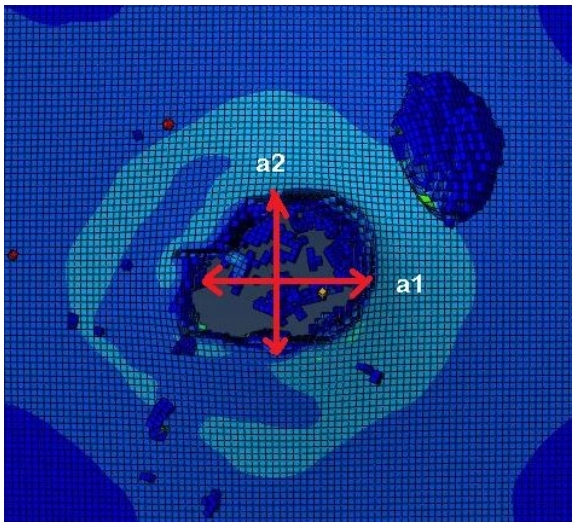

Figure 2: Damage in terms of size of the hole at rear face of baking plate.

The comparison of ogival nose head projectile have been shown in fig. 4.
The residual velocity was found to decreasing with the increase in the diameter of the projectile. The phenomenon can be attributed to the more interaction of the deformed projectile with the comminuted ceramic.
The ballistic limit velocity was found for the blunt projectiles. It was found to be increased with the increased diameter to length ratios for all cases. The ballastic velocities are mentioned in table 4.

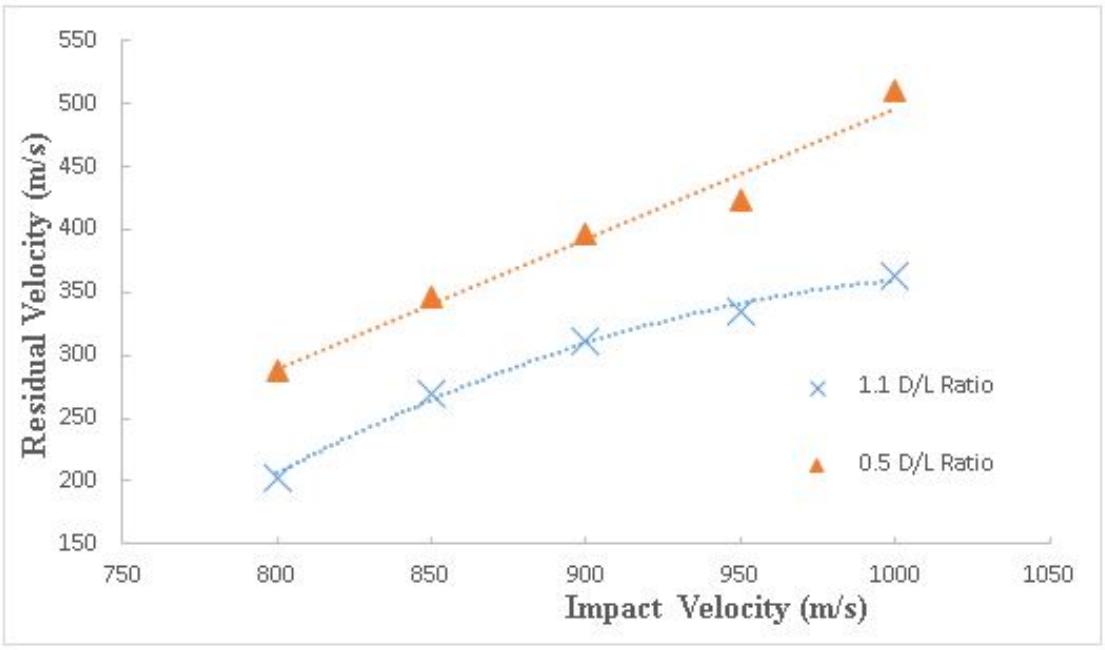

Figure 3: Residual velocity for blunt projectile.

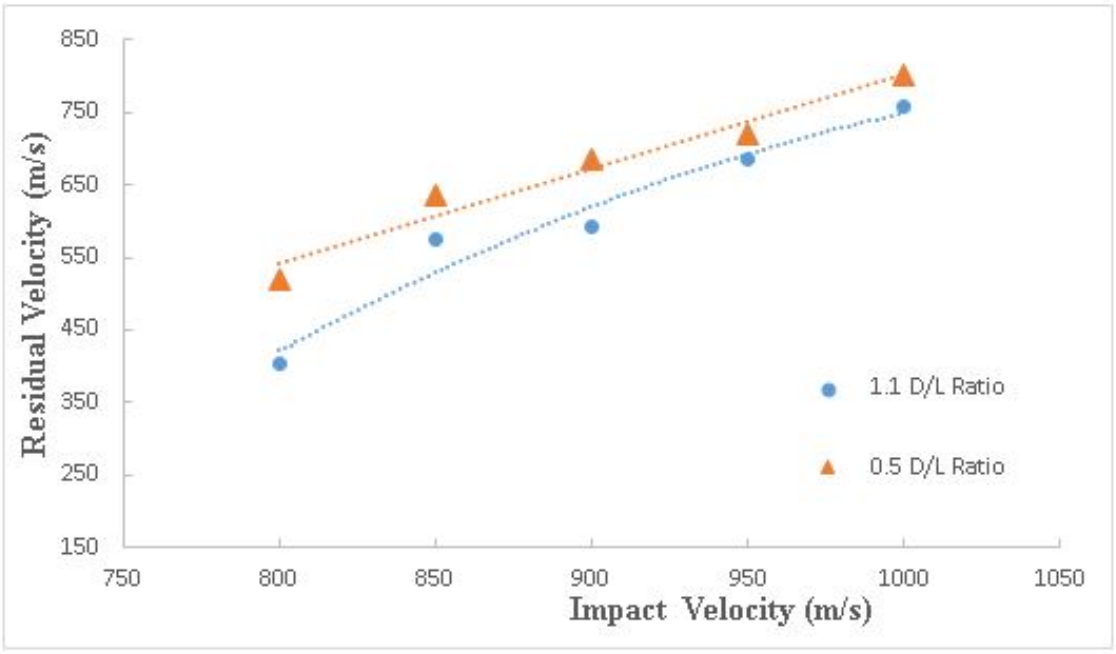

Figure 4: Residual velocity for Ogive nose projectile.

4 Conclusions

Numerical simulation was validated by using experimental data available in open literature. Effect of diameter to length ratios was studied by using 3D numerical simulation. The residual velocities was found to be decreasing with the increase in diameter of the projectile. The ballastic limit velocity was increased with the increased diameter. This can be attributed to the increased interaction between comminuted ceramic and projectile.

Acknowledgements

Authors gratefully acknowledge the financial support provided by Department of Science and Technology through grant no. INT/RUS/RFBR/P-232 under DST-RFBR scheme for carrying out this research work.

References

[1] Woodward, Raymond LA simple one-dimensional approach to modelling ceramic composite armour defeat, *International Journal of Impact Engineering*, **9**, 1990, 455–474.

[2] Woodward, RL and Gooch Jr, WA and O'donnell, RG and Perciballi, WJ and Baxter, BJ and Pattie, SD, A study of fragmentation in the ballistic impact of ceramics, *International Journal of Impact Engineering*, **15**, 1994, 605–618.

[3] Zaera, R and Sánchez-Gálvez, Vicente, Analytical modelling of normal and oblique ballistic impact on ceramic/metal lightweight armours, *International Journal of Impact Engineering*, **21**, 1998, 133–148.

[4] Wang, B and Lu, G and Lim, MK, Experimental and numerical analysis of the response of aluminium oxide tiles to impact loading, *Journal of materials processing technology*, **51**, 1995, 321–345.

[5] Hetherington, JG, The optimization of two component composite armours, *International Journal of Impact Engineering*, **12**, 1992, 409–414.

[6] Cortes, R and Navarro, C and Martinez, MA and Rodriguez, J and Sanchez-Galvez, V, Numerical modelling of normal impact on ceramic composite armours, *International Journal of Impact Engineering*, **12**, 1992, 639–650.

[7] Lee, M and Yoo, YH, Analysis of ceramic/metal armour systems, *International Journal of Impact Engineering*, **25**, 2001, 819–829.

[8] Chi, Runqiang and Serjouei, Ahmad and Sridhar, Idapalapati and Tan, Geoffrey EB, Ballistic impact on bi-layer alumina/aluminium armor: A semi-analytical approach, *International Journal of Impact Engineering*, **52**, 2013, 37–46.

[9] Serjouei, Ahmad and Chi, Runqiang and Zhang, Zhiyuan and Sridhar, Idapalapati, Experimental validation of BLV model on bi-layer ceramic-metal armor, *International Journal of Impact Engineering*, **77**, 2015, 30–41.

[10] Venkatesan, J and Iqbal, MA and Gupta, NK and Bratov, V and Kazarinov, N and Morozov, F, Ballistic Characteristics of Bi-layered Armour with Various Aluminium Backing against Ogive Nose Projectile, *Procedia Structural Integrity*, **6**, 2017, 40–47.

[11] Venkatesan, J and Iqbal, MA and Madhu, V, Ballistic performance of bilayer alumina/aluminium and silicon carbide/aluminium armours, *Procedia Engineering*, **173**, 2017, 671–678.

[12] Johnson, Gordon R and Holmquist, Tim J, An improved computational constitutive model for brittle materials, *AIP Conference Proceedings*, **309**, 1994, 981–984.

[13] Johnson, Gordon R, Cook W.H., A constitutive model and data for metals subjected to large strains, high strain rates and high temperatures, *Proceedings of the 7th International Symposium on Ballistics*, 1983.

M. A. Iqbal, Department of Civil Engineering, IIT Roorkee, Roorkee-247667, India

Decimal-by-decimal analysis of the gravitational constant value as exemplified by torsion balance

Dmitry G. Kiryan, George V. Kiryan
diki.ipme@gmail.com

Abstract

Term "gravitational constant" was for the first time introduced more than 200 years ago, and since that time attempts have been made to refine its value. As per the materials of *Committee on Data for Science and Technology* (CODATA), all indirect measurements of the "gravitational constant" obtained by various research groups exhibit in the SI system equality of two first decimals and spread in subsequent decimals. We have analyzed this situation by using the torsion balance mathematical model. This paper shows that this situation might be explained by solving the direct metrological problem, namely, calculation of the necessary measurement accuracies of each of the torsion balance parameters from the preset accuracy of the "gravitational constant" value. Decimal-by-decimal analysis of the torsion balance sensitivity, jointly with the CODATA data, has lead us to the assumption that all the variety of the "gravitational constant" values was obtained at experimental setups without appropriately planning the final result accuracy.

1 Problem definition

In his work "Traitè de mècanique" (1809), Simèon Denis Poisson introduced into the law of gravitational interaction between two material bodies factor **G** named "gravitational constant"[1]. The law states that the force of gravitational interaction between two homogeneous spheres (material points) is directly proportional to their gravitating[2] masses and inversely proportional to the squared distance between their

[1]The history of the "gravitational constant" is presented in detail in the K. F. Tomilin's book "*Fundamental physical constants in the historical and methodological aspects*" [1, pp. 106–126]

[2]The concept of the material body gravitating mass is considered in papers [2, 3]. Briefly speaking, the material body gravitating mass $\widetilde{m}$ is a function of density of its material environment. The gravitating mass functional expression looks as follows:

$$\widetilde{m} = m\,(1 - \rho_0/\rho)\,, \quad m > 0\,,$$

centers of symmetry. Later a scale-dimension factor was introduced into the law of gravitation, which was titled "gravitational constant".

Let us consider two homogeneous spheres $\mathfrak{m}^*$ and $\mathfrak{m}$ in masses in the Cartesian coordinate system $Oxyz$ (Fig. 1). Positions of the spheres are defined by radius-

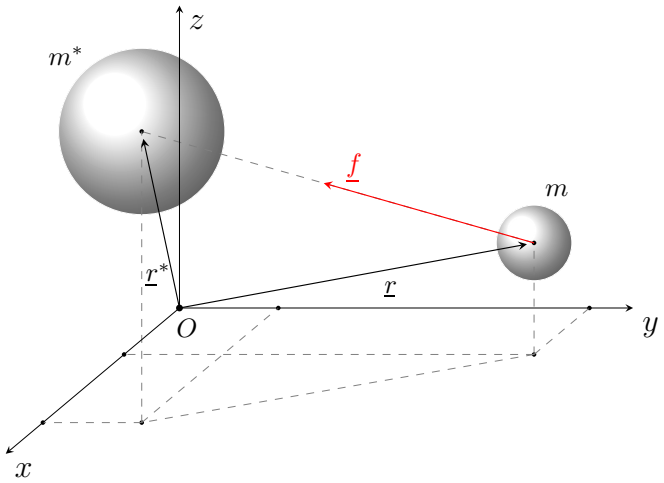

Figure 1: Gravitational force $\underline{f}$ acting upon a homogeneous sphere with mass $\mathfrak{m}$ from a homogeneous sphere with mass $\mathfrak{m}^*$.

vectors $\underline{r}^*$ and $\underline{r}$, respectively. In this case, the law of gravitational interaction (i.e., the expression for gravitational force $\underline{f}$ acting upon mass $\mathfrak{m}$ from mass $\mathfrak{m}^*$) obtains the following form:

$$\underline{f} = \underline{E}(\mathfrak{m}^*, \underline{r}^* - \underline{r})\ \mathfrak{m}\ , \quad \underline{E}(\mathfrak{m}^*, \underline{r}^* - \underline{r}) = \left(G\ \frac{\mathfrak{m}^*}{|\underline{r}^* - \underline{r}|^2} \right) \frac{\underline{r}^* - \underline{r}}{|\underline{r}^* - \underline{r}|}\ . \tag{1}$$

Here $\underline{E}$ is intensity of the gravitational field generated by mass $\mathfrak{m}^*$. Certainly, mass $\mathfrak{m}$ is also a source of the gravitational field and attracts mass $\mathfrak{m}^*$ with exactly the same force as mass $\mathfrak{m}^*$ attracts mass $\mathfrak{m}$.

At present, international committee CODATA[3] recommends the following value of the "gravitational constant" [4]:

$$G = 6.67384(80) \times 10^{-11}\ m^3/(kg \cdot s^2)\ . \tag{2}$$

At the same time, the CODATA data [4] given in Tab. 1 demonstrate that all the "gravitational constant" values coincide only in *two first decimals*.

General experience in purposeful and conscious instrumental observation of planet orbits, galaxies dynamics [5], tides on land and sea, and the Earth's gravitational field strength allows us to state that gravitational interaction between material bodies depends exclusively on their masses, geometry and distance between them.

where ρ_0 is the medium density, ρ is the averaged density of the material body, $\mathfrak{m}$ is the gravitating mass of the body at $\rho_0 = 0$ (i.e., in the absence of the material medium). Hereinafter term "gravitating" is omitted for brevity, however, it is necessary to keep in mind that the medium factor always exists and needs proper attitude from researchers.

[3]Committee on Data for Science and Technology & The CODATA Task Group on Fundamental Constants. `http://www.codata.org`

TABLE XXIV Summary of values of G used to determine the 2010 recommended value

Item number	Value[1] (10^{-11} m^3 kg^{-1} s^{-2})	Relative standard uncertainty u_r	Identification
$G1$	6.672 48(43)	6.4×10^{-5}	NIST-82
$G2$	6.672 9(5)	7.5×10^{-5}	TR&D-96
$G3$	6.673 98(70)	1.0×10^{-4}	LANL-97
$G4$	6.674 255(92)	1.4×10^{-5}	UWash-00
$G5$	6.675 59(27)	4.0×10^{-5}	BIPM-01
$G6$	6.674 22(98)	1.5×10^{-4}	UWup-02
$G7$	6.673 87(27)	4.0×10^{-5}	MSL-03
$G8$	6.672 28(87)	1.3×10^{-4}	HUST-05
$G9$	6.674 25(12)	1.9×10^{-5}	UZur-06
$G10$	6.673 49(18)	2.7×10^{-5}	HUST-09
$G11$	6.672 34(14)	2.1×10^{-5}	JILA-10

[1]Correlation coefficients: $r(G1, G3) = 0.351$; $r(G8, G10) = 0.234$.

Table 1: Values of the "gravitational constant" obtained by different research groups [4].

In other words, *the observed gravitational interaction is defined only by the character of the physical-spatial distribution of the material medium as a whole.*

With the passage of time the method of refining the "gravitational constant" became a separate challenge. The more than 200-year history of improving the techniques an increasing the instrumental sensitivity has not resulted in at least the naturally expected asymptotic refining of constant **G**. In the SI system, only two first decimals of the **G** values obtained by each research group are equal. As an example of a commonly accepted approach to indirect measurement of the "gravitational constant", paper *"Measurement of Newton's Constant Using a Torsion Balance with Angular Acceleration Feedback"* [6] may be considered.

What is the practical meaning of the difference in the third and subsequent decimals? What is the reason for this almost two-century epic of the fruitless search for the precise value of "gravitational constant" **G** by indirect measurements? Let us consider the current situation from the point of view of both our main goal (refining of the "gravitational constant") and the available capabilities. For this purpose, let us solve the direct metrological problem.

2 The torsion balance schematic model

As a basic model, we have taken the simplest torsion balance design that allows the mass-to-mass gravitational interaction to be detected via the static torsion angle of the quartz fiber. Transient oscillation processes are neglected. We will not analyze other structural and methodological versions of indirect "gravitational constant" measurements since, as shown further, they have the same disadvantages as the classical measurement scheme based on measuring the fiber torsion angle.

Fig. 2 presents the torsion balance schematic model in the Cartesian coordinate system Oxyz. Axis Oz is perpendicular to the picture plane and directed toward the

reader. Weightless and rigid beam A_1A_2 with two equal masses m_A at the ends is suspended at point O by using a weightless and tensionless quartz fiber L in length and d in diameter. The beam arms are equal to each other: $|OA_1| = |OA_2| = h$. The plane of the beam A_1A_2 rotation about point O is perpendicular to the vector of the Earth's gravitational field intensity $\underline{E}_{Terra}$.

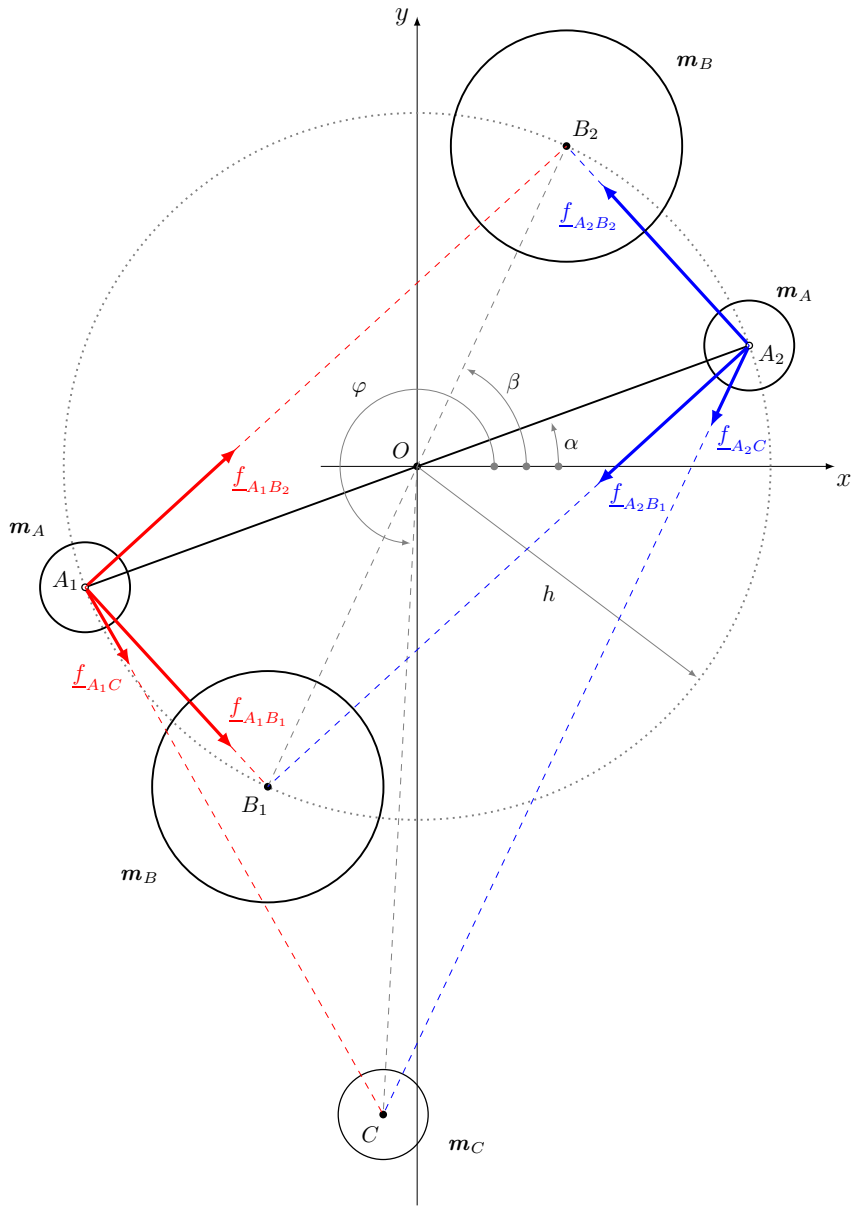

Figure 2: The torsion balance schematic model.

The controllable gravitational action on the torsion balance masses is realized through two motionless masses m_B located at points B_1 and B_2 on the circle of radius h. Orientation of the motionless masses m_B is defined by angle β between axis Ox and the line connecting points B_1 and B_2. As the positive direction, the counterclockwise rotation is taken. In addition, let us take into account the effect of gravitational anomaly m_C located outside the torsion balance at the distance h_C from point O with azimuth φ that is the angle between axis Ox and straight line OC.

To prevent displacement of the point where the quartz fiber is connected to the beam with respect to motionless masses m_B, let us forbid the point O motion within plane Oxy. This will cause an appropriate response at point O, but it will not affect the static equilibrium of the system.

Static equilibrium of beam A_1A_2 is characterized by angle α, therefore, positions of moving masses m_A at points A_1 and A_2 may be defined by the following radius-vectors:

$$\underline{r}_{A_1} = h \begin{pmatrix} \cos(\pi+\alpha) \\ \sin(\pi+\alpha) \\ 0 \end{pmatrix} , \quad \underline{r}_{A_2} = h \begin{pmatrix} \cos(\alpha) \\ \sin(\alpha) \\ 0 \end{pmatrix} . \tag{3}$$

Positions of the motionless masses at points B_1 and B_2 are defined in the similar way:

$$\underline{r}_{B_1} = h \begin{pmatrix} \cos(\pi+\beta) \\ \sin(\pi+\beta) \\ 0 \end{pmatrix} , \quad \underline{r}_{B_2} = h \begin{pmatrix} \cos(\beta) \\ \sin(\beta) \\ 0 \end{pmatrix} , \tag{4}$$

as well as the radius-vector of gravitational anomaly m_C:

$$\underline{r} = h_C \begin{pmatrix} \cos(\varphi) \\ \sin(\varphi) \\ 0 \end{pmatrix} . \tag{5}$$

When the system is in equilibrium, this means that the sum of all the torsional moments acting on the quartz suspension fiber is equal to zero.

The beam suspension fiber response to torsion manifests itself through the elastic force moment $\underline{M}_\alpha$ and may be expressed as follows:

$$\underline{M}_\alpha = \left(0 \quad 0 \quad -\alpha \frac{Y_\tau J_p}{L} \right)^T , \quad \text{where} \quad J_p = \frac{\pi d^4}{32} . \tag{6}$$

Here α is the suspension fiber torsion angle, Y_τ is the shear modulus of the fiber material [7], J_p is the polar moment of inertia of the round fiber cross-section, and L, d are the suspension fiber length and diameter, respectively.

The moments of gravitational forces twisting the suspension fiber may be subdivided into two components: the moment of gravitational action from motionless masse $\underline{M}_\beta$ and moment from gravitational anomaly $\underline{M}_\varphi$.

Taking into account axial symmetry of the masses (Fig. 2), let us consider gravitational interaction between mass m_A with radius-vector $\underline{r}_{A_1}$ and two motionless masses m_B with radius-vectors $\underline{r}_{B_1}$ and $\underline{r}_{B_2}$, and then double the moment:

$$\underline{M}_\beta(\alpha) = 2 \cdot \underline{r}_{A_1} \times (\underline{f}_{A_1B_1} + \underline{f}_{A_1B_2}) , \tag{7}$$

where

$$\begin{aligned} \underline{f}_{A_1B_1} &= \underline{E}(m_B, \underline{r}_{B_1} - \underline{r}_{A_1})\, m_A , \\ \underline{f}_{A_1B_2} &= \underline{E}(m_B, \underline{r}_{B_2} - \underline{r}_{A_1})\, m_A . \end{aligned} \tag{8}$$

Now let us introduce the effect of gravitational anomaly m_C on the masses located at the ends of the A_1A_2 beam:

$$\begin{aligned} \underline{f}_{A_1} &= \underline{E}(m_C, \underline{r} - \underline{r}_{A_1})\, m_A \,, \\ \underline{f}_{A_2} &= \underline{E}(m_C, \underline{r} - \underline{r}_{A_2})\, m_A \,. \end{aligned} \tag{9}$$

Due to geometrical asymmetry, forces $\underline{f}_{A_1}$ and $\underline{f}_{A_2}$ cause additional rotation of the beam and its displacement in the Oxy plane. Within our task, only the additional contribution of gravitational anomaly m_C to the suspension fiber torsion angle is of interest. Therefore, displacement of point O, i.e., of the point where the beam is suspended, is forbidden ($|\underline{r}_O| = 0$).

Thus the torsional moment induced by gravitational anomaly m_C with radius-vector $\underline{r}_C$ takes the following form:

$$\underline{M}_\varphi(\alpha) = \underline{r}_{A_1} \times \underline{f}_{A_1C} + \underline{r}_{A_2} \times \underline{f}_{A_2C} \,. \tag{10}$$

The torsion balance is in the static equilibrium, which means that the sum of gravitational moments $\underline{M}_\beta$ eq. (7), $\underline{M}_\varphi$ eq. (10) and elastic force moment $\underline{M}_\alpha$ eq. (6) is zero:

$$\underline{M}_\alpha(\alpha) + \underline{M}_\beta(\alpha) + \underline{M}_\varphi(\alpha) = 0 \,. \tag{11}$$

This transcendental equation gives us the static torsion angle α and thus establishes the interrelation between the beam rotation angle α and torsion balance parameters. Angle α is bounded from above, the limiting value being dependent on the schematic model geometry (Fig. 2). The maximum permissible angle of the beam A_1A_2 rotation may be defined as

$$\alpha_{max} = \beta - \arccos\left(1 - \frac{1}{2}\left(\frac{R_A + R_B}{h}\right)^2\right) \,, \tag{12}$$

where α_{max} is the maximum permissible rotation angle of the beam, R_A, R_B are the radii of the moving and motionless spheres, respectively.

To continue analyzing the accuracy of the preset torsion balance parameters, let us deduce "gravitational constant" **G** from (11):

$$\mathbf{G} = \alpha\, \frac{Y_\tau}{L}\, \frac{\pi d^4}{32}\, \frac{2h}{m_A m_B} \left(\frac{\cos\xi}{\sin^2\xi} - \frac{\sin\xi}{\cos^2\xi}\right)^{-1}, \quad \xi = \frac{\beta - \alpha}{2} \,. \tag{13}$$

This relation enables determination of the necessary accuracy of each of the torsion balance key parameters which ensures the required accuracy of the "gravitational constant" value. Since we are interested in the accuracy characteristics of just the torsion balance with calibrated masses m_A and m_B, we have neglected the anomaly m_C gravitational effect on masses m_A in deducing relation (13). The effect of gravitational anomaly on the suspension fiber torsion angle will be considered later, after solving the main problem.

3 Calculation of the necessary accuracy of the system parameters

Let us set the required calculation accuracy of the "gravitational constant" value and calculate the necessary measurement error in the beam rotation angle and also in key design and physical/mechanical parameters of the torsion balance.

As the required calculation accuracy of the "gravitational constant" in the SI system, we regard the number of significant decimals. Thus we assign increment $\Delta\mathbf{G}$ to each decimal in the "gravitational constant" value:

$$\Delta\mathbf{G} = [\ 0.1;\ 0.01;\ 0.001;\ 0.0001;\ \ldots\ ] \times 10^{-11}\ m^3/(kg \cdot s^2)\ . \tag{14}$$

Being under the action of the gravitational forces induced by masses m_B, the initially weightless beam with masses m_A at the ends is in static equilibrium at the angle α to the Ox axis. Angle α can be found from equation (13) by using the unperturbed "gravitational constant".

After setting the "gravitational constant" increment $\Delta\mathbf{G}$ by selecting it from sequence (14), we can find a corresponding correction to the chosen torsion balance parameter which will completely compensate the effect of the preset $\mathbf{G}$ perturbation, namely, preserve the initial static equilibrium characterized by angle α. This compensative correction will be just the maximum permissible absolute error in the chosen parameter of the system.

First let us estimate the necessary measurement accuracy of torsion angle α. Let us vary "gravitational constant" $\mathbf{G}$ in (6) by $\Delta\mathbf{G}$ and find a new torsion angle different from the initial one. Designate this difference as $\Delta\alpha$. This means that to calculate the "gravitational constant" with the preset accuracy $\Delta\mathbf{G}$ it is necessary to have instruments able to measure the suspension fiber torsion angle[4] with absolute accuracy $\Delta\alpha$.

After that, maintaining the static equilibrium characterized by invariable torsion angle α eq. (13), let us find the interrelation between the preset "gravitational constant" increment $\Delta\mathbf{G}$ and corresponding compensative corrections to the basic torsion balance parameters, namely, m_B, L, d and Y_τ. Tab. 2 shows the torsion balance parameters used in the schematic model (Fig. 2). Calculations of the necessary measurement accuracy of the torsion balance parameters are listed in Tab. 3. The results obtained are shown in Figs. 3,4 that clearly demonstrate a significant increase in the required measurement accuracy of the torsion balance basic parameters with increasing number of decimals in the "gravitational constant" value. The maximal

[4]In case the interacting material bodies m_A and m_B are homogeneous spheres, the beam suspension torsion angle is essentially a strict angular equivalent of the distance between geometric centers of the spheres and hence it is quite reasonable to use relation (1) to calculate the "gravitational constant".

When the pair of masses consists of bodies with the shape different from spherical (e.g., cylinders), there arises a problem with applying the law of universal gravitation (1) since in this case the gravitational interaction force does not correlate with the distance between the cylinder's centers of mass. In this case correction factors should be used which arise from an approximate solution of the problem of gravitational interaction between cylindrical material bodies, which, in its turn, contributes additional uncertainty in the "gravitational constant" calculations.

Table 2: Basic parameters of the torsion balance.

$L = 0.7\ m$	— length of the beam suspension fiber;
$d = 50\ \mu m$	— suspension fiber diameter;
$h = 100\ mm$	— beam arm length;
$Y_\tau = 31.1966\ GPa$	— shear modulus of the suspension fiber (material: SiO_2);
$R_A = 10\ mm$	— radius of the spheres (moving masses) at the beam ends;
$m_A = 0.0821\ kg$	— moving sphere mass (material: W);
$R_B = 70\ mm$	— radius of the spheres (motionless masses);
$m_B = 28.1604\ kg$	— motionless sphere mass (material: W);
$\beta = 57°$	— angle determining location of motionless masses m_B;

Table 3: Maximum permissible absolute measurement errors of the torsion balance parameters for various values of the "gravitational constant" absolute accuracy.

$\Delta G \times 10^{-11}$	$\Delta\alpha$, *arcsec*	Δm_B, *g*	ΔL, *mm*	Δd, μm	ΔY_τ, *GPa*
0.1	662.654	415.696	10.333	0.18624	0.46741
0.01	65.541	42.129	1.047	0.01872	0.04674
0.001	6.547	4.219	0.105	0.00187	0.00467
0.0001	0.655	0.422	0.010	0.00019	0.00047
0.00001	0.065	0.042	0.001	0.00002	0.00005

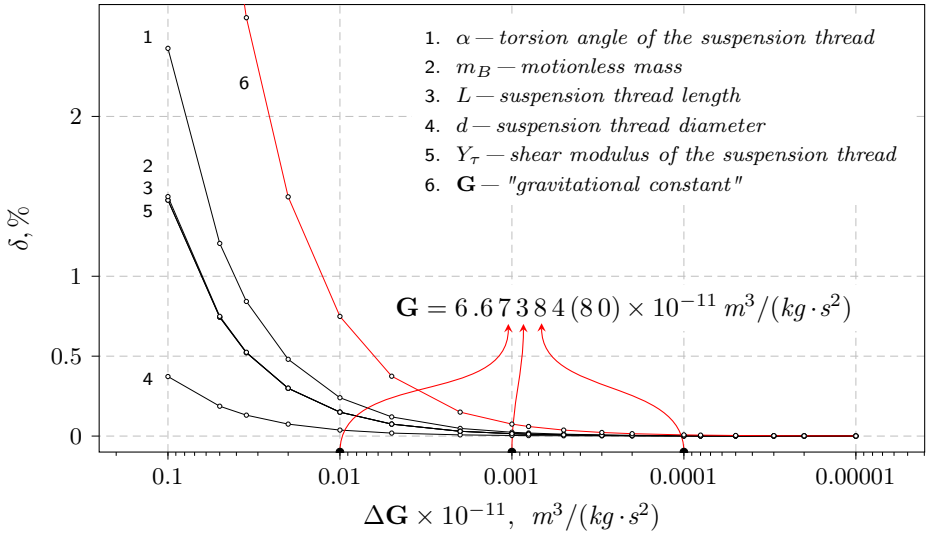

Figure 3: Relative accuracy of the schematic model parameters versus the number of decimals in the "gravitational constant" value.

error of the "gravitational constant" indirect measurement is graphically represented in Figs. 3,4. The error was calculated via the following formula:

$$\delta G = \frac{1}{G} \sum_{i=1}^{5} \left| \frac{\partial G}{\partial q_i} \right| \Delta q_i \,, \quad \text{where} \quad q_i = \{\, \alpha,\ m_B,\ L,\ d,\ Y_\tau \,\}\,. \tag{15}$$

Based on the data of Tab. 3, Figs. 3,4 and also on the fact that errors are ac-

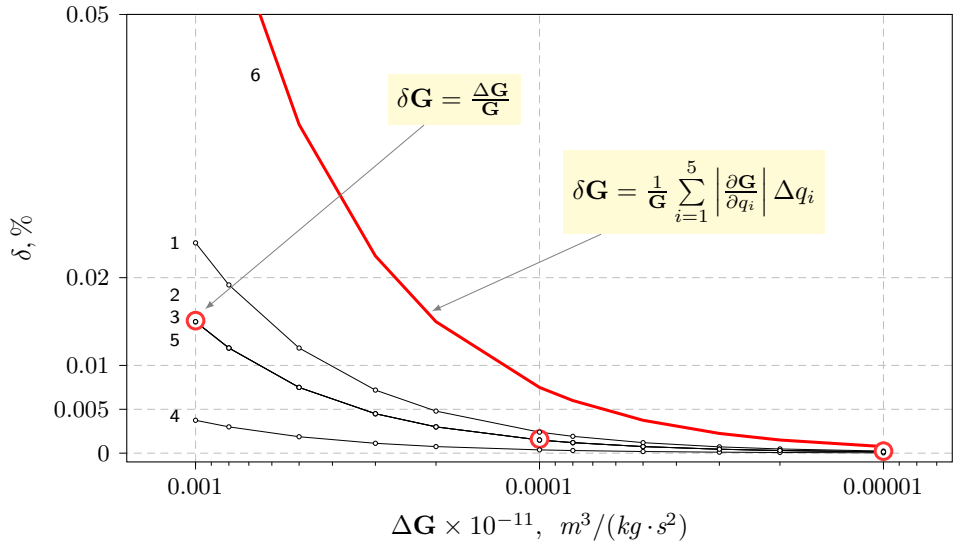

Figure 4: A Figure 3 fragment presented in a larger scale.

cumulative as relation (15) shows, it is possible to define an empiric rule stating that when the "gravitational constant" is found with the accuracy of, e.g., $\Delta\mathbf{G} = 0.001 \times 10^{-11}\, m^3/(kg \cdot s^2)$, the maximum permissible absolute measurement error of each torsion balance parameter should be calculated based on the $\Delta\mathbf{G}$ value lower by an order of magnitude.

It is possible to reject direct measurement of parameters L, d, Y_τ and replace them with only one parameter, i.e., torsional stiffness factor. For this purpose it is necessary to conduct an additional experiment in which masses m_B are removed in-situ without violating the experimental setup integrity. In the course of this experiment the actual suspension fiber torsional stiffness was determined via the fixed period of the beam torsion motion. However, in this case the measurement accuracy of such parameters as mass, torsion angle, linear dimensions and time (the torsion oscillation period) still remains problematic.

The effect of gravitational anomaly m_C on the torsion angle α. Now let us estimate the effect of gravitational anomaly m_C on the experimentally measured torsion angle of the beam A_1A_2 suspension fiber (Fig. 2). Assume that when anomaly m_C was absent, the torsion balance beam was turned by angle α. Using the torsional moment balance equation (11), calculate the new static torsion angle α_C allowing for the presence of gravitational anomaly m_C at point C defined by radius-vector $\underline{r}_C$. The asymmetric location of mass m_C gives rise to an additional torsional moment and response at point O. Here we consider only the torsional moment since within our task beam A_1A_2 can rotate only in plane Oxy about point O. Tab. 4 lists the calculations reflecting the effect of the gravitational anomaly on the torsion angle of the beam suspension fiber. Analysis of the Tab. 4 data unambiguously shows that it is necessary to ensure local axial symmetry of the gravitational field within a radius of minimum 5 meters from the suspension fiber of the torsion balance beam. As for celestial bodies, in the framework of our schematic model such gravitational anomalies as e.g. Moon (in perigee) produce extremely minor (instrumentally non-

Table 4: The effect of gravitational anomaly ($m_C = 100\,kg$, azimuth $\varphi = 90°$) on the suspension fiber torsion angle.

$\lvert\underline{r}_C\rvert, m$	$(\alpha_C - \alpha)$, *arcsec*	$\delta\alpha, \%$
2	6.4526091	0.0236213
3	1.9179015	0.0070209
5	0.4149482	0.0015190
10	0.0519051	0.0001900
30	0.0019228	0.0000070
Moon	0.0008894	0.0000033
50	0.0004153	0.0000015

measureable) effect on the suspension fiber torsion angle. Thus celestial bodies may be excluded from consideration.

4 Conclusions

Solving of the direct metrological problem by using the torsion balance mathematical model indeed gives an answer on the question why there has been no progress in refining the "gravitational constant" value during so many years and why it can hardly be expected in the foreseeable future. The decimal-by-decimal analysis has shown that the current problems with the accuracy of determining the "gravitational constant" are caused by a quite real and ordinary fact, i.e., by limited metrological capacity of experimental setups in combination with methodological stereotypes.

To reach the preset accuracy of the "gravitational constant", the experimentalist should artificially increase it by an order of magnitude and then find the maximum permissible measurement errors of the system key parameters corresponding to this increased accuracy. Just these measurement errors will enable calculation of the "gravitational constant" with that preset accuracy provided the laboratory metrological capability is sufficiently high.

In addition, note that the gravitational effect of celestial bodies may be ignored due its insignificance but only under the condition of the gravitational field axial symmetry with respect to the suspension fiber of the torsion balance beam.

To summarize the above, we can state that at present the "gravitational constant" has been calculated accurately to the second decimal, and the spread in subsequent decimals (see Tab. 1) is caused by specific features of particular experimental setups and metrological capabilities of laboratories, experimental techniques, external factors, etc. Thus the process of refining the "gravitational constant" has turned into senseless waste of time and resources though the search for *experimentum crucis*[5] for indirect measurement of the "gravitational constant" seems to be important and useful from the metrological and engineering point of view.

[5]Crucial experiment — an experiment held to decide with certainty between two rival hypotheses about some matter. (`http://philosophy.enacademic.com/588/crucial_experiment`)

References

[1] Томилин К. А. Фундаментальные физические постоянные в историческом и методологическом аспектах. — ФИЗМАТЛИТ, 2006. — 368 с.

[2] Kiryan D. G., Kiryan G. V. On the Gravitational Mass // International Journal Of Applied And Fundamental Research. — 2013. — Vol. 1. — URL: http://www.science-sd.com/452-24059.

[3] Kiryan D. G., Kiryan G. V. Gravitational interaction in the medium of non-zero density // e-prints viXra:1406.0128v2. — 2014. — Jul. — P. 24. — URL: http://vixra.org/abs/1406.0128.

[4] Mohr P. J., Taylor B. N., Newell D. B. CODATA recommended values of the fundamental physical constants: 2010 // Reviews of Modern Physics. — 2012. — Nov. — Vol. 84, no. 4. — P. 1527–1605.

[5] Kiryan D. G., Kiryan G. V. The Evolution of the System of Gravitating Bodies // Advanced Problems in Mechanics. — 2017. — Jun. — P. 219–234.

[6] Gundlach J. H., Merkowitz S. M. Measurement of Newton's Constant Using a Torsion Balance with Angular Acceleration Feedback. — 2000. — 11. — Vol. 85. — P. 2869–72.

[7] Strong J. Physical experiment technology. — Leningrad News-paper, Magazine and Book Publishing House, 1948.

Dmitry G. Kiryan, Institute of Problems of Mechanical Engineering of RAS
61 Bolshoy Prospect V.O., 199178, Saint-Petersburg, Russia

George V. Kiryan, Saint-Petersburg, Russia

Electro-acoustic estimation of the compensatory method of electric motor noise decrease

V.M. Kolykhalin
cap-007@mail.ru

Abstract

Electromagnetic interaction between stator and rotor fields, mechanical motor vibrations and air fluctuations from ventilation motor impeller compose the basic components of electric motor noise in a wide frequency range. Magnetostrictive forces causing radial deformation of the stator core rings under alternate field action bring the special addition in motor noise in basic 100 Hz frequency. The compensation method consists on reduction 100 Hz frequency and its harmonics as an interference interaction between two antiphase sources is considered. The air volume formed by the winding stator and several rotor core elements is fluctuated. External side of stator magnetic core is appeared as first source and internal side of stator magnetic core is applied as second source influencing fluctuations through the hole drilled in bearing motor side with an allowance for adding the short pipe used as resonant cavity. The most compensation effect in 100 Hz frequency as close as possible to resonant frequency of resonator is fixed. The asynchronous electric motor into the small volume chamber SVC with rubber damping construction is installed. The greatest linear size SVC less than half of wave length of the longest eighen frequency is used. Interaction between external side of stator magnetic core and resonant source into SVC is modeled on the forepole system with coefficient taking into account the difference between areas of both sources by transformation coefficient. The dependence of the sound noise pressure from electromagnetic vibrations inside of the SVC with and without compensation effect is considered. The spectrograms illustrating of magnetic motor noise decrease are shown and the adjustment for decrease of magnetic motor noise is supported.

1 Formulation of the problem of the motor noise reduction

The increase quantity and power of electric machines and aspiration to facilitate designs cause increased requirements to noise machine characteristics which in the list of the basic parameters of quality are included. First of all it is caused by harmful influence of noise on a person.

Not expensive but most applied asynchronous electric motors with such basic noise components as magnetic, mechanical and aerodynamic with typical ventilation systems are used. The stator core fluctuations by the magnetostrictive forces are excited. During each half of a cycle of alternative electrical field the stator core has one compression-stretching cycle. The doubling network frequency corresponding of mechanical fluctuations 100 Hz is prevailed.
The main idea is to reduce of electric motor noise by negative correlation of a pier of sound harmonic sources: stator core 100 Hz fluctuations and resonator with antiphase 100 Hz fluctuations. Therefore the motor installed into the small volume box (SVB) having the maximum size not more than half of air wave length corresponded the double frequency network 100 Hz are investigated. Thus acoustical field as statistical is considered when the level of sound pressure is the same in all points of the SVB and does not depend on coordinates. It is exact restriction for low frequencies while eighen frequencies of the SVB considerably above frequencies investigated are excited [1].
The effect of acoustic short circuit is well known especially for developing of a loudspeaker enclosure. The corresponding sound pressure excited by alternative cycles of air compression-stretch of the opposite loudspeaker diaphragm surfaces are created. If loudspeaker acoustic baffle is absent the effect of acoustic short circuit in low frequencies is happened because of the diffraction of sound waves. In this way the sound pressure in surrounding space is decreased.
The similar acoustic effect to reduce of low frequency electric motor noise is applied. The reduction of the basic magnetic noise component with carrying frequency 100 Hz in broadband spectrum of pressure is examined [2].

2 Acoustic - mechanical system

Some air capacity inside of the electric motor formed by winding stator and rotor elements is considered. The aperture S_2 through a motor beating side for passing out internal stator core fluctuations was drilled. The internal stator core fluctuations with external stator core fluctuations being antiphase each other are summarized. Then motor noise pressure into SVB as result of the interference of such fluctuations is decreased (Fig.1).
The aperture with the piece of a pipe installed as a resonator throat is supplemented. The construction on rubber shock-absorber into SVB was fixed.
The installation for analysis of magnetic noise reduction including the SVB with the linear sizes 0,4m 0,5m 0,6m and the asynchronous electric motors 800 Wt was developed.
Application of the resonator system allows forcing sound radiation in the resonant frequency 100 Hz by ratio determined as

$$f_{@} = \frac{1}{\sqrt{m_2 \cdot c_a}} \tag{1}$$

Here *m2* is the sum of air weight in the resonator throat and the air weight of environment; *ca* is air flexibility in the SVB divided to aperture *S2, S1* is the fluctuation surface of the stator core.

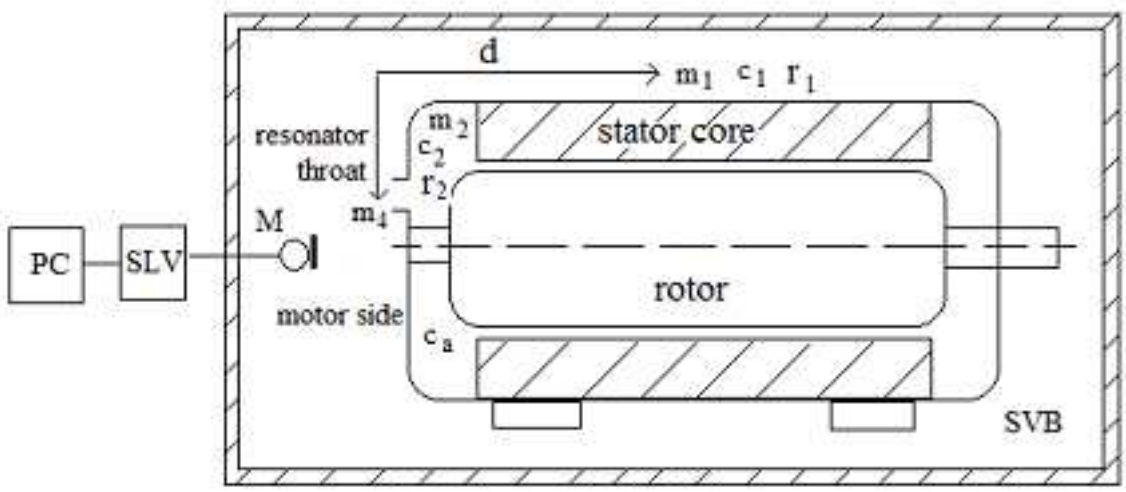

Figure 1: Installation for analysis of magnetic noise reduction: M is the microphone with the amplifier; SLV is the sound level meter; PC is the computer; d is distance between centers of sources

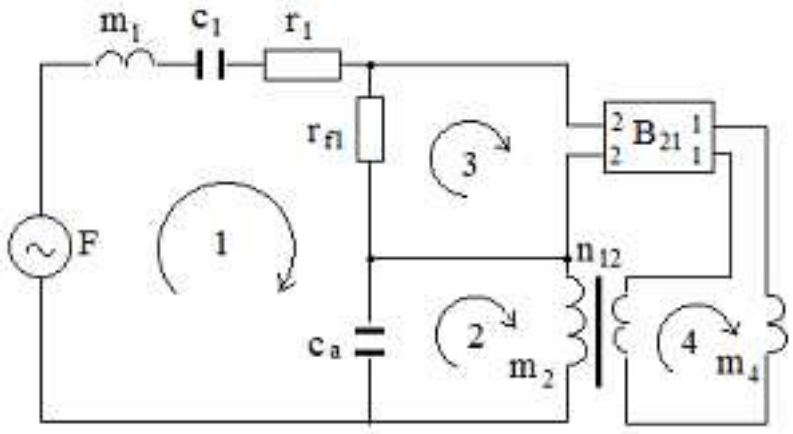

Figure 2: Equivalent electric scheme showing interactions of four contours between stator core and resonator with the aperture S2 into SVB

The internal stator core fluctuations by flexibility ca to air weight $m2$ are transferred. So $m2$ serves as the second radiator. On the resonant frequency of the resonator with aperture S2 $f = fres$ or frequencies as close as $fres$ the fluctuations of weight $m2$ achieve the highest amplitudes.

The equivalent electric scheme acoustic-electrical system on Fig.1 is considered and allowing to estimate quantitatively the interaction of fluctuations between stator core and resonator into SVB.

The contour 1 in Fig.2 is the basic source of excitation (external stator core fluctuations) with oscillatory speed $\dot{\xi}_1, m1, c1, r1$.

By contour 2 in Fig.2 the fluctuations with the oscillatory speed $\dot{\xi}_2$ between equivalent air weight inside electric motor and air weight in the resonator throat are considered.

By contour 3 in Fig.2 the interaction with the oscillatory speed $\dot{\xi}_3$ between external

stator core radiations and air resistance into SVB is considered.
By contour 4 in Fig.2 the fluctuations with the oscillatory speed $\dot{\xi}_4$of air weight in SVB oscillating in common with air weight of resonator throat are considered.

3 Interpretation of the interaction between stator core and resonator fluctuations

Interaction between stator core and resonator fluctuations by two-port network *b21* (Fig.2) with transfer coefficient is modeled

$$b_{21} = \frac{\dot{\xi}_3}{\dot{\xi}_4} = \frac{S_2}{S_1} e^{-jkd} = n_{21} e^{-jkd}. \tag{2}$$

The difference between of the areas stator core S1 and the aperture S2 of the resonator by transfer coefficient *n21* and the delay of a stream $\dot{\xi}_2 S_2$ from the aperture on a way d with a phase member e^{-jkd} is considered.
The main parameter explaining the interaction between stator core and resonator in Fig.2 is the common radiation resistance *rf*. Then the *rf* can be determined as the sound radiating power W in common fluctuations of the stator core and the resonator with aperture S2by two ways: with oscillatory speed $\dot{\xi}_1$ stator core ore as the difference $\dot{\xi}_1 - \dot{\xi}_3$. Then

$$W = \left|\dot{\xi}_1\right|^2 \cdot r_f = \left|\dot{\xi}_1 - \dot{\xi}_3\right|^2 \cdot r_{f1}, \tag{3}$$

thus

$$r_f = r_{f1} \left|1 - \frac{\dot{\xi}_3}{\dot{\xi}_1}\right|^2. \tag{4}$$

In these expressions *rf1* is the resistance of fluctuation of stator core radiation without an aperture in motor but *rf* is with an aperture. For finding *rf* from (3) the scheme on Fig.2 is used.
The following features of the scheme in Fig.2 are taken into account. The resistance *rf1* and the target resistance of the two-port network *b21* parallel connected with *rf1* between points *2-2* are summarized as the resistance *rf*.
The entrance resistance between points *1-1* of the two-port network *b21*is the same as target resistance but in n_{21}^2 time increased. At recalculation in the contour 2 with oscillatory speed $\dot{\xi}_2$ the active resistance is *rf* and the reactive resistance is $\omega m_2 = \omega m_4 n_{12}^2$. Here $\dot{\xi}_2$is the speed determined to aperture *S2*.
Considered from this point of view the expression is found

$$\frac{\dot{\xi}_2}{\dot{\xi}_1} = \frac{1}{j\omega c_a \left(r_f + j\omega m_2 + 1/j\omega c_a\right)} = \frac{1}{j\omega c_a Z}, \tag{5}$$

were $Z = r_f + j\omega m_2 + 1/j\omega c_a$.
In the other side according (2) and taking a form as $e^{-jkd} \approx 1 - jkd$ the expression $\dot{\xi}_4 \approx \dot{\xi}_3 / (1 - jkd)$ is found.

Thereby

$$1 - \frac{\dot{\xi}_3}{\dot{\xi}_1} = \frac{r_f + j\omega m_4 + kd/\omega c_a}{Z}. \tag{6}$$

The numerical $\frac{kd}{\omega c_a} = \frac{d}{c_0 c_a} = \rho_0 c_0 \frac{d \cdot S_1^2}{V} \gg r_f$ being of value in (7) is used.
Here V is the air volume into electric motor, co is the sound speed in air, ca is the air flexibility into electric motor (Fig.1).
Neglecting r_f and substituting the module (5) in (4) the common radiation resistance rf is received

$$r_f = r_{f1} \frac{(d/c_0 c_a)^2 + (\omega m_4)^2}{r_f^2 + (\omega m_4 - 1/\omega c_a)^2}. \tag{7}$$

To find out numerical value rf du to three frequency ranges $\omega \gg \omega_{res}, \omega \ll \omega_{res}, \omega = \omega_{res}$the expression (7) is investigated. Here ω_{res} is the resonant frequency of the resonator.
If the first frequency range is $\omega \gg \omega_{res}$then $\omega m_2 \gg \frac{1}{\omega c_a}, \omega m_2 \gg \frac{d}{c_0 c_a}$ and after some simplifications the expression (7) is transformed

$$r_f \approx r_{f1}. \tag{8}$$

If the second frequency range is $\omega \ll \omega_{res}$ then $\omega m_2 \ll \frac{1}{\omega c_a}, \omega m_2 \ll \frac{d}{c_0 c_a}$ and after simplifications the expression (7) is transformed

$$r_f \approx \frac{\rho_0}{4\pi c_0^3} d^2 S_1^2 \omega_{res}^4. \tag{9}$$

The third expression $\omega = \omega_{res}$ is more important. Then $\omega_{res} m_2 > \frac{d}{c_0 c_a}$ and after simplifications the expression (7) is transformed

$$r_f \approx \sqrt[3]{r_{f1} \cdot \omega_{res}^2 m_2^2}. \tag{10}$$

4 The results of measurements of the acoustic short circuit effect for motor noise reduction

For discussion about acoustic short circuit effect there are two motor noise pressure spectrograms into SVB: without the resonator (Fig.3) and having the resonator with aperture S2 in motor side (Fig.4).
The frequency on abscissa (Hz) and the relative acoustic noise pressure (dB) on ordinate axis are constructed. The integrate level noise pressure 89 dB measured by sound level meter $RFT0024$ was fixed (Fig.3). The maximum noise pressure value is corresponding of the basic magnetic motor noise frequency 100 Hz.
The frequency on abscissa (Hz) and the relative acoustic pressure (dB) on ordinate axis are constructed. The acoustic short circuit effect for motor noise reduction used in the frequency 100 Hz and the first harmonics in Fig.4 is shown. The integrate level noise pressure 82 dB measured by the sound level meter was fixed.

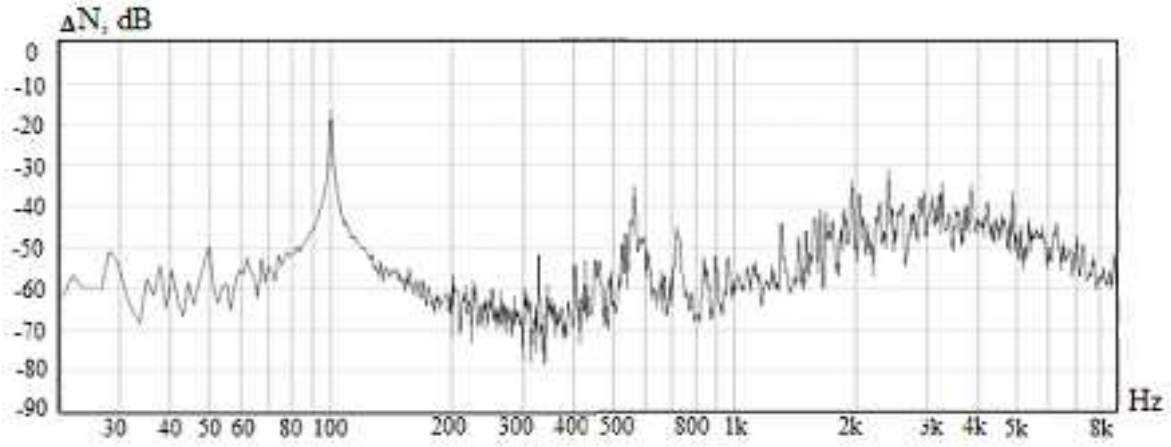

Figure 3: Noise pressure spectrogram for motor without resonator

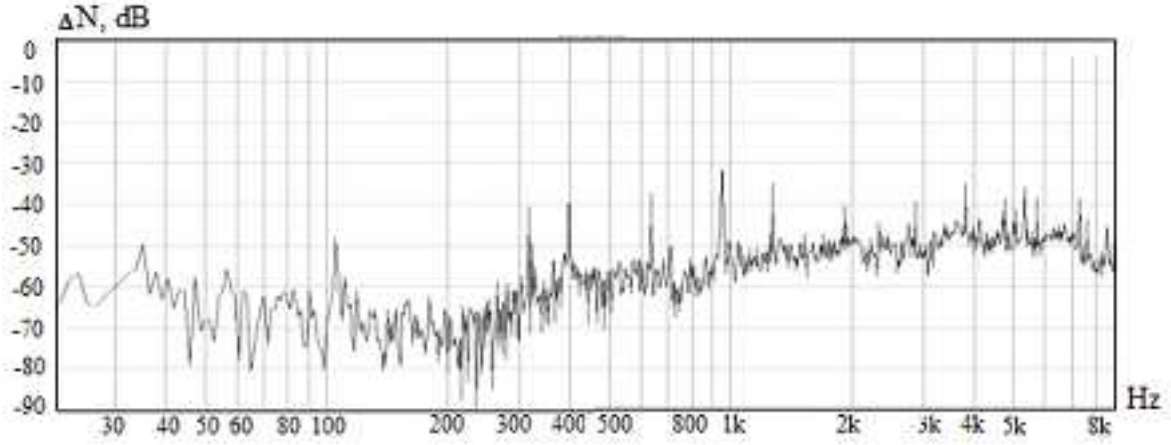

Figure 4: Noise pressure spectrogram for motor having the resonator with aperture S2 in motor side

Comparing spectrograms in Fig.3 and in Fig.4 the integrate level pressure from 89 dB (without resonator) to 82 dB (with resonator) in wide strip is decreased.
As follows from stated the effective method developed making quieter electric motors for person protection in low frequencies and increasing functions of power electronics on transport is provided.

References

[1] Davydov V. V., Kolykhalin V. M. About compensation method of the electric motor noise.- B.: Vestnik BGTU named V.G. Shukhov, 2014.

[2] Kolykhalin V.M., Davydov V.V. Device of the electric motor noise compensation. Patent of the Russian Federation є2528552, M. Federal serv., RU RU 2528552 C1, published 20.09.2014 Bul. 26.

Modeling of the equilibrium component of the stress tensor of filled elastomeric materials with consideration of the Mullins softening effect

Kseniia A. Mokhireva, Alexander L. Svistkov
lyadovaka@icmm.ru

Abstract

Elastomers are viscoelastic materials and their properties significantly depend on the loading rate. The actual stress experienced by these materials is the sum of equilibrium and dissipative (inelastic) terms. At very low loading rates we can eliminate the significant influence of time effects and model the material as hyperelastic. In this paper, the features of the experimental determination and subsequent mathematical description of equilibrium stresses are considered. Verification of the proposed equations has been carried out for a series of experiments - cyclic uniaxial tests of samples of materials on the basis of the same matrix, but with different filler contents and under different maximum degrees of deformation.

1 Introduction

Rubber products are widely used in different fields of modern world due to their physical and mechanical properties. However, the complex nature of their behavior (finite deformations, dependence of polymer properties on strain rate, hysteresis losses, stress relaxation, softening effect, etc.) causes difficulties with creation of a system of constitutive equations for this class of materials. In order to take into account the effect of loading rate on the elastomers behavior, two approaches are usually used: integral and differential [1, 2]. Despite the differences in the methods of constructing equations, both approaches have one similar feature. In each approach we can directly determine equilibrium (elastic) stresses, which are independent of time processes.

As a rule, most researchers do not pay special attention to the description of the elastic component and define it with the help of "simple" elastic potentials. Such simplification is not correct when modeling the properties of high-filled rubbers under conditions of large deformations. In addition, it has been long established that the material softens (stresses fall) under reloading – the Mullins effect [3]. This feature should also be taken into account when describing the experimental data. In this article, the peculiarities of the experimental procedure aimed to determine the equilibrium component of stresses are considered and equations describing the elastic component of the stress tensor are proposed

2 Elastic properties. Formulation of the elastic potential

As it has been mentioned before, the viscoelastic behavior of the elastic material is described by the models of integral and differential forms [1, 2], of which the differential models are most frequently used. This is due to the simplicity and clarity of the tensor functions used in the equations, which reflect the physics of the processes occurring during deformation. It is proposed to consider the free energy in the form of a sum of equilibrium and nonequilibrium (dissipative) parts [4]:

$$\mathbf{T} = \mathbf{T}_e + \mathbf{T}_d, \tag{1}$$

where $\mathbf{T}_e$ is the actual equilibrium stress at given deformation after the completion of all transient processes, and $\mathbf{T}_d$ is the dissipative stress (difference between real $\mathbf{T}$ and equilibrium $\mathbf{T}_e$ stresses).
Let us consider the construction of the constitutive equations for the equilibrium component only. Usually, this component of the stress tensor is determined by specifying an elastic potential, the form of which can be chosen from the enormous variety of potentials already proposed [3, 5]. The presence of a large number of representations for describing the elastic deformation energy can be attributed to attempts to specify an optimal form providing a reliable description of the experimental data regardless of the material and the way of its loading. Furthermore, this potential should include a small number of constants to be determined.

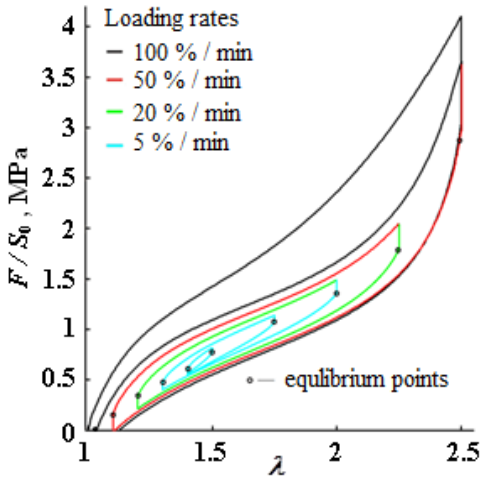

Figure 1: Uniaxial loading of the sample made of the material filled with 50 phr carbon black N220. From one sample, it is possible to obtain the data on the viscoelastic behavior of the material, residual strains, the Mullins softening effect, and equilibrium points at different degrees of the sample elongation. F – acting force, S_0 – initial cross section of the sample, λ – sample stretch ratio.

Before choosing the shape of the potential for describing the elastic properties of elastomers, it is necessary to determine the method of finding elastic (equilibrium) stresses. To this end, we have performed the experiments, in which the samples

were subjected to uniaxial cyclic loading according to the loading scheme described in patent [6] and illustrated in Figure 1. After each loading and unloading of the sample, a 20-minute delay was set for the first deformation cycle and a 10-minute delay for the subsequent cycles. After 20- or 10-minute "rest" of the material, the curve breakpoints (equilibrium points) were formed at each of the unloading and loading sections (Figure 1). In our opinion, these points characterize adequately the state of the material under equilibrium (quasistatic) tension.
This type of the test was performed for the samples based on the same matrix with different filler concentration. As an elastomeric base, we have used styrene-butadiene rubber SBR-1502, which has found wide application in the tire, rubber, cable and footwear industries. The filler was carbon black ISAF N220 with spherical particles of low density $\rho = 1.8$ g/cm^3. The filler content was as follows: 1) 10 parts by weight of carbon black per 100 parts by weight of rubber, i.e. 10 phr, 2) 30 phr, 3) 50 phr. Accordingly, the volume fraction occupied by the filler in the composite for each case was: 1) $\phi \approx 4.8\%$, 2) $\phi \approx 13.3\%$ and 3) $\phi \approx 20.4\%$.
Since the material behavior depends on the degree of loading, in order to determine the universal shape of the potential and to more accurately specify the values of the constants of this potential, we performed a series of tests on cyclic loading of samples at different maximum stretch ratios: a) $\lambda = l/l_0 = 2$, b) $\lambda = 2.5$, c) $\lambda = 3.5$, d) $\lambda = 4$.
By analyzing the obtained experimental data, we have defined the potential describing the elastic strain energy density as follows:

$$\omega = aC\ln(I_1) - C\ln(1 - \frac{I_1}{I_*}) + const, \tag{2}$$

where a, C is the material constants, $I_1 = \lambda_1^2 + \lambda_2^2 + \lambda_3^2$, $\lambda = l/l_0$ is the stretch ratio, and I_* is the limiting value for I_1. The material is assumed to be incompressible ($\lambda_1\lambda_2\lambda_3 = 1$). The proposed potential is a combination of two parts: the first term for the initial loading segment and the second term for the sudden increase in stresses with increasing strains. The second component is the variation of the Ghent potential [5], where I_* characterizes the limiting extensibility of the rubber network so that the value of this parameter depends on the degree of the sample elongation. The use of this potential in calculating the equilibrium component of the stress tensor requires determination of two material constants and one parameter characterizing the behavior of elastomers. For this purpose, we have minimized the sum of squares of normalized deviations of the model data from the experimental results. Normalization of the differences between the numerical and experimental results is given via dividing by the value of the experimental data. Being subjected to loading, the material accumulates residual strains; the higher is the loading force, the larger are the residual strains. In order that the error of the model does not exceed 5% it is necessary to shift the curve along the X-axis by the value equal to the residual strain. Since the model has been developed under the assumption of a multiplicative decomposition of the deformation gradient into elastic and inelastic parts, the following condition is valid: $\lambda = \lambda_e\lambda_p$, where λ is the total stretch ratio, λ_e is the elastic (equilibrium) stretch ratio and λ_p is the inelastic (plastic) stretch ratio. Therefore, the displacement of the curve along the X-axis with the aim to

describe the equilibrium curve of the stress-softened material behavior is stated as:

$$\lambda_e = \frac{\lambda}{\lambda_p} \tag{3}$$

In further equations and calculations, instead of λ, we use λ_e and $\lambda_i^e (i = 1, 2, 3)$ correspond to the elastic components of the stretch ratio found from (3).
For constructing theoretical вГЁstress-stretch ratioвГ№ curves, elastic stresses are calculated based on the formula:

$$\sigma_1^e = \frac{F_e}{S_0} = \lambda_1^e \frac{\partial \omega_e}{\partial \lambda_1^e} - p = 2\lambda_1^e C \left(\lambda_1^e - \frac{1}{(\lambda_1^e)^2}\right)\left(\frac{\alpha}{I_1^e} + \frac{I_*}{(I_* - I_1^e)}\right) \tag{4}$$

where p is the Lagrange parameter defined by the condition ($\sigma_2^e = \sigma_3^e = 0$). Thus, according to equation (3), the constants α, C and the parameter I_* determine the stretching of the curve along the Y-axis, and only I_* specifies the stretching along the X-axis. We assume that the constant α is invariable for all materials to exclude the mutual influence of α and C on each other. We also assume that $\alpha = 5$, then, minimizing the sum of squares of the deviations between the numerical and experimental results, we arrive at the conclusion that the constant C varies insignificantly within the framework of one material. Let this constant C be the same in the calculations and have a certain value for each material.
Changes in the model constants (α, C) and the parameter I_* for the examined elastomer samples is given in Table 1.

Material	Total stretch ratio λ	Constant α	Constant C	Parameter I_*
filler volume fraction $\phi \approx 4.8\%$	2	5	0.93	16.857
	2.5			18.71
	3.5			23.805
	4		-	-
filler volume fraction $\phi \approx 13.3\%$	2		0.106	9.534
	2.5			11.134
	3.5			15.684
	4			19.557
filler volume fraction $\phi \approx 20.4\%$	2		0.125	7.324
	2.5			8.857
	3.5			12.828
	4			16.406

Table 7: The constants and parameters of the developed model for different materials

Figure 2 presents examples showing how the experimental results can be approximated by the proposed model in accordance to the values from Table 1. It is seen that the theoretical curves approximate the experimental data well.
Based on the obtained constitutive equations (2) and the calculated results (Table 1), we put forward some assumptions. Firstly, for all materials the constant α is regarded as an invariable value and, therefore, characterizes the properties of the

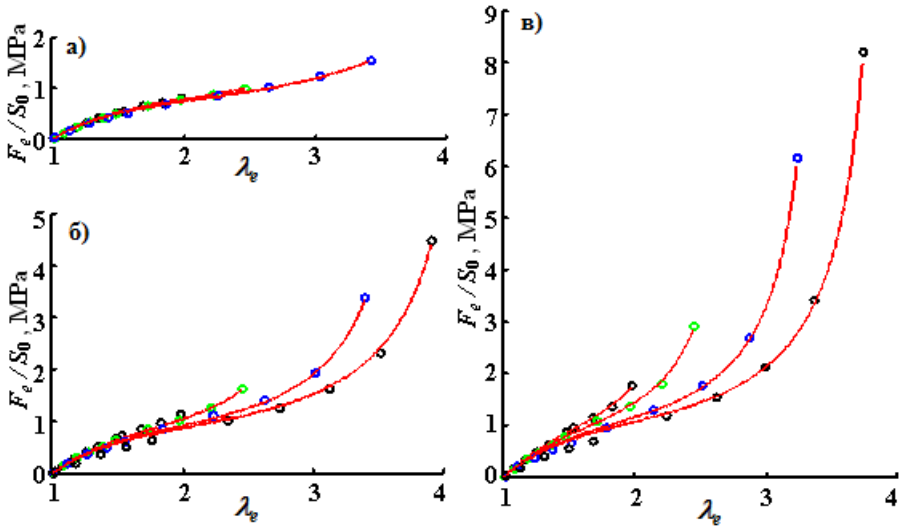

Figure 2: Plots of the experimental data (points) and the theoretical curves (lines) for materials with filler content: a) 10 phr; b) 30 phr; c) 50 phr

material matrix. The constant C increases with increasing filler concentration in the elastomer and, in fact, shows the degree of reinforcement depending on the degree of filler concentration. Secondly, the parameter I_*, as already mentioned, reflects the limiting value of the network extensibility. In the case of the material with a filler content of 10 phr, the value of this constant has exceeded the maximum permitted value and because of this the results for the sample stretched to 300% are absent; a break occurs.

Using the results obtained in our investigation, we have derived an elastic potential (2) that involves constants, which are able to characterize the elastomer properties. With this potential, we can provide a relative evaluation of the reinforcement degree of elastomers (the smaller is the constant value, the less is the active filler concentration in the material). The parameter I_* allows one to determine the elongation degree of the sample (the higher is its value, the higher is the stretch ratio and the greater is the probability of a break).

3 Analysis of the relations between the model constants. The Mullins softening effect.

Let us consider the dependence of the constant C and the parameter I_* of the elastic potential on the choice of the material (the degree of its filling) and the peculiarities of the testing procedure (different maximum strain levels).

The calculations of the model constant C (Table 1) have shown that its value increases with higher concentration of active filler particles in the material. Comparison of the obtained calculations with the experimental data indicates that the relationship between the constant C and the filler concentration ϕ is linear (Figure 3) and can be determined as:

$$C = C_1 + C_2\phi = 0.082 + 0.2\phi \tag{5}$$

where C_1 and C_2 are the constants, and ϕ is the volume fraction of filler in the material.

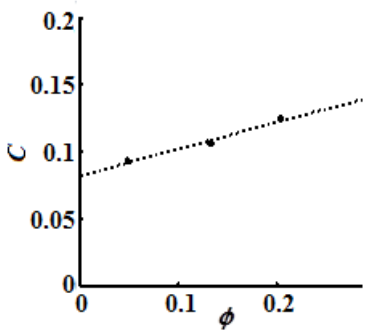

Figure 3: Linear relationship between the material constant C and the filler volume fraction ϕ of the composite

Besides, it has been found that the parameter I_* depends on the stretch ratio, and the parameter increases as the prescribed maximum strain grows (Figure 4). For each of the materials, this relationship is inherently linear:

$$I_* = C_3^* + C_4^* \max(I_1^e) = \begin{cases} 11.4 + \max(I_1^e), & \phi \approx 0.048 \\ 3.8 + \max(I_1^e), & \phi \approx 0.133. \\ 1.9 + \max(I_1^e), & \phi \approx 0.204 \end{cases} \tag{6}$$

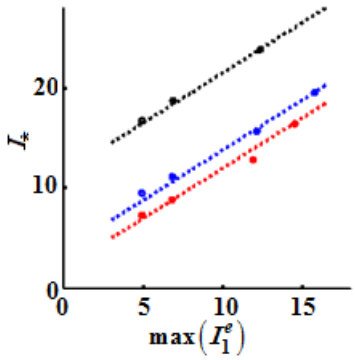

Figure 4: Linear relationship between the model parameter I_* and the stretch ratio

It follows from the previous calculations of the parameter I_* that the constant $C_4^* = 1$, and therefore it is not further considered for the term $\max(I_1)$ in equations (6), but C_3^* depends on the variable ϕ (Figure 5):

$$C_3^* = C_3 \phi^{-C_4} = 0.2\phi^{-1.4} \tag{7}$$

Taking into account equations (5), (6) and (7), potential (2) can be written in the generalized form as

$$\omega_e = (C_1 + C_2\phi)\left(\alpha \ln(I_1^e) + \ln\left(1 - \frac{I_1^e}{C_3\phi^{-C_4} + \max(I_1^e)}\right)\right) + const \tag{8}$$

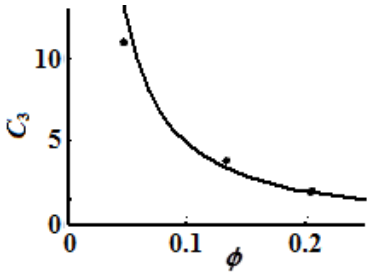

Figure 5: Power-law dependence of the constant C_3 on the filler volume fraction ϕ of the material

Thus, equation (8) allows us to find and describe the entire spectrum of the equilibrium curves of the behavior of stress-softened materials, regardless of their filler concentration in them and the maximum stretch ratio given in the experiment.
The equilibrium strain curves received from the experiments show that the material has softened after being subjected to loading, and this reduces the material stiffness during the repeated loading cycles (the Mullins effect) [7, 8]. From the practical point of view and modeling the softening of elastomers under deformations is an undesirable effect. If the material is able to soften completely, then there is no need to take this effect into account in calculations, but in practice the material is able to recover its properties with time partially or almost completely, especially during "rest" at high temperatures [9]. Furthermore, in real conditions rubber products experience nonuniform loads and, consequently, the material exhibits the nonuniform softening effect. Therefore, within the framework of numerical and finite-element calculations it is necessary to take into account the Mullins effect and to determine the behavior of the non-softened material.
In our case, the relationship represented by equation (8) with consideration of (4) permits us to determine the equilibrium stress-strain curves of the non-softened material. Figure 6 shows the equilibrium tensile curves of the material deformed for the first time (blue lines) and the set of equilibrium curves of the stress-softened material (red lines). These lines are the stain-stress curves of the material that experienced a total stretch of 100%, 150%, 250% and 300%, respectively. It is worthy to note that the current deviations between the equilibrium tensile curves of the stress-softened and non-softened materials with the test data indicate only possible experimental and computational errors.
As a result, we have derived the constitutive equation (8) for describing and finding the elastic properties of materials.

Conclusions

A possible way of determining and describing the elastic component of the stress tensor, which is needed for modeling the viscoelastic behavior of elastomers, is considered. We have developed a five-constant elastic potential that involves the constants characterizing the properties of elastomers depending on their structure (the amount of the filler introduced) and the peculiarities of the testing procedure (the degree of loading). The efficiency of the proposed model has been validated by com-

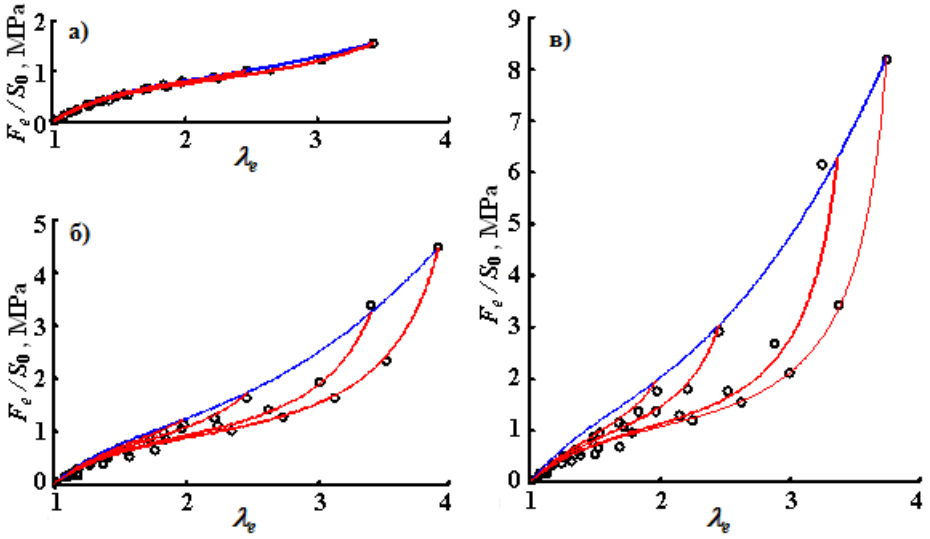

Figure 6: Curves of the elastic behavior of the material deformed for the first time (blue lines) and the stress-softened material (red lines) with filler concentrations: a) 10 phr; b) 30 phr; c) 50 phr

parison with the experimental data for materials based on the same matrix with different filler contents.

Acknowledgements

The study was supported by RFBR (grant numbers 16-08-00914, 17-08-01118).

References

[1] Svistkov A. L., Lauke B. Differential constitutive equations of incompressible media with finite deformations //J APPL MECH TECH PHY. – 2009. – V. 50, Is. 3. – P. 493-503.

[2] Petiteau J.–C., Verron E., Othman R., Sourne H., Sigrist J.–F., Barras G. Large strain rate-dependent response of elastomers at different strain rates: convolution integral vs. internal variable formulations //MECH TIME DEPEND MAT. – 2012. – P. 349-367.

[3] Aidy Ali, Hosseini M., Sahari B.B. A review of constitutive models for rubber-like materials //AJEAS. – 2010. – V. 3, Is. 1 – P. 232-239.

[4] Reese S., Govindjee S. A theory of finite viscoelasticity and numerical aspects //INT J SOLIDS STRUCT. – 1998. – V. 35, Is. 26-27. – P. 3455-3482.

[5] Arruda E.M., Boyce M.C. Constitutive models of rubber elasticity: A review //RUB CHEM TECH. – 2000. – V. 73. – P. 504-523.

[6] Svistkov A.L., Shadrin V.V. Patent RF No. 2549841. – 2015. *(in Russian)*

[7] Mullins L. Softening of Rubber by Deformation //RUB CHEM TECH. – 1969. – V. 42, No. 1. – P. 339-362.

[8] Ogden R.W., Roxburgh D.G. A pseudo-elastic model for the Mullins effect in filled rubber //PROC R SOC LOND. – 1999. – V. 455, No. 1988, Series A. – P. 2861-2877.

[9] Shadrin V.V. Recovery of the Mechanical Properties of Rubber under Thermal Treatment //POLYM SCI. Series B. – 2005. – V. 47, No. 7-8. – P. 220-222.

Kseniia A. Mokhireva, Perm, Russia
Alexander A. Svistkov, Perm, Russia

Algebraic Poincaré equations

R.P. Moshkin[1]

[1]*M. V. Lomonosov Moscow State University, Moscow, Russia*

rmoshkin@yandex.ru

Abstract

As examples, we specify the Poincaré-Chetaev equations. The review article of V.V. Rumyantsev can be supplement with data on works devoted to other forms of equations of motion of nonholonomic systems.

The original source of this idea, the work of Poincaré published in 1901, actually introduced the expansion of the vector of generalized velocities with respect to a moving frame (although the term appeared later at E. Cartan) composed from vector fields forming the Lie algebra (in modern terminology), that is, their Lie brackets have constant ("structural") coefficients in the same fields. Thus, Poincaré has already used the idea of pseudo velocities, although this idea was clearly introduced by Boltzmann in 1902. It is interesting that the constancy of structural coefficients is not necessary for Poincaré equations in reality. The work of Hamel in 1904 has no reference to Poincaré, but clearly operates with vector fields. The Hamel equations are different from the Poincaré equations only terminologically. Hamel clearly point out that the constancy of structural coefficients is not required; he generalizes his "Euler-Lagrange equations" to nonholonomic systems.

It is interesting that, often, parallel works are also historically simultaneous. The next burst of activity in the field of equations of motion of nonholonomic systems was in 1926 and during next five years. On the one hand, N.G. Chetaev published the Hamiltonian version of the Poincaré equations and anticipates the Dirac approach to exposition of Hamiltonian mechanics. On the other hand, in 1926-31 Vranceanu, Singh and Shouten introduced and developed the notion of nonholonomic connection, due to which they tie a nonholonomic mechanics to Riemannian geometry. At the same time, they relied on the work of Ricci and Levi-Civita published in 1900!

There are a number of different forms of equations of motion of nonholonomic systems. We will consider the main of them and show that they can be obtained from the Maggi's equations. We will derive the most commonly used forms for noting the equations of motion of nonholonomic systems from the Maggi's equations.

1 Introduction

Earlier [1-3], the direct calculations showed the equivalence of the Poincaré equations of motion of nonholonomic systems to the Chaplygin, Appell, Hamel, Volterra, and Ferres equations and some other equations. The equivalence of the equations of motion in quasicoordinates to the Appell equations, as well as Chaplygin's equations, was proved [6] by derivation of these sets of equations

from the d'Alembert-Lagrange principle. The Voronets equations were derived from the Poincaré equations (5.6) in [4].

We will show that the Poincaré equations are equivalent to some other forms of equations of motion of nonholonomic systems.

2 The equations of Volterra, Appell, Kane

Maggi [5] showed that the Appell and Volterra equations follow from the equations established by him. Maggi considered a mechanical system with coordinates $x_i (i = 1,...,n)$, subject to linear constraints, which can be both holonomic and nonholonomic, explicitly dependent or independent on time. When solving the constraint equations in relation to $\dot{x}_i$, he presented the latter in the following form

$$\dot{x}_i = b_{is}(x)\eta_s, \qquad i = 0,1,...,n, \qquad s = 0,1,...,l, \qquad b_{i0} = \delta_{i0},$$

the quantities η_s (he denoted by e_s), are called motion characteristics of the system under consideration, where

$$b_{is} = \frac{\partial \dot{x}_i}{\partial \eta_s} = \frac{\partial \ddot{x}_i}{\partial \dot{\eta}_s}, \qquad s = 1,...,l = n - m.$$

Proceeding to the derivation of Volterra equations, Maggi converted his equations of the form

$$\left(\frac{d}{dt}\frac{\partial L}{\partial \dot{x}_i} - \frac{\partial L}{\partial x_i} - Q_i\right) b_{is} = 0, \qquad s = 1,...,k$$

(in which the kinetic energy T occurs instead of L, while Q_i denotes all the active forces applied to the system) to the form

$$\frac{d}{dt}\frac{\partial T}{\partial \eta_r} = \frac{db_{ir}}{dt}\frac{\partial T}{\partial \dot{x}_i} + b_{ir}\frac{\partial T}{\partial x_i} + P_r, \qquad r = 1,...,l, \qquad P_r = Q_i b_{ir}. \tag{1}$$

Volterra [7] considered a system with N point masses, the velocities of which in a Cartesian system of coordinates are related to the motion characteristics of the form

$$\dot{x}_i = b_{is}\eta_s, \qquad i = 1,...,3N, \qquad s = 1,...,l,$$

where $b_{is} = b_{is}(x_1,...,x_{3N})$. In this case, the Maggi's equations (1) take the form of Volterra equations

$$\frac{d}{dt}\frac{\partial T}{\partial \eta_r} = c_{rs}^{(k)}\eta_k\eta_s + P_r, \qquad k,s = 1,...,l,$$

$$c_{rs}^{(k)} = m_i b_{ik}\frac{\partial b_{ir}}{\partial x_j}b_{js}, \qquad m_i = m_{i+1} = m_{i+2}, \qquad i,j = 1,...,3N,$$

where $T(x_1,...,x_{3N},\eta_1,...,\eta_l) -$ is the kinetic energy.

Without giving Maggi's derivation of Appell equations from equations

$$\left(\frac{d}{dt}\frac{\partial L}{\partial \dot{x}_i} - \frac{\partial L}{\partial x_i} - Q_i\right) b_{is} = 0, \qquad s = 1,...,k,$$

here, we note that they are simpler to derive directly from the following equations

$$\left(m_\nu \ddot{\bar{r}}_\nu - \bar{F}_\nu\right)\cdot \delta\bar{r}_\nu = 0, \qquad \nu = 1,...,N.$$

Differentiating equations

$$\dot{x}_i = b_{is}(x)\eta_s, \qquad i = 0,1,...,n, \qquad s = 0,1,...,l, \qquad b_{i0} = \delta_{i0}$$

with respect to time, we have $\ddot{x}_i = b_{is}\dot{\eta}_s + ...,$ where three dots denote the members not containing $\dot{\eta}_s$.

Hence, we find that $\frac{\partial \ddot{x}_i}{\partial \eta_s} = b_{is}$, as a result of which, we obtain from $\left(m_\nu \ddot{\bar{r}}_\nu - \bar{F}_\nu\right)\cdot \delta\bar{r}_\nu = 0,$ $\nu = 1,...,N$ the Appell equations

$$\frac{\partial S}{\partial \dot{\eta}_s} = \Pi_s, \qquad s = 1,...,l, \tag{2}$$

where $S = \frac{1}{2} m_\nu \ddot{\bar{r}}_\nu^2 -$ is the energy of accelerations, $\Pi_s = \bar{F}_\nu \cdot \bar{b}_{s\nu} -$ is the generalized force referred to the quasicoordinate π_s [6].

Finally, we will show that Kane's equations [8] are equivalent to the Poincaré equations. According to the relations

$$\delta f = \omega_r X_r f, \quad r = 1,...,k, \quad df = \eta_s X_s f dt, \quad s = 0,1,...,k,$$
$$\delta\bar{r}_\nu = \omega_s X_s \bar{r}_\nu \left(\nu = 1,...,N, s = 1,...,l\right).$$

Substitution of these expressions into $\left(m_\nu \ddot{\bar{r}}_\nu - \bar{F}_\nu\right)\cdot \delta\bar{r}_\nu = 0,$ $\nu = 1,...,N$ leads to equations of motion of the form

$$m_\nu \ddot{\bar{r}}_\nu \cdot X_s \bar{r}_\nu = \bar{F}_\nu \cdot X_s \bar{r}_\nu, \qquad s = 1,...,l. \tag{3}$$

For a system with Lagrangian coordinates q_i, subject to nonintegrable constraints

$$\dot{q}_j = b_{js}(t,q)\dot{q}_s + b_j(t,q), \qquad j = l+1,...,n, \qquad s = 1,...,l,$$

and operators $X_s f = b_{is}\frac{\partial f}{\partial x_s}, \quad s = 0,1,...,k, \quad f(x) \in C^2$ of the form

$$X_s f = \frac{\partial f}{\partial q_s} + b_{js}\frac{\partial f}{\partial q_j},$$

equations (3) coincide with Kane's equations (19) [8]

$$K_{q_s} + K'_{q_s} = 0, \quad s = 1,...,l,$$

which, consequently, are equivalent to the Poincaré equations.

3 The equations of Chaplygin and Voronets

Let us suppose that stationary linear nonholonomic constraints are imposed on the system under consideration, which equations can be represented in the form

$$\dot{q}^{l+k} = \beta_\lambda^{l+k}(q)\dot{q}^\lambda, \qquad \chi = 1,2,...,k; \qquad \lambda = 1,2,...,l. \tag{4}$$

Then, assuming

$$\upsilon_*^\lambda = \dot{q}^\lambda, \quad \lambda = 1,2,...,l;$$
$$\upsilon_*^{l+\chi} = \dot{q}^{l+\chi} - \beta_\lambda^{l+\chi}(q)\dot{q}^\lambda, \qquad \chi = 1,2,...,k,$$

we have

$$\frac{\partial \dot{q}^\mu}{\partial \upsilon_*^\lambda} = \begin{cases} 1, & \mu = \lambda, \\ 0, & \mu \neq \lambda, \end{cases} \qquad \mu = 1,2,...,l,$$

$$\frac{\partial \dot{q}^{l+\chi}}{\partial \upsilon_*^\lambda} = \beta_\lambda^{l+\chi}, \qquad \chi = 1,2...,k; \qquad \lambda = 1,2,...,l.$$

From these expressions it follows that for nonholonomic constraints given in the form (4), the Maggi's equations

$$(M\omega_\sigma - Q_\sigma)\frac{\partial \dot{q}^\sigma}{\partial \upsilon_*^\lambda} = 0, \qquad \lambda = 1,2,...,l.$$

can be written in the form:

$$M\omega_\lambda + M\omega_{l+\chi}\beta_\lambda^{l+\chi} = Q_\lambda + Q_{l+\chi}\beta_\lambda^{l+\chi}, \tag{5}$$
$$\lambda = 1,2,...,l; \qquad \chi = 1,2,...,k.$$

Let us suppose that kinetic energy T does not depend on the generalized coordinates and $q^{l+\chi}$ и $Q_{l+\chi} = 0 \quad (\chi = 1,2,...,k)$. Then equations (5) can be represented in the form

$$\frac{d}{dt}\frac{\partial T}{\partial \dot{q}^\lambda} - \frac{\partial T}{\partial q^\lambda} + \beta_\lambda^{l+\chi}\frac{d}{dt}\frac{\partial T}{\partial \dot{q}^{l+\chi}} = Q_\lambda, \qquad \lambda = 1,2,...,l. \tag{6}$$

Let us transform equations (6). Let us eliminate all the velocities $\dot{q}^{l+\chi}$ from the expression for the kinetic energy T using the constraint equations (4), and denote the resulting expression for the kinetic energy by T_*.

In this case, the following equalities are correct

$$\frac{\partial T_*}{\partial \dot{q}^\lambda} = \frac{\partial T}{\partial \dot{q}^\lambda} + \frac{\partial T}{\partial \dot{q}^{l+\chi}}\frac{\partial \dot{q}^{l+\chi}}{\partial \dot{q}^\lambda} = \frac{\partial T}{\partial \dot{q}^\lambda} + \frac{\partial T}{\partial \dot{q}^{l+\chi}}\beta_\lambda^{l+\chi}, \tag{7}$$

$$\frac{\partial T_*}{\partial q^\lambda} = \frac{\partial T}{\partial q^\lambda} + \frac{\partial T}{\partial \dot{q}^{l+\chi}}\frac{\partial \dot{q}^{l+\chi}}{\partial q^\lambda} = \frac{\partial T}{\partial q^\lambda} + \frac{\partial T}{\partial \dot{q}^{l+\chi}}\frac{\partial \beta_\mu^{l+\chi}}{\partial q^\lambda}\dot{q}^\mu, \tag{8}$$
$$\lambda, \mu = 1,2,...,l.$$

Let us suppose that the coefficients $\beta_\lambda^{l+\chi}$ do not depend on $q^{l+\chi}$, $\chi = 1,2,...,k$. Then, differentiating the expression (7) with respect to time, we obtain

$$\frac{d}{dt}\frac{\partial T_*}{\partial \dot{q}^\lambda} = \frac{d}{dt}\frac{\partial T}{\partial \dot{q}^\lambda} + \beta_\lambda^{l+\chi}\frac{d}{dt}\frac{\partial T}{\partial \dot{q}^{l+\chi}} + \frac{\partial T}{\partial \dot{q}^{l+\chi}}\frac{d}{dt}\beta_\lambda^{l+\chi} =$$

$$= \frac{d}{dt}\frac{\partial T_*}{\partial \dot{q}^\lambda} + \beta_\lambda^{l+\chi}\frac{d}{dt}\frac{\partial T}{\partial \dot{q}^{l+\chi}} + \frac{\partial T}{\partial \dot{q}^{l+\chi}}\frac{\partial \beta_\lambda^{l+\chi}}{\partial q^\mu}\dot{q}^\mu, \qquad \lambda, \mu = 1,2,...,l. \tag{9}$$

Computing the quantities $d/dt(\partial T/\partial \dot{q}^\lambda)$ and $\partial T/\partial q^\lambda$ by formulas (9) and (8) and substituting them into equations (6), we get

$$\frac{d}{dt}\frac{\partial T_*}{\partial \dot{q}^\lambda} - \frac{\partial T_*}{\partial q^\lambda} - \frac{\partial T}{\partial \dot{q}^{l+\chi}}\left(\frac{\partial \beta_\lambda^{l+\chi}}{\partial q^\mu} - \frac{\partial \beta_\mu^{l+\chi}}{\partial q^\lambda}\right)\dot{q}^\mu = Q_\lambda, \tag{10}$$
$$\lambda, \mu = 1,2,...,l; \quad \chi = 1,2,...,k.$$

These equations were obtained by S.A. Chaplygin [10].

If in the equations (10) we eliminate the dependent velocities $\dot{q}^{l+1}, \dot{q}^{l+2}, ..., \dot{q}^{l+\chi}$, in the expressions $\partial T/\partial \dot{q}^{l+\chi}$ using the constraint equations (4), then we obtain a system of l equations with respect to unknown functions $q^1, q^2, ..., q^l$. Thus, Chaplygin's equations allow us independently of the constraints (4) to find $q^1(t), q^2(t), ..., q^l(t)$, then to define the remainder $q^{l+1}(t), q^{l+2}(t), ..., q^{l+k}(t)$ from equations (4).

The Chaplygin's equations are transformed into ordinary Lagrange's equations of the second kind, if the constraints (4) are integrable, that is, the coefficients $\beta_\lambda^{l+\chi}$ satisfy the following conditions:

$$\frac{\partial \beta_{\mu}^{l+\chi}}{\partial q^{\lambda}} - \frac{\partial \beta_{\lambda}^{l+\chi}}{\partial q^{\mu}} = 0, \qquad \lambda, \mu = 1,2,...,l; \;\; \chi = 1,2,...,k. \tag{11}$$

Let us suppose, for example, at $\lambda = 1$ we have

$$\frac{\partial \beta_{\mu}^{l+\chi}}{\partial q^{1}} - \frac{\partial \beta_{1}^{l+\chi}}{\partial q^{\mu}} = 0, \qquad \mu = 1,2,...,l; \;\; \chi = 1,2,...,k. \tag{12}$$

Let us derive the functions $u^{l+\chi} = u^{l+\chi}(q^1, q^2, ..., q^s)$ as follows:

$$u^{l+\chi} = \int_{q^{1,0}}^{q^1} \beta_1^{l+\chi} dq^1, \qquad \chi = 1,2,...,k,$$

where $q^{1,0}$ - is an arbitrary constant value. Using conditions (12), we obtain

$$\frac{\partial u^{l+\chi}}{\partial q^{\mu}} = \int_{q^{1,0}}^{q^1} \frac{\partial \beta_1^{l+\chi}}{\partial q^{\mu}} dq^1 = \int_{q^{1,0}}^{q^1} \frac{\partial \beta_{\mu}^{l+\chi}}{\partial q^{1}} dq^1 =$$
$$= \beta_{\mu}^{l+\chi}(q^1, q^2, ..., q^s) - \beta_{\mu}^{l+\chi}(q^{1,0}, q^2, ..., q^s),$$

or

$$\beta_{\mu}^{l+\chi} = \frac{\partial u^{l+\chi}}{\partial q^{\mu}} + \beta_{\mu}^{l+\chi}(q^{1,0}, q^2, ..., q^s), \qquad \mu = 2,3,...,l; \;\; \chi = 1,2...,k.$$

Hence and from expressions

$$\beta_1^{l+\chi} = \frac{\partial u^{l+\chi}}{\partial q^{1}}; \qquad \chi = 1,2,...,k,$$

it follows that equation (10) by the coordinate q^1 will have the form of Lagrange's equation of the second kind in the case when the constraint equations (4) can be reduced to the form

$$\dot{q}^{l+\chi} = \dot{u}^{l+\chi} + \beta_{\mu}^{l+\chi}(q^{1,0}, q^2, ..., q^s)\dot{q}^{\mu}, \qquad \mu = 2,3...,l; \;\; \chi = 1,2,...,k.$$

Now we derive the equations of motion in the form obtained by P.V. Voronets [11]. We consider a mechanical system with constraints given in the form (4) without making those additional assumptions that lead to the Chaplygin's equations. In the case, when the kinetic energy T depends on all the coordinates, the Maggi's equations (5) will be written in the form

$$\frac{d}{dt}\frac{\partial T}{\partial \dot{q}^{\lambda}} - \frac{\partial T}{\partial q^{\lambda}} + \left(\frac{d}{dt}\frac{\partial T}{\partial \dot{q}^{l+\chi}} - \frac{\partial T}{\partial q^{l+\chi}} \right) \beta_{\lambda}^{l+\chi} = Q_{\lambda} + Q_{l+\chi}\beta_{\lambda}^{l+\chi}, \tag{13}$$
$$\lambda = 1,2,...,l; \;\; \chi = 1,2,...,k.$$

In order to bring these equations to the Voronets equations, we proceed similarly to the previous case. Relations (8) save their form, and expressions (9), taking into account that now the coefficients $\beta_{\lambda}^{l+\chi}$ depend on all q^{σ}, take the form

$$\frac{d}{dt}\frac{\partial T_*}{\partial \dot{q}^{\lambda}} = \frac{d}{dt}\frac{\partial T}{\partial \dot{q}^{\lambda}} - \beta_{\lambda}^{l+\chi}\frac{d}{dt}\frac{\partial T}{\partial \dot{q}^{l+\chi}} - \frac{\partial T}{\partial \dot{q}^{l+\chi}}\frac{\partial \beta_{\lambda}^{l+\chi}}{\partial q^{\mu}}\dot{q}^{\mu} +$$
$$+ \frac{\partial T}{\partial \dot{q}^{l+\chi}}\frac{\partial \beta_{\lambda}^{l+\chi}}{\partial q^{l+\nu}}\beta_{\mu}^{l+\nu}\dot{q}^{\mu}, \tag{14}$$
$$\lambda, \mu = 1,2,...,l; \;\; \chi, \nu = 1,2,...,k.$$

In this case, along with relations (8) and (14), we should take into account the following equalities

$$\beta_{\lambda}^{l+\chi}\frac{\partial T_*}{\partial q^{l+\chi}} = \beta_{\lambda}^{l+\chi}\left(\frac{\partial T}{\partial q^{l+\chi}} + \frac{\partial T}{\partial \dot{q}^{l+\nu}}\frac{\partial \beta_{\mu}^{l+\chi}}{\partial q^{l+\chi}}\dot{q}^{\mu} \right).$$

This expression, as well as relations (8) and (14) allows us to represent the equations (13) in the form

$$\frac{d}{dt}\frac{\partial T_*}{\partial \dot{q}^\lambda} - \frac{\partial T_*}{\partial q^\lambda} - \beta_\lambda^{l+\chi}\frac{\partial T_*}{\partial \dot{q}^{l+\chi}} - \frac{\partial T}{\partial \dot{q}^{l+\chi}}\beta_{\lambda\mu}^{l+\chi}\dot{q}^\mu = \\ = Q_\lambda + Q_{l+\chi}\beta_\lambda^{l+\chi}; \qquad \lambda,\mu = 1,2,...,l; \quad \chi = 1,2,...,k, \tag{15}$$

where

$$\beta_{\lambda\mu}^{l+\chi} = \frac{\partial \beta_\lambda^{l+\chi}}{\partial q^\mu} - \frac{\partial \beta_\mu^{l+\chi}}{\partial q^\lambda} + \frac{\partial \beta_\lambda^{l+\chi}}{\partial q^{l+\nu}}\beta_\mu^{l+\nu} - \frac{\partial \beta_\lambda^{l+\chi}}{\partial q^{l+\nu}}\beta_\lambda^{l+\nu}.$$

The equations (15) are called the *Voronets equations*. Joining the constraint equations (15) with the equations of motion (4), we will obtain a system of differential equations for obtaining the functions $q^\sigma(t),\ \sigma = 1,2,...,s.$

In the case of motion of a constrained system under action of forces, which have a potential, the equations (15) take the form

$$\frac{d}{dt}\frac{\partial T_*}{\partial \dot{q}^\lambda} - \frac{\partial (T_* + U)}{\partial q^\lambda} - \beta_\lambda^{l+\chi}\frac{\partial (T_* + U)}{\partial q^{l+\chi}} - \frac{\partial T}{\partial \dot{q}^{l+\chi}}\beta_{\lambda\mu}^{l+\chi}\dot{q}^\mu = 0, \qquad \lambda,\mu = 1,2,...,l.$$

In the particular case when the coordinates $q^{l+1}, q^{l+2}, ..., q^{l+k}$, corresponding to the eliminated velocities is not explicitly included into the relations for kinetic and potential energy, as well as into the constraint equations, the Voronets equations (15) coincide with the Chaplygin's equations (10).

4 The equations of motion in quasicoordinates (Hamel-Novoselov, Voronets-Hamel, Poincaré – Chetaev equations)

In the case of rotation of a rigid body around a fixed point, it was shown that the projections of the vector of instantaneous angular velocity $\overline{\omega}$ on the fixed axes cannot be considered as derivatives with respect to the new angles that uniquely determine the position of rigid body. Similarly, it may turn out that quantities υ_*^ρ, which are one-to-one connected with generalized velocities by the relations

$$\upsilon_*^\rho = \upsilon_*^\rho(t, q, \dot{q}), \qquad \rho = 1,2,...,s,$$

and

$$\hat{\upsilon}^\sigma \equiv \dot{q}^\sigma = \dot{q}^\sigma(t, q, \upsilon_*), \qquad \upsilon_* = (\upsilon_*^1, \upsilon_*^2, ..., \upsilon_*^s),$$

cannot be considered as derivatives with respect to the certain new coordinates q_*^ρ, that is, cannot be supposed that $\upsilon_*^\rho = \dot{q}_*^\rho$. In this case, the quantities υ_*^ρ are called the *quasivelocities*, and the variables $\tilde{\upsilon}_*^\rho$, given by formulas

$$\tilde{\upsilon}_*^\rho = \int_{t_0}^{t} \upsilon_*^\rho dt$$

are called quasicoordinates.

In the expression for the kinetic energy T, the generalized velocities $\dot{q}^\sigma$ are replaced by quasivelocities υ_*^ρ. We denote the resulting function by T^*. We find out, which form can have the Maggi's equations $(M\omega_\sigma - Q_\sigma)\frac{\partial \dot{q}^\sigma}{\partial \upsilon_*^\lambda} = 0, \qquad \lambda = 1,2,...,l$, written in the form

$$\left(\frac{d}{dt}\frac{\partial T}{\partial \dot{q}^{\sigma}}-\frac{\partial T}{\partial q^{\sigma}}-Q_{\sigma}\right)\frac{\partial \dot{q}^{\sigma}}{\partial \upsilon_{*}^{\lambda}}=0, \qquad \lambda=1,2,...,l;\ \ \sigma=1,2,...,s, \tag{16}$$

when using the function T^{*}.

Taking into account the relations

$$\frac{\partial T^{*}}{\partial \upsilon_{*}^{\lambda}}=\frac{\partial T}{\partial \dot{q}^{\sigma}}\frac{\partial \dot{q}^{\sigma}}{\partial \upsilon_{*}^{\lambda}}, \qquad \frac{\partial T^{*}}{\partial q^{\sigma}}=\frac{\partial T}{\partial q^{\sigma}}+\frac{\partial T}{\partial \dot{q}^{\rho}}\frac{\partial \dot{q}^{\rho}}{\partial q^{\sigma}},$$
$$\lambda=1,2...,l;\ \ \rho,\sigma=1,2,...,s,$$

we have

$$\left(\frac{d}{dt}\frac{\partial T}{\partial \dot{q}^{\sigma}}\right)\frac{\partial \dot{q}^{\sigma}}{\partial \upsilon_{*}^{\lambda}}=\frac{d}{dt}\left(\frac{\partial T}{\partial \dot{q}^{\sigma}}\frac{\partial \dot{q}^{\sigma}}{\partial \upsilon_{*}^{\lambda}}\right)-$$
$$-\frac{\partial T}{\partial \dot{q}^{\sigma}}\frac{d}{dt}\frac{\partial \dot{q}^{\sigma}}{\partial \upsilon_{*}^{\lambda}}=\frac{d}{dt}\frac{\partial T^{*}}{\partial \upsilon_{*}^{\lambda}}-\frac{\partial T}{\partial \dot{q}^{\sigma}}\frac{d}{dt}\frac{\partial \dot{q}^{\sigma}}{\partial \upsilon_{*}^{\lambda}}, \tag{17}$$

$$\frac{\partial T}{\partial q^{\sigma}}\frac{\partial \dot{q}^{\sigma}}{\partial \upsilon_{*}^{\lambda}}=\frac{\partial \dot{q}^{\sigma}}{\partial \upsilon_{*}^{\lambda}}\left(\frac{\partial T^{*}}{\partial q^{\sigma}}-\frac{\partial T}{\partial \dot{q}^{\rho}}\frac{\partial \dot{q}^{\rho}}{\partial q^{\sigma}}\right)=$$
$$=\frac{\partial \dot{q}^{\sigma}}{\partial \upsilon_{*}^{\lambda}}\frac{\partial T^{*}}{\partial q^{\sigma}}-\frac{\partial T}{\partial \dot{q}^{\rho}}\frac{\partial \dot{q}^{\rho}}{\partial q^{\sigma}}\frac{\partial \dot{q}^{\sigma}}{\partial \upsilon_{*}^{\lambda}}. \tag{18}$$

In the right-hand side of expression (18) in the double sum, we exchange the indices of summing ρ and σ. As a result, we have

$$\frac{\partial T}{\partial q^{\sigma}}\frac{\partial \dot{q}^{\sigma}}{\partial \upsilon_{*}^{\lambda}}=\frac{\partial \dot{q}^{\sigma}}{\partial \upsilon_{*}^{\lambda}}\frac{\partial T^{*}}{\partial q^{\sigma}}-\frac{\partial T}{\partial \dot{q}^{\rho}}\frac{\partial \dot{q}^{\rho}}{\partial \upsilon_{*}^{\lambda}}\frac{\partial \dot{q}^{\sigma}}{\partial q^{\rho}}. \tag{19}$$

Let us consider the operator

$$\frac{\partial}{\partial \tilde{\upsilon}_{*}^{\rho}}=\frac{\partial \dot{q}^{\sigma}}{\partial \upsilon_{*}^{\rho}}\frac{\partial}{\partial q^{\sigma}}, \qquad \rho,\sigma=1,2,...,s, \tag{20}$$

which, under assumption $\upsilon_{*}^{\rho}=\dot{\tilde{\upsilon}}_{*}^{\rho}=\dot{q}_{*}^{\rho}$, passes into the operator of partial derivative with respect to the new coordinate q_{*}^{ρ}, since we have

$$\frac{\partial \dot{q}^{\sigma}}{\partial \upsilon_{*}^{\rho}}\frac{\partial}{\partial q^{\sigma}}=\frac{\partial \dot{q}^{\sigma}}{\partial \dot{q}_{*}^{\rho}}\frac{\partial}{\partial q^{\sigma}}=\frac{\partial q^{\sigma}}{\partial q_{*}^{\rho}}\frac{\partial}{\partial q^{\sigma}}=\frac{\partial}{\partial q_{*}^{\rho}}.$$

The relation (19), taking into account expression (20), can be written in the form

$$\frac{\partial T}{\partial q^{\sigma}}\frac{\partial \dot{q}^{\sigma}}{\partial \upsilon_{*}^{\rho}}=\frac{\partial T^{*}}{\partial \tilde{\upsilon}_{*}^{\lambda}}-\frac{\partial T}{\partial \dot{q}^{\sigma}}\frac{\partial \dot{q}^{\sigma}}{\partial \tilde{\upsilon}_{*}^{\lambda}}.$$

Hence and from expression (17) it follows that the Maggi's equations (16) can be represented in the form

$$\frac{d}{dt}\frac{\partial T^{*}}{\partial \upsilon_{*}^{\lambda}}-\frac{\partial T^{*}}{\partial \tilde{\upsilon}_{*}^{\lambda}}-\frac{\partial T}{\partial \dot{q}^{\sigma}}\left(\frac{d}{dt}\frac{\partial \dot{q}^{\sigma}}{\partial \upsilon_{*}^{\lambda}}-\frac{\partial \dot{q}^{\sigma}}{\partial \tilde{\upsilon}_{*}^{\lambda}}\right)=Q_{\lambda}^{*}, \tag{21}$$
$$\lambda=1,2,...,l;\ \ \sigma=1,2,...,s.$$

Here

$$Q_{*}^{\lambda}=Q_{\sigma}\frac{\partial \dot{q}^{\sigma}}{\partial \upsilon_{*}^{\lambda}}. \tag{22}$$

Equations (21) are sometimes called the equations of Chaplygin's type [12].

Let us consider the particular case when the generalized velocities $\dot{q}^{\sigma}$ are related to quasivelocities υ_{*}^{ρ} by linear, homogeneous, stationary relations:

$$\upsilon_*^\rho = \alpha_\sigma^\rho(q)\dot{q}^\sigma,$$
$$\rho,\sigma = 1,2,...,s, \tag{23}$$
$$\dot{q}^\sigma = \beta_\rho^\sigma(q)\upsilon_*^\rho,$$

and the constraint equations are the following:

$$\upsilon_*^{l+\chi} \equiv \alpha_\sigma^{l+\chi}(q)\dot{q}^\sigma = 0. \tag{24}$$

In this case, using expressions (23) and operator (20), and also taking into account that after performing the operations of differentiation it can be assumed that $\upsilon_*^{l+\chi} = 0 \quad (\chi = 1,2,...,k)$, we have

$$\frac{d}{dt}\frac{\partial\dot{q}^\sigma}{\partial\upsilon_*^\lambda} = \frac{d}{dt}\beta_\lambda^\sigma(q) = \frac{\partial\beta_\lambda^\sigma}{\partial q_\sigma^\rho}\dot{q}^\rho = \frac{\partial\beta_\lambda^\sigma}{\partial q^\rho}\beta_\mu^\rho\upsilon_*^\mu =$$
$$= \upsilon_*^\mu\frac{\partial\dot{q}^\rho}{\partial\upsilon_*^\mu}\frac{\partial\beta_\lambda^\sigma}{\partial q^\rho} = \upsilon_*^\mu\frac{\partial\beta_\lambda^\sigma}{\partial\widetilde{\upsilon}_*^\mu}, \qquad \lambda,\mu = 1,2,...,l;\ \ \rho,\sigma = 1,2,...,s;$$
$$\frac{\partial\dot{q}^\sigma}{\partial\widetilde{\upsilon}_*^\lambda} = \frac{\partial\dot{q}^\rho}{\partial\upsilon_*^\lambda}\frac{\partial\dot{q}^\sigma}{\partial q^\rho} = \frac{\partial\dot{q}^\rho}{\partial\upsilon_*^\lambda}\frac{\partial\beta_\mu^\sigma}{\partial q^\rho}\upsilon_*^\mu =$$
$$= \upsilon_*^\mu\frac{\partial\beta_\mu^\sigma}{\partial\widetilde{\upsilon}_*^\lambda}, \qquad \lambda,\mu = 1,2,...,l;\ \ \rho,\sigma = 1,2,...,s.$$

Consequently, equations (21) take the form

$$\frac{d}{dt}\frac{\partial T^*}{\partial\upsilon_*^\lambda} - \frac{\partial T^*}{\partial\widetilde{\upsilon}_*^\lambda} - \frac{\partial T}{\partial\dot{q}^\sigma}\left(\frac{\partial\beta_\lambda^\sigma}{\partial\widetilde{\upsilon}_*^\mu} - \frac{\partial\beta_\mu^\sigma}{\partial\widetilde{\upsilon}_*^\lambda}\right)\upsilon_*^\mu = Q_\lambda^*, \tag{25}$$
$$\lambda,\mu = 1,2,...,l;\ \ \sigma = 1,2,...,s.$$

These equations are usually called the *Chaplygin's equations in quasicoordinates* [6]. Let us note that the equations (21) and (25) should be considered together with the equations of nonholonomic constraints given respectively in the form

$$\varphi^\chi(t,q,\dot{q}) = 0, \qquad \chi = 1,2,...,k,$$

and (24).

Equations (21) include both the function T^* and the function T. Now, we reduce the Maggi's equations (16) to the form that involves the function T^* only.

The following relation

$$\frac{\partial T}{\partial\dot{q}^\sigma} = \frac{\partial T^*}{\partial\upsilon_*^\rho}\frac{\partial\upsilon_*^\rho}{\partial\dot{q}^\sigma}, \qquad \rho,\sigma = 1,2,...,s,$$

yield the relation

$$\left(\frac{d}{dt}\frac{\partial T}{\partial\dot{q}^\sigma}\right)\frac{\partial\dot{q}^\sigma}{\partial\upsilon_*^\lambda} = \frac{\partial\dot{q}^\sigma}{\partial\upsilon_*^\lambda}\frac{d}{dt}\left(\frac{\partial T^*}{\partial\upsilon_*^\rho}\frac{\partial\upsilon_*^\rho}{\partial\dot{q}^\sigma}\right) =$$
$$= \left(\frac{d}{dt}\frac{\partial T^*}{\partial\upsilon_*^\rho}\right)\frac{\partial\upsilon_*^\rho}{\partial\dot{q}^\sigma}\frac{\partial\dot{q}^\sigma}{\partial\upsilon_*^\lambda} + \frac{\partial T^*}{\partial\upsilon_*^\rho}\frac{\partial\dot{q}^\sigma}{\partial\upsilon_*^\lambda}\frac{d}{dt}\frac{\partial\upsilon_*^\rho}{\partial\dot{q}^\sigma}.$$

Since

$$\frac{\partial\upsilon_*^\rho}{\partial\dot{q}^\sigma}\frac{\partial\dot{q}^\sigma}{\partial\upsilon_*^\lambda} = \begin{cases}1, & \rho = \lambda,\\ 0, & \rho \neq \lambda,\end{cases}$$

we have

$$\left(\frac{d}{dt}\frac{\partial T}{\partial \dot{q}^{\sigma}}\right)\frac{\partial \dot{q}^{\sigma}}{\partial \upsilon_{*}^{\lambda}} = \frac{d}{dt}\frac{\partial T^{*}}{\partial \upsilon_{*}^{\lambda}} + \frac{\partial T^{*}}{\partial \upsilon_{*}^{\rho}}\frac{\partial \dot{q}^{\sigma}}{\partial \upsilon_{*}^{\lambda}}\frac{d}{dt}\frac{\partial \upsilon_{*}^{\rho}}{\partial \dot{q}^{\sigma}}. \tag{26}$$

Taking into account the expressions

$$\frac{\partial T}{\partial q^{\sigma}} = \frac{\partial T^{*}}{\partial q^{\sigma}} + \frac{\partial T^{*}}{\partial \upsilon_{*}^{\rho}}\frac{\partial \upsilon_{*}^{\rho}}{\partial q^{\sigma}}$$

and operator (20), we obtain

$$\frac{\partial T}{\partial q^{\sigma}}\frac{\partial \dot{q}^{\sigma}}{\partial \upsilon_{*}^{\lambda}} = \frac{\partial T^{*}}{\partial \widetilde{\upsilon}_{*}^{\lambda}} + \frac{\partial T^{*}}{\partial \upsilon_{*}^{\rho}}\frac{\partial \dot{q}^{\sigma}}{\partial \upsilon_{*}^{\lambda}}\frac{\partial \upsilon_{*}^{\rho}}{\partial q^{\sigma}}.$$

Then from the above and from formulas (22) and (26), it follows that the Maggi's equations (16) can be represented in the form

$$\frac{d}{dt}\frac{\partial T^{*}}{\partial \upsilon_{*}^{\lambda}} - \frac{\partial T^{*}}{\partial \widetilde{\upsilon}_{*}^{\lambda}} + \frac{\partial T^{*}}{\partial \upsilon_{*}^{\rho}}\frac{\partial \dot{q}^{\sigma}}{\partial \upsilon_{*}^{\lambda}}\left(\frac{d}{dt}\frac{\partial \upsilon_{*}^{\rho}}{\partial \dot{q}^{\sigma}} - \frac{\partial \upsilon_{*}^{\rho}}{\partial q^{\sigma}}\right) = Q_{\lambda}^{*}, \tag{27}$$

$$\lambda = 1,2,...,l;\ \ \rho,\sigma = 1,2,...,s.$$

The equations (21) and (27) can be applied to both holonomic and nonholonomic systems, with either the linear or nonlinear with respect to velocities ideal constraints. In the case when the time does not enter into the kinetic energy and the constraint equations in explicit form, the equations (21) and (27) were obtained by G. Hamel [14] and in the general case by V.S. Novoselov. Therefore, these equations should be called the *Hamel-Novoselov equations.*

In the case when the quasivelocities are defined by formulas (23) and the constraints are given by equations (24), we have

$$\frac{\partial \dot{q}^{\sigma}}{\partial \upsilon_{*}^{\lambda}}\frac{d}{dt}\frac{\partial \upsilon_{*}^{\rho}}{\partial \dot{q}^{\sigma}} = \beta_{\lambda}^{\sigma}\frac{d\alpha_{\sigma}^{\rho}}{dt} = \beta_{\lambda}^{\sigma}\frac{\partial \alpha_{\sigma}^{\rho}}{\partial q^{\tau}}\dot{q}^{\tau} = \beta_{\lambda}^{\sigma}\beta_{\mu}^{\tau}\frac{\partial \alpha_{\sigma}^{\rho}}{\partial q^{\tau}}\upsilon_{*}^{\mu},$$

$$\frac{\partial \dot{q}^{\sigma}}{\partial \upsilon_{*}^{\lambda}}\frac{\partial \upsilon_{*}^{\rho}}{\partial \dot{q}^{\sigma}} = \beta_{\lambda}^{\sigma}\frac{\partial \alpha_{\tau}^{\rho}}{\partial q^{\sigma}}\dot{q}^{\tau} = \beta_{\lambda}^{\sigma}\beta_{\mu}^{\tau}\frac{\partial \alpha_{\tau}^{\rho}}{\partial q^{\sigma}}\upsilon_{*}^{\mu},$$

$$\lambda,\mu = 1,2,...,l;\ \ \rho,\sigma,\tau = 1,2,...,s.$$

Consequently, in this case, equations (27) take the form

$$\frac{d}{dt}\frac{\partial T^{*}}{\partial \upsilon_{*}^{\lambda}} - \frac{\partial T^{*}}{\partial \widetilde{\upsilon}_{*}^{\lambda}} + c_{\lambda\mu}^{\rho}\upsilon_{*}^{\mu}\frac{\partial T^{*}}{\partial \upsilon_{*}^{\rho}} = Q_{\lambda}^{*},$$

$$c_{\lambda\mu}^{\rho} = \left(\frac{\partial \alpha_{\sigma}^{\rho}}{\partial q^{\tau}} - \frac{\partial \alpha_{\tau}^{\rho}}{\partial q^{\sigma}}\right)\beta_{\lambda}^{\sigma}\beta_{\mu}^{\tau}, \tag{28}$$

$$\lambda,\mu = 1,2,...,l;\ \ \rho,\sigma,\tau = 1,2,...,s.$$

In the case of $l = s$ these equations, as well as the expressions for the coefficients $c_{\sigma\tau}^{\rho}$ were obtained first by P.V. Voronets in 1901. In 1904 for $l < s$ these results were obtained once more by G. Hamel [15]. Therefore, these equations are usually called the *Voronets-Hamel equations*, but Hamel himself called them the Euler-Lagrange equations. We remark that in the literature they are also called the *Hamel-Boltzmann equations*.

A little before the work of P.V. Voronets, it was appeared an article by H. Poincaré [16], who obtained equations highly close to equations (28). Poincaré equations correspond to the case when in equations (28) for $l = s$ the coefficients $c_{\sigma\tau}^{\rho}$ are constant and the forces are expressed via the forcing function U :

$$Q_{\tau}^{*} = \beta_{\tau}^{\sigma}\frac{\partial U}{\partial q^{\sigma}}, \qquad \sigma,\tau = 1,2,...,s.$$

In this case, equations (28) can be written in the form proposed by H. Poincaré:

$$\frac{d}{dt}\frac{\partial L^*}{\partial \upsilon_*^\tau} = c_{\sigma\tau}^{\rho}\upsilon_*^{\delta}\frac{\partial L^*}{\partial \upsilon_*^{\rho}} + \beta_\tau^\sigma \frac{\partial L^*}{\partial q^\sigma}, \qquad L^*(q,\upsilon_*) = T^* + U,$$

$$\rho,\sigma,\tau = 1,2,...,s.$$

On derivation of equations of motion, H. Poincaré used the group theory. The Poincaré approach was subsequently developed in the works of N.G. Chetaev, L.M. Markhashov, V.V. Rumyantsev, Fam Guen. They generalized the Poincaré equations to the case when the coefficients of $c_{\sigma\tau}^{\rho}$ are not constant and the motion occurs under the action of both potential and non-potential forces. The equations derived by them describing the motion of nonholonomic systems are called *Poincaré-Chetaev equations* [4], [13].

References

[1] *Fam Guen*. On the equations of motion of non-holonomic mechanical systems in Poincare-Chetaev variables. // PMM.-1967.-Vol. 31, no. 2.- P. 253-259.

[2] *Fam Guen*. On the equations of motion of non-holonomic mechanical systems in Poincare-Chetaev variables. // PMM.-1968.-Vol. 32, no. 5.- P. 804-814.

[3] *Fam Guen*. On one form of the equations of motion of mechanical systems. // PMM.- 1969.- Vol. 33, no. 3.- P. 397-402.

[4] *Rumyantsev V.V.* On Poincaré-Chetayev equations. // PMM.-1994.-Vol. 58, no. 3. - P. 3-16.

[5] *Maggi G.A.* Da alcune nuove forma della equazioni della dinamica applicabile ai sistemi anolonomi // Atti della Reale Acad. Naz. dei Lincei. Rend. Cl. fis. e math. Ser. 5. 1901.- V. 10, № 2.- P. 287-291.

[6] *Neimark Ju.I., Fufaev N.A.* Dynamics of nonholonomic systems. Moscow: Nauka, 1967.- P. 519.

[7] *Volterra V.* Sopra una classe di equazioni dinamiche // Atti della R. Accad. delle sci. di Torino.- 1897.-T. 33.-P. 451-475.

[8] *Kane T.R.* Dynamics of nonholonomic systems // Trans. ASME. Ser. E. J. Appl. Mech.- 1961.-V. 28, № 4.- P. 574-578.

[9] *Rumyantsev V.V.* On general equations of dynamics. // Nonlinear mechanics / Edited by V. M. Matrosov, V. V. Rumyantsev, A. V. Karapetyan. - M.: FIZMATLIT, 2001. – P. 432. - ISBN 5-9221-009-2.

[10] *Chaplygin S.A.* On a motion of a heavy body of revolution on a horizontal plane. // Trudy otdeleniya fizicheskikh nauk Obshchestva lyubitelei estestvoznaniya. 1897. Vol. 9. no. 1. (See Complete Works, Vol. 1. 1948).

[11] *Voronets P.V.* On the equations of motion for non-holonomic systems.// Mat. Sbornik, Moscow Mathematical Society. 1901. Vol. 22. no. 4.

[12] *Novoselov V.S.* Application of nonlinear nonholonomic coordinates in analytical mechanics // Uch. zap. Leningrad State University. 1957. No. 217. no. 31.

[13] *Chetaev N.G.* On Poincaré equations // Applied Mathematics and Mechanics. Vol. V. 1941. no. 2. P. 253-262.

[14] *Hamel G.* Nichtholonome Systeme höherer Art // Sitzungberichte der Berliner Mathematischen Gesellschaft. 1938. Bd. 37. S. 41-52.

[15] *Hamel G.* Die Lagrange-Eulerischen Gleichungen der Mechanik // Zeitschrift für Mathematik und Physik. 1904. bd. 50. S. 1-50.

[16] *Poincaré H.* Sur une forme nouvelle des équations de la mécanique // Comptes Rendus. 1901. Vol. 132. P. 369-371.

[17] *XLV International Summer School-Conference* «Advanced Problems in Mechanics» 2017, Russia, St. Petersburg, June 22-27, 2017.

[18] *International conference* "Fundamental and applied problems of mechanics FAPM-2017", dedicated to the 170th anniversary of the birth of the great Russian scientist Nikolai Yegorovich Zhukovsky, Moscow, October 24 - 27, 2017.

Turbine blade vibration analysis using helicoidal shell model

Artem A. Moskalets, Tatiana V. Zinovieva, Alexander K. Belyaev
artem.moskalec@gmail.com

Abstract

Short turbine blades with comparable height and length are often used in turbine construction. In service, the blades are subject to various periodical impacts, and to prevent the fatigue failures, resonance vibrations should be avoided. Therefore, determination of natural frequencies and normal modes are of crucial importance. We consider free vibrations of a blade modeled by a helicoidal Kirchhoff shell. In the paper we use the variational approach based on the Lagrange mechanics in which the generalized coordinates play the role of factors for the displacement approximation. The displacement approximation are taken from the beam theory for the naturally twisted beam with an additional component taking into account the in-plane deformation of the cross-section. The algorithm of calculations by means of computer mathematics is proposed and an example of modal analysis of the helicoidal shell with variable section is presented. An example of modal analysis of the helicoidal shell with variable cross-section is provided, too. A three-dimensional computer model of the blade is developed and analyzed by ANSYS. Comparison of calculation results for shell and the three-dimensional model is demonstrated.

1 Introduction

The impacts of gas or fluid jets on a blade of the power plant is of the periodical character. Therefore, the blades are affected by the forced oscillations [1, 2, 3]. Some frequencies of these pulsating loads can be close to one of the normal frequencies of the blade, and resonance vibrations can cause the fatigue failure of the blade. In this regard, at the design should take into account the anticipated operating regimes and frequencies of alternating impacts, so that the blade could be "detuned" from the resonance frequencies by changing the mechanical and geometrical parameters of the blade. For this reason, the vibration analysis is an important part of the turbine design.

In power engineering, the engineers often use blades which have comparable length and width, therefore, from a mechanical perspective the blades can be considered shells.

In this work we propose to consider a short twisted blade as the helicoidal shell and apply the classical theory of thin shells [4, 5]. Based on the tensor equation of

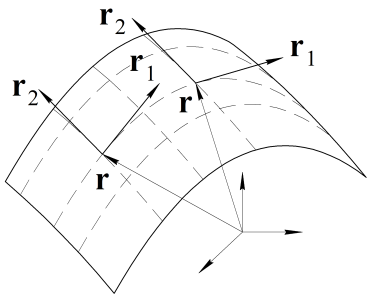

Figure 1: Shell surface

the shell theory, the scalar equations are derived and the energy relationships are obtained. Then the Lagrange equations, in which coefficients of the displacement approximation play the role of generalized coordinates, are used for construction of the global inertia and stiffness matrices for the further modal analysis. This approach was tested on the helicoidal blade in [6] in the present paper we give more attention to detailed consideration of the method. Natural frequencies and normal modes are to be calculated in the Wolfram Mathematica system [7]. It is reasonable to compare them with the results of the 3D-model finite element analysis by ANSYS [8], so that we judge the applicability of the approximations used.

2 Brief information from the theory of Kirchhoff-ʙΓЄs shells

According to the approach of the Lagrange analytical mechanics one must first determine the degrees of freedom of the examined object and introduce the generalized coordinates and then apply the principle of virtual work for determination of the generalized forces.

A classical shell can be presented as a deformable surface with material normal unit vectors which have three translational degrees of freedom and two rotational ones. It is assumed that the shell does not resist the rotation of the normal around its axis and therefore no corresponding degree of freedom is needed. The movement of the shell is then defined by the small displacement vector $\mathbf{u}$ and the small rotation vector $\boldsymbol{\theta}$ in the tangent plane [9].

It is convenient to use the vector of change of the normal $\mathbf{n}$ to the shell as a generalized coordinate: $\boldsymbol{\varphi} \equiv \boldsymbol{\theta} \times \mathbf{n} = \widetilde{\mathbf{n}}$. The sign of tilde implies a small increment with deformation.

Any surface is known to be defined by the dependence of the radius vector on the curvilinear coordinates $\mathbf{r}\,(\gamma^1,\gamma^2)$.

Thus, each point of this surface is the point of intersection of two coordinate curves (Fig. 1). Vectors of derivatives of the radius vector are tangential to these curves and form the basis:

$$\mathbf{r}_\beta = \partial\mathbf{r}/\partial\gamma^\beta = \partial_\beta\mathbf{r}. \tag{1}$$

The unit normal vector to the surface formed by these two vectors is

$$\mathbf{n} = \frac{\mathbf{r}_1 \times \mathbf{r}_2}{H},\ H \equiv |\mathbf{r}_1 \times \mathbf{r}_2|\,. \tag{2}$$

Any vector is known to be decomposed into components in both covariant and contravariant bases as follows: $\boldsymbol{\chi} = \chi_\beta \mathbf{r}^\beta + \chi_n \mathbf{n} = \chi^\beta \mathbf{r}_\beta + \chi_n \mathbf{n}$. Here the components χ_β of the vector $\boldsymbol{\chi}$ are called "covariant" and χ^β are called "contravariant".
The contravariant basis is constructed according to the condition $\mathbf{r}_\alpha \cdot \mathbf{r}^\beta = \delta_\alpha^\beta$ where δ_α^β is the Kronecker symbol.
It is necessary to introduce both bases to obtain the sought-for equations. Firstly, we can find the expression for the Hamilton operator:

$$\nabla = \mathbf{r}^\beta \partial_\beta. \tag{3}$$

Then we compose expressions for the first and second metric tensors

$$\mathbf{a} = \nabla \mathbf{r},\ \mathbf{b} = -\nabla \mathbf{n}. \tag{4}$$

It is known that the surface form is completely defined by covariant components of these metric tensors [10]. Therefore, the surface deformation is quite defined by the small increments of these components and can be determined by two symmetrical tensors in the tangent plane:

$$\boldsymbol{\varepsilon} \equiv \frac{1}{2}\widetilde{a_{\alpha\beta}} \mathbf{r}^\alpha \mathbf{r}^\beta,\ \boldsymbol{\kappa} \equiv \widetilde{b_{\alpha\beta}} \mathbf{r}^\alpha \mathbf{r}^\beta,\ a_{\alpha\beta} = \mathbf{r}_\alpha \cdot \mathbf{r}_\beta,\ b_{\alpha\beta} = -\partial_\alpha \mathbf{n} \cdot \mathbf{r}_\beta. \tag{5}$$

The first of these tensors defines the change of lengths and angles on the surface whereas the second one defines the change of its curvature. Accounting for $\mathbf{u} \equiv \widetilde{\mathbf{r}}$ and eq. (5) we obtain

$$\boldsymbol{\varepsilon} = (\nabla \mathbf{u})_\perp^{\mathrm{S}}\,,\ \boldsymbol{\kappa} = -(\nabla \mathbf{u})_\perp + \mathbf{b} \cdot \nabla \mathbf{u}^{\mathrm{T}}. \tag{6}$$

Here $(\ldots)_\perp$ denotes the part of the tensor in the tangential plane, the signs $(\ldots)^{\mathrm{S}}$ and $(\ldots)^{\mathrm{T}}$ denote symmetrization and transposition, respectively.
It follows from KirchhoffвЂ Єs kinematic hypothesis that the rotation is related with the displacement by the orthogonality condition:

$$\mathbf{r} \cdot \mathbf{n} = 0 \Rrightarrow \boldsymbol{\varphi} = -\nabla \mathbf{u} \cdot \mathbf{n}. \tag{7}$$

The strain energy and the kinetic energy of the shell are integrals over the surface area:

$$\Pi = \int \widehat{\Pi} \mathrm{d}o,\ K = \int \rho h \left|\dot{\mathbf{u}}\right|^2 \mathrm{d}\,o, \tag{8}$$

where ρ is the mass density, $\mathrm{d}o = H \mathrm{d}\gamma^1 \mathrm{d}\gamma^2$ is the surface element, $(\ldots)^{\cdot}$ denotes differentiation with respect to time t, $\widehat{\Pi}$ is the specific strain energy of the isotropic shell, which is the function of both strain tensors $\boldsymbol{\varepsilon}$, $\boldsymbol{\kappa}$:

$$\widehat{\Pi}(\boldsymbol{\varepsilon}, \boldsymbol{\kappa}) = \frac{Eh}{2(1-\nu^2)} \left[\nu\varepsilon^2 + \left(1-\nu^2\right) \boldsymbol{\varepsilon} \cdot\cdot \boldsymbol{\varepsilon} + \frac{h^2}{12}\left(\nu\kappa^2 + (1-\nu)\, \boldsymbol{\kappa} \cdot\cdot \boldsymbol{\kappa}\right)\right], \tag{9}$$

where E is the Young modulus, ν is the Poisson ratio, and ε, κ are the traces of respective strain tensors.

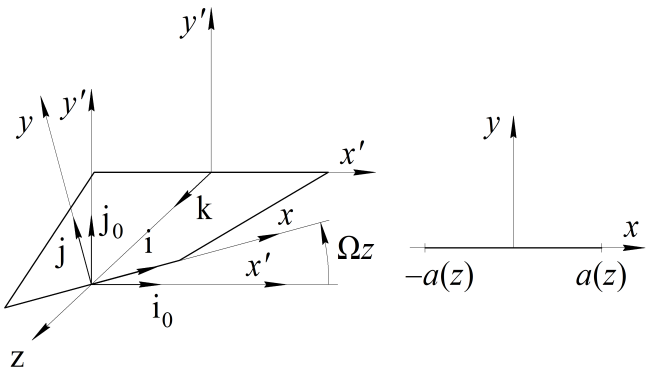

Figure 2: Helicoid model

3 Geometry and deformation of the blade

Helicoid blade is formed by helical motion of a thin strip with the thickness h and width $2a(z)$ (Fig. 2) rotating about axis z by angle per unit length Ω. Axis z is passing through the center of mass of all cross-sections. Cartesian axes x', y' (with unit vectors $\mathbf{i}_0$, $\mathbf{j}_0$) are fixed, while axes x, y (with the unit vectors $\mathbf{i}$, $\mathbf{j}$) are rotating together with the section (Fig. 2). The unit vectors of both coordinate systems are related by the following relations:

$$\mathbf{i}_0 = \cos(\Omega z)\,\mathbf{i} - \sin(\Omega z)\,\mathbf{j},\ \mathbf{j}_0 = \sin(\Omega z)\,\mathbf{i} + \cos(\Omega z)\,\mathbf{j}. \tag{10}$$

The radius vector is defined as

$$\mathbf{r}(z,x) = z\mathbf{k} + x\mathbf{i}(z),\ -a(z) \le x \le a(z). \tag{11}$$

Accounting for the following formulas for differentiating the unit vectors $\mathbf{i}' = \Omega\mathbf{j}$, $\mathbf{j}' = -\Omega\mathbf{i}$, we can form the basis in the tangent plane:

$$\mathbf{r}_1 = \partial_z\mathbf{r} = \mathbf{k} + \Omega x\mathbf{j} \equiv H\mathbf{e},\ \mathbf{r}_2 = \partial_x\mathbf{r} = \mathbf{i}, \tag{12}$$

where $H = |\mathbf{r}_1 \times \mathbf{r}_2| = \sqrt{1+\Omega^2x^2}$. Therefore, the unit normal vector is

$$\mathbf{n} = \frac{1}{H}(\mathbf{j} - \Omega x\mathbf{k}). \tag{13}$$

Now we can construct the contravariant basis:

$$\mathbf{r}^1 = \frac{1}{H}\mathbf{e} = \frac{1}{H^2}(\mathbf{k} + \Omega x\mathbf{j}),\ \mathbf{r}^2 = \mathbf{i}, \tag{14}$$

and obtain the Hamilton operator afterward:

$$\nabla = \mathbf{r}^\beta\partial_\beta = \frac{1}{H}\mathbf{e}\partial_z + \mathbf{i}\partial_x. \tag{15}$$

Now we can derive the relations between the unit vectors:

$$\begin{cases} H\mathbf{n} = \mathbf{j} - \Omega x\mathbf{k}, \\ H\mathbf{e} = \Omega x\mathbf{j} + \mathbf{k}, \end{cases} \Rightarrow \begin{cases} \mathbf{k} = \dfrac{1}{H}(\mathbf{e} - \Omega x\mathbf{n}), \\ \mathbf{j} = \dfrac{1}{H}(\mathbf{n} + \Omega x\mathbf{e}). \end{cases} \tag{16}$$

One obtains

$$\mathbf{k}_\perp = \frac{1}{H}\mathbf{e},\ \mathbf{j}_\perp = \frac{\Omega x}{H}\mathbf{e} \tag{17}$$

from (16) to separate the tangential components of $\nabla\mathbf{u}$ and $\nabla\boldsymbol{\varphi}$ when constructing the strain tensors (6). Hence the first and second metric tensors are

$$\mathbf{a} = \nabla\mathbf{r} = \mathbf{r}^\beta\mathbf{r}_\beta = \mathbf{ee} + \mathbf{ii},\ \mathbf{b} = -\nabla\mathbf{n} = \frac{\Omega}{H^2}(\mathbf{ei} + \mathbf{ie}). \tag{18}$$

We define the displacement vector as

$$\mathbf{u} = u_x\mathbf{i} + u_y\mathbf{j} + u_z\mathbf{k}, \tag{19}$$

after what, in accordance with (7), we can introduce the rotation vector of the normal:

$$\boldsymbol{\varphi} = -\nabla\mathbf{u}\cdot\mathbf{n} = \varphi_x\mathbf{i} + \varphi_y\mathbf{j} + \varphi_z\mathbf{k}. \tag{20}$$

Taking (13) and (15) into account we obtain the components of $\boldsymbol{\varphi}$:

$$\begin{aligned}
\varphi_x &= \frac{1}{H}(\Omega x\partial_x u_z - \partial_x u_y),\\
\varphi_y &= \frac{\Omega x}{H^3}\left(\Omega x u_z' - u_y' - \Omega u_x\right),\\
\varphi_z &= \frac{1}{H^3}\left(\Omega x u_z' - u_y' - \Omega u_x\right).
\end{aligned} \tag{21}$$

Hereafter $(\ldots)'$ denotes the differentiation with respect to coordinate z.
It is convenient to introduce the strain tensors $\boldsymbol{\varepsilon}$ and $\boldsymbol{\kappa}$ as follows:

$$\begin{aligned}
&\boldsymbol{\varepsilon} = \varepsilon_x\mathbf{ii} + \varepsilon_1\mathbf{ee} + \varepsilon_{1x}(\mathbf{ei} + \mathbf{ie}),\\
&\boldsymbol{\kappa} = \kappa_x\mathbf{ii} + \kappa_1\mathbf{ee} + \kappa_{1x}(\mathbf{ei} + \mathbf{ie}),\\
&\varepsilon_x = \mathbf{i}\cdot\boldsymbol{\varepsilon}\cdot\mathbf{i} = \partial_x u_x,\\
&\varepsilon_1 = \mathbf{e}\cdot\boldsymbol{\varepsilon}\cdot\mathbf{e} = \frac{1}{H^2}\left[\Omega x\left(\Omega u_x + u_y'\right) + u_z'\right],\\
&\varepsilon_{x1} = \mathbf{i}\cdot\boldsymbol{\varepsilon}\cdot\mathbf{e} = \varepsilon_{1x} = \frac{1}{2H}\left[u_x' - \Omega u_y + \Omega x\partial_x u_y + \partial_x u_z\right],\\
&\kappa_x = \mathbf{i}\cdot\boldsymbol{\kappa}\cdot\mathbf{i} = -\partial_x\varphi_x + \frac{\Omega}{H^3}\left[\Omega x\partial_x u_y + \partial_x u_z\right],\\
&\kappa_1 = \mathbf{e}\cdot\boldsymbol{\kappa}\cdot\mathbf{e} = -\frac{1}{H^2}\left[\Omega x\left(\Omega\varphi_x + \varphi_y'\right) + \varphi_z'\right] + \frac{\Omega}{H^3}\left(u_x' - \Omega u_y\right),\\
&\kappa_{x1} = \mathbf{i}\cdot\boldsymbol{\kappa}\cdot\mathbf{e} = \kappa_{1x} = \frac{1}{H}\left[-\varphi_x' + \Omega\varphi_y\right] + \frac{\Omega}{H^2}\partial_x u_x.
\end{aligned} \tag{22}$$

4 Displacement approximations and vibration analysis

Following the approach proposed in [6, 12], we use the Lagrange equations for vibration analysis of the shell. Having applied the Lagrange equations

$$\left(\frac{\partial K}{\partial \dot{q}_i}\right)^{\cdot} - \frac{\partial K}{\partial q_i} = -\frac{\partial \Pi}{\partial q_i} + Q_i, \tag{23}$$

we obtain the system of equation in terms of generalized coordinates q_i. However we have to choose the displacement approximation first. In this paper we derive the bending vibrations of the shell by taking the displacement vector as

$$\mathbf{u} = \mathbf{U}(z,t) - \mathbf{U}'(z,t) \cdot x\mathbf{ik} + S(z,t)\left[x^2 - a^2(z)\right]\mathbf{j}. \tag{24}$$

The two first terms in (24) correspond to the elementary beam theory where deflection vector $\mathbf{U}$ is

$$\mathbf{U}(z,t) = U_x(z,t)\,\mathbf{i}_0 + U_y(z,t)\,\mathbf{j}_0, \tag{25}$$

cf. [11]. The third term in (24) determines the deformation of the cross-section in its plane. We supposed that the deformed cross-section takes a parabolic shape. The components of $\mathbf{u}$ according to the relations (10) are

$$\begin{aligned} u_x &= U_x(z,t)\cos(\Omega z) + U_y(z,t)\sin(\Omega z), \\ u_y &= U_y(z,t)\cos(\Omega z) - U_x(z,t)\sin(\Omega z) + S(z,t)\left[x^2 - a^2(z)\right], \\ u_z &= -x\left[U_x'(z,t)\cos(\Omega z) + U_y'(z,t)\sin(\Omega z)\right]. \end{aligned} \tag{26}$$

Now we can proceed to the discrete model by approximating the introduced functions U_x, U_y, S in accordance with the Ritz method:

$$\begin{aligned} U_x(z,t) &= \sum_{i=1}^{N} U_{xi}\,\Phi_i(z) = {U_x}^{\mathrm{T}}\Phi, \\ U_y(z,t) &= \sum_{i=1}^{N} U_{yi}\,\Phi_i(z) = {U_y}^{\mathrm{T}}\Phi, \\ S(z,t) &= \sum_{i=1}^{N} S_i\,\Psi_i(z) = S^{\mathrm{T}}\Psi. \end{aligned} \tag{27}$$

We have thus presented the generalized coordinates whose roles are played by functions U_{xi}, U_{yi}, S_i. Then Φ and Ψ in (28) are columns of the coordinate functions satisfying the boundary conditions. The "rigid support" in the root cross-section $z = 0$ corresponds to the following condition

$$\Phi(0) = \Phi'(0) = \Psi(0) = 0. \tag{28}$$

For instance, the power functions satisfy these conditions:

$$\Phi_1 = z^2,\ \Phi_2 = z^3,\ \Psi_1 = z,\ \Psi_2 = z^2,\ \ldots \tag{29}$$

The number of the coordinate functions is denoted by N in (24).
Now we can obtain the potential and kinetic energy. The area element is $\mathrm{d}o = \mathbf{r}_1 \times \mathbf{r}_2 = H\mathrm{d}z\mathrm{d}x$; then according to (8)

$$\Pi = 2\int_0^L \int_0^{a(z)} \widehat{\Pi} H \mathrm{d}z\mathrm{d}x,\ K = 2\int_0^L \int_0^{a(z)} \rho h \left(\dot{u_x}^2 + \dot{u_y}^2 + \dot{u_z}^2\right) H\mathrm{d}z\mathrm{d}x, \tag{30}$$

where L is the blade length.
The final equations for energies expressed in terms of the generalized coordinates are obtained by means of the Wolfram Mathematica. They are too cumbersome to be presented in the paper.
Now the Lagrange equations (23) are given by:

$$M\ddot{U} + CU = Q(t), \tag{31}$$

in which the block columns and matrices are used.

$$\begin{aligned} M &\equiv \begin{pmatrix} M_{xx} & M_{xy} & M_{xs} \\ M_{xy} & M_{yy} & M_{ys} \\ M_{xs} & M_{ys} & M_{ss} \end{pmatrix},\ U \equiv \begin{pmatrix} U_x \\ U_y \\ S \end{pmatrix}, \\ C &\equiv \begin{pmatrix} C_{xx} & C_{xy} & C_{xs} \\ C_{xy} & C_{yy} & C_{ys} \\ C_{xs} & C_{ys} & C_{ss} \end{pmatrix},\ Q(t) \equiv \begin{pmatrix} Q_x \\ Q_y \\ Q_s \end{pmatrix}. \end{aligned} \tag{32}$$

Here M and C are the global matrices of the inertia and stiffness, U and Q are the global columns of the unknowns and the generalized forces, respectively. The latter can be found from the expression for the virtual work of the external load.
In the case of the free harmonic oscillations we have a zero column in the right part of (31) and can replace $\ddot{U}$ by $-\omega^2 U$. The result is the generalized eigenvalue problem:

$$\left(C - \omega^2 M\right) U = 0 \tag{33}$$

When the global matrices of inertia and stiffness are constructed we can use such special commands as *Eigenvalues* and *Eigenvectors* for solving (33) in the Wolfram Mathematica. In the result we can compute values of the first N normal frequencies.
We have analyzed the blade with the following parameters: $\Omega \approx 1.745$ (the tip cross-section is turned by a 30° angle against the root section), $h = 0.01$ m, $L = 0.3$ m, the width ranging from 0.4 m to 0.2 m. The material characteristics are: $\rho = 7800$ kg/m^3, $\nu = 0.3$, $E = 2 \cdot 10^{11}$ Pa.
For our calculation we took $N = 5$.
The results of the finite element analysis for the two first normal modes are shown in Fig. 3.
Values of the two first natural frequencies (Hz) are as follows:

	3D-model	shell model
f_1	109.2	101.5
f_2	552.5	498.3

The difference between the results of the two approaches is less than ≈ 10 %.

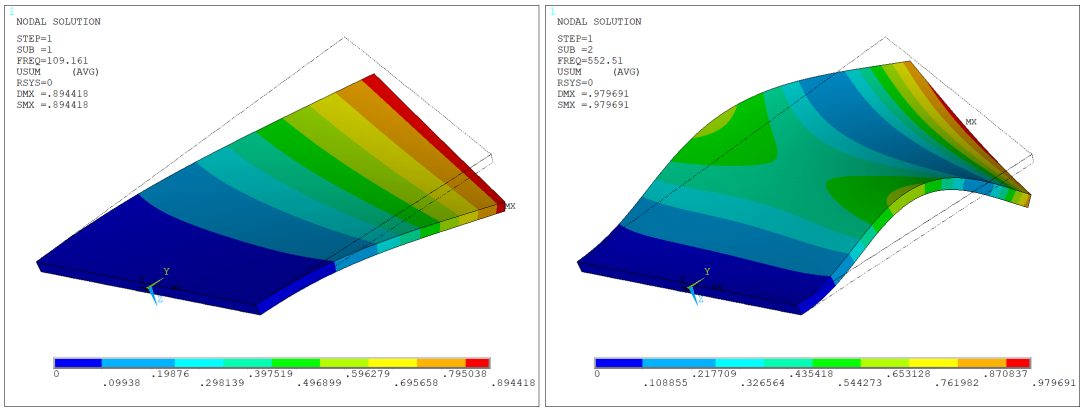

Figure 3: The first and second normal modes and their natural frequencies calculated by ANSYS

5 Conclusion

In this paper we presented a brief review of formalism of the Kirchhoff shells. The geometry of a blade is described as a helicoidal shell. The translational and rotational displacements were found from the tensor equations of the shell theory. The approximation for the displacement was considered as for the twisted beam with an additional term that takes into account the in-plane deformation of the cross-section. The displacement was approximated in terms of the chosen functions and the Ritz method was applied. It should be noted that the number of the coordinate functions N, as well as the type of these functions should be a subject for tests. For example, the results of the authors' analyses of the long blades' vibrations [12, 13] performed by using several different techniques showed that the increase in N may not necessarily lead to a more accurate result.

Having approximated the displacement functions, we proceeded to the discrete model and introduced the generalized coordinates. After that we derived the expression of potential and kinetic energies and then obtain the system of the Lagrange equations. The formulated generalized eigenvalue problem allows one to carry out the modal analysis for the blade. The problem was solved by means of special functions embedded in the Wolfram Mathematica.

We compared the results of our approach with the ANSYS finite element analysis of a 3D-model. The certain difference between these results could be explained by the properties of the coordinate functions. However, the actual choice of the type and number of coordinate functions is a topic of separate study which the authors intend to perform in the nearest future.

The presented algorithm allows us to analyze forced vibrations: the generalized forces can be derived from the expression for the virtual work. One can also consider the transient oscillations in the manner suggested in [12] for the long blades handled as rods.

References

[1] H. P. Bloch , M. P. Singh. Steam Turbines: Design, Applications and Relating. McGraw-Hill, 2009. 433 p.

[2] A. S.Leyzerovich. Wet-Steam Turbines for Nuclear Power Plants. Penn Well, 2005. 481 p.

[3] A. Kostjuk. Dinamika i prochnost' turbomashin. M.: Mashinostroenie, 1982. 264 p.

[4] V. Eliseev, Yu. Vetyukov, T. Zinovieva. Divergentsiya gelikoidalвЃЄnoy obolochki v trube s tekushey zhidkostвЃЄyu // PMTF, 2011. Vol. 52. вЊЦ 3. P. 143-152.

[5] V. Eliseev. Mechanics of elastic bodies (Mekhanika uprugih tel). St. Petersburg State Polytechnic University Publishing House, St. Petersburg, 2003. P. 336 (in Russian)

[6] V. Eliseev, A. Moskalets. Vibrations of Turbine Blades as Elastic Shells //Advances in Mechanical Engineering. вЃY Springer, Cham, 2018. P. 53-60.

[7] J. M. Borwein, M. B. Skerritt. An introduction to modern mathematical computing: with Mathematica. вЃY Springer, 2012. вЃY Vol. XVI. 224 p.

[8] T. Stolarski, Y. Nakasone, S. Yoshimoto. Engineering analysis with ANSYS software, 2007.

[9] V. Eliseev, T. Zinovieva. Lagrangian mechanics of classical shells: theory and calculation of shells of revolution // Shell Structures: Theory and Applications. вЃY Vol. 4 вЃY Pietraszkiewicz & Witkowski (eds). Proceedings of the 11th International conference "Shell structures: theory and applications". October 11-13, 2017, Gdansk, Poland. Published by Taylor & Francis Group, London, 2018. P. 73-76

[10] P. Grinfeld. Introduction to tensor analysis and the calculus of moving surfaces. New York: Springer, 2014.

[11] V. Eliseev, T. Zinovieva. Mekhanika tonkostennyh konstrukcij: teoriya sterzhnej. Ucheb. posobie. вЃY SPb.: Izd-vo SPbGPU, 2008. вЃY 96 p. (in Russian)

[12] V. Eliseev, A. Moskalets, E. Oborin. One-dimensional models in turbine blades dynamics // Lecture Notes in Mechanical Engineering. 2016. V. 9. P. 93-104

[13] T. Zinovieva, A. Moskalets. Modal Analysis of Turbine Blade as One-and Three-Dimensional Body // Advances in Mechanical Engineering. вЃY Springer, Cham, 2018. P. 195-204.

Artem A. Moskalets, Peter-the-Great Polytechnic University, Polytechnicheskaya str. 29, 195251 St. Petersburg, Russia

Tatiana V. Zinovieva, Institute for Problems in Mechanical Engineering of Russian Academy of Sciences, V.O., Bolshoj pr., 61, 199178 St. Petersburg, Russia
Alexander K. Belyaev, Institute for Problems in Mechanical Engineering of Russian Academy of Sciences, V.O., Bolshoj pr., 61, 199178 St. Petersburg, Russia

Investigation and development of an actuator based on an elastic element

Kirill A. Nuzhdin, Victor M. Musalimov
nkirill74@gmail.com

Abstract

The main purpose of this work is development and investigation of power-efficient actuator for transforming an applied force into translatory motion. An elastic element (which has the functioning principle based on the phenomenon of loss of stability) is used as an operating element of this device. In addition, there is made the analysis of the analogues of the proposed mechanism. In this paper we propose the actuator design and demonstrate the main components of the mechanism. Moreover, we have described the calculation of the mechanical properties and conditions for the applicability of a working link of the mechanism (an elastic element). Also this research is focused on the study of recuperation mechanisms which is used in actuators for partially restore of the spent energy.

1 Introduction

In the modern world one of the main functions of technology is the partial or complete replacement of a person production functions. Thus, the use of high-tech mechatronic devices allows to save a person from heavy physical activity (labouring job), routine and monotonous work, to eliminate the impact on personnel of harmful factors, and to liquidate the influence of the human factor during work that requires high accuracy, productivity and quality of tasks.

Currently, there are a large number of different types of actuators which are used in virtually all areas of robotics for energy transfer from the controlling object to the controlled object. Along with the most common types of actuators, such as mechanical, electrical, hydraulic and pneumatic, there are complex and "exotic" types of actuators, for example, pneumatic muscle, actuators based on electroactive polymers and metals with memory effect. However, these actuators are not always able to meet the demands for the design of complex mechatronic devices and sometimes designers have to solve the task of developing a new type of execution units. Thus, the main purpose of this work is development and investigation of power-efficient actuator for transforming an applied force into translatory motion.

Like any high-tech mechanisms, the actuator based on an elastic element is energy-dependent. For this reason, one of the central tasks to solve the problems of efficiency and productivity of such machines remains energy performance (energy efficiency).

As one of the solutions to this problem, it is possible to use the introduction of recuperation mechanisms that are aimed at partial restoration of the spent energy with the help of various actuating elements. The elements can be made in the form of elastic elements (for example, springs or elastic rods)[1].

2 Dynamics of recuperation mechanisms

Undoubtedly, a decrease in power consumption increases the time of autonomous operation of various mechanisms and actuators. Therefore, at the moment, various recuperation mechanisms are becoming widely used. The purpose of these mechanisms is partially restore of the spent energy (not only thermal and electrical but also mechanical) for reuse or its accumulation.
The present work is devoted to the investigation of recuperation mechanisms used to restore mechanical energy. We know two types of these devices.
The first type is recuperation mechanism of the executive device designed to convert the applied force into translational motion, where partial energy regeneration occurs due to the elastic properties of the working link in the process of restoring the initial form (further we will consider this mechanism in more detail).
The second type of recuperation mechanisms is a spring accumulator with an output rotary link used for rotational motion [2, 3]. The scheme of this device is shown in Fig. 1

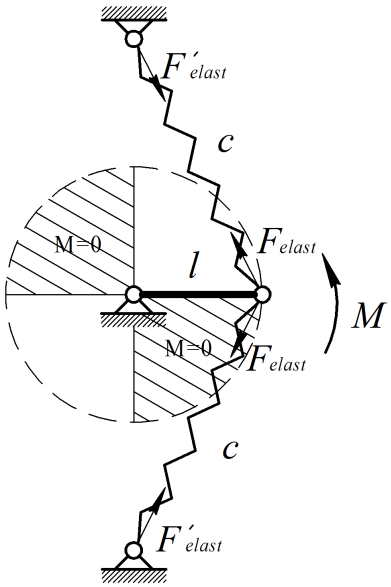

Figure 1: Scheme of the cyclic rotation mechanism with spring accumulator: l — length of the rotating crank; M — engine torque; F_{elast} and F'_{elast} — spring force; c — spring stiffness.

Consider the second device in more detail.
The mechanism is a rotating crank, to the free end of which are attached two springs of equal constant (spring force). The opposite ends of the spring are attached to the base, and are located on the same line and at the same distance from the axis of

the crank rotation. The initial length of these springs is assumed to be 0.1 m, also during the functioning of the mechanism, each of them is in a deformed (stretched) state and reaches the initial length only at the time when the other spring has the largest value of stretching. The described scheme allows the most effective use of a spring accumulator for energy recovery.
The working cycle of turning the mechanism, i.e. the complete turn of the working link about the rotation axis can be mentally divided into four parts (see Fig. 1). Unshaded areas correspond to the stage of "charging" the spring accumulator. Under the action of the drive torque, here takes place the rotational movement of the working link, which acts on the springs, shifts them from the balanced state, compressing one and stretching the other. In this part we should make some explanation: according to the theory of catastrophes and the theory of stability, this mechanism with a spring accumulator (consisting of two identical springs) has two stability positions, i.e. such conditions under which no vibrations of the working link are made, and the state and position of the springs do not change arbitrarily long. In our case at the initial moment of time the mechanism is in the first stable state equal to the zero deviation of the working link relative to the rotation axis. The second stable position is symmetric to it, i.e. it is located at the point of deviation equal to 180 deg. These two states are a kind of attractor for the right and left semicircles of the trajectory of movement of the worker, respectively.
The shaded areas of the trajectory of the working link correspond to the operation cycle of the spring accumulator. Here, the drive is disconnected and the motion is made only by the accumulated springs energy.

3 Modeling of recuperation mechanism

At the next stage of the work, a model of this mechanism was built using the SimMechanics/MATLAB environment (Fig. 2).
The Machine Environment and Ground (1,2) blocks specify the gravitational forces for the model and the mounting and positioning conditions of the machine parts, respectively. Revolute, Body - form the geometry of the rotating working link. Joint Actuator1 is a kinematic drive providing rotational motion. Joint Sensor is designed to obtain output characteristics of the working (actuating) link. Body Spring & Damper (1) perform the roles of non-linear springs. The Subsystem block specifies the input signal which is passed to the Joint Actuator1 drive. The Coulomb & Viscous Friction block is used to account for the effect of friction in the Revolute joint.
Let's talk in more detail about the modeling of friction in this mechanism.
If we take into account all theories of friction, it can be concluded that under friction processes it can be observed the following main effects: elastic deformation of surfaces, plastic deformation of surfaces, ploughing effect, shear of adhesion junctions [4].
This means that under modeling of the friction process, it is necessary to take into account both elastic and viscosity characteristics of friction surfaces.
In our model (Fig. 2) the input of the Coulomb & Viscous Friction block has a value of the body speed, the output has a value of the frictional force. The work basis of

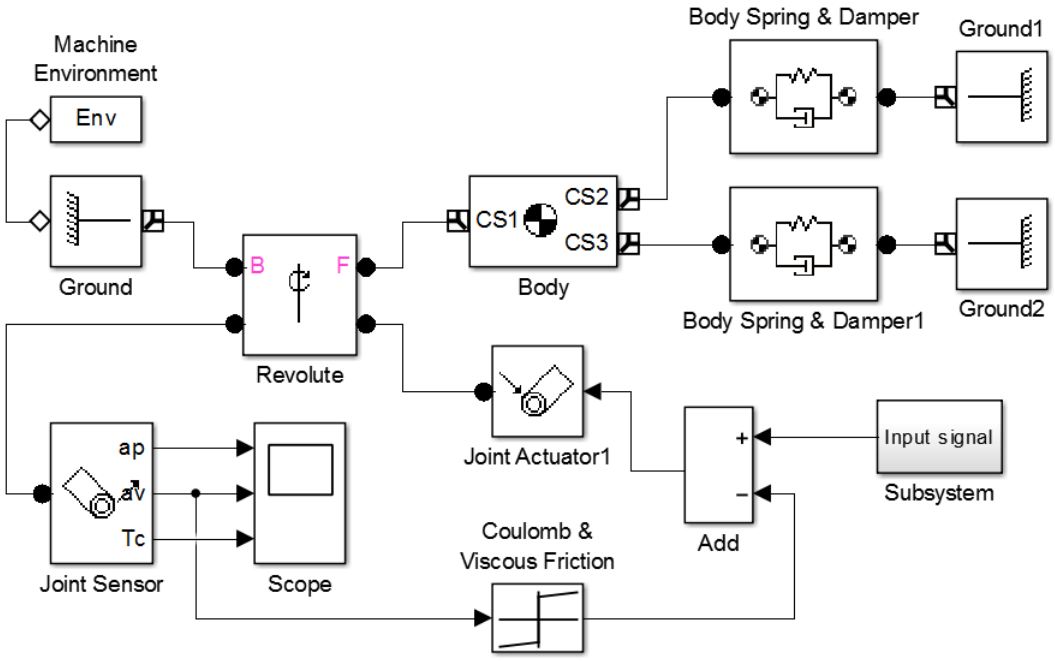

Figure 2: Model of recuperation mechanism with spring accumulator in SimMechanics.

the block is a well-known equation:

$$f = sign(v)(\mu|v| + \eta) \tag{1}$$

where f — friction coefficient; $sign$ — function of variable sign determination; v — velocity; μ — coefficient of viscous friction; η — coefficient of dry friction.
At the next stage, experiments for evaluation of the recuperation properties of the resulting mechanism were conducted. As the initial (ideal) device, the mechanism was considered without the use of a spring accumulator. To compare the properties of the two devices, the same signal (corresponding to one complete turn of the actuator) was applied to their inputs of the drive blocks. After that, the data which are characterizing the angle of rotation of the actuator (Angle, deg.), the angular velocity of rotation (Angular velocity, degree/s) and the drive torque (Torque, N*m) were recorded. The obtained graphical results are shown in Fig. 3.
Analyzing the results obtained, it can be noticed that the use of a spring accumulator can significantly reduce the operating time of the drive. This accordingly leads to a reduction of power consumption (this can be seen when comparing the Torque/Time graphs). However, on the other hand, the use of elastic elements increases the frequency of vibrations of the working link, thereby increasing the runtime of the working cycle.
At conclusion, during the work with the application of the MATLAB application package and the SimMechanics library we were able to build a model of the recuperation mechanism and, on its example, show the expediency of using spring accumulators in cyclic rotational mechanisms for energy recovery.

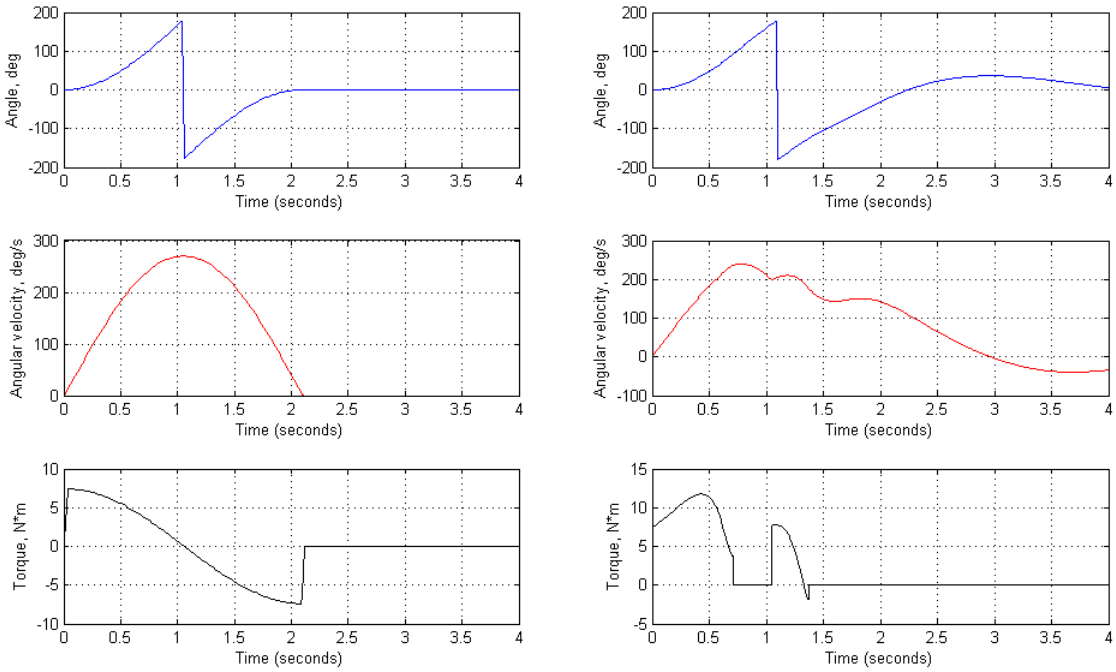

Figure 3: The obtained results for the ideal mechanism (left) and the mechanism with spring accumulator (right).

4 Design and investigation of the actuator based on an elastic element

4.1 Analogues

We know the next analogues. The first one is Mobile mechanism for converting the applied force into translational motion (Fig. 4).

The invention relates to a manpower walking mechanism. A travel mechanism is provided with a foreleg mechanism and a rear leg mechanism which are respectively hinged with a machine frame, the foreleg mechanism and the rear leg mechanism are of L-shaped cranks, unidirectional wheels are arranged at the bottom end of the cranks, the horizontal end heads of the cranks of the foreleg mechanism and the rear leg mechanism are respectively hinged and connected with a connected plate. The structure of the invention is simple and reasonable, the foreleg mechanism is designed into the L-shaped crank, through the hinging with the machine frame and the horizontal end head of the crank, only two point hinge is utilized to realize that the foreleg mechanism moves back and forth under the functions of the upper part pressure and the lower part pressure, thus a large quantity of parts are decreased, and the assembly and the regulation are convenient. Simultaneously, two connecting rod type cradle mechanisms are arranged at the upper parts of the foreleg mechanism and the rear leg mechanism, the power is directly exerted on the foreleg mechanism and the rear leg mechanism through a cradle to lead the mechanism to move smoothly, a pedal mechanism is connected with a drive mechanism, in

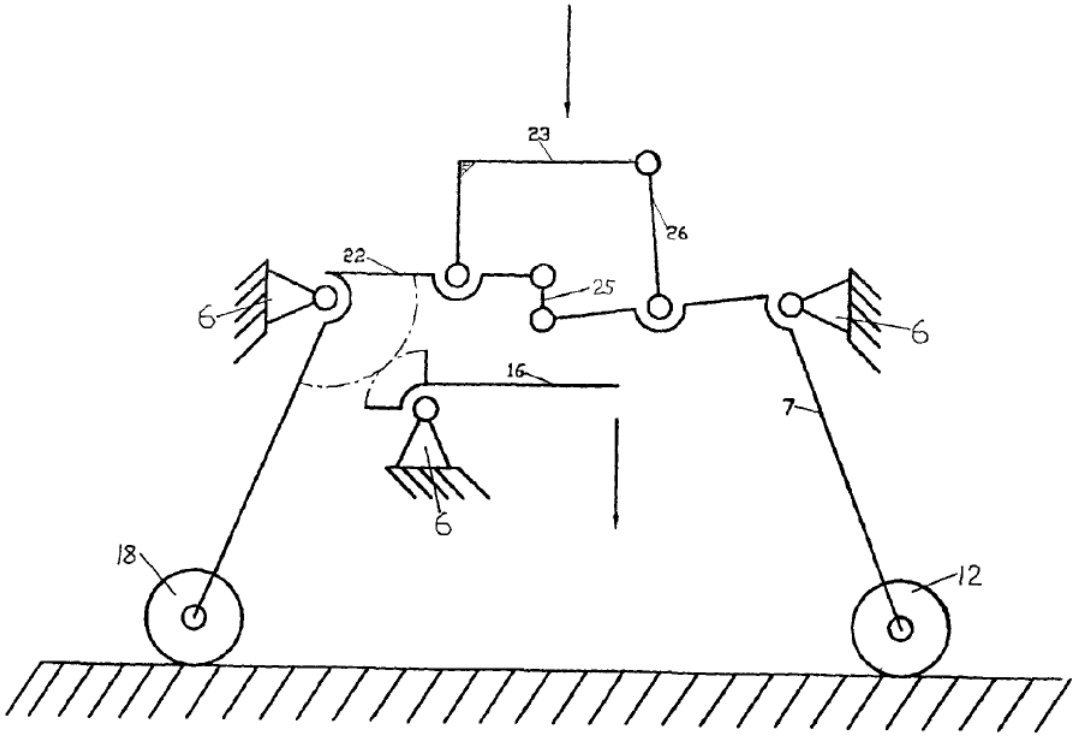

Figure 4: Mobile mechanism.

particular a gear drive mechanism or a lever drive mechanism, the guidance quality is good, and the connecting rod is arranged in a pressure spring frame, thus the position limit is accurate. The disadvantages of this device include the complexity of design and energy loss due to frictional resistance in kinematic nodes [5].
The second one is Bionic mechanical walking animal (Fig. 5).
The utility model provides a bionic mechanical walking animal, comprising a quadruped imitated outer shell, forelimbs with single direction rotating wheels, hind limbs with two-way rotating wheels, a cradle, pedals and a limb driving mechanism in the outer shell. The bionic mechanical walking animal is characterized in that the forelimbs and the hind limbs are respectively connected with the front and back ends of a cross beam through a rotation shaft, and the limb driving mechanism is hinged by the middle part of a front upper connecting rod and the middle part of the cross beam; the upper end of the front upper connecting rod is provided with the cradle, and the lower end of the front upper connecting rod is hinged with the connection shafts of the two forelimbs; a back upper connecting rod is also hinged with the middle part of the cross beam, and the other end of the back upper connecting rod is hinged with the connection shafts of the two hind limbs; one end of a front lower connecting rod is hinged together with one end of a back lower connecting rod, and the other end of the front lower connecting rod is hinged with the lower part of the front upper connecting rod; the other end of the back lower connecting rod is hinged with the lower part of the back upper connecting rod; the two pedals are respectively arranged at both ends of a horizontal connecting rod, and the middle part of the horizontal connecting rod is connected with the lower

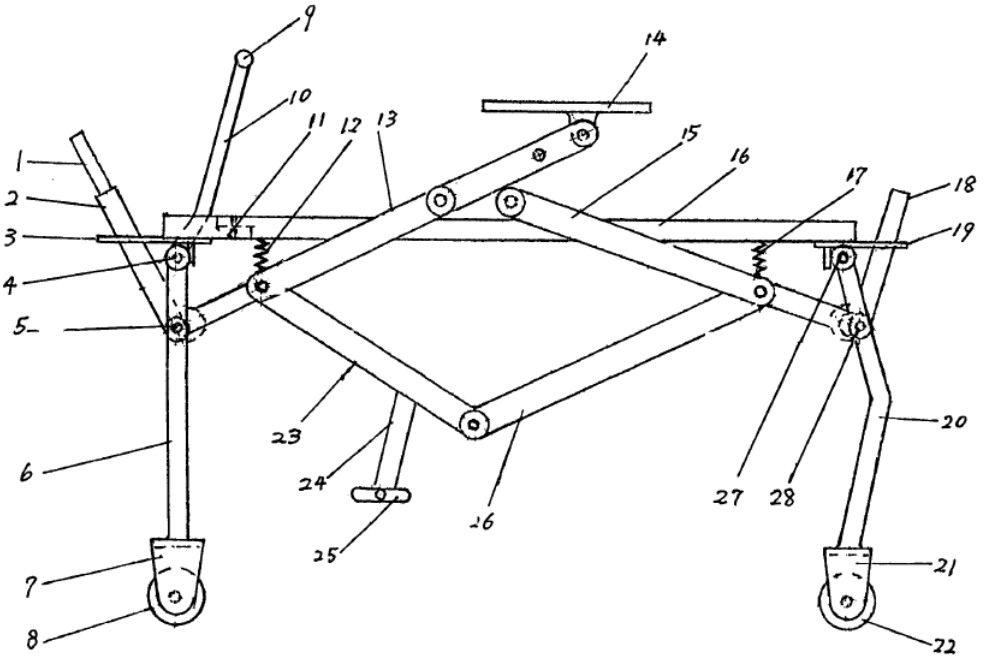

Figure 5: Bionic mechanical walking animal.

part of the front lower connecting rod or the back lower connecting rod via a vertical connecting rod. The bionic mechanical walking animal has simple structure, low cost, portable operation, safety and reliability. As the shortcomings of the above mechanism, we can distinguish: the complexity of the design, numerous connection joints that introduce significant friction resistance of the mechanism, as well as the dependence of the speed and distance of movement on the time and impulse of the applied force [6].

4.2 Modeling and operating peculiarities of the device

To eliminate the shortcomings of analogues and to solve the aforementioned problem, the mechanism was proposed and constructed (the scheme is shown in Fig. 6) [7]. The proposed device is a new type of energy-efficient actuators, where an elastic element is used as a working link. Its operation is based on the phenomenon of loss of stability under the action of the applied external force. The purpose of this mechanism is to demonstrate the properties and behavior of an elastic element whose design features can be used in the modeling of bionic systems.

It should be noted that the movable base (including frame 1 and mobile supports 3 in Fig. 6) is used only to demonstrate the force action that occurs under the process of buckling failure (loss of stability) of elastic element.

The principle of operation of the proposed mechanism is as follows: at the initial moment of time a force P (which is directed vertically downwards) is applied on the area of the conjugation of the motion platform for transferring the loading force 4 and the elastic element 5. When the applied force reaches a critical value, a loss of stability of the elastic element occurs, in other words the rectilinear shape of

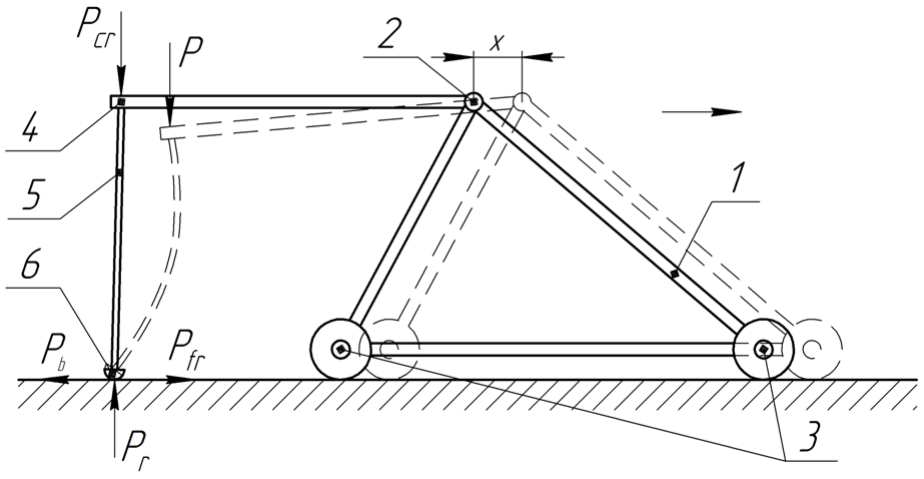

Figure 6: Proposed scheme of the actuator based on an elastic element: 1 — base; 2 — joint hinge; 3 — mobile supports (equipped with a ratchet mechanism); 4 — motion platform for transfer of the applied loading force P; 5 — elastic element; 6 — semicircular support tip; P_{cr} — the critical loading force; P_{fr} — the friction force; P_r — the support reaction force; P_b — the bending force; x — device displacement.

the elastic element changes under the action of the bending moment. Due to this phenomenon, the free end of the elastic element (in the present case, we consider that the free end is the lower edge of the elastic element with the semicircular support tip) will begin to deviate from the rectilinear steady state. However, under the condition of the appearance of frictional force P_{fr} (it is directed opposite to action of the bending force P_b) the entire energy of the elastic element (which was accumulated under process of loss of stability) is redistributed and reverses direction toward translational motion of the base of the actuator. When the applied force P is removed, an inverse process is occurring. The elastic element recovers an initial rectilinear shape, but the movable base (like the whole mechanism) will not change its position due to reaction of the ratchet mechanisms of the movable supports [8, 9, 10].

The whole process of moving the actuator can be divided into two cycles. The first cycle is a "loading cycle". Under the influence of the applied force, here is occurring the loading of elastic element that causes a change in the rectilinear shape, which in turn ensures the movement of the entire mechanism. The second cycle is "recuperation cycle". Here, on the condition that the value of the applied force is less than the critical value, the process of restoring the original shape of the elastic element takes place by virtue of the stored energy in the process of loss of stability.

4.3 Selection of the device working link and the way of functions

In the next step, an elastic element is selected. The selection of a suitable working link is expedient to begin with the calculation of elastic properties, the selection of

suitable materials and forms.
In general, the proposed device can be designed in a wide range of the size range — from millimeters to several tens of centimeters. The overall dimensions of the device (in particular, the linear dimensions of the elastic element) directly affect on the properties of the operating link and, consequently, on the technical characteristics of the entire mechanism. This feature allows us to expand an application area of the proposed actuator.
When making a selection of a material for the elastic element, attention should be paid to the following parameters: high elastic properties, durability, endurance range, and also its mechanical characteristics have to be stability over time.
In this work, as an example of parameters calculation of elastic element were used solid rods of rectangular cross section with dimensions of 5x10 and 7x10 mm, and 70 mm length. As materials for manufacturing, the following were selected: high-quality carbon steel (65), manganese steel (65G), silicium steel (60S2) and chromium-vanadium steel (50HFA).
To determine the mechanical properties of an elastic element, let us consider it as a rectilinear rod which is fixed one end and being under the influence of pressure force, that directed along the longitudinal axis of the rod and acting on its free end (see Fig. 7) [4].

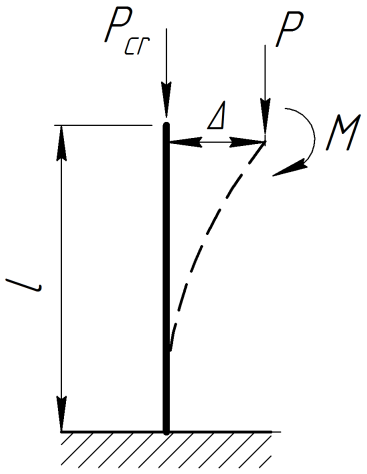

Figure 7: The process of changing a shape of the rod under action of force: P — load force, P_{cr} — critical force, M — bending moment, Δ — deviation of the rod end, l — length of the elastic rod.

For $P < P_{cr}$ only the central compression of the rod occurs. For $P > P_{cr}$ the rod operates on the joint action of compression and bending. Even with a small excess of the critical load, the deflections of the rod end and the occurred flexural stress are quite significant. To determine P_{cr}, we used the following expression:

$$P_{cr} = \frac{\pi^2 EJ}{\mu l^2} \tag{2}$$

where EJ — flexural stiffness, which is determined as a product of the Young's modulus of material elasticity E and the moment of inertia of the cross-sectional

J; μ — factor depending on the end conditions of the rod (in our case $\mu = 2$); l — length of the elastic rod [11].
The loss of stability of the rod occurs until the critical longitudinal compressive stress of the rod is reached which is equal to a yield stress or a proof strength for ductile materials, or ultimate compressive strength for brittle materials [12].
The peculiarity of the loss of stability lies in the fact that it occurs suddenly and at low stress values, when the strength of the material is nowhere near exhausted [13].
From the foregoing, it can be concluded that for deviation of the free end of the rod (as a consequence, the displacement of the movable base of the actuator), it is necessary to apply a force which is greater than the critical value, but the magnitude of this applied force should be less than the value at which the rod reaches the critical longitudinal compressive stress. Therefore, in this paper, only the rods of great flexibility are considered, i.e. those for which Euler's formula is valid.
Thus, it is possible to compose a system of equations describing the application condition of an elastic element:

$$P_{cr} = \frac{\pi^2 EJ}{(\mu l)^2} \leq P \tag{3}$$

$$\sigma_{cr} = \frac{\pi^2 E}{\lambda^2} = \frac{\pi^2 EJ_{min}}{(\mu l)^2 A} < \sigma_T \tag{4}$$

$$\lambda = \frac{\mu l}{i_{min}} \geq \lambda_s = \sqrt{\frac{\pi^2 E}{\sigma_p}} \tag{5}$$

where P — the applied force; σ_{cr} — the critical longitudinal compressive stress; λ — the slenderness ratio of a rod; $P\Theta$ — the cross-section area; σ_T — the yield stress; i_{min} — the minimum cross section radius of inertia; λ_s — the limit slenderness ratio of a rod; σ_p — the proportional elastic limit.
Using the conditions of application of the elastic element that were described above, we can complete a table in which all the mechanical properties and features of the elastic rods for some materials are displayed (see Table 1). The materials, which for their properties are most suitable in the manufacture of elastic elements, were listed in this table as examples.

5 Conclusions

In conclusion we have researched recuperation mechanisms which is used in actuators for partially restore of the spent energy. In the course of the work, we have designed the recuperation mechanism of an energy-efficient actuator based on an elastic element and have selected and calculated parameters of the working link which was made in the form of an elastic solid steel rod of rectangular cross-section. This mechanism has a simpler construction in comparison with the studied analogues due to reducing of connecting nodes and kinematic pairs number. The proposed device can find its application in many areas of mechanical engineering, especially under designing of various actuated parts of machines and mechanisms which have a purpose to convert an applied force into translational motion. Also, this actuator can be used in robotechnics area as a new type of energy efficient mechanism.

Table 8: The calculated parameters of the elastic rod.

Material	Cross-section dimension, mm x mm	Length of elastic rod, mm	Critical force P_{cr}, N	Applied (loading) force $P\prime$, N	Deflection of the rod end, mm	Bending force, N
Steel 65	5 x 1	70	1.2	43.01	43.1	0.006
			4		44	0.019
			6.9		46.15	0.033
	7 x 1	70	1.4	60.21	60.3	0.005
			5.8		61.7	0.02
			6.9		62.4	0.024
Steel 65G	5 x 1	70	1.2	45.12	45.2	0.006
			4.9		46.7	0.023
			6.7		48.2	0.032
	7 x 1	70	1	63.15	63.2	0.004
			5.4		64.5	0.018
			7.7		66	0.026
Steel 60S2	5 x 1	70	0.59	44.48	44.5	0.003
			5.1		46.2	0.024
			7.2		48	0.034
	7 x 1	70	0.59	62.27	62.3	0.003
			2.9		63	0.014
			6.6		66.4	0.031
Steel 50HFA	5 x 1	70	0.98	45.74	45.8	0.005
			3.4		46.5	0.016
			5.7		48	0.027
	7 x 1	70	0.87	64.03	64.1	0.004
			4.6		66	0.022
			6.4		68	0.03

References

[1] K.A. Nuzhdin. System issues of a creation of actuators based on elastic // Journal of Instrument Engineering, 61, 2018, pp. 148–153.

[2] V.M. Musalimov, K.A. Nuzhdin. Study and design of the actuator based on elastic element // Week of Science SPbPU: Proceedings of a scientific conference with international participation. Institute of Metallurgy, Mechanical Engineering and Transport, 2017, pp. 32–35.

[3] D.S. Pelupessi, M.V. Zhavner, Spring-Loaded Accumulators with the Output Rotary Link for Step Movements // Proceedings of Higher Educational Institutions. PËPөchine Building, 679, 2016, pp. 9–17.

[4] V.M. Musalimov, K. Nuzhdin. The experimental determination of bifurcation components of friction // Procedia Engineering, 199, 2017, pp. 1478–1483.

[5] Nie Wenlong, Mobile mechanism // CN Patent 101172203B.

[6] Sheng Ming Yi, Bionic mechanical walking animal // CN Patent 2734289Y.

[7] V.M. Musalimov, K.A. Nuzhdin, The actuator based on an elastic element // RU Patent 172799.

[8] I.V. Kragelsky, M.N. Dobychin, V.S. Kombalov // Principles calculations on friction and wear, 1977, p. 526.

[9] V.M. Musalimov. Bifurcation component of sliding friction // Journal of Instrument Engineering, 60, 2017, pp. 793–796.

[10] V.M. Musalimov, K.A. Nuzhdin, A.E. Tyurin. Modeling of external dynamic of the friction engagement // Book of papers. 24th International Congress of Theoretical and Applied Mechanics, 2016, pp. 1802–1803.

[11] J.M.T. Thompson // Instabilities and Catastrophes in Science and Engineering, 1985, p. 254.

[12] R. Gilmor // Applied theory of catastrophes, 1984, p. 350.

[13] Y. Panovko // Fundamentals of applied theory of vibrations and shock, 1976, p. 320.

Victor M. Musalimov, 197101, 49 Kronverksky Pr., Saint Petersburg, Russian Federation
Kirill A. Nuzhdin, 197101, 49 Kronverksky Pr., Saint Petersburg, Russian Federation

Model of the effect of low concentrations of diffusion - mobile hydrogen on the cracks propagation

V.A. Polyanskiy, Y.A. Yakovlev, A.S. Zegzhda
alex.zegzhda@gmail.com

Abstract

Small amount of hydrogen concentration impact appears significantly in material fatigue and cracks propagation. Resonant effect is observed at fatigue. This effect was described by a model of bicontinuous medium containing hydrogen [1], [2] and was detected experimentally later [3].

Significant impact of small diffusion - mobile hydrogen concentration to metal fatigue was observed in non-cyclic static and dynamic loading. Hydrogen embrittlement areas were localized. Hydrogen embrittlement sites were formed during metal fracture. Model HELP (Hydrogen-enhanced localized plasticity) is generally used to describe the observed phenomena [4]. The base physical mechanism couldn't be represented in the critical hydrogen concentration, which could be observed experimentally. This and calculation complication are major weak points of the model.

During the testing it had been found that hydrogen was concentrated in a thin boundary layer at the surface of a metal specimen [8]. The result makes it possible to describe new models of hydrogen effect to material mechanical properties.

A boundary layer mechanical properties degradation effect due to accumulation of diffusion - mobile hydrogen was modeled by finite element method.

The cylindrical corset samples with the annular crack were examined because extensive experimental data exist for such cases.

The results of hydrogen concentration from [8] were applied in the model. The bicontinuous model of a boundary layer was chosen as a base model for material properties examination.

A boundary layer thickness and mechanical properties degradation effect on tensile strength, which mostly used in previous studies, was analyzed. Tensile strength dependence on deteriorated layer thickness and level of the properties degradation was plotted.

Degradation of mechanical properties at a depth of the grain size of polycrystalline metal doesn't lead to significant tensile strength change. Only a model of bicontinuous material for the entire specimen could explain experimentally observed effects.

1 Introduction

Hydrogen effect on high strength steel is well known problem due to the degradation of mechanical properties caused by hydrogen accumulation. Moreover, small amount of hydrogen concentration impact appears significantly in material fatigue and cracks propagation.
Resonant effect is observed at fatigue. This effect was described by a model of bicontinuous medium containing hydrogen [1], [2] and was detected experimentally later [3].
Significant influence of small diffusion – mobile hydrogen concentration was observed during the non-cyclic static and dynamic loading. Hydrogen embrittlement areas were localized. Hydrogen embrittlement sites were formed during metal fracture. Model HELP (Hydrogen-enhanced localized plasticity) is generally used for description of the observed phenomena [4]. But the base HELP physical mechanism couldn't be represented, because it is possible only with the hydrogen concentration, which couldn't be observed experimentally. This and calculation complication are major weak points of the model. Model HEDE (hydrogen-enhanced decohesion) [5] doesn't correlate with experimental data about the critical concentrations of hydrogen too. As a result, last articles [6] propose to synergy between HELP and HEDE models. This approach looks universal. However both models consider nonlinear equations and simple linear combination is impossible. Model HELP proposed for description of cracks propagation and it's localized model. HEDE describes grains cohesion and shift. Most likely, they are couldn't be combined in one material without prior linearizing of defining equations [7].
During the testing it had been found that hydrogen was concentrated in a thin boundary layer at the surface of a metal specimen [8]. Testing was performed to observe different specimens fracture under various mechanical loadings. There are a number of studies to describe hydrogen effect in various materials consider condition with or without concentrator, as example [9].
New models are required to describe hydrogen effect to material mechanical properties. And existing independent experimental data create base for models verification.

2 Material and methods

2.1 Hydrogen distribution

The plane corset samples of steel 14HGNDC were examined. Sample size is $900 \times 120 \times 17\ \mathrm{mm}^3$. Width of the working portion of the sample was 70 mm. Series of tests were performed to study tensile strength, low-cycle and multicycle fatigue. Samples were cutting on pieces with size $6 \times 6 \times 17\ \mathrm{mm}^3$ after failure for measurement of the hydrogen concentration. Hydrogen analyzer AV-1 was used for measurements.
The half of specimens analyzed without additional polishing. The another half was polished manually in the depth of 0.1 mm layer. Upper and lower specimen edge's had been polished only. Therefore, rolled boundary layer was deleted, which contacts with the environment air during mechanical testing. Specimens were cut also from

unloaded part of sample, as well as from loaded.
Average hydrogen concentration in specimens with removed boundary layer is 0.25 ppm. Unloaded part of corset samples with boundary layer consider 0.42 ppm hydrogen concentration.
Loaded part of samples with boundary layer consider hydrogen concentration in range of 0.42 ppm to 0.95 ppm. Maximum values observed in the main crack, which lead to samples fracture.
Hydrogen concentration could be calculated by subtraction method, considering thickness of boundary layer. Initially boundary layer accumulates approximately 10 ppm hydrogen during rolling stage. Hydrogen are redistributed and accumulated additionally, during tensile phase. Boundary layer around main crack consider up to 60 ppm hydrogen. This means that there is the hydrogen induced fracture during mechanical testing under normal environment conditions.
Nonetheless, this phenomenon should be further analyzed. It would be feasible to use the model for this purpose.

2.2 Hydrogen-induced fracture model

The purpose of this study is the modeling of fracture in cylindrical steel samples, caused by mechanical properties degradation created by diffusion – mobile hydrogen accumulation in the boundary layer.
The simple model of material heterogeneity examined to study impact of mechanical properties degradation. Plasticity is simulated by bilinear material model.
The cylindrical corset samples with the annular crack examined because extensive experimental data exist for such cases (see Fig. 1). ANSYS/LS-DYNA is used for fracture simulation.
The explicit dynamic structural analysis method used for modelling. Axisymmetric 2D model used assumes that a 3D model and its loading can be generated by revolving a 2D section 360° about the y-axis. It reduces number of elements in the model, increases solving time and allows to plot section strain-stress result without additional tools. The geometry has to lie on the positive x-axis of the x-y plane due to symmetry with dimensions shown in the figure 1. Boundary layer thickness is in range of 0..50 Bxm.
2D model are meshed by 2D Solid 162 axisymmetric elements. The Fig. 2 are show 3D revolving a section in 270° with specific mesh in stress concentrations area.
Boundary conditions (loads and constraints) are:

$$y = 0: \quad u_y = 0,$$

$$y = L: \quad u_y = v_y \cdot t,$$

$$x = R: \quad n \cdot \sigma = 0.$$

The lowest edge of section is fixed. The upper edge is moved with constant velocity $v_y = 3$ mm/c. Material properties are based on data from cf. [8] about hydrogen concentration and from cf. [10] about high strength steel AISI 4135 (see table 9).

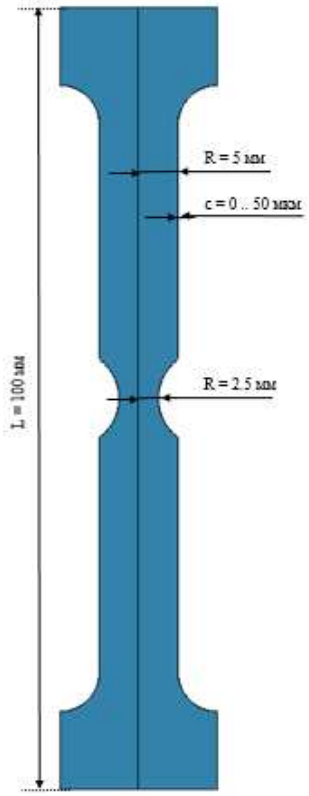

Figure 1: Cylindrical model with concentrator

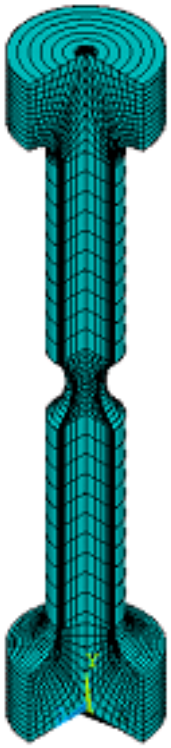

Figure 2: Finite element model revolved in 3/4

Table 9: Material properties

Steel AISI 4135	E	200 GPa
	ν	0.32
	σ_y	1 350 MPa
	E_T	763 MPa
	ρ	7 865 kg/m^3
	$\varepsilon_{failure}$	0.003
Boundary layer	$\sigma_{y\ H\ concentration\ I}$	500 MPa
	$\varepsilon_{failure\ H\ concentration\ I}$	0.00065
	$\sigma_{y\ H\ concentration\ II}$	400 MPa
	$\varepsilon_{failure\ H\ concentration\ II}$	0.0005

3 Results and discussion

Boundary layer thickness and mechanical properties degradation effects on the maximum of the first principal stress were analyzed. The maximum of the first principal stress measured in the point, shown in the Fig. 3. Relation between the maximum

stress and boundary layer thickness is plotted in the Fig. 4.

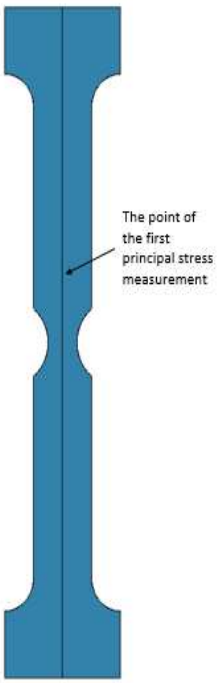

Figure 3: The first principal stress point

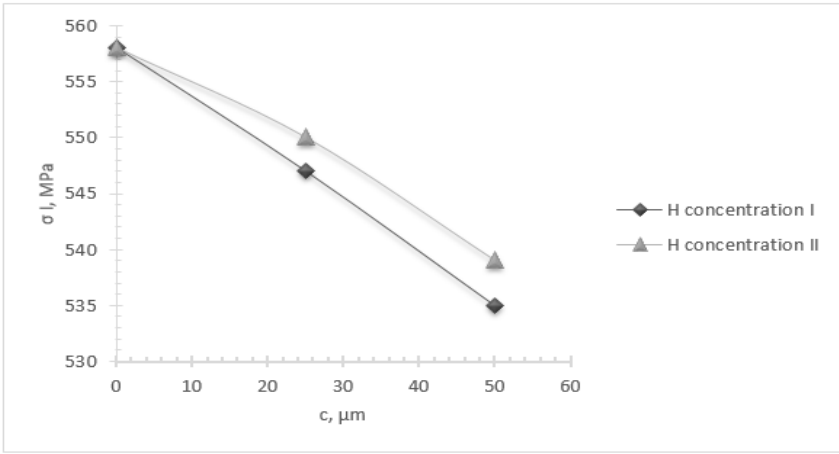

Figure 4: Maximum stress vs boundary layer thickness dependence

The maximum stress decrease is 19 MPa as shown in the graph and it is not more than 4% from decreasing of the initial value. Consequently, degradation of mechanical properties at a depth of the grain size of polycrystalline metal does not lead to significant tensile strength change.
However, effect of the hydrogen accumulation into the boundary layer and hydrogen-induced fracture, which we detected in case of mechanical fracture, was explained in the research [11] for other cases. It may be assumed that surface sorption of hydrogen from environmental is one of the main fracture mechanisms. The model of bicontinuous material, which was developed in [12], has not consider this effect of boundary layer.

4 Conclusions

Experimental data is collected for single-axis tensile loading of corset samples. It shows that leading mechanisms of fracture is hydrogen accumulation in the thin boundary layer with further creation and propagation of cracks.
Hydrogen-induced mechanical properties degradation analyzed on cylindrical corset samples from high strength steel. Degradation of mechanical properties at a depth of the grain size of polycrystalline metal does not lead to significant tensile strength change.

Only a model of bicontinuous material for the entire specimen could explain experimentally observed effects.
This phenomenon should be further analyzed by the model, which explain degradation of boundary layer with high hydrogen concentration during fracture.

Acknowledgements

The financial support of the Russian Foundation for Basic Research, grants No. 17-08-00783-a, 18-08-00201-a and 18-31-00329, is acknowledged.

References

[1] V.Polyanskiy, A.Polyanskiy, Y.Yakovlev. The material interaction with the solute hydrogen during fatigue failure //W. Eichlseder, F. Grun, 3rd Fatigue Symposium Leoben. Lightweight design. 18-19 April 2012 Leoben, Austria. Conference transcript. ISBN: 978-3-902544-03-02.-Leoben:Montanauniversitat.-2012.-p.191-201.

[2] A.K. Belyaev, A.M. Polyanskiy, V.A. Polyanskiy and Yu.A. Yakovlev, "Parametric Instability in Cyclic Loading as the Cause of Fracture of Hydrogenous Materials," Mech. Solids. 47 (5), 533-537 (2012)

[3] J. Yamabe, M. Yoshikawa, H. Matsunaga, S. Matsuoka, Effects of hydrogen pressure, test frequency and test temperature on fatigue crack growth properties of low-carbon steel in gaseous hydrogen// Procedia Structural Integrity, Vol. 2, 2016, pp. 525-532.

[4] Birnbaum H.K., Sofronis P. Hydrogen-enhanced localized plasticity – a mechanism for hydrogen-related fracture . Mat. Sci. and Eng.: A. 176(1-2) 1994. -pp. 191–202.

[5] Varias A.G., Massih A.R. Simulation of hydrogen embrittlement in zirconium alloys under stress and temperature gradients. J. of Nuclear Mat. 279(2-3) 2000. -pp. 273–285.

[6] M.B. Djukic, V. Sijacki Zeravcic, G.M. Bakic, A. Sedmak, B. Rajicic, Hydrogen damage of steels: A case study and hydrogen embrittlement model// Engineering Failure Analysis, Vol.58, 2015, pp. 485-498, http://dx.doi.org/10.1016/j.engfailanal.2015.05.017.

[7] Ignatenko A.V., Pokhodnya I.K., Paltsevich A.P., Sinyuk V.S. Dislocation model of hydrogen-enhanced localizing of plasticity in metals with BCC lattice. The Paton Weld J. (3) 2012. -pp. 15–19.

[8] A. K. Belyaev, D. E. Mansyrev, V. A. Polyanskiy, A. M. Polyanskiy, D. A. Tretyakov, Yu. A. Yakovlev, Boundary layer of hydrogen concentration under plastic deformation, Diagnostics, Resource and Mechanics of materials and structures. - 2017. - Iss. 4. - P. 32-43 - DOI: 10.17804/2410-9908.2017.4.032-043

[9] A. Laureysa, T. Depovera, R. Petrova,b, K. Verbekena, Influence of sample geometry and microstructure on the hydrogen induced cracking characteristics under uniaxial load, Materials Science & Engineering, 2017, DOI: 10.1016/j.msea.2017.02.094

[10] Nie, Y., Kimura, Y., Inoue, T., Yin, F., Akiyama, E., & Tsuzaki, K. (2012). Hydrogen embrittlement of a 1500-MPa tensile strength level steel with an ultrafine elongated grain structure. Metallurgical and Materials Transactions A: Physical Metallurgy and Materials Science, 43(5), 1670-1687. DOI: 10.1007/s11661-011-0974-7

[11] Garkunov DN, Suranov G.I., Khrustalev Yu.A., Hydrogen wear of parts of machines Ukhta: Ukhta State Technical University 199p. ISBN: 5-88179-319-6

[12] A. K. Belyaev, N.R. Kudinova, V.A. Polyanskiy, Yu. A. Yakovlev, The description of deformation and destruction of materials containing hydrogen by means of rheological model, St. Petersburg Polytechnical University Journal: Physics and Mathematics, Volume 1, Issue 3, 2015, Pages 305-314, ISSN 2405-7223, doi:10.1016/j.spjpm.2015.12.002.

V.A. Polyanskiy, IPME RAS, V.O., Bolshoj pr., 61 , 199178 St.-Petersburg, Russia and St.-Petersburg State Polytechnic University, 195251 Politekhnicheskaya, 29 St.-Petersburg, Russia

Y.A. Yakovlev, IPME RAS, V.O., Bolshoj pr., 61 , 199178 St.-Petersburg, Russia and St.-Petersburg State Polytechnic University, 195251 Politekhnicheskaya, 29 St.-Petersburg, Russia

A.S. Zegzhda, SPbSTU, St.-Petersburg State Polytechnic University, 195251 Politekhnicheskaya, 29 St.-Petersburg, Russia

Non-isothermal steady power-law fluid flow through an axisymmetric sudden contraction

Kira E. Ryltseva, Oleg Yu. Frolov, Gennady R. Shrager
kiraworkst@gmail.com

Abstract

In this work, the laminar steady power-law fluid flow in a pipe with sudden contraction is considered taking into account viscous dissipation, dependence of the rheological characteristics on the temperature, and constant temperature on the rigid wall. The flow is described by the motion, continuity, and energy equations using stream function, vorticity, and temperature variables. This system of equations is enclosed by the Ostwald de Waele power law with a temperature dependence of the consistency coefficient defined by exponential law. For numerical solving, the finite-difference method based on the alternative directions scheme is used. The difference equations are solved by the sweep method.

As a result of parametrical calculations, the flow kinematic characteristics were studied depending on the power-law index and dimensionless criteria. The effect of viscous dissipation on the flow structure was determined, and the temperature field was obtained in a wide range of basic parameters. The calculated results were verified and compared with available data.

1 Introduction

Laminar fluid flows in pipes with sudden contraction are frequently encountered in various technical applications. In particular, these same flows are realized in the industrial equipment applied for a polymer processing by casting method. Arranging of efficient manufacturing procedures requires both a detailed investigation of the flow structure, head and rate determining, and estimation of hydraulic resistance provided by processing line components. In general, polymeric fluid flows are characterized by non-Newtonian rheological behavior and non-isothermal properties caused by mechanical energy dissipation, chemical heat sources, and various heat-transferring boundary conditions. In such processes, physical properties of the medium are temperature-dependent.

Since the flows through sudden contraction find a widespread industrial application, they attract much attention of the researchers, at least from the middle of last century. The results of investigation on the laminar isothermal fluid flow through contracting geometries available at that time were considered in [1, 2]. These papers include a detailed discussion on the flow structure and kinematics, pressure losses

depending on the Reynolds number and contraction ration for Newtonian and non-Newtonian fluids. The more recent studies were carried out and reflected in [3, 4, 5, 6].

The number of significant difficulties appears when solving the problem of non-isothermal non-Newtonian fluid flow taking into account mechanical energy dissipation and temperature-dependent rheological parameters. Therefore, in most cases, the theoretical studies of the flow and heat transfer with varying physical characteristics of the fluid are implemented using approximate solution or numerical methods at simplifying assumptions.

One-dimensional problems on the steady non-isothermal viscous flow can be solved analytically. The pioneering works containing analytic solutions of such problems appeared in the middle of last century [7, 8, 9, 10]. The stability of obtained stationary solutions and a corresponding phenomenon referred to as a hydrodynamic thermal explosion are discussed in [11, 12]. The research results regarding considered problem are described in the following monographies [13, 14, 15]. Non-isothermal Newtonian and non-Newtonian fluid flows in sudden contractions are studied in [16, 17, 18].

The purpose of this work is to simulate numerically a steady non-isothermal power-law fluid flow in a pipe with sudden contraction in order to evaluate the effect of viscous dissipation on the kinematics of the process, flow structure, and temperature and apparent viscosity distributions.

2 Formulation of the Problem

The laminar steady power-law fluid flow through an axisymmetric sudden contraction under non-isothermal conditions is considered. The flow region is depicted in Fig. 1.

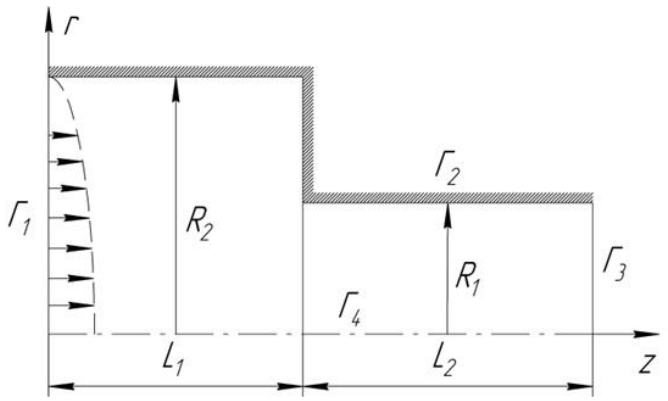

Figure 1: Flow region

The mathematical model of the flow includes the following dimensionless equations in terms of stream function, vorticity, and temperature [19]:

$$\frac{\partial(v\omega)}{\partial r} + \frac{\partial(u\omega)}{\partial z} = \frac{2^n \cdot B}{Re}\left(\Delta\omega - \frac{\omega}{r^2}\right) + \frac{2^n \cdot S}{Re}, \tag{1}$$

$$\Delta\psi - \frac{2}{r}\frac{\partial\psi}{\partial r} = -r\omega, \tag{2}$$

$$\frac{\partial(v\theta)}{\partial r} + \frac{\partial(u\theta)}{\partial z} = \frac{2}{Pe}\left(\Delta\theta + 2^{n-1}A^2B\cdot Br\right) - \frac{v\theta}{r}, \tag{3}$$

where, the source term (S) and the intensity of the rate of strain tensor (A) are given as

$$S = 2\frac{\partial^2 B}{\partial r\partial z}\left(\frac{\partial v}{\partial r} - \frac{\partial u}{\partial z}\right) + \left(\frac{\partial^2 B}{\partial z^2} - \frac{\partial^2 B}{\partial r^2}\right)\left(\frac{\partial u}{\partial r} + \frac{\partial v}{\partial z}\right) +$$

$$+2\frac{\partial B}{\partial z}\cdot\frac{\partial\omega}{\partial z} + 2\frac{\partial B}{\partial r}\cdot\frac{\partial\omega}{\partial r} + \frac{\partial B}{\partial r}\cdot\frac{\omega}{r},$$

$$A = \sqrt{2\left(\frac{\partial u}{\partial z}\right)^2 + 2\left(\frac{\partial v}{\partial r}\right)^2 + 2\left(\frac{v}{r}\right)^2 + \left(\frac{\partial u}{\partial r} + \frac{\partial v}{\partial z}\right)^2}.$$

The stream function (ψ) and vorticity (ω) are defined as follows:

$$v = -\frac{1}{r}\frac{\partial\psi}{\partial z},\ u = \frac{1}{r}\frac{\partial\psi}{\partial r}, \tag{4}$$

$$\omega = \frac{\partial v}{\partial z} - \frac{\partial u}{\partial r}. \tag{5}$$

The system of equations is completed by a rheological power law, which specifies temperature-dependent apparent viscosity by formula [19]:

$$B = \exp\left[-\theta\right]A^{n-1}, \tag{6}$$

where, n is the power-law index. For values of n between 0 and 1, the apparent viscosity is shear-thinning, for $n > 1$, the apparent viscosity is shear-thickening, and for $n = 1$, the Newtonian apparent viscosity model occurs.
In the equations stated above, v, u are the radial and axial velocity components, respectively, $\theta = \beta\left(T - T_1\right)$ is the dimensionless temperature, T and T_1 are the dimensional temperatures of the fluid in the flow and on a solid wall, respectively, and $D = 2R_1$ is the diameter of the downstream pipe. The typical scales for space, velocity, and apparent viscosity are the radius of the downstream pipe (R_1), the average velocity in the downstream pipe (U), and the value of $k_1\left(\frac{U}{R_1}\right)^{n-1}$, respectively.
The dimensionless Reynolds, Peclet, and Brinkman numbers are represented as

$$Re = \frac{\rho U^{2-n}D^n}{k_1},\ Pe = \frac{c\rho UD}{\lambda},\ Br = \frac{k_1D^2\beta}{\lambda}\left(\frac{U}{D}\right)^{n+1}.$$

Here, $k_1 = k_0\exp\left[-\beta\left(T_1 - T_0\right)\right]$ is the consistency coefficient at T_1, k_0 is the consistency coefficient at T_0, β is the temperature dependency coefficient; ρ is the fluid density, c is the heat capacity, and λ is the thermal conductivity, which are considered to be constant.

At the inlet boundary (Γ_1), the velocity and temperature profiles are calculated corresponding to a fully developed one-dimensional non-isothermal fluid flow with a specified constant flow rate in the infinite pipe. Based on the obtained velocity profile, the stream function and vorticity are calculated according to Eqs.(4,5), and assigned as an inlet boundary conditions. On the rigid walls (Γ_2), the no-slip boundary conditions are realized, and the dimensionless temperature is set to zero. At the output boundary (Γ_3), the derivatives of stream function, vorticity, and temperature with respect to z are set to zero. The inlet and outlet boundaries are supposed to be remote from contraction plane to exclude the effect of the latter on the flow behavior in the vicinity of inlet and outlet sections. Along the axis of symmetry (Γ_4), the symmetry conditions are applied.
Consequently, the boundary conditions are written as follows:

$$\Gamma_1 : u = f_1(r), \quad \psi = \int_0^r urdr, \quad \omega = -\frac{\partial u}{\partial r}, \quad \theta = f_2(r), \quad z = 0, \quad 0 \le r \le \frac{R_2}{R_1};$$

$$\Gamma_2 : \psi = const, \quad \omega = -\frac{1}{r}\frac{\partial^2 \psi}{\partial r^2}, \quad \theta = 0, \quad r = \frac{R_2}{R_1}, \quad 0 \le z \le \frac{L_1}{R_1},$$

$$\psi = const, \quad \omega = -\frac{1}{r}\frac{\partial^2 \psi}{\partial z^2}, \quad \theta = 0, \quad 1 \le r \le \frac{R_2}{R_1}, \quad z = \frac{L_1}{R_1},$$

$$\psi = const, \quad \omega = -\frac{\partial^2 \psi}{\partial r^2}, \quad \theta = 0, \quad r = 1, \quad \frac{L_1}{R_1} \le z \le \frac{L_1}{R_1} + \frac{L_2}{R_1};$$

$$\Gamma_3 : \frac{\partial \psi}{\partial z} = 0, \quad \frac{\partial \omega}{\partial z} = 0, \quad \frac{\partial \theta}{\partial z} = 0, \quad z = \frac{L_1}{R_1} + \frac{L_2}{R_1};$$

$$\Gamma_4 : \psi = 0, \quad \omega = 0, \quad \frac{\partial \theta}{\partial r} = 0, \quad r = 0.$$

3 Method of Solution

During numerical simulation of the considered flow, an asymptotic time solution of the unsteady flow equations was obtained in order to yield a steady-state solution of the initial problem [20]. The finite-difference method based on the alternative directions scheme is used to implement the difference approximation for governing equations [21]. The obtained difference equations are solved by the sweep method [20].
A set of calculations was carried out on the sequence of square grids intended to validate the numerical algorithm and to verify the approximating convergence. Distributions of the axial velocity and temperature along contraction plane are presented at various grid steps (h) in Fig. 2. A resulting data analysis shows an approximating convergence of the method. The following calculations are implemented for a difference grid with h=0.025.

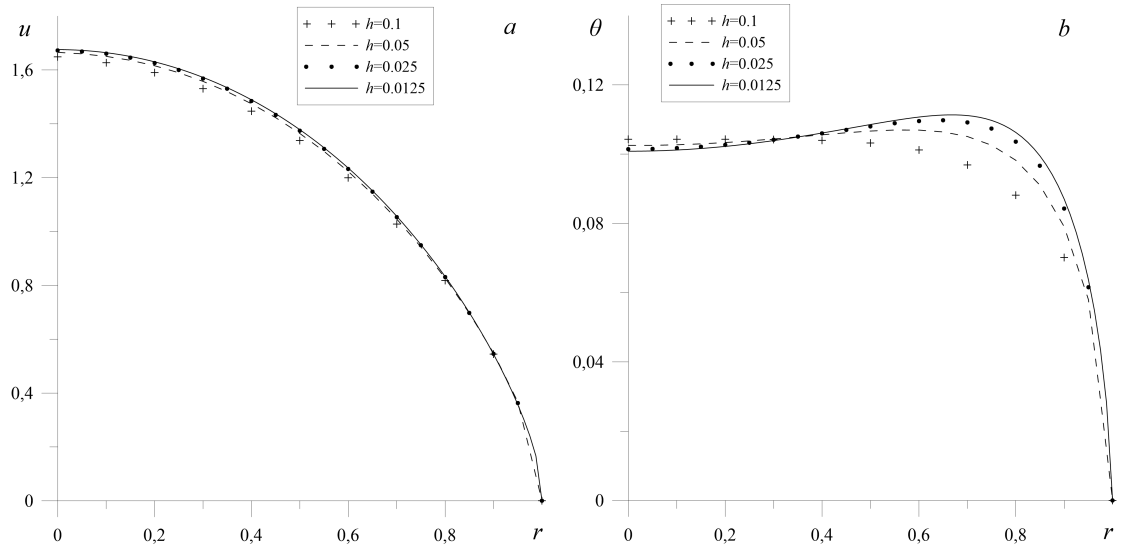

Figure 2: Distributions of the (a) velocity and (b) temperature along contraction plane at Re=1, Pe=100, n=0.8, and $\frac{R_2}{R_1}$=2

4 Results and Discussion

In the considered problem of the power-law fluid flow in a pipe with sudden contraction ($\frac{R_2}{R_1}$=2), the lengths of upstream and downstream pipes are assumed to be $\frac{L_1}{R_1}$=8 and $\frac{L_2}{R_1}$=40, respectively. Due to the fact that such flows are typically characterized by small Reynolds numbers, the value of Re is fixed at 1 in this work. The Brinkman number was stated to be Br=1, providing an existence of stable stationary solution. In general, the flow field observed in a pipe with sudden contraction consists of three distinct flow regions in both isothermal and non-isothermal cases. The first is a one-dimensional flow zone appearing near the inlet section, which is referred to as a fully developed flow and is recognized by the parallel to the wall streamlines (Fig. 3). The second is a two-dimensional flow zone occurring upstream and downstream of contraction plane including recirculating region at the corner. This zone is characterized by distortion of the streamlines towards the centerline as the contraction plane is approached. The extension of this region is strongly dependent upon the governing parameters such as Reynolds number, Peclet number, power-law index, and contraction ratio. As the downstream pipe is entered, the flow tends to reach the fully developed flow conditions, where the third (one-dimensional) zone appears.

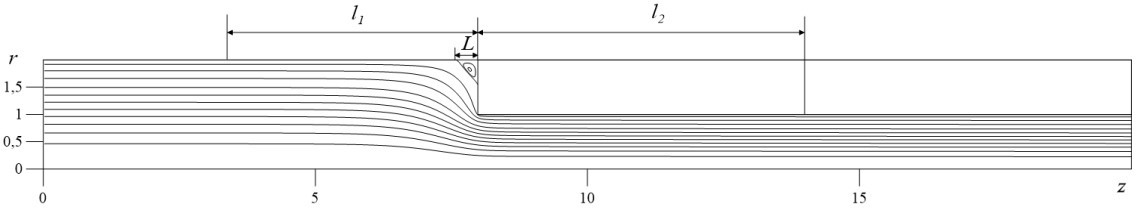

Figure 3: Non-isothermal flow pattern (Pe=100, n=0.8)

Based on the obtained flow pattern, the non-dimensional geometrical characteristics are imposed in order to implement a quantitative analysis of the flow. These are

the length of recirculating flow region (L), and the length of upstream (l_1) and downstream (l_2) two-dimensional flow zones (Fig. 3). Since the flow structure is strongly dependent upon rheology and temperature, it is of major interest to consider both isothermal and non-isothermal flow formation at varying power-law index. The results of parametric study revealing the effect of power-law index on the lengths of two-dimensional flow zones at various thermal conditions are presented in Table 1.

Table 10: The lengths of two-dimensional flow zones versus power-law index

	isothermal flow			non-isothermal flow (Pe=10)			non-isothermal flow (Pe=100)		
n	0.8	1.0	1.2	0.8	1.0	1.2	0.8	1.0	1.2
l_1	3.85	3.225	2.75	3.975	3.375	2.875	3.875	3.25	2.775
l_2	1.325	1.025	0.875	4.275	4.725	5.025	12.775	16.225	19.025
L	0.3811	0.4854	0.5955	0.3470	0.4162	0.4876	0.3963	0.4501	0.5589

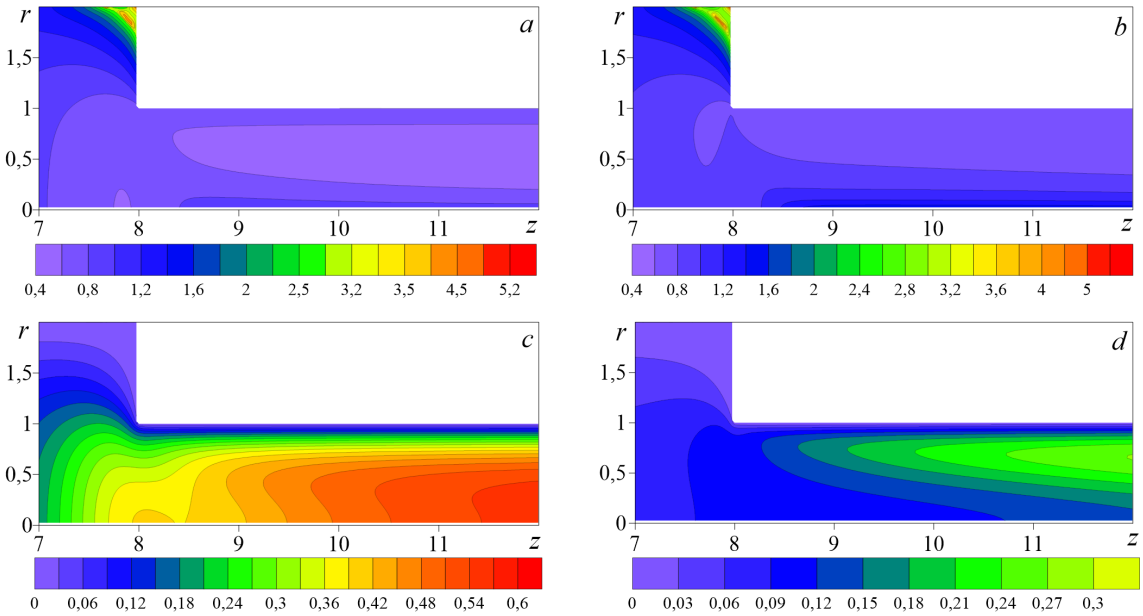

Figure 4: Distribution of the apparent viscosity (a,b) and temperature (c,d) in the vicinity of contraction plane at n=0.8: (a,c) Pe=10 and (b,d) Pe=100

Comparing isothermal and non-isothermal flows, the tendencies for l_1 and L are found to be similar, i.e. increasing power-law index leads to a decrease in the length of upstream two-dimensional flow zone and to an increase in recirculating flow region. However, behavior of the downstream two-dimensional flow zone is significantly affected by non-isothermality. The values of l_2 obtained for isothermal flow are different from those for non-isothermal flow: in the first case, l_2 is found to

decrease in size with increasing power-law index, and in the second case, an increase in l_2 is observed.
Figures 4,5 demonstrate the effect of power-law index and Peclet number on the apparent viscosity and temperature distribution in the immediate vicinity of contraction plane. It is evident that increase in Pe provides changes in the apparent viscosity and temperature fields, and those are more significant for the latter. An increased heat transfer due to convection (as compared to conduction) displaces the heated region towards outlet section and changes the temperature maximum in the flow field. Thus, the fully developed temperature distribution is reached at a certain distance from contraction plane, and this distance increases with higher Peclet number.

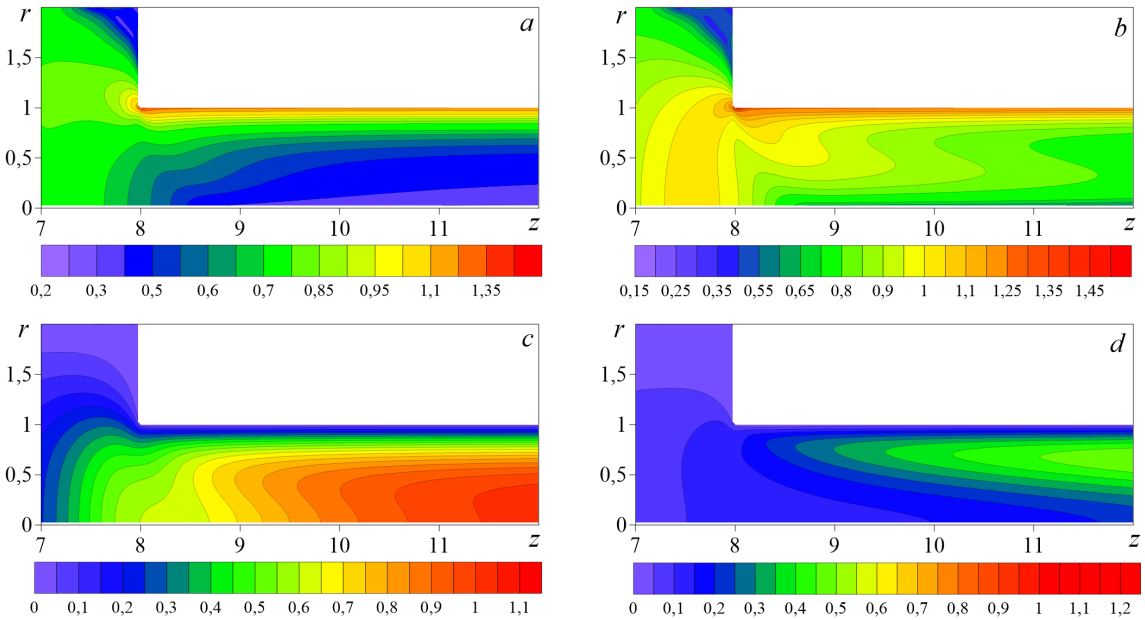

Figure 5: Distribution of the apparent viscosity (a,b) and temperature (c,d) in the vicinity of contraction plane at n=1.2: (a,c) Pe=10 and (b,d) Pe=100

5 Conclusion

A steady power-law fluid flow through an axisymmetric sudden contraction under non-isothermal conditions was numerically simulated using the finite-difference method. The flow kinematic characteristics such as the lengths of two-dimensional flow regions were obtained for shear-thinning, Newtonian, and shear thickening fluids, and compared with those determined in the isothermal case. It was revealed that the accounted heat generation due to viscous dissipation had little effect on the length of both recirculating region and upstream two-dimensional flow zone, and, in contrast, it provided a significant increase in the length of downstream two-dimensional flow zone, which enhanced with higher power-law index.
A parametric study was implemented in order to evaluate the impact of rheology and thermo-physical properties on the apparent viscosity distribution and heat transfer

behavior. An increase in the Peclet number was found to extend a distance from contraction plane to the region where the fully developed temperature distribution occurred.

Acknowledgements

This work was supported by the grant of the President of the Russian Federation (MK-710.2017.1) and the Russian Foundation for Basic Research (project no. 18-08-00412).

References

[1] White S.A., Gotsis A.D., Baird D.G. Review of the entry flow problem: experimental and numerical // J. Non-Newtonian Fluid Mech. 1987. V.24. P. 121-160.

[2] Boger D.V. Viscoelastic flows through contractions // Ann. Rev. Fluid Mech. 1987. V.19. P.157-182.

[3] Oliveira M.S.N., Oliveira P.J., Pinho F.T., Alves M.A. Effect of contraction ratio upon viscoelastic flow in contractions: The axisymmetric case // J. Non-Newtonian Fluid Mech. 2007. V.147. P. 92-108.

[4] Kfuri S.L.D., Silva J.Q., Soares E.J., Thompson R.L. Friction losses for power-law and viscoplastic materials in an entrance of a tube and an abrupt contraction // Journal of Petroleum Science and Engineering. 2011. V.76. P. 224-235.

[5] Borzenko E., Boyarkina K., Shrager G. Pressure losses of power-law fluid flow through an axisymmetric sudden contraction // Key Engineering Materials. 2016. V.685. P. 47-50. DOI: 10.4028/www.scientific.net/KEM.685.47.

[6] Borzenko E., Ryltseva K., Frolov O., Shrager G. Calculation of the local resistance coefficient of viscous incombressible fluid flow in a pipe with sudden contraction // Tomsk State University Journal of Mathematics and Mechanics. 2017. V.48. P. 36-48. DOI: 10.17223/19988621/48/4.

[7] Regirer S.A. Some thermohydrodynamic problems on a one-dimensional steady-state flow of viscous dropping liquid // Journal of Applied Mathematics and Mechanics. 1957. V.21. I.3. P. 424-430. (in Russian)

[8] Kaganov S.A. On a steady laminar flow of incompressible fluid in plane channel and round cylindrical tube with allowance for heat of friction and temperature dependence of viscosity // Journal of Applied Mechanics and Technical Physics. 1962. V.3. P. 96-99. (in Russian)

[9] Kearsley E.A. The viscous heating correction for viscometer flows // Trans. Soc. Rheol. 1962. V.6. P. 253-261. DOI: 10.1122/1.548925.

[10] Martin B. Some analytical solutions for viscometric flows of power-law fluids with heat generation and temperature dependent viscosity // Ind. J. Non-Linear Mech. 1967. V.2. I.4. P. 285-301. DOI: 10.1016/0020-7462(67)90001-7.

[11] Bostandzhiyan S.A., Merzhanov A.G., Khudyaev S.I. On the hydrodynamic thermal explosion // Dokl. Akad. Nauk SSSR. 1965. V.163. I.1. P. 133-136. (in Russian)

[12] Bostandzhiyan S.A., Chernyaeva S.M. On the hydrodynamic thermal explosion in a non-Newtonian fluid flow // Dokl. Akad. Nauk SSSR. 1966. V.170. I.2. P. 301-304. (in Russian)

[13] Petukhov B.S. Heat transfer and resistance in a laminar fluid flow in the pipes. Moscow: Energiya, 1967. 409 p. (in Russian)

[14] Froyshteter G.B., Danilevich S.Yu., Radionova N.V. Flow and heat transfer of non-Newtonian fluids in the pipes. Kiev: Naukova dumka, 1990. 216 p. (in Russian)

[15] Kutepov A.M., Polyanin A.D., Zapryanov Z.D. et al. Chemical Hydrodynamics: Handbook. Moscow: Byuro Kvantum, 1996. 336 p. (in Russian)

[16] Wachs A., Clermont J.-R. Non-isothermal viscoelastic flow computations in an axisymmetric contraction at high Weissenberg numbers by a finite volume method // J. Non-Newtonian Fluid Mech. 2000. V. 95. P. 147-184.

[17] Han X., Li X. An iterative stabilized CNBS-CG scheme for incompressible non-isothermal non-Newtonian fluid flow // International Journal of Heat and Mass Transfer. 2007. V.50. P. 847-856.

[18] Habla F., Woitalka A., Neuner S., Hinrichsen O. Development of a methodology for numerical simulation of non-isothermal viscoelastic fluid flows with application to axisymmetric 4:1 contraction flows // Chemical Engineering Journal. 2012. V. 207-208. P. 772-784.

[19] Yankov V.I., Boyarchenko V.I., Pervadchuk V.P. et al. Fiber-forming polymer processing. Fundaments of polymer rheology and polymer flows in channels. Izhevsk: Regulyarnaya i khaoticheskaya dinamika, 2008. 264p. (in Russian)

[20] Godunov S.K., Ryabenkiy V.S. Difference Schemes. North-Holland: Elsevier Science Ltd, 1987. 440p.

[21] Yanenko N.N. The Method of Fractional Steps: The Solution of Problems of Mathematical Physics in Several Variables. Springer-Verlag, 1971. 160p. DOI: 10.1007/978-3-642-65108-3.

Kira E. Ryltseva, National Research Tomsk State University, Lenin Ave. 36, Tomsk, Russian Federation
Oleg Yu. Frolov, National Research Tomsk State University, Lenin Ave. 36, Tomsk, Russian Federation

Gennady R. Shrager, National Research Tomsk State University, Lenin Ave. 36, Tomsk, Russian Federation

Mathematical Model of Micropolar Elastic Thin Beams with Constrained Rotations and The Finite Element Method

Samvel H. Sargsyan, Knarik A. Zhamakochyan
sargsyan@yahoo.com

Abstract

In this paper hypotheses are accepted, which adequately replace properties of asymptotic solution of boundary-value problem of plane stress state of micropolar theory of elasticity with constrained rotation in thin two-dimensional region. On the basis of them applied model of bending deformation of thin beams is constructed. The appropriate algorithm of the finite element method is developed for solving boundary problems of statics and free oscillations of bending deformation of micropolar elastic thin beams with constrained rotation. On the basis of the analysis of the numerical results effective properties of the micropolarity of the material are established compared to the classical case.

1 Introduction

The question of mathematical modeling of an object [1] generates a clear action plan. It can be conditionally divided into three stages: model-algorithm-program.
This paper relates to the mathematical modeling of bending deformation of elastic thin beam in the formulation of the moment theory of elasticity with constrained rotation and with consideration of transverse shear strains, also to the development of the finite element method for solving applied problems in this field.
In the first part of the paper previously accepted approach approach [2-4] is developed and based on the equations of the plane problem of the moment theory of elasticity with constrained rotation [5] an applied model of bending deformation of thin beam is constructed with the derivation of the formula for the density of the potential energy of deformation.
The finite element method (FEM), which is closely connected to a personal computer and completely corresponds to it, is very popular now among the numerical methods. The main functional For FEM in the form of displacements is the total potential energy of the system [6,7].
In the second part of the paper an FEM is developed for solving concrete problems of determination the stress-strain state of the bending deformation of micropolar elastic thin beams with constrained rotation, which is realized on a personal computer.

2 Problem statement

An isotropic micropolar elastic parallelepiped of constant height $2h$, length a and thickness $2h_1 = 1$ is considered. The coordinate plane x_1x_3 is placed in the middle plane of the parallelepiped. The axis x_3 is directed along the height and x_1-along the length of the parallelepiped, which divides the height $2h$ in half. It is assumed that plane stress state is realized in direction of the axis x_2. Basic equations of the generalized plane stress state of micropolar theory of elasticity with constrained rotation are given in paper [5].

Our aim is to construct an applied (one-dimensional) model of bending deformation of thin beam with transverse shear deformations, taking the equations of the two-dimensional theory of the generalized plane stress state of micropolar elasticity with constrained rotation as a basis, with application of the already developed [2-4] approach.

The description of the law of the change of displacements and rotation along the beam's thickness is taken to be linear[2]:

$$V_3 = w(x_1), \;\; V_1 = x_3\psi_1(x_1), \;\; \omega_2 = \Omega_2(x_1). \tag{1.1}$$

In papers [2-4] the kinematic hypothesis (1.1) is called Timoshenko's generalized hypothesis for the micropolar case (since the formulas for displacements in (1.1) coincide with the formulas of Timoshenko's kinematic hypothesis [8] in the classical theory of elasticity).

In the micropolar theory of elasticity with constrained rotation, the rotations of body particles are expressed through displacements as in the classical theory of elasticity ($\overrightarrow{\omega} = \frac{1}{2} rot \overrightarrow{V}$), so that in this case we will have:

$$\omega_2 = \Omega_2(x_1) = \frac{1}{2}(\psi_1 - \frac{dw}{dx_1}). \tag{1.2}$$

Besides the kinematic hypothesis (1.1), static hypotheses were developed in paper [2] to reduce two-dimensional problem to one-dimensional one.

On the basis of these hypotheses one-dimensional model (applied model) of the bending deformation of micropolar elastic thin beams with constrained rotation will be obtained from the above mentioned two-dimensional theory:

Equilibrium equations(motion)

$$\frac{\partial N_{13}}{\partial x_1} = -2q(+2\rho h\frac{\partial^2 w}{\partial t^2}),$$

$$\frac{\partial M_{11}}{\partial x_1} - N_{31} = -h \cdot 2q_1(+\frac{2\rho h^3}{3}\frac{\partial^2 \psi_1}{\partial t^2}),$$

$$\frac{\partial L_{12}}{\partial x_1} + N_{31} - N_{13} = -2m_3(+2Jh\frac{\partial^2 \Omega_2}{\partial t^2}). \tag{1.3}$$

Elasticity relations

$$N_{13} + N_{31} = 4h\mu\Gamma_{13},$$

$$M_{11} = \frac{2Eh^3}{3}K_{11}, \;\; L_{12} = 2Bhk_{12}. \tag{1.4}$$

Geometrical relations

$$\Gamma_{13} = \frac{\partial w}{\partial x_1} + \psi_1, \;\; K_{11} = \frac{\partial \psi_1}{\partial x_1},$$

$$k_{12} = \frac{\partial \Omega_2}{\partial x_1}, \;\; \Omega_2 = \frac{1}{2}(\psi_1 - \frac{\partial w}{\partial x_1}). \tag{1.5}$$

Here N_{13}, N_{31} are averaged forces along the beam thickness; M_{11}, L_{12} are averaged moments of power stress σ_{11} and moment stress μ_{12} along the beam thickness; Γ_{13} is shear deformation; K_{11} is beam axis bending (connected with transfer moment M_{11}), and k_{12} is beam axis bending (connected with transfer moment L_{12}); $2q$ is intensity of the load distributed normally to the beam axis; $2q_1$ is intensity of the load distributed parallel to the beam axis; $2m_3$ is intensity of external moment; E and μ are classical modules of elasticity and shear of beam material; B is new elastic constant of beam micropolar material.

Boundary conditions on the edge (on $x_1 = 0$ or $x_1 = a$) of the beam are the followings:

$$M_{11} = M_{11}^*, \;\; \text{or} \;\; \psi_1 = \psi_1^*,$$

$$N_{13} = N_{31}^*, \;\; \text{or} \;\; w = w^*,$$

$$L_{12} = L_{12}^*, \;\; \text{or} \;\; \Omega_2 = \Omega_2^*. \tag{1.6}$$

General form of the total potential energy functional of the system is expressed as follows:

$$U = \int_0^a (W - 2q_1 h\psi_1 - 2qw - 2m_3\Omega_2)\, dx_1 -$$

$$- \left((M_{11}\psi_1 + N_{13}w + L_{12}\Omega_2)_{x_1=a} - (M_{11}\psi_1 + N_{13}w + L_{12}\Omega_2)_{x_1=0}\right), \tag{1.7}$$

where

$$W = E\frac{h^3}{3}K_{11}^2 + h\mu\Gamma_{13}^2 + Bhk_{12}^2\,. \tag{1.8}$$

W is linear density of deformation potential energy of micropolar beam during the bending (Ω_2 expressed by formula (1.2)).

Minimizing the functional (1.7) basic differential equations (1.3)-(1.5) and natural boundary conditions (1.6) will be obtained for bending deformation of micropolar beam.

3 Stiffness matrix of finite element of micropolar beam

Let's consider determination of stiffness matrix of micropolar beam finite element.

Following expansions in the form of cubic polynomials are chosen for deflection w, complete rotation ψ_1 of normal element:

$$w(x_1) = a_0 + a_1 x_1 + a_2 x_1^2 + a_3 x_1^3,$$
$$\psi_1(x_1) = b_0 + b_1 x_1 + b_2 x_1^2 + b_3 x_1^3. \tag{2.1}$$

Here a_i, b_i are coefficients, which are expressed with the help of nodal displacements and rotations. Nodal displacements are denoted as follows:

$$w(0) = \delta_1,\ w'(0) = \delta_2,\ \psi_1(0) = \delta_3,\ \psi_1'(0) = \delta_4,$$
$$w(a) = \delta_5,\ w'(a) = \delta_6,\ \psi_1(a) = \delta_7,\ \psi_1'(a) = \delta_8,\ . \tag{2.2}$$

As we can see above mentioned finite element has eight degrees of independence. Substituting (2.1) into (2.2), coefficients a_i, b_i will be expressed with the help of nodal displacements and rotations δ_k. Substituting a_i, b_i into (2.1), we obtain following approximations for displacements and rotations.

$$w(x_1) = \sum_{i=1,2,5,6} \delta_i N_i(x_1),$$
$$\psi_1(x_1) = \sum_{i=3,4,7,8} \delta_i N_i(x_1), \tag{2.3}$$

here $N_i(x)$ are form functions of the element:

$$N_1 = N_3 = 1 - \frac{3}{a^2}x_1^2 + \frac{2}{a^3}x_1^3,\ N_2 = N_4 = x_1 - \frac{2}{a}x_1^2 + \frac{1}{a^2}x_1^3,$$
$$N_5 = N_7 = \frac{3}{a^2}x_1^2 - \frac{2}{a^3}x_1^3,\ N_6 = N_8 = -\frac{1}{a}x_1^2 + \frac{1}{a^2}x_1^3. \tag{2.4}$$

Substituting (2.3) into functional (1.7), after integration we obtain function of eight independent variables $\delta_1, \delta_2, \delta_3, \delta_4, \delta_5, \delta_6, \delta_7, \delta_8$. The minimization of functional (1.7) reduces to the determination of the minimum of function of eight independent variables:

$$\frac{\partial U}{\partial \delta_k} = 0 \quad (k = 1, 2, 3, \ldots, 8).$$

Calculating corresponding partial derivatives, we obtain system of linear algebraic equations:

$$[K] \cdot \{\delta\} = \{P\}. \tag{2.5}$$

Here K is stiffness matrix of element with size 8×8, which is the most important concept of the finite element method; $\{\delta\}^T = \{\delta_1, \delta_2, \delta_3, \delta_4, \delta_5, \delta_6, \delta_7, \delta_8\}$ is vector of nodal displacements and rotations; $\{P\}^T$ is vector concentrated nodal forces and moments.

Expressions for the elements of the stiffness matrix of a finite element are introduced below:

$$K_{11} = -K_{15} = K_{55} = \frac{6h(5B + 2a^2\mu)}{5a^3},$$
$$K_{12} = K_{16} = -K_{25} = -K_{76} = \frac{3Bh}{a^2} + \frac{h\mu}{5},$$

$$K_{13} = K_{17} = -K_{35} = -K_{57} = -h\mu,$$

$$K_{14} = -K_{18} = -K_{23} = K_{27} = K_{36} = -K_{45} = K_{58} = -K_{67} = \frac{Bh}{2a} - \frac{ha\mu}{5},$$

$$K_{22} = K_{66} = \frac{2Bh}{a} + \frac{4ah\mu}{15}, \quad K_{24} = K_{68} = \frac{Bh}{4}, \quad K_{26} = \frac{Bh}{a} - \frac{ha\mu}{15},$$

$$K_{28} = -K_{46} = -\frac{Bh}{4} + \frac{a^2h\mu}{30}, \quad K_{33} = K_{77} = \frac{h(21B + 26a^2\mu + 28h^2E)}{35a},$$

$$K_{34} = -K_{78} = \frac{h(21B + 44a^2\mu + 28h^2E)}{420},$$

$$K_{37} = \frac{h(-21B + 9a^2\mu - 28h^2E)}{35a},$$

$$K_{38} = -K_{47} = \frac{h(21B - 26a^2\mu + 28h^2E)}{420},$$

$$K_{44} = K_{88} = \frac{ah(21B + 6a^2\mu + 28h^2E)}{315},$$

$$K_{48} = -\frac{ah(21B + 18a^2\mu + 28h^2E)}{1260}.$$

4 Model calculation of micropolar elastic beams with constrained rotation for the static problem

As an example we'll consider problem of the bending of the beam when evenly distributed load with intensity q is acting along the axis x_1 (in this case $q_1 = 0, q \neq 0, m_3 = 0$) and the edges are hinged-supported. Boundary conditions for hinged supported beam are follows:

$$w = 0, \quad M_{11} = 0, \quad L_{12} = 0, \quad \text{on} \quad x_1 = 0; a. \tag{3.1}$$

We obtain following expression for functional (1.7) with consideration of (3.1):

$$U = \int_0^a (W - 2qw)dx_1.$$

After the constructing of the stiffness matrix K, the vector of equivalent nodal forces and moments P, with consideration of the boundary conditions (3.1), we form a system of linear algebraic equations (2.5) corresponding to the considered problem for different numbers of dividing the beam into finite elements.

We consider the case when the beam is divided into two finite elements. Numerical results (maximum deflection) of the calculation are given for the case, when the physical constants have following values: $\mu = 0,75MPa$, $E = 191MPa$, $B = 1000N$, load is $q = 0,5 \cdot 10^3 Pa$, and geometrical dimensions of the beam are the followings: $a = 8mm$, $h = 0.2mm$ (we also introduce the result for classical theory of elastic thin beam, when it is bent).

As can be seen from the given values of Table 1, the micropolarity of the material of the beam increases the stiffness of the beam compared with the classical case of the material.

Table 11: The maximum deflection of micropolar and classical beam.

	Micropolar beam			Classical beam			
w_{max}	Exact value	2 finite elements	4 finite elements	Exact value	2 finite elements	4 finite elements	$\frac{w_{max}^{cl}-w_{max}^{mic}}{w_{max}^{cl}}$
(m)	$2,86 \cdot 10^{-8}$	$2,59 \cdot 10^{-8}$	$2,77 \cdot 10^{-8}$	$4 \cdot 10^{-8}$	$3,62 \cdot 10^{-8}$	$3,86 \cdot 10^{-8}$	0,285

5 Dynamic problem of a micropolar elastic beam with constrained rotation

The general form of the functional of the total mechanical energy (the sum of the potential energy of deformation and kinetic energy) of a micropolar-elastic beam for bending deformation is expressed as follows:

$$\widetilde{U} = \int_0^a (W + \rho h \frac{\partial^2 w}{\partial t^2} \cdot w + \frac{\rho h^3}{3} \frac{\partial^2 \psi_1}{\partial t^2} \cdot \psi_1 + Jh \frac{\partial^2 \Omega_2}{\partial t^2} \cdot \Omega_2) dx_1. \tag{4.1}$$

In case of free oscillations the main kinematic functions of the problem are introduced in this way:

$$\begin{aligned} w(x_1, t) &= (a_0 + a_1 x_1 + a_2 x_1^2 + a_3 x_1^3) \sin \omega t, \\ \psi_1(x_1, t) &= (b_0 + b_1 x_1 + b_2 x_1^2 + b_3 x_1^3) \sin \omega t, \end{aligned} \tag{4.2}$$

where ω is frequency of the natural oscillation.
Substituting (4.2) into (4.1), the problem of minimizing the functional (4.1) is reduced to the obtaining of the minimum of the function of eight independent variables ($\frac{\partial U}{\partial \delta_k} = 0, k = 1, 2, 3, ...8$).
Calculating the corresponding partial derivatives, we obtain the following matrix equation:

$$(K - \omega^2 M) \cdot \{\delta\} = 0, \tag{4.3}$$

where K is stiffness matrix of finite element, M is the matrix of masses of a finite element.
Expressions for the elements of the matrix of masses of the finite element are introduced below:

$$M_{11} = M_{55} = \frac{3hJ}{5a} + \frac{26ha\rho}{35}, \quad M_{12} = -M_{56} = \frac{hJ}{20} + \frac{11ha^2\rho}{105},$$

$$M_{13} = M_{17} = -M_{35} = -M_{57} = \frac{hJ}{4},$$

$$M_{14} = -M_{18} = -M_{23} = M_{27} = M_{36} = -M_{45} = M_{58} = -M_{67} = \frac{ahJ}{20},$$

$$M_{15} = -\frac{3hJ}{5a} + \frac{9}{35}ah\rho, \quad M_{16} = -M_{25} = \frac{h(21J - 26a^2\rho)}{420},$$

$$M_{22} = M_{66} = \frac{h(7aJ + 2a^3\rho)}{105}, \quad M_{24} = M_{68} = 0,$$

$$M_{26} = \frac{h(-14aJ - 12a^3\rho)}{840}, \;\; M_{28} = -M_{46} = -\frac{a^2hJ}{120},$$

$$M_{33} = M_{77} = \frac{13}{210}ah(3J + 4h^2\rho), \;\; M_{34} = -M_{78} = 11a^2h(\frac{J}{420} + \frac{h^2\rho}{315}),$$

$$M_{37} = \frac{3}{140}ah(3J + 4h^2\rho), \;\; M_{38} = -M_{47} = -\frac{13}{2520}a^2h(3J + 4h^2\rho),$$

$$M_{44} = M_{88} = \frac{ha^3J}{210} + \frac{2}{315}h^3a^3\rho, \;\; M_{48} = -\frac{3ha^3J}{840} - \frac{1}{210}h^3a^3\rho.$$

We formulate the equation to determine the frequencies of free oscillations:

$$|K^{-1}M - \frac{1}{\omega^2}E| = 0.$$

The results of numerical calculations (when the beam is divided into two finite elements) we given for the case, when physical constants of the beam have the values of the previous problem, and $\rho = 7700kg/m^3$, $J = 5,3 \cdot 10^{-6}kg/m$.

Table 12: The lowest frequency of free oscillation ω.

		Micropolar beam(sec^{-1})		Classical beam(sec^{-1})	
$a(m)$	$h(m)$	Exact value	2 finite elements	Exact value	2 finite elements
$8{\cdot}10^{-3}$	$0,2 \cdot 10^{-3}$	$0,848 \cdot 10^5$	$0,849 \cdot 10^5$	$0,7181 \cdot 10^5$	$0,7184 \cdot 10^5$
10^{-7}	$0,5 \cdot 10^{-9}$	$0,1965{\cdot}10^{11}$	$0,1969{\cdot}10^{11}$	$0,1404{\cdot}10^{10}$	$0,1408{\cdot}10^{10}$
10^{-8}	$0,5{\cdot}10^{-10}$	$0,1965{\cdot}10^{12}$	$0,1969{\cdot}10^{12}$	$0,1404{\cdot}10^{11}$	$0,1408{\cdot}10^{11}$

As can be seen from the tables above, the micropolarity of the beam material increases the frequency of oscillations, and in the nanosized region, the frequencies are in the terahertz range.

Acknowledgements

This work was supported by the RA MES State Committee of Science, in the frames of the research project e 15T-2C138.

References

[1] Samarskii A. A., Mikhailov A.P. Mathematical modeling. M.: Physmathlit. 2005. 320 p. (in Russian)

[2] Sargsyan S. H. Effective Manifestations of Characteristics of Strength and Rigidity of Micropolar Elastic Thin Bars // Journal of Materials Science and Engineering. 2012. V. 2. No 1. P. 98-108.

[3] Sargsyan S. H. Mathematical model of micropolar elastic thin plates and their strength and stiffness characteristics// Journal of Applied Mechanics and Technical Physics. 2012. V. 53. No 2. P. 275-282.

[4] Sargsyan S. H. General Theory of Micropolyar Elastic Thin Shells// Physical Mesomechanics. 2011. V. 14. No 1. P. 55-66. (in Russian)

[5] Nowacki W. Theory of asymmetric elasticity. Oxford, etc.: Pergamon-Press. 1986. 383 p.

[6] Trushin S. I. Finite Element Method. Theory and problems M.: Publishing House of the Association of constructional Universities. 2008. 256 p.(in Russian)

[7] Samogin Yu. N., Khromatov V. Ye., Chirkov V. P. The finite element method in problems of material resistance. M.: Physmathlit. 2012. 200 p.(in Russian)

[8] Timoshenko S. P. Oscillations in engineering. M.: Nauka. 1967. 444 p.(in Russian)

Samvel H. Sargsyan, Sayat Nova str. 2/11, Gyumri, Armenia
Knarik A. Zhamakochyan, Hakobyan str. 50, Gyumri, Armenia

Thermo-electro-mechanical modeling of thermal fatigue failure process of corset samples from single-crystal nickel superalloys

Artem V. Savikovskii, Artem S. Semenov, Leonid B. Getsov
temachess@yandex.ru

Abstract

The results of computations of the thermal and stress-strain state of single-crystal corset specimens subjected to the action of periodic electric current, leading to variable inhomogeneous heating and subsequent thermal fatigue failure, are presented. The influence of maximum value and range of temperature and also delay time at the maximum temperature on the number of cycles before the macrocrack formation is investigated. Comparison of the computational results with the experimental data for various single-crystal nickel-based superalloys showed a good accuracy.

1 Introduction

Single-crystal nickel-based superalloys [1] are widely used for the manufacture of nozzle and working blades of gas turbine engines (GTE). The thermal-fatigue strength of such materials with a pronounced anisotropy and a sensitivity of mechanical properties to the temperature is currently not fully studied. For the investigation of thermal fatigue durability under a wide range of temperatures with and without intermediate delays the experiments are carried out on different types of samples, including corset (plane) specimen on the installation developed in NPO CKTI [2] (see Fig. 1 a). Fixed in axial direction by means of two bolts with a massive foundation the corset sample (see Fig. 1 b) is heated periodically by passing electric current through it. During cycling the maximum and minimum temperatures are automatically maintained constant.

The objective of the study is to determinate numerically the thermal and stress-strain states of the corselet specimens under cyclic electric loading and to study systematically the effect of delay at maximum temperature on the thermal fatigue durability on the base of the deformation criterion [3, 4, 5] of thermal-fatigue failure for single crystal superalloys using the results of finite element (FE) simulation of full-scale experiments. The results of simulation and their verification are obtained for the different single-crystal nickel-based superalloys: VZhM4, VIN3 and ZhS32.

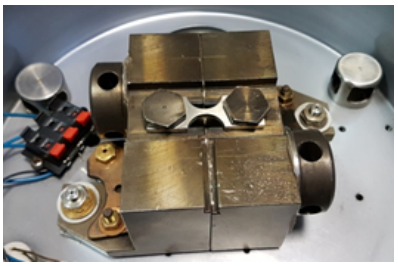
a)

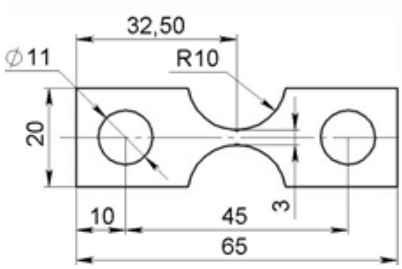

b)

Figure 1: a) Installation for carrying out experiments on thermal fatigue, b) Geometry corset sample for thermal fatigue experiment.

2 Results of thermo-electric analysis

Modeling of heating process in the corset samples was carried in the FE program ANSYS with taking into account the temperature dependence of all material properties, nonstationary Joule heating, the convective heat exchange and radiative heat transfer between the sample and the environment. The full-scale FE model of experimentation object including discrete models of the specimen and the setup is presented in Fig. 2.

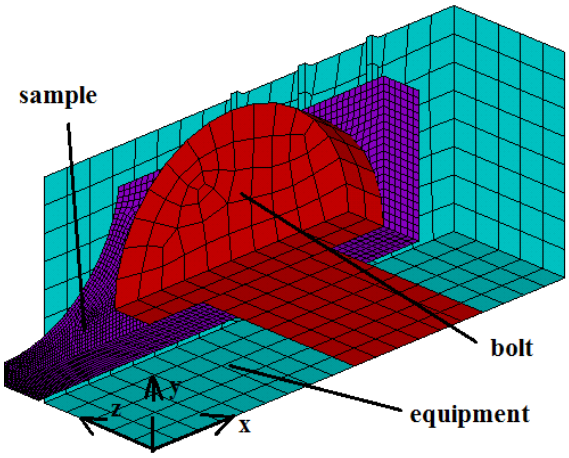

Figure 2: Finite-element model for thermoelectric problem.

Modeling of heating processes and thermal fatigue fracture of sample was carried out for four temperature regimes (modes): $150 \div 900$, $250 \div 1000$, $500 \div 1050$ and $700 \div 1050°C$. The used in FE simulations material properties for the single crystal nickel superalloy sample and for the steel equipment were taken from literature [6], [13, 14, 15] (see also Table 1). While specifying the properties of nickel alloy and steel the implementation of the Wiedemann-FranzвГЄs law was controlled: $\lambda\rho_e =$ LT, where λ is the thermal conductivity,ρ_e is the specific electrical resistance, T is the temperature in K, $L = 2.22 \cdot 10^{-8} W\Omega K^{-2}$ is the *Lorentz's* constant.

Table 1. Thermo-electric properties of nickel superalloy used in FE simulations.

T	$°C$	20	200	400	800	1000	1150	Ref.
ρ	$\frac{kg}{m^3}$	8550	8500	8450	8350	8330	8310	[13]
C_ρ	$\frac{J}{kg \cdot K}$	440	520	520	575	590	600	[13]
λ	$\frac{W}{m \cdot K}$	7.4	11.2	14.1	19.8	26.7	36.7	[6]
ρ_e	$\Omega \cdot m$	$8.7 \cdot 10^{-7}$	$9.3 \cdot 10^{-7}$	$1.1 \cdot 10^{-6}$	$1.2 \cdot 10^{-6}$	$1 \cdot 10^{-6}$	$8.9 \cdot 10^{-7}$	[6]

The coupled three-dimensional transient thermo-electrical analysis has been performed. Due to the symmetry in respect to the xz and yz planes, a quarter of the structure was considered. The thermal and electric contacts between the sample and bolts, between the sample and the foundation were taken into account. The initial temperature for the sample and the equipment was set to 30 $°C$. For the free surface of sample the boundary condition of convective heat transfer is used:

$$q_n = h(T - T_0), \tag{1}$$

where n is the normal to body, q_n is the heat flux density, $h = 20\frac{W}{m^2 K}$ is the coefficient of convective heattransfer, T_0 is the ambient temperature. The condition of radiative heat transfer was also set on the surfaces of central (high temperature) part of the sample (10 mm length):

$$q_n = \varepsilon \sigma_{SB}(T^4 - {T_0}^4), \tag{2}$$

where $\varepsilon = 0.8$ is the black factor of the body, $\sigma_{SB} = 5.67 \cdot 10^{-8} W m^{-2} K^{-4}$ is the coefficient of Stefan-Boltzmann.
The temperature field distribution in the VZhM4 sample is shown in Fig. 3a for the loading regime with $T_{max} = 1050°C$. Note that the solution of thermo-electric problem has been obtained for the complete FE model shown in Fig. 2 with taking into account the equipment.The evolution of temperature spatial-distribution is given in Fig. 3b (x is a distance from the sample center). The bell-form of the curve is keeping during whole heating process.

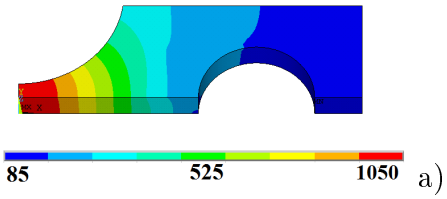

a)

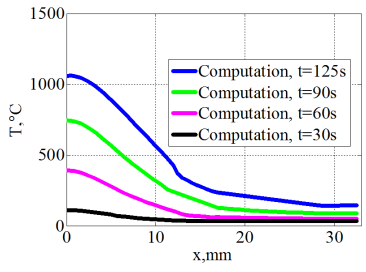

b)

Figure 3: a) Temperature field distributions in VZhM4 sample by heating for regime with $T_{max} = 900°C$, b) Evolution of temperature distribution along the VZhM4 sample axis for different heating times.

The comparison of FE results with experimental data for axial temperature distribution demonstrates a good agreement for the all considered loading regimes (see, for example, Fig. 4).

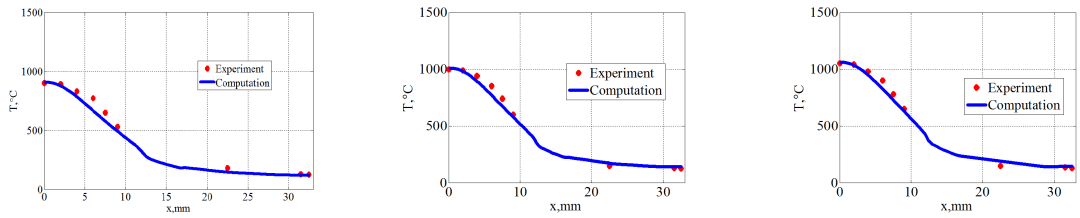

Figure 4: Comparison of computational results with experimental data for axial temperature distributions in VZhM4 sample for regimes with: a) $T_{max} = 900°C$,b) $T_{max} = 1000°C$, c) $T_{max} = 1050°C$

3 Results of thermo-elasto-visco-plastic analysis

The obtained in thermo-electric problem the spatial and temporal distribution of the temperature field is the base for the strain and stress field computation within the framework of thermo-elasto-visco-plastic problem solution.
The fixing of sample under heating leads to the high stress level and inelastic strain appearance. The local strain and stress concentration is observed in the central (working) part of sample. The FE simulation is required for the computation of inhomogeneous stress and inelastic strain fields. Modeling of inelastic deformation in the corset samples has been performed with taking into account of the temperature dependence of all material properties, anisotropy of mechanical properties of single crystal sample, kinematic hardening, inhomogeneous nonstationary temperature field, mechanical contacts bolt/specimen and specimen/foundation, friction between the contact surfaces, temperature expansion in the specimen, bolt and foundation. The two FE formulations for the thermo-mechanical problem have been considered:

- with taking into account of equipment;
- without taking into account equipment (simplified formulation [7] for the sample only).

Using the second formulation provides significant saving computational time due to reduction in the number of degrees of freedom and refusal to solve a contact problem that is very actual for the numerous multivariant computations for different regimes of loading and the crystallographic orientations. One of the aims of the investigations was the selection of the equivalent (effective) length of the sample for the simplified formulation. The validity of the simplified formulation is based on the comparison with the results of full-scale formulation (with taking into account equipment), as well as on the comparison with the relative displacements of two markers measured in experiments.
In the general case there is no symmetry in the problem (see Fig.4 a) due to anisotropy of mechanical properties of single crystal sample. However in the important for practice case of [001] crystallographic orientation of sample the symmetry in respect to planes xz and yz (see Fig.4 b) can be introduced. Equipment and bolts were modeled by linear elastic material (steel), and for the sample the elasto-viscoвГУplastic model of the material was used.

The problem was solved in a three-dimensional, quasi-static formulation. As boundary conditions the symmetry conditions were set: zero displacements on the y-axis on the xz plane and zero displacements on the x-axis on the yz plane. On the lower side of the equipment zero displacements along the x and z axes were set. On the bolt cap the pressure of 100 MPa has been applied that is equivalent to the tightening force of the bolt. The mechanical properties for the alloys VZhM4 and VIN3 were taken from the papers [11, 12] and for ZhS32 from [2] (see Table 2 for details). The mechanical properties of bolts are taken for pearlitic steel [13].

Table 2. Mechanical properties of VZhM4 used in simulations [11]:

T	$^{\circ}C$	20	700	900	1000	1050
E_{001}	MPa	130000	96000	91000	86000	82000
ν	-	0.39	0.422	0.425	0.428	0.43
α	1/K	$1.1 \cdot 10^{-5}$	$1.7 \cdot 10^{-5}$	$1.9 \cdot 10^{-5}$	$2.1 \cdot 10^{-5}$	$2.3 \cdot 10^{-5}$
${\sigma_Y}^{001}$	MPa	846	950	-	-	820
n	-	8	8	8	8	8
A	$MPA^{-n}c^{-1}$	$1 \cdot 10^{-42}$	$1 \cdot 10^{-29}$	$1 \cdot 10^{-28}$	$2 \cdot 10^{-27}$	$1 \cdot 10^{-26}$

In simplified formulation (see Fig. 5 d) we consider only the sample without equipment, in which zero displacements on the symmetry planes xz and yz were set, the outer face of the sample parallel to the symmetry plane xz was fixed in the direction of the axis x. To exclude solid body motions, a number of points on this face were also fixed in the direction of the y and z axes.

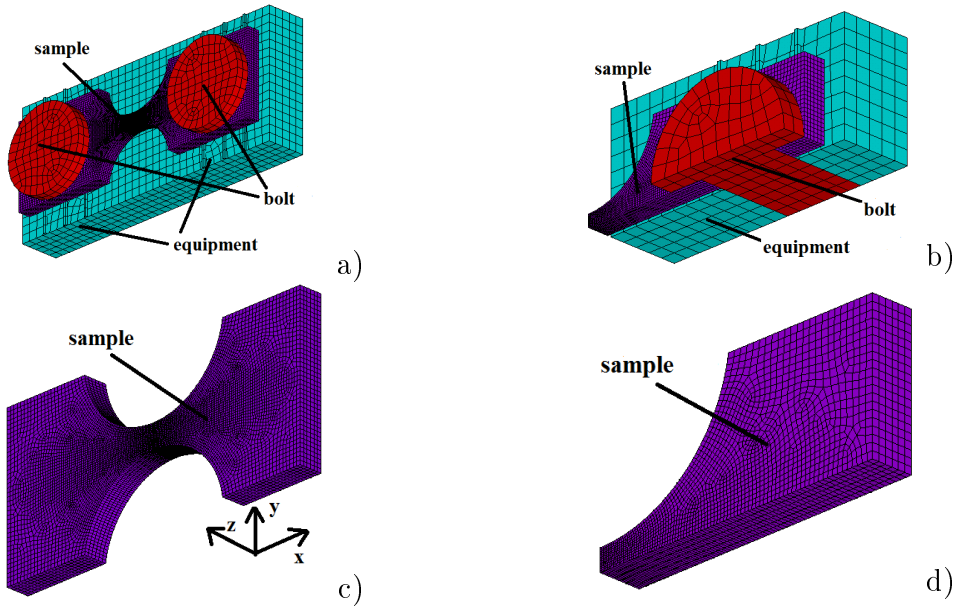

Figure 5: Finite-element models in mechanical problem: a) complete model (sample/bolt/equipment) without symmetry account, b) complete model (sample/bolt/equipment) with symmetry account, c) simplified model (sample only) without symmetry account, d) simplified model (sample only) with symmetry account.

Fig. 6 shows distributions of plastic strain intensity for nickel superalloys and three temperature modes after 7 cycles for thermoplasticity problem in ANSYS

(for VZHM4 and VIN3 the length of the sample is 42 mm, for ZHS32 is 50 mm).

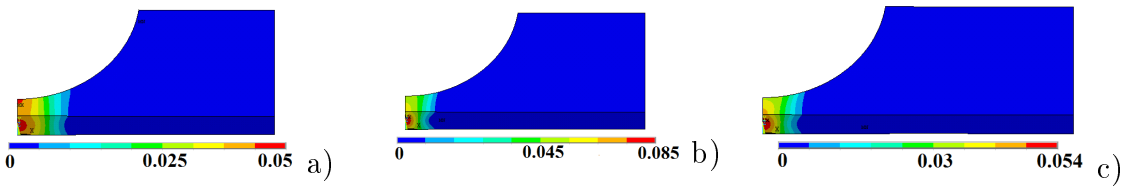

Figure 6: Distributions of plastic strain intensity for a) superalloy VZhM4, mode $700 \div 1050°C$; b) superalloy VIN3, mode $500 \div 1050°C$; c) superalloy ZhS32, mode $150 \div 900°C$ after 7 cycles.

The Table 6 shows the equivalent (effective) length of the sample for the simplified formulation, which has been found from the condition of equality of the inelastic strain ranges with complete model for different alloys. In the FE simulations with acceptable engineering accuracy can be used the value 40 mm. Effective length takes into account the compliance of equipment and its variation in considered range has no appreciable on the results.

Table 6. The equivalent length of the corset sample for different alloys.

VZhM4	VIN3	ZhS32
34-42 mm	38-46 mm	40-52 mm

4 Influence of delay on the thermal fatigue durability

Simulations of inelastic cyclic deformation of corset samples were performed by means of the FE program PANTOCRATOR [8], which allows to use the micromechanical (physical) models of plasticity and creep for single crystals [9, 10]. The Norton power-type law without hardening was applied to describe creep properties. The micromechanical plasticity model accounting 12 octahedral slip systems with lateral and nonlinear kinematic hardening [9] was used in the FE computation for single crystal alloy.

FE computations were carried out for a part of a corset sample (simplified FE model with effective length of sample equal 40 mm, see Fig. 7a.

The influence of the delay at maximum temperature on the number of cycles to the formation of macro cracks is analyzed in the range from 1 min to 1 hour for the cyclic loading regimes (see, for example, Fig. 7b) with:

- maximum temperature of $1000°C$ and a temperature range of $350°C$ and $550°C$;
- maximum temperature of $1000°C$ and a temperature range of $750°C$;
- maximum temperature of $900°C$ and a temperature range of $750°C$.

The heating times in the cycle were 7s, 25s, 18 s and 28s, the cooling time was 15s, 17s, 40s and 52s for VZhM4. The heating time in the cycle was 25 s, the cooling

time was 17s for VIN3. The heating times in the cycle was 25 s and 15s, the cooling time was 15s and 75s for ZhS32. The mechanical properties for the alloys VZhM4 and VIN3 were taken from the papers [11, 12] and for ZhS32 from [2].

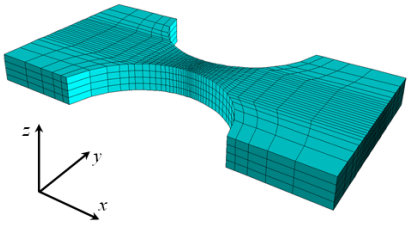

a)

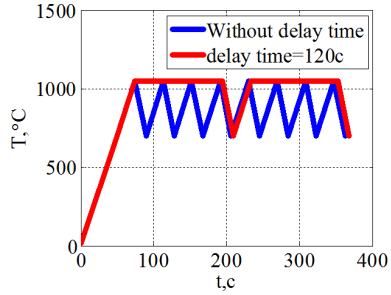

b)

Figure 7: a) Finite element model of sample (simplified formulation) for analysis of delay influence;b) temperature evolutions in central point of sample with and without delay for temperature regime 700-1050 $°C$

Damage calculation and estimation of the number of cycles before the formation of macrocracks were made on the basis of deformation four-member criterion [3],[4],[5]:

$$D = \sum_{i=1}^{N} \frac{\left(\Delta\varepsilon_{eq_i}^{p}\right)^{k}}{C_1(T)} + \sum_{i=1}^{N} \frac{\left(\Delta\varepsilon_{eq_i}^{c}\right)^{m}}{C_2(T)} + \max_{0\le t\le t_{max}} \frac{\varepsilon_{eq}^{p}}{\varepsilon_r^{p}(T)} + \max_{0\le t\le t_{max}} \frac{\varepsilon_{eq}^{c}}{\varepsilon_r^{c}(T)}, \tag{3}$$

where the first term takes into account the range of plastic strain within the cycle, the second term is the range of creep strain within the cycle, the third term is unilaterally accumulated plastic strain (ratcheting), the fourth term is unilaterally accumulated creep strain. The number of cycles before the formation of macrocracks N is determined from the condition D = 1. The maximum shear strain in the sliding system with normal to the slip plane n and the sliding direction l is considered as equivalent deformation. The values k=2, m = 5/4 , $C_1 = (\varepsilon_r^p)^k$, $C_2 = 3/4 * (\varepsilon_r^c)^m$ are usually accepted, where ε_r^p and ε_r^c ultimate strains of plasticity and creep under uniaxial tension.

In the FE computations the values of ultimate strain $\varepsilon_r^p = 0.40$ for VZhM4, $\varepsilon_r^p = 0.36$ for ZhS32, $\varepsilon_r^p = 0.42$ for VIN3 were used. Improvement of the accuracy of prediction of influence the delay time on durability can be achieved by the refinement of the constant ε_r^p on the basis of data without delay.

The comparison of the results of FE simulations and experiments concerning the effect of the delay time at the maximum temperature on the thermal fatigue durability for single-crystal superalloys VZhM4, VIN3 and ZhS32 is given in Fig. 8,9,10.

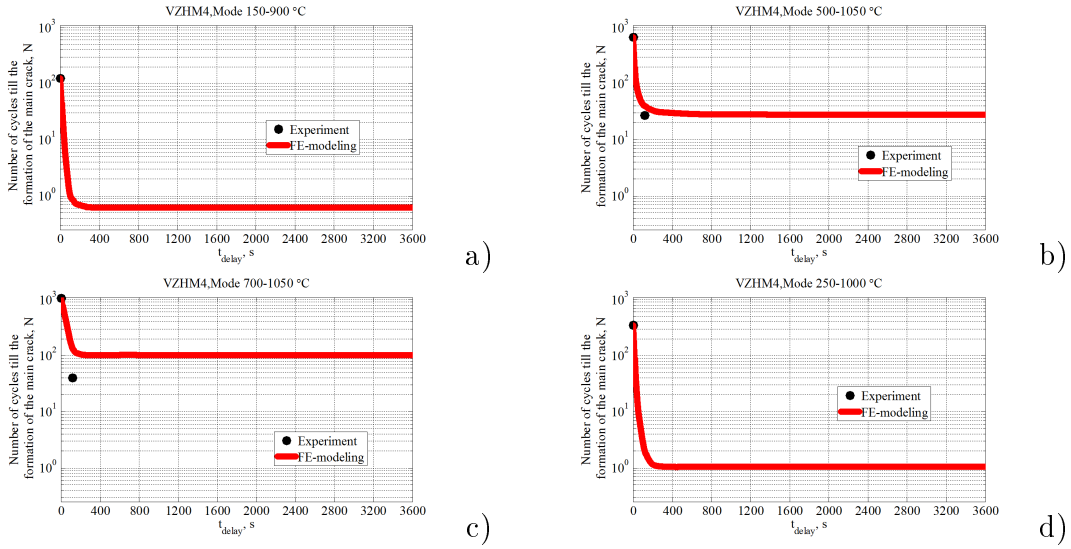

Figure 8: Comparison of results of FE simulation and experimental data for the alloy VZhM4: a)mode $150 \div 900°C$, heating time is 28s, cooling time is 52s,b)mode $500 \div 1050°C$, heating time is 7s, cooling time is 15s,c)mode $700 \div 1050°C$ heating time is 25s, cooling time is 17s,d)mode $250 \div 1000°C$ heating time is 18s, cooling time is 40s.

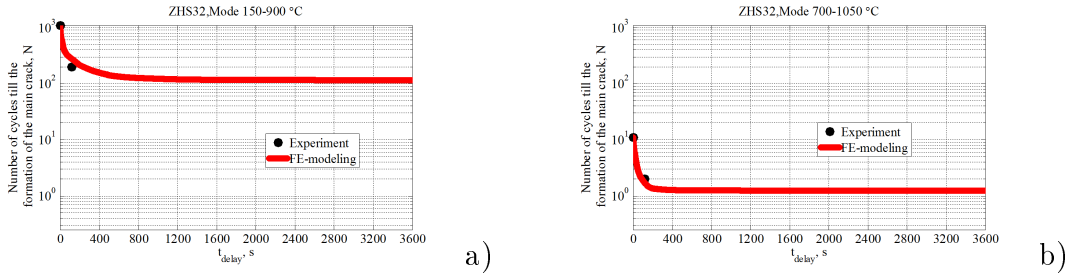

Figure 9: Comparison of results of FE simulation and experimental data for alloy ZhS32: a) mode $150 \div 900°C$, heating time is 25 s, cooling time is 75 s, b) mode $700 \div 1050°C$, heating time is 15 s, cooling time is 15 s.

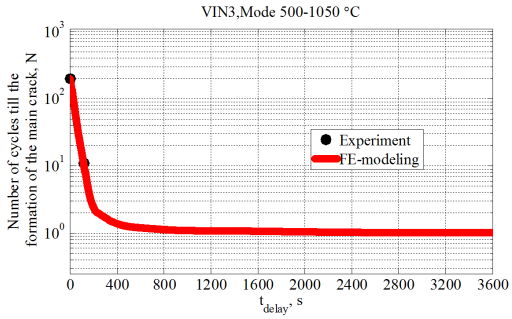

Figure 10: Comparison of calculation and experiment for alloy VIN3, mode 500-1050 $°C$, heating time-25 s, cooling time-17s

5 Conclusions

The results of the computations show a good agreement with the experiment, which suggests that the finite-element computations in combination with application of deformational criterion can be used to predict the thermal-fatigue strength of various single-crystal superalloy samples in wide range temperatures.

Acknowledgements

The study was performed under financial support of RFBR grant No. 16-08-00845 and scholarship program Siemens.

References

[1] Shalin R.E., Svetlov I.L., Kachalov E.B. and other Single crystals of nickel heat-resistant alloys-M.: Mashinostroenie, 1997. - 336 p.

[2] Getsov L. B. Materials and strength of gas turbine parts.-Rybinsk: Publishing House Gas Turbo Technology. 2010- 2011

[3] Getsov L. B., Semenov A. C. Criteria of fracture of polycrystalline and single crystal materials under thermal cyclic loading // Proceedings of CKTI. Vol. 296, 2009, pp. 83-91.

[4] Semenov A.S., Getsov L.B. Thermal fatigue fracture criteria of single crystal heat-resistant alloys and methods for identification of their parameters // Strength of Materials, 2014. Vol. 46, No. 1, p. 38-48.

[5] Getsov L.B., Semenov A.S., Staroselsky A. A failure criterion for single-crystal superalloys during thermocyclic loading // Materials and technology. 2008. Vol. 42, P. 3вГУ12.

[6] Petrushin N. Oh. Logunov A.V., Kovalev A. I., Zverev A. F., Toropov V. M., Fedotov N. H. Thermophysical properties of Ni_3Al-Ni_3Nb directly crystallized eutectic composition / / High temperature thermophysics, 1976, вНЦ 3.

[7] May S., Semenov A.S. Modeling of inelastic cyclic deformation of monocrystalline specimens // Proc. of the XXXIX week of science of SPbGPU. 2010. Vol. 5. P. 73-74.

[8] Semenov A. S. PANTOCRATOR is a finite-element software package focused on solving nonlinear problems of mechanics / Proceedings of the V-th International. Conf. "Scientific and technical problems of forecasting reliability and durability of structures". SPb.: Izd-vo SPbSPU, 2003. p. 466-480.

[9] Cailletaud G.A. Micromechanical approach to inelastic behaviour of metals // Int. J. Plast., 1991, 8, p. 55-73.

[10] A. S. Semenov. Identification of anisotropy parameters of phenomenological plasticity criterion for single crystals on the basis of micromechanical model // Scientific and technical sheets SPbGPU. Physical and mathematical Sciences. 2014. No. 2 (194). p. 15-29.

[11] Kablov E. N., Petrushin N. O. Svetlov I. L., Demonis I. M. Nickel casting heat-resistant alloys of the new generation. The jubilee nauch.- tech. sat. Aviation materials and technologies. M: Proceedings of VIAM 2012, p. 36-52.

[12] Semenov S. G., Getsov L. B., Semenov A. S., Petrushin N. V., Ospennikova O. G., A. A. Zhivushkin The issue of enhancing resource capabilities of nozzle blades of gas turbine engines through the use of new single crystal alloy // Journal of Machinery Manufacture and Reliability. 2016. No.4, p.30-38.

[13] Zinoviev V.E., Thermo-physical properties of metals at high temperatures. Moscow: Metalurgia, 1989.

[14] Chirkin V.S. Thermophysical properties of nuclear materials. Moscow:Atomizdat, 1968, p. 161.

[15] Maslenkov S.B., Maslenkova E.A. Steels and alloys for high temperatures. Moskow: Metallurgia, 1991.

Artem V. Savikovskii,SPbSPU,Politechnicheskaya 29;195251,St.Petersburg,Russia
Artem S. Semenov,SPbSPU,Politechnicheskaya 29;195251, St.Petersburg, Russia
Leonid B. Getsov,NPO CKTI,Politechnicheskaya 24;194021,St. Petersburg,Russia

Impact Strength of Mild Steel and Armox 500T Steel

K. Senthil, M.A. Iqbal, N.K. Gupta
urssenthil85@yahoo.co.in

Abstract

A study is based on the finite element investigation of the response of Mild Steel (MS) and Armox 500T Steel (AS) target subjected to macro and micro size impactor. The simulations were carried out on target against penetrator with varying masses, sizes, shapes and different in nature (rigid and deformable projectiles) using ABAQUS/Explicit. The material parameters of the Johnson-Cook elasto-viscoplastic model was employed for predicting the behaviour of target. The impact resistance of MS and AS target plates have been studied against flat nose having masses of 4, 8, 13.5, 27, 32 and 64 kg. The influence of temperature has also been studied numerically for particular penetrator of large masses. To study the influence of nature of projectile, the simulation were performed on MS and AS targets against deformable 2024 aluminium flat, hardened steel flat and hardened steel conical impactor at 950 and 150 m/s incidence velocity. The study thus presents a detailed investigation in terms of penetration, perforation and failure mechanism of MS and AS target and leads to some important conclusions pertaining to the force and resistance offered by the target.

Keywords: Finite element analysis, Armox 500T steel, Mild steel, Flat and conical nose impactor, Rigid and deformable projectiles

1 Introduction

For successful military operations, high strength steel may be widely considered however, the structural steels like low strength steels are used in the building, automobile and industrial applications. For instance, the tallest structures are constructed using structural steel due to its constructability. High strength and low strength steel plates are predominantly used as civil, aerospace and military protective structures. The idea of using these plates is to protect the personnel against accidental loads, terrorist attacks or international peace keeping operations. Bhat [2] discussed some basic principles that underlie design of materials effective for armour. Brian [3] observed that the IRHA performed better than standard RHA against the L/D 5KE penetrators. Buchar et al. [5] concluded that the targets of dual hardness exhibit very good resistance against the impact of AP projectile. Although the increase in

the hardness of the steel improved its ballistic behaviour, the steel specimens having either 50 or 60 HRc were broken in a brittle manner rather than perforation by the projectiles [6]. Hardness levels in steel plates played an important role in the ballistic performance. When the hardness of the steel plates increased, the penetration and the ballistic performance. When the hardness of the steel plates increased, the penetration and propagation ability of the projectile decreased significantly [19]. A detailed literature survey has been carried out on the target and projectiles in the present study have been carefully identified. The selection of suitable armour materials for defence applications is very crucial in order to design military vehicles, structural occupancy and military bunkers. The ideal material should possess the lowest areal density, high ductility and high strength [8, 9, 18, 7]. However, high strength steel still seems to be an ideal material for armour applications due to high strength and superior mechanical properties. Also, the investigations on armour steel plates against normal and oblique impact by different penetrator and fragments with help of computer tool is interesting [4, 12]. Based on the detailed literature survey, it is observed that the ballistic resistance of Armox 500T steel could not be found much studies in the available literature despite the fact that it possesses high strength, high hardness and high ductility which have been identified as the ideal properties for armour. The numerical reproduction of the experimental results is however limited due to the unavailability of strength and fracture parameters required for the Johnson-Cook constitutive modeling. It is observed that the studies on numerical investigations on ballistic resistance of mild steel, Armox steel target with elevated temperature against large mass flat impactor is limited. Also, it is observed that the ballistic resistance of Armox 500T steel against different penetrator with varying shape, size and mass is limited. In the present study, impact resistance of Armox 500T steel and mild steel targets has been studied against flat nose and conical nose at normal obliquity using ABAQUS/Explicit finite element code. The influence of temperature has also been studied numerically considering the fact that target may experience the temperature load from accidently/man made sources. The temperature was varied as 500, 900 and 1300 °K in light of various scenarios like protective structures against vehicle engine, special application in industry and blast waves cause various level of temperature. The Johnson-Cook constitutive model has been employed for predicting the material behavior of the Armox 500T steel (AS) and mild steel (MS) targets.

2 Constitutive Modelling

The flow and fracture behavior of projectile and target material was predicted employing the Johnson-Cook [15] elasto-viscoplastic material model available in ABAQUS [1] finite element code. The material model is based on the von Mises yield criterion and associated flow rule. It includes the effect of linear thermo-elasticity, yielding, plastic flow, isotropic strain hardening, strain rate hardening, softening due to adiabatic heating and damage. The Johnson and Cook [15] extended the failure criterion proposed by Hancock and Mackenzie [10] by incorporating the effect of strain path, strain rate and temperature in the fracture strain expression, in addition to stress triaxiality. The fracture criterion is based on the damage evolution wherein

the damage of the material is assumed to occur when the damage parameter, exceeds unity: The strain at failure is assumed to be dependent on a non-dimensional plastic strain rate, a dimensionless pressure-deviatoric stress ratio, (between the mean stress and the equivalent von-Mises stress) and the non-dimensional temperature, $\hat{T}$ defined earlier in the Johnson-Cook hardening model. When material damage occurs, the stress-strain relationship no longer accurately represents the material behavior [1]. The use of stress-strain relationship beyond ultimate stress introduces a strong mesh dependency based on strain localization i.e., the energy dissipated decreases with a decrease in element size. Hillerborg's [11] fracture energy criterion has been employed in the present study to reduce mesh dependency by considering stress-displacement response after the initiation of damage.

3 Finite Element Modelling

The finite element simulation of the problem was carried out using ABAQUS/-Explicit finite element code. The explicit algorithm of the code was employed for predicting the perforation phenomenon. The AS and MS target of thickness 3.18 and 4.7 mm was modelled in ABAQUS/CAE as three dimensional deformable continuum. The targets were restrained at periphery with respect to all degree of freedom. The calibrated JC model discussed in Iqbal et al. [12, 13] was employed to assign the flow and fracture behaviour of the target material. The geometry of flat and conical nose impactor was also created in accordance with its actual dimensions of Goldsmith and Finnegan [8] as a three dimensional deformable body. The geometry of large mass flat nose impactor was also created in accordance with its actual dimensions of Jones and Kim [16], as a three dimensional deformable body. As discussed above the steel core of the projectile has been modelled for all the finite element simulations assuming that the brass jacket has stripped off and had no influence the perforation process. The flow and fracture behaviour of target [12, 13] as well as projectile [17] was modelled employing the JC model. The target was meshed with eight node linear hexahedral elements with hourglass control. The finite element model of of a typical target with impactor are shown in Fig. 1. The element size in the impact zone of the targets for all the simulations of MS and AS were considered 0.2 and 0.35 mm^3 respectively and the aspect ratio close to unity. Away from the impact region, however, the size of element was slightly increased keeping the aspect ratio unity. The hexahedral elements of 0.9 mm^3 was used to discretize the conical and flat 2024 aluminium deformable projectile throughout its body. The contact between the projectile and target was modelled by employing the Kinematic contact algorithm, ABAQUS. The projectile was considered as master and the through thickness contact region of the target as node based slave surface. In the present study, a coefficient of friction of 0.02 was assumed between the projectiles and target.

4 Results and Discussion

The simulations were performed on various target and impactor configuration and classified into six phases. First phase, the simulations were performed on 4 mm

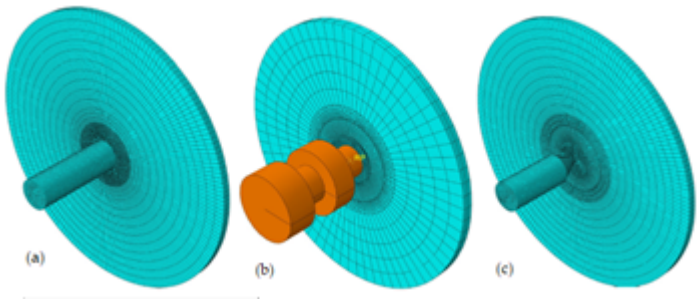

Figure 1: Target with (a) flat (b) double nose flat (c) conical (d) 12.7 mm and (e) 7.62 mm impactor

thick targets against 4, 8, 13.5, 27 and 64 Kg mass by 8.1 m/s incidence velocity (considering the drop of mass from 3.2 m height). Also, the influence of temperature on both the target against varying temperature was studied. Second phase, the simulation was performed on 3.18 mm thick targets against solid deformable 2024 aluminium flat impactor at 0° obliquity against 150 and 950 m/s incidence velocity. Third phase, the simulation was performed on 3.18 mm thick targets against solid deformable hardened steel flat impactor against 150 and 950 m/s incidence velocity. Fourth phase, the simulation was performed on 3.18 mm thick targets against solid deformable hardened steel conical impactor at 0° obliquity against 150 and 950 m/s incidence velocity. The ballistic resistance for all chosen target thicknesses has been studied numerically at given incidence velocities. The resistance of monolithic and layered targets studied in terms of forces and acceleration has been compared and discussed.

4.1 Response of target by varying mass of flat nose impactor

The impact resistance of 4 mm thick MS plates have been studied against blunt nose cylindrical object having masses of 4, 8, 13.5, 27, 32 and 64 kg at 8.1 m/s incidence velocity through numerical simulations using ABAQUS/Explicit. The numerical results pertaining to the resistance of 101 mm span target has been compared in our previous studies and validated with experiments conducted by Jones and Kim [16], see Figs. 2-4.

The forces offered by the target has been simulated within 10% deviation from the experimental results, Fig. 2(a). However, the predicted as well as measured maximum force offered by the target was found to be same 35.8 kN at 1.8 milli seconds. The penetration and perforation of target by striker at various time step has been shown in Fig. 2(b)-(d). It is observed that the predicted force was found to be overestimated upto 2 milli seconds whereas it is found under estimated after 2 milli seconds. The residual velocity of penetrator has been simulated within 15% deviation from the experimental results, Fig. 3(a). The simulated and measured residual velocity was found to be 0 and 1.68 m/s respectively, at 1.9 milli seconds. It is observed that the predicted residual velocity was found to be under predicted near about to 2 milli seconds whereas it is found in close agreement to their actual results upto 1.5 milli seconds. The penetration event of target by striker at 1, 2 and

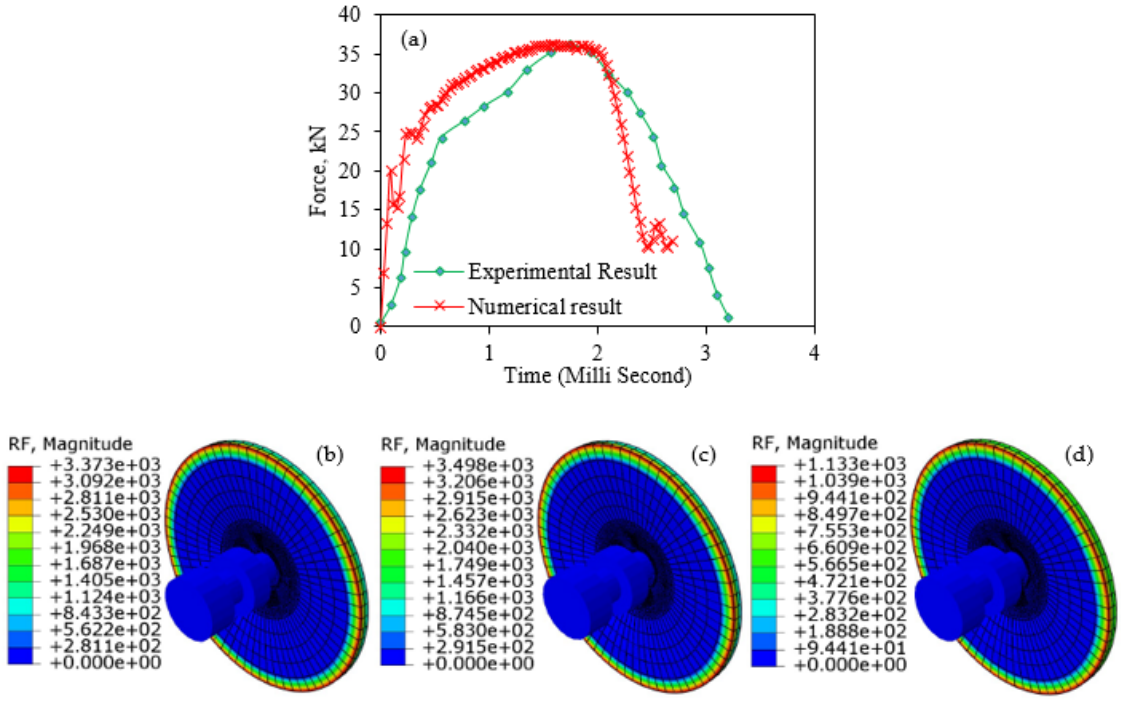

Figure 2: Comparison of (a) actual and simulated results of force by 8 Kg penetrator at (b) 1.0 (c) 2.0 and (d) 2.5 milli second and enlarged view at (e) 1.0 (f) 2.0 and (g) 2.5 milli second

2.5 milli seconds time step has been shown in Fig. 3(b)-(d).

The deflection of target has been predicted maximum 17% deviation from the experimental results, Fig. 4(a). The simulated as well as measured deflection of the target was found to be same, till 1.6 milli seconds. After 1.6 milli seconds, the predicted deflection was found to be lesser than measured deflection. It is also observed that the simulated residual velocity was found to be underestimated near about to 2 milli seconds whereas it is found in close agreement to their actual results upto 1.6 milli seconds. The deflection of target at 1, 2 and 2.5 milli second time step has been shown in Fig. 4(b)-(d). Therefore, it is concluded that the deflection of target and residual velocity of penetrator were in close agreement to their actual results upto 1.6 milli seconds, whereas the force offered by the target found deviated maximum of 10%. After 1.6 milli seconds, the force offered by the target was found in good agreement to their experimental results, whereas the deflection and residual velocity of projectile was found deviated to maximum of 16%.

The influence of temperature on MS and AS target has been studied by varying the temperature. Fig. 5 shows the effect of temperature at 230, 500, 900 and 1300 °K on both the target impacted by 8 Kg mass at 8.1 m/s incidence velocity. The maximum forces offered by the MS target was 37, 37, 24 and 15 kN against 230, 500, 900 and 1300 °K temperature, respectively. The maximum resistance offered by AS target was 93, 86, 66 and 42 kN against 230, 500, 900 and 1300 °K temperature, respectively. It is observed that the resistance of target was found to decrease almost 50% when the target temperature increased from ambient temperature to 1300 °K.

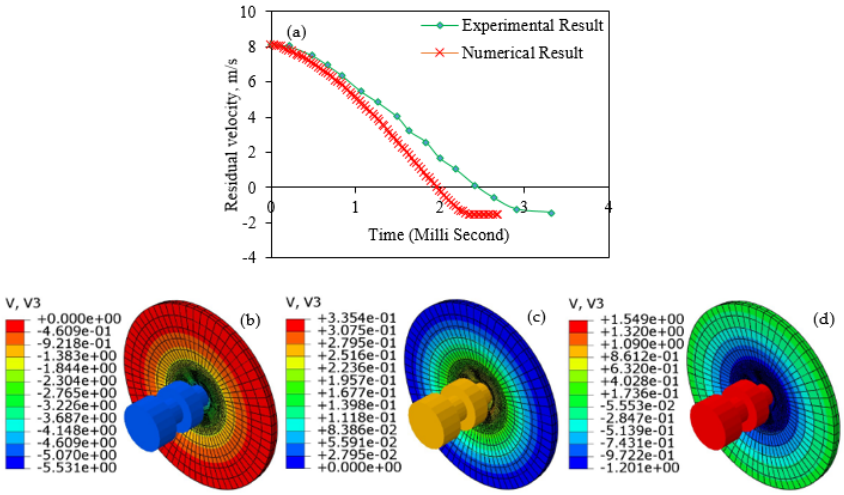

Figure 3: Comparison of (a) actual and simulated results of residual velocity by 8 Kg penetrator at (b) 1.0 (c) 2.0 and (d) 2.5 milli second and enlarged view at (e) 1.0 (f) 2.0 and (g) 2.5 milli second

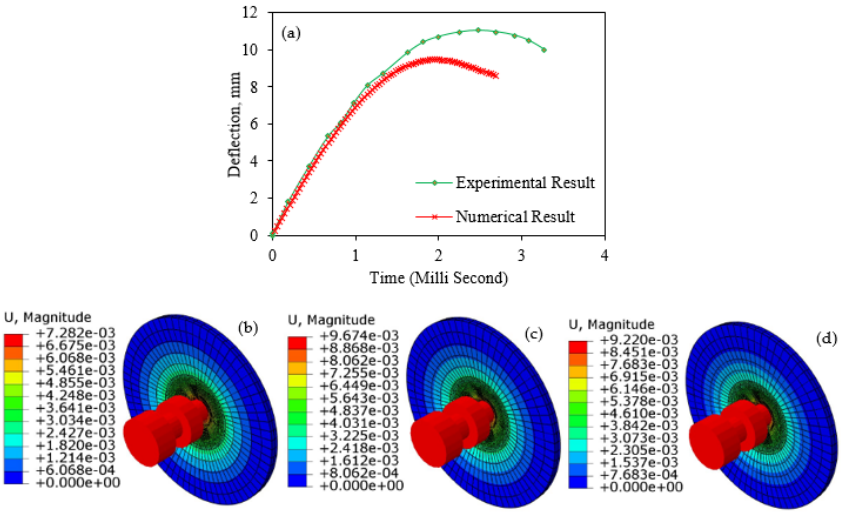

Figure 4: Comparison of (a) actual and simulated results of deflections of target by 8 Kg penetrator at (b) 1.0 (c) 2.0 and (d) 2.5 milli second and enlarged view at (e) 1.0 (f) 2.0 and (g) 2.5 milli second

The MS target has experienced penetration when the temperature of target was 1300 °K whereas AS target offered resistance significantly and doesnвГЄt experience perforation under high temperature, i.e. upto 1300 °K.

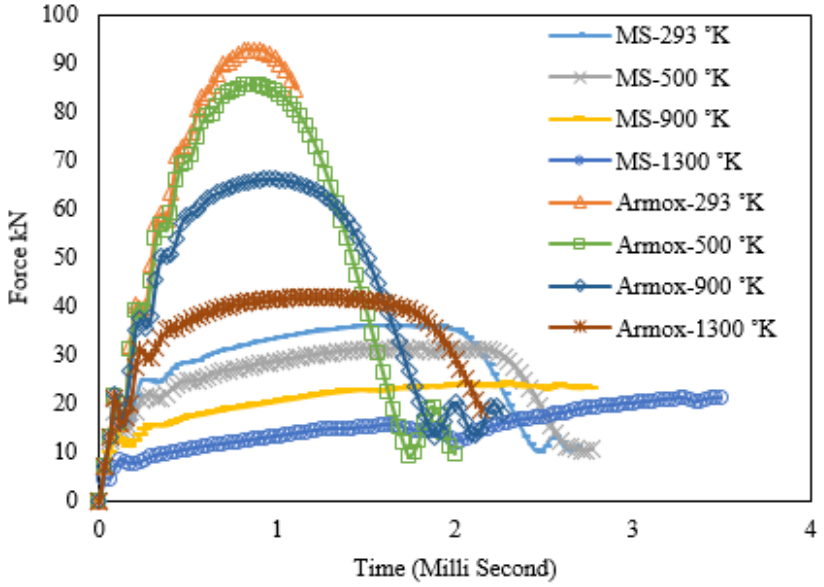

Figure 5: Resistance offered by the target against varying temperature

4.2 Response of target by deformable aluminium flat nose impactor

The simulations were performed on 3.18 mm thick targets of 118 mm span against solid deformable 2024 aluminium flat impactor of 37 grams by 150 and 950 m/s incidence velocity. The influence of low and high incidence velocity of impactor on mild steel and Armox 500T steel has been studied. At 150 m/s incidence velocity, both the target offered resistance significantly without any perforation and the impactor was found rebound back into same direction. The maximum forces offered by the MS and AS target at 150 m/s velocity was 17.6 and 26.3 kN respectively corresponding to 100 micro Seconds, see Fig 6(a)-(l). At 950 m/s velocity, Armox target offered resistance significantly without any penetration whereas the mild steel target was found perforated. It is observed that the AS target has experienced global deformation due to deformable impactor found deformed into mushroom shape, see Fig 6(d, h and l). The maximum forces offered by the mild steel and Armox target at 950 m/s velocity was 12.8 and 128 kN respectively. It is observed that the AS target offering resistance was found to be increased almost 30% as compared to MS target for low velocity whereas in case of high velocity, AS target offering resistance was found to be increased almost 90% as compared to MS target. Therefore, it is concluded that at low incidence velocity, the forces of both the target found almost similar whereas at high incidence velocity AS target was found to be superior against flat nose deformable projectiles.

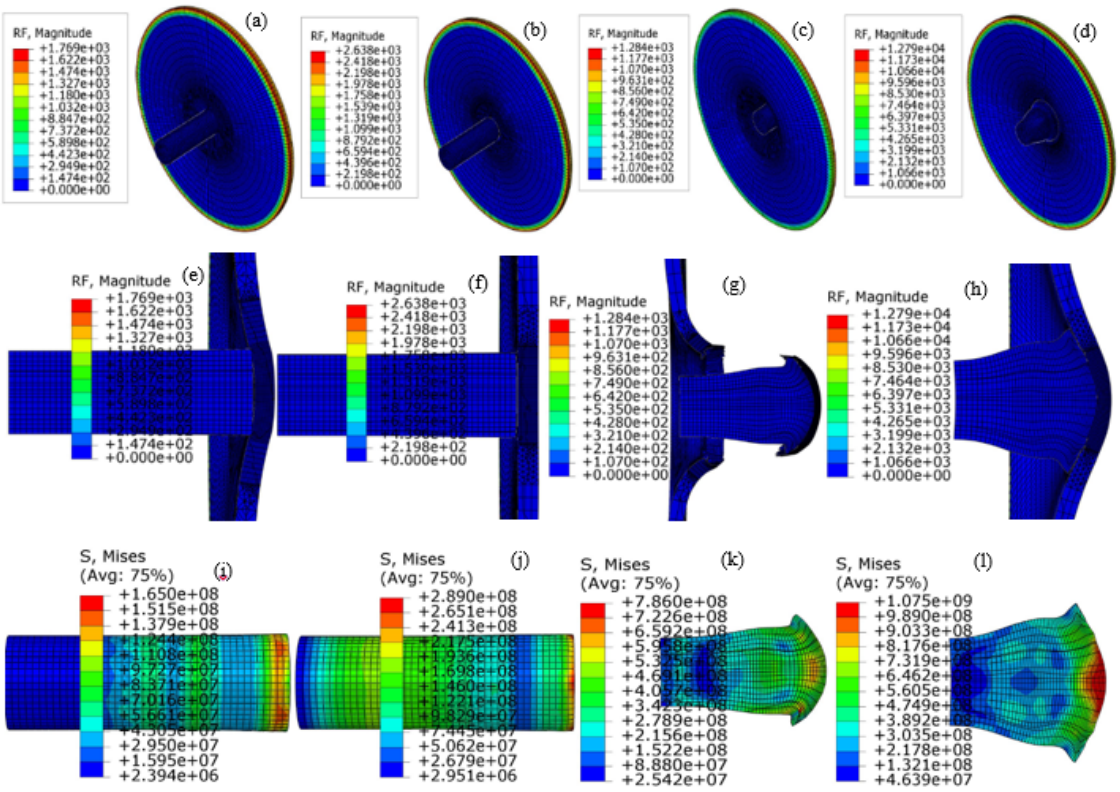

Figure 6: Resistance (Kg) offered by the target against deformable aluminium flat impactor of (a) MS-150 m/s (b) AS-150m/s (c) MS-950 m/s and (d) AS-950 m/s targets at 100 micro second, enlarged view of (e) MS-150 m/s (f) AS-150m/s (g) MS-950 m/s and (h) AS-950 m/s targets and deformation of projectiles by (i) MS-150 m/s (j) AS-150m/s (k) MS-950 m/s and (l) AS-950 m/s target in terms of von-Mises stresses

4.3 Response of target by hard steel flat nose impactor

The simulations were performed on 3.18 mm thick targets against solid hardened steel flat impactor by 150 and 950 m/s incidence velocity. Fig. 7(a)-(b) shows the effect of incidence velocity of 150 and 950 m/s on both the target impacted by 37 grams mass flat impactor. At 150 m/s incidence velocity, both the target offered resistance significantly without any perforation and the impactor was found rebound back into same direction, see Fig. 8. The maximum forces offered by the MS and AS target at 150 m/s velocity was 12 and 56 kN respectively corresponding to 100 Bxs, see Fig. 8(a)-(b) and Fig. 8(a). It is observed that the Armox target has experienced global deformation whereas the mild steel target has experienced local deformation. At 950 m/s velocity, both the target was found perforated. The maximum forces offered by the MS and AS target at 950 m/s velocity was 4.7 and 12.3 kN respectively, Fig. 7(b). It is observed that the AS target offering resistance was found to be increased almost 78% as compared to MS target for low velocity whereas in case of high velocity, AS target offering resistance was found to be increased almost 62% as compared to MS target.

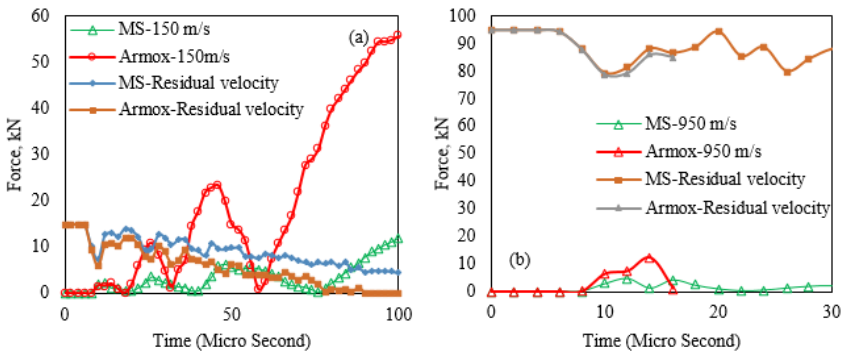

Figure 7: Resistance offered by the target against flat impactor at (a) 150 and (b) 950 m/s incidence velocity

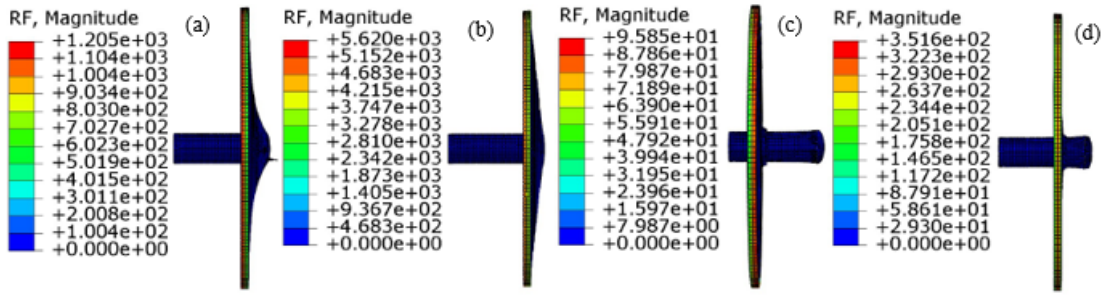

Figure 8: Resistance (Kg) offered by the target against hard steel flat impactor by (a) MS-150 m/s (b) AS-150m/s (c) MS-950 m/s and (d) AS-950 m/s configuration at 100 μs

4.4 Response of target by conical impactor

The simulations were performed on 3.18 mm thick targets against hardened steel conical impactor by 150 and 950 m/s incidence velocity. At 150 m/s incidence velocity, both the target offered resistance significantly without any perforation and the impactor was found struck inside the target, Fig. 9(a)-(b). The maximum forces offered by hard steel conical impactor on MS and AS target at 150 m/s velocity was 36.3 and 50.2 kN respectively corresponding to 250 and 150 Bxs respectively, see Fig. 9(a). It is observed that the AS target has experienced global deformation whereas the MS target has experienced local deformation, see Fig. 10(a)-(b). At 950 m/s velocity, both the target was found perforated. At 950 m/s incidence velocity, the maximum forces offered by hard steel conical impactor on MS and AS target was 4.17 and 46.9 kN respectively, see Fig. 10(c)-(d). It is observed that the forces of AS target found better resistance for both high as well as low incidence velocity, whereas both the target was found to offer resistance better against low incidence velocity. Therefore, it is concluded that when incidence velocity of conical projectiles increases from low to high, the response of AS target is found insignificant whereas MS target is found to decrease by 90%. It may be due to the low stiffness and low strength of MS target and sharp nose of projectiles, the target loses its resistance quickly.

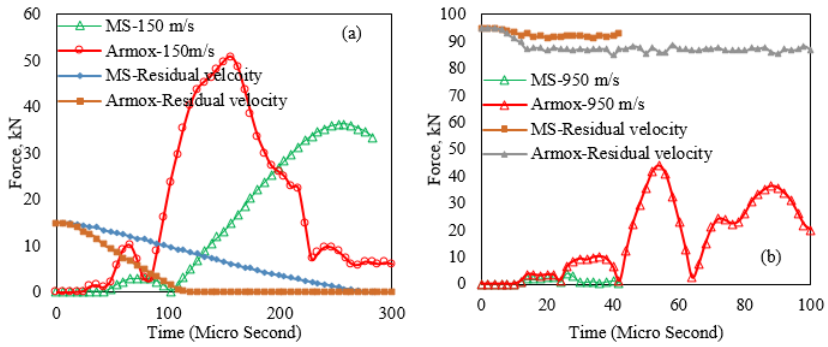

Figure 9: Resistance offered by the target against conical impactor at (a) 150 and (b) 950 m/s incidence velocity

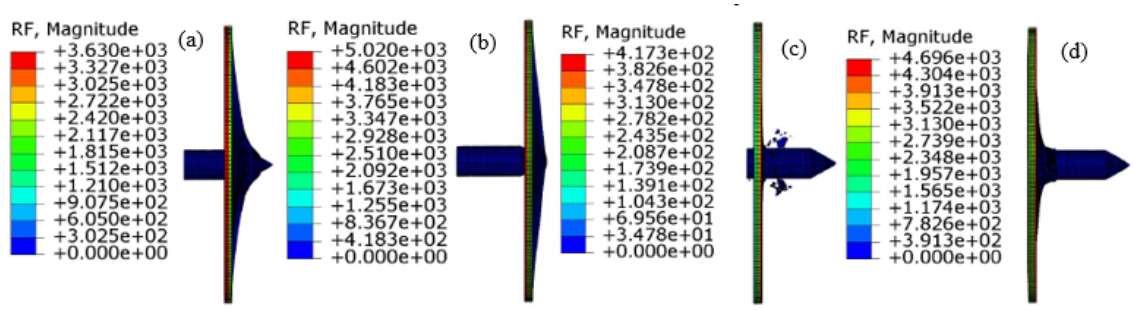

Figure 10: Resistance (Kg) offered by the target against hard steel flat impactor of (a) MS-150 m/s (b) Armox-150m/s (c) MS-950 m/s and (d) Armox-950 m/s configurations

5 Conclusions

A detailed numerical investigation has been carried out on Armox 500T steel and mild steel targets against flat, conical and ogival nosed projectiles. The results wherein the induced peak force and damage of target were predicted and compared with each other. The influence of temperature has also been studied numerically for particular penetrator and the following conclusions are drawn.

The maximum forces offered by AS and MS target was 121 and 41 kN and corresponding mass 27 and 13.5 Kg mass respectively. It is concluded that this behavior describes that the ballistic performance of target has improved significantly with increase in strength and hardness of target. It is observed that the resistance of both the target found to decrease almost 50% when the target temperature increased from ambient temperature to 1300 °K.

It is observed that at low incidence velocity of deformable flat nose projectiles, the forces of both the target found almost similar whereas at high incidence velocity AS target was found to be superior due to the high resistance capacity and high stiffness. In case of hard flat nose projectiles, the trend is reverse that at high incidence velocity, the acceleration of both the target found almost similar whereas in case of low incidence velocity, AS target was found superior.

It is concluded that the AS target offered better resistance against high as well as low incidence velocity of conical nose projectiles, whereas both the target was found to be better against low incidence velocity. It is also concluded that the acceleration of AS target was found to be increased by only 16% as compared to MS target for both the incidence velocity.

References

[1] ABAQUS (2010) Explicit User's Manual Version 6.14.

[2] Bhat TB (1985) Science of armour materials. Defence Science Journal 35: 219-223.

[3] Brian LR (1996) Improved rolled homogeneous armor. Army Research Laboratory. ARL-CR-285: 1-28.

[4] Borvik T, Dey S and Clausen AH (2009) Perforation resistance of five different high-strength steel plates subjected to small-arms projectiles. International Journal of Impact Engineering 36: 948-964.

[5] Buchar J, Voldrich J, Rolc S and Lisy J (2002) Ballistic performance of dual hardness armour. In. Proc: 20th international symposium of ballistics. 23-27 September; Orlando; p. 1-8.

[6] Demir T, Ubeyli M and Yildirim RO (2008) Investigation on the ballistic impact behavior of various alloys against 7.62 mm armor piercing projectile. Materials and Design 29: 2009-2016.

[7] Dikshit SN (1998) Ballistic Behaviour of thick steel armor plate under oblique impact: Experimental investigation. Defence Science Journal 48: 271-276.

[8] Goldsmith W and Finnegan SA (1986) Normal and oblique impact of cylindro-conical and cylindrical projectiles on metallic plates. International Journal of Impact Engineering 4: 83-105.

[9] Gupta NK and Madhu V (1997) An experimental study of normal and oblique impact of hard-core projectile on single and layered plates. International Journal of Impact Engineering 19: 395-414.

[10] Hancock JW and Mackenzie AC (1976) On the mechanisms of ductile failure in high-strength steels subjected to multi-axial stress-states. Journal of the Mechanics and Physics of solids 24: 147-169.

[11] Hillerborg A, Modeer M and Petersson PE (1976) Analysis of crack formation and crack growth in concrete by means of fracture mechanics and finite elements. Cement and Concrete Research 6: 773-782.

[12] Iqbal MA, Senthil K, Bhargava P, et al. (2015) The characterization and ballistic evaluation of mild steel. International Journal of Impact Engineering 78: 98-113.

[13] Iqbal MA, Senthil K, Sharma P, et al. (2016) An investigation of constitutive behavior of Armox 500T steel and armour piercing incendiary projectile material. International Journal of Impact Engineering 96: 146-164.

[14] Iqbal MA, Senthil K, Madhu V, et al. (2017) Oblique impact on single, layered and spaced mild steel targets by 7.62 AP projectiles. International Journal of Impact Engineering 110: 26-38.

[15] Johnson GR and Cook WH (1985) Fracture characteristics of three metals subjected to various strains, strain rates, temperatures and pressure. Engineering Fracture Mechanics 21: 31-48.

[16] Jones N and Kim SB (1997) A study on the large ductile deformations and perforation of mild steel plates struck by a mass - Part I: Experimental results. Transactions of the ASME 119: 178-184.

[17] Kay G (2003) Failure modeling of titanium 6Al-4V and aluminum 2024-T3 with the JohnsonвЃ“YCook material model. Rep. No. DOT/FAA/AR-03/57, Federal Aviation Administration, Washington, D.C.

[18] Pritti J, Castro M, Squillacioti R, et al. (1997) Improved rolled homogeneous armour (IRHA) steel through higher hardness, ARL-TR-1347, 1-49.

[19] Ubeyli M, YДçldДçrДçm RO and Ogel B (2007) On the comparison of the ballistic performance of steel and laminated composite armors. Materials and Design 27: 1257-1262.

K. Senthil, Assistant Professor, Department of Civil Engineering, NIT Jalandhar, Punjab, 144011
M.A. Iqbal, Associate Professor, Department of Civil Engineering, IIT Roorkee, Uttarakhand, 247667
N.K. Gupta, Emeritus Professor, Department of Applied Mechanics, IIT Delhi, New Delhi, 110016

Non-smooth first integrals of dissipative systems with four degrees of freedom

Maxim V. Shamolin
shamolin@rambler.ru, shamolin@imec.msu.ru

Abstract

In this study, we show the integrability of certain classes of dynamic systems on the tangent bundle to a four-dimensional manifold. In this case, the force fields have so-called variable dissipation and generalize the cases considered previously.

1 Introduction

In many problems of dynamics, mechanical systems arise with the space of positions — a four-dimensional manifold. Their phase spaces naturally become the tangent bundles to these manifolds. Thus, for example, the study of a five-dimensional generalized spherical pendulum in a nonconservative force field leads to a dynamic system on the tangent bundle to a four-dimensional sphere, while the special metric on it is induced by an additional symmetry group. In this case, the dynamic systems describing the motion of such a pendulum have alternating dissipation and the complete list of first integrals consists of transcendental functions expressed through a finite combination of elementary functions.
We also single out the class of problems on the motion of a point along a four-dimensional surface, the metric on it being induced by the Euclidean metric of a comprehensive space. In a number of cases, the complete list of first integrals consisting of transcendental functions can also be found in systems with dissipation. The results obtained are especially important in the sense of the presence of a precisely nonconservative force field in the system.

2 Equations of geodesic lines under a change of coordinates and its first integrals

It is well known that, in the case of a four-dimensional Riemannian manifold M^4 with coordinates (α, β), $\beta = (\beta_1, \beta_2, \beta_3)$, and affine connection $\Gamma^i_{jk}(x)$ the equations of geodesic lines on the tangent bundle $T_*M^4\{\dot\alpha, \dot\beta_1, \dot\beta_2, \dot\beta_3; \alpha, \beta_1, \beta_2, \beta_3\}$, $\alpha = x^1$, $\beta_1 = x^2$, $\beta_2 = x^3$, $\beta_3 = x^4$, $x = (x^1, x^2, x^3, x^4)$, have the following form (the

derivatives are taken with respect to the natural parameter):

$$\ddot{x}^i + \sum_{j,k=1}^{4} \Gamma^i_{jk}(x)\dot{x}^j\dot{x}^k = 0,\ i = 1, \ldots, 4. \tag{1}$$

Let us study the structure of Eqs. (1) under a change of coordinates on the tangent bundle T_*M^4. Consider a change of coordinates of the tangent space:

$$\dot{x}^i = \sum_{j=1}^{4} R^{ij}(x)z_j, \tag{2}$$

which can be inverted:

$$z_j = \sum_{i=1}^{4} T_{ji}(x)\dot{x}^i,$$

here $R^{ij}, T_{ji}, i, j = 1, \ldots, 4$, are functions of x^1, x^2, x^3, x^4, and

$$RT = E,$$

where

$$R = (R^{ij}),\ T = (T_{ji}).$$

We also call Eqs. (2) new kinematic relations, i.e., relations on the tangent bundle T_*M^4.

The following equalities are valid:

$$\dot{z}_j = \sum_{i=1}^{4} \dot{T}_{ji}\dot{x}^i + \sum_{i=1}^{4} T_{ji}\ddot{x}^i,\ \dot{T}_{ji} = \sum_{k=1}^{4} T_{ji,k}\dot{x}^k, \tag{3}$$

where

$$T_{ji,k} = \frac{\partial T_{ji}}{\partial x^k},\ j, i, k = 1, \ldots, 4.$$

We also have:

$$\dot{z}_i = \sum_{j,k=1}^{4} T_{ij,k}\dot{x}^j\dot{x}^k - \sum_{j,p,q=1}^{4} T_{ij}\Gamma^j_{pq}\dot{x}^p\dot{x}^q. \tag{4}$$

Otherwise, we can rewrite Eq. (4) in the form

$$\dot{z}_i + \sum_{j,k=1}^{4} Q_{ijk}\dot{x}^j\dot{x}^k|_{(2)} = 0, \tag{5}$$

where

$$Q_{ijk}(x) = \sum_{s=1}^{4} T_{is}(x)\Gamma^s_{jk}(x) - T_{ij,k}(x). \tag{6}$$

Proposition 2.1. *System (1) is equivalent to compound system (2), (4) in a domain where* $\det R(x) \neq 0$.

Therefore, the result of the passage from equations of geodesic lines (1) to an equivalent system of equations (2), (4) depends both on the change of variables (2) (i.e., introduced kinematic relations) and on the affine connection $\Gamma^i_{jk}(x)$.

3 A fairly general case

Consider next a sufficiently general case of specifying kinematic relations in the following form:

$$\begin{aligned}
&\dot{\alpha} = -z_4,\\
&\dot{\beta}_1 = z_3 f_1(\alpha),\\
&\dot{\beta}_2 = z_2 f_2(\alpha) g_1(\beta_1),\\
&\dot{\beta}_3 = z_1 f_3(\alpha) g_2(\beta_1) h(\beta_2),
\end{aligned} \tag{7}$$

where $f_k(\alpha)$, $k = 1, 2, 3$, $g_l(\beta_1)$, $l = 1, 2$, $h(\beta_2)$ are smooth functions on their domain of definition. Such coordinates z_1, z_2, z_3, z_4 in the tangent space are introduced when the following equations of geodesic lines are considered [1, 2, 3] (in particular, on surfaces of revolution):

$$\begin{cases}
\ddot{\alpha} + \Gamma^{\alpha}_{11}(\alpha,\beta)\dot{\beta}_1^2 + \Gamma^{\alpha}_{22}(\alpha,\beta)\dot{\beta}_2^2 + \Gamma^{\alpha}_{33}(\alpha,\beta)\dot{\beta}_3^2 = 0,\\
\ddot{\beta}_1 + 2\Gamma^{1}_{\alpha 1}(\alpha,\beta)\dot{\alpha}\dot{\beta}_1 + \Gamma^{1}_{22}(\alpha,\beta)\dot{\beta}_2^2 + \Gamma^{1}_{33}(\alpha,\beta)\dot{\beta}_3^2 = 0,\\
\ddot{\beta}_2 + 2\Gamma^{2}_{\alpha 2}(\alpha,\beta)\dot{\alpha}\dot{\beta}_2 + 2\Gamma^{2}_{12}(\alpha,\beta)\dot{\beta}_1\dot{\beta}_2 + \Gamma^{2}_{33}(\alpha,\beta)\dot{\beta}_3^2 = 0,\\
\ddot{\beta}_3 + 2\Gamma^{3}_{\alpha 3}(\alpha,\beta)\dot{\alpha}\dot{\beta}_3 + 2\Gamma^{3}_{13}(\alpha,\beta)\dot{\beta}_1\dot{\beta}_3 + 2\Gamma^{3}_{23}(\alpha,\beta)\dot{\beta}_2\dot{\beta}_3 = 0,
\end{cases} \tag{8}$$

i.e., other connection coefficients are zero. In case (7) Eqs. (4) take the form

$$\begin{aligned}
\dot{z}_1 &= \left[2\Gamma^{3}_{\alpha 3}(\alpha,\beta) + \frac{d\ln|f_3(\alpha)|}{d\alpha}\right] z_1 z_4 - \left[2\Gamma^{3}_{13}(\alpha,\beta) + \frac{d\ln|g_2(\beta_1)|}{d\beta_1}\right] f_1(\alpha) z_1 z_3 -\\
&- \left[2\Gamma^{3}_{23}(\alpha,\beta) + \frac{d\ln|h(\beta_2)|}{d\beta_2}\right] f_2(\alpha) g_1(\beta_1) z_1 z_2,\\
\dot{z}_2 &= \left[2\Gamma^{2}_{\alpha 2}(\alpha,\beta) + \frac{d\ln|f_2(\alpha)|}{d\alpha}\right] z_2 z_4 - \left[2\Gamma^{2}_{12}(\alpha,\beta) + \frac{d\ln|g_1(\beta_1)|}{d\beta_1}\right] f_1(\alpha) z_2 z_3 -\\
&- \Gamma^{2}_{33}(\alpha,\beta)\frac{f_3^2(\alpha)}{f_2(\alpha)}\frac{g_2^2(\beta_1)}{g_1(\beta_1)} h^2(\beta_2) z_1^2,\\
\dot{z}_3 &= \left[2\Gamma^{1}_{\alpha 1}(\alpha,\beta) + \frac{d\ln|f_1(\alpha)|}{d\alpha}\right] z_3 z_4 - \Gamma^{1}_{22}(\alpha,\beta)\frac{f_2^2(\alpha)}{f_1(\alpha)} g_1^2(\beta_1) z_2^2 -\\
&- \Gamma^{1}_{33}(\alpha,\beta)\frac{f_3^2(\alpha)}{f_1(\alpha)} g_2^2(\beta_1) h^2(\beta_2) z_1^2,\\
\dot{z}_4 &= \Gamma^{\alpha}_{11} f_1^2(\alpha) z_3^2 + \Gamma^{\alpha}_{22} f_2^2(\alpha) g_1^2(\beta_1) z_2^2 + \Gamma^{\alpha}_{33} f_3^2(\alpha) g_2^2(\beta_1) h^2(\beta_2) z_1^2,
\end{aligned} \tag{9}$$

and Eqs. (8) are almost everywhere equivalent to compound system (7), (9) on the manifold $T_*M^4\{z_4, z_3, z_2, z_1; \alpha, \beta_1, \beta_2, \beta_3\}$.

To integrate system (7), (9) completely, it is necessary to know, generally speaking, seven independent first integrals.

Proposition 3.1. *If the system of equalities*

$$\begin{cases} 2\Gamma^1_{\alpha 1}(\alpha,\beta)+\dfrac{d\ln|f_1(\alpha)|}{d\alpha}+\Gamma^{\alpha}_{11}(\alpha,\beta)f_1^2(\alpha)\equiv 0,\\ 2\Gamma^2_{\alpha 2}(\alpha,\beta)+\dfrac{d\ln|f_2(\alpha)|}{d\alpha}+\Gamma^{\alpha}_{22}(\alpha,\beta)f_2^2(\alpha)g_1^2(\beta_1)\equiv 0,\\ \left[2\Gamma^2_{12}(\alpha,\beta)+\dfrac{d\ln|g_1(\beta_1)|}{d\beta_1}\right]f_1^2(\alpha)+\Gamma^1_{22}(\alpha,\beta)f_2^2(\alpha)g_1^2(\beta_1)\equiv 0,\\ 2\Gamma^3_{\alpha 3}(\alpha,\beta)+\dfrac{d\ln|f_3(\alpha)|}{d\alpha}+\Gamma^{\alpha}_{33}(\alpha,\beta)f_3^2(\alpha)g_2^2(\beta_1)h^2(\beta_2)\equiv 0,\\ \left[2\Gamma^3_{13}(\alpha,\beta)+\dfrac{d\ln|g_2(\beta_1)|}{d\beta_1}\right]f_1^2(\alpha)+\Gamma^1_{33}(\alpha,\beta)f_3^2(\alpha)g_2^2(\beta_1)h^2(\beta_2)\equiv 0,\\ \left[2\Gamma^3_{23}(\alpha,\beta)+\dfrac{d\ln|h(\beta_2)|}{d\beta_2}\right]f_2^2(\alpha)g_1^2(\beta_1)+\Gamma^2_{33}(\alpha,\beta)f_3^2(\alpha)g_2^2(\beta_1)h^2(\beta_2)\equiv 0, \end{cases} \tag{10}$$

is valid everywhere in its domain of definition, system (7), (9) has an analytic first integral of the form

$$\Phi_1(z_4,\ldots,z_1)=z_1^2+\ldots+z_4^2=C_1^2=const. \tag{11}$$

One can prove a special existence theorem for the solution $f_k(\alpha)$, $k=1,2,3$, $g_l(\beta_1)$, $l=1,2$, $h(\beta_2)$ of system (10) for the presence of analytic integral (11) for system (7), (9) of equations of geodesic lines. Below, however, we do not need all conditions (10) in studying dynamic systems with dissipation. Nevertheless, in what follows, we suppose that the condition

$$f_1(\alpha)=f_2(\alpha)=f_3(\alpha)=f(\alpha), \tag{12}$$

is satisfied in Eqs. (7); the functions $g_l(\beta_1)$, $l=1,2$, $h(\beta_2)$ must satisfy the transformed third equality from (10):

$$\begin{cases} 2\Gamma^2_{12}(\alpha,\beta)+\dfrac{d\ln|g_1(\beta_1)|}{d\beta_1}+\Gamma^1_{22}(\alpha,\beta)g_1^2(\beta_1)\equiv 0,\\ 2\Gamma^3_{13}(\alpha,\beta)+\dfrac{d\ln|g_2(\beta_1)|}{d\beta_1}+\Gamma^1_{33}(\alpha,\beta)g_2^2(\beta_1)h^2(\beta_2)\equiv 0,\\ 2\Gamma^3_{23}(\alpha,\beta)+\dfrac{d\ln|h(\beta_2)|}{d\beta_2}+\Gamma^2_{33}(\alpha,\beta)h^2(\beta_2)\equiv 0. \end{cases} \tag{13}$$

Thus, the functions $g_l(\beta_1)$, $l=1,2$, $h(\beta_2)$ depend on the connection coefficients; as for restrictions on the function $f(\alpha)$ they are given below.

Proposition 3.2. *If properties (12) and (13) are valid, and the equalities*

$$\Gamma^1_{\alpha 1}(\alpha,\beta)=\Gamma^2_{\alpha 2}(\alpha,\beta)=\Gamma^3_{\alpha 3}(\alpha,\beta)=\Gamma_1(\alpha), \tag{14}$$

are satisfied, system (7), (9) has a smooth first integral of the following form:

$$\Phi_2(z_3,z_2,z_1;\alpha)=\sqrt{z_1^2+z_2^2+z_3^2}\;\Phi_0(\alpha)=C_2=const, \tag{15}$$

$$\Phi_0(\alpha)=f(\alpha)\exp\left\{2\int_{\alpha_0}^{\alpha}\Gamma_1(b)db\right\}.$$

Proposition 3.3. *If the properties in proposition 3.2 are valid, and also*

$$g_1(\beta_1) = g_2(\beta_1) = g(\beta_1), \tag{16}$$

herewith the equalities

$$\Gamma^2_{12}(\alpha,\beta) = \Gamma^3_{13}(\alpha,\beta) = \Gamma_2(\beta_1), \tag{17}$$

are valid, that system (7), (9) has a smooth first integral of the following form:

$$\Phi_3(z_2, z_1; \alpha, \beta_1) = \sqrt{z_1^2 + z_2^2}\Phi_0(\alpha)\Psi_1(\beta_1) = C_3 = const, \tag{18}$$

$$\Psi_1(\beta_1) = g(\beta_1)\exp\left\{2\int_{\beta_{10}}^{\beta_1}\Gamma_2(b)db\right\}.$$

Proposition 3.4. *If the properties in propositions 3.2, 3.3 are valid, herewith the equality*

$$\Gamma^3_{23}(\alpha,\beta) = \Gamma_3(\beta_2), \tag{19}$$

are valid, that system (7), (9) has a smooth first integral of the following form:

$$\Phi_4(z_1; \alpha, \beta_1, \beta_2) = z_1\Phi_0(\alpha)\Psi_1(\beta_1)\Psi_2(\beta_2) = C_4 = const, \tag{20}$$

$$\Psi_2(\beta_2) = h(\beta_2)\exp\left\{2\int_{\beta_{20}}^{\beta_2}\Gamma_3(b)db\right\}.$$

Proposition 3.5. *If the properties in propositions 3.2, 3.3, 3.4 are valid, that system (7), (9) has a first integral of the following form:*

$$\Phi_5(z_2, z_1; \alpha, \beta) = \beta_3 \pm \int_{\beta_{20}}^{\beta_2}\frac{C_4 h(b)}{\sqrt{C_3^2\Phi_2^2(b) - C_4^2}}\,db = C_5 = const. \tag{21}$$

Under the conditions listed above, system (7), (9) has a complete set (five) of independent first integrals of the form (11), (15), (18), (20), and (21).

4 Equations of motion on the tangent bundle of a three-dimensional manifold in a potential field of force and its first integrals

Let us now somewhat modify system (7), (9) under conditions (12)–(14), (16), (17), and (19), which yields a conservative system. Namely, the presence of the force field is characterized by the coefficient $F(\alpha)$ in the second equation of system (22). The

system under consideration on the tangent bundle $T_*M^4\{z_4, z_3, z_2, z_1; \alpha, \beta_1, \beta_2, \beta_3\}$ takes the form

$$\begin{cases} \dot{\alpha} = -z_4, \\ \dot{z}_4 = F(\alpha) + \Gamma^{\alpha}_{11} f_1^2(\alpha) z_3^2 + \Gamma^{\alpha}_{22} f_2^2(\alpha) g_1^2(\beta_1) z_2^2 + \Gamma^{\alpha}_{33} f_3^2(\alpha) g_2^2(\beta_1) h^2(\beta_2) z_1^2, \\ \dot{z}_3 = \left[2\Gamma^1_{\alpha 1}(\alpha, \beta) + \dfrac{d \ln |f_1(\alpha)|}{d\alpha} \right] z_3 z_4 - \Gamma^1_{22}(\alpha, \beta) \dfrac{f_2^2(\alpha)}{f_1(\alpha)} g_1^2(\beta_1) z_2^2 - \\ - \Gamma^1_{33}(\alpha, \beta) \dfrac{f_3^2(\alpha)}{f_1(\alpha)} g_2^2(\beta_1) h^2(\beta_2) z_1^2, \\ \dot{z}_2 = \left[2\Gamma^2_{\alpha 2}(\alpha, \beta) + \dfrac{d \ln |f_2(\alpha)|}{d\alpha} \right] z_2 z_4 - \left[2\Gamma^2_{12}(\alpha, \beta) + \dfrac{d \ln |g_1(\beta_1)|}{d\beta_1} \right] f_1(\alpha) z_2 z_3 - \\ - \Gamma^2_{33}(\alpha, \beta) \dfrac{f_3^2(\alpha)}{f_2(\alpha)} \dfrac{g_2^2(\beta_1)}{g_1(\beta_1)} h^2(\beta_2) z_1^2, \\ \dot{z}_1 = \left[2\Gamma^3_{\alpha 3}(\alpha, \beta) + \dfrac{d \ln |f_3(\alpha)|}{d\alpha} \right] z_1 z_4 - \left[2\Gamma^3_{13}(\alpha, \beta) + \dfrac{d \ln |g_2(\beta_1)|}{d\beta_1} \right] f_1(\alpha) z_1 z_3 - \\ - \left[2\Gamma^3_{23}(\alpha, \beta) + \dfrac{d \ln |h(\beta_2)|}{d\beta_2} \right] f_2(\alpha) g_1(\beta_1) z_1 z_2, \\ \dot{\beta}_1 = z_3 f(\alpha), \\ \dot{\beta}_2 = z_2 f(\alpha) g(\beta_1), \\ \dot{\beta}_3 = z_1 f(\alpha) g(\beta_1) h(\beta_2), \end{cases} \tag{22}$$

and it is almost everywhere equivalent to the following system:

$$\begin{cases} \ddot{\alpha} + F(\alpha) + \Gamma^{\alpha}_{11}(\alpha, \beta) \dot{\beta}_1^2 + \Gamma^{\alpha}_{22}(\alpha, \beta) \dot{\beta}_2^2 + \Gamma^{\alpha}_{33}(\alpha, \beta) \dot{\beta}_3^2 = 0, \\ \ddot{\beta}_1 + 2\Gamma_1(\alpha) \dot{\alpha} \dot{\beta}_1 + \Gamma^1_{22}(\alpha, \beta) \dot{\beta}_2^2 + \Gamma^1_{33}(\alpha, \beta) \dot{\beta}_3^2 = 0, \\ \ddot{\beta}_2 + 2\Gamma_1(\alpha) \dot{\alpha} \dot{\beta}_2 + 2\Gamma_2(\beta_1) \dot{\beta}_1 \dot{\beta}_2 + \Gamma^2_{33}(\alpha, \beta) \dot{\beta}_3^2 = 0, \\ \ddot{\beta}_3 + 2\Gamma_1(\alpha) \dot{\alpha} \dot{\beta}_3 + 2\Gamma_2(\beta_1) \dot{\beta}_1 \dot{\beta}_3 + 2\Gamma_3(\beta_2) \dot{\beta}_2 \dot{\beta}_3 = 0. \end{cases}$$

Proposition 4.1. *If the conditions of Proposition 3.1 are satisfied, system (22) has a smooth first integral of the following form:*

$$\Phi_1(z_4, \ldots, z_1; \alpha) = z_1^2 + \ldots + z_4^2 + F_1(\alpha) = C_1 = const, \; F_1(\alpha) = 2 \int_{\alpha_0}^{\alpha} F(a) da. \tag{23}$$

Proposition 4.2. *If the conditions of Propositions 3.2, 3.3, and 3.4 are satisfied, system (22) has three smooth first integrals of form (15), (18), and (20).*

Proposition 4.3. *If the conditions of Proposition 3.5 are satisfied, system (22) has first integral of form (21).*

Under the conditions listed above, system (22) has a complete set of (five) independent first integrals of form (23), (15), (18), (20), and (21).

5 Equations of motion on the tangent bundle of a two-dimensional manifold in a force field with dissipation and its first integrals

Let us now consider system (24). In doing this, we obtain a system with dissipation. Namely, the presence of dissipation (generally speaking, sign-alternating) is characterized by the coefficient $b\delta(\alpha)$ in the first equation of system (24):

$$\begin{cases} \dot{\alpha} = -z_4 + b\delta(\alpha), \\ \dot{z}_4 = F(\alpha) + \Gamma^{\alpha}_{11} f_1^2(\alpha) z_3^2 + \Gamma^{\alpha}_{22} f_2^2(\alpha) g_1^2(\beta_1) z_2^2 + \Gamma^{\alpha}_{33} f_3^2(\alpha) g_2^2(\beta_1) h^2(\beta_2) z_1^2, \\ \dot{z}_3 = \left[2\Gamma^1_{\alpha 1}(\alpha,\beta) + \dfrac{d\ln|f_1(\alpha)|}{d\alpha} \right] z_3 z_4 - \Gamma^1_{22}(\alpha,\beta) \dfrac{f_2^2(\alpha)}{f_1(\alpha)} g_1^2(\beta_1) z_2^2 - \\ - \Gamma^1_{33}(\alpha,\beta) \dfrac{f_3^2(\alpha)}{f_1(\alpha)} g_2^2(\beta_1) h^2(\beta_2) z_1^2, \\ \dot{z}_2 = \left[2\Gamma^2_{\alpha 2}(\alpha,\beta) + \dfrac{d\ln|f_2(\alpha)|}{d\alpha} \right] z_2 z_4 - \left[2\Gamma^2_{12}(\alpha,\beta) + \dfrac{d\ln|g_1(\beta_1)|}{d\beta_1} \right] f_1(\alpha) z_2 z_3 - \\ - \Gamma^2_{33}(\alpha,\beta) \dfrac{f_3^2(\alpha)}{f_2(\alpha)} \dfrac{g_2^2(\beta_1)}{g_1(\beta_1)} h^2(\beta_2) z_1^2, \\ \dot{z}_1 = \left[2\Gamma^3_{\alpha 3}(\alpha,\beta) + \dfrac{d\ln|f_3(\alpha)|}{d\alpha} \right] z_1 z_4 - \left[2\Gamma^3_{13}(\alpha,\beta) + \dfrac{d\ln|g_2(\beta_1)|}{d\beta_1} \right] f_1(\alpha) z_1 z_3 - \\ - \left[2\Gamma^3_{23}(\alpha,\beta) + \dfrac{d\ln|h(\beta_2)|}{d\beta_2} \right] f_2(\alpha) g_1(\beta_1) z_1 z_2, \\ \dot{\beta}_1 = z_3 f(\alpha), \\ \dot{\beta}_2 = z_2 f(\alpha) g(\beta_1), \\ \dot{\beta}_3 = z_1 f(\alpha) g(\beta_1) h(\beta_2), \end{cases} \tag{24}$$

which is almost everywhere equivalent to the following system

$$\begin{cases} \ddot{\alpha} - b\dot{\alpha}\delta'(\alpha) + F(\alpha) + \Gamma^{\alpha}_{11}(\alpha,\beta)\dot{\beta}_1^2 + \Gamma^{\alpha}_{22}(\alpha,\beta)\dot{\beta}_2^2 + \Gamma^{\alpha}_{33}(\alpha,\beta)\dot{\beta}_3^2 = 0, \\ \ddot{\beta}_1 - b\dot{\beta}_1\delta(\alpha)W(\alpha) + 2\Gamma_1(\alpha)\dot{\alpha}\dot{\beta}_1 + \Gamma^1_{22}(\alpha,\beta)\dot{\beta}_2^2 + \Gamma^1_{33}(\alpha,\beta)\dot{\beta}_3^2 = 0, \\ \ddot{\beta}_2 - b\dot{\beta}_2\delta(\alpha)W(\alpha) + 2\Gamma_1(\alpha)\dot{\alpha}\dot{\beta}_2 + 2\Gamma_2(\beta_1)\dot{\beta}_1\dot{\beta}_2 + \Gamma^2_{33}(\alpha,\beta)\dot{\beta}_3^2 = 0, \\ \ddot{\beta}_3 - b\dot{\beta}_3\delta(\alpha)W(\alpha) + 2\Gamma_1(\alpha)\dot{\alpha}\dot{\beta}_3 + 2\Gamma_2(\beta_1)\dot{\beta}_1\dot{\beta}_3 + 2\Gamma_3(\beta_2)\dot{\beta}_2\dot{\beta}_3 = 0, \\ W(\alpha) = 2\Gamma^1_{\alpha 1}(\alpha,\beta) + \dfrac{d\ln|f_1(\alpha)|}{d\alpha}. \end{cases}$$

Now we pass to integration of the sought six-order system (24) under condition (13), as well as under the equalities

$$\Gamma^{\alpha}_{11}(\alpha,\beta) = \Gamma^{\alpha}_{22}(\alpha,\beta) g^2(\beta_1) = \Gamma^{\alpha}_{33}(\alpha,\beta) g^2(\beta_1) h^2(\beta_2) = \Gamma_4(\alpha), \tag{25}$$

hold.

We also introduce (by analogy with (13)) a restriction on the function $f(\alpha)$. It must satisfy the transformed first equality from (10):

$$2\Gamma_1(\alpha) + \frac{d\ln|f(\alpha)|}{d\alpha} + \Gamma_4(\alpha)f^2(\alpha) \equiv 0. \tag{26}$$

To integrate it completely, one should know, generally speaking, seven independent first integrals. However, after the following change of variables,

$$w_4 = z_4,\ w_3 = \sqrt{z_1^2 + z_2^2 + z_3^2},\ w_2 = \frac{z_2}{z_1},\ w_1 = \frac{z_3}{\sqrt{z_1^2 + z_2^2}},$$

system (24) decomposes as follows:

$$\begin{cases} \dot\alpha = -w_4 + b\delta(\alpha), \\ \dot w_4 = F(\alpha) + \Gamma_4(\alpha)f^2(\alpha)w_3^2, \\ \dot w_3 = \left[2\Gamma_1(\alpha) + \dfrac{d\ln|f(\alpha)|}{d\alpha}\right] w_3 w_4, \end{cases} \tag{27}$$

$$\begin{cases} \dot w_2 = \pm w_3\sqrt{1+w_2^2}f(\alpha)g(\beta_1)\left[2\Gamma_3(\beta_2) + \dfrac{d\ln|h(\beta_2)|}{d\beta_2}\right], \\ \dot\beta_2 = \pm\dfrac{w_2w_3}{\sqrt{1+w_2^2}}f(\alpha)g(\beta_1), \end{cases} \tag{28}$$

$$\begin{cases} \dot w_1 = \pm w_3\sqrt{1+w_1^2}f(\alpha)\left[2\Gamma_2(\beta_1) + \dfrac{d\ln|g(\beta_1)|}{d\beta_1}\right], \\ \dot\beta_1 = \pm\dfrac{w_1w_3}{\sqrt{1+w_1^2}}f(\alpha), \end{cases} \tag{29}$$

$$\dot\beta_3 = \pm\frac{w_3}{\sqrt{1+w_2^2}}f(\alpha)g(\beta_1)h(\beta_2). \tag{30}$$

It is seen that to integrate system (27)–(30) completely, it is sufficient to determine two independent first integrals of system (27), by one integral of systems (28) and (29), and an additional first integral "attaching" Eq. (30) (i.e., five integrals in total).

Theorem 5.1. *Let the equalities*

$$\Gamma_4(\alpha)f^2(\alpha) = \kappa\frac{d}{d\alpha}\ln|\delta(\alpha)|,\ F(\alpha) = \lambda\frac{d}{d\alpha}\frac{\delta^2(\alpha)}{2} \tag{31}$$

be valid for some $\kappa, \lambda \in \mathbf{R}$. Then system (24) under equalities (12), (13), (16), (25), and (26) has a complete set of (five) independent, generally speaking, transcendental first integrals.

6 Conclusions

By analogy with low-dimensional cases, we pay special attention to two important cases for the function $f(\alpha)$ defining the metric on a sphere:

$$f(\alpha) = \frac{\cos\alpha}{\sin\alpha}, \tag{32}$$

$$f(\alpha) = \frac{1}{\cos\alpha \sin\alpha}. \tag{33}$$

Case (32) forms a class of systems corresponding to the motion of a dynamically symmetric five-dimensional solid body at zero levels of cyclic integrals, generally speaking, in a nonconservative field of forces [3, 4, 5]. Case (33) forms a class of systems corresponding to the motion of a material point on a four-dimensional sphere also, generally speaking, in a nonconservative field of forces. In particular, at $\delta(\alpha) \equiv F(\alpha) \equiv 0$ the system under consideration describes a geodesic flow on a four-dimensional sphere. In case (32), if

$$\delta(\alpha) = \frac{F(\alpha)}{\cos\alpha},$$

the system describes the spatial motion of a five-dimensional solid body in the force field $F(\alpha)$ under the action of a tracking force [6, 7, 8]. In particular, if

$$F(\alpha) = \sin\alpha\cos\alpha,\ \ \delta(\alpha) = \sin\alpha,$$

the system also describes a generalized five-dimensional spherical pendulum in a nonconservative force field and has a complete set of transcendental first integrals that can be expressed in terms of a finite combination of elementary functions [9, 10, 11].

If the function $\delta(\alpha)$ is not periodic, the dissipative system under consideration is a system with variable dissipation with a zero mean (i.e., it is properly dissipative). Nevertheless, an explicit form of transcendental first integrals that can be expressed in terms of a finite combination of elementary functions can be obtained even in this case. This is a new nontrivial case of integrability of dissipative systems in an explicit form [12].

Acknowledgements

This work was supported by the Russian Foundation for Basic Research, project no. 15-01-00848-a.

References

[1] M. V. Shamolin, “Comparison of complete integrability cases in Dynamics of a two-, three-, and four-dimensional rigid body in a nonconservative field”, Journal of Mathematical Sciences, 187:3 (2012), 346–359.

[2] M. V. Shamolin, “Some questions of qualitative theory in dynamics of systems with the variable dissipation”, Journal of Mathematical Sciences, 189:2 (2013), 314–323.

[3] M. V. Shamolin, “Variety of Integrable Cases in Dynamics of Low- and Multi-Dimensional Rigid Bodies in Nonconservative Force Fields”, Journal of Mathematical Sciences, 204:4 (2015), 379–530.

[4] M. V. Shamolin, "Classification of Integrable Cases in the Dynamics of a Four-Dimensional Rigid Body in a Nonconservative Field in the Presence of a Tracking Force", Journal of Mathematical Sciences, 204:6 (2015), 808–870.

[5] M. V. Shamolin, "Some Classes of Integrable Problems in Spatial Dynamics of a Rigid Body in a Nonconservative Force Field", Journal of Mathematical Sciences, 210:3 (2015), 292–330.

[6] M. V. Shamolin, "Integrable Cases in the Dynamics of a Multi-dimensional Rigid Body in a Nonconservative Force Field in the Presence of a Tracking Force", Journal of Mathematical Sciences, 214:6 (2016), 865–891.

[7] M. V. Shamolin, "Integrable Systems with Variable Dissipation on the Tangent Bundle of a Sphere", Journal of Mathematical Sciences, 219:2 (2016), 321–335.

[8] M. V. Shamolin, "New Cases of Integrability of Equations of Motion of a Rigid Body in the n-Dimensional Space", Journal of Mathematical Sciences, 221:2 (2017), 205–259.

[9] M. V. Shamolin, "Some Problems of Qualitative Analysis in the Modeling of the Motion of Rigid Bodies in Resistive Media", Journal of Mathematical Sciences, 221:2 (2017), 260–296.

[10] V. V. Trofimov, "Euler equations on Borel subalgebras of semisimple Lie algebras," *Izv. Akad. Nauk SSSR, Ser. Mat.,* **43**, No. 3 (1979), 714–732.

[11] V. V. Trofimov, "Finite-dimensional representations of Lie algebras and completely integrable systems," *Mat. Sb.,* **111**, No. 4 (1980), 610–621.

[12] V. V. Trofimov and M. V. Shamolin, "Geometric and dynamical invariants of integrable Hamiltonian and dissipative systems", Journal of Mathematical Sciences, 180:4 (2012), 365–530.

Maxim V. Shamolin, Lomonosov Moscow State University, Russian Federation

Nonlinear torsional dynamics of weakly coupled oscillatory chainse

V.V. Smirnov, M.A. Kovaleva, L.I. Manevitch
diki.ipme@gmail.com

The Compressive Response of Boron Carbide Ceramic under High Strain Rate

J. Venkatesan, M.A. Iqbal, V. Madhu
jsvenkat.c@gmail.com

Abstract

The boron carbide (B4C) ceramic is suitable material for armour application due to its low density, high hardness and compressive strength. It is subjected to high strain rate of loading during the projectile impact. Therefore, in this study, the compressive response of B4C is determined under low and high strain rate of loading using Modified Split Hopkinson Pressure Bar (MSHPB) test. The experimental results indicated that the uniaxial compressive strength of B4C ceramic is not sensitive to the strain rate of up to 103 s-1 and the failure of the B4C specimen was sudden and catastrophic under the uniaxial compressive loading at both low and high strain rate.

1 Introduction

Ceramics are suitable candidate for the armour design due to it is superior properties like high hardness and high strength to weight ratio. Boron carbide (B4C) ceramic is widely used for the armour design due to its higher hardness, compressive strength and low density among the advance ceramic materials [1].

The projectile impact on the ceramic layer develops strain rate in the range of $10^3 - 10^4\ s^{-1}$ [2]. Therefore, it is essential to understand the B4C ceramic response at these strain rates and also the effect of strain rate on its behaviour. The most of the available studies of B4C ceramic for armour application was focused on the strength of the material under shock loading where the material experiences strain rate of above $10^5\ s^{-1}$ [3]–[6]. There is very few studies are available on B4C response at the strain rate range of $10^{-3} - 10^4\ s^{-1}$.

Paliwal and Ramesh [2] conducted uniaxial compressive tests at strain rate range of $10^{-6} - 2\ \times 10^2\ s^{-1}$ to study the dynamic failure and strength of the B4C ceramic using modified split Hopkinson pressure bar test and high speed camera. Hogan et al. [7] studied the effect of processing-induced defects on the dynamic compressive strength and failure of B4C using SHPB. The material was investigate at strain rate range of $3.5 \times 10^2 - 10^3\ s^{-1}$. There is no other studies are available in these strain rate as per the author knowledge. Therefore, in this study the response of B4C ceramic was explored under high strain rate of loading. The Split Hopkinson pressure bar setup for the metal testing is modified for ceramic testing in the current study.

2 Experimental Procedure

The commercially available hot pressed boron carbide ceramic tile was used for the current study. The B4C specimens for the quasi-static, SHPB and density measurements were machined from the 100 mm × 100 mm × 5 mm and 10 mm thick tiles using the Wire-cut Electrical Discharge Machine (WEDM). The WEDM machining quality is mainly depends on the electrical conductivity and ductile or brittle nature of the material. Though the B4C ceramic has sufficient electrical conductivity to be machined using WEDM, due to its brittle nature, the machining was very difficult and time consuming process. The quality of the surface finish after machining the specimen by WEDM was extremely good due to the slow rate of machining and intense care. Density of the B4C was measured using Archimedes method as per the guidance of ASTM - C373-16 and the measured density was 2.50 g/cc.

Cylindrical B4C specimens of 5 mm diameter and 5 mm length were used for uniaxial compressive experiments at quasi-static and high strain rate loading see Fig. 1. The loading surface of the specimens were polished to 6 Bxm using the Buehler diamond impregnated metal discs of 45 Bxm to 6 Bxm to eliminate the premature failure due to the presence of surface defect. The surface of the specimens were examined by optical microscope before the testing to ensure the surface is defect free. Specimens with unpolished surface was also tested under the quasi-static and high strain rate loading. The end friction between the loading platens of the testing machine and the specimen surface builds the complex stress and the testing is no more uniaxial. Therefore, lubricant was applied on the specimen surface to minimize the interface friction during the testing.

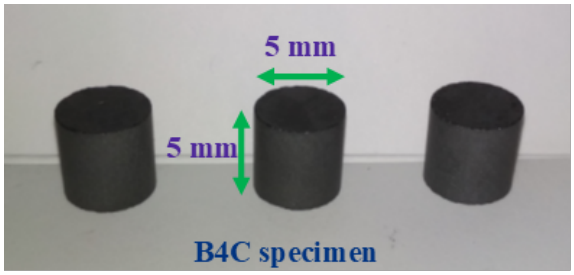

Figure 1: WEDM machined B4C specimens

The quasi-static test was carried out using the INSTRON Universal Testing Machine (UTM). The UTM loading platen hardness was lower than the hardness of B4C ceramic. The harder B4C indent into the loading platen due the large difference of hardness. Therefore, harder material of tungsten carbide (WC) platens of the diameter 13 mm, 30 mm, 50 mm with 10 mm thick was placed between the loading platen and B4C ceramic specimen. The quasi-static tests were conducted with strain rate of $10^{-3}\ s^{-1}$ and $10^{-2}\ s^{-1}$.

Modified split-Hopkinson pressure bar (MSHPB) apparatus was used to measure the uniaxial compressive strength of B4C ceramic under high strain rate. The SHPB apparatus for metal testing is modified for the ceramic testing. The apparatus contains striker of various length, incident, transmission and momentum trapper

Table 13: Detail of pulse shaper and insert

	Material	**Dimension**
Pulse shaper	Copper	5 mm diameter and 0.5 mm thick and 8 mm diameter 0.5 mm thick
Insert	Tungsten carbide	13.1 mm diameter and 6 mm length
Insert confinement	Steel	Inner diameter = 13.1 mm, Outer diameter = 20 mm,Length = 5.9 mm

bar of 2000 mm. the bar material is vascomax steel with density of 8080 kg/m^3, elastic modulus of 196.4 GPa and poisson's ratio of 0.3. The same has been modified by introducing thin copper pulse shaper between striker and the incident bar and steel confined WC inserts in the interface of incident bar-specimen and specimen-transmission bar see Fig. 2. The detail of the insert and pulse shaper is given in Table 1.
The WC inserts is protect the incident and transmission bars from the indentation of B4C specimen due to the high hardness. The WC inserts was confined by the steel rings to prevent the inserts failure beforehand the ceramic undergoes failure. The function of copper pulse shaper is to increase the rise time of the incident pulse which helps to maintain the stress equilibrium in the ceramic specimen throughout the test. Several SHPB trials with different impact velocity and striker length were conducted on copper pulse shaper to establish the required shape of the incident pulse. The dimension of the pulse shaper is finalised based on the trial test results. For further details regarding the design and modification of the SHPB for the ceramic testing can be seen in [8].

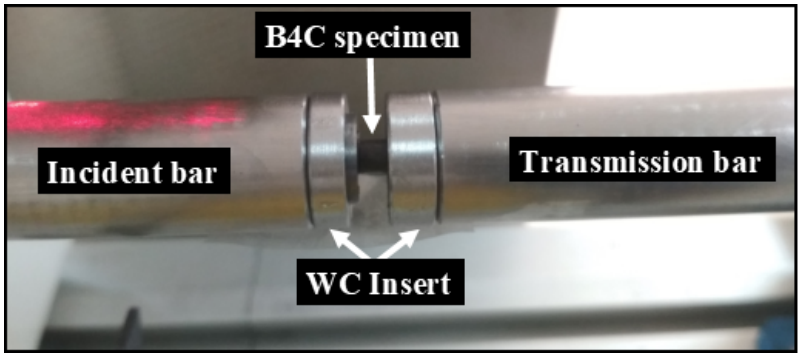

Figure 2: Modified split Hopkinson pressure bar setup for testing the ceramic material

3 Results and discussion

3.1 Quasi-static test

The B4C ceramic stress-strain relationship at the strain rate of 10^{-3} s^{-1} is shown in the Fig. 3. The average uniaxial compressive strength of the B4C ceramic was

3600 MPa. Ceramic specimen fracturing and spalling was observed during the end of test. The B4C specimen failed catastrophically after the specimen attains the capacity and the most of the ceramic specimen became powder. It was difficult to collect all the failed material due to fineness of the crushed ceramic. Therefore, the crushed B4C specimen of little quantity is collected and it will be analysed further for understand the fracture and failure mechanism of B4C ceramic under quasi-static loading.

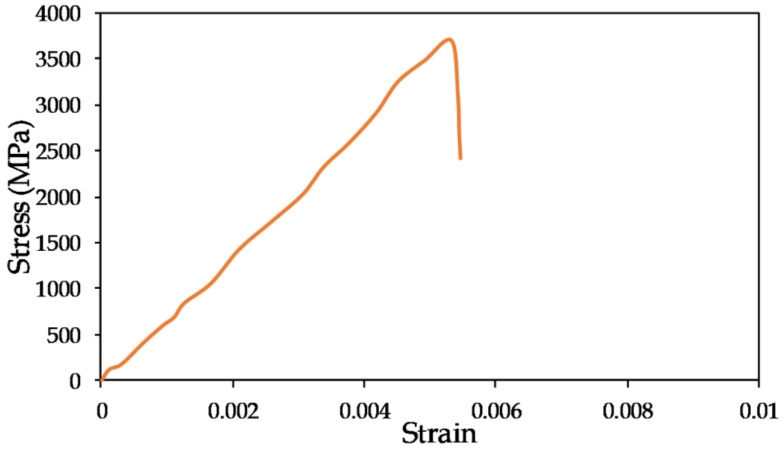

Figure 3: Stress-strain relationship of B4C at strain rate of 10^{-3} s^{-1}

3.2 High strain rate loading

The SHPB strain signal of the current experiment for 200 mm striker is shown in the Fig. 4. The rise time the signal is increased by copper pulse shaper. The impedance match of the inserts and the SHPB bars were ensured by trial experiments without any specimen and it is observed that the incident strain signal completely passed through the inserts.

Hence, the dimension and arrangement of the inserts is satisfactory for the SHPB experiment. The B4C specimens then tested under various strain rate. Maximum strain rate achieved in the current experiment was 10^3 s^{-1}. For the higher strain rate the striker velocity increased, however the signals measured in the transmission bar was not appropriate and was difficult to establish the stress-strain relationship and calculate the strength of B4C ceramic, therefore these tests results were excluded. In future, the B4C ceramic response at the strain rate above $10^3 s^{-1}$ will be studied in by fixing the strain gauges on the surface of the specimen. The strain rate sensitivity of the B4C ceramic is studied by comparing the strength at various strain rate. It is observed from the experimental results that the strength of the B4C ceramic is not sensitivity in the strain rate range of 10^{-3} to 10^3 s^{-1}(Fig. 5) and the similar behaviour was reported by [2, 7].

Therefore, it can be concluded that the B4C ceramic is strain rate independent for the strain rate up to 10^3 s^{-1}. The failure of the B4C was axially splitting and the failure was exactly at the center of the specimen for the strain rate of 3×10^2 s^{-1} and the failure surface of the B4C was rough which indicates the excellent shear

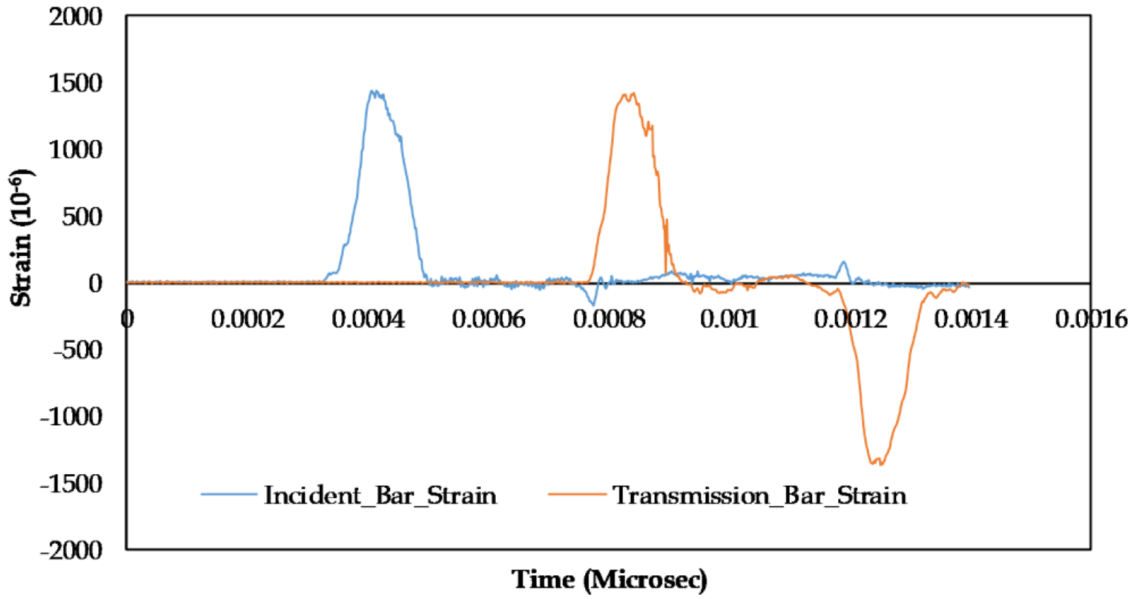

Figure 4: Strain signal of SHPB without specimen and with the 13 mm diameter insert (striker length and impact velocity is 200 mm and 13 m/s respectively)

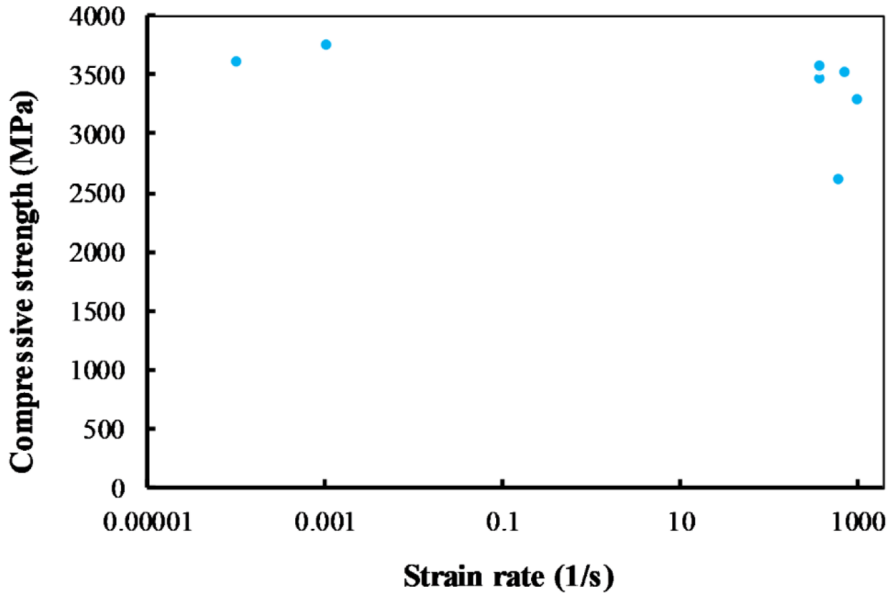

Figure 5: . Uniaxial compressive strength of B4C at various strain rate

resistance of the material. At higher strain rate the specimen becomes powder and the fractured fragments were similar to the quasi-static loading. The failed ceramic was collected for the further analysis of the fragment shape and size and the fractured surface of the B4C for the future study.

4 Conclusion

The uniaxial compressive strength of the B4C ceramic is determined at the quasi-static and dynamic loading condition and the strain rate ranged from $10^{-3}s-1$ to $10^{3}\ s^{-1}$. The specimens were machined by wire-cut EDM and tested under dynamic loading using split Hopkinson pressure bar setup. The experimental results showed that the uniaxial compressive strength of B4C is not sensitive to the strain rate as the strength was almost same in all the strain rate loading. The failure of the ceramic under both quasi-static and dynamic loading condition was catastrophic and crushed to powder. The failed B4C ceramic is collected and its failure surface and fragments will be analysed for the understanding the fracture and failure of this material under various loading condition.

Acknowledgements

The authors are gratefully acknowledging the financial support provided by DRDO through the research project grand no. ARMREB/MAA/2016/185 for carrying out the present study and also the author extends his gratitude to Mr. Bidyapati Mishra and Dr. S. G. Savio for their technical support

References

[1] Chen MW, McCauley JW, LaSalvia JC, Hemker KJ. Microstructural characterization of commercial hot-pressed boron carbide ceramics. J Am Ceram Soc 2005;88:1935вГ˙Y42.

[2] Paliwal B, Ramesh KT. Effect of crack growth dynamics on the rate-sensitive behavior of hot-pressed boron carbide. Scr Mater 2007;57:481вГ˙Y4.

[3] Vogler TJ, Reinhart WD, Chhabildas LC. Dynamic behavior of boron carbide. J Appl Phys 2004;95:4173вГ˙Y83.

[4] Holmquist TJ, Johnson GR. Characterization and evaluation of boron carbide for plate-impact conditions. J Appl Phys 2006;100.

[5] Hayun S, Paris V, Dariel MP, Frage N, Zaretzky E. Static and dynamic mechanical properties of boron carbide processed by spark plasma sintering. J Eur Ceram Soc 2009;29:3395вГ˙Y400.

[6] Grady DE. Hugoniot equation of state and dynamic strength of boron carbide. J Appl Phys 2015;117.

[7] Hogan JD, Farbaniec L, Sano T, Shaeffer M, Ramesh KT. The effects of defects on the uniaxial compressive strength and failure of an advanced ceramic. Acta Mater 2016;102:263вГ˙Y72.

[8] Chen W, Song B. Split Hopkinson (Kolsky) Bar. Boston, MA: Springer US; 2011.

J. Venkatesan, Indian Institute of Technology Roorkee, India
M.A. Iqbal, Indian Institute of Technology Roorkee, India
V. Madhu, DRDO бГY Defence Metallurgical Research Laboratory, Hyderabad, India

Automatic frequency control of the magnetron system for medical linear accelerator using fuzzy logic control

Nattawat Yachum, Nilaped Russamee, Jiraphon Srisertpol
nattawat@slri.or.th

Abstract

The Medical Linear Accelerator (MedLINAC) at Synchrotron Light Research Institute (SLRI) in Thailand is the first machine prototype that has been successfully installed and commissioned. The MedLINAC provides the radiation effect of X-RAY for cancer treatment. The control system of the MedLINAC is currently manually controlled by Users, adjusting the microwave power, provided by a magnetron, through the Graphical User Interface (GUI). The magnetron system includes the structure of anode and cathode polarities and two-polarities of permanent magnets, generates the resonant frequency to accelerator tube. The resonant frequency of 2.998 GHz and the peak power of 3.1 MW are suitable parameters with influence to the energy of an electron. The analysis of a magnetron is very complex and it usually requires solving transcendental equations. Both Hull-cutoff and Hartree conditions are estimated properly as parameters of the resonant frequency by using the fundamental principle of an electron motion in structured magnetron. This paper demonstrates the design procedures of automatic frequency control of the magnetron system for the MedLINAC using the Fuzzy Logic Control (FLC) and adjusts the parameters of fuzzy identifier model by using recursive least square algorithm. The controller has a recursive form and model uncertainties. The experimental results obtained from adjusting the desirable resonant frequency, which excites the electrons charge and makes High-power energy for performance of X-RAY radiation.

1 Introduction

The MedLINAC has been developed the capability to accelerate an energy of an electron and to generate radiation of X-RAY by SLRI for medical use in hospitals. It is a necessary equipment for the radiotherapy treatment implies a cancer. Two modes Operations of the radiotherapy treatment can be used. They are the treatment by the X-RAY and electron beam. The MedLINAC consists of 3 main parts: Linear Accelerator (LINAC), LINAC treatment head and the treatment couch system. The prototype of the MedLINAC at SLRI has used LINAC of S-band type

and the resonant frequency of 2.998 GHz. The generation of an electron is emitted by the electron-gun type of hot-cathode, which sets to be negative voltage of -30 kV. In the process for producing of frequency or the resonant frequency of 3 GHz approximately, the Magnetron system is operated the power rating of 3.1 MW and generated the frequency range between of 2,993 to 3,002 MHz by applying high-voltage from a modulator and the voltage must set at 1,043 V.
The Magnetron system has generated high-power frequency which requires to match properly the accelerator tube at resonant frequency of 2.998 GHz. Two techniques for the control of the magnetron system were currently used. They were using to tune the technique of the frequency with applied voltage for experimenting the magnetron by [11, 15] and using to tune the technique of the multiple-cavity magnetron with consideration of the internal structures such as amount, dimension, space and gap of cavities, which depends on the actuator with rod of a motor by [10, 13, 14]. A stepping-motor is manually controlled by Users via a program on computer. Result of the manual control can control constantly the resonant frequency. If the magnetron system is disturbed by the ambient temperature, it takes effect on the resonant frequency as change and canвГЄt adjust the frequency back to the reference point rapidly. The energy of an electron and the radiation are fast decreasing. Therefore, it is the unstable system. [5, 6, 7, 8, 9] The control system with the FLC Algorithm is a simple, reliable and accurate system. It usually uses in the feedback control loop and improves capable of the performance under external disturbance, which is using to control a linear or non-linear system.
In this paper, The FLC designs and applies the Automatic Frequency Control of the magnetron system for the MedLINAC and it controls to generate constantly the resonant frequency of 2.998 GHz. The FLC of the resonant frequency can control back to the reference point as automatically, although the external disturbance is occurred. The FLC is designed by LabVIEW programming. The objective of the FLC controls the position of stepping motor by keeping the voltage from modulator and shows the dynamic response of X-RAY radiation on the screen. The performance of the FLC was found better than the control of manual user.

2 Magnetron System Analysis

2.1 An electron motion in an electromagnetic field

Both electric and magnetic field influence significantly the motion of an electron, that depends on the orientation of the two fields. If the electric and magnetic field are at the right angle (90°) to each other, this type of field is called a crossed field. The electrons were emitted by the cathode polarity, which are accelerated by the electric field and the more their path is bent by the magnetic field. Since electric and magnetic field or called an electromagnetic field directly influence acting on an electron, it can be explained by Lorentz force law. [1, 2] For rectangular coordinates were written to replace by cylindrical coordinates, which are analyzed data from structure of the magnetron. Hence, the equation of motion for electrons in cylindrical

coordinates is written to rearrange the equations as.

$$\frac{d^2r}{dt^2} - r(\frac{d\phi}{dt})^2 = \frac{e}{m}E_r - \frac{e}{m}r\frac{d\phi}{dt}B_z \tag{1}$$

$$\frac{1}{r}\frac{d}{dt}(r^2\frac{d\phi}{dt}) = \frac{e}{m}B_z\frac{dr}{dt} \tag{2}$$

2.2 Hull cut-off and Hartree conditions

General operation of a cylindrical magnetron is controlled by applying the voltage (V_{OC}) at the anode and cathode polarities from a modulator, generates the characteristic dc-voltage of 980 to 1,043 V and the pulse width of 5 μS. The magnetron system connects with perpendicular fields of between the magnetic field (B_{OC}) and the electric field. The electrons are emitted by cathode. They move to the anode and be grazed by the influence of magnetic field. The electron leaves from the cathode with initial velocity of zero and the behavior of the electron grazes the anode block. It can be called the cut-off condition. From equation (2), rearrangement of the equation result in the condition of both the Hull cut-off magnetic field and dc-voltage to the equations as [3, 4, 12].

$$B_{OC} = \frac{\sqrt{\frac{8mV}{e}}}{r_a(1-\frac{r_c^2}{r_a^2})} \tag{3}$$

$$V_{OC} = \frac{e}{8m}(B_{OC})^2(r_c)^2(1-\frac{r_c^2}{r_a^2})^2 \tag{4}$$

where r_a, r_c are the radius of anode and cathode, respectively.

The Radio Frequency (RF) Field occurs, this voltage is the condition at which oscillations should start. From an equation (1) and (2), applying this synchronous condition govern an electron movement in a cylindrical coordinate system. It provides at the same time that the magnetic is sufficiently large, so the undistorted space charge does not extend to the anode. The general working operation of cylindrical magnetron is operated by applying the anode-voltage that is slightly above the Hartree-voltage curve and the magnetron system starts to oscillate. [3, 4] However, the anode-voltage of a magnetron is always set below the $\pi - 1$ mode line to avoid mode competition. The Hartree voltage V_H for RF oscillation to start in a magnetron can be obtained.

$$V_H = \frac{\omega_o B}{2}(r_a^2 - r_c^2)^2 - \frac{m}{2e}(r_a\omega_o)^2 \tag{5}$$

where $\omega_o = \frac{\omega}{n}$, ω_o is the angular frequency of the electron, ω is the angular frequency of RF field and n is the modes of oscillation.

3 Automatic Frequency Control (AFC) System

The control of the RF signal is generated by the coupling from the cavity of the magnetron. It depends on the adjustable position of the structured magnetron with the tuning on the rod of a stepping motor. The result of the tuning indicates a changing frequency. The appropriate RF signal for the LINAC of s-band type (2 to 4 GHz) requires the frequency of 2.998 GHz approximately. It is called *the resonant frequency*. An electron was emitted by the electron gun. If when it hits the resonant frequency, the electron increases more energy. After the electron with high-energy moves towards and hits the x-ray target, it causes to affect the radiation of X-Ray. In part of the resonant frequency, the disturbance of the temperature is one main factor of working operation on the magnetron system to effect of the frequency inconsistently. Therefore, the resonant frequency must be measured by using the sensors (AFC circuit). They are the Forward (FWD) power and Reflect (REFL) power. The adjustment of the resonant frequency depends on the design via the linguistic development of program and operates the frequency automatically. The algorithmic FLC is part of the key component for controlling the output signal and compensating the frequency.
The experimentation of the AFC system, the start writes the code to form based GUI on Main Computer (Main PC). The developmental code of based language uses Graphical programming language. It is called *LabVIEW*, which can write the code on the Embedded system under the real-time system (Fuzzy Controller). The Fuzzy Controller is controlled by the Ethernet network communication. It controls and monitors the positional movement of the stepping motor with the hardware and software of the National Instruments products or be called *SoftMotion Module*. This is the central communication of devices between the name of NI-9512 and Motor driver. Both the NI-9512 and Motor driver generate the pulse signal and convert the pulse signal to the position of a stepping motor, respectively. The radiation of X-Ray is caused by hitting the X-Ray target. It can use the sensor (Radiation Monitor) on the measurement of the radiation and displays on Main PC. Finally, the procedures of the AFC system are shown in Fig. 1.

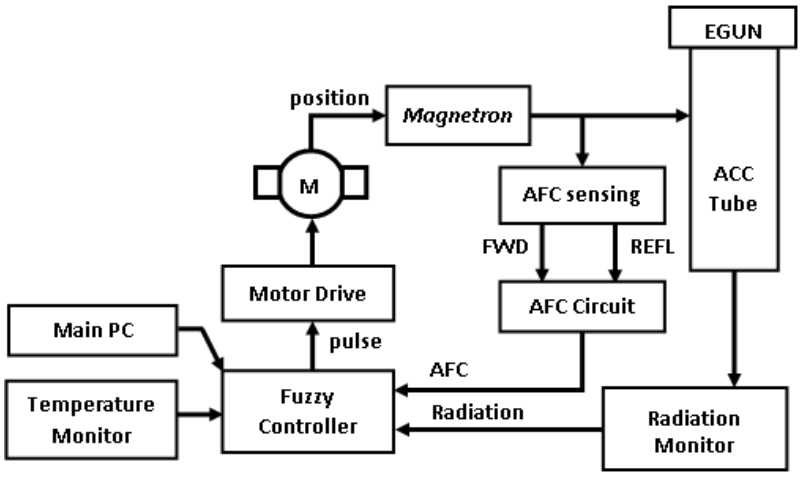

Figure 1: Block diagram of automatic frequency control

In section of tuning for the resonant frequency, the AFC sensing is the measurement device of the feedback signal system. Main components consist of Directional coupler and Circulator. Which are the monitor of the FWD and REFL signal, respectively. Both FWD and REFL signal are compared by AFC circuit module, which uses a particular frequency of 2.998 GHz. The results of the comparison signal can use in the process of the FLC towards the future. All components for the experimentation of the AFC system are shown in Fig. 2.

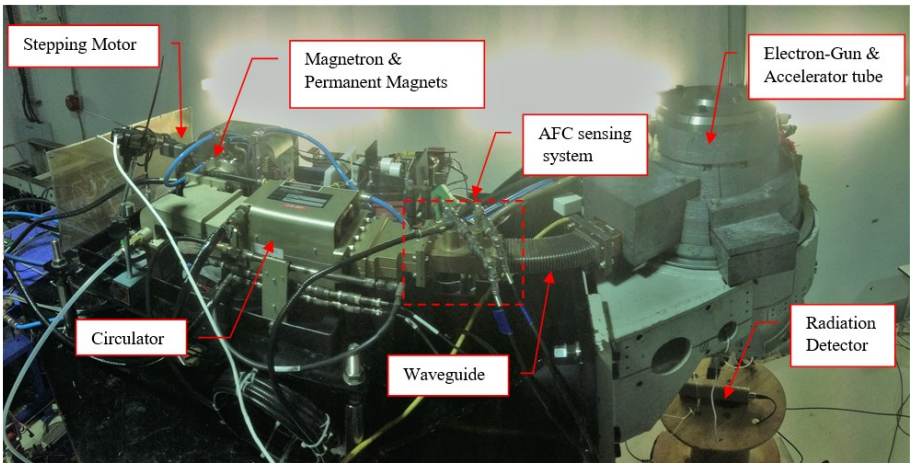

Figure 2: The AFC system of Medical Linear Accelerator

In Fig. 2, the component of the generational resonant frequency is a magnetron. It is a structured form in the shape of a cylindrical tube and that was produced by e2v technologies. The Oscillation of the magnetron (MG7095) depends on working operation by applying the anode-voltage supply between region of Hull cut-off curve and the straight Hartree line. It is always set the mode oscillation of the magnetron as $\pi - 1$ mode. [3] The anode structure of the hole-and-slot-Magnetron (MG5193) with twelve-cavity forms the same as the Magnetron (MG7095) such as the dimension shape and structured form but the output rating differs. Therefore, the MG7095 type of the magnetron can use the same specification of the dimension as the MG5193. It is presented in the Table 14 and can be calculated by using the equation (5) and illustrates results of calculation in Fig. 3.

Table 14: Hull cut-off/Hartree conditions of the cylindrical magnetron (MG7095)

No.	Magnetrons parameters	Results
1	Radius of anode (mm)	17
2	Radius of cathode (mm)	9.25
3	Permanent magnet (Tesla)	0.152
4	Hull cut-off curve (kV)	72.6378
5	Hartree line π mode (kV)	40.4312
6	Hartree line $\pi - 1$ mode (kV)	46.5712
7	Frequency (GHZ)	2.998

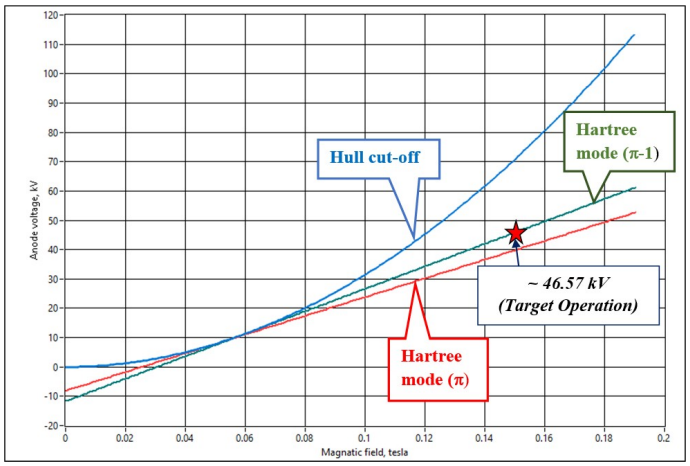

Figure 3: Operating anode-voltage of mode oscillations

4 Implementation of Fuzzy Controller

The design of Fuzzy controller is the key component of the controller for engineering design. The preprocessing and postprocessing steps depend on the determinant laws of the control such as the adjustment of the input and output membership. They must be converted by using the rules-based or the inference engine of the FLC and results in the degree of membership. The characteristic membership indicates the upper-lower and maximum-minimum value and can assign the value of membership function such as triangular shape and straight-line membership function, which uses for input and output variables, respectively. The Input and Output membership function is shown in Fig. 5, 6 . The rules-based FLC determines the human linguistic expression in the series of IF-THEN rules and is illustrated in Table 15. Hence, both the memberships and rules-based FLC should be interpreted by an expert.

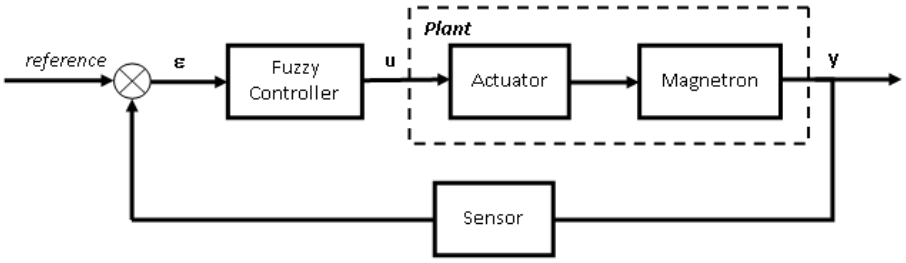

Figure 4: Block diagram of the Fuzzy controller

Block diagram of Fuzzy controller is shown in Fig. 4. An error (ϵ) of the system is the feedback signal (y) of the AFC system. The feedback signal includes of the AFC-A and AFC-B and they are compared by the AFC circuit module, which is a key component within a control loop for the frequency tuning of the operation of LINAC. After that the feedback signal compares again with the reference input. Hence an error value uses in the rules-based FLC. For Block of Fuzzy controller, the preprocessing and postprocessing data always convert the data such as a real signal to the Fuzzy sets and the Fuzzy sets to a real signal, respectively. The example of the output data (u) should convert type of data from digital signal to analog

signal and determines properly the value for moving position of the actuator. So, it can set the value in percentage unit (0-100%). Next, Block of the actuator is the stepping motor. It can control to desire the position consistently by applying the pulse signal from the motor driver. The position of the stepping motor is changed by a mechanism of the structured magnetron or space of cavity, which it changes. This directly affects the frequency output or AFC signal. The AFC system is controlled by the linguistic rules and uses in the Fuzzy Controller Block. It is used by Takagi-Sugeno or center of sum (COS) method. [5] A. Basci proposes the inference of Fuzzy, which uses an on-line method or adjusts the parameters of a Takagi-Sugeno identifier model to matching behavior of the control system. From Fig. 5, 6, it is straight line group that can be calculated as follow.

$$COS = \sum_{m=1}^{L} \frac{\mu_{(k_m)} k_m}{\mu_{(k_m)}} \tag{6}$$

where $\mu_{(k_m)}$ is the degree of membership of the input variable and k_m is the output variable range.

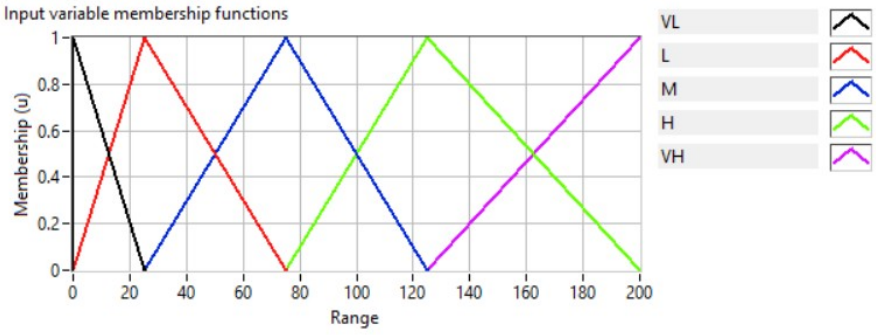

Figure 5: Membership function: Input variables

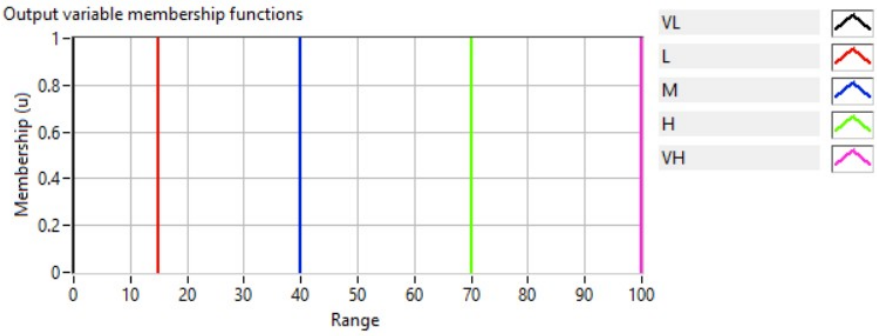

Figure 6: Membership function: Output variables

The output variable of the AFC system is chosen. It should convert to the position control of 0 to 100 %. The membership function of the rules-based FLC includes the input and output logics. They consist of very Low (VL), Low (L), Medium (M), High (H) and very High (VH). The linguistic values of Fuzzy Controller and the

Table 15: Fuzzy Rules Bases

No.	If Input is	Then Output is
1	VL	VL
2	L	L
3	M	M
4	H	H
5	VH	VH

inference system are evaluated by Takagi-Sugeno method. Therefore, the rules of the FLC are mentioned and can be edited by the Fuzzy system designer, which adds the add-on LabVIEW. The system of the fuzzy controller is a single input and single output (SISO) system. It determines the input of position error and the output of position movement. The design of the LabVIEW program writes the code with two sections such as the front panel and the block diagram, which are together called VI (Virtual Instrument).

5 Experimental Results

The magnetron system is controlled by using Algorithm of the FLC for the MedLINAC via LabVIEW program. The determined reference of the temperatures at important components consist of the magnetron system and accelerated tube. The tuning of device requires to set the constant temperature by heating of the inlet water manifolds of $40°C$. Next, the input-voltage and the output-voltage is applied by a modulator, which is capability of device generates a pulse width of 5 μS and the input and output voltage with rating of 1,043 V and 45 kV, respectively. The Magnetron system works in the region between range of the Hull cut-off and Hartree line refer to Fig. 3. The experimentations of AFC system for the MedLINAC and results are shown in Fig. 7–9.

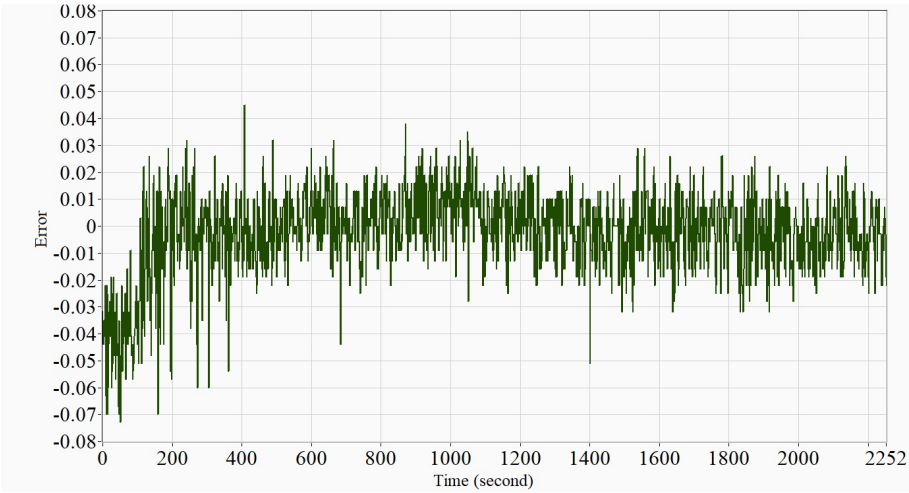

Figure 7: Fuzzy system response: Error response

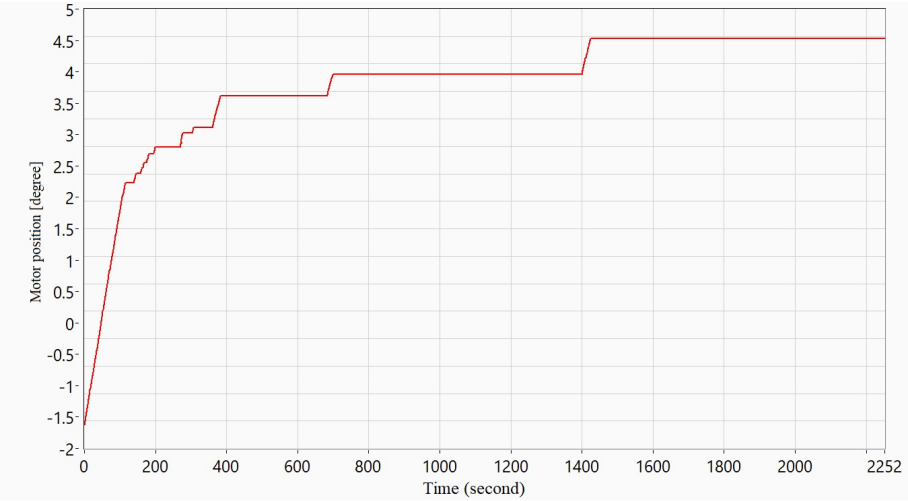

Figure 8: Fuzzy system response: Position response

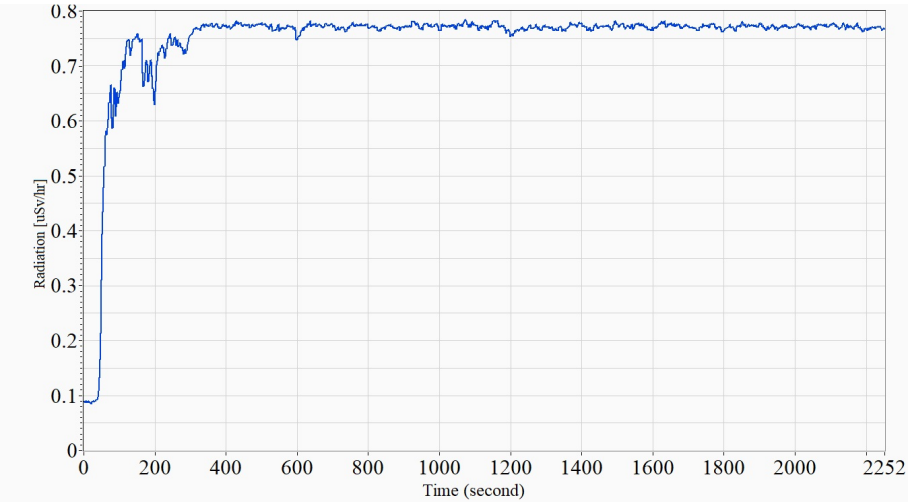

Figure 9: Fuzzy system response: Radiation response

Fig. 7–9 show all experimental results of 2,252 seconds or 38 minutes approximately. An error response (ϵ) or AFC comparative signal in Fig. 7 response compares between the frequency output and the input reference (Required 2.998 GHz). It controls the feedback frequency (Resonant frequency) of 2.998 GHz constantly. The boundary of control sets at the range of between -0.04 to +0.04 V. Results of the signal are out of range, which consist of 0 to 400 second, 700 and 1400 second approximately. In Fig. 8, the effect of the moving Stepping Motor with out of range tunes automatically the position. This moves from 1.6 to 4.6 degree approximately and the signal of the motor position response is zero overshoot, rise time of 100 second and the system of positional Motor in time of 1,430 second constantly. And finally, the results of X-RAY radiation (Fig. 9) from the MedLINAC of 0.775 μSv/hr approximately, the signal of the radiation likely follows direction of an error and the positional Motor response. It observes that the radiation signal of the AFC system. The Fuzzy logic control can control the X-RAY radiation response constantly. However, if the disturbance caused, The Stepping Motor properly moves to tune the

position by the Fuzzy logic rules and the magnetron system can adjust itself so the output converges to its desired boundary.

6 Conclusions

The experimental result presents the effective performance control system for frequency control of the magnetron system using the FLC design with LabVIEW program. The dynamic response of the frequency shows no overshoot, rise time of 100 seconds and settling time of 320 seconds. The disturbance caused in system such as the changing ambient temperature in the system. The FLC can adjust itself and output signal is in range of the desired input. This control system is an engineering research and development study for sustainable technology of the MedLINAC at SLRI, Thailand.

Acknowledgements

The Authors are grateful to Synchrotron Light Research Institute (Public Organization), Thailand, the Ministry of Science and Technology and Suranaree University of Technology for supports of the tools, equipment, budgets and research location.

References

[1] G. B. Collins, Microwave Magnetrons Vol. 6, New York: McGrew-Hill, 1948.

[2] Samuel Y. Liao, Microwave devices and circuit, Third Edition: Prentice Hall, Englewood Cliffs, New Jersey 07632, pp. 6-14, 1997.

[3] L. Ma, 3D Computer Modeling of Magnetrons, Doctor of philosophy in Electrical Engineering, Department of Electronic Engineering, Queen Mary, University of London, United Kingdom, 2004.

[4] S. Fernandez-Gutierrez, Simulation of a Magnetron using Discrete Modulated Current Source, Doctor of philosophy in Electrical Engineering, Boise State University, United State, May 2014.

[5] A. Basci and A. Derdiyok, Implementation of an adaptive fuzzy compensator for coupled tank liquid level control system, Elsevier Measurement 91, pp. 12-18, 2016.

[6] R. Paul et al., LabVIEW Implementation of Fuzzy Logic Controller for Heat Exchanger Process, 1st International conference on futuristic trend in computational analysis and knowledge management, pp. 13-17, 2015.

[7] P. Hari Krishnan and M. Arjun, Control of BLDC Motor Based on Adaptive Fuzzy Logic PID Controller, International Conference on Green Computing Communication and Electrical Engineering, 6-8 March 2014.

[8] L. Sabri and H. AL-Mshat, Implement of Fuzzy and PID controller to water Level System using LabVIEW, International Journal of Computer Applications, Vol. 116 No. 11, April 2015.

[9] K. Premkumar and Dr.B.V.Manikandan, Adaptive fuzzy logic speed controller for Brushless DC motor, International Conference on Power, Energy and Control, 6-8 Feb 2013.

[10] R. B. Nelson, Methods of Tuning Multiple-Cavity Magnetrons, Proceedings of the I.R.C., Research Laboratory, General Electric Co., Schenectady, N. Y., December 13, 1946.

[11] H. Obata, N. Tsuji and K. Furumoto, Electronic-Frequency-Tuning Magnetron, IEEE Transactions on Electron Devices, Vol. 59. No. 11, November 2012.

[12] T. Isenlik and K. Yegin, Tutorial on Design of Hole-Slot-Type Cavity Magnetron Using CST Particle Studio, IEEE Transactions on Plasma Science, Vol. 41 No. 2, February 2013.

[13] J. Turner, Magnetron Automatic Frequency Control System, EE498 senior design project report, pp. 1-8.

[14] Sungsu Cha et al., Development of an automatic frequency control system for an X-band (=9300MHz) RF electron linear accelerator, Nuclear Instruments and Methods in Physics Research A 855(2017) 102-108, 4 March 2017.

[15] H. Huang et al., Simulation and Experiments of an S-band 20-kW Power-Adjustable Phase-Locked Magnetron, IEEE Transactions on Plasma Science, Vol. 45. No. 5, May 2017.

Nattawat Yachum, Synchrotron Light Research Institute, Nakhon Ratchasima, Thailand
Nilaped Russamee, Synchrotron Light Research Institute, Nakhon Ratchasima, Thailand
Jiraphon Srisertpol, School of Mechanical Engineering, Suranaree University of Technology, Nakhon Ratchasima, Thailand

Influence of hydrogen on stress-strain state of pipeline

Tatiana V. Zinovieva
tatiana.zinovieva@gmail.com

Abstract

An essential present-day engineering problem of pipeline destruction in the result of influence of hydrogen contained in the transported medium is considered. The relevance of this topic is determined by possible environmental and economic issues, in the event of an accident resulting in gas and oil leaks.

Hydrogen affects mechanical properties of the pipe, changing its stress-strain state, which, in turn, changes the distribution of bound hydrogen in the material of the pipe. The hypothesis adopted on the nature of this connection made it possible to explain the reasons for the destruction of pipeline on a simple model.

The problem of the theory of elasticity for a hollow pipe under internal pressure is considered in a plane axisymmetric formulation; stress and strain fields are found. Estimates of stresses according to the Mises criterion have shown the appearance of plastic deformation zone in the pipe that is leading to the delamination of the material in the circumferential direction. This result corresponds to presently known experimental data.

Keywords: influence of hydrogen, stresses in pipeline, hydrogen-affected delamination.

1 Introduction

Many disasters were caused by hydrogen cracking of metals. This phenomenon is especially dangerous for engineering structures operating under high pressure, including oil pipelines. Presence of hydrogen in the transported medium leads to its quick accumulation inside the mass of metal, and, as a result, to a significant deterioration of pipeline mechanical properties [1].

A research by Nie [2] shows, that hydrogen saturation reduces the ultimate stress of metal by a factor of 3 – 5. Studies of Polyanskiy et al [3] have shown that increase of hydrogen concentration by a factor of 2 – 3 with respect to its natural concentration leads to damage of pipe material.

It is well known, that hydrogen causes crack formation inside metal pipes (fig. 1). Usually presence of such cracks is explained by microscopic defects during rolling of metal. However, analysis of experimental data shows that such defects are caused by hydrogen [4].

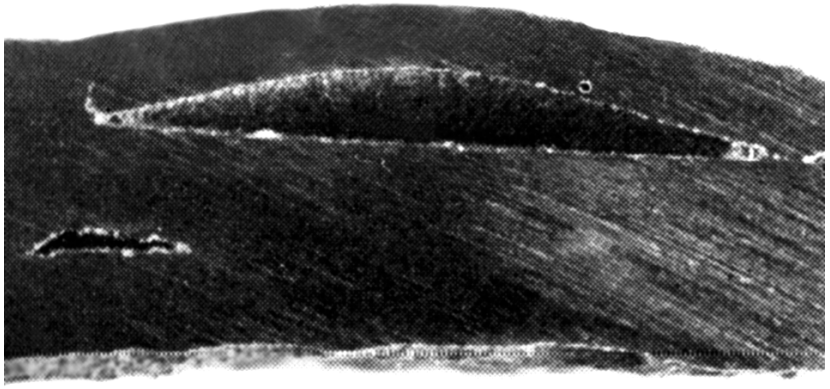

Figure 1: Hydrogen induced fracture near the external surface of a thick steel pipe

Critical reviews of a large number of modern studies on the topic of hydrogen-induced cracking and hydrogen embrittlement are given in [5, 6].
Most studies consider growth condition of a previously-formed crack, without studying of its causes. Mathematical modeling and analysis of causes are still timely issues in studies of cracks. Unfortunately, there are not enough experimental data covering influence of low concentrations of hydrogen onto mechanical properties of materials. The goal of this research is to explain causes of pipe destruction under internal pressure of hydrogen-containing feed with the methods of the theory of elasticity.

2 Prolegomena

Let us first calculate the stress-strain state of a long steel pipeline that experience a pressure onto its internal wall. For that end, let us consider a plane axisymmetric Lame's problem for a hollow pipe under a uniform internal pressure of p.
The overall solution to this problem is known, see [7, 8]:

$$\sigma_r = A - \frac{B}{r^2}, \quad \sigma_\varphi = A + \frac{B}{r^2}, \quad u = \frac{1}{E}\left[A(1-\nu)r + \frac{B(1+\nu)}{r}\right]. \tag{1}$$

Here σ_r and σ_φ are radial and circumferential stress values, u is a radial displacement, A, B are arbitrary constants determined from boundary conditions: on the internal radius (r_0) the stress is $\sigma_r = -p$, on the external radius (r_2) the stress is $\sigma_r = 0$. From that we may find

$$A = \frac{r_0^2}{r_2^2 - r_0^2}p, \quad B = \frac{r_0^2 r_2^2}{r_2^2 - r_0^2}p. \tag{2}$$

Let us determine deformation in the pipe following the formulas

$$\varepsilon_r = u' = \frac{1}{E}\left[A(1-\nu) - \frac{B(1+\nu)}{r^2}\right], \quad \varepsilon_\varphi = \frac{u}{r} = \frac{1}{E}\left[A(1-\nu) + \frac{B(1+\nu)}{r^2}\right], \tag{3}$$

here E is the elasticity modulus and ν is Poisson's ratio of material.

Let us note, that the coefficient of volumetric expansion is constant and positive

$$tr\varepsilon \triangleq \varepsilon_r + \varepsilon_\varphi = \frac{2A(1-\nu)}{E} > 0, \tag{4}$$

i.e., the pipe material is under conditions of a uniform voluminous expansion.
In this problem, displacements and deformations are two-dimensional, but stress tensor contains the third component in the perpendicular direction:

$$\sigma_z = \nu\left(\sigma_r + \sigma_\varphi\right) \ . \tag{5}$$

Figure 2a shows the calculation results for stress in the pipe with parameters corresponding to major gas and oil pipelines: internal radius of $r_0 = 680$ mm, outside radius of $r_2 = 710$ mm, working pressure of $p = 12$ MPa, steel properties: $E = 2 \cdot 10^5$ MPa, $\nu = 0.28$.
The maximum of von Mises yield criterion τ_0 is of special interest in determining pipe strength:

$$\tau_0 = \max \sqrt{\left(\sigma_\varphi - \sigma_z\right)^2 + \left(\sigma_z - \sigma_r\right)^2 + \left(\sigma_r - \sigma_\varphi\right)^2 / 2}, \tag{6}$$

its value shall not exceed the steel tensile yield stress (300 MPa). The distribution of equivalent (von Mises) stress in a pipe is shown on Figure 2a by dotted line. It is evident, that its maximum is located at the internal surface, but the pipe does not have any plastic deformations yet.
Then, it is necessary to take into account presence of hydrogen inside the pipe. It presents in the metal in its natural concentration, but it may also penetrate from medium transported through the pipeline.
Studies [9, 10] stipulate, that diffusion of hydrogen atoms in metal is influenced not only by their concentration and thermal field, but by the stress-strain state of the matrix as well. According to Gorsiy's hypothesis, hydrogen atoms are attracted to areas of tensile stress in metal. High-energy hydrogen is incorporated into crystal lattice of metal. Due to that, mechanical properties of the material undergo changes, in particular, its modulus of elasticity and yield point are reduced [5].
In the problem under consideration, the pipe material is compressed in the radial direction ($\sigma_r < 0$) and stretched out in the circumferential direction ($\sigma_\varphi > 0$); one may assume, that hydrogen will ingress the crystal lattice predominantly in the circumferential direction.
It seems, that a number of condition shall be held for hydrogen intrusion: interatomic bonds in the lattice shall be significantly stretched out, while hydrogen atoms shall have sufficient energy. These conditions are held near the internal surface of the pipe, where both tensile stress and hydrogen concentration are maximal. Thus, there is an internal layer formed in the pipe with weakened mechanical properties.
One may expect, that the properties of metal are changed non-uniformly in different directions. Young's modulus is probably more weakened in the circumferential direction, than in the radial one. For now, let us limit ourselves with analysis of isotropic material with a reduced modulus of elasticity.
The process of hydrogen redistribution through metal is very slow and may take anywhere from several hours to several years [5]. Thus, studies of pipe destruction

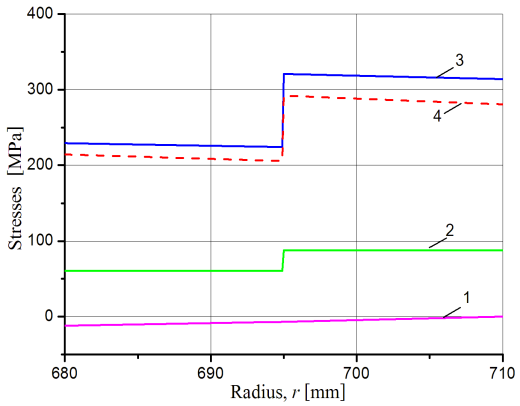

(a)

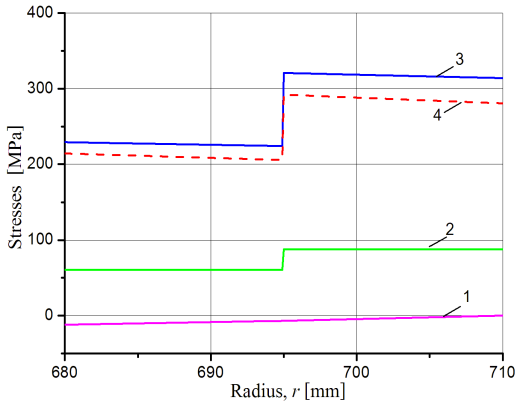

(b)

Figure 1: Figure 2: Stresses in a pipe (a) without weakened layer, (b) with weakened layer of 15 mm: 1 – radial σ_r, 2 – axial σ_z, 3 – circumferential σ_φ, 4 – equivalent stress as function of radius

mechanism under the influence of hydrogen may be considered as a sequence of static problems in the theory of elasticity.

Let us assume, that due to interactions with hydrogen, there is an internal layer of thickness h formed, characterized by weakened mechanical properties. Let us determine the stress-strain state of such a pipe.

3 A pipe with a weakened layer

Let us consider a problem similar to Lame's problem for a circular ring made of two materials. In the internal part $r_0 < r < r_1$ there is a weakened material with a constant Young's modulus of E; in the external part $r_1 < r < r_2$ there is steel with the Young's modulus of E_0. Boundary conditions are the same as in the previous problem, with two additional conditions: on the radius of conjugation (r_1) the values of σ_r and u are continuous.

Formulas (1) are written down for the internal layer with the constants A, B, while for the external layer there are A_0, B_0. Applying boundary conditions, we obtain a linear algebraic system for the four constants. Its solution will give us values of displacement and stress from the formulas (1).

Figure 2b shows diagrams of stresses and deformations for the same parameters as above, the weakened layer thickness is 15 mm ($r_1 = 695$ mm), while the modulus of elasticity is $E = 0.7E_0$.

The calculations show, that radial stress has changed insignificantly, while circumferential and axial stresses have a discontinuity at the boundary between the two layers and there's maximum values increased. The maximum value of the von Mises yield criterion has increased to $\tau_0 = 292$ MPa.

Let us note, that the maximum tensile stress values are now localized in a hydrogen-free layer of steel near the boundary between the layers. As a result, the hydrogen atoms, having ingressed into the crystal lattice in this area, are going to weaken the material. Thus, the thickness of the weakened layer is going to gradually increase.

Obviously, the increase in the thickness of the weakened layer will be accompanied with increasing equivalent stresses. At some critical value of h a yield stress will be attained and plastic deformations appear. The area of such deformations is a circle, marking the boundary of hydrogen-weakened layer of material.

Figure 3 shows maximum equivalent stress as a function of weakened layer thickness; it may be seen that the critical value is h=18 mm.

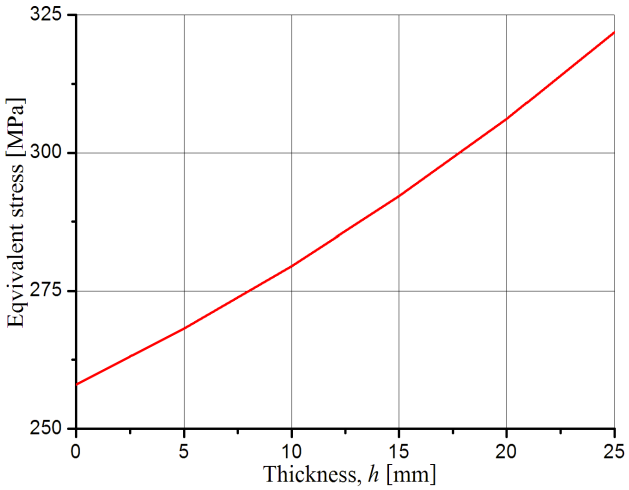

Figure 3: Equivalent stress in a pipe with a weakened layer

The calculation results support the available experimental data, showing that hydrogen damage in pipes happens along a circle.

4 Conclusion

The mathematical modeling study explains the cause of damage of pipeline material as a result of hydrogen impact.
It is shown, that during the transportation of hydrogen-containing feed through the pipeline, a stress-strain state appears that facilitates redistribution of hydrogen through the pipe material. As a result, there is an internal layer formed in the pipe with weakened mechanical properties. Analysis of stress in such a two-layer pipe has shown appearance of a plastic deformation area in the form of a circle along the boundary between layers. This leads to appearance of circular cracks and longitudinal delamination of pipe walls.
Exact quantitative assessment requires new experimental data on influence of small concentrations of hydrogen onto the properties of structural materials.

References

[1] M. Elboujdaini. Initiation of Near Neutral pH Environmentally Assisted Cracking in Line Pipe Steel // Proceedings of the 16th European Conference of Fracture, Alexandroupolis, Greece, July 3 – 7, 2006.

[2] Y. Nie, Y. Kimura, T. Inoue, et al. Hydrogen embrittlement of a 1500-MPa tensile strength level steel with an ultrafine elongated grain // Metallurgical and Materials Trans. A. 2012. Vol. 43. No. 5. Pp. 1670–1687.

[3] A.M. Polyanskiy, V.A. Polyanskiy, Yu.A. Yakovlev. Issledovaniye protsessov ustalosti i razrusheniya metallicheskikh materialov s privlecheniyem metoda

opredeleniya energii svyazi vodoroda v tverdom tele [Investigation of metal fatigue and destruction by method of determination of hydrogen binding energy in solid] // Deformatsiya i razrusheniye materialov. No. 3 (2009). Pp. 39–43. (rus.)

[4] A. Balueva. Modeling of hydrogen embrittlement cracking in pipe-lines under high pressures // Procedia Materials Science 3, 2014. Pp. 1310–1315.

[5] A.K. Belyaev, N.R. Kudinova, V.A. Polyanskiy, Yu.A. Yakovlev. The Description of deformation and destruction of materials containing hydrogen by means of rheological model // St. Petersburg Polytechnical University Journal: Physics and Mathematics є 3 (225) 2015. Pp. 134–149. (rus.)

[6] M.B. Djukic et al. Towards a unified and practical industrial model for prediction of hydrogen embrittlement and damage in steels // Procedia Structural Integrity 2 (2016). Pp. 604-611.

[7] V.V. Eliseev. Mekhanika uprugih tel [Mechanics of elastic bodies]. SPb.: Izd-vo SPbGPU, 2003. 336 p. (rus.)

[8] A.I. Lurie. Theory of Elasticity. Springer Science & Business Media, 2010. 1050 p.

[9] W.S. Gorsky. Theorie der ordnungsprozesse und der Diffusion in Mischkristallen von CuAu // Sow. Phys. 1935. Bd. 8. Pp. 433–456.

[10] W.S. Gorsky. Theorie des elastichen Nachwirkung in ungeordneten Mischkristallen (elastische Narchwirkung zweiter Art) // Phys. Zeitschrift der Sowjetunion. 1935. Bd. 8. Pp. 457–471.

Tatiana V. Zinovieva, Institute of Problems of Mechanical Engineering RAS, Bolshoj 61, Vas. Ostrov, Saint-Petersburg, 199178, Russia

Alternative seating of the drum in a separation line

Bosak M.[1], Tarca A.[1]

[1]University of Economics in Bratislava

martin.bosak@euke.sk

Abstract

Separation processes are used in order to separate substances in homogeneous and heterogeneous substance systems. Fabric systems are mostly the product of chemical transformation obtained by chemical or biochemical reaction in some apparatus or they may occur as a natural source (air, water, mineral deposits). They are further used for cleaning e.g. desulphurisation of gases from combustion or water purification. Continuous working filters are often part of the separation line. In this case, it is a drum rotary filter. The rotating drum has a filter partition on the side, which is outside. The drum is partially immersed in a slurry vessel and the filtrate passes through the forming cake, the filtering baffle, through the individual drum segments to the axis of rotation through the distributor head outwards. Formed cake is continuously washed, blown and removed. The solids content of the slurry should be relatively low (from 3% to 5%) because thanks to that sediment often does not have to be emptied (cleaned).

1 Introduction

The drum rotary filter operates with a horizontal axis of rotation and it is filled along an axis, which is near the bottom part of the drum. Emptying is manual and the drum holder is rigid by means of the two pressed pins according to Fig. 1

During operation of the device due to external and internal factors at the place where the pivot was attached to the drum, the pins were often broken. The demandingness of the work on the replacement of the new pin contributed to the consideration of applying the pins as a mechanically dismountable screw connection. In this case, as a screw connection there were used the pre-assembled screws. The bolt would be screwed through the flange to the front of the drum, as shown in Fig 2.

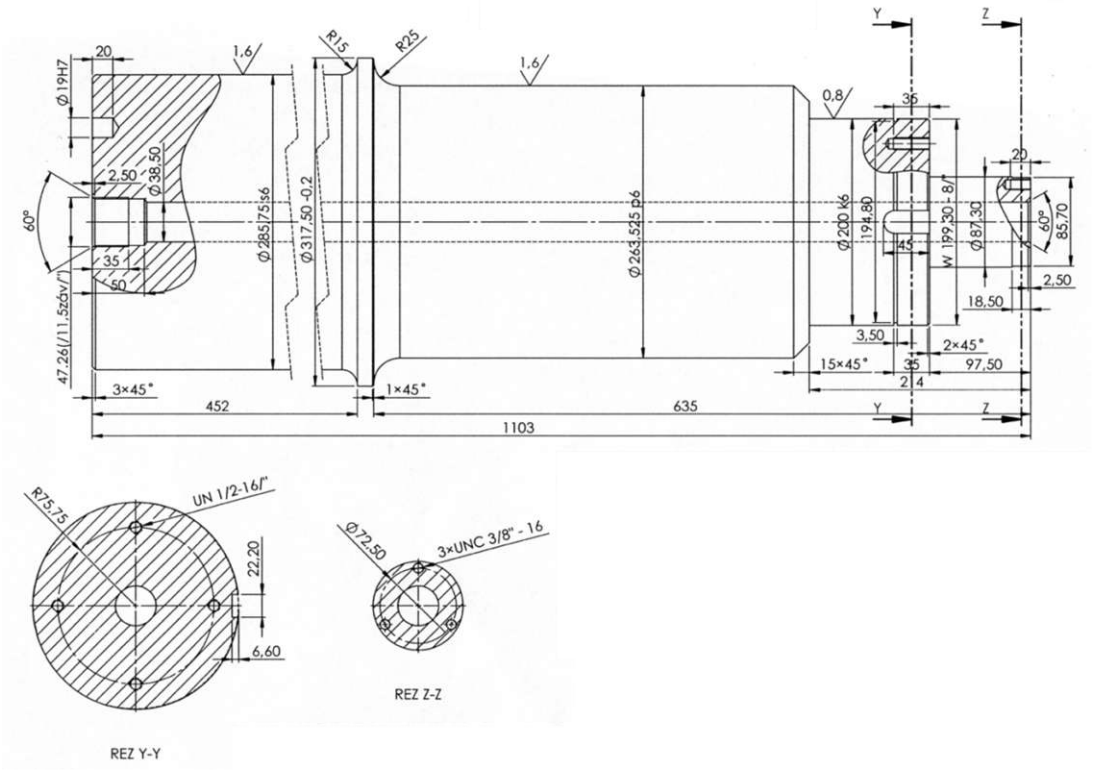

Fig. 1 Drum holder bar

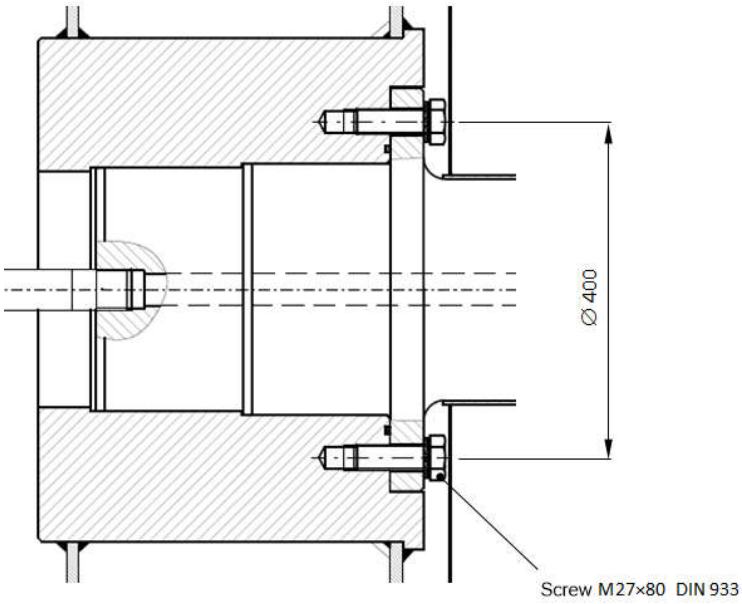

Fig. 2 Mounting of the pin on the front side of the drum

Advantage or the disadvantage of such a solution was verified by the performed calculation and FEM analysis. The creation of a computational model for FEM analysis was based on the work of various authors. Bocko et al. [1] analyze the impact of screw connections on stress and deformation as a whole. It indicates that the type of used calculation model depends on the desired calculation goal. In the case of a strength test,

the joint recommends using a model to determine axial force, transverse force and bending moment, or to create a sufficiently accurate model for voltage-based evaluation. The calculation shows 5 types of calculation models. Krištofovič [2] works on the dynamic interaction of the liquid with the tank, which leads to complex motion equations and indicates the simplification of the hydrodynamic side of the problem. Koves [3] in his contribution provides a method for sizing flanges and screws. The optimization of the shape of the joint is discussed by [4], where it states that the optimized shape has a positive effect on the maximum stress which results in a more even distribution of the load along the threads in the engagement. The problem of the sensitivity of the torsion stiffness of the bolt is analyzed in [5], for example and with changes in the dynamics of the rotor when loosening the screws it is analyzed in [6]. The effects of clamping forces on fatigue life of screw connections are examined by [7].

2 Computational model - static analysis using FEM

The object of the analysis is the pin consisting of material Fe 510 (11 523.1), which has a value of f_y (Re) = 345 MPa, the strength of f_u (Rm) = 490 - 630 MPa [9].

The pin is designed in two cases of hub connection, both as a pressed joint and as a screw connection after design modifications.

The input data for the calculation of the reactions were taken from a static calculation [8] where a total load of 1 452 kN was assumed to consist of the drum's own weight and the weight of the load plus the dynamic coefficients. The test pin is located at reaction site B, Fig. 3.

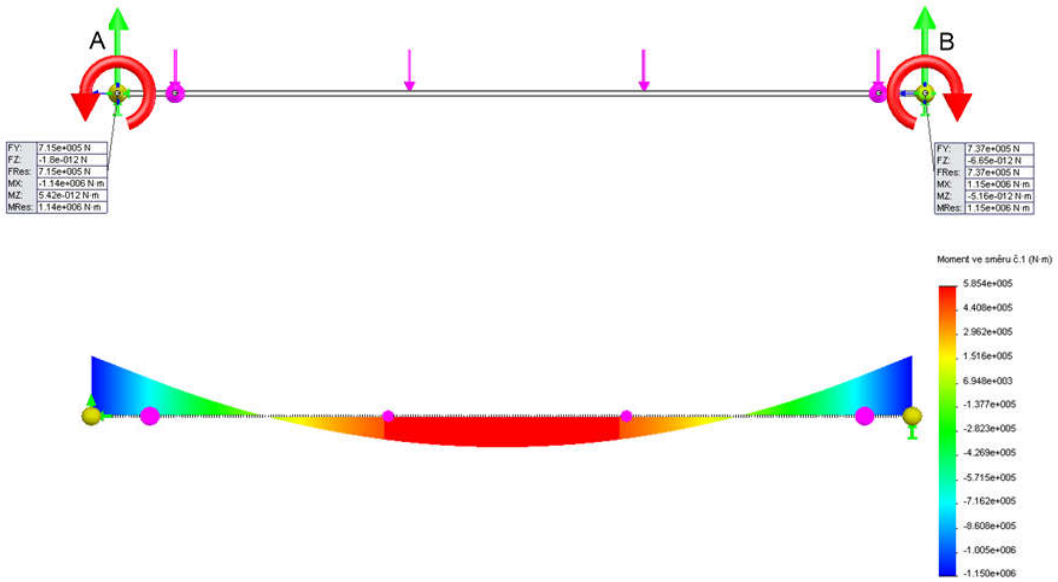

Fig. 3 The magnitude of the reactions at the locations of the bearing supports

3 Pin fastening made as a moulded joint

In Fig. 1 is shown a pin whose connection to the face of the drum is made by pressing (used housing H7 / s6). The following tolerance values [11] are used for the used storage:

$$Ø285{,}75\ H7^{+0{,}052}_{0}$$

$$Ø285{,}75\ s6^{+0{,}202}_{+0{,}170}$$

On the pressed joint with a hollow pin, according to [10], the relative pressures p0 - in the hole of the hollow pin, p1 - in the contact surface at the radius r1 and the relative pressure p2 - act on the surface of the hub at the radius r2.

Simplified 3D pin model was created for simulation purposes. The boundary conditions, applied loads, and a finite element network have been defined on the model.

The result of the simulation is the total stress distribution in the pins (Figure 4), which does not exceed the value of the tread of the material.

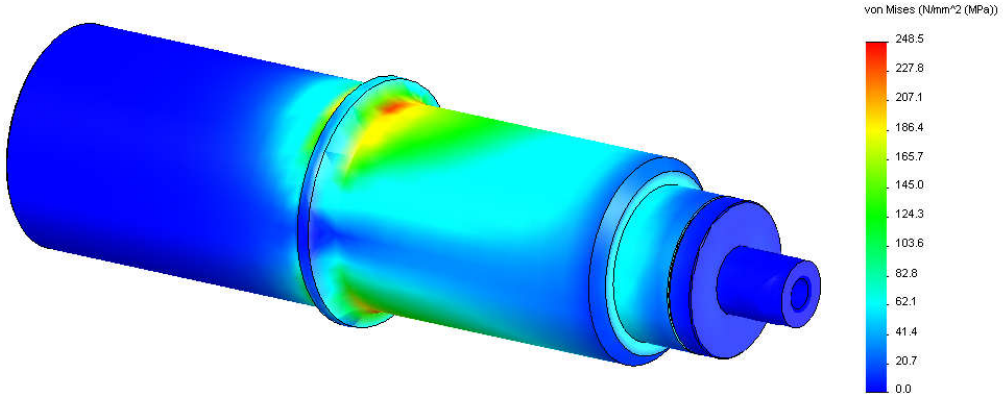

Fig. 4 Total tension distribution in the pin

4 Pin bolt made as a screw connection

A design was made on the pin, which consisted of changing the pin attachment to the front wall of the press from the pressed joint to the screw connection. The drawing of the pin adjustment is shown in Fig. 5.

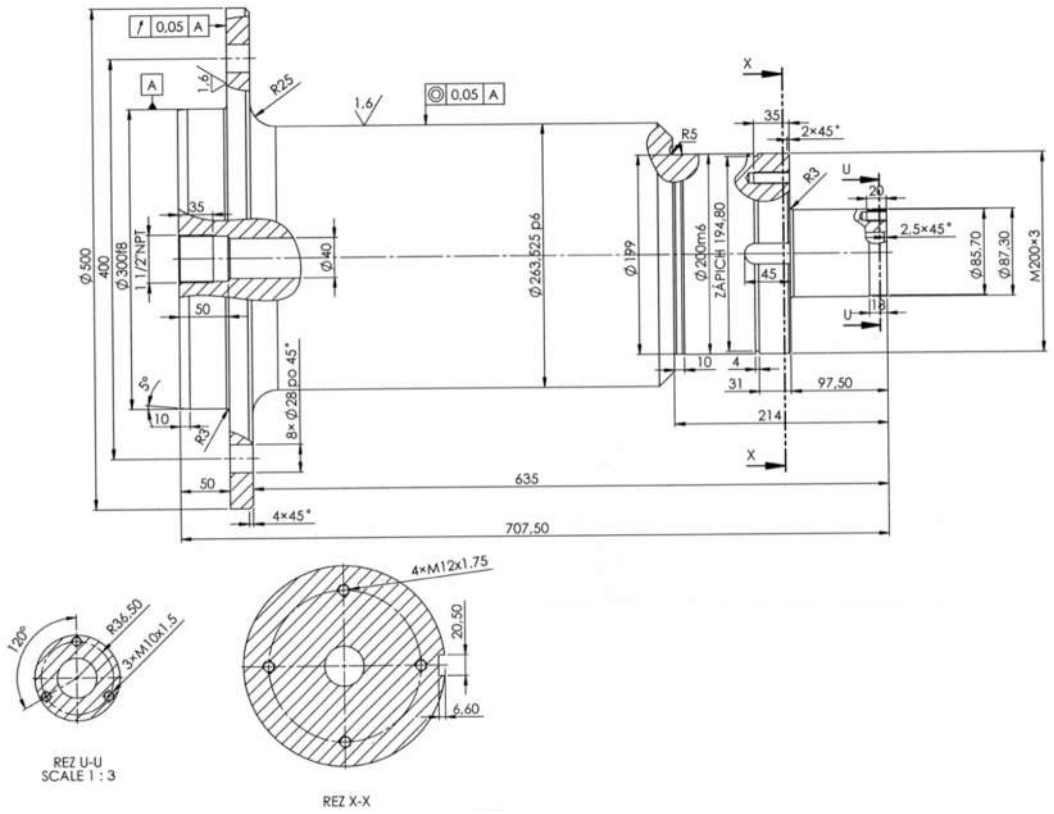

Fig. 5 Drawing of a modified pin

In this case, the pin attachment to the front of the drum is realized by means of 8 screws M27. Analogously, the pattern was applied to the model, with the marginal conditions adjusted for the new drum connection. The simulation result is shown in Fig. 6.

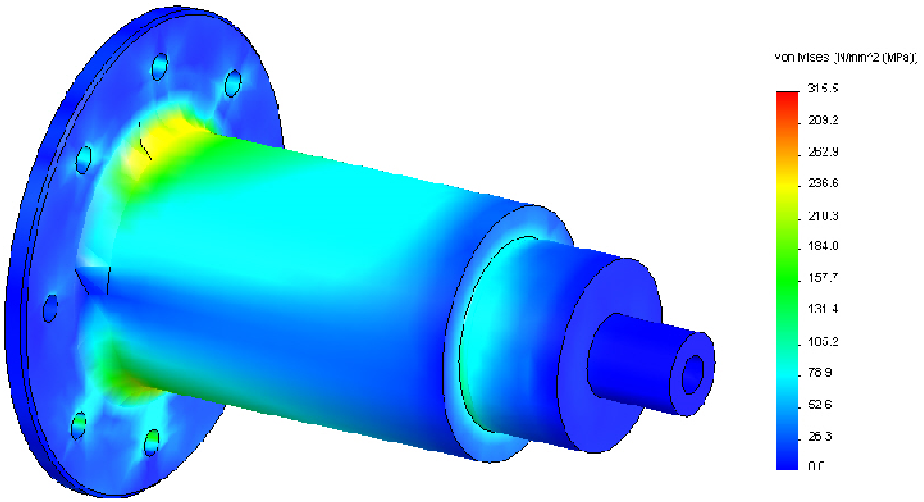

Fig. 6 Total tension distribution in the adjusted pins

From the Fig. 6 it can be seen that even in this case the maximum voltage does not exceed the value of the slump of the material.

5 Calculation of torque and shear force on screws

The pin to the drum is bolted by means of 8 screws M27 x 80 DIN 933 with the diameter 400 mm. The most unfavourable situation may occur in the case of locking of the bearing on the pin, which results in a maximum load on the pin at the point of attachment to the drum

The torque required for the analysis was calculated from the engine power and the drum speed. The engine power is P = 30 kW, drum speed is $n_b = 2\ min^{-1}$.

$$M_K = \frac{P}{2 \cdot \pi \cdot n_b} \tag{1}$$

$$M_k = 143{,}3\ kNm$$

The cutting force applied to the bolts at the point of attachment of the pin to the drum is determined according to the following equation:

$$F_c = \frac{2 \cdot M_K}{D_S} \tag{2}$$

where D_s is the diameter of the bolt attachment.

$$F_c = 716{,}5\ kN.$$

The force acting on one screw (Figure 7) is given as a proportion of the total shear force and number of screws (3) used.

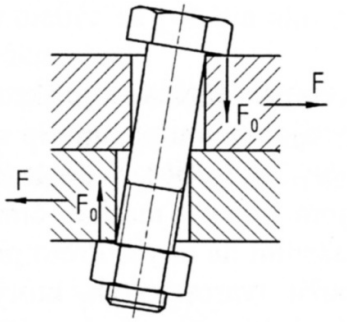

Fig. 7 Dynamically loaded coupling

F - the shear force, F_0 - the preload obtained by tightening the screw

$$F = F_c / 8 = 89{,}6\ kN. \tag{3}$$

The recommended tightening torque for screws M27 DIN 933 of the strength class 8.8 (without pre-tensioning) is, according to the manufacturer, $F_0 = 109$ Nm.

Screw parameters M27 x 80 DIN 933:

thread pitch p = 3 mm,

mean diameter $d_2 = 25{,}051$ mm,

small diameter d_3 = 23,319 mm,
cross-section of the screw core A = 459 mm^2.

According to [12], for the strength class of screws 8.8, the following nominal values of the fluctuation factor f_{yb} = 640 N/mm^2 and tensile strengths f_{ub} = 800 N/mm^2.

The resistance of the shear bolt for a single shear plane is determined according to the relationship (4) as follows:

$$F_{v,Rd} = \frac{\alpha_v f_{ub} A}{\gamma_{M2}} \quad (4)$$

where α_v = 0,6 for strength classes 4.6, 5.6 a 8.8,
γ_{M2} - is the partial confidence factor = 1,25

$F_{v,Rd}$ = 176 256 N = 176,3 kN.

For the resistance of the cutting screw, the condition must be met:

$$F \leq F_{v,Rd}$$
$$89{,}6 \text{ kN} \leq 176{,}3 \text{ kN}$$

6 Shear resistance of screw for one shear plane using the FEM

For the loads weighing on one bolt, finite element analysis for shear bolt resistance was performed (Figure 8).

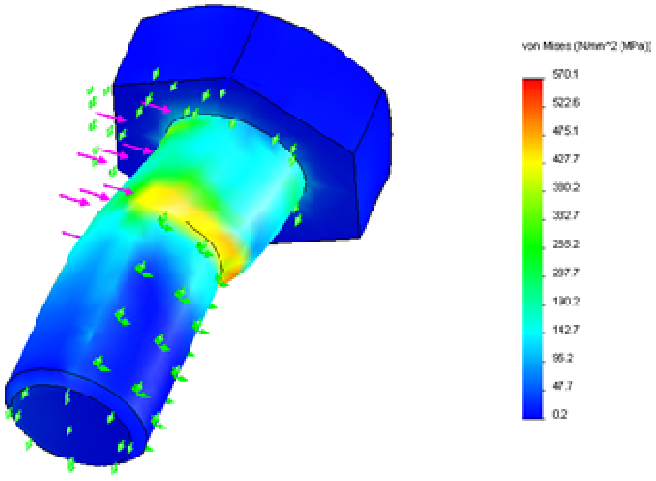

Fig. 8 Result of analysis for cutting screw resistance

According to the results of the analysis, the yield curve of the material was not exceeded, which confirmed the calculation of the cutting screw resistance described above.

The most unfavourable case of pivot loading is assumed to be an extreme load case when the bearing on the pins under investigation is completely blocked, thereby resulting in a combined load of force from the drum's own gravity to the drum load in conjunction with the maximum torque transmitted from the propulsion system.
The simulation model of this extreme load condition and the simulation results are shown in Fig. 9.

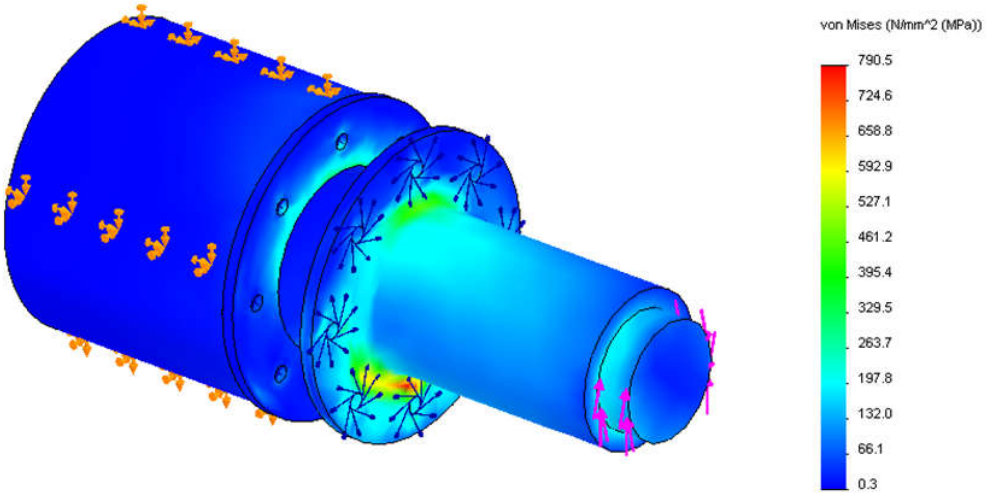

Fig. 9 Simulation results

For more accurate results, it is necessary to create a simulation of the load on the whole system, since the partial simulation for the pin only represents a rough approximation of the boundary conditions, causing uncertainties in the resulting voltage values.

7 Summary of results and conclusion

Based on the computational simulations for extreme load conditions, the analysis showed that the proposed adjustment of the pin in terms of stress is not as advantageous as, for the same load conditions, it shows 27% higher stresses but not exceeding the allowable values. However, considering the costs associated with the replacement of the damaged pin and the total line shutdown time and then despite this aspect, it is advantageous to use the proposed adjustment of the pin for the screw connection.

References

[1] Bocko, P., Mantič, M.: Input data for preloaded bolted connection design in FEM. In: Nové trendy v konštruovaní a v tvorbe technickej dokumentácie. Nitra SPU. 2005: 24-27. ISBN 8080695172.
[2] Krištofovič, V., Kotrasová, K.: Interaction of steel water tank tower with subsoil under Earthquake excitation. Modelování v mechanice, Ostrava, 2006: 1-13.
[3] Koves, W.J.: Flange joint bolt spacing requirements. Am Soc Mech Eng Press Vessel Pip Div PVP 2008;3:3–10. doi:10.1115/PVP2007-26089.
[4] Pedersen, N.L.: Overall bolt stress optimization. J Strain Anal Eng Des 2013;48:155–65. doi:10.1177/0309324712470233.

[5] Smith, L.M., Nassar, S.A., Ganeshmurthy, S., Burgues, O. J.: Sensitivity analysis of a bolt-together vehicle chassis. SAE Tech Pap 2006. doi:10.4271/2006-01-1251.
[6] Qin, Z., Han, Q., Chu, F.: Bolt loosening at rotating joint interface and its influence on rotor dynamics. Eng Fail Anal 2016;59:456–66. doi:10.1016/j.engfailanal. 2015.11.002.
[7] Chakherlou, T.N., Razavi, M.J., Abazadeh, B.: Finite element investigations of bolt clamping force and friction coefficient effect on the fatigue behavior of aluminum alloy 2024-T3 in double shear lap joint. Eng Fail Anal 2013;29:62–74. doi:10.1016/j.engfailanal.2012.11.004.
[8] Argaláš, B.: Statický posudok skrutkovaného spoja pre uchytenie bubna. Stroj: Vláknitá linka-Pracie filtre (hnedá linka).
[9] Trebuňa, F., Šimčák, F.: Odolnosť prvkov mechanických sústav, Edícia vedeckej a odbornej literatúry, TU Košice, 980 s., ISBN 80-8073-148-9
[10] Málik, M., Medvecký Š. a kol.: Časti a mechanizmy strojov, Žilinská univerzita v Žiline, EDIS, 2002, 535 s., ISBN 80-8070-043-5.
[11] Leinveber, J., Řasa, J., Vávra, P.: Strojnícke tabuľky, Scientia, Praha, 1999, ISBN 80-7183-164-6.
[12] STN EN 1993-1-8 Eurokód 3 - Navrhovanie oceľových konštrukcií, časť 1-8: Navrhovanie uzlov.

Chaotic dynamics of interacting pendulums (the decision of the synchronization problem)

S.O. Gladkov, S.B. Bogdanova
sglad51@mail.ru, sonjaf@list.ru

Abstract

It's consider as an example of two coplanar metal pendulums, suspension points of which are at the same horizontal level and the same fixed distance of b from each other. It's shown that the principle of possibility of synchronization due to two main factors. The first one is the effect of electromagnetic interaction between the pendulums. The second one is taking into account of the power of EM radiation coming to the nonlinear attenuation.

1 Introduction

In this paper, we would not research internal structure of the clock mechanism. It was obtained the system of nonlinear dynamic equations of motion and it was given analytical estimates of synchronization time of t_{synch}, supported by numerical solution of the equations obtained, which has not bad agreement with the experimental results (see below).

The problem to which this paper is devoted is not new one, because dated back to Huygens time, who first turned attention to the effect of synchronization of physical metal pendulums, hanging at some distance from each other. Later the effect of synchronization have been searched in other papers (for example [1] – [4]) and in monographs (for example, [5] – [7]). We should note that in some sources (for example, [7] and [8]), the model of synchronization is based on condition of small adjustment of pendulums swing connected with "dry friction" which proportional to the velocity of pendulums motion and in the opinion of the authors, the internal structure of the clock mechanism is determined only. In this paper, we would not research internal structure of the clock mechanism, but we approach the solution of the problem from a fundamentally different physical point of view.

We should note that none of the mentioned sources estimated the time of synchronization t_{synch} was not estimated in any mentioned sources, what is more, it was not offer physically grounded interaction between pendulums, leading exactly to the effect of synchronization.

What is more, the effect of EM radiation had never been taken into account, however, as we are going to prove now, it plays a pivotal role in this interesting phenomenon. Also, in the previous papers it was not mentioned at all.

We should notice that the arguments given below can easily be transferred to any other similar problems that are somehow related to the effects of the radiation of the currently known physical fields (gravitational, electromagnetic and acoustic) and are an attribute of any moving and interacting objects. As an example we choose two absolutely identical physical pendulums, points of suspension are at the same distance b from each other. For the sake of concretization the calculations below, we should take the pendulums are coplanar as in Fig. 1. We should notice that the explained algorithm for calculation is trivially genereliazed even if the pendulums are suspended in parallel planes, however, the substance of the issue is identical in both cases.
In the general, if lengths of suspension are different or equal to l_1 and l_2 , then according to the geometry of Fig. 1, we get the following expression for the distance between the centers of the pendulums:

$$R = \sqrt{l_1^2 + l_2^2 + b^2 + 2bl_1 \sin\varphi_1 - 2bl_2 \sin\varphi_2 - 2l_1 l_2 \cos(\varphi_1 - \varphi_2)} \tag{1}$$

In our case, when both pendulums are identical, i.e. $l_1 = l_2 = l$, $m_1 = m_2 = m$from the formula (1) synchronization condition is trivially written, i.e.$R = b$ equality should be realized $R = b$. This automatically leads to the equation:

$$l + b\sin\varphi_1 - b\sin\varphi_2 - l\cos(\varphi_1 - \varphi_2) \tag{2}$$

Solving this equation in φ_2 , we obtain that:

$$\sin\varphi_2 = \sin\varphi_1 \tag{3}$$

I.e. the synchronization condition is

$$\varphi_1 = \varphi_2, \dot{\varphi}_1 = \dot{\varphi}_2 \tag{4}$$

2 Setting of the problem

Before proceeding to the direct formulation and solution of the problem, it is necessary to say a few words about the physical side of the problem. For identical pendulums when $l_1 = l_2 = l$, $m_1 = m_2 = m$ the potential energy should be represented in a symmetrical form as a half sum

$$U(R) = \frac{U_{12}(R) + U_{21}(R)}{2} \tag{5}$$

The total energy of the system should be like this

$$\begin{aligned} E = T + U = U_0 + \frac{ml_c^2\dot{\varphi}_1^2}{2} + \frac{ml_c^2\dot{\varphi}_2^2}{2} - mgl_c(\cos\varphi_1 + \cos\varphi_2) + \\ + \frac{U_{12}(R) + U_{21}(R)}{2} = const, \end{aligned} \tag{6}$$

where $U_0 = mgH$, l_c the distance of suspension point of the pendulum from its center of attraction, H height of suspension of pendulums above the Earth. In contrast to the dependence (1), the distance between the centers of the pendulums is conveniently introduced in vector form, which automatically allow for the curve trajectory of its motion. Indeed, since at the initial instant time $t = 0$, the distance is R_0 , then at any moment of the time it can be represented as

$$\mathbf{R} = \mathbf{R_0} - \int_{\mathbf{0}}^{\mathbf{t}} (\mathbf{v_1(t)} + \mathbf{v_2(t)})\, \mathbf{dt}, \tag{7}$$

where $\mathbf{v_1}, \mathbf{v_2}$ the velocities of both balls. As a result, the potential energy of interaction can be represented in the following form

$$U = U_G \left(\left| \mathbf{R_0} - \int_{\mathbf{0}}^{\mathbf{t}} (\mathbf{v_1(t)} + \mathbf{v_2(t)})\, \mathbf{dt} \right| \right) + U_{EM} \left(\left| \mathbf{R_0} - \int_{\mathbf{0}}^{\mathbf{t}} (\mathbf{v_1(t)} + \mathbf{v_2(t)})\, \mathbf{dt} \right| \right). \tag{8}$$

The first term is the usual gravitational interaction of two material objects, but we will dwell on the second term in (8) in more detail. To find it we should recall some of the basic principles of electrodynamics (see, for example, [9]) and among other factors, Maxwell's equations. In the quasi static case from classical electrodynamics it follows that the vector potential $\mathbf{A}$ of the magnetic field should satisfy equation

$$\Delta \mathbf{A} = -\frac{4\pi}{c} \mathbf{j}, \tag{9}$$

where $\mathbf{j}$ is the inertial current of the density in moving balls, c is the velocity of the light. As it's known (see ref. [9]) the interaction determined by the motion of the electrons can be represented in the form:

$$U = -\frac{1}{c} \int_V \mathbf{j} \mathbf{A} dV. \tag{10}$$

In our case, a moving pendulum, conditionally denoted by index 1, induces a potential on the second pendulum $\mathbf{A_1}$. Therefore, in the accordance with the expr. (10) and eq. (9) we have for the potential interaction energy

$$U_{EM} = \frac{1}{c^2} \int_{V_1} \int_{V_2} \frac{\mathbf{j_1 j_2}}{\tilde{R}} dV_1 dV_2, \tag{11}$$

where the vector $\tilde{\mathbf{R}}$ is determined as $\tilde{\mathbf{R}} = \mathbf{R} + \mathbf{r_1} - \mathbf{r_2}$, where radius-vectors $\mathbf{r_1}, \mathbf{r_2}$ are current directions in each of the balls counted from their centers, for which integration is carried out in (11), V_1 and V_2 the volumes of these balls. Since the current density in the moving sphere is $\mathbf{j} = \rho_\mathbf{e} \mathbf{v}$, where ρ_e electric density in the

ball, its velocity at fluctuating motion is defined as $\mathbf{v} = l_c\dot{\varphi}\boldsymbol{\tau}$, where l_c the distance of suspension center from center of attraction the system of the ball + rod.
In the result with the accordance formula (11) we can obtain that the potential energy of interaction is

$$U_{EM} = \frac{\dot{\varphi}_1\dot{\varphi}_2\left(\mathbf{k_1}\cdot\mathbf{k_2}\right)\rho_e^2}{c^2}\int\limits_{V_1}\int\limits_{V_2}\frac{\left(l_c\boldsymbol{\tau}_1 + r_1\mathbf{v_1}\right)\left(l_c\boldsymbol{\tau}_2 + r_2\mathbf{v_2}\right)dV_1dV_2}{\tilde{R}} =$$
$$= \frac{\dot{\varphi}_1\dot{\varphi}_2\left(\mathbf{k_1}\cdot\mathbf{k_2}\right)\rho_e^2}{c^2}\left[l_c^2\left(\boldsymbol{\tau}_1\cdot\boldsymbol{\tau}_2\right)\int\limits_{V_1}\int\limits_{V_2}\frac{dV_1dV_2}{\tilde{R}} + l_c\int\limits_{V_1}\int\limits_{V_2}\frac{r_1\left(\boldsymbol{\tau_1}\cdot\mathbf{v_2}\right)dV_1dV_2}{\tilde{R}} + \right.$$
$$\left. + l_c\int\limits_{V_1}\int\limits_{V_2}\frac{r_2\left(\boldsymbol{\tau_2}\cdot\mathbf{v_1}\right)dV_1dV_2}{\tilde{R}} + \int\limits_{V_1}\int\limits_{V_2}\frac{r_1r_2\left(\mathbf{v_1}\cdot\mathbf{v_2}\right)dV_1dV_2}{\tilde{R}}\right], \tag{12}$$

where $\mathbf{k_1}$ and $\mathbf{k_2}$ - unit vectors directed along the angular velocities ω_1 and ω_2 and along the axis$z$, perpendicular to the plane of the Fig. 1
As we can see from the Fig. 1, scalar product of unit vectors $\boldsymbol{\tau_1}$ and $\boldsymbol{\tau_2}$ is $\boldsymbol{\tau_1}\cdot\boldsymbol{\tau_2} = \cos\left(\pi - \varphi_1 + \varphi_2\right) = -\cos\left(\varphi_1 - \varphi\right)$. For other scalar products in (15), we are finding that $\boldsymbol{\tau_1}\cdot\mathbf{v_2} = \cos\left(\varphi_1 - \varphi_2\right)$, $\boldsymbol{\tau_2}\cdot\mathbf{v_1} = \cos\left(\varphi_2 - \varphi'\right)$, $\mathbf{v_1}\cdot\mathbf{v_2} = \cos\left(\varphi - \varphi'\right)$, where angles φ and φ' are the current vector angles in the plane $x - y$ of the spherical coordinate system for which integration is carrying out, i.e.$dV_1 = r_1^2\sin\theta_1 dr_1 d\theta_1 d\varphi$ and $dV_2 = r_2^2\sin\theta_2 dr_2 d\theta_2 d\varphi'$.
After all calculation we are finding from the expr. (12)

$$U_{EM} = \frac{\dot{\varphi}_1\dot{\varphi}_2\left(\mathbf{k_1}\cdot\mathbf{k_2}\right)\rho_e^2}{c^2}\left[-l_c^2\cos\left(\varphi_1 + \varphi_2\right)\int\limits_{V}\int\limits_{V}\frac{dV_1dV_2}{\tilde{R}} + F\right], \tag{13}$$

where the function

$$F = \int\limits_0^{r_0} r_1^3 dr_1 \int\limits_0^{r_0} r_2^3 dr_2 \int\limits_0^{\pi}\sin\theta_1 d\theta_1 \int\limits_0^{\pi}\frac{\left(\sqrt{A-B} - \sqrt{A+B}\right)\sin\theta_2}{2r_1r_2\sin\theta_1\sin\theta_2}d\theta_2 =$$
$$2\int\limits_0^{r_0} r_1^2 dr_1 \int\limits_0^{r_0} r_2^2 dr_2 \int\limits_0^{\pi} d\theta_1 \int\limits_0^{\pi}\Big(\sqrt{R^2 + 2Rr_1\cos\theta_1 - 2Rr_2\cos\theta_2 + r_1^2 + r_2^2 - 2r_1r_2\left[\cos\left(\theta_1 - \theta_2\right) -}$$
$$- \sqrt{R^2 + 2Rr_1\cos\theta_1 - 2Rr_2\cos\theta_2 + r_1^2 + r_2^2 - 2r_1r_2\cos\theta_1\cos\theta_2}\Big)d\theta_2$$

and approximately we have that the interaction is

$$U_{EM} = \frac{\dot{\varphi}_1\dot{\varphi}_2\left(\mathbf{k_1}\cdot\mathbf{k_2}\right)\rho_e^2V^2l_c^2\cos\left(\varphi_1 + \varphi_2\right)}{c^2b}\xi \tag{14}$$

where ξ – is a numerical dimensionless factor of the order of unity. It is not so important for our investigation. As we can easily understand, scalar product of unit vectors $\mathbf{k_1}$ and $\mathbf{k_2}$ should be written as $\mathbf{k_1} \cdot \mathbf{k_2} = \cos\psi$ and the sign of this expression at certain times must change. Essentially, such a fact could have significance, however, it does not carry a fundamental and profound meaning. Therefore for all analytic calculations carried out below the solution will be given at $\cos\psi = \pm 1$. So $\mathbf{v_1} = \dot{\varphi}_1 \mathbf{l}\boldsymbol{\tau_1}$ and $\mathbf{v_2} = \dot{\varphi}_2 \mathbf{l}\boldsymbol{\tau_2}$, where $\boldsymbol{\tau_{1,2}}$ is an unit vectors tangent to the trajectory of motion that can be represented as an expansion in a fixed two – dimensional basis $\mathbf{i}, \mathbf{j}$.

3 The power of the electromagnetic radiation of the moving pendulums

Herein we are going to pay attention on the most important moment of our theory and give a detailed calculation of the power of the EM radiation of pendulums, leading ultimately to their synchronization. For this goal we should recall some properties of the LiГкnard-Wiechert potentials. According to for example ref. [12] any moving charge creates a scalar potential and a vector potential $\mathbf{A}$ at some distance r from itself, which are given by the following symmetric formulas

$$\begin{aligned} \psi(\mathbf{r},t) &= \frac{e}{2}\left(\frac{1}{R-\dfrac{\mathbf{v}\cdot\mathbf{R}}{c}}+\frac{1}{R+\dfrac{\mathbf{v}\cdot\mathbf{R}}{c}}\right)=\frac{e}{R\left[1-\left(\dfrac{\mathbf{v}\cdot\mathbf{n}}{c}\right)^2\right]}, \\ \mathbf{A}(\mathbf{r},t) &= \frac{e\mathbf{v}}{2c}\left(\frac{1}{R-\dfrac{\mathbf{v}\cdot\mathbf{R}}{c}}+\frac{1}{R+\dfrac{\mathbf{v}\cdot\mathbf{R}}{c}}\right)=\frac{e\mathbf{v}}{Rc\left[1-\left(\dfrac{\mathbf{v}\cdot\mathbf{n}}{c}\right)^2\right]} \end{aligned} \tag{15}$$

where $\mathbf{n} = \dfrac{\mathbf{R}}{R}$ - is an unit vector, $R = |\mathbf{r} - \mathbf{r_0}(t)|$ is the distance, where $\mathbf{r_0}(t)$ is the trajectory of the charge and r is the point of observation. For our specific case these formulas we are completely trivially generalized to a moving metal pendulum and in the accordance of expr. (15), we obtain after the integration on volumes V_1 and V_2

$$\begin{aligned} \psi(\mathbf{r},t) &= \frac{enV}{R\left[1-\left(\dfrac{\mathbf{v}\cdot\mathbf{n}}{c}\right)^2\right]} \approx \frac{enV}{R}\left[1-\left(\frac{\mathbf{v}\cdot\mathbf{n}}{c}\right)^2\right], \\ \mathbf{A}(\mathbf{r},t) &= \frac{enV\mathbf{v}}{Rc\left[1-\left(\dfrac{\mathbf{v}\cdot\mathbf{n}}{c}\right)^2\right]} \approx \frac{enV\mathbf{v}}{R}\left[1-\left(\frac{\mathbf{v}\cdot\mathbf{n}}{c}\right)^2\right], \end{aligned} \tag{16}$$

where n is the charge concentration, V is the volume of pendulum (see above). The potentials (16) give us a possible to calculate the distributions of EM fields outside

pendulums. Indeed, in the accordance with the formulas which good known from the electrodynamics (see ref. [12]) we have for the electric and magnetic fields

$$\mathbf{E} = -\frac{1}{c}\frac{\partial \mathbf{A}}{\partial t} - \nabla\psi, \mathbf{B} = rot\mathbf{A}. \tag{17}$$

Substituting here expr. (16), we are getting that

$$\begin{aligned}
\mathbf{E} &= -\frac{enV}{c^2}\left(\frac{\dot{\mathbf{v}}}{R} + \frac{\mathbf{v}\left(\mathbf{v}\cdot\mathbf{R}\right)}{R^3}\right) + \frac{enV\mathbf{R}}{R^3} + \frac{enV\mathbf{R}}{R^3}\left(\frac{\mathbf{v}\cdot\mathbf{n}}{c}\right)^2 + \frac{2enV\mathbf{v}}{R^3}\left(\frac{\mathbf{v}\cdot\mathbf{R}}{c}\right)^2 = \\
&= \frac{enV\mathbf{R}}{R^3} - \frac{enV}{c^2}\frac{\dot{\mathbf{v}}}{R} + \frac{enV\mathbf{R}}{R^3}\left(\frac{\mathbf{v}\cdot\mathbf{n}}{c}\right)^2 + \frac{2enV\mathbf{v}}{R^3}\left(\frac{\mathbf{v}\cdot\mathbf{R}}{c}\right)^2, \\
\mathbf{B} &= \frac{enV}{cR^3}\left[\mathbf{v}\times\mathbf{R}\right],
\end{aligned} \tag{18}$$

Where we have accounted that $\mathbf{R} = \mathbf{r} - \mathbf{r_0}(t)$ and accounted that $\dot{\mathbf{R}} = -\dot{\mathbf{r_0}} = -\mathbf{v}$. As it is known from the ref. [12] the radiation should be determined only by terms that include a derivative of the velocity with respect to time. This is due to the fact that when the emission intensity of the squared absolute value of the fields and and multiplied by the element of the spherical surface R^2dO where the solid angle element $dO = \sin\theta d\theta d\varphi$ and in the limit $R \to \infty$ of the sum of the squares of the fields defined in (18) will only the term of $\dot{\mathbf{v}}$. Therefore from the expr. (18) we can take only the radiation part of the electric field, i.e.

$$\mathbf{E}^{rad} = -\frac{enV}{c^2}\frac{\dot{\mathbf{v}}}{R}. \tag{19}$$

Since $\mathbf{v} = v\boldsymbol{\tau}$ for the acceleration we have $\dot{\mathbf{v}} = \dot{v}\boldsymbol{\tau} + \frac{v^2}{l}\mathbf{n}$, where $\mathbf{n}$ the unit vector of the normal to the trajectory of motion (in our case to a circle of radius l equal to the length of the suspension). Therefore following the definition of the emission intensity according I as it's shown in the ref. [12] and taking into account formula (19) above, we are getting that

$$I = \frac{c\mathbf{E}^2_{rad}}{8\pi} = \frac{c}{8\pi}\left(\frac{enV}{c^2}\frac{\dot{\mathbf{v}}}{R}\right)^2 = \frac{(enV)^2}{8\pi c^3}\frac{1}{R^2}\left(\dot{\mathbf{v}}^2 + \frac{\mathbf{v}^4}{l^2}\right). \tag{20}$$

As far as the tangential velocity is $v = l\dot{\varphi}$ we have, hence

$$I = \frac{(enV)^2}{8\pi c^3}\frac{l^2}{R^2}\left(\ddot{\varphi}^2 + \dot{\varphi}^4\right). \tag{21}$$

So as the power of radiation is define as $W = \int IR^2dO = 4\pi IR^2$, from the expr. (21) we are obtain

$$W = \frac{(enVl)^2}{2c^3}\left(\ddot{\varphi}^2 + \dot{\varphi}^4\right) \tag{22}$$

4 Derivation of the motion equations in general form and the analysis

As it's shown in the ref. [11], in the general case we can write the following equation

$$\sum \dot{E} + \sum \dot{Q} + \sum W = 0 \tag{23}$$

where$\dot{Q}$ – is the dissipation function. Neglecting by the dissipative properties of the continuum from the expr. (32), we have

$$\sum \dot{E} + \sum W = 0. \tag{24}$$

After differentiating of the total energy over the time and using (6), (22) and (24), we are getting the following equation

$$\begin{aligned} & ml_c^2\dot{\varphi}_1\ddot{\varphi}_1 + ml_c^2\dot{\varphi}_2\ddot{\varphi}_2 + mgl_c\left(\dot{\varphi}_1\sin\varphi_1 + \dot{\varphi}_2\sin\varphi_2\right) + \\ & + \frac{\partial U_{EM}}{\partial R}\frac{\partial R}{\partial \varphi_1}\dot{\varphi}_1 + \frac{\partial U_{EM}}{\partial R}\frac{\partial R}{\partial \varphi_2}\dot{\varphi}_2 + \frac{(enV)^2}{8\pi c^3}\frac{l^2}{R^2}\left(\ddot{\varphi}^2 + \dot{\varphi}^4\right) = 0 \end{aligned} \tag{25}$$

Where the distance are

$$\begin{aligned} R = \Bigg(& \left(R_{0x} + l_c\left(\sin\varphi_1 - \sin\varphi_{01} + \sin\varphi_2 - \sin\varphi_{02}\right)\right)^2 + \\ & + \left(R_{0y} - l_c\left(\cos\varphi_1 - \cos\varphi_{01} + \cos\varphi_2 - \cos\varphi_{02}\right)\right)^2 \Bigg)^{\frac{1}{2}}. \end{aligned} \tag{26}$$

As we can see from the expr. (22) the emission power consists from two parts. The first part of the summand turns is much less than the second one and it's connected with the following simple reason. According to the numerical solutions of the resulting system of equations (25) (see below) the nonlinear "damping" due to the radiation leads to the fulfillment of the condition $|\ddot{\varphi}_{1,2}| \ll \left|\dot{\varphi}_{1,2}^2\right|$, which is confirmed by a graphic comparison of these two terms (see Fig. 2). This means that we can write the formula (22) in approximate form as $W \approx \frac{(enVl)^2}{2c^3}\dot{\varphi}^4$, as we written in the eq. (25).

After the substitution in the eq. (25), we obtain the following system of equations

$$\begin{cases} \varphi_1'' + \omega_0^2 \sin\varphi_1 + \omega_1^2 q_1 \left[\sin(\varphi_1 - \varphi_2) - a\cos\varphi_2\right] - \lambda_2 q_2 (\varphi_2'' cos\psi - \varphi_2'\psi' \sin\psi)\cos(\varphi_1 + \varphi_2) - \\ - 3\lambda_2 q_2 (\varphi_1' - \varphi_2')\sin(\varphi_1 - \varphi_2)\cos(\varphi_1 + \varphi_2)\varphi_2' \cos\psi + \kappa\varphi_1'^3 - \\ - \dfrac{3\lambda_2 a}{2}\cos(\varphi_1 + \varphi_2)\left[\dfrac{\varphi_1'\cos\varphi_1 - \varphi_2'\cos\varphi_2}{Q_{12}^5} + \dfrac{\varphi_2'\cos\varphi_2 - \varphi_1'\cos\varphi_1}{Q_{21}^5}\right]\varphi_2'\cos\psi = 0, \\ \varphi_2'' + \omega_0^2 \sin\varphi_2 + \omega_1^2 q_1 \left[\sin(\varphi_1 - \varphi_2) + a\cos\varphi_1\right] - \lambda_2 q_2 (\varphi_1'' cos\psi - \varphi_1'\psi' \sin\psi)\cos(\varphi_1 + \varphi_2) - \\ - 3\lambda_2 q_2 (\varphi_1' - \varphi_2')\sin(\varphi_1 - \varphi_2)\cos(\varphi_1 + \varphi_2)\varphi_1' \cos\psi + \kappa\varphi_2'^3 - \\ - \dfrac{3\lambda_2 a}{2}\cos(\varphi_1 + \varphi_2)\left[\dfrac{\varphi_1'\cos\varphi_1 - \varphi_2'\cos\varphi_2}{Q_{12}^5} + \dfrac{\varphi_2'\cos\varphi_2 - \varphi_1'\cos\varphi_1}{Q_{21}^5}\right]\varphi_1'\cos\psi = 0. \end{cases} \tag{27}$$

where the frequencies are

$$\omega_0^2 = \frac{g}{l_c}, \omega_1^2 = \frac{Gm}{l_c^3} \tag{28}$$

and the parameters are

$$\lambda_2 = \frac{\rho_e^2 V}{\rho_b c^2 b}\xi, \kappa = \frac{\rho_e^2 l^2 V}{2\rho_b c^3 l_c^2}\xi. \tag{29}$$

New functions are

$$q_1 = \frac{1}{2}\left(\frac{1}{Q_{12}^3} + \frac{1}{Q_{21}^3}\right), q_2 = \frac{1}{2}\left(\frac{1}{Q_{12}^5} + \frac{1}{Q_{21}^5}\right), \tag{30}$$

where the denominators are $Q_{12} = \sqrt{a^2 + 2\left(1 - \cos(\varphi_1 - \varphi_2)\right) + 2a\left(\sin\varphi_1 - \sin\varphi_2\right)}$ and $Q_{21} = \sqrt{a^2 + 2\left(1 - \cos(\varphi_1 - \varphi_2)\right) - 2a\left(\sin\varphi_1 - \sin\varphi_2\right)}$. Here $a = \dfrac{b}{l_c}$ – is a new dimensionless parameter. As we can see form the system (27) as it must be it is symmetric with respect to the change inversion operations $\varphi_1 \to -\varphi_1, \varphi_2 \to -\varphi_2$ and $\varphi_1 \to \varphi_2, \varphi_2 \to \varphi_1$. Introducing for convenience else one dimensionless parameter $\lambda_1 = \dfrac{\omega_1^2}{\omega_0^2}$, as well as dimensionless time $\tau = \omega_0 t$, we are finding in the result

$$\begin{cases} \varphi_1'' + \sin\varphi_1 + \lambda_1 q_1 \left[\sin(\varphi_1 - \varphi_2) - a\cos\varphi_2\right] - \lambda_2 q_2 (\varphi_2'' cos\psi - \varphi_2'\psi' \sin\psi)\cos(\varphi_1 + \varphi_2) - \\ - 3\lambda_2 q_2 (\varphi_1' - \varphi_2')\sin(\varphi_1 - \varphi_2)\cos(\varphi_1 + \varphi_2)\varphi_2' \cos\psi + k\varphi_1'^3 - \\ - \dfrac{3\lambda_2 a}{2}\cos(\varphi_1 + \varphi_2)\left[\dfrac{\varphi_1'\cos\varphi_1 - \varphi_2'\cos\varphi_2}{Q_{12}^5} + \dfrac{\varphi_2'\cos\varphi_2 - \varphi_1'\cos\varphi_1}{Q_{21}^5}\right]\varphi_2'\cos\psi = 0, \\ \varphi_2'' + \sin\varphi_2 + \lambda_1 q_1 \left[\sin(\varphi_1 - \varphi_2) + a\cos\varphi_1\right] - \lambda_2 q_2 (\varphi_1'' cos\psi - \varphi_1'\psi' \sin\psi)\cos(\varphi_1 + \varphi_2) - \\ - 3\lambda_2 q_2 (\varphi_1' - \varphi_2')\sin(\varphi_1 - \varphi_2)\cos(\varphi_1 + \varphi_2)\varphi_1' \cos\psi + k\varphi_2'^3 - \\ - \dfrac{3\lambda_2 a}{2}\cos(\varphi_1 + \varphi_2)\left[\dfrac{\varphi_1'\cos\varphi_1 - \varphi_2'\cos\varphi_2}{Q_{12}^5} + \dfrac{\varphi_2'\cos\varphi_2 - \varphi_1'\cos\varphi_1}{Q_{21}^5}\right]\varphi_1'\cos\psi = 0. \end{cases}$$

(31)

where the primes are means the differentiation over τ . The dimensionless parameter $k = \dfrac{\rho_e^2 l^2 V \omega_0}{2\rho_b c^3 l_c^2}$ (see expr. (29)), where $\rho_b = \dfrac{m}{V}$ – is a density of the metal balls. As we mentioned above, appearing in (27) the parameter $\cos\psi$ and it derivative for simplifying the analysis we are putting that $\cos\psi = \pm 1, (\cos\psi)' = 0$. Moreover, we take into account that $Q_{12} \approx Q_{21} = a$. In the result the equations (31) are simplified and we obtain the compact system of equations

$$\begin{cases} \varphi_1'' + \sin\varphi_1 + \gamma\varphi_2'' \cos(\varphi_1 + \varphi_2) + 3\gamma(\varphi_1' - \varphi_2')\sin(\varphi_1 - \varphi_2)\varphi_2' \cos(\varphi_1 + \varphi_2) + k\varphi_1'^3 = 0, \\ \varphi_2'' + \sin\varphi_2 + \gamma\varphi_1'' \cos(\varphi_1 + \varphi_2) + 3\gamma(\varphi_1' - \varphi_2')\sin(\varphi_1 - \varphi_2)\varphi_1' \cos(\varphi_1 + \varphi_2) + k\varphi_2'^3 = 0 \end{cases} \tag{32}$$

where the parameter $\gamma = \dfrac{\lambda_2}{a^5}$. To solve the equations (32), we should also define initial conditions, which we choose in the following form:

$$\varphi_1(0) = -\varphi_{01}, \varphi_2(0) = \varphi_{02}, \dot{\varphi_1}(0) = \dot{\varphi_2}(0) = 0. \tag{33}$$

The rigorous proof of the principle possibility of synchronization, given by us, is based only on two factors: 1. The potential energy of electromagnetic interaction between metallic spheres and 2. EM radiation. The numerical solution of the systems (32) at initial conditions (33) can be illustrated by the Figs. 3 – 6 (on this Fig. we are choice the parameters $\gamma = 10^{-2}$ and $k = 10^{-3}$).
So, as it's shown above analytical and numerical solution of the equations (32) and their analysis help us to realize that the eye of the synchronization problem is more understandable. The solution described above, explaining the mechanisms of interaction of pendulums and answers to the question about the physical nature of this interesting and very curious phenomenon. From the point of view of numerical analysis, graphical illustration of the solutions of the equations (32) is very important, because of its clarity, which allows us to show the entire synchronization stage in the figures, and numerically estimate the synchronization time t_{synchr} for different values of the parameters γ and k .

5 On physical nature of synchronization

We need to say that at first the issue of the synchronization of the pendulums, as a historical fact, applied to ordinary mechanical watches. Evidence of this is the very first experiment in this direction, conducted by Huygens with the aid of ship clocks, which for the first time established the fact of their synchronization. All subsequent studies, one way or another, were reduced to mechanical watches (see, for example, the monograph [7]), i.e. on the clockwork. The task posed in this article, as it appears from the previous text, was devoted to solving a purely physical problem, which is completely unrelated to the mechanics of the clockwork mechanism, and

pursued only one goal. To show the principle possibility of synchronization due to taking into account the two most important physical factors, the nature of which is purely electromagnetic, i.e. 1. EM interaction between pendulums and 2. EM radiation. It is quite clear that out of all the many interactions currently known, this is gravitational, electromagnetic, Van der Waals and magnetic dipole. The last one is the most effective only for magnetic materials. This means that in case you want this to happen. However, in this case the physics becomes completely different because it will be too small in comparison with metals, and the main role will shift to the effect of EM wave emission due to the precession of the magnetization vector, as its shown in the papers [14], [15] (see also [16]). As it turned out, the greatest contribution to the attraction effect of metal pendulums is provided by electromagnetic interaction, accompanied by inhibition in the form of EM radiation, and that was described in some detail a little higher. At the moments of closest approach of pendulums, the interaction effect reaches a maximum, as a result of which the pendulums begin to intensely "feel" each other. One at the same time slightly slows down, and the other – slightly accelerated due to the more intense radiation coming from the opposite pendulum, but the total energy of both pendulums in the absence of dissipation should remain constant. It is rather subtle moment tells us only that the formal languages for describing any non-equilibrium phenomena with or without energy dissipation will be very different from the formalism of the description of phenomena in the language of radiation powers. The only essential condition for this is the movement of the object along the curvilinear trajectory.

6 Conclusion

1. Due to the assumption that the interaction between pendulums is of a long-range nature of electromagnetic interaction a system of symmetric relatively permutations and non-linear differential equations are obtained, which are the invariant relative to the transformations: $\varphi_1 \to \varphi_2, \varphi_2 \to \varphi_1$ and $\varphi_1 \to -\varphi_1, \varphi_2 \to -\varphi_2$. The EM radiation is a main factor of synchronization phenomenon. Based on these two physical factors, we have a possible to describe mathematically the entire synchronization process.

2. It is strictly analytically shown that in the approximation of small oscillations the synchronization effect occurs after a time t_{synchr}. The numerical values of which corresponds to the experimentally observed times.

3. Using numerical integration methods, we give a general solution of the non-linear system (32) of the differential equations illustrated by the Fig. 3 - 6.

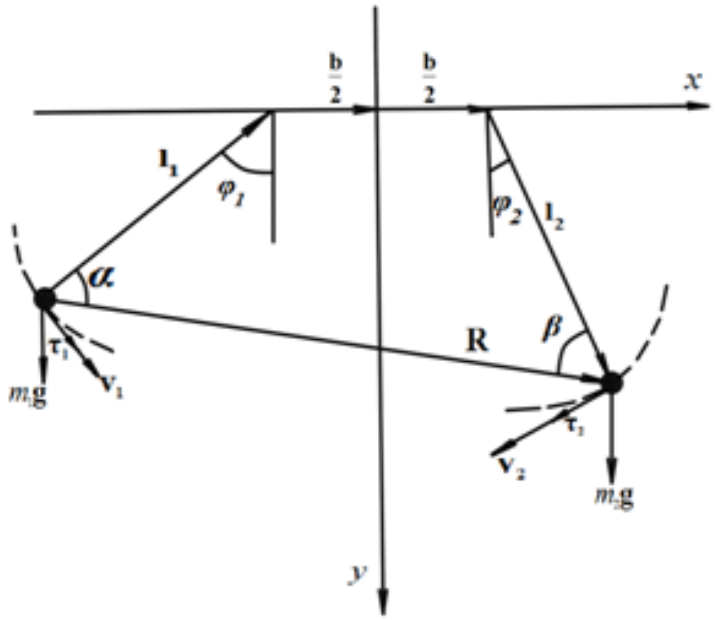
b/2
b/2
x
l1
φ1
φ2
l2
α
β
R
τ1
v1
m1g
τ2
v2
m2g
y

Fig. 1

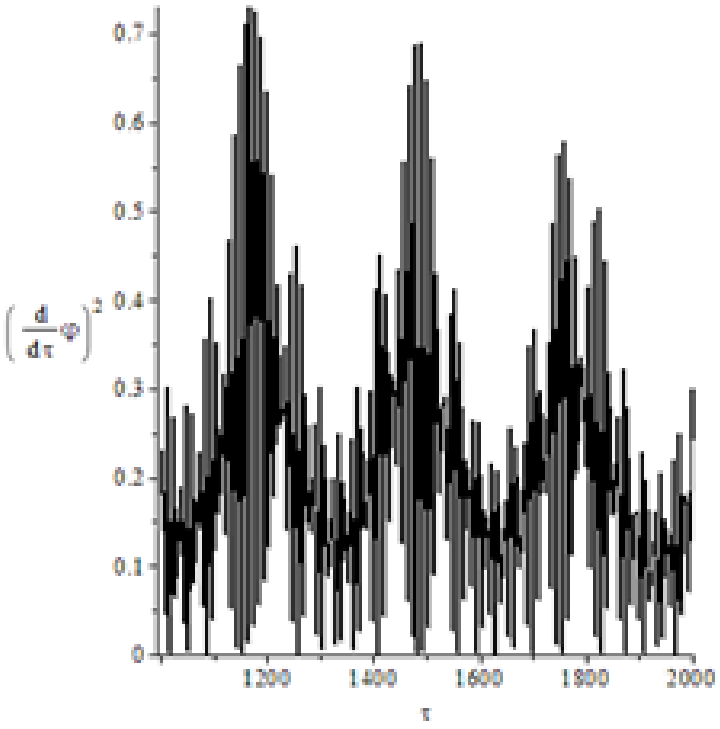
0.7
0.6
0.5
0.4
0.3
0.2
0.1
0
1200
1400
1600
1800
2000
τ

Fig. 2

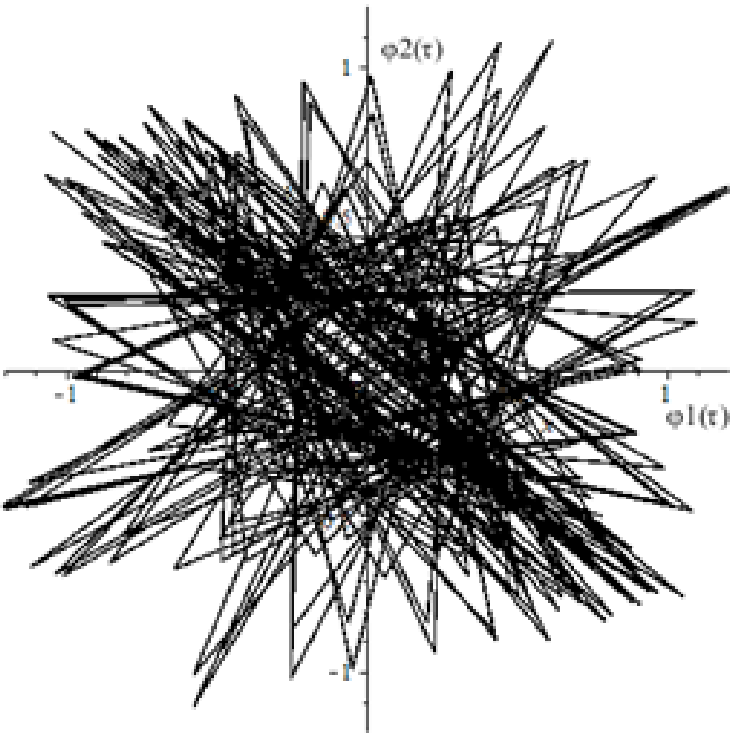

Fig. 3

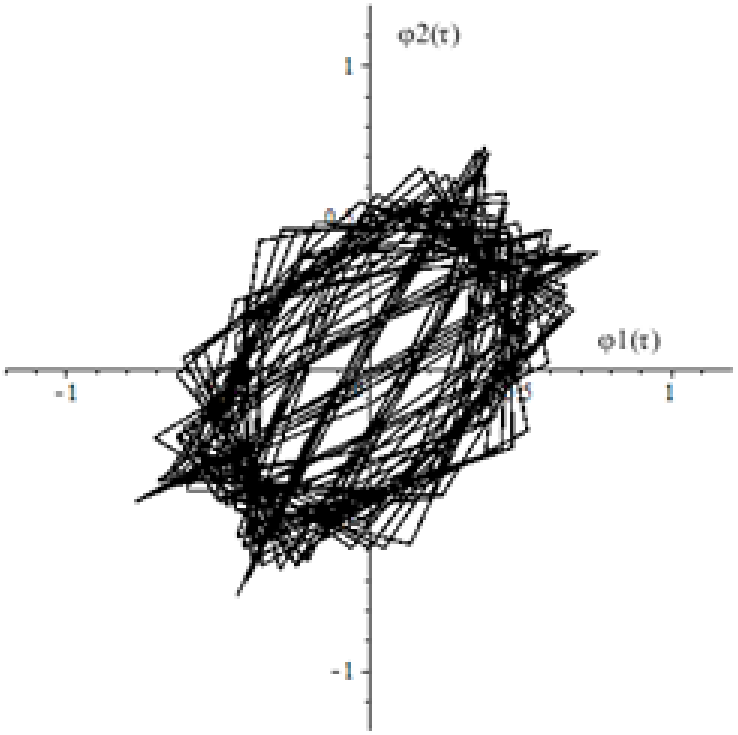

Fig. 4

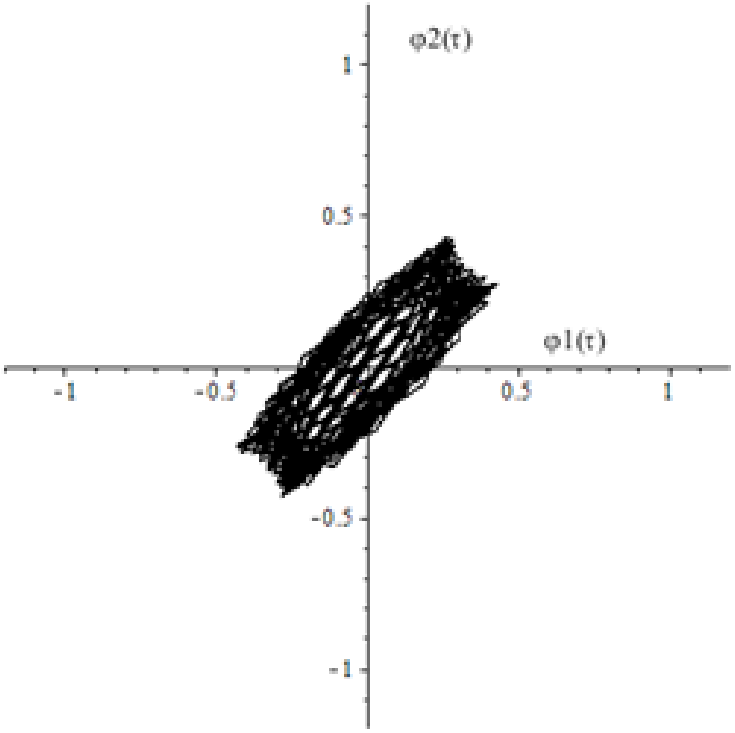

Fig. 5

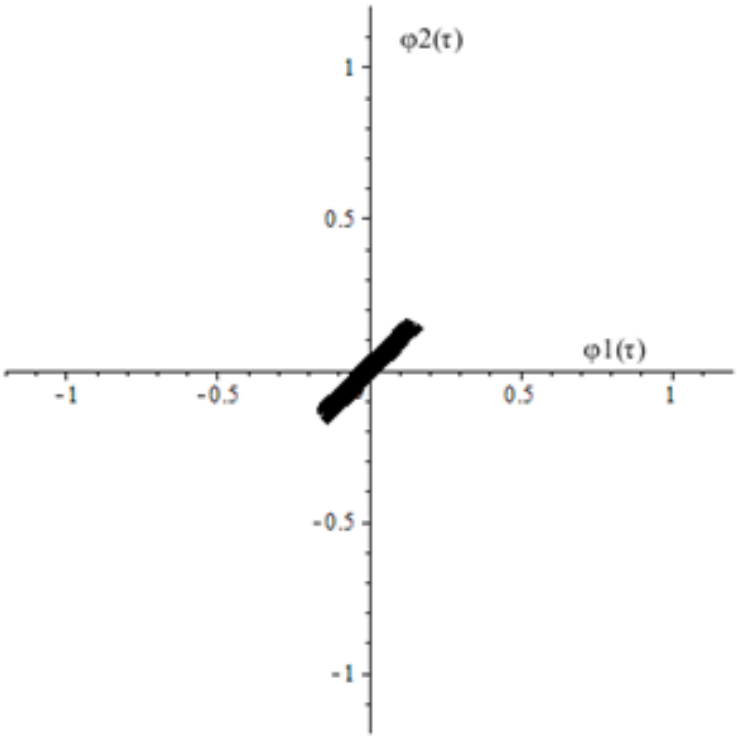

Fig. 6

Caption

Fig. 1 Schematic geometry of the problem
Fig. 2 Dependence $\dot{\varphi}^2_{1,2}(\tau)$ and $\ddot{\varphi}_{1,2}(\tau)$. In the given metric scale essentially, function $\ddot{\varphi}_{1,2}$ merges with abscissa τ . I.e., condition $|\ddot{\varphi}_{1,2}| \ll \left|\dot{\varphi}^2_{1,2}\right|$ realizes.
Fig. 3 Dependence $\varphi_2(\varphi_1)$ on the interval time $\tau \in [0, 500]$
Fig. 4 Dependence $\varphi_2(\varphi_1)$ on the interval time $\tau \in [2000, 3000]$
Fig. 5 Dependence $\varphi_2(\varphi_1)$ on the interval time $\tau \in [8000, 9000]$
Fig. 6 Dependence $\varphi_2 \approx \varphi_1$ on the interval time $\tau \in [48000, 49000]$

References

[1] T. Yamada, H. Fujisaka. Stability theory of synchronized motion in coupled – oscillator system. The mapping approach. Progr. Theor. Phys. 1983. V. 70. PP. 1240 – 1248.

[2] N.N. Verichev, A.G. Maximov. On synchronization of stochastic oscillations of parametrically excited nonlinear oscillators. Physics journal. Radiophysics. 1989. V 32. S. 8. 962 – 965p.

[3] L.M. Pecora, T.L. Carroll. Synchronization in chaotic systems. Phys. Rev. Lett. 1990. V. 64. PP. 821 – 824.

[4] M.G. Rosenblum, A.S. Pikovsky, J. Kurths. From phase to lag synchronization in coupled chaotic oscillators. Phys. Rev. Lett. 1997. V. 78. PP. 4193 – 4196.

[5] I.I. Blehman. Synchronization in nature and technics. M.: Science. 1981. 320 p.

[6] V.N. Akimov, L.N. Beluystina and others. The systems of phase synchronization. M.: Radio and connection. 1982. 288p.

[7] A.A. Andronov, A.A. Witt, S.E. Haikin. Theory of oscillations. Moscow Fizmatlit. 1959. 916 p.

[8] Henrique M. Oliveria, Luis V. Melo. Huygens synchronization of two clocks. Scientific Reports. July 2015. DOI: 10.1038/srep11548.

[9] L.D. Landau, E.M. Lifshitz. Electrodynamics of continuous media. V.8. M.: Science. 1982. 620 p.

[10] L.D. Landau, E.M. Lifshitz. Mechanics. V.1. M.: Science. 1973. 207 p.

[11] S.O. Gladkov. On the calculation of the stopping time of a cylindrical body rotating in a viscous continuum and the time of entrainment of a coaxial external cylinder. Journal of Technical Physics. 2018. V. 63. N. 3. PP. 325 – 330.

[12] L.D. Landau, E.M. Lifshitz. Field theory. 2004. V.2. M.: Science.

[13] L.E. El'sgolz. Differential equations and bases of the calculus of variations. Fizmatlit. 1969. 424 p.

[14] S.O. Gladkov. On the calculation of the radiation intensity of the electromagnetic energy by a stationary ferromagnetic spherical particle in a constant and homogeneous magnetic field. Journal of Technical Physics. 2015. V. 85. N. 7. PP. 138 – 141.

[15] S.O. Gladkov, S.B. Bogdanova. Rotating ferromagnetic ball, as a source of the long-wave EM radiation. Radio engineering and electronics. 2016. V. 62. N. 7. PP. 632 – 641.

[16] Belyaev, A.K., Eliseev, V.V., Irschik, H., Oborin, E.A. Contact of two equal rigid pulleys with a belt modelled as Cosserat nonlinear elastic rod (2017) Acta Mechanica, 228 (12), pp. 4425-4434. DOI: 10.1007/s00707-017-1942-0.